Fundamental and Applied Catalysis

Catalytic Ammonia Synthesis

Fundamentals and Practice

Edited by J. R. Jennings

Catalytic Ammonia Synthesis

Fundamentals and Practice

FUNDAMENTAL AND APPLIED CATALYSIS

Series Editors: M. V. Twigg
Imperial Chemical Industries P.L.C.
Billingham, Cleveland, United Kingdom

M. S. Spencer
School of Chemistry and Applied Chemistry
University of Wales College of Cardiff
Cardiff, United Kingdom

CATALYTIC AMMONIA SYNTHESIS: Fundamentals and Practice
Edited by J. R. Jennings

PRINCIPLES OF CATALYST DEVELOPMENT
James T. Richardson

Catalytic Ammonia Synthesis

Fundamentals and Practice

Edited by

J.R. Jennings
ICI Chemicals and Polymers Ltd.
Wilton, Cleveland, England

Springer Science+Business Media, LLC

Library of Congress Cataloging-in-Publication Data

Catalytic ammonia synthesis : fundamentals and practice / edited by
J.R. Jennings.
p. cm. -- (Fundamental and applied catalysis.)
Includes bibliographical references and index.

1. Ammonia. I. Jennings, J. R. II. Series.
TP223.C33 1991
661'.34--dc20 91-10702
CIP

ISBN 978-1-4757-9594-3 ISBN 978-1-4757-9592-9 (eBook)
DOI 10.1007/978-1-4757-9592-9

Originally published by Plenum Press, New York in 1991
Softcover reprint of the hardcover 1st edition 1991

CONTRIBUTORS

G. Ertl • Fritz-Haber-Institut der Max-Planck-Gesellschaft, Faradayweg 4-6, D-1000 Berlin 33, Federal Republic of Germany

J. W. Geus • Department of Inorganic Chemistry, Debije Institute, University of Utrecht, 3522 AD Utrecht, The Netherlands

Giorgio Gramatica • Agrimont S.p.A., Enimont Group, 20138 Milano, Italy—*Deceased.*

P. E. Højlund Nielsen • Haldor Topsøe A/S, Nymøllevej 55, DK-2800 Lyngby, Denmark

C. W. Hooper • ICI Katalco, Billingham, Cleveland TS23 1LB, England

G. J. Leigh • AFRC Institute of Plant Science Research, Nitrogen Fixation Laboratory, University of Sussex, Brighton BN1 9RQ, England

Nicola Pernicone • Ausimont Catalizzatori S.z.l., Montedison Group, 28100 Novara, Italy; *present address*: Via Pansa 7, 28100 Novara, Italy

Robert Schlögl • Fritz-Haber-Institut der Max-Planck-Gesellschaft, Faradayweg 4-6, D-1000 Berlin 33, Federal Republic of Germany; *present address*: Institut für Anorganische Chemie, Universität Frankfurt, Niederurseler Hang, D-6000 Frankfurt 70, Federal Republic of Germany

G. A. Somorjai • Department of Chemistry, University of California-Berkeley, and Center for Advanced Materials, Lawrence Berkeley Laboratory, Berkeley, California 94720

D. R. Strongin • Department of Chemistry, University of California-Berkeley, and Center for Advanced Materials, Lawrence Berkeley Laboratory, Berkeley, California 94720; *present address*: Department of Chemistry, State University of New York at Stony Brook, Stony Brook, New York 11794

Kenzi Tamaru • Department of Chemistry, Faculty of Science, Science University of Tokyo, Shinjuku-ku, Tokyo 162, Japan

S. R. Tennison • New Technology Division, BP International Limited, Sunbury Research Centre, Sunbury on Thames, Middlesex TW16 7LN, England

K. C. Waugh • Catalysis Research Centre, ICI Chemicals and Polymers Ltd., Billingham, Cleveland TS23 1LB, England

FOREWORD

The phenomenon of catalysis is found in many homogeneous and heterogeneous systems undergoing chemical change, where it effects the rates of approach to the equilibrium state in processes as diverse as those found in the stars, the earth's mantle, living organisms, and the various chemistries utilized by industry. The economies and the living standards of both developed and developing countries depend to varying degrees upon the efficacy of their chemical industries. Consequently, this century has seen a wide exploration and expansion of catalytic chemistry together with an intensive investigation of specific, essential processes like those contributing to life-supporting agricultures. Prime among the latter must surely be the "fixation" of atmospheric nitrogen by catalytic hydrogenation to anhydrous ammonia, still the preferred synthetic precursor of the nitrogenous components of fertilizers. In each decade contemporary concepts and techniques have been used to further the understanding, as yet incomplete, of the catalyst, the adsorbates, the surface reactions, and the technology of large-scale operation. The contributors to the present volume review the state of the art, the science, and the technology; they reveal existing lacunae, and suggest ways forward.

Around the turn of the century, Sabatier's school was extending the descriptive catalytic chemistry of hydrogenation by metals to include almost all types of multiple bond. The triple bond of dinitrogen, which continued to be more resistant than the somewhat similar bonds in carbon monoxide and ethyne, defied their efforts. During the following decade, Haber and Bosch developed their process for the large-scale production of ammonia by the hydrogenolysis of atmospheric nitrogen over promoted and stabilized, iron-based contacts: it was an epoch-making advance. The work assured not only adequate world food-production, but also gave impetus to the science of catalysis by solids and the associated chemical engineering. Exploding populations could now be properly provisioned with victuals or otherwise provided with munitions, while most of the essential empirical features of catalyst activity were revealed.

Professor Tamaru, prominent among catalytic chemists even as a babe-in-arms (photo page 5), tells something of the formidable minds and institutions which drove the research forward in a style now classic and probably unparalleled outside the German chemical industry. This paradigm of major invention possessed a

clearly defined objective, presented by an emergent universal need and a massive potential market. The objective was judged to be attainable by knowledgeable scientists despite uncertain data, and had champions among the most able contemporary industrial managers. The cognate sciences and technologies were pushed ahead by cooperating chemists and engineers, notably by men of broad and deep understanding. The science of both Haber and Bosch had an industrial background, making their story timely reading now that the so-called "relevance" issue intrudes increasingly upon the research within academic institutions, and as the higher management of industry becomes ever more remote from its scientific bases.

The magnitude of the achievements in the more quantitative, physical science of the Haber–Bosch program has tended to outshine the contributions from both the associated exploratory catalytic chemistry and the concepts derived therefrom. The work of Mittasch was absolutely vital and led ultimately to the development of the more effective catalysts which had commercial potential and to improved gas purification. As pointed out in this volume, some of those ideas have had to be abandoned, but it is inescapable that the notion of multifunctionality, implying jumpover, spillover, or switchover of intermediates, was contained therein, albeit formalized much later by Weiss and others. Indeed, phenomena at interfaces between solids remained unapproachable until the application of the latest physical techniques (Chapters 2–5).

The best testimony to the pioneers' accomplishments, beyond the award of two Nobel prizes, must be the fact that, after almost eighty years of research and development, the modern iron-based catalysts are hardly more than tidied-up versions of the originals. Subsequent improvements to the process have derived in the main from the generation of purer synthesis gases, the optimization of the preparation of the catalysts and their induction procedures, the determination of better kinetics (Chapter 6) with the consequent advance in the chemical engineering applications (Chapters 6 and 7). All of these improvements were directed to the lowering of reaction pressures and temperatures, and ultimately of capital costs.

To place the recent contributions on ammonia synthesis in context, the broad historical background on the one hand, and the sheer complexity of the operating process on the other must be considered. Prior to the advent of modern surface physics there existed a modest consensus among practitioners; the views were common but not universal, reasonable but equivocal, and often implicit rather than explicit. By the late fifties it had been accepted that the essential active phase is body-centered cubic metallic iron, that the likely most active crystal face is (111), that the refractory oxide components serve primarily to hinder sintering, and that one function of the alkali promoter is to lower, somehow, the work function of the iron. Already some believed that alkali metal, formed *in situ* by reduction under pressure as dilute adsorbed atoms, facilitated the transfer of electrons from the Fermi level of iron to the antibonding π-orbitals of physisorbed dinitrogen, and that a chemisorbed, "side-on" state of dinitrogen was possible (by analogy with contemporary hypotheses involving adsorbed ethene and ethyne as π-complexes on metals such as palladium). The anionic dinitrogen intermediate was not, however, perceived to be an adsorbate of measurable lifetime, although the existence of precursor states had just been signalled.

The second feature to be noted is the complicacy of the working industrial catalyst as compared with its models, which have often been devised as alkali metal-atom doped specific faces, planar or stepped, of massive single crystals of the purest iron, prepared with all the resources of high-vacuum technology. In contrast, real catalysts are porous aggregates of small particles, more or less crystalline, usually containing, beside iron and potassium, two or more refractory oxides of different acid-base properties. They are always prepared by hydrogen reduction of a somewhat inhomogeneous but intimate mixture of binary and ternary oxides of sufficient purity, thus inducing contingent, interdependent solid-gas and solid-solid, nucleated reactions, necessarily under finite partial pressures of water having catalytic or anticatalytic effects (Chapters 2, 3, 5, and 9). An adequate reproducibility of designed activity and life can be obtained only by rigid adherence to a set of procedures, scientifically based but established empirically; it usually involves some minor, intrinsic variability due to the exigencies of process control and the intrusion of hidden variables (e.g., dissimilar motivations among process operators and catalyst designers!). Oldsters would say that activity depends upon the "prehistory" of the catalyst; alteration of a component or a parameter entails a change of activity having downstream consequences in kinetics, incongruent reactor design, and costs, for which no algorithm yet exists.

Schlögl's article shows why. He tells of the application of old and new techniques to the characterization of the processes, phases, and interfaces occurring in the evolution of the working catalyst from its oxide precursors. He arrives at conclusions which are quite similar to those derived from chemical principles, while finding further complexities. It is in this area that surface physics demonstrates its greatest value to applied catalysts.

The electropositive-electronegative (basic-acidic, etc.) counterpoint runs through all catalysis, so that the various correlates of the promotor's polarity are no doubt to be detected at all stages of the genesis and maintenance of the active interface, and of its accessibility.

The desired holistic solution remains remote but is foreshadowed in the reports by Ertl, Somorjai, and Strongin on the interactions at the atomic level between adsoptives, surface geometries, promotors, and stabilizers in model catalysts. Ertl demonstrates the central role of a precursor state [the inclined α-state, metal^{+}-N_2^{-}, on Fe(111), not unlike the "side-on" adsorbate suggested earlier] in the dissociative chemisorption, and its additional stabilization by potassium adatoms. He, and in a subsequent chapter Geus and Waugh, use the data to derive potential energy diagrams for the reaction chain, and from which they calculate overall reaction rates. Although there are some differences of opinion between the two groups, the fact that such methods give results of the right magnitude affirms the advance of the last decade.

Somorjai and Strongin extend the theme, narrowing the gap between the models and the real catalyst, especially to discern mutual effects in the Fe-Al-K-O-N-H system. As in the work described by Schlögl, some expected chemistry is found but it is illuminated by the discovery of unpredicted surface reconstructions in the presence of alumina and water. The presence of potassium adatoms, as such *in situ*, is discounted in favor of a KO_x adsorbate which retains the alkali while

yet stabilizing Ertl's precursor and also loosening the bound ammonia. In normal practice alkali compounds are not found downstream of industrial reactors, and one is reminded of the old observations on the photoelectric emission of complex surfaces which showed that alkali adatoms adjacent to oxygen adatoms (W-Cs-O) are not only more strongly bound but induce dramatic decreases in the work function. A clear definition of the role(s) of the alkali promotor, electronic, geometric, or both seems near, and although rather late in the history of ammonia synthesis must remain a major objective in view of the ubiquity of such effects in catalysis (Fischer-Tropsch, higher alcohols, etc.).

Impure feedstocks add other dimensions to the matrix; reactive contaminants usually behave as permanent or temporary poisons according to whether they are strongly or weakly bound to active sites under reaction conditions. Nielsen (Chapter 8) describes the principal types, e.g., inhibitors yielding strongly electronegative adsorbates (halogens, oxygenated, and sulfuretted species) or the rarer polyvalent adatoms (phosphorus, arsenic). He mentions the empirically determined tolerable concentrations and gives some quantitative analysis of the relationship with active area. The effects of chlorine on the alkali promotor provide a nice illustration of the acid-base counterpoint, and the acceleration of sintering by steam is an important example of a less well-known effect of steam, additional to poisoning. Some corresponding chemisorptions and solid reactions are included by Geus and Waugh (Chapter 5).

Nowhere is the reacting catalyst system at true equilibrium. Furthermore, much academic experimentation is done far from equilibrium, but the industrial reactor is designed to approach that state at its exit. In Chapter 6, Gramatica and Pernicone show how useful, essentially empirical, kinetic equations have been put together on the basis of the earlier classical adsorption isotherms associated with the names of Langmuir, Tempkin, and others. Kinetics which describe accurately the degree of advancement of the reaction with time, over a range of pressures, temperatures, and contents of common impurities, are vital to reactor and process design, and the authors give an outline of the procedures which have led to the evolution of the modern plant systems of Hooper's Chapter 7. It will be appreciated that the cost of the research and development leading to such kinetic equations, and their importance to competitive design, makes them a valuable commercial property.

However, the large investments in established processes and plants naturally impose an enormous inertia, among producers and contractors alike, toward all radical change. It is therefore exciting to escape from the claustrophobia of the iron-based Haber-Bosch system into the wider regions of the Periodic Table, and the "greener," more exploratory areas of homogeneous and enzyme catalysis, in the reviews by Tennison (Chapter 9) and by Leigh (Chapter 10). Anhydrous ammonia will continue to be the commodity in demand for the foreseeable future; dilute ammonia, commonly aqueous, incurs large cost penalties for transport and concentration unless made to suit local circumstances. So the first approach to novelty is by way of a radically new catalyst tailored to fit the existing type of plant, while any enzyme-like reaction must involve hydrogenated dinitrogen only as an intermediate en route to more complex compounds.

Tennison explores the patterns of behavior, in absorption, adsorption, and activity, among the transitional elements of the long periods, with timely emphasis upon the more precious metals and the alloys of iron with its base-metal congeners of group 8. The relatively high activity of the Fe–Ru–Os triad has long been known and, in the early days of the rigid-band theory of metals, was correlated with the presence of three "holes" in their *d*-bands. Japanese research in the last twenty years has restressed the possible potential of ruthenium as an alternative to iron and it is of great interest to see that its exploitation has become a distinct possibility. Currently, the preferred support appears to be carbon, a material whose properties can be so irreproducible that its use was once generally avoided, unless essential as in dispersing precious metals in hydrogenation catalysts for the fine-chemical and pharmaceutical industries. Alkali promotors are again necessary, and their function in the new catalysts is investigated in detail but with conclusions similar to those reached by the other authors. The ubiquity of the effect would seem to support a general electronic influence rather than sets of related geometries.

It is a cause for wonder that the elements iron and molybdenum should be so prominent in catalysts as diverse as the metalloenzymes of nitrogen-fixing bacteria and the Haber–Bosch contacts. Perhaps the link may lie in some similarity between the proposed active K–Fe–O surface complex and the organo-Fe(Mo)–S organo–Fe(Mo)–S complexes wherein the sulfur ligands maintain the metals in low valency states. Leigh surveys succinctly the enzyme field and the related models among the dinitrogen-carrying complexes which have raised many false hopes since the middle sixties and the isolation of the first such molecules; photo- and electrochemical inputs have been used but commercial applications are not yet feasible.

The implications of Leigh's view of future developments in nitrogen fixation apply equally to all catalysis: we are unlikely to find more targets as "simple" and profitable as ammonia synthesis. Even before interdisciplinary projects such as the forementioned photoheterogeneous catalysis, the coming years should see the coupling of heterogeneous with homogeneous catalysis as in the present pursuit of routes from methane to higher hydrocarbons using radicals generated at oxide surfaces. It is known already, for instance, that oxygen can be hydrogenated to yield aqueous hydrogen peroxide, which with Fenton's reagent forms hydroxyl radicals and thence phenol from benzene continuously. Similarly, nitric oxide gives hydroxylamine and amidogen radicals. The core of the problem is to target a valuable product other than ammonia (an amino acid or a nitrogen heterocycle, say) and then to devise means for its economic extraction. The field is not at the present time sufficiently developed to allow this to be done, in either its chemistry or its chemical engineering.

D. A. Dowden

Stockton-on-Tees

PREFACE TO THE SERIES

Catalysis is important academically and industrially. It plays an essential role in the manufacture of a wide range of products, from gasoline and plastics to fertilizers and herbicides, which would otherwise be unobtainable or prohibitively expensive. There are few chemical- or oil-based material items in modern society that do not depend in some way on a catalytic stage in their manufacture. Apart from manufacturing processes catalysis is finding other important and ever increasing uses; for example, successful applications of catalysis in the control of pollution and its use in environmental control are certain to increase in the future.

The commercial importance of catalysis and the diverse intellectual challenges of catalytic phenomena have stimulated study by a broad spectrum of scientists, including chemists, physicists, chemical engineers, and materials scientists. Increasing research activity over the years has brought deeper levels of understanding, and these have been associated with a continually growing amount of published material. As recently as sixty years ago, Rideal and Taylor could still treat the subject comprehensively in a single volume, but by the 1950s Emmett required six volumes, and now no conventional multivolume text can cover the whole of catalysis in any depth. In view of this situation, we felt there was a need for a collection of monographs, each one of which would deal at an advanced level with a selected topic so as to build a catalysis reference library. This is the aim of the present series, Fundamental and Applied Catalysis.

These books in the series will deal with particular techniques used in the study of catalysts and catalysis; these will cover *the scientific basis of the technique, details of its practical applications,* and *examples of its usefulness.* The volumes concerned with an industrial process or a class of catalysts will provide information on the *fundamental science of the topic, the use of the process or catalysts,* and *engineering aspects.* For example, the inaugural volume, *Principles of Catalyst Development,* looks at the science behind the manufacture of heterogeneous catalysts and provides practical information on their characterization and their industrial uses. Similarly, an upcoming volume on ammonia synthesis will extend from the surface science of single iron crystals to the design of reactors for the special duty of ammonia manufacture. It is hoped that this approach will give a series of books that will be of value to both academic and industrial workers.

The series will deal with both heterogeneous and homogeneous catalysis, and will include processes in the heavy chemicals and oil refining industries, the smaller-scale manufacture of pharmaceuticals, and various aspects of pollution control. The series editors would welcome any comments on the series and suggestions of topics for future volumes.

Martyn Twigg
Michael Spencer

Billingham and Cardiff

PREFACE

The story of the catalytic synthesis of ammonia from its elements ranks as a classic in the development of the chemical industry during the twentieth century. The enabling research work began at a time when it was not even known whether the required reaction between hydrogen and nitrogen was thermodynamically feasible. Nevertheless, several leads from different research groups were followed and this culminated eventually in the demonstration by Fritz Haber of the catalytic synthesis of ammonia at elevated pressures. The major new technologies of catalyst promotion and high-pressure chemical engineering were born and new challenges associated with stress corrosion were presented to the metallurgists. That these problems were solved is now history, due to the efforts of Alwyn Mittasch, Carl Bosch, and many others. The lead in high-pressure technology gained by BASF also resulted in the development of the first process for the production of synthetic methanol by the hydrogenation of carbon monoxide. So successful were the team from BASF in their development of the ammonia synthesis reaction that, after the initial breakthrough, most of the subsequent major developments have been in the generation and purification of synthesis gas.

Scientific studies on the precursor and the active catalyst followed rapidly and the adsorption studies of Emmett and his colleagues set the principles which are still used in the development and understanding of most new catalysts, even today. A high level of understanding of the catalyst was gained in the early studies, but it was the development of ultrahigh vacuum (UHV) techniques and electron spectroscopy which led to the advances in the seventies and eighties. Fascinating differences in the reactivity and properties of iron crystals, according to which the crystallographic plane was examined, have emerged. Furthermore, some correlation between UHV data and kinetic measurements under process conditions can now be made.

Amid the excitement of this "UHV era" substantial progress was being made on the process itself. Operating pressures and temperatures have gradually been reduced in the quest for maximum efficiency in the use of energy, and new low-pressure processes are available in the market for license. The possibility remains that with further catalyst development, including perhaps the use of precious metal catalysts, the severity of the process conditions may be reduced further still.

All of the authors who have contributed to this volume are true experts in their chosen field of study and have a wealth of experience in the science and technology of ammonia synthesis. Both academia and industry are well represented and this leads to a fine balance between the science and the technology. Furthermore, in keeping with the international nature of the ammonia business, the range of authors also represents a wide geographical spread. The book begins with a history of the early developments of ammonia synthesis leading to four chapters devoted essentially to fundamental scientific investigations of the catalyst and its promoters. Three chapters on technological aspects of ammonia synthesis follow: kinetics, commercial operation, and catalyst deactivation. The book then concludes with chapters on novel alternatives to the conventional promoted iron catalyst and some thoughts as to how the ammonia synthesis industry might develop in future years.

We have endeavored to present a complete but balanced view of ammonia synthesis at a time when both the science and process are relatively mature. It is, however, a sobering thought that despite all the high-quality studies on this simplest of reactions, some questions still remain to occupy the minds of scientists in the years ahead.

All of the people concerned with this book were saddened by the death of Giorgio Gramatica while the volume was in press, and we regret he was unable to see his chapter, coauthored with Nicola Pernicone, in its final published form.

J. R. Jennings

Middlesborough

CONTENTS

CHAPTER 3. ELEMENTARY STEPS IN AMMONIA SYNTHESIS: THE SURFACE SCIENCE APPROACH

G. Ertl

CHAPTER 4. A SURFACE SCIENCE AND CATALYTIC STUDY OF THE EFFECTS OF ALUMINUM OXIDE AND POTASSIUM ON THE AMMONIA SYNTHESIS OVER IRON SINGLE-CRYSTAL SURFACES

D. R. Strongin and G. A. Somorjai

CHAPTER 5. CHEMISORPTION AT MORE ELEVATED PRESSURES ON INDUSTRIAL AMMONIA SYNTHESIS CATALYSTS

J. W. Geus and K. C. Waugh

CHAPTER 10. WHAT DOES THE FUTURE HOLD? A SURVEY OF POSSIBLE TECHNICAL DEVELOPMENTS

G. J. Leigh

APPENDIXES

1

THE HISTORY OF THE DEVELOPMENT OF AMMONIA SYNTHESIS

Kenzi Tamaru

1.1. INTRODUCTION

The synthesis of ammonia from its elements ranks as one of the most important discoveries in the history of the science of catalysis, not only because of its industrial application in which synthetic fertilizers have contributed enormously to the survival of mankind, but also from the viewpoint of fundamental science. Even today, some eighty years after the first demonstration of ammonia synthesis, many original scientific papers on the mechanism of the catalytic synthesis of ammonia are still published. Every time a new method, technique, or concept has appeared in the field of heterogeneous catalysis, it has been applied to this reaction. Specific examples of these applications over the years include the concepts of gas equilibrium,[1] activated adsorption,[2] structure sensitivity,[3] stoichiometric number and kinetic studies,[4] nonuniform surfaces,[5] the measurements of surface area,[6] surface composition and promoter distributions,[7] and the use of isotopic and spectroscopic techniques.[8] In particular, various surface science techniques have been applied successfully to this reaction system over well-defined single crystal surfaces in recent years. In this way the effect of promoters on the iron catalyst has been elucidated.[9] Accordingly, the history of ammonia synthesis parallels not only that of industrial catalysis, but also the development of the science of catalysis.

Review articles on each of the topics relevant to ammonia synthesis follow in this book. This chapter contains the history of ammonia synthesis, with particular emphasis on the story of how ammonia has come to be manufactured on the

Kenzi Tamaru • Department of Chemistry, Faculty of Science, Science University of Tokyo, Shinjuku-ku, Tokyo 162, Japan.

industrial scale, after many heated disputes between such great pioneers of modern science as, for instance, Ostwald, Haber, and Nernst.

Social Requirement of Fixed Nitrogen toward the End of the 19th Century

Many of the great discoveries made in the past were in response to a social or economic need of the time. T. R. Malthus proposed his famous principle of population in 1798 saying that, in the absence of any external constraints, the world population always increases in a geometric progression, while the production of food increases in an arithmetic progression. According to this principle, mankind at some time in the future must inevitably suffer from a shortage of food which will in turn lead to serious social and political difficulties of various kinds. In practice, the real situation regarding social problems of this kind is not so simple. Major developments in agricultural technology to produce more food have been effective in alleviating many of the difficulties. However, it is quite clear that without synthetic fertilizer, the developments in agricultural technology would scarcely have been possible.

In 1840 Justus von Leibig[10] studied plant nutrition, with particular emphasis on those elements essential for the healthy growth of plants. He concluded that one of the three most important components of a fertilizer is "fixed" nitrogen. In the last century, nitrogen-containing fertilizer was obtained as ammonium sulfate, a by-product from the destructive distillation of coal to produce coke and town gas. The total amount was, however, insufficient for the needs of the time. Another source of nitrogenous fertilizer was from Chile in South America. This consisted mainly of sodium nitrate, and was exported in increasing amounts to European countries. However, since sodium nitrate is readily soluble in water, the Chilean nitrate could only accumulate in limited areas with low rainfall, such as the Atacama Desert. Although this nitrate deposit was considered to be of vast commercial importance, the total amount was nevertheless limited, and would certainly become exhausted in the fullness of time.

The available natural reserves of fixed nitrogen were also used at that time for other miscellaneous purposes, such as for dyestuffs and explosives required by the military and the mining and construction industries. Alfred Nobel, for instance, discovered dynamite in 1866 and, with the large amount of wealth obtained from it, was able in 1901 to establish the Nobel Foundation, which awards the Nobel Prizes. It is clear that large and ever-increasing amounts of nitrate were being consumed by the explosives industry, in addition to the growing requirement for fertilizers.

Under these circumstances, toward the end of the last century, there were serious concerns that the nitrate reserves in nature would become exhausted, and that mankind would be confronted with devastating food shortages in the future.

In September 1898, Sir William Crookes[11] made a famous speech in his presidential address to the British Association for the Advancement of Science, warning that the supply of fixed nitrogen for agricultural use was rapidly reaching a point where it was insufficient to support an ever-increasing population. In his

address, he said: "England and all civilized nations stand in deadly peril of not having enough to eat," and indicated the solution to the problem as follows: "It is the chemist who must come to the rescue of the threatened communities. It is through the laboratory that starvation may ultimately be turned into plenty. Before we are in the grip of actual dearth, the chemist will step in and postpone the day of famine to so distant a period that we and our sons and grandsons may legitimately live without undue solicitude for the future" and also that "the fixation of atmospheric nitrogen is one of the great discoveries awaiting the ingenuity of chemists." William Ostwald[12] of Leipzig University also discussed the fixation of atmospheric nitrogen in 1900. Atmospheric nitrogen was seen as an inexhaustible supply if mankind had the ingenuity to devise a fixation process.

1.2. FIXATION OF ATMOSPHERIC NITROGEN

In 1895 Frank and Caro discovered a process to fix atmospheric nitrogen using barium or calcium carbide at high temperatures, as follows:

$$CaC_2 + N_2 = CaCN_2 + C \tag{1.1}$$

It was recognized that the calcium cyanamide thus formed could be used directly as a fertilizer. Caro obtained a patent in 1900 for the generation of ammonia from the cyanamide by hydrolysis.

Although the formation of calcium carbide from calcium oxide and carbon requires temperatures as high as 2300 K, the overall power necessary for this fixation process was only one quarter of that required by the arc process. The reasons for the observation are described below.

A few years before this discovery, Crookes himself and also Lord Rayleigh had studied the fixation of atmospheric nitrogen in an electric discharge between the terminals of an induction coil to give nitrous and nitric acids. Similar effects of a discharge in air had also already been studied by Cavendish toward the end of the 18th century. The method of fixing atmospheric nitrogen by means of an electric arc was developed commercially by Birkeland and Eyde, after whom the process is now named.

The thermodynamic equilibrium concentration of nitric oxide is very low at normal temperatures, and in order to obtain an appreciable amount of nitric oxide it is necessary to heat up the air to temperatures above 3000 K. This was only possible at that time by the use of an electric arc and, even then, a very large quantity of electric energy was necessary.

The concentration of nitric oxide in the effluent gas produced by this process was only 2%. The energy consumption was enormous and, consequently, the process could only be viable in countries where cheap electric power was available. This is the reason why the first plant was operated in Notodden, Norway, in 1904, using hydroelectricity.

The process was developed further by other groups, such as Badische Anilin und Soda Fabrik (BASF) of Germany, later in collaboration with Haber. It was

through this process that Haber had his first connections with BASF. Haber had studied the oxidation of nitrogen in an electric arc and had proposed a mechanism for the reaction. Since the nitric oxide content in the stationary state is greater than the thermal equilibrium amount and the excess amount decomposes on the removal of the electric field, to approach its equilibrium value, high yields of nitric oxide could be obtained by using low temperature which avoided the thermal decomposition of nitric oxide.

The fixation of atmospheric nitrogen through both the electric arc and calcium cyanamide routes were thus put into commercial practice. Both processes suffered from large requirements of electrical energy for the synthesis and were replaced before long by the direct synthesis of ammonia from its elements, which has become known as the Haber-Bosch process. Since Ostwald had developed a method for the oxidation of ammonia to produce nitric acid at the beginning of the century (1902), synthetic ammonia provided the basis for an industrial route to nitric acid.

At the beginning of this century, there were heated debates as to whether or not the synthesis of ammonia from its elements was actually possible. The first problem of critical importance was to determine the equilibrium point of the synthesis reaction. If the equilibrium lies too far on the side of the elements at reaction temperatures, the conversion will be low and the synthesis will not be viable for industrial application. The combination of nitrogen and hydrogen is an exothermic reaction, in which the total number of reacting molecules decreases to half. Therefore the synthesis should be operated at temperatures as low as possible, under pressures as high as possible. Consequently, the feasibility of direct synthesis is also dependent upon various technological innovations, required to overcome the difficulties in the development of good catalysts which would be able to activate molecular nitrogen at low temperatures, and also reactor systems which are capable of operation under high pressures at the reaction temperature.

1.3. THE PEOPLE WHO CONTRIBUTED TO THE DEVELOPMENT OF THE "HABER–BOSCH PROCESS" FOR AMMONIA SYNTHESIS

Major scientific discoveries and technical innovations are frequently accomplished by prominent scientists and engineers. It is therefore interesting to describe briefly the careers of the two principal people who contributed to the success of the Haber-Bosch process, with a further paragraph on BASF.

1.3.1. Fritz Haber

Haber[13,14] was born on December 9, 1868 in Breslau, Germany. His father was a rich chemical and dye merchant. During his school years, the young Haber became interested in chemistry through the influence of his father's business, and he practiced chemistry at home. He later studied at the Universities of Berlin and Heidelberg (when Bunsen was a professor) and at the Technische Hochschule of

Charlottenburg, where he carried out research in the field of organic chemistry under Professor Liebermann.

After graduation, he fulfilled his father's hopes by working in the chemical industry and his father's business for a period of time. However, he was unable to satisfy his personal ambitions in industry and he finally decided to seek academic freedom by working in a university. His first position was at the University of Jena under Professor Knorr. He then joined the Technische Hochschule in Karlsruhe at the age of twenty-five as a research assistant, in the Department of Chemical and Fuel Technology working on the thermal decomposition of hydrocarbons.

He must have gained valuable experience working not only in industry, but also in a department which had close connections with industry. Although he was deeply involved in pure science in his later life, he never forgot his industrial training which stood him in good stead to help overcome the various difficulties encountered in converting the significance of his thermodynamic measurements into an industrial process.

His approach toward research was to penetrate to the roots of the problem, with "thoroughness and intolerance of vagueness and superficiality." For instance, the author was told by his father,[15] who incidentally worked with Haber for more than six years, that Haber spent many hours in the preparation of manuscripts, almost as long as the time spent obtaining the actual experimental data. He paid much attention to detail in order to avoid any misunderstanding, and developed his own style using rhyme.

F. Haber visiting the author's home in Kamakura, Japan in 1924. Professor and Mrs. F. Haber, the author's parents and brother. The author is in the arms of his mother.

Haber then moved into the newly developing field of fundamental physical chemistry, which had attracted the interests of such pioneers as, for instance, van't Hoff, Arrhenius, and Ostwald. His interest, however, shifted from organic chemistry (in which he started his academic career) to physical chemistry, with particular emphasis on thermodynamics and electrochemistry. Although self-taught, he made significant contributions toward establishing the modern science of these fields. His accomplishment in these fields may be judged by the two books he published, *Foundation of Technical Electrochemistry on a Theoretical Basis* in 1898 and also *Thermodynamics of Technical Gas Reactions* in 1905, both of which were milestones in these fields, written as a "model of accuracy and critical insight." His interests had therefore shifted from organic chemistry via the fuel gas industry, to electrochemistry and physical chemistry, and finally to physics where he later become president of the Physical Society of Germany. His achievements are all the more impressive since he was largely self-taught.

1.3.2. Carl Bosch

Bosch[14,16] was born on August 27, 1874. His family owned a business dealing in piping materials for the supply of gas and water. He was keenly interested in natural sciences, in particular chemistry, and as a teenager he conducted chemical experiments at home. Bosch worked for a year at an iron and steel works following his father's advice. He became familiar with mechanics through this experience and entered the Technische Hochschule at Charlottenburg in 1894 to study foundry technology and mechanics. This Technische Hochschule is the same establishment where Haber had been fascinated by organic chemistry while studying under Professor Liebermann some years previously. In Charlottenburg, Bosch also attended lectures in chemistry and mineralogy as well as those in his major subjects. In 1896 he entered the University of Leipzig to gain further training in organic chemistry. He received his doctorate and became a research assistant in 1898 before joining Badische Anilin und Soda Fabrik (BASF) in April 1899. During his career he always worked diligently and was interested in a wide range of science and technology. He was most capable in every respect, and exhibited a remarkable ability in the design and construction of apparatus for the laboratory.

When he entered BASF his manager was Dr. R. Knietch, who is now famous for his successful development of the oxidation of sulfur dioxide over a platinum catalyst. Dr. Knietch asked Bosch to follow up the results of ammonia synthesis generated by Ostwald. Ostwald[12] at that time was interested in the fixation of molecular nitrogen to form ammonia. It was known in those days that ammonia could be decomposed to hydrogen and nitrogen over an iron catalyst. Since a catalyst does not change the chemical equilibrium but only changes the rate at which the equilibrium is attained, any catalyst which accelerates the decomposition of ammonia may also be a good catalyst for the reverse reaction. Ostwald investigated the reverse reaction in the attempted synthesis of ammonia over an iron catalyst, since no one knew in those days whether or not ammonia synthesis from its elements was even possible. He successfully obtained high concentration (6%) of ammonia by the activation of nitrogen over iron catalysts. Instead of publishing

his results, he immediately entered into negotiations with industry (BASF, Hoechst) and took out a patent on ammonia synthesis. Bosch repeated Ostwald's experiments and finally concluded that the high concentration of ammonia obtained by Ostwald came from an impure iron catalyst which still contained considerable amounts of residual ammonia and nitride. Bosch was destined in this manner to participate in ammonia synthesis from the very beginning of his career in BASF.

1.3.3. Badische Anilin und Soda Fabrik

In the latter half of the 19th century and at the beginning of the 20th century, the industrial application of organic chemistry enjoyed one of the most prosperous and fruitful periods in German history, especially in the synthesis of dyestuffs. In particular, BASF was successful in the synthesis of indigo in the year 1897, after a costly research program spread over a long period of time, but at last they could finally enjoy the profits deserved from this great success. Such a pioneering spirit must have stimulated the young, capable scientists and engineers such as Bosch and Mittasch who joined the company around the turn of the century.

In those days German scientists contributed enormously to the "enabling" studies in the fields of basic sciences, led by prominent scientists especially in chemistry and physics, such as Roentgen, Fisher, Arrhenius from Sweden, Ostwald, Laue, Willstatter, Haber, Planck, Nernst, and Einstein. Those pioneers were indeed prolific during the golden age of science in Germany, both in numbers and output.

1.4. FUNDAMENTAL RESEARCH ON THE THERMODYNAMICS OF DIRECT AMMONIA SYNTHESIS FROM ITS ELEMENTS

Haber began his work on the thermodynamic equilibria between ammonia, hydrogen, and nitrogen in 1904. In the opening paragraph of his paper entitled "Uber die Bildung von Ammoniak aus den Elementen," in 1905, he wrote as follows[17]: "Die Herren Dr. O. and Dr. R. Margulies warfen die Frage auf, ob es aussichtsvoll sei, nach einem Metal zu suchen, dessen abwechselnde Uberführung in Nitrid und Hydrur mit Stickstoff und Wasserstoff zur Ammoniakdarstellung verwendet werden konne." By repeating the process of hydrogenation of the nitride and its formation under steady-state conditions, ammonia may be formed catalytically over a metal. His interest in this problem covered not only the thermodynamics (equilibria) of this reaction, but also the rate at which the equilibrium composition from nitrogen and hydrogen is approached. Since a catalyst does not change the equilibrium composition and the maximum yield from the synthesis reaction is therefore determined by that equilibrium, his first concern was to measure the composition of the gas mixture at equilibrium.

By the time Haber had initiated his measurements on the nitrogen/hydrogen/ammonia equilibrium point, many attempts had been made to study the synthesis and decomposition of ammonia. Some of them had been successful to

a limited extent, but none had converted more than a small amount of nitrogen. In 1823, Dobereiner[18] had reported the direct combination of nitrogen and hydrogen to form ammonia for the first time. According to his report, ammonia was formed during the combustion of hydrogen with a deficiency of air in the presence of a platinum catalyst. The presence of ammonia may have been due to the formation of a small amount of nitric oxide at the high temperatures generated during the combustion of hydrogen, with subsequent reduction of the nitric oxide by hydrogen to ammonia over the platinum catalyst. In 1839, Kuhlmann[19] obtained ammonia by passing a mixture of nitric oxide and hydrogen over a platinum sponge. Ammonia was not formed from a mixture of nitrogen and hydrogen under similar conditions. Accordingly, he proposed his "status nascendi" theory which said that only "nascent" nitrogen could combine with hydrogen to form ammonia. Tessie du Motay obtained a patent for ammonia synthesis, which was effected by passing hydrogen and nitrogen alternatively over heated titanium nitride. Reduction of the nitrides, Ti_3N_2 and TiN, with molecular hydrogen led to the production of Ti_5N_3. The Ti_5N_3 was converted to Ti_3N_2 and TiN by molecular nitrogen. In a British patent, Charles Tellier reported that a considerable amount of nitrogen was absorbed by spongy iron, which could be reduced by hydrogen to form ammonia. On repetition of such a process, namely, by passing nitrogen and hydrogen over the iron sponge alternately, ammonia could be produced via the intermediate formation of iron nitride.

It was reported by Ramsay and Young[20] in 1884 that while the decomposition of ammonia took place over iron and porcelain catalysts at 800 °C, the decomposition never went to completion. It was also claimed in an Austrian patent that ammonia could be synthesized by passing a mixture of hydrogen and nitrogen over a catalyst comprising titanium or titaniferous compounds in admixture with platinum supported on porous materials. Later, in 1901, Henri Louis Le Chatelier, who is still famous for his general principle of equilibrium, obtained a patent for the direct combination of molecular hydrogen and nitrogen to form ammonia. He also claimed that higher pressures, up to 100 bar, would facilitate the reaction. However, he was obliged to stop his high-pressure experiments because of an accidental explosion in which one of his assistants was killed.

It was already generally accepted that molecular nitrogen was too inert to react directly with hydrogen at moderate temperatures. Unfortunately, at high temperatures where reaction with hydrogen becomes possible, the decomposition of ammonia also takes place, hence the need for a catalyst to allow synthesis at the reaction temperature. Perman[21] used iron as a catalyst in 1904 and studied the formation of ammonia from its elements, but, unfortunately for him, in the presence of moisture which we now know retards the reaction. Haber immediately realized that the equilibrium concentration of ammonia should not be influenced by the presence of moisture.

Haber started his work on measurement of the equilibrium point using iron as a catalyst at temperatures around 1300 K, and at atmospheric pressure. He knew, of course, that higher pressures would give higher concentrations of ammonia, but the measurements at atmospheric pressure could be carried out much more simply and easily. He placed two reaction tubes in series and measured

the equilibrium composition by approaching the equilibrium from both sides, namely, synthesis from the elements and decomposition of ammonia using both nickel on silica catalysts and, subsequently, iron on asbestos. The composition of the catalyst surface may be quite different under reaction conditions far from equilibrium, but, as the equilibrium point is approached, the catalyst should stabilize and give the true equilibrium value. The equilibrium value thus obtained should lie somewhere between the two values obtained by approaching the equilibrium from opposite directions.

The values obtained by Haber and van Oordt for the concentration of ammonia at equilibrium from a stoichiometric mixture of hydrogen and nitrogen, at 1020 °C under atmospheric pressure, are as follows[22]:

°C	27	327	627	927	1020
% NH_3	98.51	8.72	0.21	0.024	0.012

The values at lower temperatures were derived using the van't Hoff equation, $d \ln K/dT = Q/RT^2$, where K, Q, and T are the equilibrium constant, heat of reaction, and temperature, respectively. These were the first reported measurements of the equilibrium between ammonia, hydrogen, and nitrogen.

The total amount of ammonia which Haber obtained at equilibrium was quite small, and he estimated that the reaction temperature necessary for commercial success of the synthesis at atmospheric pressure would need to be lower than 300 °C, a temperature considerably below the minimum for which he could hope. Although the accuracy of the estimated compositions at equilibrium at room temperature was not high, it was of great importance to learn that the major proportion of a nitrogen and hydrogen mixture could convert to ammonia at room temperature. It was a significant step forward to discover that it was not necessary for the synthesis of ammonia from its elements to depend upon the generation of "nascent" nitrogen. Furthermore, the possibility for the synthesis of ammonia from the elements, at room temperature, was proposed for the first time provided that a suitable catalyst could be discovered. Haber himself, however, thought at that time that the manufacture of ammonia from its elements was not feasible on the industrial scale and he preferred to study the arc method in more detail.

1.4.1. Dispute between Haber and Nernst

The values obtained by Haber were considerably higher than those calculated by Nernst, using his heat theorem. Nernst therefore redetermined the equilibrium values at higher pressures (30–75 atm at 700–1000 °C) using an autoclave, since higher partial pressures of ammonia would lead to the generation of more accurate data. In practice, this constituted the first high-pressure experiment on ammonia synthesis. The values of the equilibrium constants thus obtained can be derived from the following equation[23]:

$$\log K = 24{,}000/4.571T + 3.5 \log T + 2.6 \qquad (1.2)$$

This suggests that the concentration of ammonia at atmospheric pressure is 0.012% at 893 K. In contrast, Haber's group reported that temperatures of 1293 K were required to maintain this concentration at equilibrium. Nernst's results were again in reasonable agreement with his theorem, but such a large discrepancy in the values of the equilibrium concentration estimated by the two eminent professors created a major dispute.

Haber and Le Rossignol[24] carried out further experiments to redetermine the equilibrium value using their same method at atmospheric pressure, but with various refinements. The principal reason why they carried out their measurements at atmospheric pressure was because they considered that their analytical methods were good enough. Furthermore, their experiment had the advantage of being able to approach the equilibrium state more easily from both sides, namely, synthesis and decomposition. They obtained a new value for the concentration of ammonia, 0.0048% at 1000 °C, which is close to the lower value (0.005%) of their former estimate. The reproducibility of their results was much better than that of Nernst. They were convinced that their results represented the true equilibrium positions more accurately than those of Nernst, since Nernst had not studied the decomposition of ammonia to complement the work on direct synthesis.

The meeting of the Deutsche Bunsen Gesellschaft in 1907 was an important meeting in the history of ammonia synthesis. Nernst presented his results obtained at high pressure which, as stated earlier, were in good agreement with his theorem, but which had been calculated using an assumed value of the specific heat of ammonia, which had never been measured accurately at high temperatures. Although Haber was quite sure of his new values, Nernst would not accept Haber's values unless Haber first measured the equilibrium concentrations at high pressures so that increased concentrations of ammonia by two orders of magnitudes would result. To quote from Nernst's closing remark: "Dann darf ich vielleicht nur noch eine Tatsache konstatieren, die von allgemeinem technischen Interesse ist. Es ist sehr bedauerlich dass das Gleichgewicht nach der Seite der viel geringeren Bildung mehr verschoben ist als man nach den stark unrichtigen Zahalen Habers bisher angenommen hat, denn man hatte wirklich daran denken konnen Ammoniak synthetisch herzustellen aus Wasserstoff und Stickstoff. Aber jetzt liegen die Verhaltnisse sehr viel ungunstiger, die Auseuten sind ungefahr dreimal kleiner als zu erwalten war." He considered that the problem of the measurement of the true equilibrium position had been resolved and that the ammonia content which Haber had measured was incorrect. He also thought that the industrial synthesis of ammonia was not feasible, since their new results suggested a much smaller yield of ammonia than one would expect from Haber's previous measurements. It is said that he reached this conclusion after discussions, as to whether or not industrial ammonia synthesis would be feasible on the basis of his results, with one of his friends who worked in industry, and who gave a negative response.

Nevertheless, Nernst contacted Chemische Fabrik Griesheim-Elektron in 1906 on the subject of ammonia synthesis and received some support. This was discontinued soon after because it was concluded that the construction of equipment to work under high pressure and temperature conditions would constitute an impossible task.

Nernst's comments at the meeting were somewhat overstated to emphasize his victory in the dispute. The outcome, however, was that most of the audience were convinced that ammonia synthesis from the elements was not a feasible process for practical operation. On the other hand, the tone of his speech showed quite decisively his negative attitude toward the future of such a process.

Haber and his group were, of course, far from happy about Nernst's comments, although they shared with Nernst doubts about the feasibility of ammonia synthesis on the industrial scale. They began to determine the equilibrium concentrations again, but this time they measured the equilibria at pressures as high as 30 bar, in addition to atmospheric pressure. The results obtained using iron and manganese catalysts were in good agreement with those obtained at one atmospheric pressure and they were able to publish their new data in 1908.[25]

Even these results, however, did not enhance the prospects for the industrial synthesis of ammonia because, according to their measurements, the equilibrium concentration of ammonia was only about 8% at 600 °C and 200 bar pressure. Pressures of this order at such a high reaction temperature were far from attainable on a large-scale operation in the chemical industry of the day. Furthermore, the reaction temperature at which the catalytic production of ammonia proceeded at a reasonable rate with the catalysts available at that time was higher than 700 °C. It was apparent to all that the next challenges for the industrial synthesis of ammonia were either to discover new catalysts with much higher activity which could consequently operate at much lower reaction temperatures, or to develop the process engineering so that the reaction could be operated on a large scale at much higher pressures.

1.5. THE SUCCESSFUL SYNTHESIS OF AMMONIA FROM ATMOSPHERIC NITROGEN[26]

It is not difficult to understand the reason why Nernst believed that the synthesis of ammonia would be formidably difficult to achieve on the basis of his estimate of the concentration of ammonia in the equilibrium mixture. However, Haber was brave enough to challenge this problem and fortunate in having such wonderful collaborating experts as Le Rossignol in his laboratory to assist in his challenge. As a result of great efforts made during their depressed period, they finally succeeded in the operation of a steel autoclave as a reactor at pressures of up to 200 atmospheres, which were the highest pressures obtainable in Karlsruhe. They also succeeded in discovering that osmium, and later uranium, were much better catalysts which gave usable rates of reaction at temperatures as low as 550 °C.

A great breakthrough in the synthesis of ammonia was achieved in this manner. However, this basic process was extended further by Haber and his group, who adopted a clever method of ammonia synthesis using a closed circulating system, as shown in Fig. 1.1. The system consisted of a synthesis reactor, and a heat exchanger to heat the reaction gas using the heat evolved by the exothermic reaction. Using such a circulating system, liquid ammonia was obtained continuously, with low overall energy consumption, by feeding a stoichiometric mixture

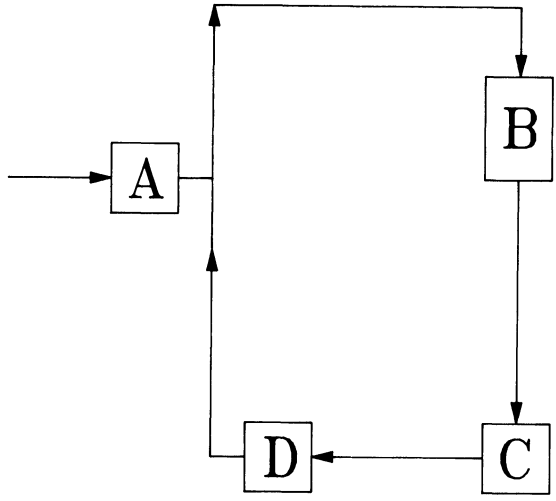

Figure 1.1. A schematic design of the circulation system used to obtain ammonia continuously from the stoichiometric mixture of hydrogen and nitrogen: (A) is the compressor, (B) the reactor, (C) the separator, and (D) the circulation pump.

of hydrogen and nitrogen to the system. This convincing demonstration in Karlsruhe provided the clear evidence that the synthesis of ammonia was indeed feasible on the industrial scale.

The success in the story so far owes much to the great challenging, unyielding, and farseeing spirit of Haber, combined with the experimental skill of the support group in his laboratory. However, the leading and still growing potential of both industry and the academic society in Germany at that time should not be overlooked, since they provided the background against which this great achievement was finally made.

BASF, as suggested above, was an ambitious and successful company with considerable interest in ammonia synthesis. They sent two young, capable engineers, Bosch and Mittasch, to visit Haber's laboratory in Karlsruhe on July 2, 1909 to see a demonstration of his process. The experiment was carried out using 98 g osmium as catalyst at a pressure of 175 bar. Ammonia was obtained at the rate of 80 g every hour. Bosch and Mittasch, who had had extensive scientific training in their early careers, were both deeply impressed by the epoch-making discoveries and dedicated themselves thereafter to the development of the process. It is important to point out that this was truly a historical day not only for Haber and his group, but also for both engineers. Bosch, later, established high-pressure technology in the chemical industry while Mittasch contributed enormously to the development and understanding of commercial catalysts. Haber was awarded the Nobel Prize in 1919 for his studies on ammonia synthesis. Bosch also received the Nobel Prize in 1931 for his achievement in high-pressure technology, jointly with Bergius who also worked with Haber's group in Karlsruhe, which had become a center of excellence in the field of high-pressure technology.

The successful demonstration of ammonia synthesis was reported in March, 1910 at a meeting in Karlsruhe.[27] It generated a sensational response as the new process to obtain "bread from the air."

Industrial Development by BASF

The industrial development of ammonia synthesis was started in BASF immediately after that day in Karlsruhe, and Bosch was made responsible for the whole project. Despite the success of the feasibility study in Karlsruhe there were still many problems to be solved before a large-scale manufacturing process could be designed and built.

In the first instance, substantially better catalysts were required for the synthesis stage. As mentioned above, active and stable catalysts allow the synthesis reaction to take place at lower pressures and temperatures. It was, accordingly, of fundamental importance to discover good catalysts which were cheaper and more stable than osmium and uranium, since both were difficult to obtain and presented handling problems.

Another serious problem was the construction of large-scale, high-pressure reactors for operation at high reaction temperatures. At that time, the highest pressure attainable in the chemical industry was 200 bar, which was used in the liquefaction of air at ambient temperature. In addition to these two major problems, the preparation of pure nitrogen and hydrogen mixtures on the large scale also presented difficulties, particularly since the reactant gases must not only be cheap, but also highly pure to minimize deactivation of the catalyst in the continuous process.

Solutions to all these problems presented considerable difficulties. Bosch and his co-workers had to overcome these hurdles, one at a time, in the embryo period of these emerging technologies. However, they worked as a powerful team, showing a great problem-solving capability. To solve the catalyst problem, they first turned to iron. This was known to be an effective catalyst for the decomposition of ammonia and Ostwald, Nernst, and Haber had all used iron as the catalyst in their early experiments. Mittasch and his co-workers noted in their experiments that the activity of iron catalysts was markedly influenced by the presence of a small amount of impurities in it. Consequently, they started to study multicomponent catalysts, by addition of other compounds to pure iron catalysts.[28]

They prepared a range of iron catalysts which contained various additives, such as chlorides, sulfates, and the oxides of the alkali and alkaline earth metals. The original idea was to promote the information of iron nitrides, which were considered to be the reaction intermediates in the reaction between nitrogen and hydrogen. Various additives were incorporated into the catalyst formulation using differing techniques, such as fusion of the required components or by coprecipitation of the mixed metal nitrates. Through extensive, thorough, and systematic research, Mittasch and his co-workers determined the general effects that additives have on the catalytic behavior of metals. Some improve the catalytic activity, some have little effect, but others are positively detrimental and poison the catalysts. After a painstaking search, it was finally discovered that alumina and magnesia

behave as promoters, and also that the combination of iron with small amounts of alumina and potash, as occurring naturally in some varieties of Swedish magnetite, generates a high and stable activity, which is suitable for the large-scale synthesis of ammonia. It is said that during this work, more than 2500 kinds of catalysts were tested during 6500 experiments before the now-accepted, promoted iron catalyst was finally found.

This was a remarkable example of systematic research into the preparation of good catalysts. The extensive information generated in this work contributed enormously to the later technology of catalyst preparation. The synthesis catalyst, based on iron, promoted by alumina and potash is still widely used in the industry today, and is prepared with only minor modifications in terms of additives and preparation methods. It is surprising to note that such a high quality catalyst could be discovered in just eighteen months after the project was started by BASF. Taking into account the limited amount of knowledge on catalysis available at the beginning of the project and the availability of high-pressure test equipment, we cannnot but admire the great achievements they accomplished in this field.

On the laboratory scale, a few grams of catalyst may be sufficient for test purposes, but with large-scale reactors, a few kilograms of catalyst are needed. For example, the tubular steel reactor employed at the beginning of 1910 was 1.8 m in length with a diameter of 14.6 cm progressing to a larger reaction 8 m long with 45 m diameter, by 1913 used in essentially the same system as that used by Haber. The reactor was housed in an explosion-proof, concrete bunker where the dangers associated with the self-ignition of high-pressure hydrogen had been taken well into account. The reaction was operated at 870 K and a pressure of 100 bar using the Swedish magnetite catalyst, but after operation for some eight hours, the tube was found to have swollen, and burst. The inner wall had completely lost its tensile strength, the failure apparently being due to chemical attack by hydrogen. The carbon-containing steel had been reduced by hydrogen to form methane and dissolution of hydrogen into the iron had also taken place. Even using the most active catalysts available, operating at a temperature of 700 K, the life of the vessel was only a few days. Ammonia synthesis on the commercial scale could never be successful until problems of this kind had been solved.

As mentioned above, Bosch was born into a family which dealt in piping materials. Furthermore, he studied not only foundry and mechanics, but also chemistry at the Technische Hochschule. With his inherent ability, and such a broad technical background, Bosch was the ideal man to tackle these difficult problems. He investigated the damaged reactor materials in detail, and discovered decarbonization and embrittlement of the steel reactor by hydrogen, and also by methane occluded within the steel under pressure. Even when various metals other than steel were tried, he was unable to achieve better results and the solution to the problem seemed to be impossible. He even attempted to use a steel tube, lined on the inside by silver, to avoid the attack of hydrogen, but since the coefficients of thermal expansion of the two metals were so different, even this method did not work well. He finally reached the solution by the use of soft iron for the catalyst-containing vessel, protected by an external vessel of steel. Since soft iron contains only a small amount of carbon, there are no problems which arise through

decarbonization. Although it does become brittle as a result of hydrogen dissolution, this is not a problem since it is protected by a pressure-resistant shell from outside. Later, Bosch further advanced his idea by the use of an external tube with small holes that did not affect its mechanical strength. The hydrogen, which passed through the inner soft iron lining by diffusion, could escape through these holes at pressures low enough to avoid attack on the outer tube. Without such technical innovations in the chemical engineering, ammonia could not have been manufactured on the industrial scale. The double tube reactor was successfully operated for the first time in March 1911.

The first ammonia plant was built at Oppau, and was capable of producing 30 tons of ammonia per day. Hydrogen was obtained initially from water gas, but this was soon replaced by the catalytic reaction between water gas and steam, the water gas shift reaction, over iron oxide:

$$CO + H_2O = CO_2 + H_2 \tag{1.3}$$

The carbon dioxide thus formed was removed by scrubbing with water, and on recovery could be used subsequently for the production of fertilizers.

Nitrogen was obtained initially by the liquefaction of air, but this, too, was soon replaced by the reaction of air with red hot coke to produce "producer gas" (60% N_2 and 40% CO), which was reacted subsequently with water gas to form carbon dioxide and hydrogen by the shift reaction mentioned above. The carbon dioxide in the gaseous product was removed by passing through water as before, while the residual carbon monoxide was removed by dissolution in ammoniacal copper liquors.

The commercial synthesis vessels were 30 cm in diameter, containing some 300 kg catalyst, and they produced 3–5 tons of ammonia each day. The factory was expanded rapidly and, by April 1915, 20 tons of ammonia were manufactured every day. This had increased to 230 tons per day by December 1917.

The most important details in the technology of ammonia synthesis were kept confidential until the factory in Oppau was opened publicly, thus allowing outsiders to visit. The British Nitrogen Products Committee had estimated that the cost of ammonia synthesized from its elements would be about 50% more expensive than that from calcium cyanamide. This is why calcium cyanamide factories were built during, and even after, the First World War.

It was, however, inevitable that such an epoch-making innovation would be applied increasingly, not only in Germany, but also in many other countries. After the initial developments of Haber and Bosch, the synthetic ammonia industry expanded rapidly throughout the world, and was applied on larger and larger scales.

At the beginning of this century, the traditional chemical processes such as dyestuffs production was always operated at pressures below 50 bar, in the temperature range below 250 °C, and on a scale of less than a few tons production per day in batch systems. The manufacture of ammonia changed that situation completely.[29] The process operated continuously at much higher temperatures, and at much higher pressures. Innovations of this type lead inevitably to the development of various new techniques, such as the preparation of synthesis gases, the development of long-lived catalysts, accurate flowmeters, better compressors,

corrosion-resistant reactors which can work at high temperature under high pressure, and so on. This is true, not only for the new style of operation and equipment, but also in establishing the connection between the chemical industry and other fields such as agriculture and process engineering. It was therefore a major step forward in the modernization of the chemical industry, and was quickly followed in 1923 by another high-pressure process, the synthesis of methanol.

In the late 1950s a further major breakthrough was achieved with the technology to build very large ammonia plants capable of manufacturing more than 1000 tons per day, using a simplified design with greatly reduced investment and operating costs. In the 1960s, the whole manufacturing system was further modified to improve the efficiency and effectiveness of each part of the system with resultant savings in energy and operating costs. This became possible because the synthesis gas was prepared more cheaply from light naphtha or natural gas rather than coal, and better catalysts, compressors, and processes to remove carbon dioxide were available. The cost of fixation of nitrogen also changed remarkably with time; for example, the energy-intensive electric arc process required a colossal 6800 therms for every ton of nitrogen fixed. The cyanamide process needed approximately 1700 therms, while with the modified Haber–Bosch process of the 1950s it had come down to 600 therms. The use of hydrocarbon feedstocks in the 1960s brought about a further reduction, down to half this value. This remarkable advancement of technology has been evident.[14,30] As a result of these innovations, the cost of ammonia has been markedly reduced, and this has contributed to the supply of cheap fertilizer to many parts of the world, thus reducing the impact of famine.

1.6. EPILOGUE

Toward the end of the 19th century, mankind was confronted with a serious problem of long-term survival due to a shortage of nitrate resources for use in fertilizers, and the production of other nitrogen-containing chemicals. In the history of nitrogen fixation we can recognize the contributions of many famous scientists who worked in this field, such as Cavendish, Ramsay, Le Chatelier, Ostwald, Nernst, and Haber. Many of those distinguished scientists were interested in solving the problem by the synthesis of ammonia from its elements and some of them, like Nernst, were almost successful in synthesizing ammonia at high pressures. They had, however, too many barriers to overcome. Although the process itself appeared simple, even Haber himself was not always optimistic about his success. He had to extricate himself repeatedly from the valley of disappointment. After overcoming many barriers he finally discovered reasonably active catalysts and successfully carried out his prototype synthesis reactions under high pressures. His deep understanding of thermodynamics and his ever-increasing efforts led to the solutions of many problems on the way. It was fortunate for Haber that he had the collaboration of genuine, excellent experts (such as Le Rossignol) in the experimentation. Bosch and Mittasch also made vital contributions to the development of high-pressure technology and search for effective catalysts respectively. Without the collaboration of these brilliant engineers from BASF, nitrogen fixation

could not have been realized so rapidly. The real lesson to learn from this extremely interesting story is that purely basic science provided the key to both this new breakthrough in the chemical industry and especially to the survival of mankind by obtaining "bread from the air."

At the end of this century, or perhaps at the beginning of the next, we may again be faced with another potential crisis. The natural hydrocarbon reserves to which we owe so much in our daily lives will increasingly become depleted. The problems associated with achieving the most effective use of our energy and natural resources must be resolved by the efforts of chemists and chemical engineers together.

REFERENCES

1. a. G. N. Lewis and M. Randall, *Thermodynamics and the Free Energy of Chemical Substances*, p. 556, McGraw-Hill, New York (1923). b. F. Haber, *Z. Elektrochem.* **20**, 597 (1914). c. F. Haber, S. Tamaru, and S. Ponnaz, *Z. Elektrochem.* **21**, 89 (1915). d, F. Haber and S. Tamaru, *Z. Elektrochem.* **21**, 191, 228 (1915). e. F. Haber, S. Tamaru, and L. N. Oeholm, *Z. Elektrochem.* **21**, 206 (1915).
2. a. H. S. Taylor, *J. Am. Chem. Soc.* **52**, 5298 (1930); **53**, 578 (1931). b. J. E. Lennard-Jones, *Proc. Roy. Soc.* **A106**, 463 (1924). c. P. H. Emmett and S. Brunauer, *J. Am. Chem. Soc.* **56**, 35 (1934). d. P. H. Emmett, in: *The Physical Basis for Heterogeneous Catalysis* (E. Drauglis and R. I. Jaffe, eds.), p. 3, Plenum Press, New York (1973). e. G. Ertl, *Catal. Rev.* **21**, 201 (1980).
3. a. M. Boudart, *Adv. Cata.* **20**, 153 (1969). b. J. A. Dumesic, H. Topsoe, S. Khammouma, and M. Boudart, *J. Catal.* **37**, 503 (1975).
4. a. J. Horiuti, *Proc. Jap. Acad.* **29**, 100 (1953); *J. Res. Inst. Catal., Hokkaido Univ.* **5**, 1 (1957). b. K. Takana, *J. Res. Inst. Catal., Hokkaido Univ.* **19**, 42 (1971).
5. S. Brunauer, K. S. Love, and R. G. Keenan, *J. Am. Chem. Soc.* **64**, 751 (1942).
6. P. H. Emmett and S. Brunauer, *J. Am. Chem. Soc.* **59**, 1553 (1937).
7. a. S. Brunauer and P. H. Emmett, *J. Am. Chem. Soc.* **59**, 310-(1937); **62**, 1732 (1940). b. G. Ertl and N. Thiele, *Appl. Surf. Sci.* **3**, 99 (1979). C. K. Hanji, H. Shimizu, H. Shindo, T. Onishi, D. C. Silverman, and M. Boudart, *J. Catal.* **77**, 208 (1982). d. G. Ertl, D. Prigge, R. Schloegl, and M. Weiss, *J. Catal.* **79**, 359 (1983).
8. a. J. C. Jungers and H. S. Taylor, *J. Am. Chem. Soc.* **57**, 679 (1935). b. R. M. Barrer, *Trans. Faraday Soc.* **32**, 490 (1936). c. G. S. Joris and H. S. Taylor, *J. Am. Chem. Phys.* **7**, 893 (1939). d. J. T. Kummer and P. H. Emmett, *J. Chem. Phys.* **19**, 289 (1951). e. R. P. Eischens and J. Jacknow, *Proc. 3rd Int. Cong. Catal.* (W. M. H. Sachtler *et al.*, eds.), p. 627, Elsevier, Amsterdam (1965). f. K. Kunimori, T. Kawai, T. Kondow, T. Onishi, and K. Tamaru, *Surf. Sci.* **54**, 525 (1976). g. G. Ertl, *Catal. Rev.* **21**, 201, 1980; *Surf. Sci.* **114**, 515 (1982). h. K. Kishi and M. W. Roberts, *Surf. Sci.* **62**, 252 (1977).
9. a. G. Ertl, S. B. Lee, and M. Weiss, *Surf. Sci.* **114**, 515, 527 (1982). b. W. L. Guthrie, J. D. Sokel, and G. A. Somorjai, *Surf. Sci.* **109**, 390 (1982).
10. J. von Leibig, *Die organische Chemie in ihre Anwendung auf agrikultural Chmie und Physiologi* (1940).
11. W. Crookes, Report of the 68th Meeting of the British Association for the Advancement of Science, Bristol, 1898, p. 3, John Murray, London (1895).
12. a. W. Ostwald, *Grundlinien der anorganischen Chemie*, p. 345, (1900). b. *Lebenslinien* (*Eine Selbstbiographie*), Klasing Co., (1927).
13. a. J. E. Coates, The Haber Memorial Lecture, *J. Chem. Soc.*, **1939**, 1642. b. M. Goran, *The Story of Fritz Haber*, University of Oklahoma Press (1967).

14. S. A. Topham, The History of the Catalytic Synthesis of Ammonia, in: *Catalysis, Science and Technology* (J. R. Anderson and M. Boudart, eds.), Vol. 7, p. 1, (1985).
15. S. Tamaru, *Kagaku-chishiki* (*Science*) **14**, 305 (1934).
16. K. Holdermann, *Im Banne der Chimie, Carl Bosch, Leben und Werk*, Econ-Verlag, Dusseldorg (1953).
17. F. Haber and G. van Oordt, *Z. Anorg. Chem.* **44**, 341 (1905).
18. J. Dobereiner, *J. Chem. Phys.* **38**, 3215 (1823).
19. F. Kuhlmann, *Justus Liebigs Ann. Chem.* **29**, 272 (1839).
20. W. Ramsay and C. Young, *J. Chem. Soc. London* **45**, 88 (1884).
21. E. P. Perman, *Proc. Roy. Soc.* **76A**, 167 (1905).
22. F. Haber and G. van Oordt, *Z. Anorg. Chem.* **44**, 341 (1905).
23. a. W. Nernst and F. Jost, *Z. Elektrochem.* **13**, 521 (1907). b. F. Jost, *Z. Anorg. Chem.* **57**, 414 (1908).
24. F. Haber and R. Le Rossignol, *Ber. Bunsenges. Phys. Chem.* **40**, 2144 (1907).
25. G. Haber and R. Le Rossignol, Z. Elektrochem. **14**, 181, 513 (1908).
26. F. Haber, *Funf Vortrage*, Julius Springer, Berlin (1924); *Aus Leben und Beruf*, Julius Springer, Berlin (1927).
27. F. Haber, *Z. Elektrochem.* **16**, 244 (1910).
28. A. Mittasch, *Geschichte der Ammoniaksynthese*, (1951); Early studies of multicomponent catalysts, *Adv. Catal.* **2**, 81 (1950).
29. Lutz F. Haber, *The Chemical Industry 1900-1930, International Growth and Technological Change*, Oxford University Press (1971).
30. H. Heinemann, *A Brief History of Industrial Catalysis, Catalysis, Science and Technology* (J. R. Anderson and M. Boudart, eds.), Vol. 1, p. 1, (1981).

2

PREPARATION AND ACTIVATION OF THE TECHNICAL AMMONIA SYNTHESIS CATALYST

Robert Schlögl

2.1. INTRODUCTION

This chapter may be opened by two statements from the scientific literature.

> "The active catalyst for the ammonia synthesis is alpha iron with small amounts of oxidic additives. ... The quality of the final catalyst is crucially influenced by the activation process which is the reduction of magnetite to metallic iron. It is important to minimise the concentration of the reaction product water which is a catalyst poison."[1]

> "... shows how the pore size distribution of the KM 1 catalyst varies with reduction temperature. ... The peak of small pores represents a pore system formed by the reduction of magnetite, while the system of larger pores is formed by the reduction of wustite ... the surface area of the catalyst reduced at higher temperature is smaller than of that reduced at a lower temperature."[2]

Just these two statements are sufficient to emphasize the complexity of the process of activation of the technical ammonia synthesis catalyst. This process is essentially the reduction of iron oxides to iron metal using synthesis gas mixtures. Each catalyst is delivered to the customer with detailed descriptions of the reduction parameters. These describe a temperature program ranging from room temperature to ca 790 K which extends typically over 50–120 hours and they further contain a set of specified boundary conditions such as space velocity, pressure, and exit water content. In order to simplify the start-up of a fresh catalyst the reduction process may now be split into a prereduction at the catalyst factory, followed by

Robert Schlögl • Fritz-Haber-Institut der Max-Planck-Gesellschaft, Faradayweg 4–6, D-1000 Berlin 33, Federal Republic of Germany. *Present address*: Institut für Anorganische Chemie, Universität Frankfurt, Niederurseler Hang, D-6000 Frankfurt 70, Federal Republic of Germany.

a short, final activation in the ammonia converter. The prereduced catalyst is protected with a thin oxide layer generated by controlled oxidation at ca 400 K.

These sets of parameters appear to be rather arbitrary and may have been established by empirical methods.[2] It is the purpose of this chapter to describe some of the underlying solid state chemical principles which will allow us to systematize the complex phenomena of activation. A description of the resulting micromorphology will be followed by an analysis of the activated surfaces. The properties of the resulting gas-solid interface, as described by elemental and structural compositions and their changes with time, determine the usefulness of the activated catalyst. Finally, an empirical model of the active catalyst surface is presented which provides the basis for the discussion of the process of ammonia synthesis in terms of a comparison between the technical catalyst and model surfaces based on single crystals of iron.

The strategy adopted in this chapter is to describe the type of information which can be obtained from a variety of analytical techniques. These techniques have been applied to a set of different industrial catalyst samples. The discussion will focus on only the qualitative results which were common for all samples. It is beyond the scope of this chapter to make a detailed analysis of the significant quantitive discrepancies found with different catalysts. It should be stressed that although such differences between the catalysts were large for bulk-sensitive properties, they were generally less pronounced in the properties of the outer (geometric) surfaces which are probed by surface-sensitive analytical methods, e.g., electron spectroscopy.

2.2. THE CATALYST SYSTEM

2.2.1. Choice of the Material

The present, doubly promoted iron catalyst emerged from extensive exploratory research that was guided by the need to choose the material which is most active for the forward reaction of nitrogen hydrogeneation, least active for the reverse reaction of ammonia decomposition, and which would be reasonably resistant toward poisoning.[3,4] The term "doubly promoted" designates an iron-based material which contains textural or "structural" promoters such as oxides of aluminum, calcium, and silicon as well as electronic promoters such as potassium-oxygen compounds. The textural promoters are characterized by their ability to form substitutional spinel-type ternary oxides within the inverse spinel structure of the host precursor magnetite (Fe_3O_4).[5] The potassium cation, K^+, has an ionic radius of 133 pm, which is comparable to the radius of the oxygen anion. Hence, substitution within the spinel structure is excluded, with the result that preferred segregation of this promoter as a binary compound occurs on the surface of the catalyst. It is concluded that solid solubility and segregation during activation or operation of the catalyst are important factors determining the effects of textural promoters in the catalyst system.

A typical chemical analysis of the catalyst precursor yields the following values: Fe_3O_4, 94.3 wt%; K_2O, 0.8 wt%; Al_2O_3, 2.3 wt%; CaO, 1.7 wt%; MgO,

0.5 wt%; SiO_2, 0.4 wt%.[1] The relative amounts of the additives have been optimized according to their apparent effectiveness. The textural promoters increase the specific surface area of the activated catalyst, which varies from a few $m^2\,g^{-1}$ for unpromoted oxide up to ca 18 $m^2\,g^{-1}$ for a promoter concentration of ca 2.5 wt%.[6] Aluminum oxide is the most efficient promoter oxide, followed by the oxides of magnesium, calcium, and silicon.[7] Larger amounts of textural promoters tend to decrease the surface area.[8] The maximum solubility of aluminum in solid solution in Fe_3O_4 is approximately 3% and this has been shown to be due to segregation of aluminum oxide.[9] The addition of potassium oxide increases the specific activity of the catalyst. The enhancement passes through a sharp maximum for amounts greater than ca 0.8 wt%. This has been ascribed to excess coverage of the surface with more than a monolayer of the potassium component and implies blocking of the active iron sites.[10,11] These results indicate that the mode of operation of the textural promoters is determined by their presence in the bulk of the material, where they help to form or stabilize both the pore and grain structures of the reduced material. Thus, activation needs to preserve the location of these oxides where they have been placed during the fusion step in the formation of the precursor. The small amount of the potassium compound and its slightly negative effect on the pore structure point to a different mechanism of promoting the ammonia synthesis activity, which indeed requires its presence as a surface compound. Activation needs to facilitate a high dispersion of the potassium on the reduced surface. The lateral distribution of the various promoters will be discussed in more detail in section 4.

2.2.2. How Important Are the Promoter Additives?

This section aims to answer the question whether it is necessary to include the promoters in any discussion dealing with the understanding of the complex reduction process of iron oxide to iron metal, or whether it is sufficient to treat their presence as no more than a side effect. This includes, of course, the question of the possible action of the promoters during the reduction process i.e., the promoters may promote the formation of active sites, rather than the rate of each turnover of a nitrogen molecule into product ammonia. As mentioned in the introduction, the structural promoters Al, Ca, and Mg generate and stabilize the pore structure, leading to a large, free iron surface in the final catalyst.[6,8] This effect requires modification of the topochemistry of the reduction process. Subsequent to activation, the active surface area of magnetite promoted with 2.5% alumina is about 20 times larger than that of pure magnetite. It is therefore clear that the mode of action of the structural promoter must be included in the discussion of the activation chemistry.

On the other hand, the effect of the electronic promoter, potassium, has been shown to be related to the kinetics of ammonia formation. Addition of 0.5% potassium oxide to the Fe-alumina catalyst resulted in a decrease in the free iron surface from 40% to ca 35% and an increase in the ammonia yield at 613 K from 0.2 mol% to 0.34 mol%. The surface fractional coverage was determined by chemisorption methods to be ca 25%.[10] This leads to the conclusion that potassium

exhibits no significant effect on the activation process itself provided it is present only as a surface compound which does not block the pore structure.

A most important result of the presence of promoters is the dramatic increase in long-term stability of catalytic activity, which is of fundamental as well as obvious practical importance. All attempts to determine the intrinsic catalytic activity of pure elemental iron under high-pressure conditions in a flow reactor are severely hampered by the pronounced sensitivity of pure iron towards contamination, and this prevents reliable steady-state measurements. Promoted iron is, on the other hand, stable in its catalytic activity for up to several years on stream.

This effect is illustrated in Fig. 2.1. The catalytic activity, normalized to the free iron surface as determined by chemisorption of carbon monoxide, is compared for different catalysts under identical testing conditions. The spread in maximum activity was large for the pure iron samples but very small for the commercial catalyst (see error bars in the figure). The rapid deactivation of unpromoted iron is evident. Activation of the commercial prereduced oxide catalyst precursor under the chosen operational conditions is far slower than under optimized conditions, but it leads to steady-state operation of the catalyst. A pulse of oxygen gas, which is an efficient temporary poison for the commercial catalyst, initially boosts the activity of the pure iron by increasing its surface area through oxidative etching. In the longer term this enlarged surface is, however, rendered more susceptible to deactivation.

In summary, the description of the activation process needs specifically to include the effects of the structural promoters on the evolution of the bulk structure

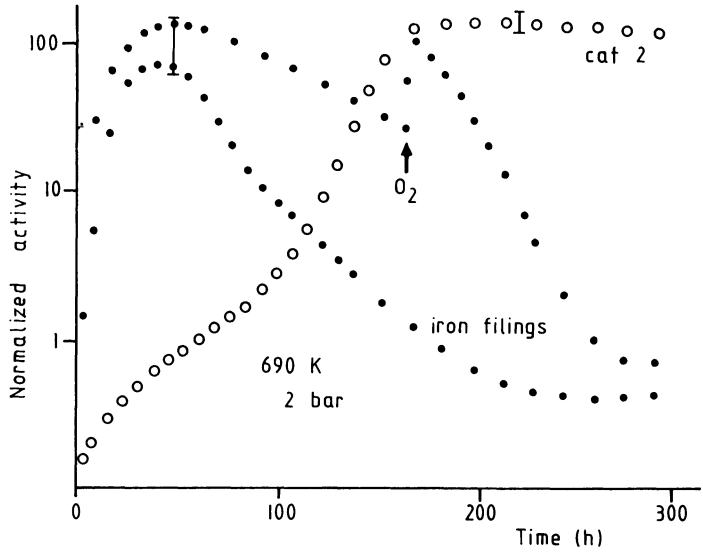

Figure 2.1. Ammonia synthesis over pure iron filings characterized by XRD and XPS and over a prereduced industrial catalyst. The activity is normalized to an equal free iron surface determined by CO adsorption. The error bars denote the spread in reproducibility. The oxygen pulse was applied for 1 min.

and surface texture of the reduced catalyst. Their presence is not merely a side effect of only technical importance but it is also of fundamental relevance.[12] The presence of the potassium promoter will be taken into account in the description of the surface chemical properties of the product of activation.

2.3. THE PRECURSOR OXIDE MIXTURE

2.3.1. Structure of the Catalyst Precursor

The catalyst components are mixtures of oxides which have been fused in an electric arc furnace at temperatures of ca 2000 K. The resulting large blocks of black hard material are broken into lumps of usually ca 1 cm diameter. The visual homogeneity of these lumps is, in general, a good indicator for the quality of the final activated catalyst. Poor catalysts exhibit white spots of segregated promoter oxides and bubble holes caused by evaporation of impurities during the fusion process. Primary sources of iron can be iron ores, scrap metal, or iron oxides (oxyhydrates) from other industrial processes. Potassium is added as potassium carbonate, nitrate, or potassium hydroxide, aluminum as alumina and calcium as oxide or carbonate.

Regardless of the experimental technique or the level of resolution, investigation of these catalyst lumps shows the heterogeneous nature of the material. While chemical and structural heterogeneity down to a level of several hundred microns is undesirable, microheterogeneity is a genuine feature of this unsupported catalyst material. Macroheterogeneity serves as reservoir for contamination and leads to mechanical disintegration of the catalyst which disturbs the gas flow pattern, thus reducing the total conversion in a reactor. This phenomenon is also observed in microreactor studies. Furthermore, when studying the bulk properties of the catalyst, using techniques such as X-ray diffraction, chemical analysis, or kinetic experiments on the reduction process, sampling methods require great care. The data presented here were obtained using particles from 5 g samples of visually homogeneous material which had been crushed in a hydraulic press and sieved to yield a fraction of 0.75 to 1.0 mm particles. From the sieve fraction only particles of the same shape were manually selected. The refined particles were then crushed in a mortar to yield less than 2 g of particles of the desirbed final grain size (usually 50 microns).

In the following discussion the X-ray diffraction (XRD) patterns of a series of six industrial catalysts are compared. High-resolution scans were obtained with monochromated Co radiation on a transmission Guinier diffractometer. Phase analyses were carried out on an automated Phillips APD 10 powder diffractometer using postmonochromated Cu radiation. In Fig. 2.2, relevant sections of the diffraction patterns of catalysts from three industrial sources are displayed. The observed reflections can be assigned to magnetite and wustite as the main components of the catalysts. The catalysts differ markedly in their content of crystalline wustite. It should be stressed here that XRD is not a suitable method for quantitative determination of the wustite content, since it depends on the crystallinity of the phase analyzed. The nonstoichiometric nature of wustite and its close structural

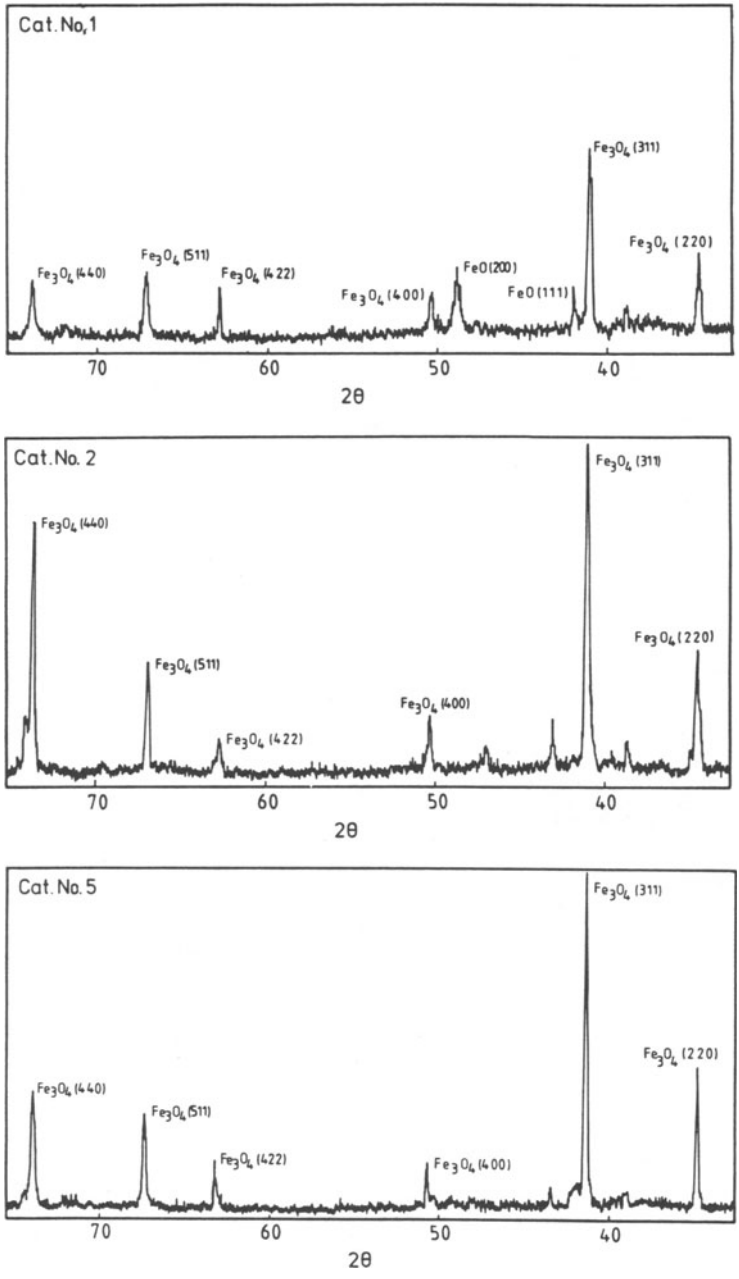

Figure 2.2. Guinier transmission diffraction patterns of industrial catalyst precursors using monochromated Co K α-radiation.

relationship to the magnetite host lattice may result in the presence of large amounts of X-ray amorphous wustite, which can only be determined by Mössbauer spectroscopy.[13,14] The presence of X-ray amorphous material in large amounts in samples 1 and 2 and in small amounts in sample 5 can be seen from the weak broad structures in the background of the diffraction patterns. The magnetite patterns are modified in terms of the relative intensities of some of the bands by the texture of the material [compare, for example, the intensity ratio of the reflections (440) to (311) which, in sample 5, is close to the expected ratio for random orientation]. The texture is not a sample preparation artefact but was found to be characteristic of each of the different batches of industrial catalysts.

The fine structure on some of the magnetite reflections, together with the deviations in the lattice constants derived from the different patterns, point to the presence of a solid solution of iron aluminum spinel hercynite ($FeAl_2O_4$), which has also been noted in previous X-ray studies.[15-17] The presence of aluminum within the magnetite lattice has also been shown by Mössbauer spectroscopy; the B-site magnetic subspectrum of magnetite is significantly broadened and asymmetrically deformed.[13] The stability of the alumina in solid solution in magnetite depends on the preparation and subsequent treatment of the catalyst. Thus, different catalysts show different degrees of decomposition (exsolution) which can be monitored by X-ray diffraction. The primary homogeneous solid solution with an overall stoichiometry given by the chemical analysis decomposes into pure magnetite, which has the largest lattice constant in the binary system magnetite—hercynite, of $a = 840.4$ pm. Other products include crystals with a larger aluminum content than the average composition which have successively smaller lattice constants (in hercynite $a = 813.5$ pm). These exsoluted phases give rise to structures at higher 2θ values than expected for pure magnetite. In Fig. 2.3, a collection of high-resolution scans of "magnetite" reflections of different catalysts is shown, which underline the strongly varying degree of exsolution and thus microheterogeneity in different precursor materials.

The dependence of the lattice parameter on the stoichiometry of the spinel phase can be used to determine the integral content of alumina within the magnetite lattice, and this is demonstrated for the present samples in the graph of Fig. 2.3. Also included are some reference data[15] which correspond to magnetite (M) singly promoted with 1%, 2%, and 3% of alumina. Unfortunately, this method is not unambiguous with multiply promoted samples, since calcium tends to enlarge the lattice constant in almost the same way as alumina reduces it. The reason for this difference is the different charge-to-radius ratio for the two cations, which leads to a net lattice expansion for the incorporation of the large calcium atom into the octahedral sites and to a net contraction for the presence of the small aluminum atom, also in the octahedral sites. The small values for the lattice contraction found for the industrial catalysts is consequently not a sign of minor incorporation of alumina into the magnetite lattice of the doubly promoted industrial catalysts in comparison with the singly promoted laboratory samples [a value between M1 and M2 (singly promoted magnetite with alumina; see the figure caption) is expected for all technical samples 1 to 5]. Alternatively, it reflects the simultaneous presence of calcium and aluminum in almost equivalent amounts in

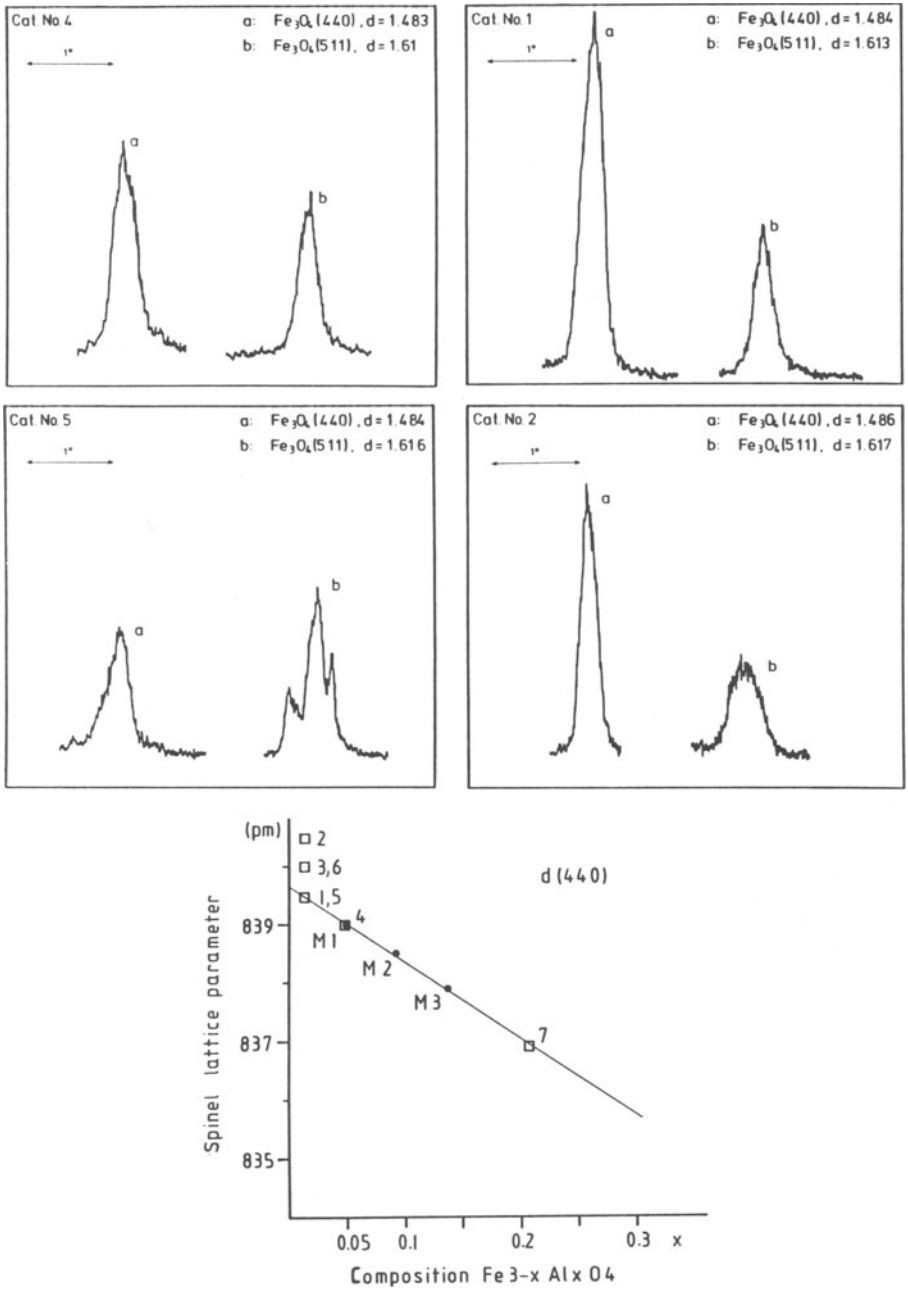

Figure 2.3. High-resolution scans over characteristic spinel reflections of some catalyst precursors using the Guinier transmission geometry and monochromated Co radiation. The graph indicates the dependence of the spinel lattice parameter determined from the dependence of the spinel lattice parameter determined from the (440) reflection on the aluminum content built into the lattice. Note that all catalyst samples contain nominally the same amount of aluminum. Lattice parameters above the line indicate the presence of an excess of calcium besides aluminum. The data M1–3 are pure alumina spinel samples.

sample catalysts 2, 3 and calcium in somewhat smaller amounts than aluminum in catalysts 1, 4, 5. Sample 6, which nominally contains only potassium as promoter, exhibits a larger lattice constant than that of pure magnetite that indicates the presence of calcium as impurity. This was later established in an EDX analysis of activated samples. The precise determination of the lattice constant is useful because it is sensitive to the effective amount of structural promoter incorporated in the lattice, while chemical analysis cannot discriminate between effective ternary componends and the ineffective binary oxides.

Singly promoted catalysts, i.e., samples of magnetite, alumina, or magnetite potassium oxide, were used to elucidate the effects of textural and electronic promotion, respectively. In Fig. 2.4, the phase composition and the crystallinity of a doubly promoted sample (catalyst 3) are compared with a sample singly promoted by alumina (catalyst 7) and a second sample, singly promoted by potassium (catalyst 6). All samples were prepared from the same iron oxide precursor and synthesized under identical conditions according to the specifications of the manufacturer. The sample, catalyst 7 (2.2% Al), consists of almost equal amounts of well-ordered magnetite and less well crystallized wustite and exhibits effects due to the texture [compare intensities of the (511) and (440) reflections]. Promotion by potassium alone (catalyst 6, 0.7% K) did not lead to the formation of large amounts of wustite but caused the crystallinity of the magnetite to decrease. The intensity ratios of the magnetite reflections are considerably different from those of the aluminum promoted sample indicating again texture effects with a preferred orientation similar to that seen in catalyst 1. The doubly promoted sample exhibits a magnetite diffraction pattern which is not, however, a simple superposition of patterns from the two singly promoted samples. The texture is the same as in the pattern of the alumina promoted sample. It is beyond the scope of this chapter to discuss the quantitative differences. It is demonstrated, however, that XRD can pick up structural differences of catalyst precursors made from the same iron source under nominally identical conditions. If such samples were activated under the same reaction conditions, it would be difficult to compare their catalytic performance in terms of direct promoter influence only, since these samples may yield catalysts with entirely different textures as well as different surface species.

If the phase analysis by XRD is carried out with much better counting statistics, a large number of additional weak reflections are observed and can be assigned to a variety of ternary oxides, such as hercynite or $CaFe_3O_5$, and to binary compounds such as CaO. Frequently, the presence of potassium bicarbonate, the decomposition product of all potassium compounds in the system after prolonged exposure to air, can also be detected. The diffraction pattern of catalyst 3 shown in Fig. 2.5 was obtained after 110 hours of data accumulation from a prereduced sample. It accounts for the presence of free α-iron. It is pointed out that in this prereduced sample, a significant amount of crystalline wustite is still present. The importance of the coexistence of magnetite, wustite, and α-iron within a single sample will become apparent in the discussion of the reduction mechanism. The wustite must be present in the precursor or have been formed in the prereduction process, since reoxidation of iron leads directly to the formation of magnetite. The

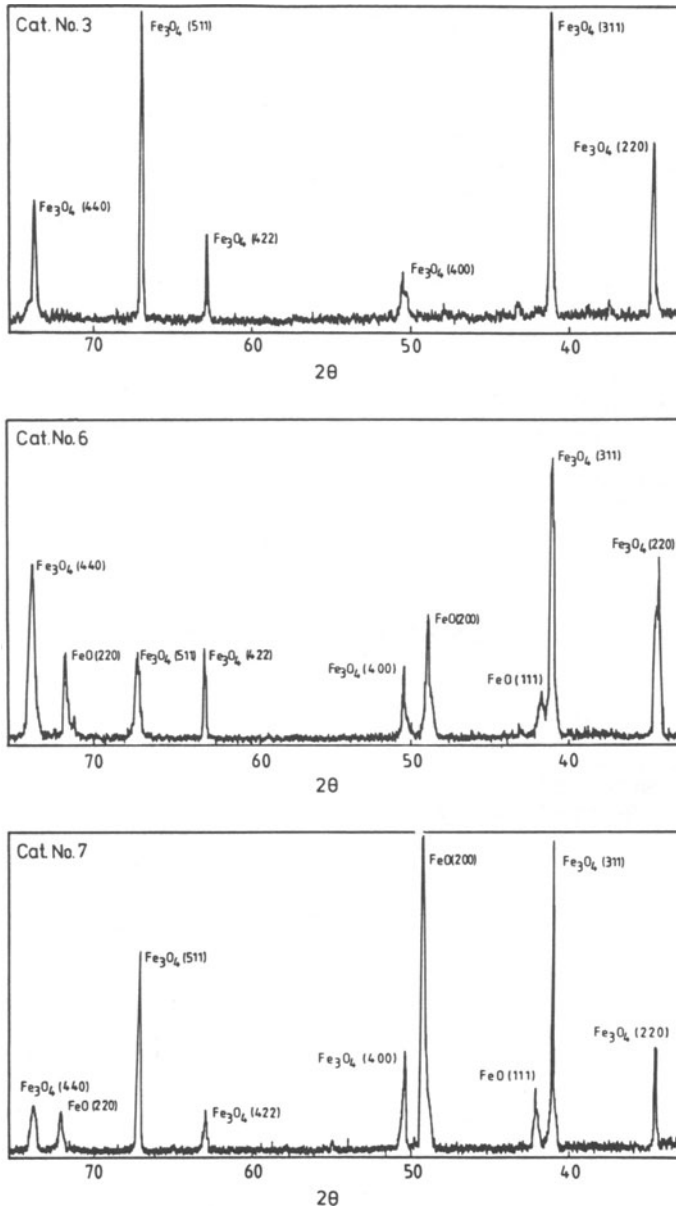

Figure 2.4. Guinier transmission scans (Co K α-radiation) of a set of differently promoted catalysts prepared from the same iron oxide. Catalyst 3 is nominally doubly promoted, containing extra calcium and silicon, catalyst 6 is singly potassium promoted, and catalyst 7 is singly alumina promoted. Both single promoted samples contain also calcium impurities.

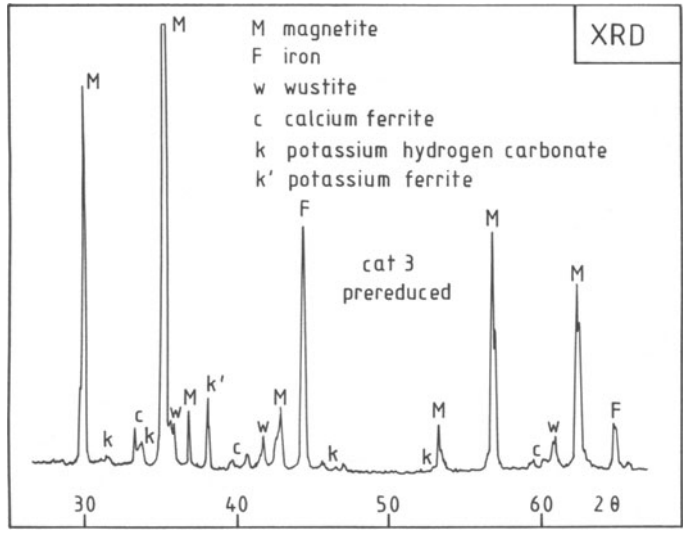

Figure 2.5. Phase analysis of a prereduced sample of catalyst 3 using postmonochromated Cu K α-radiation and a standard reflection geometry.

assignment is not unambiguous since textural effects and nonstoichiometry render a straight comparison with JCPDS reference data difficult. Different catalyst samples and even different lumps within the same catalyst batch exhibit marked differences in these weak lines, as would be expected from the heterogeneity mentioned previously.

The description of the structure of the catalyst precursor would be incomplete without mentioning the presence of noncrystalline material. Using optical microscopy with polarized light, amorphous patches can be detected in polished catalyst samples. EDX showed that such areas are rich in promoter oxides and represent inclusions of unreacted starting materials or of promoter material segregated during the initial high-temperature processing of the precursor. The phase may further contain some wustite which is strongly disordered, due to its metastable nature.

It should be pointed out here that areas of amorphous or "glassy" material can also be found in reduced catalysts (see later in Section 2.6). This material, which is also rich in promoter oxides, remains therefore unreduced in the activation process but is, in contrast to the large inclusions in the catalyst precursor, very finely divided between the iron crystallites. Using selected area electron diffraction, it can be identified as a mixture of a highly defective spinel phase with a truly amorphous (ring pattern) phase. The nature of this material, which seems to be a common ingredient in all types of iron catalyst, is difficult to assess because of the notorious analytical difficulties presented by amorphous minor phases. It may, however, play an important role for the operation of the catalyst in acting as an inert spacer material between active iron particles. This role will be further discussed in the final section of the chapter.

In summary, we see that the catalyst precursor consists of the dominant phases, magnetite and wustite, within small amounts of various ternary iron oxides and binary promoter additives. The crystallinity and texture of the samples differ widely. It is concluded that the initial solid state for the reduction process catalyst of activation is inhomogeneous for a given catalyst. It is further concluded that it is difficult to derive characteristic differences for a set of catalysts from XRD alone and also that very accurate quantitative chemical analyses are of limited value only, since they will not necessarily be representative for the catalyst charge as a whole.

2.3.2. The Morphology of the Precursor Catalysts

Surface areas of the precursor oxides by the BET method are usually low, with characteristic values of 0.15–0.7 $m^2 g^{-1}$ found for the samples used in the present work. These values exclude any pores in the meso- or microrange, and only compact particles with some large intergranular voids as the characteristic texture are expected. This is in line with earlier porosimetry studies[6] which revealed only pores of several microns to be present.

The morphology of unreduced catalysts has been studied using both the SEM technique[11] and with TEM.[2,18] All data show that unreduced catalysts exhibit dense surfaces having no pore structure within a single granule. The shapes of the granules differ for different catalysts. Those which exhibit texture effects by XRD also show texture in their behavior toward fracture. They consist of platelets—like granules of approximately micron size, which are frequently covered with segregates of ternary oxides appearing as bunches of needles of ca 500 nm size.[11] Catalysts with little texture effects, such as sample catalyst 2, fracture more isotropically and exhibit spherical granules with a microstructure of small and very thin platelets. The microheterogeneity in all samples is expressed by the variety of small ternary oxide particles (as shown by EDX analysis) and is also reflected in the lateral distribution of elements at the surface, which is strongly enriched in promoter elements[11,19] (see Section 2.7).

In summary, morphological investigations show that the precursor oxides consist of dense granules of iron oxides with some of the promoter oxides enclosed. Their surfaces are enriched with promoter oxides in both binary and ternary forms. This enrichment can be detected at the level of a few monolayers with inhomogeneous lateral dispersion, as well as the agglomeration of crystallites of ternary oxides. This suggests that the promoter oxides are enriched, at least in part, at the boundaries of the individual granules as exsoluted crystals from the initial bulk solid solution. The shape of the granules is different for different degrees of anisotropy of the oxide matrix, as is evident from the texture effects observed in the XRD data. All catalysts exhibit as their ultimate microstructure stacks of platelets, with typical lateral dimensions of 150 nm and a typical thickness of 15 nm.

2.4. SOME UNDERLYING PRINCIPLES OF ACTIVATION

Catalyst activation is a complex sequence of gas-solid reactions of

inhomogeneous mixtures of magnetite and wustite with ternary oxides formed by reaction with the additives. In the following section the structural chemistry of the various oxides is described briefly, together with the iron–oxygen phase diagram and the mechanism of magnetite reduction as established by metallurgists for the model reduction of magnetite ores with hydrogen.

2.4.1. The Structural Chemistry of the Precursor Oxides

Magnetite is a ferromagnetic and electrically conducting iron oxide with the composition 72.4 wt% Fe and 27.6 wt% O. It crystallizes in a cubic structure of the inverse spinel type. The structure is described on the basis of the crystallographic unit cell illustrated in Fig. 2.6. The formula of the unit cell is $Fe_8Fe_{16}O_{32}$. The spinel structure is built from three elements: a large face-centered cube of Fe-8 ions containing in its equally divided volume four smaller cubes of 4 Fe-16 and 4 O together with four tetrahedra of Fe-8 and 4 O. The unusual transport properties of this oxide arise from a fast valence fluctuation of the Fe-16 iron atoms, which exchange their valency between Fe^{2+} and Fe^{3+}. The Fe-8 ions are trivalent. The valence fluctuation of the Fe-16 ions, which is energetically favored by a significant ligand field stabilization energy of Fe^{2+} in octahedral sites (d-6 system), explains why the Mössbauer spectrum at 300 K[13] of magnetite shows only two species (Fe-8 and Fe-16) rather than the expected three, which can only be observed below 120 K where a phase transition freezes the electron hopping process.

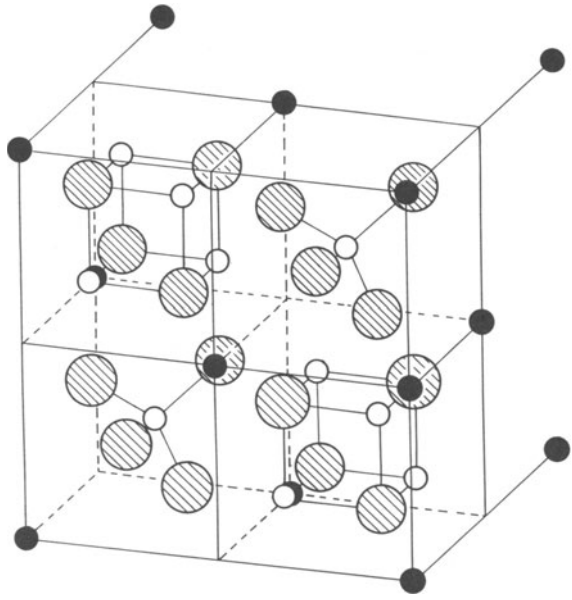

Figure 2.6. Crystal structure of magnetite. The spinel structure is shown in a representation describing the crystallographic unit cell (large cube). The iron and oxygen atoms are shown in their relative sizes.

Wustite is a nonstoichiometric microheterogeneous solid. Its idealized structure is rather similar to the magnetite structure. Both lattices are built from a cubic, close packed, oxygen lattice with the iron ions located only in octahedral voids for wustite, and in both octahedral and tetrahedral voids for magnetite. Wustite is thermodynamically metastable below 833 K but can be easily supercooled to room temperature. The composition of the material is variable and always deficient in iron: $Fe_{1-x}O$ with x varying from 4.5% to 11%. Electroneutrality is preserved by the presence of Fe^{3+} ions. These ions and the holes in the iron sublattice are not statistically distributed throughout the material but form a variety of clusters centered around the ferric ions placed in tetrahedral interstitial sites.[20,21]

Hercynite, $FeAl_2O_4$, is an example of the normal spinel structure which is also built around a cubic, close packed, oxygen sublattice. The cation distribution within the magnetite model is as follows: Fe-8 ions form the large cube and occupy the four tetrahedra and Al-16 ions occupy the four cubes. This coordination, which forces Fe^{2+} ions in tetrahedral positions, is caused by the large charge-to-radius ratio of the strongly polarizing Al^{3+} ion, which gives rise to a large lattice energy contribution to the octahedrally coordinated aluminum ions.

The other ternary oxides also occur as spinel superstructures such as $CaFe_2O_4$ (ferrite) or potassium iron oxides which contain the spinel structure as a building block. These complex structures of the beta alumina type consist of the formal composition ($K_2O \times 11\ Fe_2O_3$) and can be described as a layer structure with unit cells of spinel linked by layers of potassium ions octahedrally coordinated to the (4 + 4) oxygen ions of two adjacent spinel units.

In summary, it is seen that the crystal structures of all compounds relevant to the catalyst precursors have the same anion sublattice and are closely related to one another. This is the reason for the miscibility of all the compounds, where little internal stress is introduced into the whole structure and explains the relative stability against segregation. This concept is illustrated by the complete solubility range of alumina in magnetite giving rise to a relationship of the Vegard law type between the lattice constants of magnetite and hercynite (see Fig. 2.3). The structural complexity and microheterogeneity of the precursor oxides can be regarded as arising from the flexibility of the spinel structure to accommodate different cation distributions as well as superlattices and ordered defect structures.

2.4.2. The Iron–Oxygen Phase Diagram

A section of the iron–oxygen phase diagram is shown in Fig. 2.7. The dashed line represents a typical path for the manufacture and activation of an ammonia synthesis catalyst. All effects due to the promoter are omitted.

Manufacture of the catalyst starts from a hematite-based material (h) which is fused in the electric arc furnace above the solidus maximum of 1597 °C. Hematite does not form congruent melts but decomposes into a solid solution of magnetite (m) and oxygen. Some of this oxygen is lost from the melt into the atmosphere above the liquid. The process is sufficiently controlled to reach a composition which, after cooling to below 1400 °C, falls into the region for the coexistence of both magnetite and wustite (w). Rapid quenching to below the disproportionation

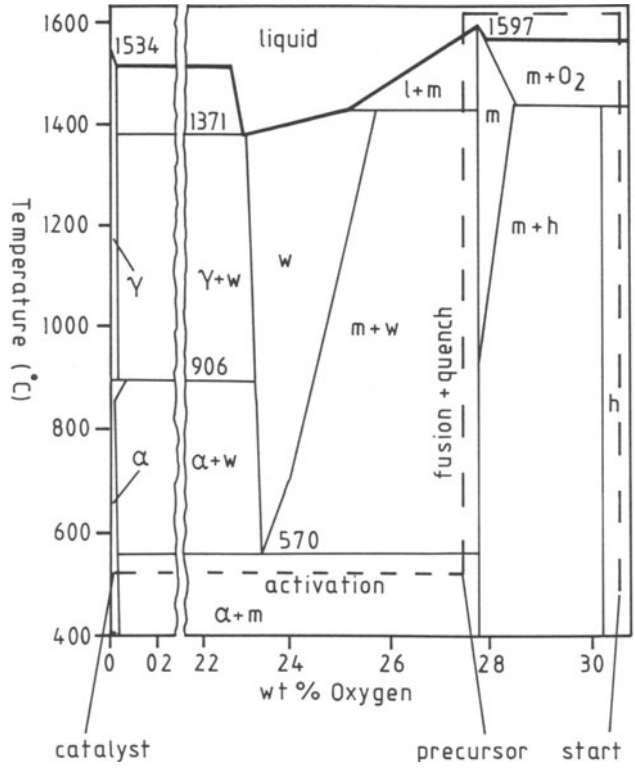

Figure 2.7. Section of the iron–oxygen phase diagram: "m" denotes magnetite, "h" hematite, and "w" wustite; α and γ stand for these modifications of iron metal. The dashed line describes the path of synthesis of the ammonia catalyst in the phase diagram.

temperature of 570 °C leads to the precursor oxide mixture, which is a supercooled solid solution of wustite in magnetite. At the temperatures employed for the reductive activation of the oxide, wustite is unstable with respect to a disproportionation reaction leading to another solid solution of α-iron (α) in magnetite. The activation process reduces the oxygen content by chemical means (formation of water with hydrogen) to such an extent that the final product is essentially pure α-iron.

The phase diagram shows some further relevant details. The solubility of oxygen in iron is very low (about 0.03 wt% up to 600 °C) which is a consequence of the high affinity of iron for oxygen to form oxides. Furthermore, we see in the whole range of compositions between the precursor oxides and the final catalyst, complete stability in all mixtures of metal and the oxide, magnetite. An intermediate phase with a composition between that of iron metal and wustite is thermodynamically unstable, from which it is concluded that an activation process under equilibrium conditions would involve a direct transition of magnetite into iron metal.

The metastable wustite can decompose at any temperature between room temperature and 570 °C into iron and magnetite according to the equation

$$4FeO \rightarrow Fe + Fe_3O_4$$

without the evolution of oxygen. This means that simple annealing of the precursor mixture under any atmosphere can generate iron metal nuclei from finely divided wustite inclusions. Pure wustite is not stable under the conditions of ammonia synthesis or activation of ammonia synthesis catalyst precursor. This is reflected in the poor crystallinity of the wustite (quenching) seen in the XRD analysis. Solid solutions of hematite and magnetite or of γ-iron (γ) and wustite are of little relevance for technical ammonia synthesis catalysts or technical precursors. The unusual shape of the region which covers the conditions required for the existence of wustite is due to the temperature-dependent nonstoichiometry which has been described in the literature.[20,21] This is of relevance, since the details of the cooling process of the precursor melt determine the nonstoichiometry of the wustite inclusions. The stability of wustite is strongly dependent on its nonstoichiometry, and is reflected in the variation of its heat of formation from 265.44 kJ mol^{-1} for $Fe_{0.947}O$ to 319.87 kJ mol^{-1} for $FeO_{1.20}$.[22] This stability determines the temperature required for the decomposition process and hence the conditions of formation of α-iron nucleii from wustite.

Finally, it should be kept in mind that the application of the phase diagram for prediction of phase composition is only valid for equilibrium conditions. The precursor oxide mixture is, however, metastable and, furthermore, contains impurities (promoters) which may affect activation, so that the process is not always carried out under equilibrium conditions. This makes it possible for solid solutions of α-iron, wustite, and magnetite to exist as metastable forms of the catalyst. The phase boundary from pure iron to such a solid solution is so sharp, and the region for the existence of pure iron so small, that very precise methods of analysis of the final catalyst will be required to determine whether the active form of the catalyst is pure iron or any of the contributing solid solutions.

2.4.3. The Mechanism of the Reduction of Magnetite

The mechanism of the gas-solid reaction between magnetite and hydrogen has been studied in great detail. The summary given here is based upon four studies[23-26] employing rate measurements, microscopy, and X-ray diffraction as the experimental techniques on both single crystals and powder briquets.

A common feature of all gas-solid reactions is that they are determined by several fundamental processes. The overall chemical reaction

$$Fe_3O_4 + 4H_2 \rightarrow 3Fe + 4H_2O$$

does not describe the reaction scheme and has no mechanistic relevance. The mechanism of magnetite reduction has been found to involve the formation of wustite as an intermediate product for each of the different precursors and reduction

conditions studied. Furthermore, it is now clearly established that the reaction is controlled by nucleation. This involves nucleation of wustite within the magnetite framework in addition to nucleation of alpha iron within the wustite intermediate phase. The nucleation process is entirely heterogeneous and consequently is highly sensitive to the structural perfection and the texture of the embedding matrix. In the case of the ammonia synthesis catalyst, three types of defects determine the nucleation process; (a) point defects in the oxides, (b) grain boundaries, and (c) related mechanical defects with inclusions of the promoters and iron (see below).

On the atomic scale, the reduction has been found to be controlled by two different processes. Metallic iron from wustite is formed through the direct chemical reaction:

$$FeO + H_2 \rightarrow Fe + H_2O$$

The kinetics of this thermally activated process (activation energy ca 65 kJ mol^{-1}) is governed in the initial phase by the chemical reaction rate and in the final stages of reduction by diffusion processes of hydrogen and water at the reaction interface.

The chemical reaction generates a gradient of ferrous ion concentration throughout the solid. This gradient leads to a rapid diffusion of ferrous ions from magnetite, through wustite, to the chemical reaction interface where they are reduced and precipitated as iron nuclei. This becomes an efficient process, due to the structural peculiarities of the spinel lattice described above, provided a certain number of defects is present. These defects are provided by the nonstoichiometry of the wustite. The precipitation of wustite nuclei at the reaction interface magnetite–wustite is now also believed to be caused by ion/electron diffusion processes rather than by direct contact of magnetite with hydrogen[27]:

$$O^{2-} + H_2 \rightarrow H_2O + 2 \text{ electrons}$$

$$Fe_3O_4 + Fe^{2+} + 2 \text{ electrons} \rightarrow 4FeO$$

This mechanism involving ion diffusion separates spatially the two processes of the generation of reducing electrons (reaction of hydrogen and oxygen), and the subsequent transfer of these electrons onto the species to be reduced (the iron ions). Such a complication of a simple chemical reaction is a result of the rigidity and density of the solid reactant, magnetite, which prevents direct access of the gaseous reactant hydrogen to the solid–solid reaction interface.

Turning to the macroscopic aspects of the reduction process, it has been noted that the porosity of the oxide, as defined by the percent of voids within a unit volume of magnetite, is a crucial parameter for the reducibility of an oxide. Reducibility may be defined as the time required to reduce a unit volume of iron oxide by 90% under standard conditions of temperature and gas flow. It is shown in Fig. 2.8a that the reducibility can vary over almost an order of magnitude with experimentally attainable variations in porosity. The shape of the curve suggests that two different reaction mechanisms for the extremes in porosity can exist. The catalyst precursors used in this study exhibit porosities below 5% when analyzed at room temperature. Thus, the following discussion concentrates on the mechanism appropriate to the low porosity extreme.

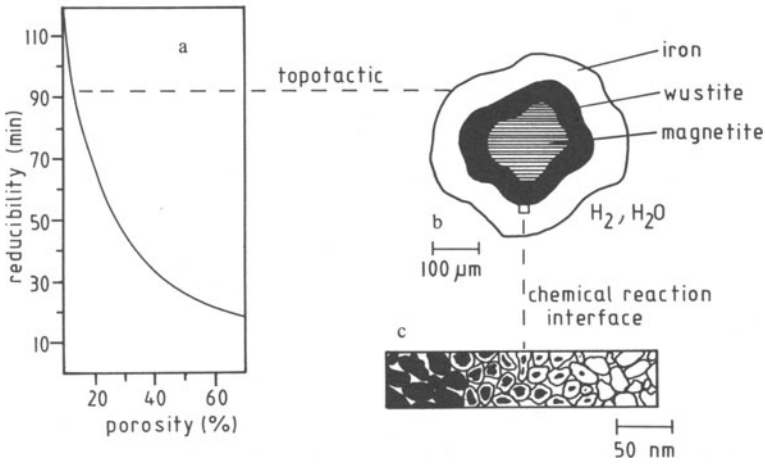

Figure 2.8. The mechanism of magnetite reduction: (a) describes the reducibility of a magnetite brick under standard conditions as a function of its porosity. In the range of poor reducibility the reaction is topotactic and leads to a core and shell structure visible in an optical microscope and shown schematically in (b). Section (c) describes the situation at the wustite-magnetite interface as can be seen in an electron microscope.

Of all iron oxides, the dense magnetite is the most difficult one to reduce. In the pyrometallurgical extraction of iron, such ores are therefore preoxidized to hematite before reduction. The conversion of hematite back to magnetite results in a 15% increase in volume due to the change from a hexagonal, close-packed lattice (hematite) into cubic close-packing (magnetite and wustite). This increases the fraction of voids improves the reducibility by ca a factor of two. The discrepancy between these facts and the low-temperature process for the activation of the dense magnetite catalyst precursors is apparent; we will return to it later.

From a large body of microscopic examinations of partially reduced dense grains of magnetite a topotactic reaction model has been derived, and is presented schematically for different levels of resolution in Figs. 2.8b, c. The term "topotactic" designates a reaction mechanism in which the spatial arrangement of the reaction interfaces is not random or defect-controlled, but is strongly related to the macroscopic edges of the reacting solid. The underlying principle is that topotactic reactions proceed by a lattice plane manner from the surface into the bulk, with reaction rates characteristic of the crystallographic orientation of the respective lattice planes.

The so-called core and shell model (Fig. 2.8b) suggests that a reacting magnetite grain consists of a core of dense unreduced magnetite, surrounded by a dense layer of the reaction intermediate wustite, which itself is surrounded by a porous layer of the final product iron. This layer forms the gas-solid interface for reactant hydrogen and product water. The product water is an efficient poison for the reaction since it reacts vigorously with the metallic iron interface to regenerate iron oxyhydroxides or magnetite, according to the temperature of the interface.

Water must therefore be removed from the reaction interface as quickly as possible to ensure net progress of the reduction process.

The magnetite-wustite interface is sharp even when observed at high resolution. The wustite-iron interface, however, is diffuse at higher resolution as illustrated in Fig. 2.8c. Close examination reveals that iron formation occurs through precipitation of iron metal nuclei, resulting from diffusion of hydrogen into the pores of the interface region followed by a slow growth of the nuclei. The lower rate of chemical reaction compared to the faster rate of the gaseous diffusion process causes the finite thickness of the diffuse interface.

If the reduction process is carried out at temperatures at which the new surface adjacent to the iron nuclei precipitated in the early stages of reduction can grow into large iron particles at the expense of nuclei precipitated later (Ostwald ripening), the remaining core of wustite becomes difficult to reduce. This is because access of hydrogen is prevented and the high degree of crystallinity of the iron slows down ion diffusion. Hence, the final stage of reduction is significantly slowed and total reduction may even be prevented. The temperature regime in which this unwanted Ostwald ripening occurs before the complete reduction of the wustite lies between 900 K and 1000 K. The phenomenon is called "recrystallization" in metallurgy and "sintering" in catalysis. Metallurgical reductions are therefore carried out above 1000 K (fast reduction, well-crystallized iron), while the catalyst activation process proceeds in a slow reaction, below the recrystallization temperature, in order to maintain small iron particles.

The situation described so far and the label "topotactic" is valid only if the starting magnetite grain is a single crystal. The pores shown in Fig. 2.8c are formed as a consequence of nucleation, together with the growth of many wustite and iron particles. The volume of the single crystal after reduction is typically 5% less than the starting material.

A catalyst particle is, however, a polycrystalline, sintered solid made up from oxide particles of ca 100 nm size, in which the following sequence of events will occur. It is pointed out that at low spatial resolution such a polycrystalline solid will show the same core and shell pattern, i.e., a partially reduced and cross-sectioned particle exhibits a layer of iron around a core of oxide.[28] The interface is, however, diffuse and ca 0.1 micron wide. In the initial phase, the ion diffusion mechanism will result in precipitation of a few nuclei at the most reactive sites of the solid, which are located predominantly at the grain boundaries of the magnetite single crystals. These nuclei will grow, and layers of wustite surround the magnetite crystals to mark, like a mosaic, the locations of the former magnetite grain boundaries. At this stage further growth is almost inhibited, and any new nuclei within the magnetite cores will be formed by the ion diffusion mechanism. Also, the initial hydrogen molecules can penetrate into the newly formed pores between the wustite crystals. Ion diffusion is hindered by the large number of grain boundaries formed and the material has a much smaller average particle size than the starting oxide.

Reduction of the wustite by hydrogen will also start at the most reactive sites, which are the small nuclei in the interior of the parent magnetite crystals. The first iron metal nuclei grow in the center of the magnetite crystals and the large wustite

crystals at the initial grain boundaries are the last part of the solid to be converted to iron. In the very final stage of reduction, iron crystals of about the same size and grain structure as the starting magnetite are seen, with small remnants of wustite and, ultimately, segregated impurities which decorate the initial framework.

Finally, the apparent contradictions on the direct application of the kinetic and mechanistic results from metallurgical studies to the case of catalyst activation will be discussed. The main points are: (1) the poor reducibility of dense magnetite vs the low activation temperature (kinetic) and (2) the clear reduction of the average particle size of the activated catalyst compared to the precursor oxide (mechanistic). This should not occur according to the multiparticle mechanism sketched above.

These discrepancies can be resolved by taking into account the fact that catalyst precursors are quite unlike the metallurgical test specimen. They do not consist of pure magnetite but contain metastable wustite and textural promoter oxides. The consequences arising from the different starting composition are illustrated in Fig. 2.9. The structural framework of magnetite is stable up to the reduction temperature of above 800 K. The catalyst oxide, however, contains wustite and ternary oxides precipitated at the grain boundaries. Upon slow heating the metastable solid solution is annealed, allowing the system to equilibrate. Thus, the wustite disproportionates into elemental iron nuclei and magnetite. If hydrogen is present at the wustite locations, one of the disproportionation products, magnetite, is chemically reduced to metallic iron using the other disproportionation product, iron, as nuclei. The fact that these nuclei are available at lower temperatures (ca 550 K) than those at which the bulk reduction of magnetite occurs, allows some shrinkage of part of the volume of the oxide, and thus enhances the formation of voids at the annealing temperature. This is illustrated in the bottom part of Fig. 2.9. The presence of wustite thus transforms the bulk magnetite, which

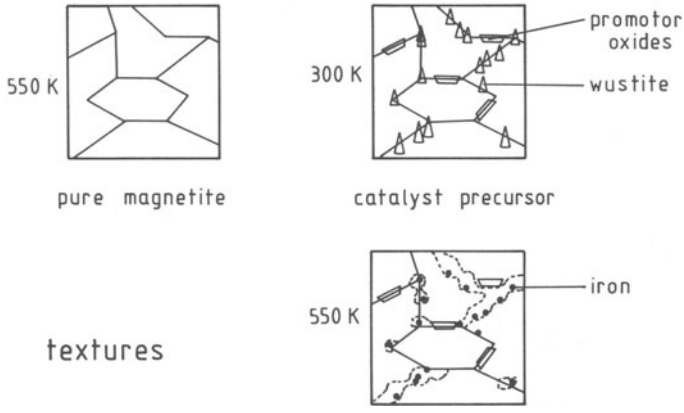

Figure 2.9. The textural difference between magnetite and the catalyst precursor. The prereduction of wustite opens up voids and provides nucleation centers for the main reduction, which starts at ca 550 K. The promoter oxides prevent the crystallites of iron oxide from growing into large homogeneous and thus unreactive crystals.

is dense at room temperature, into a porous magnetite at a temperature lower than that at which the bulk reduction process commences. It can be seen from Fig. 2.8a that even a comparatively small increase in porosity will greatly facilitate the reduction.

Increasing amounts of wustite in the precursor are therefore favorable, owing to their porosity-enhancing effect. Above an optimum concentration, however, any further increase in the amount of wustite will be detrimental. This is because a pore system which is too large will separate the individual crystallites of magnetite to such an extent that the fast ion diffusion mechanism is blocked. This, in turn, prevents the formation of intermediate wustite nuclei, resulting in an increase in the activation energy of the bulk reduction.

The second contradiction mentioned above, namely, the particle-size effect, can be attributed to the presence of textural promoters. We have seen from the X-ray analyses that textural promoters are present, with a wide range of particle sizes and compositions. The larger particles will be located between the magnetite crystals, as shown in Fig. 2.9, where their effect is to prevent aggregation of the magnetite crystals during annealing. They act as spacers which prevent any crystal growth during the removal of wustite. Alumina dissolved in the magnetite has to come out of solution during the formation of the intermediate wustite. As described above, this process reduces the average particle size, since several wustite nuclei grow within one magnetite crystal. The "nascent" alumina will thus precipitate, either as hercynite or as binary aluminum oxide, depending on the ion diffusion kinetics in the newly formed grain boundaries between the intermediate wustite crystallites, where it has the same spacer function as between the large magnetite grains. It therefore acts as a fixation agent for the fine textural framework which results as a consequence of the growth of intermediate solids in the reduction process. This redistribution may well benefit from the presence of water, which could help to segregate alumina chemically and which also slows the final chemical reduction.

2.5. THE ACTIVATION PROCESS

2.5.1. Some Typical Activation Experiments

The most obvious feature of the activation process is the evolution of water produced during the reduction of the iron oxide. The progress of activation can thus be studied by following the evolution of water during activation. In Fig. 2.10, two typical water evolution curves obtained from two different catalysts during activation in a test reactor for measuring reduction kinetics are shown. The activation was carried out with a hydrogen/helium mixture instead of the usual hydrogen/nitrogen mixture so as not to interfere with electrochemical detection of water by the product ammonia. The left-hand panel shows the temperature programs applied in accordance with the manufacturer's specifications. These specifications differ significantly for different catalysts. During our studies, it was found to be of crucial importance to follow these specifications in order to obtain a catalyst with a high, stable activity.

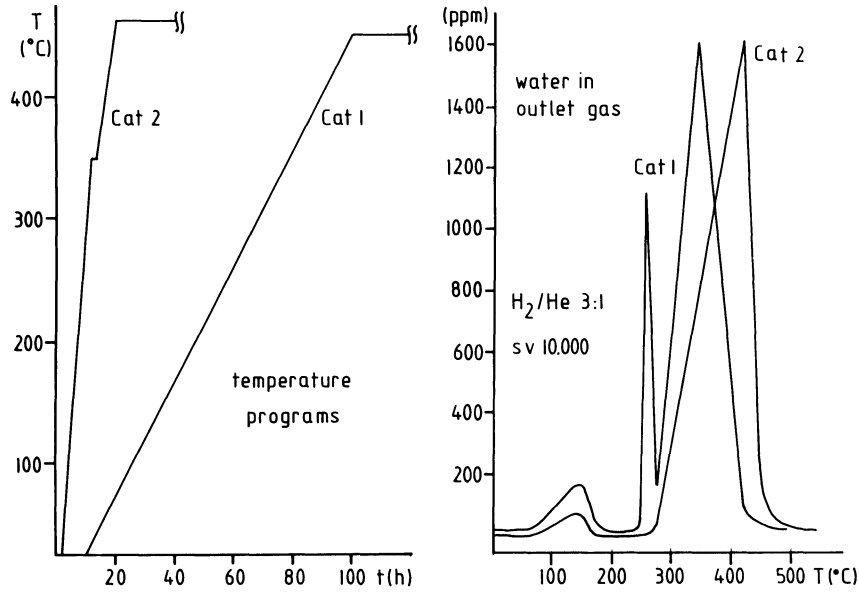

Figure 2.10. Activation of industrial catalysts. The left panel describes the temperature programs used, the right figure shows the evolution of the reaction product water with increasing temperature. The amount of catalyst was in all cases 0.6000 g.

Different water evolution profiles are characteristic for different catalyst types. A common feature is the loss of adsorbed water at ca 150 °C. The amount of water held at the surface of the oxide grains was also found to be characteristic for different catalysts. No correlation was found, however, between the BET surface of the precursor and the amount of desorbed water (catalyst 2 exhibited 0.5 $m^2 g^{-1}$ while catalyst 1 exhibited only 0.15 $m^2 g^{-1}$). The water evolution profile of catalyst 1 contains a sharp feature at 270 °C which is absent in the profile of catalyst 2. This feature is ascribed to the reduction of wustite that occurs before the bulk magnetite is attacked. From comparison of the temperatures at which reduction begins, it can be deduced that catalyst 2 contains almost no wustite. This is in good agreement with the XRD patterns shown in Fig. 2.2. The initial reduction of wustite has also been shown by Mössbauer studies of catalyst activation.[29] In this study of the activation of an industrial catalyst, the authors were able to derive activation energies for both wustite reduction (67–79 kJ mol^{-1}) and magnetite reduction (113–146 kJ mol^{-1}). Both increase monotonically with increasing extent of activation.

The main reduction process occurs at different temperatures for the two catalysts. The formation of voids and of iron nuclei by reduction of wustite is beneficial for the main reduction process, which is an expected consequence of the mechanistic model described above. Hence, the final annealing temperature is lower for catalyst 1 than for catalyst 2. These annealing periods are important for the generation of stability in the catalyst performance. If the temperature is dropped

immediately after reaching the maximum of the temperature ramp, it is difficult to sustain subsequent steady-state conversion.

Another way of following the activation kinetics is to monitor the weight loss of the sample, which for complete reduction would be 27.3 wt% in the case of pure magnetite. The experiments need to be carried out with great care since the gas flow pattern, which is a crucial parameter in the kinetics of a gas-solid reaction, will be different for a catalyst placed in a fixed bed reactor and a catalyst suspended on a weighing pan. Much of the kinetic data available on activation, and which will be discussed below, were obtained by monitoring the weight loss.

This technique can also be used to study activation in a qualitative way and to obtain information as to why it is necessary to raise the temperature so slowly during the activation process. In Fig. 2.11, weight loss curves for different catalysts and different heating rates are shown. The data were obtained using a microbalance. The most striking feature is the strong dependence on heating rate of both the temperature at which reaction begins and the overall kinetics. At high heating rates the reaction always starts at ca 570 °C, which is the temperature at which the phase separation between magnetite and wustite occurs (see Fig. 2.7). This onset is independent of sample size, flow rate, and variation in heating rate. If the heating rate is greatly reduced, however, a second regime of reactivity is reached and is characterized by the onset of reaction at ca 400 °C. Further lowering of the heating rate to the range used by industry produces a further reduction in the onset temperature. The step in the weight loss curve for catalyst 1 is assigned to initial reduction of wustite and is reminiscent of the extra water evolution peak seen in Fig. 2.10. This process is so slow that it does not appear as a distinct event at high rates of heating. At these rates, the beneficial effect of voids and iron nuclei is also

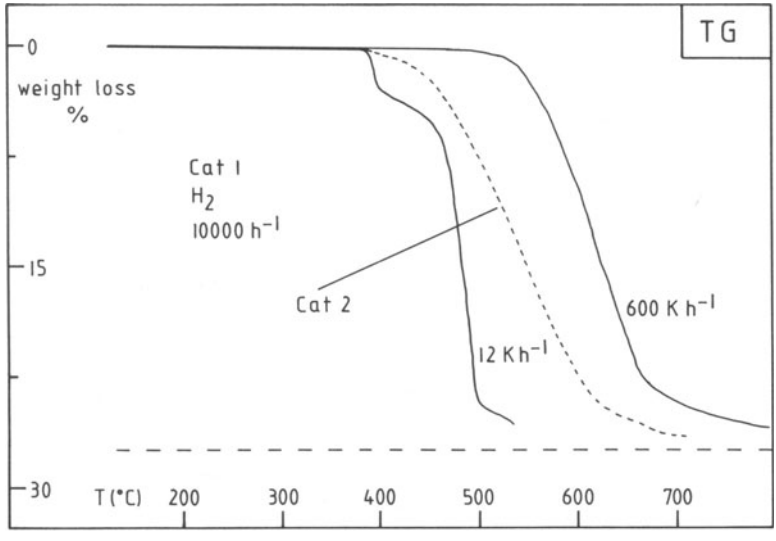

Figure 2.11. Weight loss curves of catalyst 1 and catalyst 2 in pure hydrogen for different heating rates. The dashed line indicates the theoretical weight loss for complete reduction.

lost, leading to a direct chemical attack of the whole material with little spatial selectivity. The decomposition of wustite occurs only in part as an initial reduction associated with weight loss (the step in Fig. 2.11 corresponds to ca 10% wustite while the XRD suggests more than 35% wustite) because a large amount of wustite disproportionates into iron and magnetite without any loss of weight. Comparison of the curves for catalysts 1 and 2, obtained under the same conditions with exactly the same sample sizes, shows the beneficial effect of wustite on the reduction kinetics. This is shown in the different weight loss slopes and hence in the different temperatures at which further reduction ceases.

None of these activation experiments led to complete reduction of the catalyst. The dashed line in Fig. 2.11 indicates the level required for complete reduction assuming the sample to be pure magnetite (wustite gives rise to an only marginally smaller weight loss of ca 25.5 wt%). A degree of reduction lying between 93% and 95% was always observed, independent of the catalyst type and of the activation conditions. This could be traced back to the presence of the structural promoters, since a catalyst singly promoted with potassium gave a degree of reduction of 99%.

Reaction rates, as a function of temperature, for different heating rates were obtained by differentiation of the weight loss curves and are displayed in Fig. 2.12. The two-stage reaction encountered during slow activation can now be recognized

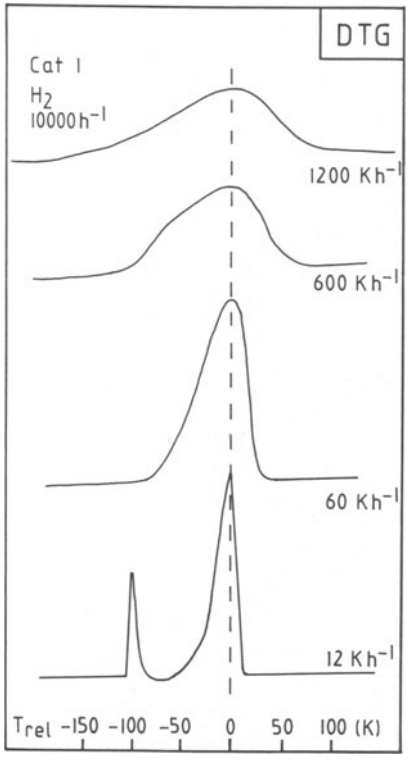

Figure 2.12. Reaction rate profiles for the activation of catalyst 1 in pure hydrogen. The effect of the heating rate on the reaction profile is clearly established. The profiles were obtained from numerical differentiation of weight loss curves.

very clearly. The two rate profiles exhibit different line shapes and hence different reaction kinetics. The beneficial effect from the initial reduction of wustite (see the valley between the two peaks) is illustrated by the increased slope of the main peak, which corresponds to the magnetite reaction. If the kinetic information is to be interpreted further, it is necessary to separate the solid state reaction kinetics from the transport kinetics of the reaction gases. The curve derived from a heating rate of 600 K h^{-1} exemplifies the superposition of the two influences. Reduction commences rapidly due to the high absolute temperature of 570 K but the rate slows down again due to the low rate of gaseous diffusion into the catalyst, and this is reflected by the bending of the curve at ca −50 K of relative temperature.

The characteristics of this kinetic superposition are strongly dependent on experimental parameters and will be different for both fixed bed reactors and the microbalance configuration. Any further interpretation of the data of Fig. 2.12 is therefore omitted. It is known, however, that under all circumstances the activation process will be controlled by a complicated interaction of kinetic influences and we should regard the curves shown in Fig. 2.12 only as a qualitative example. It is noted that line shapes, as shown in Fig. 2.12 for a heating rate of 60 K h^{-1}, have also been obtained as characteristic curves in model calculations of TPR profiles for three-dimensional phase boundary controlled reactions (topotactic reaction).[30]

Another property of the catalyst which changes during activation is its surface area, increasing from ca 0.5 $m^2 g^{-1}$ to ca 18 $m^2 g^{-1}$. In an early report,[31] a linear increase in surface area with the progress of activation (expressed as degree of reduction) was found. Those experiments were carried out at a fixed temperature of 350 °C, i.e., close to the temperature of maximum reduction rate (see Fig. 2.10). This result is consistent with the proposed core and shell reaction mechanism, bearing in mind that the surface area is a macroscopic property and assuming that the growth rate of the porous shell of a catalyst particle is linear.

Moreover, during activation the pore structure changes and this controls the reduction kinetics (see above). In an early report,[32] it was found that the pores had an average diameter of 33 nm and increased in number linearly with the progress of reduction. The average pore diameter was found to increase to 37 nm only at the end of reduction. More recently, the evolution of the pore structure was studied by mercury porosimetry employing a sample transfer technique which avoided reoxidation of the activated samples.[33] The results confirmed the existence of the 33 nm diameter pores, but also revealed that a second class of narrower pores of ca 10 nm diameter exists. During activation the wide pores develop first. At ca 20% reduction, the evolution of the narrow pores starts and, at high degrees of reduction, the increase in porosity is due only to the increasing number of small pores. These observations are consistent with the mechanism whereby the initial reduction of wustite opens up the dense magnetite structure as the first step in the overall procedure of activation.

The evolution of surface area as a function of activation temperature was followed by heating catalyst samples in synthesis gas at ambient pressure according to the manufacturers specification up to the required temperature, which was then held for 41 to 91 hours. Subsequently, the sample was transferred to the BET apparatus and finally to the Guinier powder X-ray diffractometer. Care had to be

taken to avoid oxidation of the samples, which would lead to a significant reduction in the surface area. The surface areas were found to be dependent on the flow rate of the reducing gas. The space velocity of 9000 h^{-1} was the lower limit for the generation of the expected surface areas after full activation.

The results are shown in Fig. 2.13 for the surface area evolution and in Figs. 2.14 and 2.15 for the XRD results. Evolution of the surface area starts above 350 °C, i.e., the temperature of maximum evolution of water (see Fig. 2.10). The increase in surface area occurs over a very small temperature interval, which is covered in the heating profile of the technical activation in just 3% of the total duration of the activation. From the shape of the curves, which are similar for different catalysts, it might be concluded that it is the rapid growth of iron nuclei that is related to the increase in surface area. The lower inflection of the curve falls in the temperature interval where the initial reduction of wustite was observed. As suggested by several authors,[33,34] the initial reduction of wustite forms voids (large pores[32,33]) and promotes the onset of the main reduction process.

This view is supported by the XRD results. In Fig. 2.14, wide scans of samples from catalyst 2 are shown which were taken (a) before the increase of surface area (350 °C reduction temperature), (b) at the lower inflection of the surface evolution curve (385 °C), (c) at the upper inflection of this curve (400 °C), and (d) at the point at which changes in both surface area and bulk crystal structure have ceased (423 °C). It emerges clearly that the early increase in surface area is related to the growth of iron metal as particles large enough to give Bragg reflections. The increase in surface area is terminated when all the iron oxide has been converted into α-iron. It is noteworthy that the small reflections not annotated in Fig. 2.14 that arise from ternary promoter phases have also disappeared, indicating an increased dispersion of these phases.

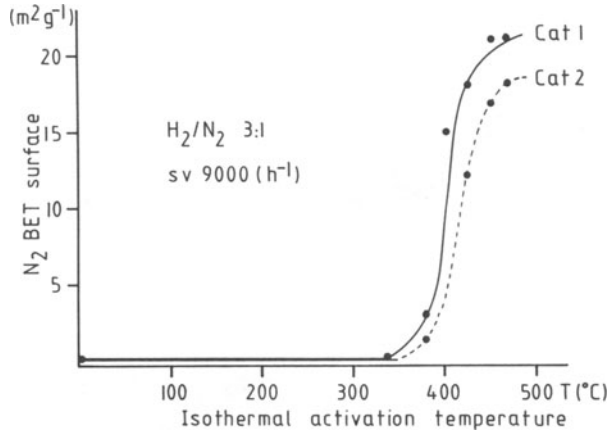

Figure 2.13. Evolution of the specific BET surface area with the activation temperature. The samples were either handled under argon or reduced in situ. No effect was found due to the method of treatment on the surface area.

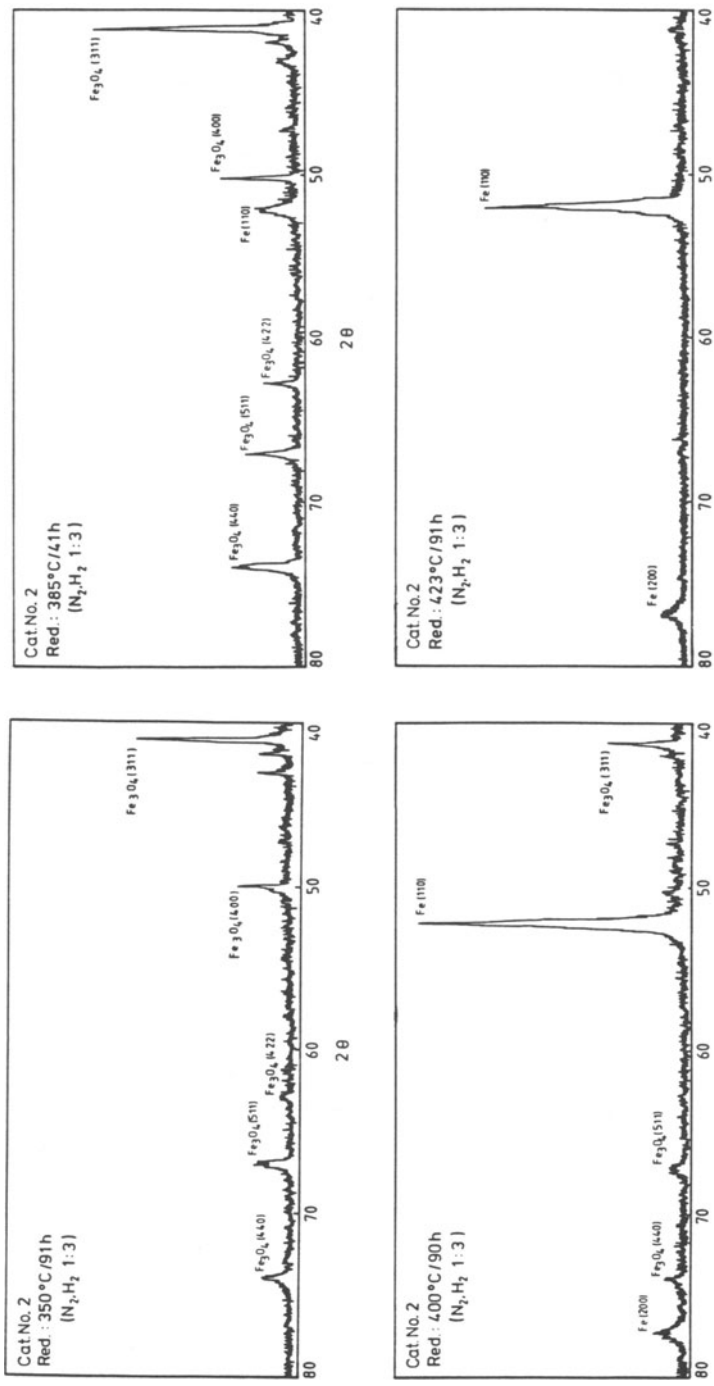

Figure 2.14. Guinier transmission diffraction patterns using Co K α-radiation. The samples were analyzed after the specific surface area determination. A special embedding technique protected the material from exposure to air, the efficiency of which is demonstrated in the scan of the sample activated at 423 °C. It can be seen that as a consequence of the fracture of the initial magnetite crystallites during reduction, the texture effect in the magnetite diffraction pattern is lost (see scan at 385 °C).

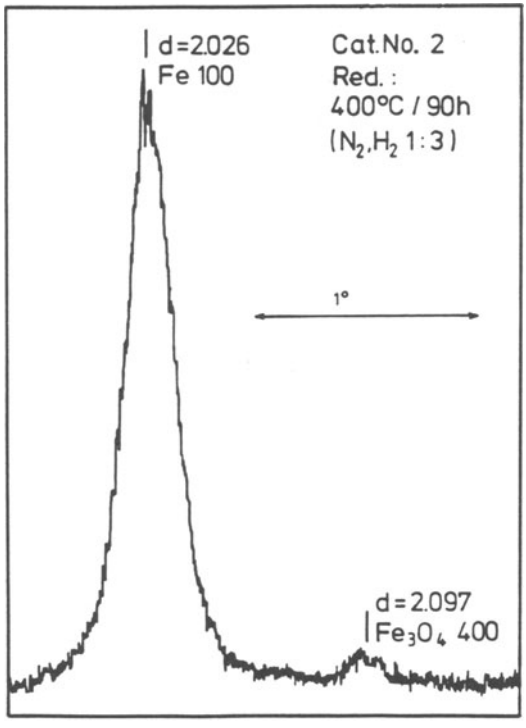

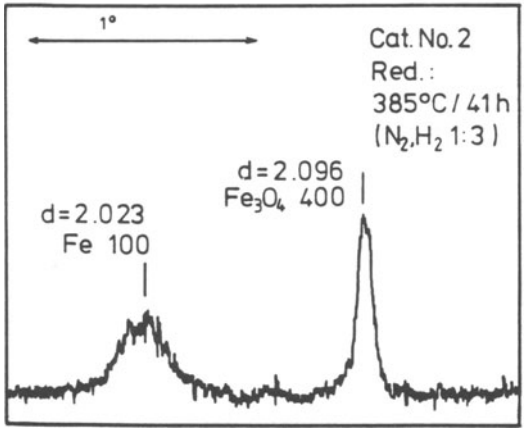

Figure 2.15. High-resolution Guinier diffraction scans over the principal iron line of partly activated samples. We note the intensity between the two clear peaks in both diffraction patterns which indicate the presence of an additional phase during activation.

In Fig. 2.15, high-resolution scans over the Fe (110) region are displayed for catalyst samples in the early stages of activation (bottom) and in the final stages of iron formation (top). The traces show that magnetite and iron coexist during reduction; this is in agreement with the phase diagram. Between the two indicated reflections, there is a tiny peak which is related to the process of reduction; it is absent before alpha iron is formed and disappears when all magnetite has been converted. This behavior is consistent with that expected from the intermediate wustite phase. However, the d-value of the reflection is smaller than expected for the standard FeO (200) reflection. It is known,[21] however, that the lattice parameter of wustite varies with composition from 437 pm down to 428 pm. This result, together with the observation of a small amount of wustite coexisting with magnetite and iron in Mössbauer experiments,[35] suggests that this peak is associated with the intermediate phase occurring during magnetite reduction.

The apparent changes in linewidth make it possible to draw the following conclusions about particle sizes. The particle size of the α-iron product is significantly smaller than that of the parent magnetite. This excludes a direct, microscopically topotactic reduction from magnetite to iron, but is in complete agreement with the nucleation mechanism described above (several wustite nuclei will precipitate within one magnetite crystal). The particle size of the iron crystallites is the same from their first appearance up to complete conversion. This shows that, under the mild conditions of activation, no recrystallization of iron occurs. The particle size of the magnetite is reduced only in the very final stages of reduction, which indicates the topotactic character of the reaction; only a small proportion of the magnetite crystals is converted at the reaction front in any given time. The alternative mechanism of random nucleation would broaden the magnetite line in a linear manner with the degree of reduction.

If the activation is carried out using wet gas mixtures and high rates of heating (ca 660 K h^{-1}), then an entirely different product from activation can be obtained.[36] The insitu XRD patterns are characteristic of a poorly ordered compound with no Bragg reflections at the positions for α-iron. The pattern may result from a layered iron oxyhydroxide. Heating to 900 K in inert gas converts this material into well-ordered α-iron. A large number of in situ XRD experiments[37] on the activation of ammonia synthesis catalysts revealed that under industrial activation conditions (slow heating rates, water concentrations up to 5000 ppm) this unidentified phase can coexist with the iron phase described above. Its morphology was found to be typically different from that of the conventional activation product. Examination by electron microscopy of a large number of activated catalysts revealed indeed that many active catalysts contain both types of product even if no indication of the second phase was suggested by XRD.

In principle, in situ XRD should be suitable to follow the structural evolution of the active phase directly, i.e., with no interruption of the activation process and using a single sample for all diffraction experiments. However, since different reaction cells would be used for this purpose, the serious disadvantage of uncontrolled gas flow and thus ill-defined reaction kinetics are seen. In Fig. 2.16, part of a series of diffraction patterns from in situ activation experiments of catalyst 3 with pure hydrogen are shown. The temperature interval is that of maximum water

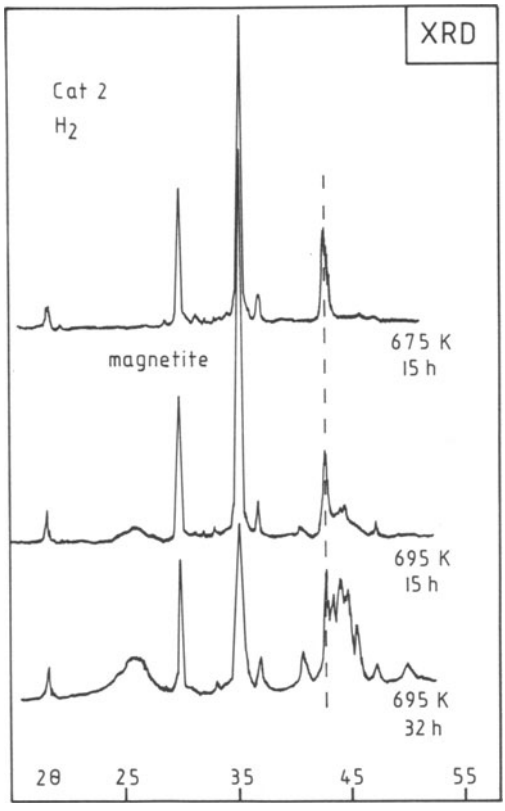

Figure 2.16. Diffraction patterns during "in situ" activation (Cu K α-radiation, postmonochromated) of a sample of catalyst 2 in a high-temperature camera (HTK 10 of Anton Paar). The dashed line denotes the position of a magnetite reflection still present besides the new intermediate phase which finally converts to alpha iron (not shown here).

evolution. At 675 K the diffraction pattern of magnetite is seen with a small contribution from hercynite expelled from solid solution. At 695 K a broad feature at higher diffraction angles from the magnetite (400) reflection (dashed line in Fig. 2.16) and a new broad line at ca $2\theta = 26°$ start to develop. Maintaining the sample at this temperature for 32 h leads to an increase in the intensity of these new features and a decrease in the intensity of the magnetite reflections. At 725 K the new features disappear and iron (110) becomes dominant, as shown in Fig. 2.15. The two intermediate features are the same as described in Ref. 36. Thus, it is concluded that the second phase is an intermediate product of the magnetite reduction. Under inappropriate reaction conditions this intermediate may become the predominant phase and is therefore characteristic of incomplete activation. The intermediate is indeed an individual phase since it results in two diffraction peaks; the line shape of the peak at $2\theta = 45°$ may be mistaken for superposition of two broad lines from magnetite and iron rather than three peaks from magnetite, the intermediate phase, and a textured form of α-iron.

Finally, activation has also been followed by an investigation of the reacting surface using UPS with parallel detection of the evolved water. To perform this experiment, activation parameters far from technical conditions had to be used.

The experiment was performed inside a UHV chamber with a dynamic atmosphere of 8×10^{-6} mbar hydrogen. The result is shown in Fig. 2.17, in which the water evolution detected by a QMS is compared to the evolution of the metallic character of the surface, as expressed by the intensity at the Fermi edge monitored by He I UPS (for the shape of the whole spectra, see Section 2.7). The water evolution curve indicates two steps in the reduction process, but only the second step leads to the formation of metallic iron in the region near the surface. This evidence provides further strong support for the suggested two-step nucleation mechanism found for the reduction of magnetite in its modified form, which is now suggested as a model for the activation of the ammonia synthesis catalyst.

2.5.2. The Kinetics of Activation

The activation kinetics have been studied by several groups over a long period of time. This discussion will be restricted to the work of Baranski and co-workers, who have studied several technical catalysts similar to the ones used for the present experiments.[29,33,38-40] Earlier work by Hall and co-workers[31] will also be used in the present discussion. The work of other groups is covered in Ref. 38.

The kinetic model starts with the basic assumption of the core and shell model. It takes into account that at least two reactions determine the overall kinetics rather than a single elementary reaction. The model is called the "mixed control type" and has been found to describe the reduction of metallurgical magnetite[41,42] in a satisfactory manner. The issue is further complicated by the fact that the two main constituents, magnetite and wustite, exhibit different reduction kinetics[29] and the initial reduction of wustite accelerates the rate of magnetite reduction (see above). The activation energies for the reduction of these two oxides differ significantly, which alters the control of the overall reaction from the faster reaction in the beginning, to a slower reaction at the point when all wustite has been

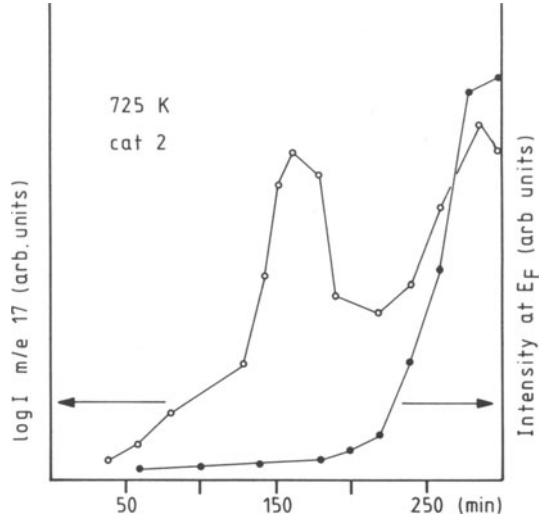

Figure 2.17. Conversion of the oxide surface into metallic iron during "in situ" activation of a sample of catalyst 2 inside a photoelectron spectrometer. The curve with the open dots shows the amount of water evolved during activation in pure hydrogen at a pressure of 8 E-6 mbar. The curve with the full dots represents the increase in intensity at the Fermi level measured with He I UPS.

consumed. This change is demonstrated in the conversion curves by a clearly visible inflection, the position of which depends on the catalyst sample, and the slope is dependent on the temperature of isothermal activation.

The formal kinetics of activation of a large variety of technical and unpromoted catalysts can also be described with the same "mixed control type" equation. This was shown to be valid for a large variation in the whole parameter space. The water content of the reduction gas was found to be the only critical parameter; at ca 5000 ppm water in the synthesis gas used for reduction, the reaction was slowed down by a factor of 7 and only followed the general kinetic equation in the early stages of reduction.

The kinetic equation for the mixed control formalism was transformed to yield a linear form of the conversion curve. It contains two variable parameters, which have been assigned to the diffusion constant of hydrogen through the already reduced shell, and the reaction constant for the chemical reduction. For simplicity, this kinetic treatment assumed a direct conversion of magnetite to metallic iron without any intermediate phases. The linear form of the rate equation is in good agreement with the activation process between 10% and 80% conversion. The discrepancies at the end points may be rationalized by domination of the reduction process with a single rate-determining stage. This could be a process of generation of voids at the beginning, and reduction of large wustite nuclei at the end of the activation. It is pointed out that the purpose of the kinetic model was to describe the activation process by an empirical equation, which does not attempt to determine the physical meaning of the parameters in the model.

From the dependence of the kinetic parameters on experimental conditions, the following conclusions have been drawn.

1. It is impossible to describe the activation process with a simple kinetic model using only one rate-determining step such as the chemical reaction itself or hydrogen diffusion. Furthermore, it has been shown that gaseous diffusion did not influence the parameters. From the particle-size dependence of the parameters, it was found that diffusion within the particle plays a dominant role; in contrast with the case of pure magnetite, it was not possible to distinguish between surface diffusion and bulk diffusion.
2. From the temperature dependence of the activation progress, an apparent activation energy of 50–65 kJ mol^{-1} was found. This value is too large to be explained by a diffusion process and the change of texture (increase in porosity) with temperature was suggested as the reason for the large value. The effect of texture on the activation process has also been pointed out by others[2,31] and is illustrated in Fig. 2.8.
3. No clear dependence of the kinetic parameters on the shape of the catalyst particles could be established. In particular, since the model was derived for spherical particles, deviations in shape from spherical particles should yield a variation in the parameters. However, a statistical analysis of the parameters gave no evidence for a meaningful difference between spherical and irregular-shaped particles. This point is of interest since the expected parameter variation would be a kinetic indication for the topotactic charac-

ter of the activation, which has been demonstrated unequivocally by microscopic techniques.[2,18,28]

Finally, we return to the effect of inhibition by water upon the activation. This is not only of academic interest but has also been established in the technical activation as a critical factor; too little water results in an unstable catalyst and too much water results in an inactive catalyst. Thus the activation procedures often specify a maximum water concentration in the outlet gas, which is then used to fine-tune the temperature program of activation. Baranski's work, with a water content in the dry gas of below 100 ppm and in the wet gas of ca 5000 ppm, is related to the technical case in the following way. The "dry" case corresponds to near-optimal conditions and may be an example for normal activation. The wet case, however, corresponds to a relative failure during the activation process, in which the activation proceeds in the top layers of the reactor too quickly so that the lower layers of catalyst are reduced in an atmosphere containing excess moisture. Special reactors have been designed to minimize this problem.[1]

It was established clearly[39,40] that the inhibiting effect of water does not act on the reduction of *pure* magnetite, where inhibiting effects of ca 1% have been found, but it is determined by the presence of the alumina promoter. Furthermore, the inhibiting effect acts only on the reduction of magnetite, the wustite reduction which occurs first being unaffected. This seems to explain the observation that the general kinetic model is also valid in a wet atmosphere at low degrees of activation. Thus, the initial suggestion that a dense iron metal layer hinders the diffusion of hydrogen is not very likely, nor is the intuitive explanation that reoxidation of already-formed iron slows the overall activation process. The effect may be interpreted alternatively as follows. Water promotes the segregation of alumina from the defected spinel starting material and thus allows reduction of the "purified" magnetite. At excessive levels of water, dense layers of alumina oxyhydroxides may form, instead of hercynite, and remain at the grain boundaries of the intermediate wustite crystals. This dense layer may hinder hydrogen diffusion by the formation of a thin shell of oxyhydroxide covering the porous shell of reduced iron and thus eventually block progress of the reaction.

It is pointed out that the presence of water in concentrations larger than a few hundred ppm (outlet stream concentration) also changes the surface constitution and the micromorphology of the activated catalyst. The phenomenon has therefore been studied in detail and will be discussed in Section 2.7.1.

2.6. THE STRUCTURE OF THE ACTIVATED CATALYST

In this section, the nature of the iron material resulting from the activation process will be described. Its bulk properties as revealed by Mössbauer spectroscopy, X-ray diffraction, and EXAFS will be discussed, followed by a description of the typical morphologies of activated particles as seen in the SEM, and finally the complex microstructure of the material as seen in the high-resolution TEM will also be demonstrated. The main purpose of the section is to illustrate the fundamental differences between the active catalyst material and pure iron powder.

2.6.1. Models of Textural Promotion

The main difference between pure iron and the activated catalyst is the presence of the textural promoters, which stabilize the initially-formed iron sponge structure against recrystallization (sintering). The effect of promoters has been studied using in the main hercynite, or physical mixtures of iron and aluminum oxide as models. Three types of dispersion of each promoter substance have been suggested in the literature, and have been reviewed elsewhere.[17] The suggestions are: (1) a thin film of oxide covers the pure iron metal crystallites, (2) "molecules" of hercynite are dispersed in each iron crystal causing paracrystalline disorder,[16] or (3) larger inclusions of either alumina or hercynite account for the stabilizing effect. Most of the experimental evidence for these theories came from X-ray diffraction and Mössbauer spectroscopy. The early theory of the alumina film is supported by selective chemisorption measurements[8,43] carried out on a historic sample singly promoted by alumina (designated no. 954), which was prepared in 1925[44] and used as a reference material. This same material was later used in a surface analysis study of ammonia synthesis catalysts using Auger electron spectroscopy,[45] which also supported the idea of a thin surface film of textural promoters. It is pointed out that XPS and scanning Auger data from industrial catalyst samples are also in full agreements[11,19] with these observations.

Measurements of the phase transition temperature for the α/γ iron transition of iron alumina model compounds gave evidence for the modification of the lattice properties of alumina-containing iron. The initial temperature was too high, but several cycles through the phase transition gradually reduced the transition temperature back to its normal value.[46]

2.6.2. Mössbauer Spectroscopy of the Activated Catalyst

Mössbauer spectroscopy is a technique which is particularly sensitive to the local chemical environment. If the chemical environment is modified locally by the presence of heteroatoms such as dispersed alumina arising from the addition of textural promoters, this would affect many iron atoms within the sample and the method should detect differences in the spectral parameters, i.e., linewidths of the iron metal in the catalyst would change. If the iron contained larger inclusions of hercynite, the spectra should exhibit a quadrupole split component, with a typical ferrous ion shift characteristic of the ternary aluminum iron oxide. Three groups have studied these problems and their results are reviewed critically in Ref. 14.

In this review it was pointed out that only in situ studies of activation could give decisive answers, since passivation of a reduced catalyst causes broadening of the iron resonance lines as well as additional absorptions from the formed oxide components.[47] A further problem with quantitative phase analysis using Mössbauer spectroscopy is the recoil-free fraction of small particles or structurally disordered components. Most studies have been carried out at room temperature or even at high temperature in order to avoid the complication of magnetic splitting. The advantage of a collapsed single line or a quadrupole doublet is countered by

a loss in the recoil-free fraction. This effect is not important for materials with high Debye temperatures, as they are typical for bulk iron oxides. However, small particles or disordered solids often show drastically reduced Debye temperatures and may therefore remain undetected in the high-temperature spectra.

The in situ studies of commercial catalysts by Topsoe and co-workers[13,14,47] can be summarized as follows. There is no suggestion of any modification of the local chemical environment of a significant number of iron atoms, i.e., they are in identical environments in both the catalyst and in pure α-iron. Furthermore, there is no evidence for any alloy formation between iron and aluminum. In their earlier studies, these authors did not find any remaining iron compound after complete reduction. In later experiments, however, both a trivalent paramagnetic species, attributed to calcium ferrite, and a magnetically split component were detected in samples which had been reduced according to the commercial activation procedure. These findings are in agreement with the weight-loss measurements discussed above. The surface characterization studies which will be discussed in Section 2.7 also revealed incomplete reduction of the iron, as a typical feature of activated catalysts.

Finally, it is pointed out that Mössbauer studies were unable to produce unambiguous evidence for the presence of highly dispersed promoters within the iron lattice. The studies revealed, however, the presence of iron compounds which were difficult to reduce, and which may be associated with ternary iron oxides of calcium, aluminum, and silicon. These compounds are present in large particles with diameters above ca 10 nm.

A large amount of Mössbauer work has been devoted to in situ surface characterization of iron catalyst. These experiments were carried out, however, using small particles of iron oxide supported on inert carriers. These materials represent a different class of catalysts to the industrial ammonia synthesis catalyst. The Mössbauer studies which has helped to evaluate the concept of structure sensitivity in ammonia synthesis will therefore not be discussed here.

2.6.3. EXAFS Studies

X-ray absorption spectroscopy can give detailed information about the local electronic (NEXAFS) and geometric structure (EXAFS) of a probe atom. Since it can be applied to a wide variety of different atoms, the technique is well suited to study both the structures of the main iron constituent and of the promoters in the catalyst. Recently, a series of in situ experiments were performed looking at the Fe K edge of doubly promoted model catalysts, which were prepared using the techniques of coprecipitation and calcination.[48] The catalysts which contained the different promoters, potassium and cesium respectively, were investigated during activation and under operating conditions.

The main results can be summarized as follows. Activation occurs as a complicated process involving the presence of more than one oxide species. The formation of metallic iron commences at ca 600 K, far below the onset of the main reduction process. This can be seen as direct experimental proof for the iron nucleation mechanism by disproportionation and prereduction of wustite. The

onset of iron formation was different for the two promoters, with the potassium-promoted sample exhibiting a 40-K lower onset temperature. The reduction was completed in the temperature range 640–670 K,[38] leading to a material with an almost identical spectrum to iron foil at the same temperature. No indication for any significant structural difference between pure iron and the catalyst was found. The normalized intensity of the EXAFS amplitude was significantly smaller than would be expected and, on this basis, a smaller average coordination number of iron in the catalyst compared to pure iron was suggested. This would be, however, in contradiction with the results from both the X-ray diffraction and Mössbauer studies, as recognized in Ref. 48. The difficulties in fulfilling the experimental requirement of a homogeneous absorber within the in situ cell are more likely to account for the lack in intensity.

We have also performed EXAFS measurements using an activated and kinetically characterized sample of catalyst 1.[49] Using X-ray diffraction, we ensured the integrity of the transfered sample which had been prepared in a beryllium cell to yield a perfectly homogeneous absorber. The measurements were performed in the transmission mode with the sample cooled to 78 K. In Fig. 2.18, the EXAFS of iron powder (top) which is identical to that of iron foil and of the activated catalyst (cat 1) are shown. The bottom trace is the corresponding Fourier transform for catalyst 1. The EXAFS features of the catalyst and the iron powder are very similar, which is in full agreement with the in situ measurements[48] of the model catalyst. The structural identity of the two materials can be seen with even higher resolution than from the data of Ref. 48 because of the optimized conditions of data acquisition. The well-resolved Fourier transform shows the same maxima in the radial distribution function as seen in the data of the in situ study. These can be assigned to the nearest Fe–Fe distance and also the second and third nearest-neighbor shells. The lack of intensity in the EXAFS amplitude of the catalyst was also noted in our study, but to a much smaller extent than in Ref. 48.

In summary, the EXAFS results show that there is no difference between pure iron and the catalyst in the average local structure. Furthermore, there are no iron atoms present in the catalyst in significant quantities which exhibit a different geometric environment to the average, i.e., there is only one type of iron atom present. This is strong evidence against the paracrystallinity theory and is more consistent with a macroscopic distribution of the promoter phases, which affects fewer iron atoms than can be detected with the X-ray absorption technique. The porosity of the reduced catalyst may account for a certain lack of EXAFS amplitude. Any significant reduction in the coordination number of the iron in the catalyst would require a cluster-like microstructure for which no evidence has yet been found.

2.6.4. X-Ray Diffraction

X-ray diffraction patterns taken in situ[36] or off line from activated catalysts exhibit only the lines characteristic of α-iron after careful reduction. In contrast, segregation of the promoter phases occurs when the activation is carried out too

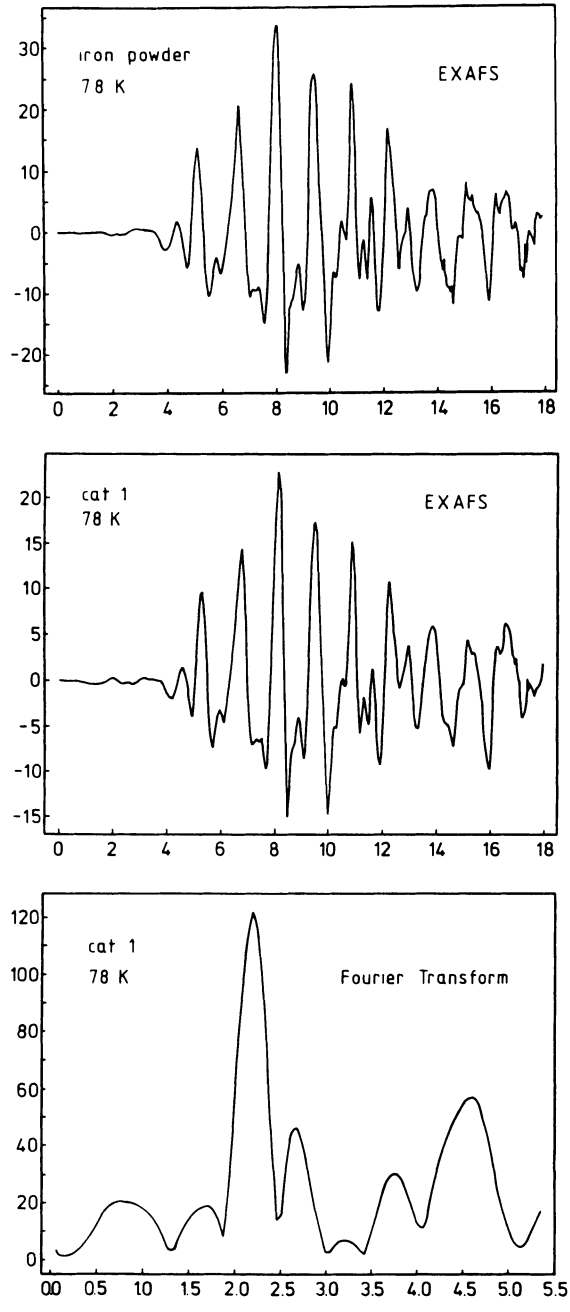

Figure 2.18. EXAFS experiments on a sample of activated catalyst 1 (in a Be container) and on iron powder. All spectra were measured at 78 K in transmission geometry at the Daresbury synchrotron radiation source. The bottom trace shows the Fourier transform of the central spectrum. A phase shift correction was done using the top spectrum as reference.

rapidly. In the extreme case, the individual diffraction patterns of the ternary oxides and basic potassium carbonate can be detected.

The average d-spacings of the iron diffraction peaks are very close to those of pure elemental iron as indicated in Fig. 2.15. This result is in good agreement with the conclusions reached from the other two methods of structural analysis discussed above. There is one difference, however, between the diffraction patterns of pure iron powder and that of the catalyst, namely, the line shape is significantly and reproducibly different. The theory of paracrystallinity was developed[15-17] from this line shape effect, which is the only experimental evidence in support of the idea that the bulk of an active ammonia synthesis catalyst may be different from iron powder.

This line shape effect is illustrated in Fig. 2.19 for a sample of catalyst 2 used for ca 4 weeks in ammonia synthesis catalysis. It is pointed out that in "off line" experiments, the process of reoxidation of the catalyst must be suppressed as much as possible, because of the thermal stress which occurs during reoxidation. This stress, which will be discussed below, seriously interferes with the line profile measurements even at such a low stage of reoxidation that no iron oxide can be detected as a separate phase in the XRD pattern. In the figure, several different peak profiles are compared. The comparison can only be of a qualitative nature, since any quantitative analysis would require much better counting statistics. However, the advantage of the monochromated focusing Guinier technique used in this study is that no X-ray satellite broadening and little instrumental broadening affect the line shape of the raw data displayed. Thus, mathematical data manipulation is not required in order to see the line-broadening effect.

The line profile of a diffraction event on a large number of coherently scattering lattice planes (Bragg diffraction) is a very sharp line of a few radians widths after correction for instrumental broadening. If the number of diffracting planes becomes small compared to the coherence length of the radiation used, the line is successively broadened. In the limit, the transition from diffraction to inelastic scattering changes the type of intensity distribution from a Bragg pattern to the radial distribution function of the material. The result of this effect is that, in the present case, any number of parallel Bragg planes amounting to a thickness between 2 and 200 nm will give rise to a broadened Bragg reflection. Only in the case of spherical particles can the thickness of the package of lattice planes be correlated with the particle size. In the general case of particles with an anisotropic shape, the thickness can be correlated with the dimension of the single crystallite in the direction given by the Miller index of that particular reflection. This effect is shown in the upper part of Fig. 2.19, in which two reflection profiles characteristic of two directions intersecting at an angle of 45° are compared. The different sizes of the average single crystal in these two directions can be seen clearly and it is concluded that the microstructure of the catalyst must be made up from anisotropic, nonspherical single crystals of iron. The dimensions of the crystal can also be estimated[50] from the linewidths shown in the figure, and the value of ca 25 nm for the (110) reflection agrees well with accepted literature data.[15,17,48]

The second cause of line broadening in the XRD pattern arises from many kinds of defects and internal stresses within a ductile material such as iron. The

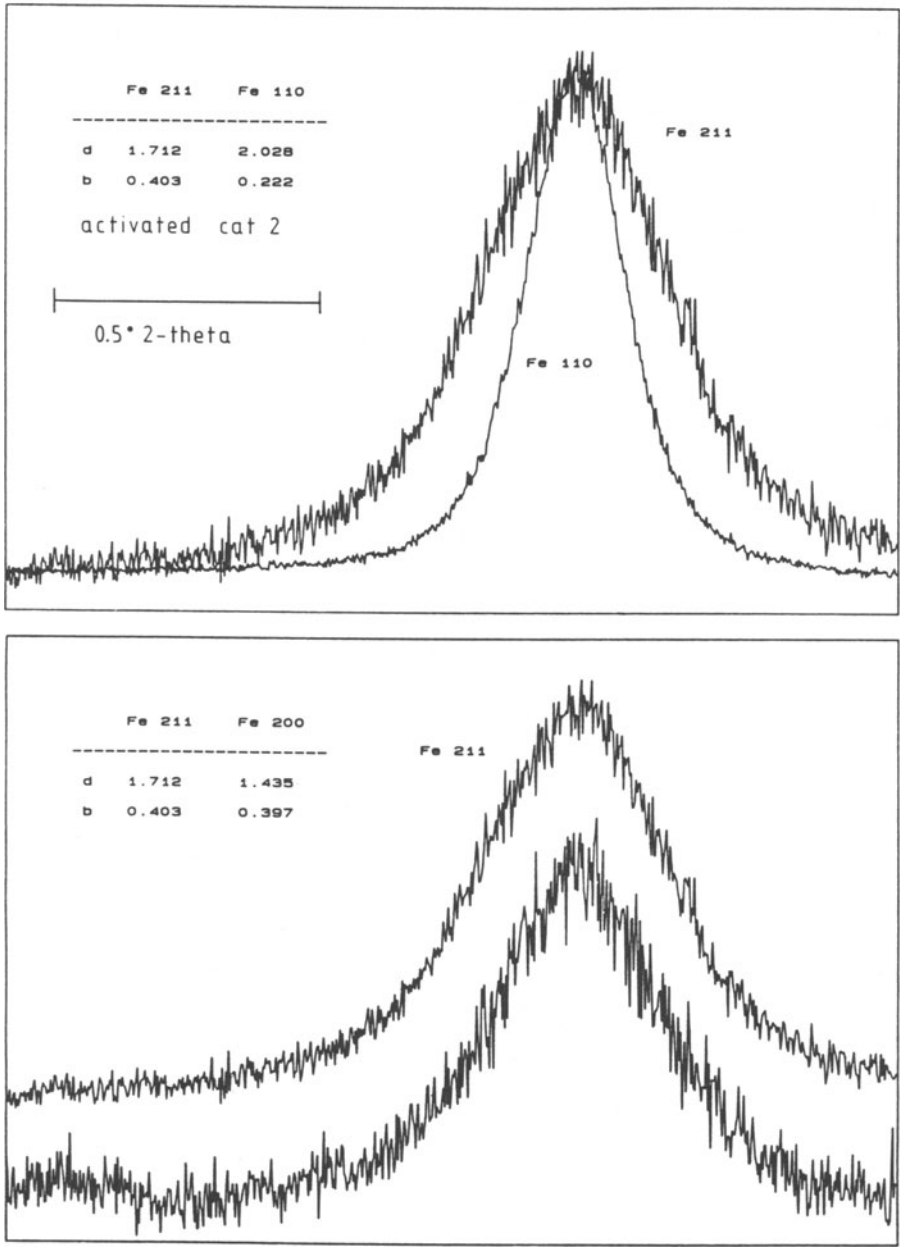

Figure 2.19. High-resolution Guinier scans over several reflections of α-iron of a sample of fully activated catalyst 2 which was 4 weeks on stream prior to analysis. The numbers report the *d* spacings (d) and linewidths (b) as FWHM without instrumental broadening correction. The natural linewidth of the instrument measured with silicon is 0.08° 2-theta at the position of Fe(110). The *x*-axis is the same for all profiles; the intensities were normalized to the respective maxima.

d-spacing, characteristic of a perfect single crystal, is a fixed, single value. If, however, large crystals (100–1000 nm) (1) contain large amounts of point defects (voids), (2) are elastically distorted, (3) exhibit deformation faulting, or (4) suffer from a combination of these effects, then a distribution of d-spacings within the crystal results. This Gaussian distribution of d-spacings is convoluted with the peak profile, derived from coherent scattering given by that specific particle size. In order to separate the two effects, the fact that the d-spacing distribution leads to a widening of the diffraction peaks with increasing diffraction angles is utilized. If the linewidths of a series of reflections belonging to one crystallographic direction are determined and plotted against the diffraction angle, a straight line can be obtained, the slope of which is proportional to the width of the distribution of the d-spacings. This method of analysis was applied in the theory of paracrystallinity and the slope was designated as the paracrystallinity index, given as the percent deviation from the averaged-spacing. These deviations are small for the ammonia synthesis catalysts, with typical values of ca 5% for the (110) direction. An illustration is given in the lower part of Fig. 2.19. The line profiles shown are asymmetric, due to an asymmetric distribution of the d-spacings. Their integral widths are, however, the same within experimental error. The experimental error is too large to detect linewidth differences of only a few percent. It is concluded that the line shape of the iron diffraction pattern is affected by both particle-size broadening and stress-induced broadening.

The theory of paracrystallinity links the strain broadening with the action of the textural promoters. It suggests that individual "molecules" of hercynite should be incorporated within the lattice of the metallic iron. One such molecule would replace seven iron atoms. This replacement would result in elastic deformations in the vicinity of the hercynite molecule due to differences in the molecular structure compared with the metallic iron lattice and so account for the variation in d-spacing. This model, which is based upon treatment of a crystalline solid within the hard-sphere approximation and without taking into account chemical bonding effects, appears unlikely for the following reasons. First, any ternary spinel oxide such as hercynite is not made up of discrete molecules as such. It only exists because of electrostatic, long-range interactions which are characteristic of a large number of identical unit cells. Second, coordination polyhedra containing both metallic and ionic iron species would be chemically very unstable. The compensation of the formal charges occurring at the periphery of these molecules by conduction band electrons of the surrounding metal appears difficult. Such an inclusion of a charged cluster within a metal matrix would have a high tendency to segregate to a grain boundary. There it would form a larger aggregate of oxidic material which is exactly the opposite effect from the desired stabilization of the iron crystallite by the promoter phase.

There is little doubt about the experimental observation of characteristic line broadening in ammonia synthesis catalysts. Accurate measurements were first made by Hosemann *et al.* and these have been confirmed recently.[17] However, all of the arguments cited in favor of the "molecular dispersion of the promoter oxide" thesis also hold for a different distribution of the promoters. It was pointed out in the conclusion of the work by Borghard and Boudart[17] that there are several

different locations for the promoter oxides. Some material covers the outer surface of a crystal as a thin layer. A large amount of ternary oxide is also located at the grain boundaries within the initial magnetite framework. A third location would be along the new grain boundaries formed during reduction of the precursor, which determined the final particle size of ca 20 nm. The promoters present at both grain boundary locations prevent recrystallization of the microstructure during activation as well as during use of the catalyst. The X-ray line broadening is thus a reflection of the complex reduction mechanism of iron oxide. The effects of the reduction mechanism on particle size and strain have been determined by the promoter oxides, which prevent any annealing of the ductile iron metal.

2.6.5. The Micromorphology of the Activated Catalyst

The catalyst activation process results in transformation of the compact nonporous precursor solid into a porous material, containing two types of pores with diameters of ca 30 nm and ca 10 nm.[2,38] From XRD data, anisotropic particles with a diameter of ca 25 nm and smaller dimensions in the perpendicular directions are expected. Furthermore, from the heterogeneous nature[2,4] of the elemental compositions, particles other than pure iron metal are also expected. Such expectations from the catalyst in the reduced state have indeed been observed in an earlier SEM study.[11] The active catalyst appears to consist of a sponge-like structure of spherical particles separated by pores of ca 10 nm. The surface of the sponge is covered with crystals of the promoter oxide and with patches of highly dispersed potassium and alumina promoters. These are distributed in such a way that the potassium forms an adlayer over the iron with aluminum and calcium covering the remaining areas. This leaves almost no free iron metal surface. These latter results were deduced from scanning Auger spectroscopy data obtained from the same catalyst as was used in the SEM investigation. Little information was given, however, about the true particle shapes, their lateral arrangement, and their microscopic elemental bulk composition. The present discussion will focus on these subjects with only a brief comment on low- and medium-resolution images.

The high-resolution images presented in this section were all obtained from various catalysts after activation without any sample preparation. In particular, surface coating treatments were avoided. Suitable 50-micron particles of precursor oxide were examined using a Jeol CX 200 TEMSCAN apparatus. Extensive tests of the sample transfer procedure and of beam stability ensured that no imaging artefacts interfered with the image interpretation.

In Fig. 2.20, a typical low-resolution image of an activated sample of catalyst 1 is shown. The particles, of ca 1 mm diameter, appear rather isotropic and exhibit sharp edges. The spotty surfaces reveal the segregation of promoter oxides into the voids along which fracture had occurred. The other catalysts were quite different, with an anisotropic, needle-like shape and did not show segregation similar to catalyst 1 when they were investigated without exposure to air. After mild reoxidation under controlled conditions and subsequent storage in air for a few days, the samples exhibited the same spotty appearance as seen in Fig. 2.20 and also as described in Ref. 11. This suggests that the reoxidized, activated samples

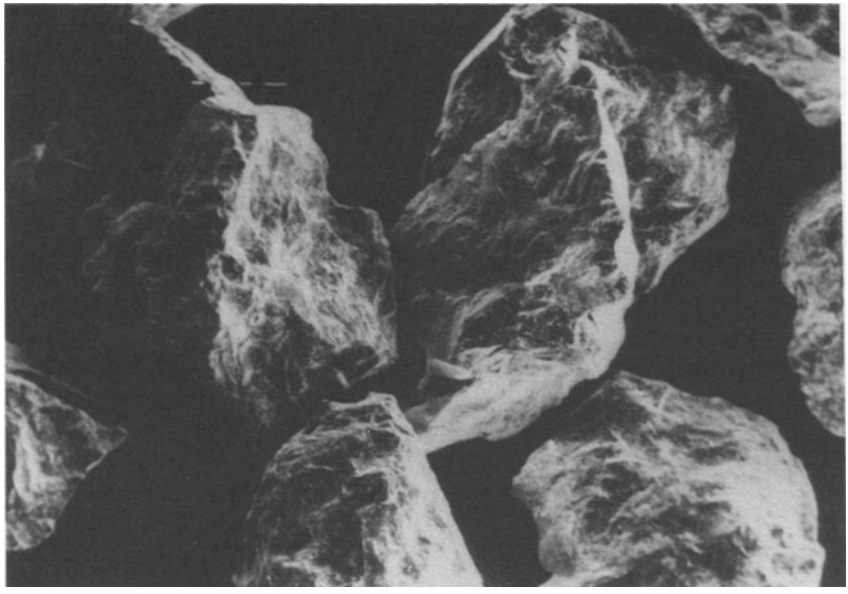

Figure 2.20. Low-resolution SEM image (15 kV) of a sample of activated catalyst 1. The particles are ca. 1 mm in diameter.

were not completely stable to air, and tend to form large (several microns) segregates consisting of a mixture of iron and promoter oxides. Samples of catalysts 2, 3, 5, 6, and 7 were investigated in this way and they all show a common anisotropic behavior on fracture, resulting in needles and platelets after isostatic pressing of large lumps of the precursor oxide.

The macroheterogeneous nature of a reduced sample of catalyst 1 is shown in Fig. 2.21. Similar pictures showing the lateral bulk distribution of promoter elements have also been reported in Ref. 4. It is emphasized that of the catalysts studied, only catalyst 1 exhibited this heterogeneity on a large scale both before and after activation. With all the other catalysts, it was observed that the process of activation resulted in an increase in the dispersion of the promoter elements beyond the resolution of the X-ray distribution images (ca 2 micron). The line scan experiment in the left-hand side of Fig. 2.21 demonstrates how two large grains of almost pure magnetite can be interconnected by a sliver of calcium iron oxide. The small peaks beside the main feature in the calcium line scan indicate the presence of thin layers of calcium enriched iron oxide near the internal surface of the large grains. Such an arrangement of the promoter oxides is consistent with the schematic picture given in Fig. 2.8. The potassium distribution image at the right-hand side of Fig. 2.21 shows an aggregate of mixed potassium iron oxides consisting of large platelets. The small droplets at the front of the agglomerate which might intuitively be identified with potassium oxide, in reality, contain only iron. The sharp steps of the underlying iron grains are also recognized. The fracture surfaces in both images reveal that the large grain texture of the original oxide

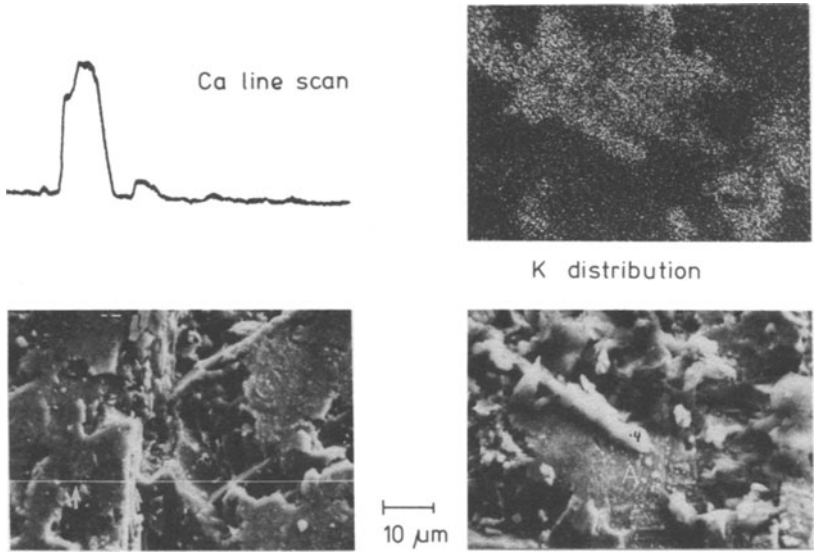

Figure 2.21. Macroheterogeneity of catalyst 1 in the precursor state. The two left-hand figures show how two magnetite grains are separated by a crystal of calcium iron oxide (boundaries marked by arrows). The right-hand figures demonstrate the uneven potassium distribution. The area A contains spherical particles of iron oxide.

precursor is preserved on reduction, giving a system of large intergranular voids in the resulting iron material. All of these main features were also seen with the other catalysts, but the dimensions of the promoter species and of the voids were ca 10 times smaller.

The consequence when internal strain in an activated sample of catalyst 1 is liberated by rapid reoxidation in dry air is shown in Fig. 2.22. A system of large cracks decorates the blocks of grains with parallel orientation. These indicate the major sites of segregation of the promoter oxides found within the cracks, in full agreement with the external fracture planes as shown in Fig. 2.20. The system of small cracks is indicative of the anisotropic nature of the grains. These cracks decorate the boundaries of the initial platelets of magnetite generated during synthesis of the precursor oxide and they are a clear indication of the effect the promoters have in the conservation of the texture of the catalyst.

Activated catalysts may be described by the following textural hierarchy. A macroscopic particle is confined by fracture lines running through a system of blocks consisting of stacks of platelets in a parallel orientation. This texture is formed during preparation of the oxide precursor. Upon reduction, each of the platelets may be subdivided into even smaller platelets. The initial texture is defined by a system of pores which accounts for the formation of the internal surface area. This textural system is stabilized by promoter oxides, which act as a glue, separating neighboring platelets and leaving voids for the interconnection of the pore system. Such an arrangement renders the activated material brittle and accounts for the glass-like fracture behavior of active catalysts. This is in striking contrast to pure

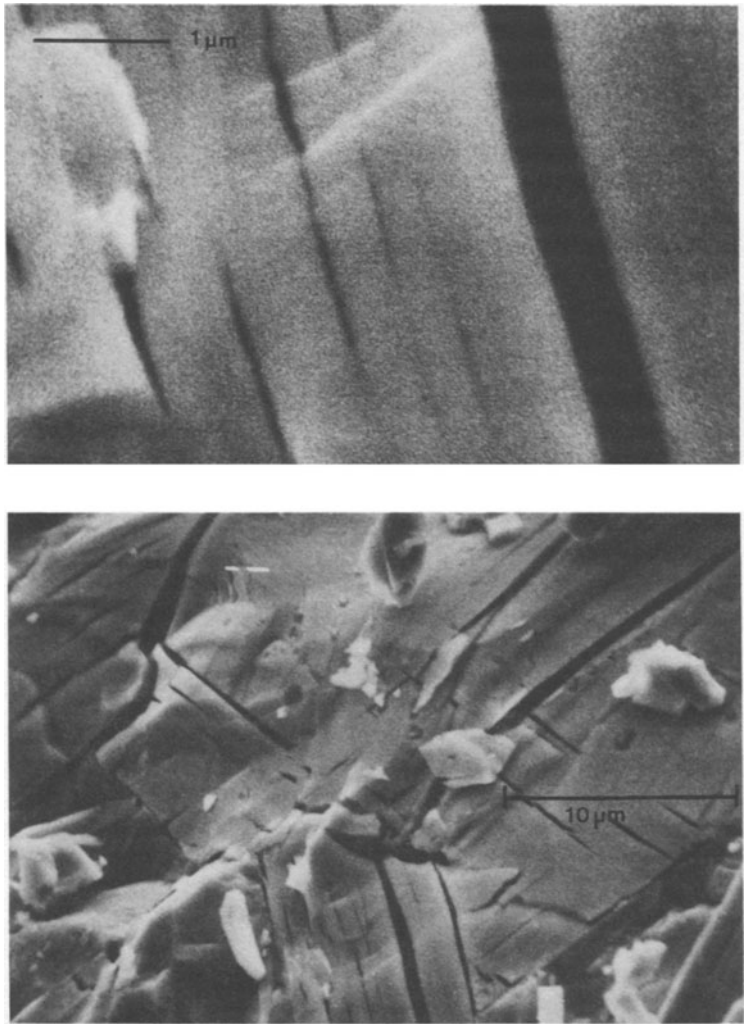

Figure 2.22. The effect of internal strain released upon reoxidation of an activated sample of catalyst 1 (SEM, 10 kV). The system of cracks demonstrates how the macroscopically isotropic material is built from thin platelet-like subunits.

iron metal which exhibits ductile behavior. The rigid interfaces, iron–promoter oxide–iron, also conserve any strain induced during activation, unless they are disrupted by either chemical reaction (reoxidation) or prolonged thermal annealing above 900 K. It is the purpose of this section to demonstrate the existence of the large platelets, which themselves are subdivided into smaller ones and which are held in place by small aggregates of promoter oxides.

In Fig. 2.23, the aggregates of the large platelets are shown. The multiple bendings indicate a significant internal strain. The roughness of the surface that

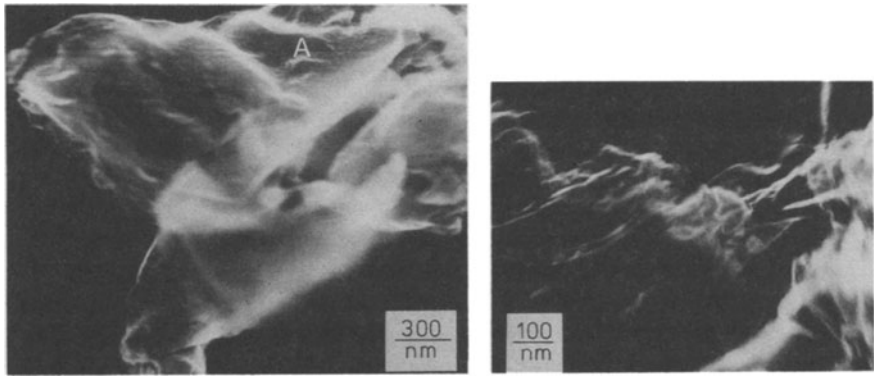

Figure 2.23. Fluffy catalyst obtained after rapid activation of a sample of catalyst 2. The material is made up from thin platelets bearing significant internal strain which causes the bending of the particle. The rough region A is caused by the system of ca 10 nm pores (SEM, 200 kV).

can be seen in the left-hand micrograph of Fig. 2.23 is caused by the small pores, clear images of which have been shown previously in Ref. 11. The platelets were obtained in this isolated form by rapid activation of the catalyst. Such treatment results in the transformation of the compact solid into a fluffy material.[36,37]

Samples from slow activation also contain isolated flakes that peel from the edges of the bulk of the material, as can be seen in Fig. 2.24, which presents images of catalyst 2 after slow activation. The sponge-like texture built from stacks of parallel platelets can be seen clearly. It can further be recognized that the large platelets are subdivided into small compact areas and holes. Having an average diameter of 10 nm, these form the pore system within the stacks of platelets. The orientation of the specimen was chosen so as to highlight the pore structure. In Fig. 2.25, different orientations were chosen to illustrate as clearly as possible the stacking of the thin platelets. The left-hand micrograph shows the rare occurrence of a boundary between two orthogonal platelet stacks. This situation occurs along the texture line between two blocks of large platelet stacks. Large voids are usually observed at these locations (see Fig. 2.21).

At the highest possible resolution attainable by the SEM technique, some information about the surface of the small platelets can be obtained. These surfaces are characteristic of the different methods of activation, irrespective of the catalyst sample being examined. In Fig. 2.26, images are presented of catalyst 2 after activation in the presence of ca 6000 ppm of water (designated in Section 2.7 as wet activation). The smooth surfaces show both small and large segregates of promoter species, namely, potassium in the background of the top image and calcium at the center left edge of the top image. These islands of promoters can be distinguished from metallic iron platelets by the shape of their respective perimeters; they are sharp for iron and diffuse for promoters. The inset in Fig. 2.26 indicates the typical surface structure of samples reduced under conditions containing about 350 ppm water in the outlet gas (designated in Section 2.7 as dry activation). The same diffuse islands of promoter species (right edge) can be seen,

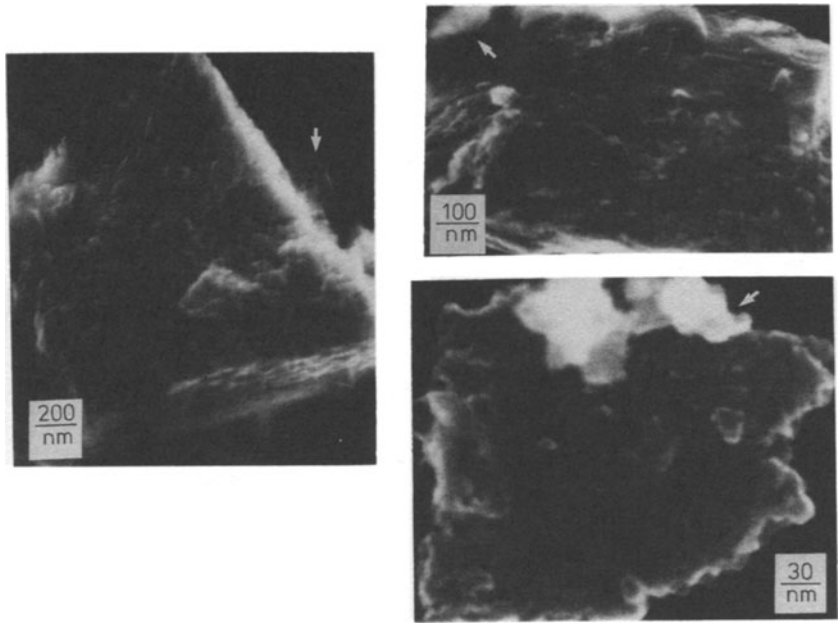

Figure 2.24. Surface morphology of slowly activated catalyst 2. The arrows indicate the presence of individual platelets peeling off the main body of the porous catalyst. This material consists of stacks of this iron platelets with sharp but irregular edges and a turbostatic stacking sequence (SEM, 120 kV).

supported by a well-developed crystalline structure of iron. This structure can be seen in more detail in Fig. 2.27, which suggests that the thin platelets may be built from single crystals of iron with well-developed edges and sizes compatible with the X-ray line-broadening data. The resolution of ca 4 nm steps (ca 10 unit cells of iron) in the left image excludes any uniform coverage of the iron surface with a film of promoter species. These photographs suggest a high reactivity of such iron particles toward sintering and thus underline the need for a stabilization of the structure, which is believed to represent the active state of the catalyst.

The internal structure of the small platelets was also investigated by scanning transmission electron microscopy (STEM). Specimen preparation, such as microtoming or ion milling, could not be applied since this would risk the danger of creating segregation as a consequence of specimen thinning. About 100 positions from five different samples were investigated and the typical images as shown in Fig. 2.28 were always obtained. The lower insets in the figure present SEM images of the position from which the STEM pictures were obtained, after the specimen had been tilted to the appropriate orientation. The STEM images reveal thin, regular (quadratic) crystals with a large number of promoter oxide spacers on top and underneath, as the smallest discernable unit in the catalyst. The distinction of this situation from the other alternative of promoter particles within the iron crystals (paracrystallinity) was possible by applying selected area diffraction to

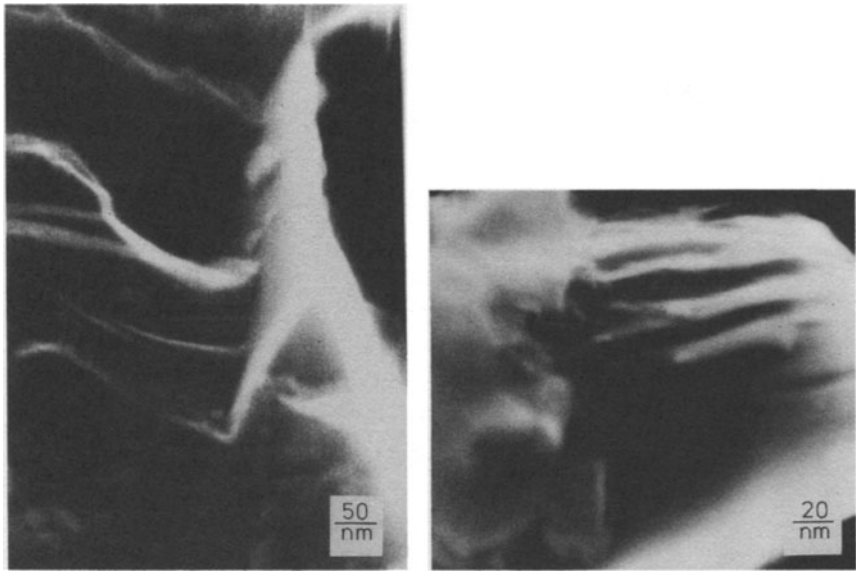

Figure 2.25. Stacks of iron platelets of activated catalyst 2. In order to emphasize the steps in the stacks, the illumination was chosen such that the rough surface structure seen in Fig. 2.24 is not resolved (SEM, 200 kV).

these crystals, which identified them unambiguously as single crystals of iron (see below).

In summary, it is seen that regular platelets of iron single crystals are arranged into irregular stacks in such a way that larger platelets result. The texture of these platelets is predetermined by the texture of the precursor oxide. The large platelets form blocks up to several micron in size, the boundaries of which eventually become the location of the fracture lines which determine the macroscopic appearance of the catalyst particles. The texture at all three levels is decorated by particles of promoter oxide species present in different sizes.

Using analytical electron microscopy it has been possible to identify the elemental composition of the individual platelets. In Fig. 2.29, energy dispersive X-ray spectra (EDX) are presented; they were obtained from thin sections of a reduced sample of catalyst 3. Trace a is typical of a region rich in promoter oxide particles. The high local concentration of oxygen as well as the significant amounts of calcium and potassium can be recognized. Areas containing small amounts of promoter oxide particles gave rise to EDX spectra as shown in trace b. The total amount of promoter oxides is about 25% of that of the area analyzed in trace a. The different relative amount of promoter elements is due more to micro-heterogeneity rather than a typical effect of the different morphologies. The only common feature of all the analyses was that no area analyzed was completely free of potassium and oxygen. This is taken as an indication that the presence of a potassium-oxygen compound in high dispersion is characteristic of reduced

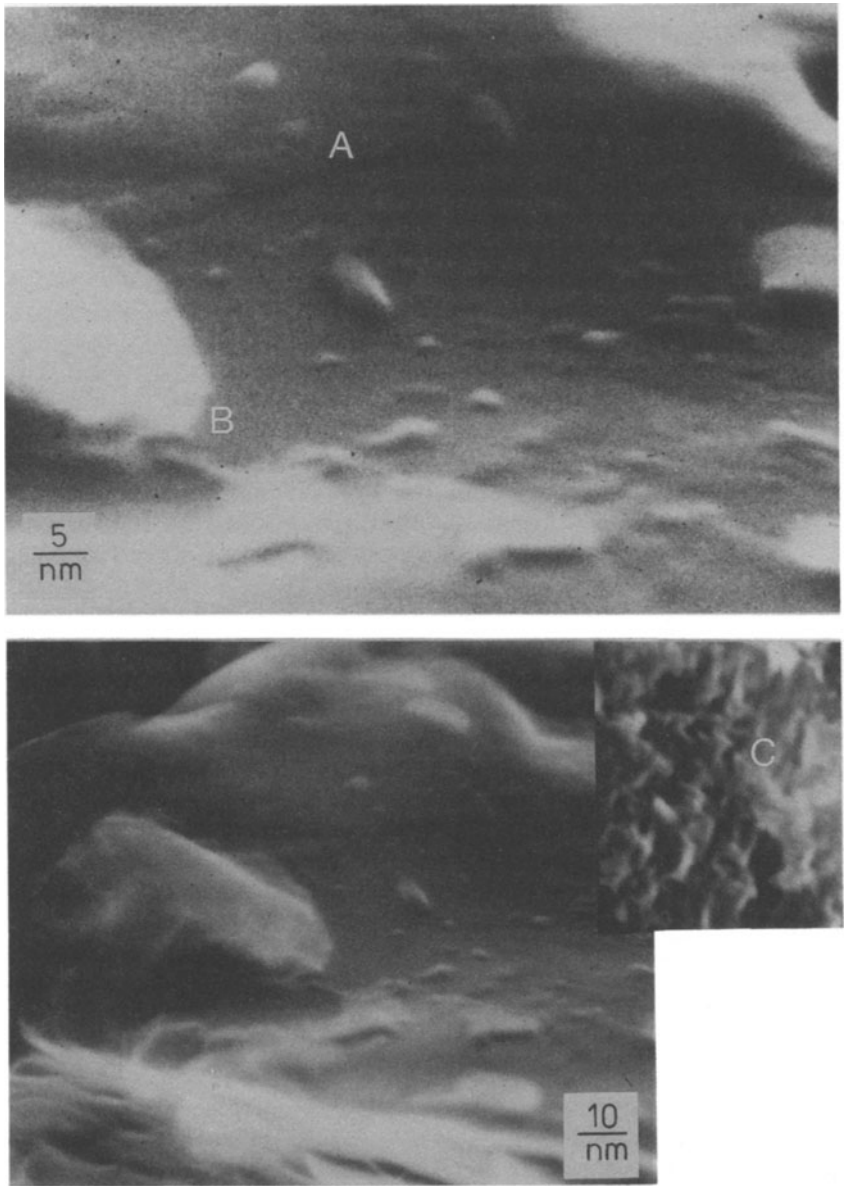

Figure 2.26. High-resolution SEM (200 kV) of activated catalyst 2. The main images were obtained from a sample activated in the presence of ca 5000 ppm water; the image in the bottom inset was obtained from a sample activated in dry synthesis gas. Region A is rich in potassium (solidified droplet of KOH), region B is rich in calcium (particle of calcium oxide), region C is also rich in potassium.

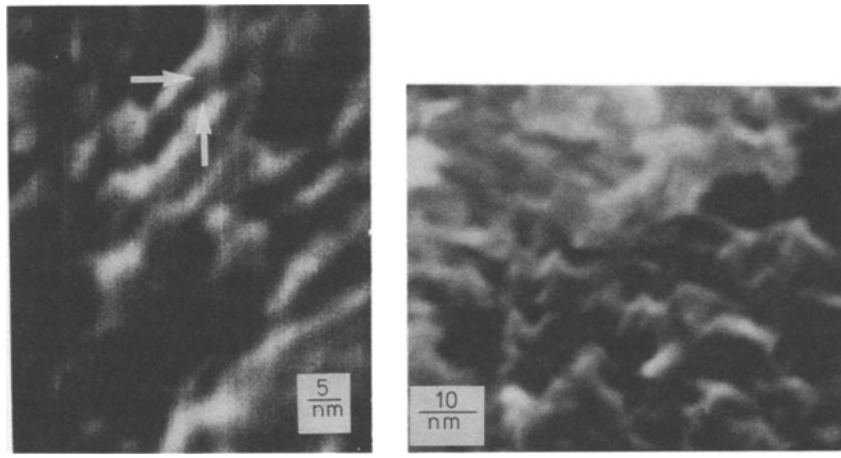

Figure 2.27. High-resolution SEM (200 kV) of catalyst 2 activated in dry synthesis gas under "industrial" conditions. The two arrows designate a step made by two superimposed platelets of iron. The thickness of the top platelet is ca 10 unit cells of iron. The irregular stacking of these primary structure elements of the catalyst can be seen in the right-hand micrograph.

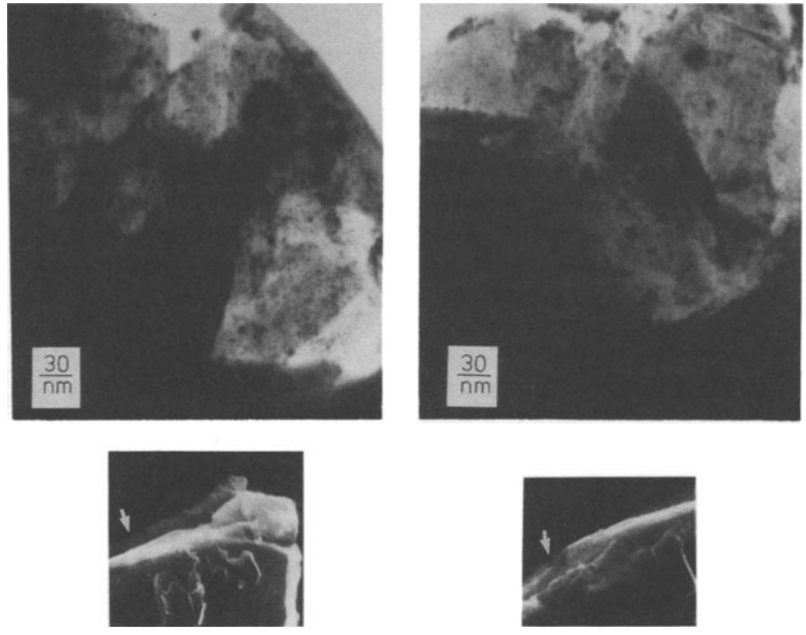

Figure 2.28. STEM images of individual platelets of activated catalyst 2 (200 kV). The arrows in the SEM insets indicate the locations from which the STEM images were obtained after suitable tilting. The platelets are single crystals of α-iron according to the corresponding selected area-diffraction patterns.

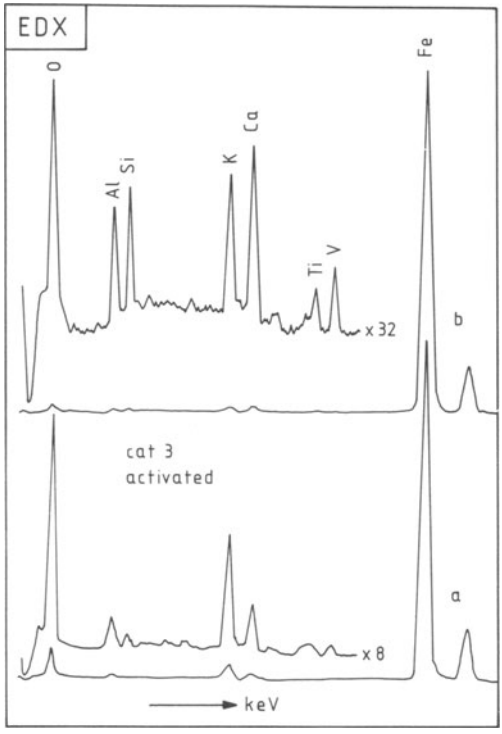

Figure 2.29. Energy dispersive X-ray analysis of two different particles of activated catalyst 3. Trace a is typically for dirty areas with many segregated particles of promoter oxides. Trace b was found characteristic for clean areas without visible particles of promoters. The spectra were taken as point analyses with ca 100,000 magnification and a very small spot of 200 kV electrons directed on a thin area of the catalyst material.

catalysts. It is also established by this bulk-sensitive technique that oxygen is a constituent element of an active catalyst. It was established beyond doubt that this oxygen was a genuine component, rather than an artefact of the transfer process. It was further demonstrated that the thin flakes of the second phase found in the XRD analysis contained significantly more oxygen than the particles of catalyst activated in a slow manner; the iron-to-oxygen ratio was typically 1:1 in the nonmetallic phase.

2.6.6. Microstructure of the Activated Catalyst

The morphology of the activated catalyst has been elucidated by studies on scanning electron microscopy. Using this information, the atomic structure of the smallest building unit to be characterized can now be analyzed using high-resolution transmission electron microscopy. It is pointed out that the resolution of lattice fringes of ca 0.2 nm, such as, e.g., the Fe (111) orientation, reaches the limit of resolution of modern commercial medium high-voltage instruments, such as the JEOL CX 200 microscope operating at 200 keV.

The crystallographic structure of the platelets can be determined by electron microdiffraction. In Fig. 2.30a, the prevailing diffraction pattern is shown. It originates from α-iron single crystals and shows the (111) orientation, which was found to constitute the basal plane of many platelets. There is no indication of

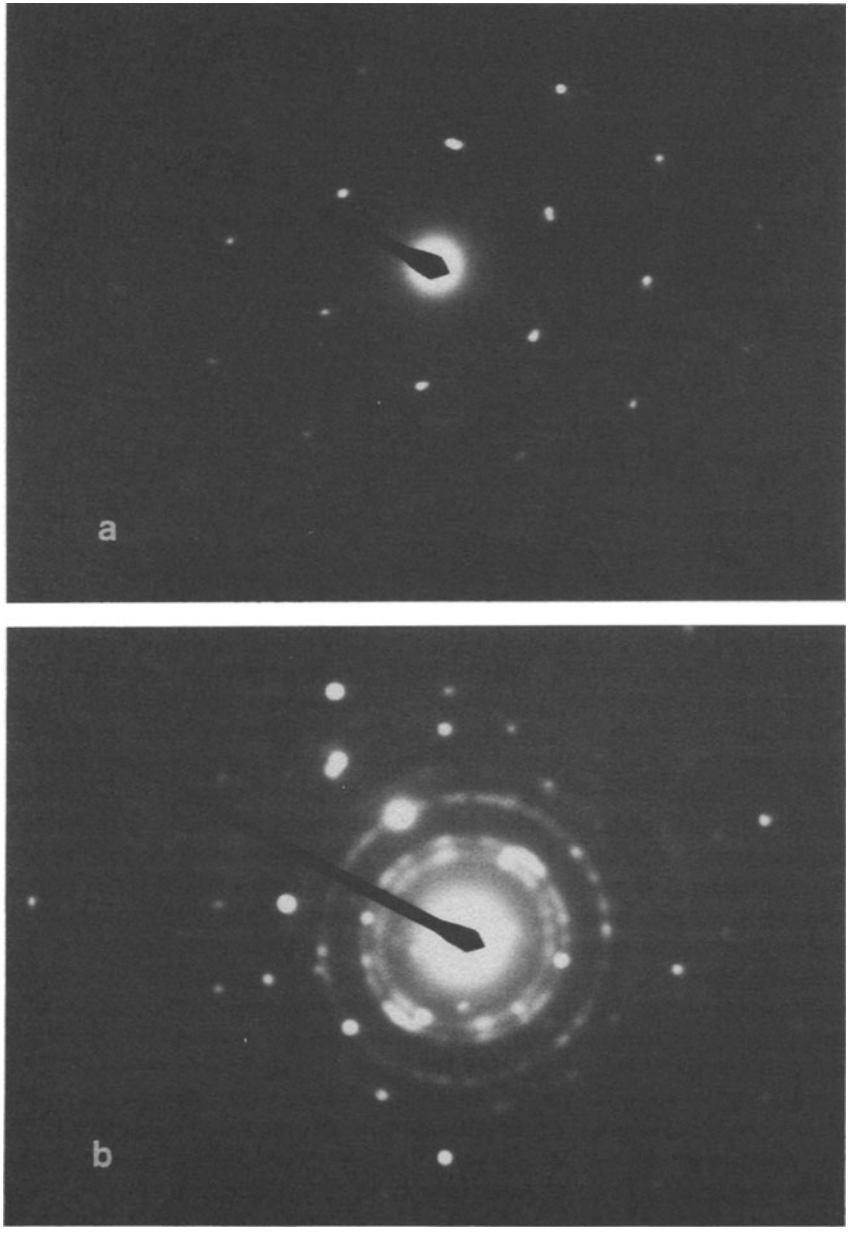

Figure 2.30. Selected area-diffraction patterns of activated catalyst 1 after successful anaerobic transfer into the electron microscope. Pattern a shows the (111) orientation of α-iron with the particles being perfect single crystals. Pattern b was taken from an area between two stacks of platelets and is typical of a strongly disordered spinel oxide lattice.

intrinsic structural disorder, as would be predicted by the theory of paracrystallinity. The fact that this information is obtained from individual particles of the catalyst, rather than from a large ensemble of crystals, strongly suggests that the XRD line broadening is an intercrystalline particle-size effect rather than an intracrystalline long-range order effect. This diffraction pattern further supports the general idea that iron (111) single crystals may constitute suitable model surfaces on which to study ammonia synthesis (see the following chapter).

Less frequently, diffraction patterns such as those seen in Fig. 2.30b were obtained, typically from areas rich in promoter oxides. They arise from the spinel structure of magnetite/hercynite particles, with little long-range order. Such particles can only diffract X-rays very poorly and may well remain undetected in a phase analysis by XRD. The existence of a disordered phase has also been mentioned in Ref. 2. The poor crystallinity of the promoter oxides is in full agreement with their genesis as a product of exsolution from the oxide precurser, which has been described in the preceding sections. The dispersion of this poorly ordered phase was found to be much higher in catalysts 2, 3, and 5 than in catalyst 1, where this phase formed seams within the activated material.

In Fig. 2.31, a sample of catalyst 1 is shown which was ca 90% reduced. The outer particles of the grains are still in the oxide state, as suggested by the

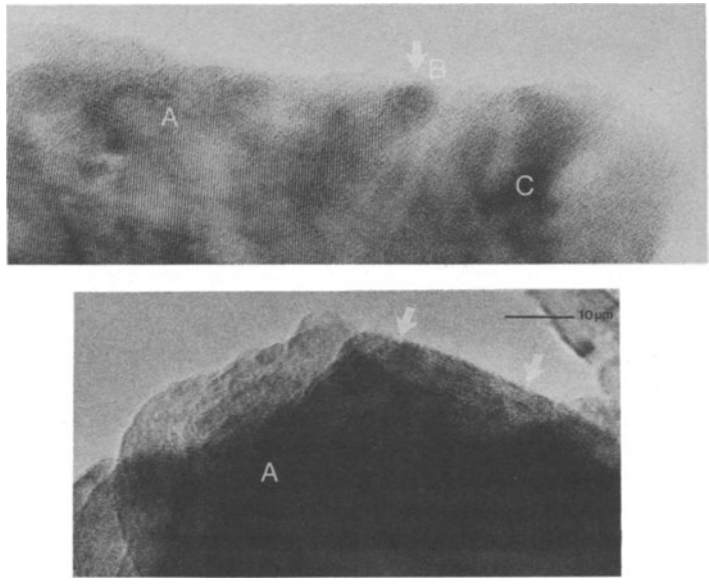

Figure 2.31. Lattice image (high-resolution TEM) of platelets of partly activated catalyst 1. The bottom image shows different orientations of the magnetite/wustite lattice; the area designated with arrows exhibits many lattice defects and shows a pronounced step structure of the edge of the platelet. The top image shows a thin section of magnetite with the (311) lattice fringes (areas A). The arrow B points at a nucleus of α-iron which grows at the interface between the still unreacted magnetite A and the amorphous reacting edge region C.

mechanistic scheme of the activation process, and the lattice image of the magnetite/wustite phase is displayed. The top image shows a single crystal of oxide exhibiting the (311) fringes. The outer right-hand edge, in the process of reduction, has already been converted into an amorphous disordered state, with a small nucleus of α-iron formed at the outer edge of the boundary region between the ordered and disordered zones. The bottom image shows the (110) orientation of the oxide phase. The irregular array of unit cells arises from the stepped structure of the edge of the platelet, as well as the large number of defects in the structure which give rise to a mosaic morphology. This structure is attributed to the presence of varying amounts of promoter ions within the iron oxide lattice. Such defects within the lattice provide good starting conditions for a solid state reaction, which involves an ion migration mechanism as postulated in the activation process.

A fully reduced sample of catalyst 1 which had been slightly reoxidized during transfer, gave rise to the images shown in Fig. 2.32. A shell of oxide particles has formed around a core of iron metal which can be identified by electron diffraction, as well as by weak fringes of Fe(111) which are visible in the bottom image. The rich mosaic structure and the average particle size of only ca 10 nm indicate clearly that these particles are not fragments of unreduced oxide from the original precursor but indicate the size of the iron single crystals. The general pattern found in a

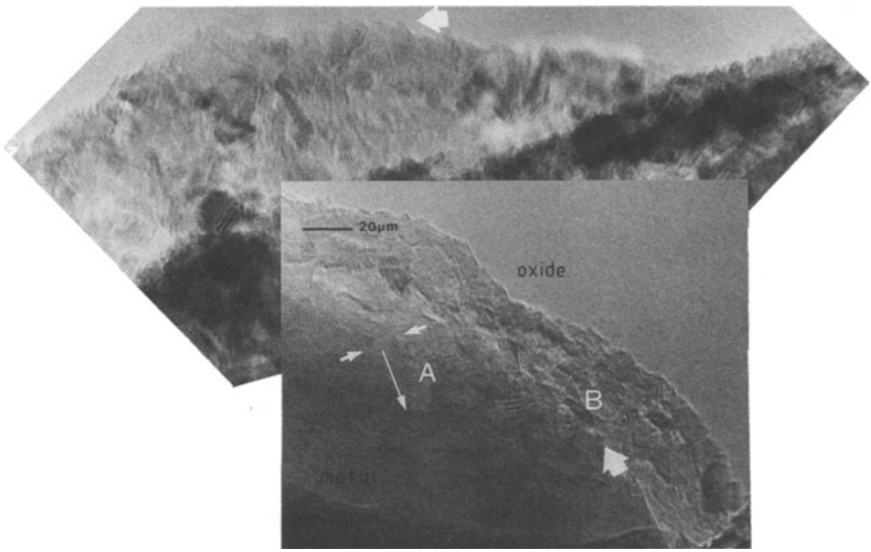

Figure 2.32. TEM images of fully activated catalyst 1 which was slowly reoxidized (passivated). Around a core of metal A exhibiting lattice fringes of Fe(111) along the direction of the long arrow a shell of tiny oxide particles B has grown. The thick arrow points at the interface between oxide and metal. The top image shows the outer section of another platelet with the arrow pointing at the sharp edges of the oxide crystallites making up the external surface, which can be seen here in cross section. There is no visible trace of contamination.

study of several samples of reduced catalyst was that, according to its variable size (from ca 30 to over 500 nm in width), a primary platelet consists of several or many single crystals of iron, with a rather uniform particle size as shown in Fig. 2.32. These crystals form an irregular mosaic, which gives rise to a rough surface exhibiting sharp edges. The direct images of these catalyst surfaces can be seen as a cross section in the top image of Fig. 2.32 and as a top view in the SEM images of Figs. 2.26 and 2.27.

When the reduced catalyst was transferred successfully in the total absence of air, it was possible to image the iron particles directly. In Fig. 2.33 the edge of a quadratic platelet is shown. The top right and bottom left insets both show Fe(111) fringes of individual crystals which constitute the platelet. The top inset shows a step structure, which indicates that the single crystals themselves exhibit a terrace structure, in the same way as seen for large single-crystal surfaces. The diffuse contrast along the steps is taken as an indication that the iron atoms in the step exhibit defective coordination, and this is responsible for a smearing of the contrast. The left bottom inset shows a perfect single crystal of iron that also exhibits the (111) orientation as its most abundant surface. It is pointed out that

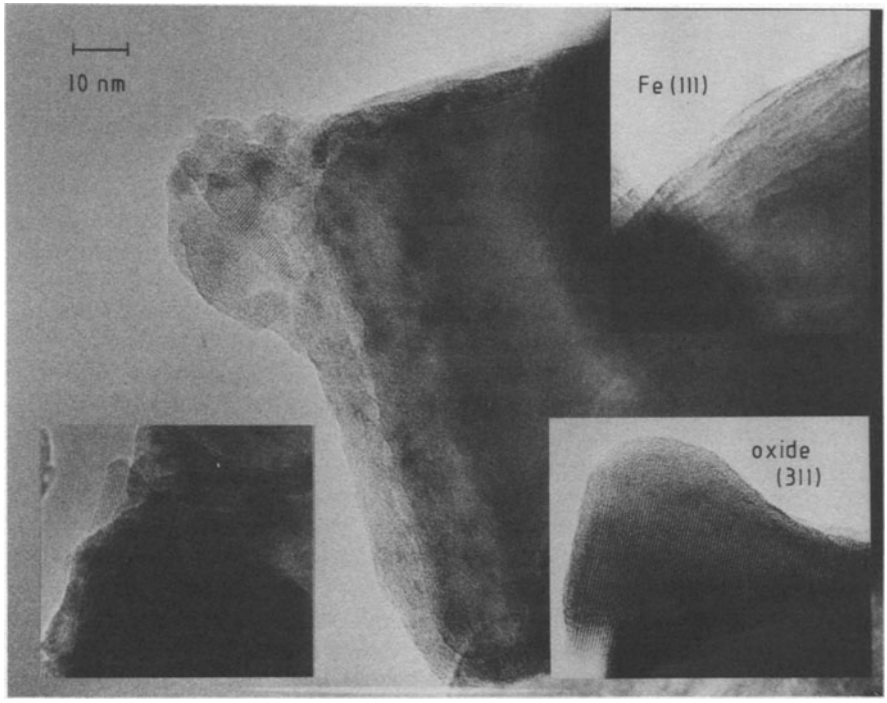

Figure 2.33. Lattice images of fully reduced catalyst 1. The insets show different areas of Fe(111) and, for comparison, an area of unreduced magnetite (311) all at the same magnification.

these and many other crystals inspected in this study are of perfect long-range order and exhibit no signs of endotactic groups within their structure. This is further illustrated in Fig. 2.34, which shows a large part of a similarly oriented iron platelet without any defects. These images demonstrate clearly that the microstructure of technical ammonia synthesis catalysts is very different from cubic iron particles and that the predominant surface orientation is the (11) plane. The images demonstrate further that a large number of iron atoms in the catalyst are in a homogeneous environment, in a similar manner to those in a macroscopic single crystal.

There is also evidence for a heterogeneous structure on the microscale. For example, the tip of the platelet shown in the main image of Fig. 2.33 is composed of intergrown oxide particles and iron nuclei which did not have the opportunity to grow larger than ca 5 nm. The frequent change in the orientation of the narrow fringes which arise from Fe(111) illustrates the misorientation of the different nuclei. This prevented their agglomeration to form a larger crystal. The iron oxide (large fringes) is most likely to be hercynite. This is difficult to reduce, and acts as a physical barrier which prevents the reorientation of the nuclei. This situation is seen to be a visible indication of the function of the structural promoters outlined

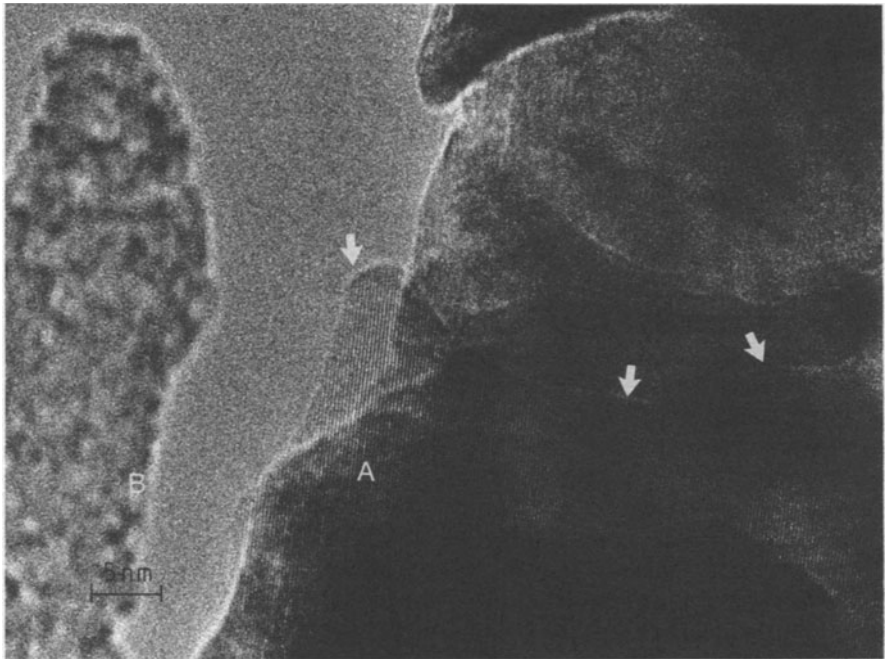

Figure 2.34. Lattice image of a perfect single crystal of iron. The anisotropic platelet exhibits the (111) orientation as basal plane A. The arrows indicate the boundary of the thin platelet standing out of a stack of similar randomly superimposed platelets. The ara B is amorphous carbon from the support grid.

above. Their main effect is to prevent the growth of the iron nuclei during activation and to preserve the microstructure during operation of the catalyst.

2.7. SURFACE ANALYSIS OF THE AMMONIA SYNTHESIS CATALYST

A detailed understanding of the mechanism of ammonia synthesis over iron metal has been obtained from single-crystal studies carried out under UHV and in situ high-pressure conditions.[51] The reaction was found to be structure-sensitive and to occur most efficiently on the Fe(111) surface, presumably on the c-7 sites.[51,52] The rate of ammonia formation is determined by the dissociative chemisorption of nitrogen. This is limited by the low adsorption probability of molecular nitrogen which gives rise to two different presursor states.[54-56] The presence of potassium was found to enhance the sticking coefficient of molecular nitrogen.[57] All of the states of chemisorbed nitrogen can be characterized by various spectroscopic techniques such as photoemission,[55,58] HREELS,[55] and XANES,[59] as well as by thermal desorption methods.[54,56]

The single-crystal studies, described in detail in the following chapter, have also been extended to high-pressure conditions[51] and to the addition of promoter compounds.[60] The latter results are consistent with the view that the reaction mechanism also applies at high pressures. The action of the potassium promoter arises from its electron-donating effect but, at high pressure and finite conversion, it has also been ascribed to a lowering of the desorption energy of the product ammonia. This arises from the repulsive interaction of the Broensted base ammonia with the basic surface groups of "potassium oxide."[53] The description of the nature of this potassium oxide is one objective of the surface characterization and will be discussed in detail below.

In order to demonstrate the validity of the low-pressure mechanism for the high-pressure practical reaction, kinetic models have been established to bridge the pressure gap.[61-63] One model, which used only the low-pressure kinetic parameters and thermodynamic data as input, was successful in the detailed prediction of the high-pressure kinetics. One conclusion was that the overall reaction enthalpy under practical synthesis conditions can be regarded as the energy required to create new free surface sites, after the hydrogenation of the nitrogen atom. This is a consequence of the high stability of the reaction intermediates, which had already been found from UHV studies and which would be expected to allow their direct spectroscopic identification on real catalyst surfaces. The other approach agrees well in the final result with the first model, but it uses a different kinetic model with different input parameters. A critical discussion of these two models will be given in subsequent chapters.

It should be stressed that not only is there a pressure gap between the UHV studies and the high-pressure measurements, but also a "material gap." The UHV studies use carefully cleaned iron metal in the form of single crystals as the catalyst. On the other hand, elemental polycrystalline iron without surface purification does not catalyze ammonia synthesis at high pressure (1 bar), as has been described in Section 2.2. This may be rationalized in terms of the extreme sensitivity of the

amount of chemisorbed nitrogen toward contamination by carbon, oxygen, and sulfur on the iron surfaces.[64]

A target of the work described below is the preparation of technical catalyst surfaces under in situ conditions. The state of nitrogen chemisorbed onto these surfaces will subsequently be characterized by X-ray photoelectron spectroscopy for comparison with the iron single-crystal studies.

Since a technical catalyst surface cannot accurately be defined by a single term such as "a clean iron surface," a large section of this work consists of the description of surfaces obtained by three different methods of activation.

Sieve fractions of 0.2–0.4 mm diameter from catalysts 2 and 3 were used in the photoemission experiments and were analyzed in the form of beds of ca 0.6 mm height of loose powders contained in molybdenum crucibles. Samples were mounted on variable-temperature specimen rods of two different Leybold photoelectron spectrometers, which were equipped with EA 10 and EA 11N analyzers, sources for Al X-rays (150 watt) and He I, He II UV radiation, sputtering facilities, quadrupole mass filters, and gas handling facilities. One spectrometer was also equipped with a standard Leybold high-pressure reaction cell which, after minor modification, allowed treatment of the samples in hydrogen at pressures up to 2 bar and at temperatures up to 790 K. Calibration of the spectrometer was carried out with Pd foil for the Fermi edge zero, and with gold foil (Au $4f$ = 84.0 eV) for the binding energy reference. Polycrystalline iron foil, cleaned by sputtering at 800 K, was used as the reference material in both clean and reoxidized forms. All surface preparations designated as activated were tested for catalytic activity by exposing the samples at 790 K to a 10^{-5} mbar hydrogen and nitrogen mixture for several hours and by monitoring the ammonia produced with the quadrupole mass filter. No attempt was made to quantify these crude tests.

The following reduction procedures were applied. Direct observation of the reduction process was achieved by exposure of the samples inside the analysis chamber to hydrogen pressures of typically 1×10^{-6} mbar for ca 120 h, after which time the evolution of water was almost complete.

More realistic reduction conditions were possible using the high-pressure attachment. Samples under hydrogen, usually at pressures of 1 bar, were heated to 790 K using a slow temperature program over a period of 48 h. In order to study the influence of the water content of the atmosphere, one set of experiments was carried out with flowing hydrogen which corresponded to an outlet water partial pressure of ca 150 ppm (designated as the "flowing" condition). In the other set of experiments, the hydrogen atmosphere (ca 25 ml volume with 20 mg catalyst sample) was only slowly changed, by bleeding the reaction gas mixture through a needle valve. This gave rise to an outlet partial pressure of eater of ca 700 ppm (designated as the "static" condition).

2.7.1. Surface Characterization

In the following sections, results will be presented which have been obtained for two catalysts designated catalyst 1 and catalyst 2 and which were of the same nominal bulk composition given in Section 2.2. Despite significant differences in

some of the bulk structural properties discussed in the previous sections, only small systematic differences in their surface properties could be detected.

2.7.1.1. Quantitative Surface Analysis

In this section, results are summarized that were obtained by integration of core level spectra, with subsequent correction for cross-section differences, using theoretical cross sections. The absolute accuracy of this procedure is of the order of 15%. This is due to errors in the background fitting procedures and spectroscopic problems, such as differential charge broadening, characteristic of the type of samples used in this study. The error was estimated by comparative measurements on different pure iron oxides. Surface stoichiometry problems, arising from films of water adsorbed on iron oxide powders, were minimized by insitu treatment with oxygen. The reproducibility of different surface preparations was found to be ca 3% for the data presented here. The data presented are representative values chosen from 23 data sets. Occasional large deviations were observed, caused by the inhomogeneity of the industrial catalyst material. This compositional inhomogeneity was also established by powder X-ray diffraction and energy dispersive X-ray analysis.

A specific problem consequent upon these inhomogeneous samples arises in the quantification of XPS results, which requires the assumption that the depth probed by XPS has a homogeneous composition. While XPS is a surface-sensitive technique, only ca 30% of the total intensity arises from the top atomic layer which may contain adsorbates and promoter films. The deeper layers, which may be of variable composition in catalyst samples, contribute the other 70% of spectral intensity in a section of ca 2 nm in thickness. Furthermore, very little information can be obtained from the inner surfaces of the pore system of an activated catalyst. It has therefore generally been assumed that the inner surface of the catalyst can be considered to be similar to the outer surface. These assumptions limit the significance of quantitative surface analysis techniques when applied to heterogeneous porous solids and do not allow clear conclusions to be drawn, as can be done in the case of single-crystal samples.

Typical elemental compositions of catalyst surfaces are given in Table 2.1. The two different samples of catalysts (see the first rows in Table 2.1) yielded similar iron-to-oxygen ratios in the activated catalyst surface regardless of the method of activation employed. The two oxide precursors, however, differ significantly in their carbon content and in the iron-to-oxygen ratio. The enrichment in carbon found for catalyst 1 arises from elemental carbon rather than from segregation of potassium carbonate, as could be shown from the chemical shift of the carbon 1 *s* line. Segregation of potassium carbonate was typical of catalyst surfaces that had for several weeks been exposed to air.

In both samples, the iron-to-oxygen ratio is lower than the calculated value for pure magnetite (nominally 0.75, with an experimental value for a powder sample of 0.70). The chemical state of much of the excess oxygen was found to be adsorbed water. Desorption of the water layer at ca 650 K caused an increase in the iron-to-oxygen ratio. Pretreatment of the catalyst in the high-pressure cell

TABLE 2.1. Surface Compositions (in at%)

Treatment	Fe	O	K	Ca	Al	C
Catalyst 1/flowing						
as received	10	45	5	1	5	34
650 K/8 h	18	41	9	3	4	25
790 K/10 h	49	38	1	3	7	
active/60 h	38	41	3	2	6	6
Catalyst 2/static						
as received	22	58	7	2	1	9
650 K prered	22	52	7	2	3	14
790 K/14 h	33	42	11	2	3	9
active/70 h	33	42	11	2	3	9

Elemental Ratios

Treatment	Fe:O	Fe:K	Fe:Ca	Fe:Al	Fe:C
Catalyst 1/flowing					
as received	0.22	2.0	10	2.0	0.29
650 K/8 h	0.44	2.0	6	4.5	0.72
790 K/10 h	1.32	16	50	16	7
active/80 h	0.93	12	19	6	6
Catalyst 2/static					
as received	0.38	3.1	11	22	2.4
650 K/prered	0.42	3.1	11	7	1.6
790 K/14 h	0.78	3.0	17	11	3.7
active/70 h	0.78	3.0	17	11	3.7

at 650 K in flowing hydrogen at 1 bar for 60 h caused only a slight change in the iron-to-oxygen ratio. Reduction in flowing dry hydrogen always led to a larger increase in the iron-to-oxygen ratio than reduction under wet conditions. In dry hydrogen, the iron-to-oxygen ratio is increased to 1.85, implying that a significant amount of iron must be in the zero-valent state. In the case of wet reduction, the ratio only reaches 1.75, indicating a lower content of zero-valent iron in the surface.

Prolonged exposure of the reduced surface to ammonia synthesis gas mixtures at low pressure did not result in further reduction of the residual iron oxide. A beneficial effect of synthesis gas might have been expected from the decomposition of catalytically formed ammonia on iron oxide, which could act as a source of atomic hydrogen. A significant lowering of the iron-to-oxygen ratio with prolonged exposure to synthesis gas mixtures was found with all catalysts reduced under dry conditions. Samples reduced in wet hydrogen were much more stable.

The ammonia synthesis catalyst exhibits a remarkable ability for self-purification. Heating in hydrogen results in removal of a large fraction of the carbon contamination. This is in contrast to elemental iron, where similar treatment only causes segregation of carbon to the surface. An intense signal at mass 15 arising from a CH_3 fragment in the mass spectrum of the exit gas during reduction shows that carbon is removed as a hydrogenated species, possibly methane. Residual carbon contamination in the surface below 10 at% cannot be removed by hydrogenation, which is indicative of a graphitic deposit (see below).

Changes in the surface concentrations of the promoter elements are also dependent on the mode of reduction. Subsequent to wet reduction, potassium and aluminum are destributed at the surface, while their concentrations are lowered when dry hydrogen is used. Redispersion of aluminum occurred in samples of both catalysts that had been reduced in dry hydrogen during ammonia synthesis. The redispersion was complete within ca 30 hours of exposure to synthesis gas mixture and did not occur when the samples were kept at 790 K in pure hydrogen.

It is interesting to note the large difference in potassium dispersion as indicated by the iron-to-potassium ratios. Wet reduction seems to support the formation of a potassium species which is dispersed over the surface of the catalyst.

In summary, quantitative results indicate a strong influence of the reduction conditions on the composition of the resulting surface. The most abundant element on the active surface is oxygen. Iron must be present in several different chemical states, and a large fraction is present as elemental iron. A common observation is the efficient removal of carbon contamination during reduction. There are indications of two types of carbon contaminants, each with a different chemical reactivity.

2.7.1.2. UPS Results

UV excited valence-band spectra (UPS) are not often used in the characterization of real catalyst systems. In the present study they were measured for two purposes. First, in a mixture of iron metal and iron oxide, UPS allows accurate definition of the zero of the energy scale and the detection of charging phenomena. In addition, the characteristic dependence of spectral features on excitation energy permits the qualitative separation of the valence band features due to oxygen-derived states from those of the iron $3d$ valence states. It is therefore possible to follow the reduction process of the surface. In addition, these spectra can indicate that there are no small molecules such as molecular oxygen, water, or carbon monoxide on the activated surface, by the absence of characteristic "fingerprint" patterns.

In Fig. 2.35, a set of He I (top) and He II (bottom) excited UPS data for a reduction experiment inside the analysis chamber is shown. The He I spectra are dominated by a feature at 6.5 eV and an additional structure around 10.8 eV. The most significant change as reduction proceeds is the appearance of a new feature at the Fermi level (compare the spectra after 1 h and 70 h). The formation of a Fermi edge indicates that the chemical reaction produces a species of metallic iron, even at the low partial pressure of hydrogen used in the reduction experiment. A comparative experiment using an oxidized iron foil under the same reaction conditions did not lead to the formation of an equivalent feature at the Fermi edge.

The main peak at 6.5 eV is composed of both oxygen $2p$ and iron 3d states, which indicate the presence of iron–oxygen bonds. The peak at 10.8 eV arises from the OH groups of chemisorbed water. This was established by drying a slurry of magnetite in water, inside the UHV system. This assignment is also in agreement with literature data of other hydroxide systems.[65]

As indicated above, changes in the shape of the spectrum around the main peak as the excitation energy is increased can be used to separate, qualitatively,

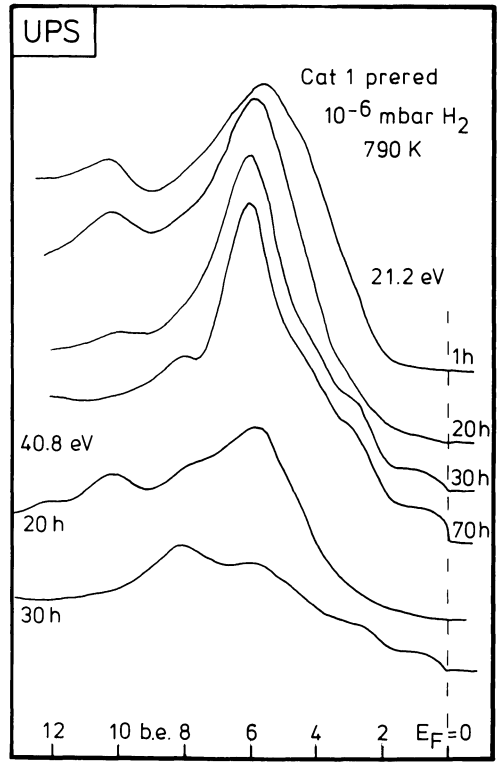

Figure 2.35. UPS data of an "in situ" reduction experiment of catalyst 1 which was prepared outside the spectrometer and transferred in dry air. The spectrum of the genuine precursor was very similar to the top spectrum in the figure. The top four spectra were taken with He I excitation, the two bottom spectra with He II excitation (analyzer in the FRR 4 and FAT 20 eV mode, respectively).

the oxygen and iron contributions to the valence band spectrum. This is illustrated in Fig. 2.36 in which a data set obtained from an intermediate state of a high-pressure reduction experiment is shown (see below). For comparison, the spectrum of clean, polycrystalline iron, with its characteristic iron 3*d* band, is also shown. All spectra have been normalized to a point at 12.2 eV, which is free from contributions due to characteristic structures.

With increasing photon energy, the sharp structure of the oxygen 2*p* states disappears and a double peak structure, which can be clearly seen in the bottom traces of Fig. 2.35, becomes apparent. In Fig. 2.36, additional features can be seen at ca 1.0 eV and 3.0 eV. These four structures arise mainly from iron 3*d* states, which extend over a wide energy range in the partly covalent iron oxides. This is in marked contrast to elemental iron, where they form a characteristic narrow conduction band which contains the Fermi edge. This observed trend in the energy dependence of the cross sections is consistent with the theoretical values of 4.83 and 8.75 for iron and 10.67 and 6.81 for oxygen when using excitation energies of 21.2 and 40.8 eV, respectively.[66]

From comparison with data reported previously in the literature, the double peak structure and the feature at ca 1 eV are indicative of ferrous ions (Fe^{2+}), and

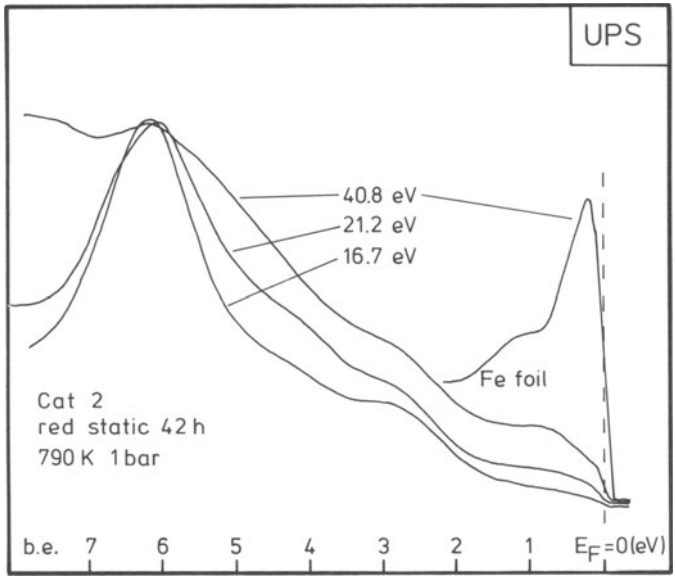

Figure 2.36. Dependence of the valence band features of a partly reduced catalyst on the excitation energy. This dependence is used to discriminate oxygen states from the iron 3*d* states (analyzer mode FAT 10 eV for all spectra).

they occur both in the magnetite precursor and in the expected reduction intermediate, wustite (FeO). Ferric ions (Fe^{3+}) give rise to a single peak around 5.5 eV. Chemisorbed carbon monoxide gives rise in the He II spectra to two peaks at 7.6 eV and 10.7 eV ($5\sigma/1\pi$ and 4σ, respectively). Having established a set of fingerprint spectra for several relevant species which would normally be difficult to obtain from XPS data, it was possible to follow the reduction of the oxide precursors under the different conditions of activation. There was no significant difference between the two types of catalyst used.

The unreduced surface of the catalyst used for the experiment described in Fig. 2.35 contains iron only in the ferric state, indicating that the surface of bulk magnetite is fully oxidized. Moreover, it contains a significant amount of chemisorbed water. The very low intensity of the spectrum within the first 2 eV is consistent with the semiconductor nature of hematite. If the intensity scale is greatly expanded, it can be seen that the spectrum begins exactly at the point of zero energy, as determined by the palladium Fermi edge (indicated by the dashed line in the figure). This is taken as proof that specimen charging had not occurred. Hence, the binding energy scale established with metallic reference elements is also valid for these catalyst samples.

After 20 hours of reduction at low hydrogen pressure, some of the iron had been reduced to the divalent state, as indicated by a shoulder below 8 eV in the He II spectrum. After 30 hours, the spectrum of ferrous ions had become dominant in the data obtained using both He I and He II excitation. A significant intensity

at the zero-energy point indicates a shift of part of the iron $3d$ intensity to zero energy, which is characteristic of the formation of elemental iron. Further heating in hydrogen removes all of the water and a large fraction of the oxygen, as shown by a narrowing of the structure at 5.5 eV. The step at the zero-energy point is characteristic of elemental iron. This iron, however, is either present as small particles below 10 nm in size or, alternatively, is contaminated by oxygen. These two effects may explain the absence of the triangular conduction band feature normally found in clean, bulk, elemental iron. In control experiments with a partly oxidized iron foil, it was found that contaminated iron exhibits a very low cross section for both He I and He II spectra. It is therefore difficult to estimate the amount of zero-valent iron present in the catalyst surface. The majority of the surface iron is, however, present in the form of ferrous ions.

In summary, observation of reduction in situ revealed that the hydroxylated ferric surface of the precursor is converted into a largely ferrous surface, free of water after a long induction period. Only a fraction of the surface iron is reduced to an ill-defined metallic state. Neither a film of chemisorbed water nor other molecular contaminants block the surface and prevent the reduction from proceeding. This is in contrast to the kinetic studies described in Section 2.5, which deal with the high-pressure reduction of iron oxides where, under identical conditions, ferrous ions are more easily reduced than ferric ions.

The UPS data from surfaces reduced for 70 hours under high pressure are compared in Fig. 2.37. Spectra of elemental iron and an unreduced oxide precursor are also shown. No further changes in the patterns were observed following a further period of 24 hours of additional exposure to hydrogen. These spectra, which are significantly different to those of both the precursor and elemental iron, appear to represent the catalyst surfaces in their final stage of reduction.

Reduction of the oxide using wet hydrogen results in a surface constitution very similar to that obtained during the low-pressure reduction. The presence of a critical concentration of water seems to cancel the effect of a partial pressure of hydrogen which is nine orders of magnitude higher. Only a small amount of elemental iron is present in the surface, but this is, however, very stable against reoxidation. Neither storage in UHV for 48 hours, not cooling to room temperature and reheating to 790 K, caused any change in the spectrum.

In contrast, reduction under dry conditions results in the conversion of most of the iron to the metallic state. The top spectrum in Fig. 2.37 shows clearly the formation of the iron $3d$ conduction band in coexistence with some residual ferrous ions. The main feature at ca 6 eV is at the same position as in the unreduced sample. This result provides further evidence that the spectra are free from charging effects. When a sample has become charged, inhomogeneities in the surface potential arise from the coexistence of insulating patches and metallic particles, and these should influence the peak positions of the insulating phase.

Spectra similar to the top trace in Fig. 2.37, showing the characteristic distortion of the conduction band feature, were obtained after exposure of the iron foil to 2 L (L is the Langmuir unit, 1 L = 10^{-6} Torr sec) of oxygen at 300 K. The shoulder around 4 eV is indicative of the presence of ferrous ions. These are not normally formed in the initial phase of oxidation of elemental iron. The catalyst surface is

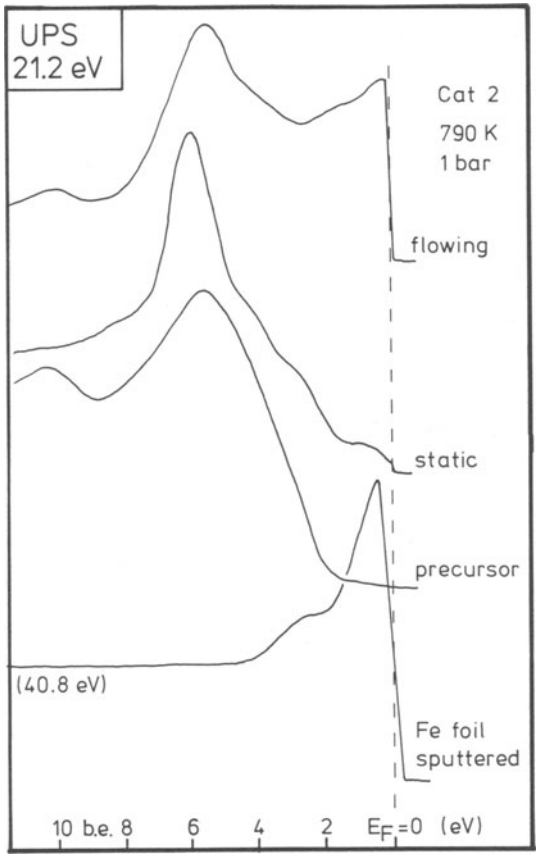

Figure 2.37. Comparison of the valence band spectra of differently activated catalyst samples. The reactions in static or flowing hydrogen were carried out in a high-pressure attachment to the spectrometer (analyzer mode FRR 4 and FAT 20 eV for the iron metal spectrum).

thus composed of a large fraction of elemental iron and chemisorbed oxygen, with a small fraction of ferrous iron oxide. The surface is unstable, and reoxidation can occur during storage in UHV at room temperature, or during heating in UHV to 790 K. This sensitivity was also found to be typical of clean elemental iron. The chemisorbed oxygen and the presence of water on the catalyst surface may therefore be an artefact of the sample transfer, which involved cooling to room temperature and mechanical movement through a viton-sealed compartment.

Finally, the UPS results are compared with the valence band XPS data presented in Fig. 2.38. These spectra are very weak and require accumulation times of ca 10 hours, which may be compared to the UPS data which are available within 5 minutes. The spectra were obtained after 72 hours of reduction. The intensity at the zero-energy point implies the presence of different amounts of elemental iron in the two samples. This assignment is, however, not wholly unambiguous. Ferrous ions exhibit a characteristic structure at a binding energy of 1 eV (arrow in Fig.

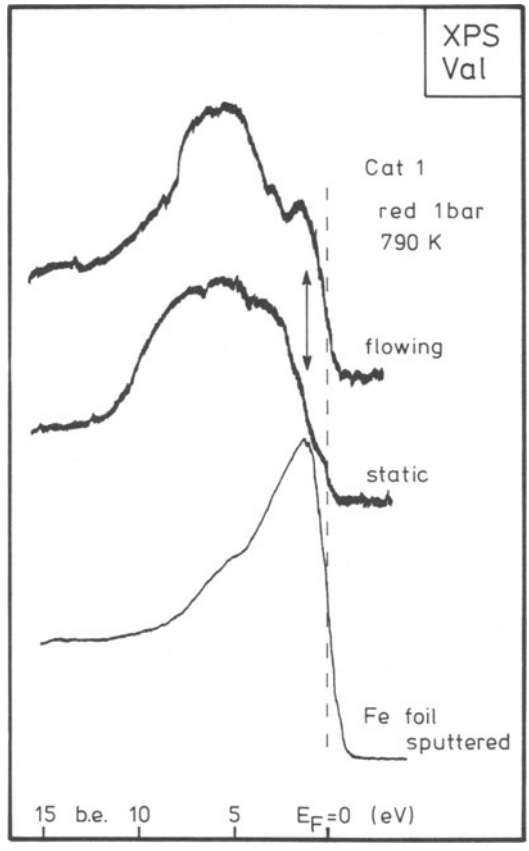

Figure 2.38. Valence band spectra of the catalyst samples used for Fig. 2.37 with Mg X-ray excitation. The arrow indicates a characteristic structure for Fe^{+2} states (analyzer mode FAT 50 eV).

2.38) which may be mistaken for the top of the iron conduction band, taking into account the poor resolution of nonmonochromated valence band XPS (ca 1.0 eV).

Both catalysts exhibit a broader iron 3*d* band than that of elemental iron. A large fraction of the total valence band intensity arises from these iron 3*d* states (cross section of Fe 3*d* 4.5×10^{-3} compared to O 2*p* with 5×10^{-4}). This reflects the presence of covalently bonded iron compounds in the mixed surface of the catalysts. The broad feature at 5.5 eV in the top spectrum arises largely from oxygen, since a similar structure with low intensity at the Fermi edge was found for iron foil exposed to 8 L oxygen at room temperature. The shoulder around 10 eV, indicative of iron oxides, was not observed in the chemisorption experiment.

The XPS valence band data represent, in a less well resolved manner, the same situation on the catalyst surfaces as the UPS data. The significantly different degrees of reduction, which result from different levels of water and the presence of nonreduced iron oxides in both samples, are the main characteristics of the surfaces, which will subsequently be used as substrates for nitrogen chemisorption

experiments. The UPS data also show that reduction proceeds via intermediate ferrous ions, starting from a surface containing exclusively ferric.

2.7.1.3. Iron and Oxygen Core Levels

Core level spectroscopy of iron compounds is a prototype example, showing the distortions of the frozen orbital model, which describes photoemission from many bodies. The iron M transitions are governed by coupling of the core hole with the unfilled *d* orbitals of the valence shell (multiplet splitting). The iron L transitions are, in addition, strongly influenced by the large number of final states with finite transition probability arising from the partly covalent character of the iron–oxygen bond. The energy distribution of these shake-up satellites extends over ca 15 eV and reduces the intensity of the main transition significantly. Instead of a clearly resolved iron 2*p* spectrum, consisting essentially of two lines, a broad intensity distribution over ca 30 eV is obtained with all iron oxide systems. The strong variation in background, which can be seen in the inset of Fig. 2.6, further complicates the evaluation of all spectral components.

The result of these spectroscopic problems, together with the notorious non-stoichiometry of all iron oxides, is that the definition of reference data becomes rather complicated, as has been illustrated in a recent review article.[67,68] Combination of literature data with results from the UPS experiments allows an interpretation of the iron 2*p* 3/2 spectrum of the catalyst surfaces. During data analysis, the background subtraction procedure influenced the interpretation to a major extent. Linear backgrounds caused omission of part of the spectrum, which at no point reached the base line between the two spin–orbit maxima (see raw data presented in Fig. 2.41). Shirley-type stepped backgrounds overemphasized or created satellite structures. A compromise was found by postulating a curved background, represented by an empirical polynomial function, the nonlinear coefficients of which were kept constant throughout the analysis of all data.

The results of the in situ reduction experiments are summarized in Fig. 2.39. The positions of the Fe 2*p* 3/2 maxima for different valencies are given as dotted lines. Despite pronounced multibody effects, the literature values follow the general rule of equidistant shifts for a change in valency (the oxidation of Fe 0 to Fe 2+ results in twice the shift which accompanies further oxidation of Fe 2+ to Fe 3+).

The reduction reaction starts from an entirely ferric surface (bottom spectrum in Fig. 2.39). After a short time, a ferrous intermediate is present in addition to the ferric main component. Subsequently, very little change occurs until, after several additional hours of reduction, sudden step changes in both spectral shape and intensity are observed (top spectrum in Fig. 2.39). These are caused by the very rapid reduction of most of the oxide to zero-valent iron. The reduction process causes the loss of the satellite structure, with the consequence that most of the spectral intensity is concentrated into the main transition. This accounts for the apparent increase in total integrated spectral intensity.

These results demonstrate a gradual interconversion of the starting oxide into a ferrous intermediate, followed by total reduction which is qualitatively consistent with the UPS observations. The time scales of the chemical events in both spectros-

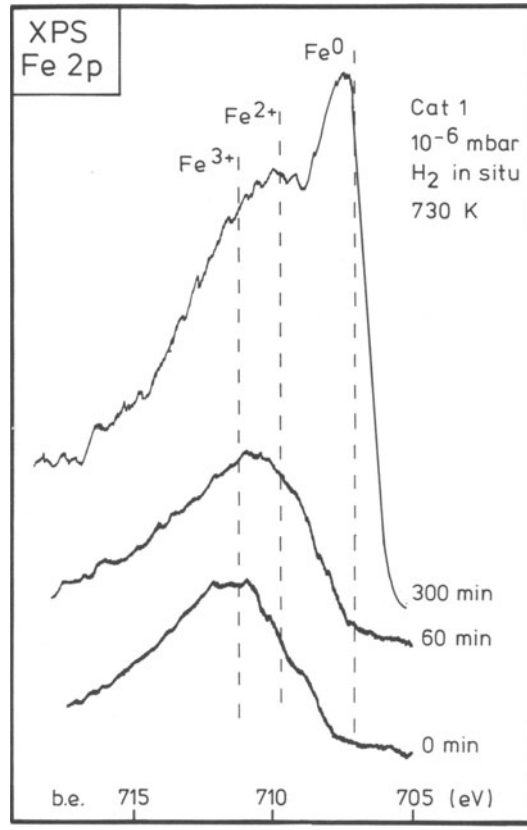

Figure 2.39. Core level spectra of the Fe 2*p* 2/3 line during "in situ" activation of a genuine precursor sample. The ordinate scale is the same for all spectra (analyzer mode FAT 50 eV).

copies are, however, vastly different owing to the different sampling depths of the two methods. XPS probes a significant depth into the sample with only a relatively minor contribution from the surface. A steady state derived from various reversible reactions is reached in the near-surface ("XPS") zone within a few hours. Reduction within the deeper volume elements of the catalyst requires permanent diffusion of water through to the surface. This bulk reduction cannot be investigated by XPS, though it does interfere with the establishment of a steady-state surface composition. Only when the bulk reduction is complete does the surface region probed by UPS reach the steady state. The distribution of iron valencies which correspond to this steady state is determined by the reduction conditions (see Section 2.8).

The results of reductions at high pressure are compared with the spectrum of elemental iron in Fig. 2.40. The spectrum of elemental iron (bottom in Fig. 2.40) is characterized by a single asymmetric line, typical of metallic elements. The weak structure at 711 eV is attributed to a satellite, since the presence of possible oxide contamination is excluded by both the corresponding UPS data and the absence of an oxygen Auger line (see inset in Fig. 2.40).

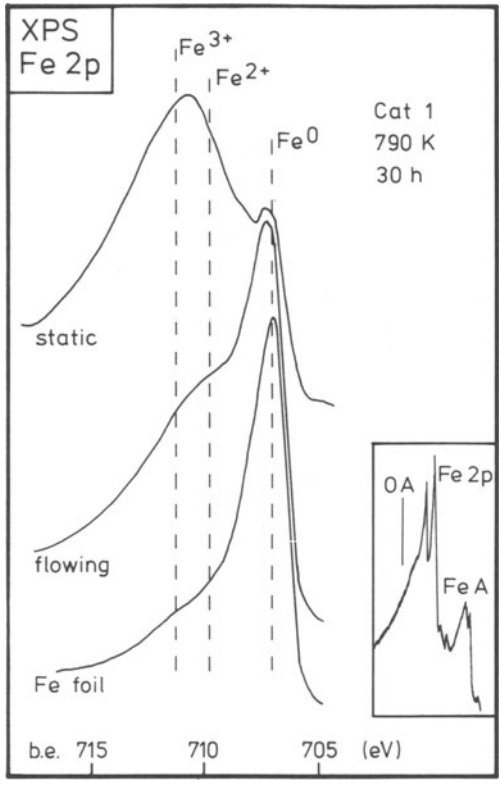

Figure 2.40. Core level spectra of the Fe 2*p* 3/2 line of differently reduced samples of catalyst 1. The inset shows a section of the survey spectrum of pure iron indicating the absence of any oxygen contamination which could have caused the shoulder at 711 eV in the main bottom reference spectrum (analyzer mode FAT 50 eV).

Spectra from surfaces prepared under dry reduction conditions are dominated by the peak for elemental iron. They all, however, showed a shoulder at 710 eV, characteristic of the presence of unreduced material in, presumably, both ferrous and ferric oxidation states. The position and linewidth of the zero-valent iron peak are different from those of iron foil. A shift of 0.2–0.3 eV to higher binding energy was typical as well as a broader linewidth (2.2 eV for ion foil and ca 3.0 eV for the catalyst). There was no detectable relaxation shift in the iron spectrum. Therefore, the possibility of small-particle effects seems unlikely. The presence of large concentrations of local defects, in addition to possible spectroscopic effects of local variations in the position of the Fermi level, offer plausible explanations for the differences in spectral parameters.

Under wet reduction conditions, the amount of zero-valent iron is much smaller than after dry reduction, which is in agreement with the UPS data. The peak maximum for the oxidized species lying between the typical binding energies of ferrous and ferric iron is not indicative of a special chemical state. This arises from a superposition of two asymmetric subspectra, each centered at the typical ferrous and ferric positions. Comparison of the sample spectrum with the spectrum of magnetite shows that the amount of ferrous ions in the catalyst is much larger

than in magnetite itself, as expected from the quantitative data (see Table 2.1). Attempts to deconvolute the spectrum by subtraction of a reference spectrum of unreduced magnetite or wustite were not successful, leaving behind only distorted residual intensity distributions. A modification of the satellite structure of the oxides is therefore assumed to cause these features either by the presence of promoter elements (ternary oxides), or by the intergrowth of the zero-valent iron into the oxide matrix. In either case, reduction resulted in a modification of the chemical nature of the residual iron oxide and the final spectrum is not simply a superposition of unreduced starting material and reduced iron.

The position of the zero-valent iron is shifted by the same value in both types of catalyst surfaces, irrespective of the amount of oxide present. This observation renders unlikely any influence caused by local variations of the Fermi level on the spectra. It is assumed that in both reduction processes the same type of defective zero-valent iron is formed. Such an analysis is in agreement with the bulk analytical results from XRD, EXAFS, and Mössbauer spectroscopy which were described above.

In Fig. 2.41, a raw data set from a wet reduction experiment is shown. The catalyst had, however, been stored in air for several years before it was used. Segregation of potassium compounds had led to a color change from black to gray. The reduction was carried out on such a gray surface, cut from the catalyst lump using a diamond saw. The left-hand side of Fig. 2.41 shows iron 2*p* data

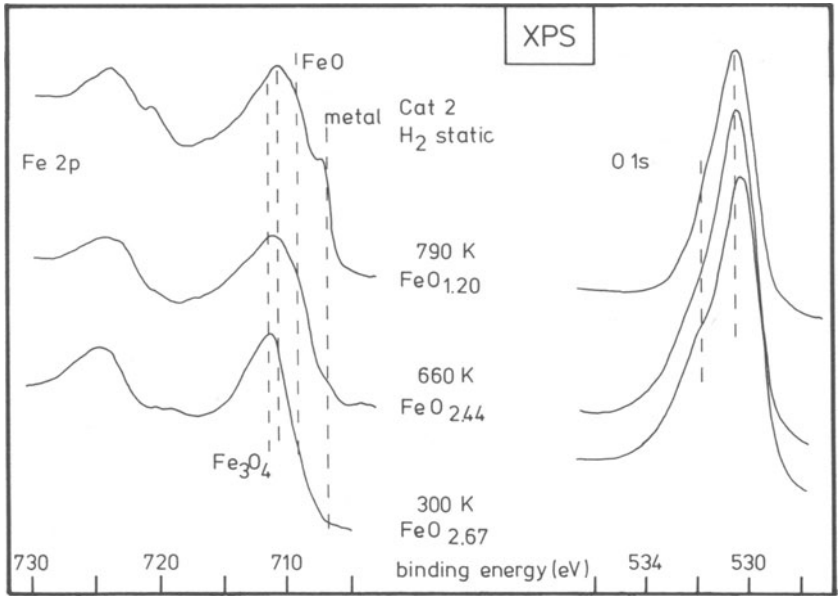

Figure 2.41. Raw data of core level spectra of an activation experiment of catalyst 2 in static hydrogen. The compositions were derived from integration of the Fe 2*p* and O 1*s* core level spectra. No significant difference in the Fe:O ratios was obtained if the Fe 3*p* core level spectra were used indicating a largely correct background subtraction (analyzer mode FAT 50 eV).

obtained after keeping the catalyst for 24 h at the indicated temperatures, under 1 bar of hydrogen. The bottom trace is typical of a totally oxidized ferric surface of the catalyst precursor. The sharp line as 711.4 eV and the satellite structure at ca 719 eV indicate the presence of hematite as the surface species. The Fe:O ratio of 1:2.67 is much larger than would be expected for bulk hematite, which has a Fe:O ratio of 1:1.5. The excess oxygen is present as surface hydroxyl groups, which give rise to the shoulder at 531.9 eV in the corresponding oxygen 1*s* spectrum (at the right-hand side of Fig. 2.41). Chemisorbed molecular water would give rise to a peak at ca 533 eV, which had been observed previously on freshly introduced samples of prereduced catalysts (not discussed here).

Heating to 66 K in hydrogen resulted in reduction of the surface hematite to magnetite, as indicated by the appearance of spectral intensity below 710 eV (typical for ferrous iron) and the shift of the satellite structure closer to the main Fe 2*p* 3/2 structure (intensity around 715 eV). This reduction did not result in the loss of the surface hydroxyl groups, as indicated by the large excess of oxygen (Fe:O ratio for bulk magnetite 1:1.33, observed ratio 1:2.44). The presence of surface hydrogen groups can also be deduced from the still strongly asymmetric oxygen 1*s* line profile. The shift of the apparent maximum in the oxygen 1*s* spectrum is caused by the high dispersion of the oxidic potassium promoter (see below).

Reduction at 790 K finally led to the formation of zero-valent iron, as indicated by the shoulder below 707 eV. The close similarity between this spectrum and the one shown in Fig. 2.40 is a measure of the reproducibility of spectral features under the same reduction conditions. Here, the Fe:O ratio of 1:1.2 is slightly below the value for bulk magnetite, namely, 1:1.33. The observation that the oxygen 1*s* spectrum is less asymmetric and the loss of spectral intensity above 532 eV indicate that a large amount of hydrogen-bridged surface hydroxyl groups (with chemical shifts more similar to those of water) has now disappeared. Only isolated hydroxyls (with shifts more similar to main group element oxides) and oxide anions, a large fraction of which may be coordinated to the cationic promoters, potassium and aluminum, still remain. This could account for the high binding energy of the center of gravity of the oxygen 1*s* line which lies at a value of 530.4 eV, larger than that of oxygen in pure iron oxides, with typical binding energies in the range 529.7–530.0 eV. The unchanged position of the oxygen 1*s* maximum, before and after reduction to a partly metallic surface, is further evidence for the absence of surface charging in this system.

In summary, the iron core level data have shown that different methods of reduction result in different completeness of conversion to zero-valent iron, in agreement with the more surface-sensitive UPS data. The residual oxide, which was present in all cases investigated, is a mixed ferrous and ferric oxide with a different chemical identity to the precursor magnetite, i.e., the oxidic residue is modified chemically during the reduction procedure and is therefore not merely a simple residue of unreduced starting material. After reduction, the spectral parameters of the zero-valent iron are slightly different to bulk iron foil and it is assumed that the iron is present as large particles (above 10 nm diameter) but with disordered surfaces. All activated catalyst surfaces contain zero-valent iron, and also significant levels of iron bound to oxygen.

After reduction, the oxygen 1*s* spectra are dominated by species bound to main group elements. The possibility cannot be excluded, however, that, in addition to the expected cations of the promoter elements, there may also be some isolated hydroxyl groups present on the activated catalyst surfaces.

2.7.1.4. Promoters and Impurities

This section will concentrate on a few effects which can be characterized as typical, although large nonsystematic variations in the distribution of both the promoters and the carbon impurity have been observed throughout this study. Typical spectra are summarized in Fig. 2.41. The calcium 2*p* spectra shown on the left-hand side of the figure indicate some of the chemical changes that can be observed in the structural promoter calcium oxide. The shift of the spectrum, relative to the position of a thin layer of CaO supported on graphite (no charging), indicates either differential charging of large crystals of CaO relative to the catalyst surface, or a high dispersion of the calcium giving rise to relaxation shifts. Because of the observed low total abundance of calcium at the surface (see Table 2.1) and the absence of any detectable relaxation shift, differential charging is assumed to cause the shift, which is too large to be explained by a chemical shift of the closed shell cation Ca^{2+}. The changes in the line shapes during catalyst treatment at 660 K indicate the transformation of calcium hydroxide and calcium carbonate present as surface compounds into a single chemical species calcium oxide. This "cleaning" is associated with a change in differential charging.

The broadening of the spectrum upon treatment at 790 K is similar to observations made when calcium carbonate single crystals are subject to argon ion bombardment. The "defects" induced in the calcium oxide component of the catalyst cannot be caused by an initial reduction of the oxide, because calcium oxide is stable to hydrogen at 790 K. The "defects" may be indicative of the formation of a ternary calcium iron oxide since there is no observed increase in the dispersion of calcium, which would be associated with a disintegration of the CaO crystals. It should be pointed out that the other structural promoter element, aluminum, exhibits the same spectral changes in its Al 2*s* emission. The dispersion of the alumina increases, however, with reduction of the catalyst, particularly when the wet reduction method is applied (see Table 2.1).

The spectra of the electronic promoter, potassium, indicate different changes during reduction to those of the structural promoters (see central part of Fig. 2.42). The observed binding energy of 293.6 eV agrees well with previous observations of potassium oxide in iron oxide catalysts.[69] This binding energy does not change upon reduction, i.e., the oxidic potassium is not reduced to the metallic state and this behavior was found with all of the samples investigated. The promoting action of potassium in these catalysts therefore cannot be associated with a metallic state. The spectra also show that the dispersion increases while reduction proceeds, but only when the wet activation method is applied. On dry reduction, the potassium compound appears to agglomerate. This is associated with a shift of the potassium 2*p* line to 293.8 eV, which has been found to be characteristic of pure bulk potassium hydroxide in the absence of electrostatic charging.[69,70] The spectra at 300 K and

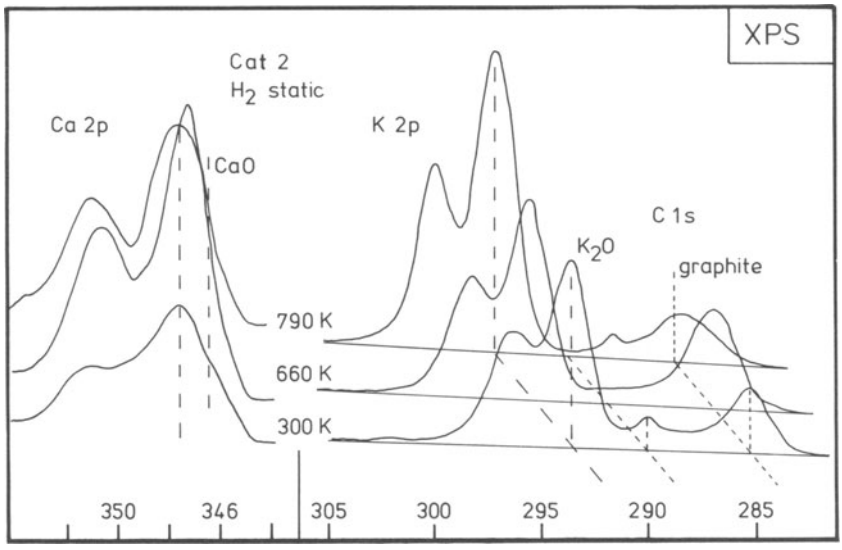

Figure 2.42. Typical core level spectra of promoter and impurity elements. The sample was the same as that used for the spectra of Fig. 2.41 (analyzer mode FAT 50 eV).

at 660 K show some tailing to higher binding energy (poor separation of the spin-orbit doublet), which was more pronounced for the sample that exhibited visual segregation of the potassium compounds. This is assumed to be caused by differential charging of some large crystals of insulating potassium oxide. As dispersion increases and large particles disintegrate, differential charging disappears and the spectrum becomes sharper.

The spectra of the main impurity, carbon, are displayed on the right-hand side of Fig. 2.42. The low intensity, compared to the potassium spectra, is caused by the fourfold smaller cross section for carbon 1*s* emission relative to potassium 2*p* emission. At room temperature, carbon is present in two forms: as organic carbon, CH_x (peak at 285 eV), and as carbonate carbon, bound to the alkaline surface of the calcium and potassium compounds (peak at 289.8 eV). The spectral intensity lying between the two peaks indicates the presence of oxygenated carbon compounds. Reduction in wet hydrogen at 660 K always results in segregation of the carbon to the surface. However, reduction in dry hydrogen at 660 K caused removal of ca 30% of the total carbon present. As shown in Fig. 2.42, the carbonate species disappears completely upon heating to 660 K. The wet atmosphere seems to act as an oxidizing agent, producing a large amount of C—O—H fragments, as indicated by the increase in intensity around 286.5 eV.

The carbon spectrum at 790 K is an example of the ability of the catalyst to purify itself. Under these conditions, the carbon compounds are present as elemental carbon with a graphitic valence structure. The wide peak at 284.8 eV and a change in the line shape of the C KVV Auger transition (not shown here) indicate a transformation of the graphitic structure to a type of carbon which is susceptible

to potassium-catalyzed steam gasification. Owing to the comparatively low concentration of the oxidizing agent, water, the process is slow enough to allow observation of the reaction intermediates C—O—K (intensity at 286.5 eV) and C—O—O (peak at 288 eV).[71-73] In dry hydrogen only the graphitic line appears, an indication that in this case the purification proceeds via methanation of carbon rather than via oxidation.

2.7.2. Nitrogen Chemisorption Experiments

The purpose of these experiments is to compare the chemisorption process of nitrogen on the model Fe(111) surface[55,58,74] with that on the reduced surfaces of technical catalysts which have been characterized in the previous sections.

From various surface science experiments it is known that nitrogen chemisorption produces three different species, the relative populations of which depend on the substrate temperature.

At 80 K, a species of molecular nitrogen bonded with the molecular axis perpendicular to the surface (γ-state) is dominant, having an XPS pattern of two peaks at 406 eV and 401 eV. At 100 K, most of the γ-state desorbs, while some nitrogen is converted into a second molecular species with the molecular axis oriented parallel to the surface (α-state). The species in the α-state exhibits a N 1*s* binding energy of 399 eV with some weak intensity at higher binding energy. This state is thought to be the immediate precursor to the dissociation of molecular nitrogen which occurs above 120 K, and which leads to the third species of nitrogen (β-state) characterized by a single nitrogen 1*s* peak at 397 eV.

In Fig. 2.43 the nitrogen 1*s* spectra of a surface of catalyst 1 activated under dry conditions is shown after exposure to an ambient pressure of nitrogen of 10^{-7} mbar at 85 K (bottom trace), after evacuation and subsequent warming to 120 K (central trace), and after further warming to 150 K (top trace).

The arrows denote the peak positions of the γ-, α-, and β-states on Fe(111).[55] The γ-state on the technical catalyst exhibits a higher binding energy than on the single crystal. The intensity ratio between main line (402.8 eV) and satellite (407.8 eV) is the same on the two surfaces, as is the splitting of 5.0 eV. The intensity ratio and the asymmetric line shape of the satellite were found to be independent of both the partial pressure of nitrogen and the surface coverage with nitrogen, which rules out the possibility that several different adsorption states contribute to the formation of these lines.

The more strongly bound species exhibit the same binding energy on both the catalyst and the model surfaces. These binding energies were found to be independent of both the amount of nitrogen adsorbed and of the method of activation or the type of catalyst used.

The total amount of adsorbed nitrogen was determined by integration of the characteristic peaks. The maximum coverage of nitrogen (ca 1.5 at%) relative to the total XPS sampling depth corresponded to rather less than 0.1 monolayers; it was achieved with the γ-state. The α- and β-states were, at the most, about half as abundant as the γ-state based on the assumption of equal cross sections for all three states.

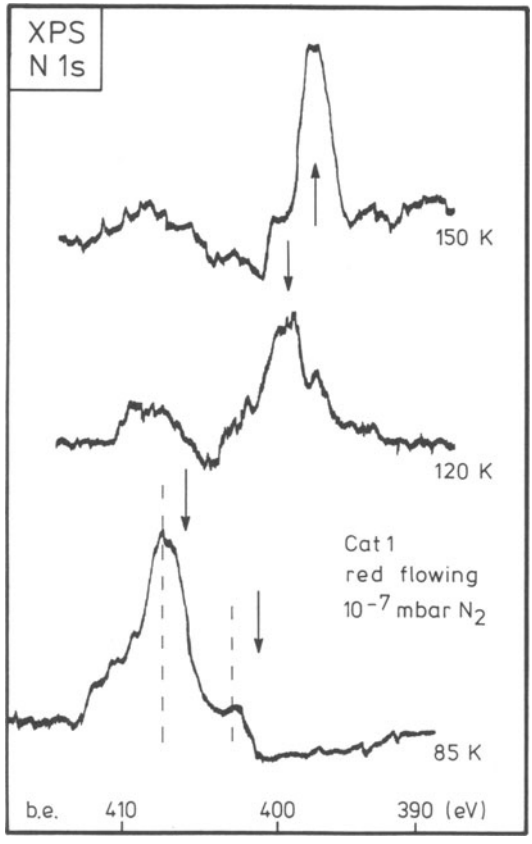

Figure 2.43. Nitrogen 1*s* spectra of an activated surface of catalyst 1 held in an atmosphere of nitrogen at the temperatures indicated. The arrows designate the peak positions of different chemisorbed species of nitrogen found with an Fe(111) single crystal as substrate (analyzer mode FAT 200 eV).

The chemisorption behavior of nitrogen on catalyst surfaces reduced with the wet activation method was typically different from that shown in Fig. 2.43. In Fig. 2.44 the nitrogen spectrum of a surface exposed to 10^{-7} mbar nitrogen at 95 K is compared with that after evacuation. The bottom trace represents a typical clean background. The curved baseline is not the result of the presence of some nitrogen species, since it does not change with excitation energy. The dashed lines show the positions for the three nitrogen species found on the same type of catalyst activated under dry conditions.

The middle spectrum shows the combination of a large amount of "normal" α-state (sharp line at 399.4 eV) with the nitrogen species exhibiting a very broad spectrum. The structure at the low binding energy part of the spectrum (at 407 eV) is reminiscent of the satellite line of the γ-state. Evacuation of nitrogen from the UHV system to a pressure of 2×10^{-10} mbar removes the broad feature completely, while the peak at 407 eV persists. The loss in intensity of the α-state is not caused by pumping, but results from either the long irradiation time (8 h) required for the accumulation of the spectrum, or from the slow coadsorption of contaminants which were found to replace chemisorbed nitrogen. When the surface containing

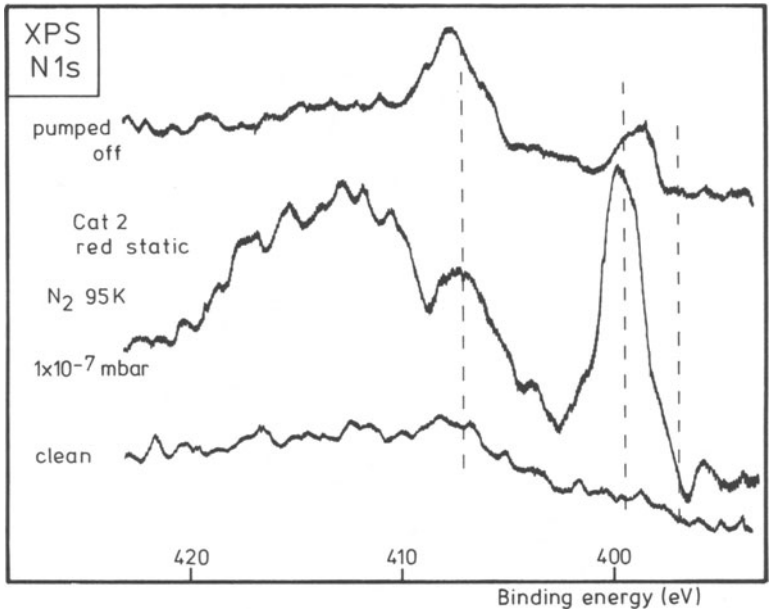

Figure 2.44. Nitrogen 1*s* spectra of an activated surface of catalyst 2 held in an atmosphere of nitrogen at 95 K. The spectral differences to the data shown in Fig. 2.43 arise from the different activation procedure rather than from the different catalyst sample (analyzer model FAT 200 eV).

the adsorbed states present in the middle spectrum of Fig. 2.44 was warmed to 150 K immediately after evacuation, the normal spectrum of the β-state at 397 eV was obtained.

Nitrogen adsorbed onto the catalyst surfaces in the β-state is a stable species, as demonstrated by the fact that the temperature can be raised to 300 K without any change in the spectrum. This species can also be obtained by exposure of the reduced surface at 300 K to one atmosphere pressure of nitrogen for one hour. No β-nitrogen was found when unreduced samples were used, or when the reduced samples were exposed to air rather than to pure nitrogen.

Several attempts were made to observe the formation of ammonia in situ. At 300 K and at a maximum partial pressure of 10^{-6} mbar hydrogen, no reaction could be observed. When samples were heated either in UHV or in hydrogen, the nitrogen spectrum was lost at temperatures above ca 400 K with the exact temperature depending on the sample. It turned out that this was not due to desorption of nitrogen since there was no TDS signal, nor was it the consequence of ammonia formation followed by desorption, since no effect of hydrogen was observed, and no signal derived from ammonia in the mass spectrum was detected. It was found that activated catalysts could absorb some nitrogen into the bulk, which is similar to the known solubility of small amounts of nitrogen in single crystals of iron.[64] A catalyst sample activated by the dry method was saturated at one atmosphere pressure with nitrogen at 700 K for 36 hours, after which the surface was found to be severely oxidized and could not adsorb additional nitrogen. Subsequent

treatment with hydrogen at 1 bar pressure produced a surface similar to those obtained with the wet reduction method, with a low dispersion of promoters (K 3 at%, Ca 2 at%, Al 3 at%).

Nitrogen was chemisorbed by this surface in the same manner as was demonstrated in Fig. 2.43. It was possible to preserve the spectrum of β-nitrogen up to temperatures of 680 K, after which a gradual loss in intensity occurred. With this catalyst sample, the effect of hydrogen on nitrogen in the β-state was observed in the experiment shown in Fig. 2.45, and described as follows. The sample surface was exposed to 1 bar nitrogen at 250 K for 1 h. The resulting nitrogen 1*s* spectrum measured at 80 K in UHV is shown in the top trace of Fig. 2.45. A strong peak at 397 eV indicates the presences of β-atomic nitrogen. The broad structure around 407 eV is though to represent molecular nitrogen, although its spectrum is different from the standard γ-state. The low-energy peak of the γ-state spectrum is situated between the two prominent structures. After accumulation of data, the sample was heated at a rate of 3 deg s^{-1} in the presence of 10^{-6} mbar hydrogen to 750 K, held for 1 min, quenched to 80 K, and the gas phase subsequently pumped away. As seen in the bottom trace of Fig. 2.43, the peak corresponding to molecular nitrogen has disappeared and the peak at 397 eV has shifted to 399 eV. This binding energy

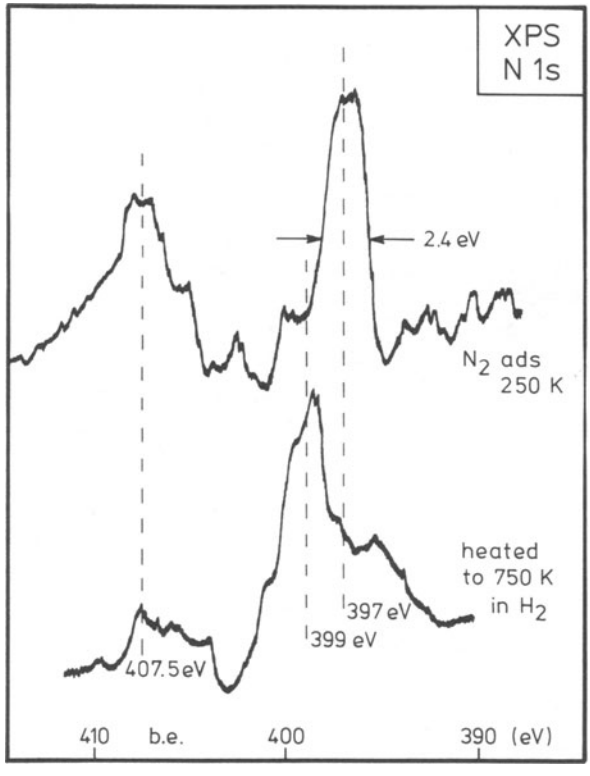

Figure 2.45. Nitrogen 1*s* spectra of a hydrogenation experiment of an activated surface of catalyst 2 saturated with nitrogen and precovered with atomic nitrogen (top trace) (analyzer mode FAT 200 eV).

is typical for either α-nitrogen or partially hydrogenated nitrogen. Since this shift occurs only in the presence of hydrogen, the spectrum is ascribed to hydrogenated atomic nitrogen species such as N—H and N—H_2. This experiment demonstrates that hydrogenated nitrogen species can be obtained on technical catalyst surfaces by the reaction of β-nitrogen with hydrogen at ca 700 K.

2.8. DISCUSSION OF THE SURFACE ANALYSIS RESULTS

2.8.1. The Catalyst Surface

Only few descriptions of the surface constitution of technical ammonia synthesis catalysts can be found in the literature.[19,11,45] An extensive investigation of such a catalyst, similar to one of the samples used in this study, was carried out by Ertl and Thiele[19] who employed a similar activation process to the dry method used in the present investigation. Although there is good general agreement between the two studies, some differences will be discussed.

First, the authors stated that the reduced catalyst surface contained only zero-valent iron. This is based on the analysis of the raw data from the Fe $2p$ 3/2 spectra. It has been found, however, that it is impossible to identify small levels of oxidized iron in the presence of a large fraction of metallic iron. This is due to the wide distribution of intensity for iron compounds caused by their satellite structure. It is therefore believed that the catalyst described in Ref. 19 contained a similar fraction of iron oxide to the present samples activated with the dry method (see Fig. 2.40). This is in line with the expectation that the presence of the spinel-forming aluminum oxide prevents complete reduction. It should be pointed out that Mössbauer spectroscopy, thermogravimetric reduction, and energy dispersive X-ray analysis all showed a small fraction of oxidized iron to be present within the bulk of fully reduced samples.

Second, the authors describe, without interpretation, spectral changes in the oxygen $1s$ line similar to the present observations exemplified in Fig. 2.41. The loss in intensity of the high-energy peak during reduction must be assigned to the loss of structural water. The fact that the peak is not present in prereduced samples shows that the water is not simply a superficial film of moisture from the air. It indicates, together with the total oxidation of the surface iron, that the catalyst is not completely stable to air after its final high-temperature calcination. Instead, it builds up a finite content of ferric oxyhydroxides, the decomposition of which during activation causes the loss of the water peak. This is considered to be an important step in the sequence of events leading to the reduced catalyst (see below).

Third, in both studies significant amounts of surface carbon impurities have been observed. Ertl and Thiele attributed the presence of the carbon to contamination, which occurred during handling of the samples. Analysis of the carbon $1s$ spectra in the present samples led to the conclusion that at least some of the carbon is an intrinsic impurity of the iron compounds. On the other hand, the carbonate species found in the catalyst precursor is attributed to uptake of carbon dioxide by the alkaline promoter phases during storage of the catalyst. Therefore, the

carbon content was included in the elemental analysis of the surface. The detrimental carbon contamination is removed either by methanation (dry activation) or gasification (wet activation). This ability of the ammonia synthesis catalyst to purify itself from residual carbon is seen as one of the reasons for the high final activity of iron, when derived from a multiply promoted precursor oxide, relative to iron derived from pure oxides, which is much less active for ammonia synthesis (see Fig. 2.1). Similarly, iron single crystals do not have this self-purification mechanism and need to be cleaned carefully before they become catalytically active.

It should be mentioned that the present samples did not contain any significant amounts of chlorine or sodium at the surface, unlike those studied by Ertl and Thiele. During their temperature programmed desorption experiments, the presence of chlorides could be observed as bulk impurities. This, and the higher dispersion of the promoters on the catalyst sample used by Ertl and Thiele, suggest that their sample was stored in air for a long time prior to analysis, giving rise to extensive segregation of promoters to the surface. This was also characteristic of one of the samples in the present study.

In a subsequent study, Ertl *et al.* reported on the overall surface composition of a reduced catalyst which had a bulk composition similar to catalyst 1 in the present study. The surface composition of the two samples is, however, vastly different. In particular, the iron content is lower than the iron content of the present sample, in the unreduced state. The levels of potassium and aluminum are, on the other hand, much larger. It was pointed out that the surface composition as determined was consistent with earlier chemisorption experiments, and led to the conclusion that ca 40% of the accessible surface should be covered with potassium oxide. If the potassium and aluminum oxides were indeed present, as suggested, in the form of surface films, then the bulk of the catalyst would consist predominantly of metallic iron. If a sampling depth of 2–4 nm for XPS is assumed, then the analysis presented in Ref. 19 would represent a catalyst which is largely covered by a multilayer of promoter oxides. Consequently, a very much smaller fraction than 60% of the surface would consist of free iron. In accordance with the SEM and Auger map images the activation procedure of Ertl *et al.*[11] led to a surface of elemental iron, which is covered almost entirely by a layer of promoter oxides that contain occasional crystals of embedded ternary oxides.

The catalyst surfaces of the study under discussion present ca 5 times more metallic iron to the gas phase than the surfaces studied by Ertl *et al.* The total abundance of the promoter cations is, on the other hand, only 25% of the level contained in the catalyst described in Ref. 19. The catalysts in the present study are therefore much less segregated, taking into account the very similar bulk composition of the starting materials, and they also contain much more iron in an oxidized form.

2.8.2. Generation and Constitution of the Catalyst Surface

In the following section, a picture will be derived of the active catalyst from the results of the present study in addition to results described earlier in the chapter.

The surface of the unreduced catalyst consists of a mixture of basic ferric oxide ("FeOOH") with aluminum oxide and the basic carbonates of potassium and calcium. The constitution of this layer is considered to be similar to rust, since it is the product of the reaction of magnetite with air during catalyst storage. This layer is seen in the intergranular spaces and is also present in the cracks between the polycrystalline particles.

The first step in the reduction process, after removal of a layer of chemisorbed water at ca 400 K, is the dehydration and partial reduction of the rust layer. This leads to the formation of a surface containing ferric and ferrous ions, together with structural promoters in the form of pure binary oxides which are dissolved in spinel structures. This step also opens up some of the cracks and pores. Eventually, wustite which initially could not be found on any of the outer surfaces is reduced to iron, and this further increases the voids between the magnetite particles. This step of widening of the cracks and defects, which can be seen only indirectly by photoelectron spectroscopy (e.g., by the induction period found in the UPS experiments), is crucial for the subsequent reduction of the bulk magnetite. This is because it is known that the reduction occurs only along such defects, which provide the sites for heterogeneous nucleation of metallic iron. This led to the core and shell model of activation described in Section 2.5.

According to this model, the proportion of the sample accessible by photoemission should be reduced to metal within a short period of time, i.e., UPS should detect metallic iron shortly after the surface has reached the reaction temperature of ca 700 K. This was not observed. Instead, the gas-solid interface only becomes metallic after reduction in the bulk of the sample has terminated. The core level data, on the other hand, showed the expected behavior, with an early formation of iron metal nuclei and subsequent growth to form particles large enough to exhibit the spectral parameters of bulk iron. It is therefore concluded that the reduction process produces two interfaces: the one, an outer gas-solid interface which remains in the magnetite form until the reaction on the other, an inner metal-metal oxide interface, is completed. For catalytic activity, only the gas-solid interface is relevant. The catalyst therefore only becomes active if the whole of the bulk is converted from oxide to metal, although the majority of the material is still not involved in catalysis.

In each of the cases examined, the reduction process was not stoichiometric. This is in accordance with bulk observations by Mössbauer spectroscopy and other techniques. It should be pointed out, however, that the amount of oxidic iron is small compared to the dominant α-iron phase, which constitutes the bulk of the catalyst. The XPS parameters of this iron are close to those of bulk iron and provide no evidence for a small, cluster-like structure. In the case of the surface iron metal, there is no indication of the significant deviation from the average coordination number of 8, which was recently suggested in an EXAFS investigation.[48] Although XPS spectra on iron are not particularly sensitive to coordination numbers the loss of ca 4 nearest neighbors should cause large alterations of both core hole screening and relaxation effects. These have been demonstrated to exist in the case of monolayers of metals. The slight shift to higher energy of the core

level positions, and the distorted iron conduction band, however, point to a nonperfect structure of bulk iron as is also reflected in the X-ray diffraction line broadening.

The nature of the unreduced iron is difficult to deduce from the spectra; the complex shape of the ionic part of the iron core level emissions results from a superposition of that of ferrous and ferric iron in relative amounts different to those found in magnetite itself. From an inspection of the iron oxygen phase diagram it emerges that a binary solid solution of oxygen in ferrous oxide, "wustite," cannot exist at reaction temperature. The presence of ferrous ions therefore suggests spinel type structures, with aluminum present as additional cations. Potassium–iron oxides are only known to exist with ferric ions. A mixture of such ternary oxides has already been suggested to exist as an amorphous phase at the grain boundaries of the iron particles. The presence of such grain boundary oxidic impurities are common in the reduction of magnetite ores with hydrogen or CO.

In summary, the activated catalyst may be described in light of the photoemission analysis as follows. The main constituent, iron metal, is present in the form of particles larger than ca 10 nm. The arrangement reflects the distribution of nucleation sites, which are performed by the defect structure of the starting magnetite. The mixture of ternary oxides separates as a continuous layer from the individual particles, and prevents the growth of large well-ordered iron. This seems to exhibit a low concentration of active sites, in comparison to the defective primary iron obtained after reduction. The recrystallization would occur as Ostwald ripening, driven by the defect energy stored in the primary particles, and the conditions for ammonia synthesis provide the activation energy. The oxide layer may be of varying thickness according to the completeness of reduction. It remains after hydrogen treatment as an essential ingredient, due to the presence of spinel-forming promoter oxides. It provides anchor sites for the fixation of patches of the potassium oxide promoter, which need to be present at the active surface.

The oxide-layer network is present essentially in the bulk of the catalyst. The significant amount of surface iron oxides found in some samples of the present study can be attributed in part to a thick layer (=incomplete reduction) of network oxides and must be ascribed in part to individual segregated oxide crystals. These segregates, which have been identified by electron microscopy as well as by differential charging in the XPS (see, e.g., Fig. 2.42), may be binary or ternary oxides. Whatever their structure, they play the role of spectator species, which have been formed as an undesirable consequence of an inappropriate choice of reduction conditions.

Such a complex picture of the catalyst cannot be derived from electron spectroscopy alone. It has been confirmed fully in a microstructural investigation and is presented here since it can account for all the spectroscopic observations. It explains, in particular, that the incomplete reduction of the surface is not a failure of the experimental technique, but rather reflects an essential component of the catalyst. It may be noted that the suggested mode of operation of the structural promoters offers a chemically realistic alternative to the phenomena discussed in the literature, such as paracrystallinity,[15] monolayer formation of binary promoter oxides,[17] and surface roughening agent.[12]

2.8.3. Nitrogen Chemisorption Experiments

These experiments were carried out on the activated catalyst, providing a substrate of patches of rough metallic iron embedded in a network of iron-containing oxides and in the presence of a dispersed potassium-oxygen species. In comparison with the Fe(111) data, good agreement of the results on model and realistic surface can be observed.

Chemisorption of nitrogen is a three-step process on both surfaces. The similarity of the N 1*s* core level spectra allows the conclusion that the same types of weakly held molecular species, a strongly held molecular precursor, and the dissociated atomic state all result from nitrogen exposure. The fact that the transitions between the three species occur on both surfaces at very similar temperatures indicates also that the energetics of nitrogen interaction on Fe(111) and the catalyst are very similar. The results further rule out any influence of "impurity" species, such as carbon or oxygen, on the energies of interaction between nitrogen and the two surfaces.

The exact correspondence of the spectroscopic parameters of the α- and β-states on the two surfaces permits the conclusion that the strongly held species interact locally with their adsorption sites. These sites are of the same nature on both surfaces (iron metal C-7 sites) and are unaffected in their electronic properties by either potassium or oxygen. The number of these sites per unit area of surface may be different on the two types of surface. The total coverage of all of the surface with nitrogen in the α- and β-states, at temperatures between 100 K and 150 K, was ca 0.6 at%, irrespective of the amount of metallic iron present, as indicated by the height of the Fermi edge. This implies that only a small fraction of the available iron metal sites are of the appropriate type, and that the ratio of useful sites relative to the total iron sites is improved by the presence of large amounts of surface oxides. In other words, very high degrees of reduction are not favorable for highly active catalysts. This degree of reduction is controlled, *inter alia*, by the partial pressure of water present at the catalyst grain. This could be one reason for the crucial effect of the water content and the flow pattern of the reducing gases on the final performance of the catalyst.

In all cases studied, the fractional surface coverage by nitrogen was below 0.2 and thus comparable to that of the Fe(111) surface which has been estimated to be ca 0.2. Such a low coverage of a poorly electron-emitting adsorbate, on a polycrystalline powder substrate, causes intensity problems associated with the data acquisition. In order to obtain useful data, the energy analyzer had to be operated in such a mode where the line shape of the peaks was determined by the transfer function of the analyzer, and not by the natural linewidth. This accounts for the larger linewidths (ca 2.4 eV, see Fig. 2.45) found for nitrogen on the catalyst surfaces, when compared to the single crystal work (line width ca 1.8 eV).

The interaction between the weakly held nitrogen and the surface seems to be different for the two surfaces. It was possible to prepare a catalyst surface covered only with γ-nitrogen (Fig. 2.43). The binding energies of the two resulting lines are 4.2-8 eV, ca 1.5 eV higher than that reported for the Fe(111) surface (401.2 eV and 405.9 eV). The splitting of the two lines in both spectra is 4.7 eV,

which is slightly larger than the prediction from the theoretical model (4.0 eV).[55] The line shapes and intensity ratios are also similar in the two spectra. In contrast to nitrogen-covered Fe(111) surfaces, which can be prepared at higher temperatures, free from any γ-nitrogen, the catalyst surfaces all showed some γ-nitrogen at temperatures up to 250 K. γ-Nitrogen can be distinguished from physisorbed nitrogen by evacuation of the gas phase. Physisorbed nitrogen (all adsorbed species held with a lower energy of interaction than that of γ-nitrogen will be referred to as physisorbed) can be removed by this treatment (see Fig. 2.44), whereas γ-nitrogen persists. These physisorbed species exist in large quantities on surfaces with a low degree of reduction and with high dispersion of potassium oxide. None of these species was observed on either clean or potassium-precovered single-crystal surfaces. It was found, however, that potassium precoverage enhances the sticking coefficient of the α-species, shifts the desorption temperature of molecular nitrogen up to ca 225 K (population of the α-2 state), and causes significant broadening of the whole TDS pattern. These observations are reflected by the large fraction of α-nitrogen on surfaces rich in potassium, and by the persistence of molecular nitrogen at temperatures up to 250 K (see Fig. 2.45).

2.8.4. The Promoter Effect of Potassium

The nature of the potassium promoter will now be discussed.[69,70,75] It is clear that potassium is present on the catalyst only in the oxide state. No metallic potassium is formed during the activation stage, during which the dispersion of the potassium oxide is increased markedly (see Fig. 2.42, which shows an increase in intensity and the loss of broadening due to differential charging). These findings render the suggested mechanism of the formation of potassium hydroxide as the active phase formed via hydrolysis of potassium amide[76] to be unlikely, since it requires the intermediate presence of metallic potassium.

The K $2p$ 3/2 binding energy at 293.6 eV relative to the Fermi edge of metallic iron is larger than it would be for hydrated potassium hydroxide (ca 293.0 eV).[69,70] This shift, which is not caused by differential charging (no dispersion dependence, no dependence on instrumental settings), was also observed in other catalyst systems which contained potassium as the active promoter.[69,77] Analysis of the O $1s$ line shapes excludes the presence of species with oxidation states higher than -2, which could be present in cluster-type potassium oxides, involving peroxy oxygen species.[75] A possible structure for the promoter may be isolated K—O groups, attached via the oxygen atom to the iron surface. Such a species would experience a highly asymmetric Coulomb field, which would account for the shift in binding energy relative to bulk potassium oxide/hydroxide (Madelung shift). A small amount of these groups, which are known to exist on carbon during gasification,[71-73] would be sufficient for the effect of promotion, and they would not cover all of the active iron with a two-dimensional film. The large islands of potassium seen in the SAM images and also predicted from previous XPS data block the active surface. They may therefore be spectator species, in the same manner as suggested in the case of the structural promoters.

It is noted that Ertl and Thiele found a binding energy of 294.5 eV for potassium in the unreduced catalyst and observed no change after reduction. This behavior has also been reproduced in the reduction experiments under dry conditions, which did not lead to an increase in dispersion of potassium (see Table 2.1). The high binding energy is ascribed to charging of the particles of the potassium compounds. The lower binding energy of 293.6 eV was only found after activation experiments under wet conditions. A very similar binding energy was found for the saturation coverage of ca 0.3 monolayers potassium and oxygen coadsorbed on polycrystalline iron as well as in experiments performed with iron foils covered with highly dispersed potassium compounds.[69,70,77]

The two binding energies in the spectrum of potassium hydroxide are likely to be caused by the presence or absence of water, solvating the strong base, potassium hydroxide. The significance of this effect, which causes extensive extra-atomic screening in electron spectroscopy, may be seen from the heat of solvation of potassium hydroxide, which amounts to 58 kJ mol^{-1}. Thus, the active species of potassium is a submonolayer film of anhydrous potassium hydroxide attached as a single layer to the iron metal. The arguments propounded in Ref. 75 against the role of potassium hydroxide relate everything to the properties of three-dimensional patches of hydrated potassium hydroxide and are therefore not necessarily relevant in the present case. The anhydrous nature of the active phase offers a good explanation for the sensitivity of highly active catalysts toward water, even in such small amounts that would be unable to oxidize the iron in the absence of additional oxygen. The active surface acts as a very efficient drying agent, by binding water to the two-dimensional potassium hydroxide film, which in turn may become three-dimensional. In this form, it could exhibit the chemical properties described in Ref. 75 and, as a consequence, may therefore lose its activity.

The anhydrous potassium hydroxide is a strongly basic material. It reacts with the weak acid, water, to form a complex hydrate. The product ammonia, on the other hand, is too weak an acid to form an adduct with potassium hydroxide. This is well known from classical chemistry, where we learn that the qualitative method for the determination of ammonium compounds is by addition of potassium hydroxide, to generate the odor from the liberated ammonia gas. This is exactly in line with the pressure-dependent effect on promotion as suggested by Somorjai.[53]

The anhydrous potassium hydroxide units are also strongly polarizing agents for the metallic iron substrate. In model studies of the sequential interaction of potassium metal and oxygen adsorbed on iron,[75,77] it was shown that the resulting K—O entity interacts via the oxygen atom with the surface, without oxidizing the iron metal. This is the basis for the suggested pressure-independent promoter effect of locally enriched electron density in the $3d$ states of iron metal. These enhance the back-donation effect in the iron–nitrogen chemical bond and thus increase the adsorption energy of nitrogen adsorbed in the molecular state. The existence of this effect on the activated technical catalyst surface has recently been demonstrated by TDS experiments,[78] which revealed the existence of an α-2 state on the technical catalyst that possessed exactly the same thermal parameters as a potassium + oxygen precovered iron (111) single crystal.

We conclude that anhydrous potassium hydroxide is the active species responsible for promotion by potassium and that the beneficial effect on ammonia synthesis is bifunctional, enhancing on the one hand the adsorption energy of molecular nitrogen, and reducing the adsorption energy of the product ammonia on the other.

2.8.5. Hydrogenation of Chemisorbed Nitrogen

The final synthesis reaction will now be discussed. Ertl and Thiele showed that catalyst surfaces under ammonia synthesis conditions, though at atmospheric pressure, were covered with a mixture of molecular ammonia (binding energy 400.7 eV), the N—H fragment (binding energy 399 eV), and also atomic nitrogen (binding energy 397.5 eV) subsequent to transfer into the UHV chamber. Ammonia was shown to desorb in UHV upon heating, while the precursor species were stable up to synthesis temperature. Such behavior could also be predicted from the model calculations performed by Stoltze and Norskov.[62]

The idea behind the present experiment was to approach the investigation of the elementary step from the other side. The attempt was made to hydrogenate nitrogen, which was first shown to be present in the atomic β-state. It turned out that only one particular combination of pressure and temperature led to the spectra as shown in Fig. 2.45. In particular, the residence time of the surface at high temperature was critical in order to observe the presence of any nitrogen species at all. A short heating time was necessary to heat the outer surface of the powder sample to the synthesis temperature, and rapid cooling prevented the intermediate species from being completely hydrogenated and desorbed as ammonia.

Following the interpretation of the spectra as proposed by Ertl and Thiele, the hydrogenation experiment led to the transformation of the β-nitrogen to N—H as the dominant species in the spectrum of the quenched catalyst surface. This experiment can therefore be considered to a link, showing that hydrogenation of atomic nitrogen and dehydrogenation of ammonia lead to a common stable intermediate N—H, as required by the principle of microscopic reversibility in heterogeneous catalysis.

2.8.6. Concluding Remarks

The analysis of a large body of data, obtained from activation of two typical industrial catalysts under two different sets of reaction conditions, has given insight into the activation process. The dominant effect is the topotactic reduction of iron oxides to metallic iron, with the external gas-solid interface only being reduced after reduction of the bulk is complete. The structural promoters stabilize some iron oxide in the form of ternary oxides. They form a network of boundaries which prevent the initial nuclei of disordered iron metal from crystallization into large perfect crystals. The presence of inefficient isolated promoter oxide particles as segregated on the surface (which play no part in the catalytic reaction) complicates the analysis. The conditions during activation need to be tailored to the solid state chemical properties of each individual catalyst precursor, since they provide the boundary conditions for the generation of metallic iron. They also suppress surfacc

segregation of the ternary oxides, which act as structural promoters. The electronic promoter, potassium, is present as an oxidic form, presumably in a mixture of isolated, active K—O groups and as patches consisting of a film of potassium oxide/hydroxide. The activation procedure determines, *inter alia*, the dispersion of the potassium hydroxide/carbonate deposits, initially present in the catalyst precursor.

The chemisorption experiments with molecular nitrogen showed complete agreement between phenomena on the real catalyst and the model surface Fe(111). Both the surface interaction energies and the nitrogen 1*s* binding energies of the strongly bonded species α- and β-nitrogen are identical on both types of surface. The nature of the active sites, which have been identified as C-7 sites at Fe(111), must be the same on the real catalyst surface. Only the weakly held γ-molecular state is influenced in its spectral parameters by the differences of the two surfaces. Its adsorption and decomposition temperature is, however, the same on both surfaces, which implies that nitrogen in the γ-state has, at least in part, a function as a precursor to the formation of the α-complex, as observed on the Fe(111) crystal. The results of this study are also fully consistent with the model studies of Stoltze and Norskov. The uniform properties of the catalytically active part of the surface, which is a prediction from their calculations, exist not only on a clean single crystal of iron, but also on the chemically and structurally heterogeneous surface of a technical catalyst.

Care must be taken, however, when the results are interpreted in a quantitative way. In particular, the question of the degree of reduction of the catalyst under optimum working conditions and the fractional coverage of the active surface with nitrogen can only be answered if the surface under investigation has been shown to produce ammonia at a rate close to the thermodynamic equilibrium. Such an experiment requires a special reactor configuration, attached to an electron spectrometer.

In general terms, it has been demonstrated that the application of electron spectroscopy, in combination with a knowledge of the system derived from model studies, is capable of bridging, experimentally, both the pressure gap and the material gap for the example of catalytic ammonia synthesis.

2.9. EPILOGUE

The reader who has followed the arguments up to this point may ask the following questions: what is the average typical structure of the activated catalyst? and what is the difference between metallic iron and the activated catalyst? If the reader is practically minded, he/she may further ask: what is the use of this information? or, less provocatively, given the well-established structure sensitivity of ammonia synthesis over single crystals, is there a similar relationship between the structure of the technical material and its catalytic usefulness? An artist's impression of the main structure features of the technical activated catalyst has been developed, to respond to these questions.

In Fig. 2.46, a front view of a small section of an activated catalyst grain is shown in schematic form. The section displayed corresponds to the size of a single

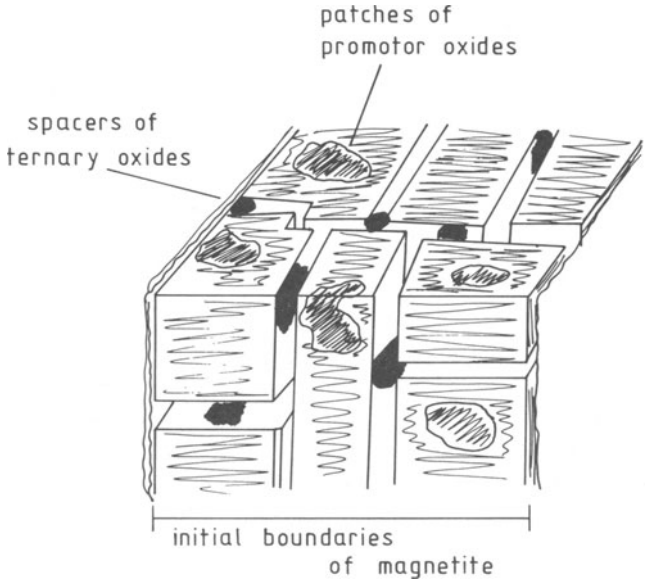

Figure 2.46. Schematic representation of the important structural features of an activated ammonia synthesis catalyst. The level of resolution is ca 30 nm as it is achieved in typical SEM micrographs. The blocks of iron are not single crystals but composites.

grain in the original magnetite precursor. Its size, composition, and defect structure had been predetermined during the synthesis of the oxide mixture. After suitable activation, which avoided any physical disintegration, the initially dense grains become agglomerates of several small iron particles, the inner structure of which is shown in Fig. 2.47. The particles themselves are separated by a pore system, which accounts for the increased surface are of the active catalyst when compared to the magnetite precursor. The pore system is stabilized against collapse via sintering of the particles, by spacers or pillars of segregated structural promoter oxides. Their anchor sites can be seen as patches on the free surface of the grain. The surface of iron metal and/or oxide is further covered with a thin film of the electronic promoter, potassium oxide.

Each of these iron particles is composed of small anisotropic platelets of α-iron, which form a loose stack containing an additional internal system of smaller pores. Such a stack is shown schematically in Fig. 2.47. Each of the platelets exhibits the thermodynamically unfavorable Fe(111) orientation as its basal plane. Thus, the material is composed of a homogeneous microstructure, but is metastable. It therefore needs to be stabilized against sintering, defined as crystallite growth to form larger isotropic iron crystals, with an equilibrium distribution of low-index Miller planes as crystal faces. The stabilization is achieved by an even distribution of the small amount of structural promoter oxides between the individual platelets. These are not shown in the figure, but see the STEM image in Fig. 2.30

It is this anisotropic microstructure that provides the main difference between isotropic, thermodynamically stable "ordinary" α-iron and the active catalyst. The

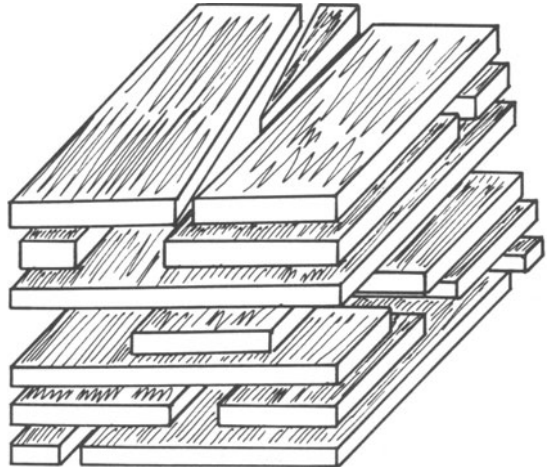

Figure 2.47. Schematic representation of a single block of iron in the activated catalyst. Each block is in fact a stack of platelets of single crystalline iron exhibiting the (111) orientation as basal plane. This unstable microstructure causes the activated catalyst to be metastable at operating temperature. The level of resolution is with ca 1 nm chosen as in low-resolution TEM micrographs.

presence of the structural promoters in the precursor during activation is the reason for the generation of this fundamental structural difference. The promoters, as well as the defects (wustite), modify the two-step nucleation process during the genesis of the active phase, such that the platelet morphology of iron grows, rather than the stable isotropic cubic form of iron particles, which is the more common form.

Any thermal or chemical stress applied to the active catalyst, which changes the distribution of the promoter oxides, may lower the activation barrier for the conversion to stable isotropic iron. Irreversible damage may then be done to the catalyst, even if any partial oxidation can be reversed by so-called reactivation.

Finally, the all-important effect of the presence of the bifunctional structural promoters will be demonstrated. They promote both formation and stabilization of the metastable, active form of α-iron. This form has been found to be exactly the same in the technical catalyst and in a model catalyst system prepared from amorphous alloy precursors.[79] In Fig. 2.48 conversion measurements are shown for a set of catalysts made from the same iron oxide starting material, but which contained different promoter additives. All three catalysts were activated in the same way, according to the manufacturer's specification.

In the first instance, it can be seen from the figure that meaningful comparison of catalytic activities can only be drawn from temperature-dependent measurements.

All three curves exhibit the same basic shape, with the high-temperature regions merging together for all of the catalysts. The conversion in this regime is determined by the thermodynamic equilibrium between ammonia and its constituent elements. The experimental curve falls along the calculated curve with a

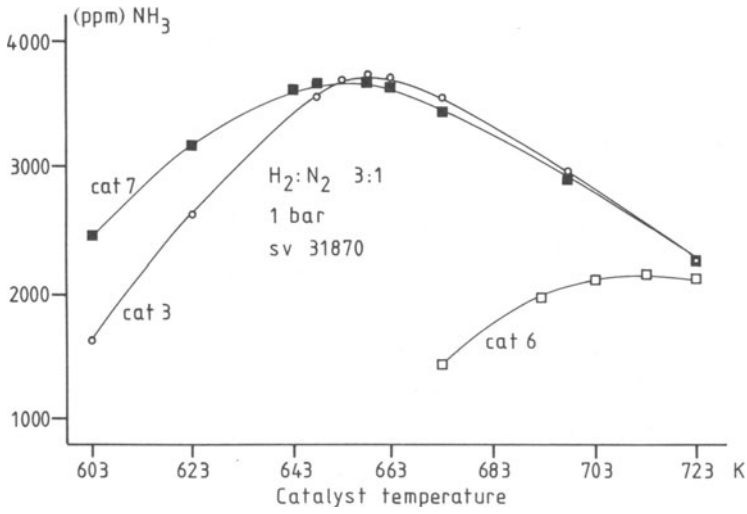

Figure 2.48. Ammonia synthesiis with differently promoted catalysts. The conversion is compared to equal amounts of 0.6000 g catalyst tested in a tubular microreactor. Each data point was taken after 24 hours of equilibration.

standard deviation of less than 10%. The point at 723 K is in exact coincidence with the theoretical conversion.

The low-temperature plots, which manifest the kinetically controlled regime of the conversion curves, are vastly different for the three catalysts. The most active catalyst is the sample promoted by alumina alone, followed by the conventional double promoted sample, while the sample promoted only by potassium is far less active. The apparent reason for this behavior is the different surface area of the catalysts. The effect of aluminum in promoting the formation of active material becomes apparent when the specific surface areas of the two alumina-containing samples, catalyst 3 ($18\ m^2\ g^{-1}$) and catalyst 7 ($21\ m^2\ g^{-1}$), with the potassium-only sample, catalyst 6 ($4\ m^2\ g^{-1}$), are compared. From these numbers, and the fact that the slopes of the conversion curves are all different, it must be concluded that there is, however, no simple linear relationship between specific surface area and catalytic activity. The fine details of the microstructure also play an important role in determining the final catalytic activity. The promotional effect of potassium can manifest itself even more strongly, if one chooses higher pressures of synthesis gas. This leads to higher conversion and thus makes the site-blocking effect of product ammonia even more important. Catalyst 7 falls then below catalyst 3. From comparison of the curves for catalyst 3 and catalyst 7, it is concluded that the conventional electronic promoting effect of potassium at low pressures, that is, enhancement of the adsorption energy of molecular nitrogen, plays only a minor role and can be overcompensated by only a 10% difference in specific surface area.

These final statements provide a means to answer some of the questions of the reader. Furthermore, they illustrate that the combination of a modern, analytical, multimethod approach with catalytic testing can indeed help to understand the complexity of real catalysis, such as is used in the example of ammonia synthesis.

ACKNOWLEDGMENTS

The author wishes to gratefully acknowledge the help with the experiments described in this work by M. Wesemann, J. Schütze, K. Grabitz, W. Mahdi, G. Weinberg, R. C. Schoonmaker, A. Reller, and T. Rayment. Critical discussions with A. Baranski, G. Ertl, R. Imbihl, S. Kipling, J. Norskow, P. Stoltze, H. Topsoe, K. C. Waugh, and D. A. Whan helped to clarify many ideas presented in this work. Special thanks are due to M. Kischke, who prepared the photographs, and to M. Muhler and J. Nickl, who helped with proofreading of the manuscript.

REFERENCES

1. W. Büchner, R. Schlibs, G. Winter, and K. H. Büchel, in: *Industrielle Anorganische Chemie*, p. 34, VCH, Weinheim, New York (1986).
2. A. Nielsen, *Catal. Rev. Sci. Eng.* **23**, 17 (1981).
3. A. Mittasch, DRP 254 437 (1910).
4. A. Ozaki and K. Akai, in: *Catalysis: Science and Technology* (J. R. Anderson and M. Boudart, eds.), Vol. 1, p. 107 ff, Springer, New York (1981).
5. A. F. Wells, *Structural Inorganic Chemistry*, 4th ed., p. 489 ff, Oxford University Press (1975).
6. C. Peters, K. Schäfer, and P. Krabetz, *Z. Elektrochem.* **64**, 1194 (1960).
7. M. E. Dry, J. A. K. Du Plessis, and G. M. Leuteritz, *J. Catal.* **6**, 194 (1966).
8. P. H. Emmett and S. Brunnauer, *J. Am. Chem. Soc.* **59**, 1553 (1937).
9. K. Schäfer, *Z. Elektrochem.* **64**, 1191 (1960).
10. R. Krabetz and C. Peters, *Angew. Chem.* **77**, 333 (1965).
11. G. Ertl, D. Prigge, R. Schlögl, and M. Weiss, *J. Catal.* **79**, 359 (1983).
12. D. R. Strongin, S. R. Bare, and G. A. Somorjai, *J. Catal.* **103**, 289 (1987).
13. B. S. Clausen, S. Morup, H. Topsoe, R. Candia, E. J. Jensen, A. Baranski, and A. Pattek, *J. Phys. (Paris)* **37**, C245 (1976).
14. H. Topsoe, J. A. Dumesic, and S. Morup, in: *Application of Mossbauer Spectroscopy*, Vol. 2, p. 55 ff, Academic Press, New York (1980).
15. H. Ludwiczek, A. Preisinger, A. Fischer, R. Hosemann, A. Schönfeld, and W. Vogel, *J. Catal.* **80**, 194 (1978).
16. R. Hosemann, A. Preisinger, and W. Vogel, *Ber. Bunsenges. Phys. Chem.* **70**, 797 (1966).
17. W. S. Borghard and M. Boudart, *J. Catal.* **80**, 194 (1983).
18. A. Nielsen, *An Investigation of Promoted Iron Catalysts for the Synthesis of Ammonia*, 3rd edn., Chapter 8, Jul Gjellerups Forlag, Copenhagen (1968).
19. G. Ertl and N. Thiele, *Appl. Surf. Sci.* **3**, 99 (1979).
20. W. L. Roth, *Acta Crystallogr.* **13**, 140 (1960).
21. S. Mrowec, *Metallugria i Odlewnictwo* **13**, 7 (1984).
22. G. V. Samsonow (ed.), *The Oxide Handbook*, 2nd edn., p. 24, Plenum Press, New York (1982).
23. T. L. Joseph, *Trans. AJME.* **120**, 72 (1936).
24. P. K. Stangway and H. U. Ross, *Trans. AJME.* **242**, 1981 (1968).
25. M. Moukassi, P. Steinmetz, B. Dupre, and C. Gleitzer, *Metall. Trans., B* **14**, 125 (1983).
26. Y. K. Rao, *Metall. Trans., B* **10**, 243 (1979).
27. J. O. Edström, *J. ISI* **175**, 289 (1953).
28. A. Reizer and A. Baranski, *Appl. Catal.* **9**, 343 (1984).
29. A. Pattek-Janczyk, A. Z. Hrynkiewicz, J. Kraczka, and D. Kulgawczuk, *Appl. Catal.* **6**, 35 (1983).
30. J. L. Lemaitre, in: *Characterisation Of Heterogeneous Catalysts* (F. Delanny, ed.), p. 52, M. Dekker, New York (1984).
31. K. W. Hall, W. H. Tarn, and R. B. Anderson, *J. Am. Chem. Soc.* **72**, 5436 (1950).
32. P. H. Emmett and T. W. DeWitt, *J. Am. Chem. Soc.* **65**, 1253 (1943).

33. A. Baranski, M. Lagan, A. Pattek, and A. Reizer, *Archiwum Hutniktwa* **25**, 143 (1980).
34. H. C. Chen and R. B. Anderson, *J. Catal.* **28**, 161 (1973).
35. B. S. Clausen and H. Topsoe, unpublished results.
36. T. Rayment, R. Schlögl, J. M. Thomas, and G. Ertl, *Nature* **315**, 311 (1985).
38. A. Baranski, A. Bielanski, and A. Pattek, *J. Catal.* **26**, 286 (1972).
39. A. Baranski, J. M. Lagan, A. Pattek, and A. Reizer, *Appl. Catal.* **3**, 207 (1982).
40. A. Baranski, A. Reizer, A. Katorba, and E. Pyrczak, *Appl. Catal.* **19**, 417 (1985).
41. B. B. Seth and H. U. Ross, *Trans. AJME* **233**, 180 (1965).
42. H. Schenk and H. P. Schulz, *Arch. Eisenhüttenwesen* **31**, 691 (1960).
43. V. Solbakken, A. Solbakken and P. H. Emmett, *J. Catal.* **15**, 90 (1969).
44. A. T. Larson and C. N. Richardson, *Ind. Eng. Chem.* **17**, 971 (1925).
45. D. C. Silverman and M. Boudart, *J. Catal.* **77**, 208 (1982).
46. G. Fagherazzi, F. Galante, F. Garbassi, and N. Pernicone, *J. Catal.* **26**, 344 (1972).
47. H. Topsoe, J. A. Dumesic, and M. Boudart, *J. Catal.* **28**, 477 (1973).
48. W. Niemann, B. S. Clausen, and H. Topsoe, *Ber. Bunsenges. Phys. Chem.* **91**, 1292 (1987).
49. M. Muhler, T. Rayment, A. Dent, and R. C. Schoonmaker, *J. Catal.* **126**, 339 (1990).
50. H. P. Klug and L. E. Alexander, *X-Ray Diffraction Procedures*, 2nd edn., p. 642 ff, Wiley, New York (1974).
51. N. D. Spencer, R. C. Schoonmaker, and G. A. Somorjai, *J. Catal.* **74**, 129 (1982).
52. R. Brill, E. L. Richter, and E. Ruch, *Angew. Chem., Int. Ed. Engl.* **6**, 882 (1967).
53. D. R. Strongin and G. A. Somorjai, *J. Catal.* **109**, 51 (1988).
54. G. Ertl, *J. Vac. Sci. Technol.* **A1**, 1274 (1983).
55. M. Grunze, M. Golze, W. Hirschwald, H. J. Freund, H. Pulm, U. Seip, M. C. Tsai, G. Ertl, and J. Küppers, *Phys. Rev. Lett.* **53**, 850 (1984).
56. G. Ertl, S. B. Lee, and M. Weiss, *Surf. Sci.* **114**, 515 (1982).
57. G. Ertl, S. B. Lee, and M. Weiss, *Surf. Sci.* **114**, 527 (1982).
58. H. J. Freund, B. Bartos, R. P. Messmer, M. Grunze, H. Kuhlenbeck, and M. Neumann, *Surf. Sci.* **185**, 187 (1987).
59. D. Arvanitis, L. Wenzel, K. Baberschke, M. Muhler, R. Schlögl, and G. Ertl, *Phys. Rev. B* **40**, 6409 (1989).
60. D. R. Strongin and G. A. Somorjai, *Catal. Lett.* **1**, 61 (1988).
61. P. Stoltze, *Phys. Scr.* **36**, 824 (1987).
62. P. Stoltze and J. Norskov, *Phys. Rev. Lett.* **55**, 2502 (1985).
63. M. Bowker, I. Parker, and K. Waugh, *Appl. Catal.* **14**, 101 (1985).
64. F. Bozso, G. Ertl, M. Grunze, and M. Weiss, *J. Catal.* **49**, 18 (1977).
65. S. D. Kelemen, H. J. Freund, and C. P. Mims. *J. Catal.* **97**, 228 (1986).
66. J. J. Yeh and J. Lindau, *At. Data Nucl. Data Tables* **32**, 1 (1985).
67. K. Wandelt, *Surf. Sci. Rep.* **2**, 1 (1982).
68. C. R. Brundle, T. J. Chuang, and K. Wandelt, *Surf. Sci.* **68**, 459 (1977).
69. H. P. Bonzel, G. Broden, and H. J. Krebs, *Appl. Surf. Sci.* **16**, 373 (1983).
70. M. Muhler and R. Schlögl, unpublished results.
71. R. Schlögl, P. Oelhafen, H. J. Güntherodt, E. Fergusson, and W. Jones, *Proc. Int. Carbon Conf. Carbon* 86, *Deutsche Keramische Gesellschaft*, (1989) *p.* 139.
72. F. Delanny, W. T. Tysoe, H. Heinemann, and G. A. Somorjai, *Carbon* **22**, 401 (1984).
73. A. J. Moulijn, B. M. Cerfotain, and F. Kaptaijn, *Fuel* **63**, 1643 (1984).
74. L. J. Whitman, C. E. Bartosch, W. Ho, G. Strasser, and M. Grunze, *Phys. Rev. Lett.* **56**, 1984 (1986).
75. Z. Paal, G. Ertl, and S. B. Lee, *Appl. Surf. Sci.* **8**, 231 (1981).
76. J. G. Van Ommen, W. J. Bolink, J. Prasad, and P. Mars, *J. Catal.* **38**, 120 (1975).
77. G. Pirug, G. Broden, and H. P. Bonzel, *Surf. Sci.* **94**, 323 (1980).
78. R. Schlögl, R. C. Schoonmaker, M. Muhler, and G. Ertl, *Catal. Lett.* **1**, 237 (1988).
79. R. Schlögl, R. Wiesendanger, and A. Baiker, *J. Catal.* **108**, 237 (1987).

3

ELEMENTARY STEPS IN AMMONIA SYNTHESIS:

The surface science approach

G. Ertl

3.1. INTRODUCTION

The net rate of a chemical reaction is determined by its mechanism, i.e., the sequence of elementary processes involved, and any attempt to gain real insight into the progress of a chemical transformation has therefore to start by studying the reaction intermediates and their individual kinetic, energetic, and structural properties on an atomic level. In heterogeneous catalysis this task is hampered in several ways: The conventional techniques used in investigations of homogeneous reactions are frequently only of limited applicability, and the catalyst surface is usually rather inhomogeneous (both structurally and chemically). Furthermore, its composition may differ considerably from that of the bulk. For these reasons information on the elementary steps of heterogeneously catalyzed reactions remained rather restricted for a long period of time. Emmett[1] concluded in a lecture on "Fifty years of progress in the study of the catalytic synthesis of ammonia" at a meeting held in 1974: "The experimental work of the past 50 years leads to conclusion that the rate-determining step in ammonia synthesis over iron catalysts is the chemisorption of nitrogen. ... The question as to whether the nitrogen species involved on the surface is molecular or atomic is still not conclusively resolved, though, in the writer's opinion, the direct participation of nitrogen in an atomic form seems more likely than that in a molecular form."

In the meantime this situation has changed markedly by the advent of new surface physical methods which enabled atomic level studies with well-defined

G. Ertl • Fritz-Haber-Institut der Max-Planck-Gesellschaft, Faradayweg 4–6, D-1000 Berlin 33, Federal Republic of Germany.

single crystal surfaces. This "surface science approach" when taken hand-in-hand with more sophisticated characterization of the surface properties of "real" catalysts has the potential, under optimum conditions, to lead to a microscopic picture of the catalytic reaction which exhibits even a quantitative predictive character for the high-pressure conditions of industrial practice. As will be shown at the end of this chapter, it now appears that in the case of ammonia synthesis this goal has been more or less reached.

The strategy adopted in this approach can be briefly outlined as follows: In order to be able to work with appropriate model systems it is at first necessary to characterize the "active site" of the real catalyst, i.e., its surface properties, as accurately as possible. Traditional methods such as X-ray crystallography, surface area determination by the BET method, and selective adsorption, etc., have now been supplemented by a whole arsenal of surface spectroscopic techniques. The actual catalyst with its rather inhomogeneous surface structure and composition may then be replaced by well-defined single-crystal surfaces (probably chemically modified in order to model also the effect of promoters) which thus enable a systematic investigation of the effect of atomic structure on the surface chemistry. Although the surface area of these single crystals is very small ($<1\ cm^2$) it is nevertheless possible to perform kinetic studies and measure reaction rates under "real" conditions by use of appropriate high-pressure cells. Identification and characterization of the adsorbed surface intermediates is, however, in general restricted to very low pressure conditions for principal experimental reasons, since most of the surface physical techniques are based on the interaction of electrons or ions with matter whose mean free paths in the gas phase decrease with pressure. Although this "pressure gap" may offer a serious problem, proper consideration of the respective thermodynamic and kinetic properties will allow the transfer of conclusions derived from ultrahigh vacuum (UHV) studies to high-pressure conditions. On the basis of the kinetic and energetic information of the elementary steps obtained from such UHV investigations, the overall reaction mechanism may finally be constructed. A kinetic model for the overall reaction may also be derived, and comparison can be made between predictions and the data measured with the real catalyst operated under practical conditions.

In the following discussion, the picture that emerges about the mechanism of the iron-catalyzed ammonia synthesis reaction along these lines will be sketched. The chapter will concentrate essentially on results obtained with well-defined Fe single-crystal surfaces, because this element is the principal component of the industrial catalyst and hence has been investigated in most detail. This subject (including the findings with other surfaces) has already been covered in several previous reviews.[2]

3.2. FROM REAL CATALYSIS TO APPROPRIATE MODEL SYSTEMS

The bulk and surface properties of the industrial ammonia catalyst have been discussed in detail in the preceding chapters. For the present purpose it suffices to remember that under working conditions it consists essentially of metallic iron

(with traces of unreduced iron). The promoters alumina and calcium oxide form a framework which stabilizes the small iron particles against sintering (structural promotion), while potassium spreads over the Fe surface and forms a (K + O) overlayer which acts as "electronic" promoter. For illustration, a series of Auger maps (recorded by means of scanning Auger electron spectroscopy) is shown in Fig. 3.1, reflecting the lateral distribution of various elements in the surface region of the reduced catalyst and demonstrating the pronounced surface enrichment of the promoters.[3]. The areas of metallic iron are covered to a substantial extent with a uniform K + O adlayer with approximate 1:1 stoichiometry. This adlayer is quite different from all bulk compounds between potassium and oxygen due to its strong interaction with the Fe substrate. The presence of oxygen increases the thermal stability of potassium on the surface (which would otherwise evaporate under reaction conditions), while the strong K–O interaction prevents complete reduction.[4]

Since the potassium overlayer merely enhances the catalytic activity but is itself inactive, the first step in the reduction of the complexity of the system consists in studying the reaction as well as the individual elementary processes on clean Fe surfaces alone without the complications arising from interactions with the

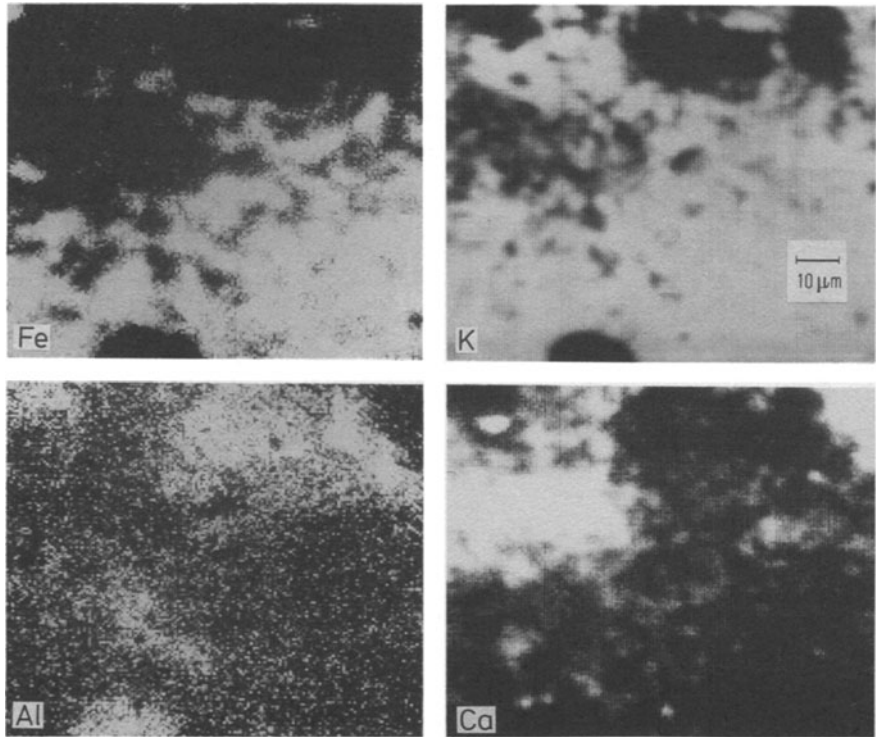

Figure 3.1. "Auger maps" from an industrial ammonia synthesis catalyst after reduction, showing the lateral distribution of Fe, K, Al, and Ca at the surface.

promoters which are then introduced at a later stage in a well-defined and controllable manner. It is essential to keep in mind that the atomic configurations in the surface of a polycrystalline material vary considerably. Therefore in order to study the influence of the surface structure, well-defined single-crystal surfaces are applied as model systems.

In Fig. 3.2 ball models are shown of the most densely packed (110), (100), and (111) planes of bcc Fe which are usually applied in such studies. The clean surfaces are not reconstructed, which means that the lateral configurations of the surface atoms are as shown here while the vertical layer separations vary typically slightly from those in the bulk (relaxation). The particular importance of the (111) plane had been recognized previously in earlier studies (and was later confirmed with single-crystal experiments to be described below): its special role in nitrogen activation was concluded by Brill[5] on the basis of observations with the field ion microscope, and by Boudart *et al.*[6] applying Mössbauer spectroscopy to small Fe particles. They suggested the preferential formation of so-called C7 sites [as characteristic for the (111) plane] after treatment of the catalyst with the gases required for ammonia synthesis.

Kinetic studies with clean iron single-crystal surfaces under high-pressure conditions were performed by Somorjai's group.[7,8] At 20 atm total pressure of a $3:1\ H_2:N_2$ mixture and at 773 K, the activity was found to vary in the order $(111) > (100) > (110)$ by more than two orders of magnitude.[7] Later this work was also extended to the (211) and (210) planes[8] and it was demonstrated that indeed the C7-type configuration of surface atoms as present with the (111) as well as (211) surfaces exhibits the highest catalytic activity. If the results reported for Fe(111) are transformed into a reaction probability for a nitrogen molecule striking the surface to become transformed into an ammonia molecule, a number of the order of 10^{-7} results. This value as well as the sequence of reactivities for the different crystal planes will be of importance in the discussion of the relevance of adsorption studies performed at low pressure that will be presented below.

A series of subsequent papers by Somorjai *et al.*[9] was concerned with the influence of potassium and aluminum oxide additives as well as of the oxidation/reduction conditions in order to get closer insight into the promoter action. The respective conclusions will be presented in the next chapter.

No information about the surface intermediates present under high-pressure conditions can be obtained by the use of electron spectroscopic techniques for obvious technical reasons. If, after high-pressure treatment, the sample is trans-

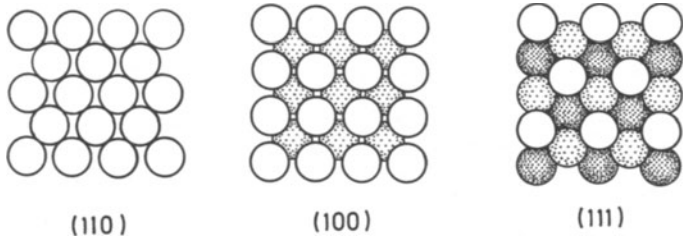

Figure 3.2. Ball models for the most densely packed surfaces of bcc Fe.

ferred to UHV conditions, it is *a priori* rather probable that the surface species will have been desorbed before their analysis. This is, of course, dependent on the strength of the surface/particle bond and, for thermodynamic reasons, also a question of temperature. This means in turn that any surface species present at high pressure can be stabilized even in UHV if the temperature is low enough. (Whether it is still formed at low temperatures because of kinetic restrictions is, of course, another question.)

It turned out[2b] that of all the surface species which may be present during ammonia synthesis at 700 K, only atomic nitrogen (N_{ad}) is sufficiently stable to survive evacuation. Determination of its concentration *in vacuo* after high-pressure operation will therefore yield information about this quantity under reaction conditions. In a series of experiments with Fe(111) performed at 580 K and $P_{N_2} = 150$ torr with varying hydrogen pressure[10] it was found that the steady-state N_{ad} concentration decreases continuously with increasing P_{H_2}. This result demonstrates directly that indeed hydrogenation of N_{ad} is an essential reaction step, and not that of $N_{2,ad}$ as was sometimes speculated in the earlier literature.[2]

The next stages of the strategy will now consist of direct investigation of the various possible surface species under UHV conditions which might be present on well-defined iron single-crystal surfaces, in order to develop (hopefully) a complete microscopic picture describing the overall reaction.

3.3. LOW-PRESSURE STUDIES WITH IRON SINGLE-CRYSTAL SURFACES

Information about the structural, electronic, energetic, or kinetic properties of chemisorbed phases formed at single-crystal surfaces can be obtained by means of a large variety of techniques, which are mainly based on the interaction of slow electrons, ions, or neutral particles with matter and the high surface sensitivity of these probes. Description of these tools can be found in the literature.[11] In the following sections we will summarize some of the results obtained using these methods with systems which are of relevance for ammonia synthesis.

3.3.1. Interaction of Hydrogen with Iron Surfaces

In common with other transition metal surfaces[12] hydrogen molecules striking a clean iron surface undergo dissociation with high probability and become atomically chemisorbed. The energetics of this process can be rationalized by the well-known Lennard-Jones diagram reproduced in Fig. 3.3. Transition from the gaseous H_2 molecule into the chemisorbed H_{ad} state can in principle occur either through intermediate trapping in the molecular "precursor" state ($H_{2,ad}$) or directly by overcoming an eventual activation barrier given sufficiently high translational energy. From recent experiments with Fe(110)[13] it was concluded that indeed the latter mechanism dominates and that there exists a small activation energy of about 3 kJ mol^{-1}. The initial (i.e., at zero coverage) sticking coefficient s_0 is fairly independent of surface temperature and of the order 0.1; above a coverage $\Theta \approx 0.1$

it decreases as $s = s_0(1 - \Theta)^2$ as would be derived for a simple Langmuir-type two-site adsorption process.[13,14] The adsorption kinetics on the Fe(100) and (111) are qualitatively similar, although they were not studied in such detail.[14]

Inspection of Fig. 3.3 shows that the strength of the metal-hydrogen bond, E_{M-H}, is obtained from $2E_{M-H} = E_{ad} + E_{diss}$, where E_{diss} ($=430\,kJ\,mol^{-1}$) is the dissociation energy of H_2 and E_{ad} the adsorption energy. Even with an *a priori* uniform single-crystal surface, the adsorption energy will in general vary as a function of coverage due to interactions between the adsorbed species. Initial adsorption energies of 109, 100, and 88 kJ mol^{-1} were determined for the Fe(110), (100), and (111) planes, respectively,[14] which are also in agreement with calorimetric data for polycrystalline Fe films.[15] The value of E_{M-H} is thus of the order of 250–270 kJ mol^{-1}. The variation of the adsorption energy with coverage is reflected by the appearance of several peaks in the thermal desorption spectra.

Recombination of adsorbed hydrogen atoms leads to the reverse process of thermal desorption whose rate is governed by $E_{ad} + E^*$, where E^* is the activation energy for dissociative adsorption. If a hydrogen-covered Fe surface is heated up in vacuo, desorption will be completed at 500 K.[14] Under the conditions of ammonia synthesis (>700 K) this step will hence be so rapid that the steady-state coverage of H_{ad} will be determined by the adsorption-desorption equilibrium $H_{2^+*} \rightleftharpoons 2H_{ad}$, where the concentration of free surface sites $*$ is, of course, affected by the presence of all other surface intermediates.

The formation of the bond between H and the metal surface takes place through coupling of the H 1*s* orbital to the metal valence states (as manifested by

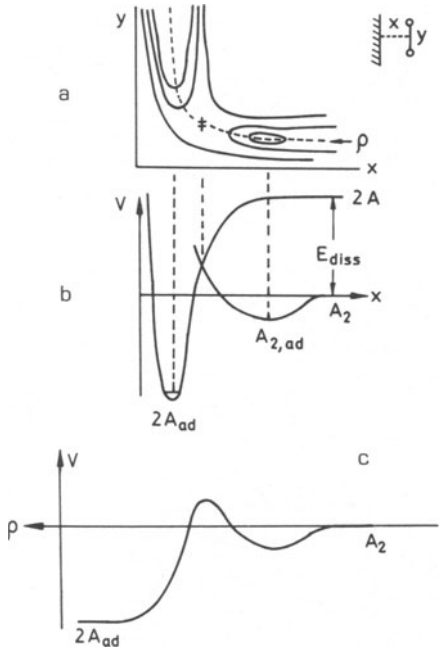

Figure 3.3. Potential energy diagrams for dissociative adsorption of a diatomic molecule approaching a surface: (a) Two-dimensional contour plot with variation of x and y. (b) One-dimensional plot, showing the potentials for the interaction of A_2 and $2A$, respectively, with the surface (Lennard-Jones potential). (c) Variation of the potential along the reaction coordinate (see a).

a peak in UPS at about 5.5 eV below the Fermi energy[14]) and is essentially covalent in nature. The latter conclusion is confirmed experimentally, e.g., by the very small dipole moments of the adsorbate complexes[14] as well as by quantum mechanical calculations.[16]

Below 250 K, chemisorbed hydrogen atoms form ordered overlayer phases on Fe(110), corresponding to coverages $\Theta = 1/2$, 2/3, and 1, respectively, as identified by LEED.[14,17] Theoretical analysis of the phase diagram[18] revealed that this long-range order is due to repulsive as well as attractive interactions between neighboring chemisorbed H atoms which are of the order of <5 kJ mol^{-1}. The structure model for the 2×1 structure at $\Theta = 1/2$ as derived from a quantitative analysis of the LEED intensities[19] is shown in Fig. 3.4. The hydrogen atoms form alternate row in the [001] direction; at $\Theta = 1$ all rows are uniformly occupied, and the adsorbed atoms are located in threefold-coordinated sites with a Fe—H bond length of 1.75 ± 0.05 Å. This result is in full agreement with the experience gained from the structural data of other transition metal/hydrogen systems.[12] Generally, atomic adsorbates prefer adsorption sites with the highest number of nearest-neighbor atoms from the substrate, a conclusion for which theoretical justification is also available.[20] Frequencies of 1060 and 880 cm^{-1} for the surface-hydrogen vibration modes were deduced from high-resolution electron energy loss spectroscopy (HREELS)[21]

Above room temperature the long-range order breaks down, because thermal disorder now overcompensates the ordering forces of the mutual interactions, and also because of the increasing mobility of the chemisorbed species. Although specific data for the present system are not available, the general experience from other systems[12] suggests that the activation energy for surface diffusion is at most of the order of only a few kJ mol^{-1}. At the high temperatures of ammonia synthesis the chemisorbed H atoms may, during their short lifetime on the surface, be safely considered to behave like a two-dimensional gas moving very rapidly parallel to the surface.

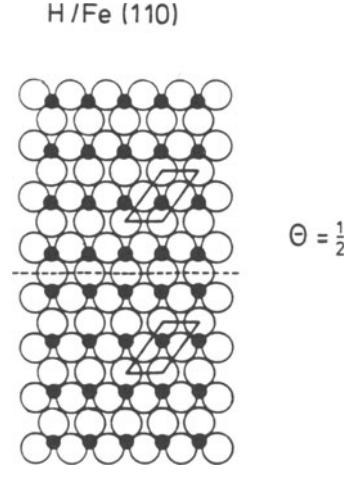

Figure 3.4. Structure of adsorbed H formed on Fe(110) at a coverage $\Theta = 1/2$ below 230 K. The broken line marks an antiphase domain boundary within the adlayer.

The presence of preadsorbed K is only of minor influence on the adsorption of hydrogen[22]: the adsorption energy is increased by about 8 kJ mol^{-1} and the sticking coefficient is somewhat enhanced, while the saturation coverge is not noticeably affected.

3.3.2. Interaction of Nitrogen with Iron Single-Crystal Surfaces

In contrast to hydrogen, the situation with nitrogen is much more complex. Three distinctly different surface species have been identified, apart from the possibility of dissolution of nitrogen atoms in the bulk: (a) a weakly held (physisorbed) molecular γ-state, (b) a chemisorbed molecular α-state on Fe(111), and (c) atomic nitrogen which may be regarded as a surface nitride. By far the most detailed investigations on molecular adsorption of nitrogen have been performed with the (111) plane and the discussion will therefore be predominantly concerned with this plane, which is also associated with the highest catalytic activity for ammonia synthesis.

3.3.2.1. The Molecular γ-State

If a clean Fe(111) surface is exposed to N_2 at $T < 80$ K, subsequent thermal desorption results in the appearance of a TPD peak around 100 K which is identified as a weakly held molecular adsorption state denoted by the symbol γ.[23] Earlier investigations with polycrystalline iron films revealed a quite similar state, namely, a molecular surface species for which an adsorption energy of 21 kJ mol^{-1} was determined calorimetrically.[31] It is unlikely that this species exhibits any pronounced specificity with respect to the surface structure. Its adsorption energy is about 24 kJ mol^{-1} and it is populated with a sticking coefficient of around 0.5.[24] It is characterized by XPS with N 1*s* spectra showing two peaks at 406 and 401 eV bonding energy[25] (Fig. 3.5), and by HREELS with a frequency of 2100 cm^{-1} ($^{15}N_2$) for the N-N stretch vibration[26] which is very close to the value of 2194 cm^{-1} for the corresponding free molecule. This suggests weak bonding with a terminal ("end-on") configuration as is also concluded from semiempirical calculations.[27] More recently the geometry of this phase, thought to consist of nitrogen molecules oriented perpendicular to the surface plane, was confirmed by analysis of angular resolved UPS data.[28]

3.3.2.2. The Molecular α-State

A second, more strongly held molecular state appears on the Fe(111) surface if it is exposed to N_2 at around 100 K. It desorbs around 150 K and its adsorption energy was determined to be 31 kJ mol^{-1} while its population from the gas phase takes place with a sticking coefficient of only about 10^{-2}.[29] XPS shows only a single N 1*s* level at 399 eV (see Fig. 3.5). Most interestingly, the frequency of the N-N stretch vibration is considerably lowered to a value of only 1490 cm^{-1} ($^{15}N_2$) reflecting a considerable reduction in the N—N bond order.[25,26,30] Comparison

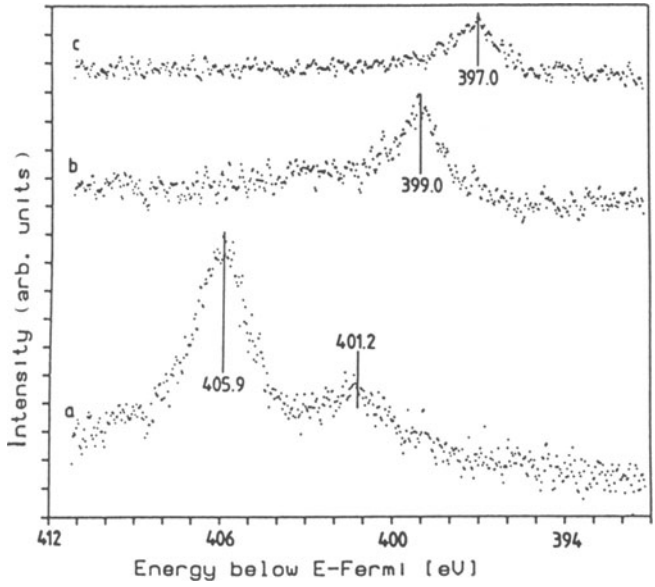

Figure 3.5. XPS data of the N 1*s* core levels for three different nitrogen species on a Fe(111) surface: (a) γ-$N_{2,ad}$, (b) α-$N_{2\text{-}ad}$, (c) N_{ad}.

with transition metal coordination complexes led to the conclusion that in this case the nitrogen molecule is bonded in a "side-on" manner. Both nitrogen atoms interact similarly with the surface atoms, as has also been corroborated by model calculations for interpretation of the XPS data.[25] The lowering of the N-N stretching frequency (which is presumably accompanied by a considerable weakening of the N—N bond and an increase in its length), together with the associated increase in the work function, suggest a π-bonding mechanism in which the antibonding π-orbitals of N_2 act as acceptors for electrons from the substrate. This view was recently confirmed by experiments using angular resolved UPS, which demonstrated that the nitrogen molecule in the α-state is strongly inclined toward the surface plane.[28] [Since the Fe(111) plane is a very open structure, a configuration of the molecular axis exactly parallel to the surface plane might be hard to realize.] In the same work a plausible theoretical model for the bond formation of this species was proposed whose properties are consistent with the known experimental data and whose possible structure is reproduced in Fig. 3.6a. In this configuration interaction of a nitrogen molecule with five Fe atoms from the three topmost layers takes place, which would also account for the low saturation coverage. This structure would correspond to the occupation of site (b) in Fig. 3.6b which had been proposed earlier as one of the possible adsorption sites,[30] while site (a) was favored in the theoretical treatment of Ref. 27. In any case, it is quite apparent that the Fe(111) plane offers a special geometry for the discussed type of bond formation, which might explain why the observation of the α-state has so far been restricted to this surface.

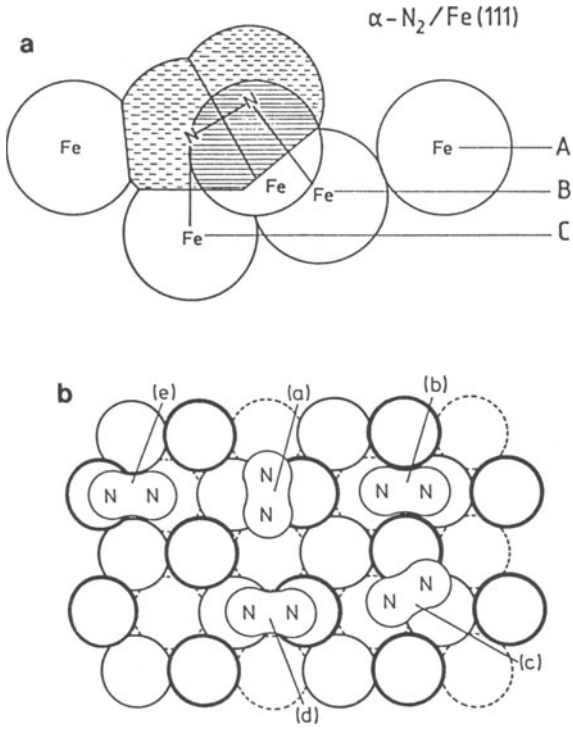

Figure 3.6. α-$N_{2\text{-ad}}$ on Fe(111): (a) Side view of the adsorption geometry as proposed in Ref. 28. (b) Top view of possible surface configurations according to Ref. 30.

3.3.2.3. The Atomic State

Warming up of the Fe(111) surface previously covered by α-N_2 leads to dissociation of this species in parallel with thermal desorption, as reflected by the disappearance of the N-N stretch band in the HREEL data, and the appearance of a new band at 450 cm^{-1} associated with the metal-nitrogen vibration. This atomic state is now characterized in XPS by a N 1*s* peak at 397 eV (Fig. 3.5). The sticking coefficient for overall dissociative adsorption from the gas phase is very small[32,33] and will be discussed in more detail below. The metal-nitrogen bond is very strong (thermal desorption occurs only above 700 K) and involves the N 2*p* levels, which show up as a single valence level at about 5 eV below the Fermi level in UPS. A series of (mostly rather complex) surface structures were detected by LEED, which for Fe(110) and (111) are associated with pronounced displacements of the surface atoms (reconstruction). In the case of the Fe(100) plane, the surface remains unreconstructed. These phases could be correlated with corresponding planes of Fe_4N (although bulk iron nitrides will not be formed by interaction between molecular nitrogen and Fe surfaces for thermodynamic reasons!) and they are therefore also denoted as "surface nitrides."[32,33] Dissociative adsorption of nitrogen on a stepped Fe(12, 1, 0) surface was found to increase the step density

and to lead to facet formation. This effect was rationalized by the tendency to achieve an epitaxial relationship between the "surface nitride" phases and the substrate.[35]

The ordered phase formed on Fe(100) (classified as c2 × 2 structure according to the standard nomenclature of surface crystallography[11]) has structural parameters similar to those found with the (002) plane of Fe_4N without distortion of the substrate lattice; this is the reason why in the case of Fe(100) no reconstruction occurs. The structure of this phase as derived from quantitative LEED analysis is reproduced in Fig. 3.7.[34] It has a coverage $\Theta = 0.5$, and the N atoms occupy fourfold hollow sites with their plane 0.27 Å above the topmost plane of Fe atoms.

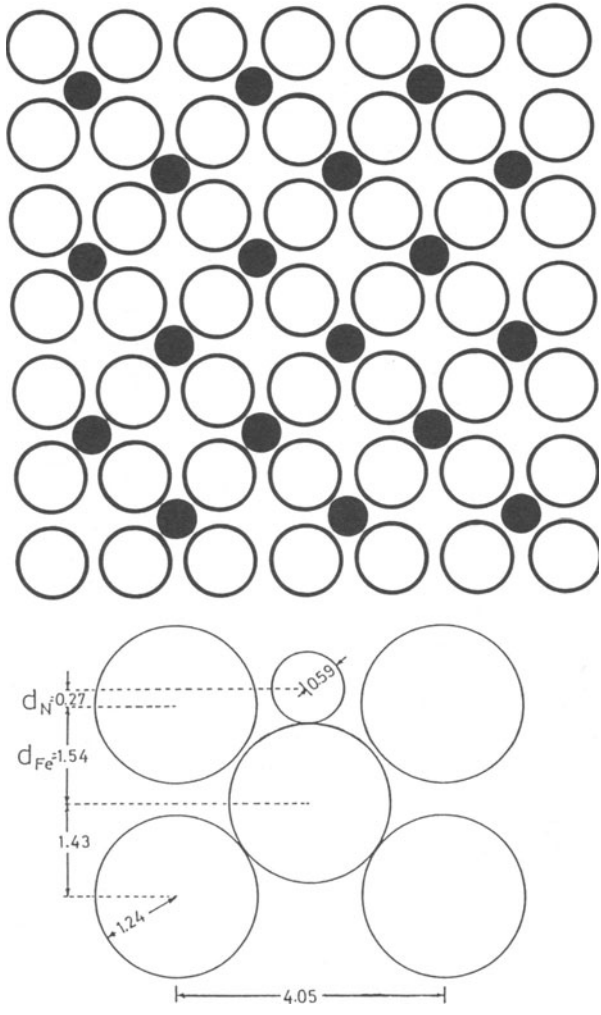

Figure 3.7. Structure (top and side views) of the c2 × 2 phase formed by N_{ad} on Fe(100).

The distance ($d_1 = 1.83$ Å) from the N atom to the underlying Fe atom is even shorter than that to the four nearest neighbors in the surface plane ($d_2 = 2.04$ Å), so it is clear that a substantial contribution to the bond formation arises from coupling of the N atoms to Fe atoms in the second layer.

Due to the strong bond with the surface, mobility of the adsorbed N atoms becomes appreciable only above about 500 K. By comparison, the mobility of the adsorbed H atoms will be higher by orders of magnitude, so that the primary step of hydrogenation can be viewed as an interaction between a two-dimensional gas of adsorbed H atoms and an essentially fixed matrix of adsorbed N atoms.

If a surface is partly precovered by N and then exposed to hydrogen, it turns out that the total amount of hydrogen adsorbed is reduced, but the shape of the thermal desorption spectrum is essentially unaffected. This indicates that the main effect of adsorbed N atoms on hydrogen adsorption is primarily one of site blocking. Preadsorbed H atoms, on the other hand, inhibit adsorption of the molecular α-N_2 state and hence decrease the rate of the dissociative nitrogen adsorption.[11] The simple assumption of mutual blocking of adsorption sites, which underlies the kinetic model to be presented in Section 3.4, is therefore a reasonable approximation.

3.3.2.4. Kinetics of Dissociative Nitrogen Adsorption

Since this step is rate-determining for ammonia synthesis, considerable effort has been expended on its detailed investigation. It has turned out to be of great complexity so that, even now, complete understanding of the underlying microscopic dynamics is still lacking, although there exists general agreement about the experimental findings.

In Fig. 3.8, the variation in the relative surface concentration of N_{ad} (as monitored by Auger electron spectroscopy) with N_2 exposure at elevated temperatures for the Fe(110), (100), and (111) surfaces[32,33] is shown. The slopes of these curves yield the sticking coefficients for dissociative chemisorption which are obviously very small and depend markedly on the surface orientation. More specifically, the initial sticking coefficient (at 683 K) changes from 7×10^{-8} to 2×10^{-7} to 4×10^{-6} in the sequence Fe(110) < (100) < (111), i.e., the (111) plane is about two orders of magnitude more active than the most densely packed (110) plane. This sequence of activity toward dissociative nitrogen adsorption at low pressures ($<10^{-4}$ torr) is in agreement with that found for the rate of ammonia production at high pressure (20 atm) described in Section 3.2.[8] Moreover, the sticking coefficients are approximately of the same orders of magnitude as the reaction probabilities derived from the quoted high-pressure work. This remarkable result demonstrates that kinetic parameters derived from well-defined single-crystal surfaces are obviously transferable over the "pressure gap" and it confirms that the dissociative nitrogen adsorption is indeed the rate-limiting step, since the rate of NH_3 formation equals that of dissociative nitrogen adsorption.

Similar conclusions had already been reached many years ago by Emmett and Brunauer,[36] who measured the uptake of nitrogen by commercial catalysts and concluded likewise that the sticking coefficient is only of the order of 10^{-6}.

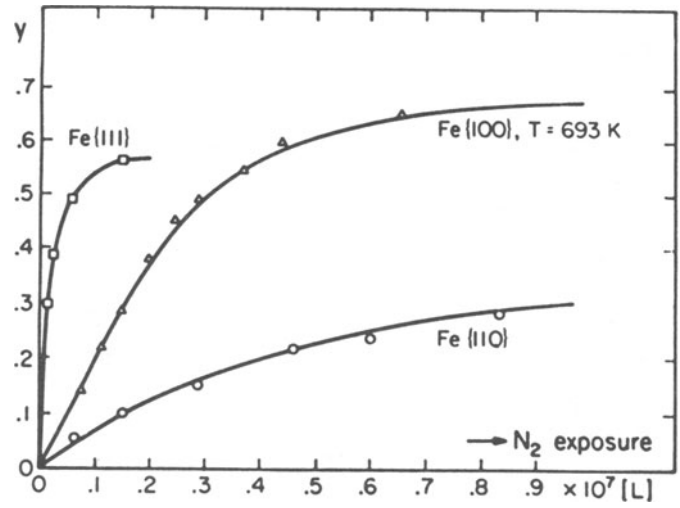

Figure 3.8. Variation in the relative surface concentration y of N_{ad} (as determined by Auger electron spectroscopy) with N_2 exposure of different Fe single-crystal planes. 1 L (Langmuir) = 10^{-6} torrs is approximately the exposure required to saturate an adlayer if the sticking coefficient is unity.

The sticking coefficient can be formulated in terms of the usual Arrhenius equation for a rate constant, $s = \nu \exp(-E^*/RT)$, with the preexponential ν and activation energy E^* as parameters. Measurements at different temperatures revealed that the differences between the three crystal planes can essentially be traced back to differences in the net activation energy E^* for the overall process $N_2 \rightarrow 2N_{ad}$, which in the limit of zero coverage was found to be about 27 kJ mol^{-1} for Fe(110), 21 kJ mol^{-1} for Fe(100), and about 0 kJ mol^{-1} for Fe(111). These activation energies increase continuously with increasing coverage, in qualitative agreement with previous measurements using supported Fe catalysts.[37]

The absolute values of the sticking coefficients cannot, however, be reconciled with the measured small activation barriers in the framework of a simple collision model. They rather demonstrate the formal existence of a very small preexponential factor ν whose origin must be sought in the dynamics of the process, a subject for continuing investigations.

Analysis of detailed kinetic data obtained with Fe(111)[29] at low temperatures yielded, for the initial overall sticking coefficient [again written as $s_0 = \nu \exp(-E^*/RT)$], a preexponential $\nu = 2.2 \times 10^{-6}$ and a negative activation energy of $E^* \approx -3$ kJ mol^{-1}. It was found that this process proceeds through molecularly adsorbed α-N_2 (see above) which acts as a "precursor" in the sense of Fig. 3.9a:

$$N_2 \underset{k_{-1}}{\overset{k_1}{\rightleftharpoons}} N_{2,ad}(\alpha) \xrightarrow{k_2} 2N_{ad}$$

The sticking coefficient into the α-state (k_1) was determined to be only about 10^{-2}; the parameters of $k_{-1} = \nu_{-1} \exp(-E_1/RT)$ were determined to be $\nu_1 = 10^{10\pm1}$ s^{-1} and $E_1 = 31$ kJ mol^{-1} and those of $k_2 = \nu_2 \exp(-E_2/RT)$ to be $\nu_2 \approx 10^7$ s^{-1} and

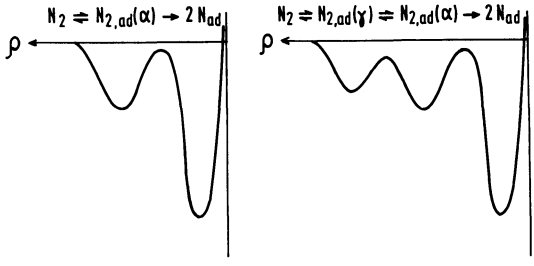

Figure 3.9. Schematic potentials illustrating the possible paths to dissociative nitrogen adsorption on Fe(111): (a) The molecular α-state is populated from the gas phase. (b) Population of the α-state is preceded by trapping in the γ-state.

$E_2 = 28$ kJ mol^{-1}. From these results it was concluded that two factors are responsible for the unusually low overall sticking coefficient: (1) The small probability of only about 10^{-2} for an impinging N_2 molecule to be trapped in the molecular precursor state, and (2) the ratio ν_2/ν_{-1} which makes it much more probable that an α-N_2 is more prone to thermal desorption than dissociation. In a subsequent theoretical study[38] it was suggested that the low preexponential of the sticking coefficient is, in this particular case, due essentially to a strongly reduced energy transfer of the impinging N_2 molecules to the phonons of the solid. As discussed in Section 3.3.2.1 above, in later work at even lower temperatures the existence of an additional molecular state (γ) had been demonstrated.[23] It was found that the α-state could be populated through thermally activated conversion of the γ-state and therefore the simple potential energy diagram of Fig. 3.9a was extended in a way as shown in Fig. 3.9b. By appropriate adjustment of the various kinetic parameters it was possible to model the experimental data on the assumption that the α-state is populated only through the γ-state and not by direct collision from the gas phase.[23,39] More recently it was found,[24] however, that this picture cannot be valid at elevated temperatures but that, under these conditions, direct adsorption of N_2 into the α-state becomes dominant, in agreement with the original model.[29] Recent molecular beam experiments have revealed that the sticking coefficient for dissociative nitrogen adsorption may be strongly enhanced by increasing the kinetic energy of the incident molecules. This result was interpreted in terms of enhanced probability for population of the α-state by increasing the probability for overcoming the $\gamma \rightarrow \alpha$ barrier without intermediate trapping of the γ-state.[40] The dependence of the sticking coefficient on the incident kinetic energy was rationalized in a qualitative manner on the basis of quantum mechanical calculations without invoking a $\gamma \rightarrow \alpha$ barrier, but interestingly it was speculated that tunneling through a narrow activation barrier is of importance for the dissociation step.[41]

Studies on the microscopic dynamics of dissociative nitrogen adsorption will certainly continue in the future, but there is now general agreement about the nature of surface species involved and the kinetic parameters of this process on the Fe(111) surface, such data being essential for the kinetics of ammonia synthesis.

3.3.2.5. The Effect of the K Promoter

The sticking coefficient for dissociative nitrogen adsorption may be enhanced by more than two orders of magnitude in the presence of preadsorbed potassium

atoms.[42] Maximum sticking coefficients of about 4×10^{-5} were obtained by optimizing the surface potassium concentration for Fe(111)[43] as well as for Fe(100)[42,43] and even polycrystalline iron.[4] Most remarkably, the pronounced difference in activity between the various clean iron single-crystal planes is practically eliminated by the presence of potassium, so that it can be concluded that the actual catalyst surface is kinetically much more uniform than one might have anticipated on the basis of the results presented so far.

The promoter action of adsorbed potassium has been attributed both to a stabilization of the molecular α-species[42,46] as well as to an enhancement of the sticking coefficient for the formation of this α-species.[39,26] On Fe(111) the adsorption energy for α-N_2 is increased locally in the vicinity of an adsorbed potassium atom from 31 to 44 kJ mol^{-1}. Parallel to this increase in the adsorption energy for the precursor state its activation energy for dissociation is lowered, as becomes apparent from inspection of Fig. 3.10. Once the nitrogen molecule has become dissociated, the adsorbed N atoms formed near the K atoms diffuse away to the bare iron patches (when the temperature is above ~400 K), so that finally the whole available surface is covered by N_{ad}.

The simplest interpretation of the promotional effect is based upon an electrostatic model.[42,43] As reflected by the strong decrease in the work function upon potassium adsorption, there is a pronounced transfer of electronic charge to the substrate, leading to the formation of a $M^{\delta-}$-$K^{\delta+}$ dipole. A nitrogen molecule adsorbed near such a site will therefore experience a more pronounced "back-bonding" effect from the metal to its antibonding π-orbitals. As a consequence its bond strength to the metal will be increased and the N—N bond strength will be weakened further, as also reflected by a further reduction in the N-N stretching

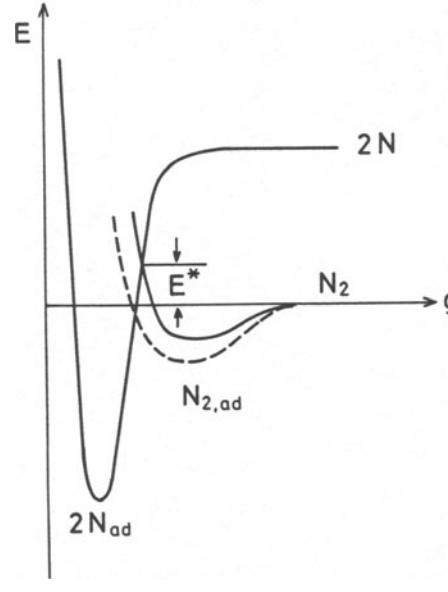

Figure 3.10. Lennard-Jones diagram illustrating schematically dissociative nitrogen adsorption through $N_{2,ad}$ adsorbed on a bare Fe patch (full line) and in the vicinity of an adsorbed K atom (broken line).

frequency.[30] This qualitative picture is corroborated by the results of theoretical treatment that confirm the localized character of this interaction. An additional prediction is that this effect will be strongly reduced for an adsorbed atom which is very close to the surface plane—hence primarily only $N_{2,ad}$, but not the N_{ad} species, will be affected.[44]

The surface of the actual catalyst will not consist of adsorbed K alone, but of a composite K + O adlayer. O is an electronegative adsorbate and therefore its presence counterbalances partly (but not completely) the promoting effect of K.[4] As a typical example s_0 on clean polycrystalline Fe at 423 K has a value of 5×10^{-6}, it increases to a maximum value of about 3×10^{-5} in the presence of K alone, and drops down to 1×10^{-5} for the composite K + O adlayer, so that the sticking coefficient with respect to the promoter-free surface is enhanced by about a factor of 2.

3.3.3. Interaction of Ammonia

The equilibrium concentration of ammonia in a nitrogen and hydrogen mixture is extremely small under low-pressure conditions, and its formation is barely seen. Desorption of this molecule from the catalyst surface is, on the other hand, the last step in the synthesis reaction, and its adsorption becomes of relevance when approaching the equilibrium state. In addition, decomposition of ammonia has to proceed through the same elementary steps as its formation, as a consequence of the principle of microscopic reversibility, so that information on the reaction mechanism is to be expected from the study of possible surface intermediates.

Below room temperature ammonia adsorbs nondissociatively on clean iron single-crystal surfaces with a rather high sticking coefficient.[45-47] The structure model proposed for the ordered phase formed on Fe(110)[46] is reproduced in Fig. 3.11. Coupling to the surface occurs through the nitrogen atom and mainly by

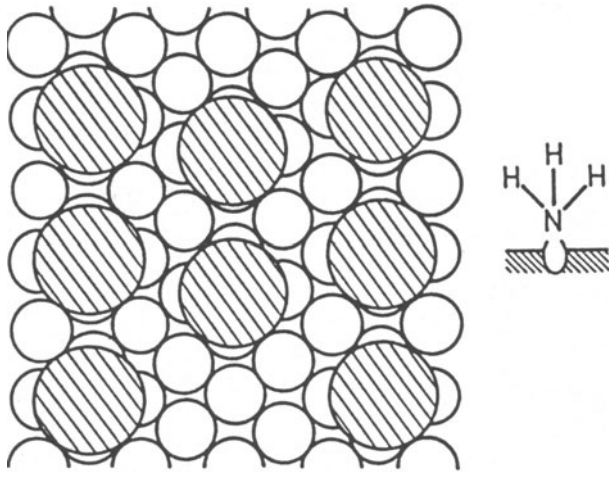

Figure 3.11. Structure model for NH_3 adsorbed on a Fe(110) surface.

σ-donation from the occupied N lone pair to the metal. These conclusions are based on the following evidence:

Two emission maxima are discernible in the UP spectrum and may be identified with the $3a_1$ (= N lone pair) and $1e$ (= N—H bond) orbitals of ammonia. The energetic separation between these two levels is decreased by about 1 eV if compared with gas phase data, and this has been attributed to the stabilization of the $3a_1$ state by bond formation with the surface. From the pronounced decrease in the work function it was concluded that the dipole moment of adsorbed ammonia is even larger than in the gas phase, which is again consistent with the proposed bond mechanism. This picture of electronic interaction is analogous to that for corresponding coordination compounds and is further confirmed by the results of *ab initio* calculations for an $Fe—NH_3$ complex.[48] Among the various vibrational bands the Fe—N stretching mode could be identified with a frequency of about 420 cm^{-1}.[47]

The adsorption energy of ammonia is dependent on the crystallographic orientation of the surface, as well as on coverage, and is typically of the order of about 70 kJ mol^{-1}.[45,46] As a consequence, rapid desorption will take place at the temperature of ammonia synthesis. The crystal face specificity of the adsorption energy is also reflected in the temperature programmed desorption (TPD) spectra, which can therefore be used as a fingerprint for monitoring possible restructuring of the surface during the synthesis reaction.[9a]

Heating up an iron surface covered by ammonia, however, not only leads to complete desorption of the adsorbate but also to stepwise thermally activated decomposition. The intermediate formation of $NH_{2,ad}$ was, for example, deduced from the observation of NH_2D production between 300 and 400 K when a Fe(111) surface had been exposed to a mixture of $NH_3 + D_2$,[45] as well as from similar features in transient UPS data from the interaction of both ammonia or hydrazine with Fe(111).[49] Intermediate formation of $NH_{2,ad}$ in the same temperature range as for Fe(111) was also concluded to take place with a Ni(110) surface on the basis of TPD and HREELS. The latter technique permitted unequivocal identification of this surface species by means of its vibrational bands.[50] In the same work, NH_{ad} could also be identified and was forming by further thermal fragmentation of $NH_{2,ad}$, with an activation energy of 85 kJ mol^{-1}. The NH_{ad} species could be isolated and identified on Fe(110). If a Fe(110) surface covered by $NH_{3,ad}$ is warmed up to around room temperature, a new 2×2 LEED pattern forms.[46,51] Attempts at a quantitative LEED structural analysis of this phase have so far been unsuccessful, presumably because this is not a simple overlayer structure but involves also some kind of reconstruction of the substrate.[52] The UP spectrum of this species exhibits two maxima at energies which are not only quite different from those of nondissociated ammonia, but also at variance with the single peak arising from the completely dissociated product N_{ad} (+ H_{ad}). Final identification of this species as NH_{ad} could be achieved by means of SIMS.[53] The variation in the intensities of different species with temperature upon heating up an NH_3-covered Fe(110) surface is shown in Fig. 3.12. The NH_3^+ signal decreases continuously due to simultaneous desorption and decomposition of $NH_{3,ad}$, while the intensity of the NH^+ species reaches its maximum at 350 K (in agreement with

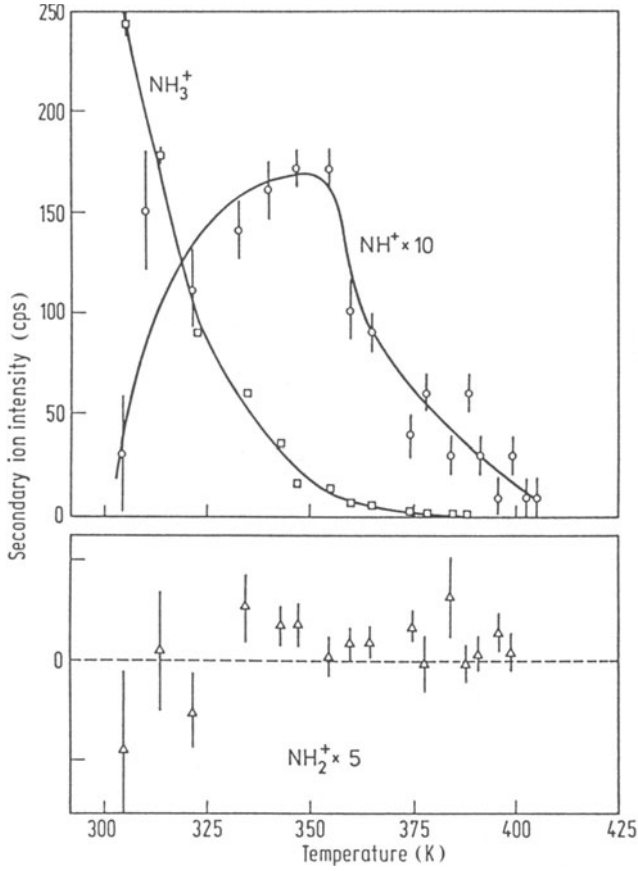

Figure 3.12. NH_3/Fe(110). Variation of the SIMS signals with surface temperature, reflecting the intermediate build-up of NH_{ad}.

LEED and UPS data) and then also decays due to further decomposition of NH_{ad}. The NH_2 concentration, on the other hand, is always below the experimental noise level.

While the adsorbed hydrogen atoms formed by decomposition of adsorbed ammonia recombine and desorb at temperatures below about 500 K (see Section 3.3.1) the simultaneously formed N_{ad} species is much more stable and needs temperatures above 700 K for desorption as N_2. This latter process is therefore the rate-limiting step in ammonia decomposition on iron surfaces under steady-state conditions.[54,55] As a consequence the reaction order with respect to NH_3 is zero and the activation energy is of the order of 200 kJ below about 800 K (desorption of N_2 being rate-limiting). The reaction order becomes unity and the activation energy negligibly small at even higher temperatures, where the rate then becomes limited by the adsorption of ammonia.[55] At higher pressures of ammonia the

transition from the zero- to first-order regime will be shifted to higher temperatures for obvious reasons, in agreement with experimental evidence.[54]

Interaction of ammonia with iron surfaces at elevated temperatures (typically 670 K) leads to the formation of γ- (Fe_4N) and even ε-nitrides.[56] These compounds, however, have no relevance under the conditions of ammonia synthesis for thermodynamic reasons.

From the electrostatic model for the promotional action of adsorbed $K^{(\delta+)}$, one would expect a destabilizing effect to the adsorption of NH_3—in contrast to N_2—since the bond with the surface is in this case dominated by electron donation to the substrate.[2e] Recent TPD measurements have indeed demonstrated a decrease in the adsorption energy induced by the presence of coadsorbed potassium, from which an additional promoter effect due to reduced site-blocking by the reaction product was concluded.[9c]

3.4. MECHANISM AND KINETICS OF AMMONIA SYNTHESIS

If all the experimental evidence presented in the preceding sections is put together, the reaction scheme for the catalytic synthesis of ammonia on iron-based catalysts can unequivocally be formulated in terms of the following steps:

$$H_2 + * \rightleftharpoons 2H_{ad} \quad (1)$$

$$N_2 + * \rightleftharpoons N_{2,ad} \quad (2)$$

$$N_{2,ad} \rightleftharpoons 2N_{ad} \quad (3)$$

$$N_{ad} + H_{ad} \rightleftharpoons NH_{ad} \quad (4)$$

$$NH_{ad} + H_{ad} \rightleftharpoons NH_{2,ad} \quad (5)$$

$$NH_{2,ad} + H_{ad} \rightleftharpoons NH_{3,ad} \quad (6)$$

$$NH_{3,ad} \rightleftharpoons NH_3 + * \quad (7)$$

where * denotes schematically an ensemble of atoms forming an adsorption site.

Suggestions that the reaction proceeds through these steps have, of course, already been made previously,[2,57] but only the surface science approach enabled direct identification of the surface intermediates and, in addition, determination of most of the relevant kinetic parameters of the elementary steps. These kinetic parameters are complex functions of the coverages (including the surface concentrations of all other surface species as well as of the promoter overlayer) and of the surface structure. At first sight it appears therefore to be a rather hopeless task to develop an adequate kinetic model which would be able to predict the rate of ammonia synthesis under industrial conditions with reasonable accuracy (say to within about one order of magnitude), even on the assumption that all these kinetic parameters were known with high precision. Surprisingly, this task could nevertheless be solved quite successfully, as will be outlined below.

Before turning to these quantitative aspects, it is first necessary to discuss the qualitative features of the presented mechanism and its energetics which provide conceptual insight into the progress of this reaction. The progress of the reaction

may be rationalized in terms of its energy profile as reproduced in Fig. 3.13. Homogeneous reaction in the gas phase would be energetically rather unfavorable because of the large dissociation energies involved in the first steps. The alternate reaction pathway offered by the catalyst avoids this problem, since the energy gain associated with the formation of the surface-atom bonds overcompensates the relevant dissociation energies, and the first steps actually become exothermic. Dissociative nitrogen adsorption is nevertheless still rate-limiting, not because of a high activation barrier, but rather because of the very unfavorable preexponential factor in its rate constant. The subsequent consecutive hydrogenation steps are energetically uphill, but the energy differences associated can easily be overcome at the temperatures (~700 K) applied under actual synthesis conditions. It is, however, quite apparent that the nature of the rate-limiting step would switch from dissociative nitrogen adsorption to hydrogenation of the adsorbed atomic nitrogen species if the temperatures were lowered sufficiently because of these differences in activation energy.

The assumption that nitrogen adsorption was the rate-limiting step of ammonia synthesis had already been applied in the derivation of the Temkin rate equations, which have proved to be quite successful in describing the kinetics of industrial ammonia synthesis provided that the empirical parameters included were properly selected.[58,59] This formalism also includes the nonuniformity of the surface, viz. the variation of the adsorption parameters with coverage. As was pointed out by Boudart,[60] integration of the rates over this (assumed) distribution yields an expression for the overall turnover rate that is interestingly rather similar to the equation which results for a uniform surface (modeled by Langmuir kinetics) with

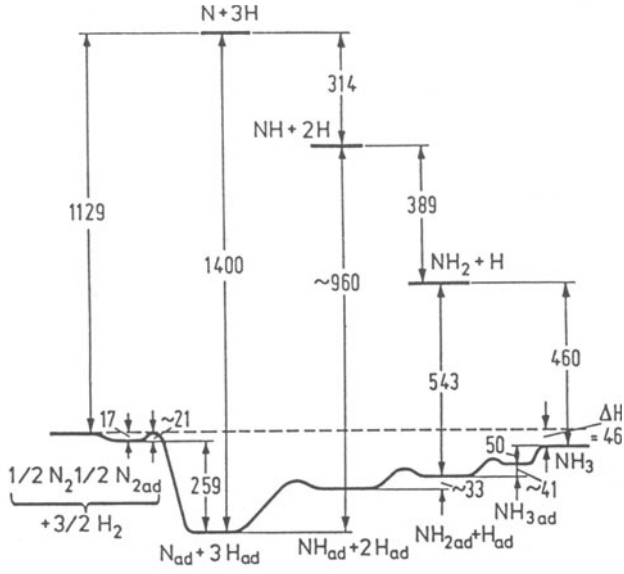

Figure 3.13. Schematic energy profile of the progress of ammonia synthesis on Fe (energies are in kJ mol^{-1}).

the kinetic parameters taken at the limit of low coverages. It was therefore recently concluded by Boudart[61] that successful approximate modeling of the kinetics with a "real" catalyst at high pressures based on data obtained with single-crystal surfaces at low coverages might not be merely accidental. This approach receives support from recent experimental comparison between an industrial ammonia synthesis catalyst and a K promoted Fe(111) surface[67]: the thermal desorption spectra for the various nitrogen species turned out to be quite similar, which demonstrates that the kinetic parameters for the model system are indeed representative for the "real" catalyst.

Attempts at theoretical modeling of the kinetics along these lines were recently performed independently by two groups. Bowker *et al.*[62] developed a computer program to calculate the rate of ammonia synthesis on the basis of the reaction scheme presented above and with rate parameters for all the individual steps as input parameters. In the first version of this treatment obviously not all of these parameters were properly chosen as provided by the experimental evidence. The resulting ammonia yields differed by 4–5 orders of magnitude from those reported for an industrial catalyst! More recently, the same authors revised their set of input parameters and applied data which they called the "Ertl kinetic model."[63] For a particular set of synthesis conditions, they calculated now an ammonia yield of 3.0%, which has to be compared with a 13.2% yield determined with the industrial catalysts operating under the same conditions. Bearing in mind all the existing experimental uncertainties with the single-crystal work, I consider this agreement to be very good and it is difficult to see why Bowker *et al.* think otherwise.[63]

The second, independent treatment was performed by Stoltze and Nørskov[64,65] and differs from the preceding work in that it starts with the experimentally well-established fact that dissociation of adsorbed nitrogen is rate-limiting. The overall rate can then be calculated from the rate of this step and the equilibrium constants of all the other steps. This reduces the number of input parameters significantly. The adsorption–desorption equilibria are treated with the approximation of competitive Langmuir-type adsorption and by evaluation of the partition functions for the gaseous and adsorbed species. The data for the potassium-promoted Fe(111) surface were used for the rate of dissociative nitrogen adsorption which are also representative of the other crystal planes of the promoted catalyst, as outlined above. The active area of the commercial catalyst was assumed to equal that derived from selective carbon monoxide chemisorption as a well-established standard procedure. A particular strength of this model is the fact that experimental data from single-crystal studies (such as TPD traces) are reproduced well with the *same* set of parameters and the same model as used for the determination of the rate under "real" conditions. Comparison of the resulting yields against those determined experimentally with a commercial Topsøe KM1 catalyst yielded general agreement to within a factor better than 2. In Fig. 3.14, a compilation of data over a wide range of conditions is presented that demonstrate this almost too perfect agreement.

Even more important than these quantitative data are the more qualitative features of this model, reproducing the trends on the rate during variation in temperature, gas flow, pressure, as well as the influence of potassium coverage

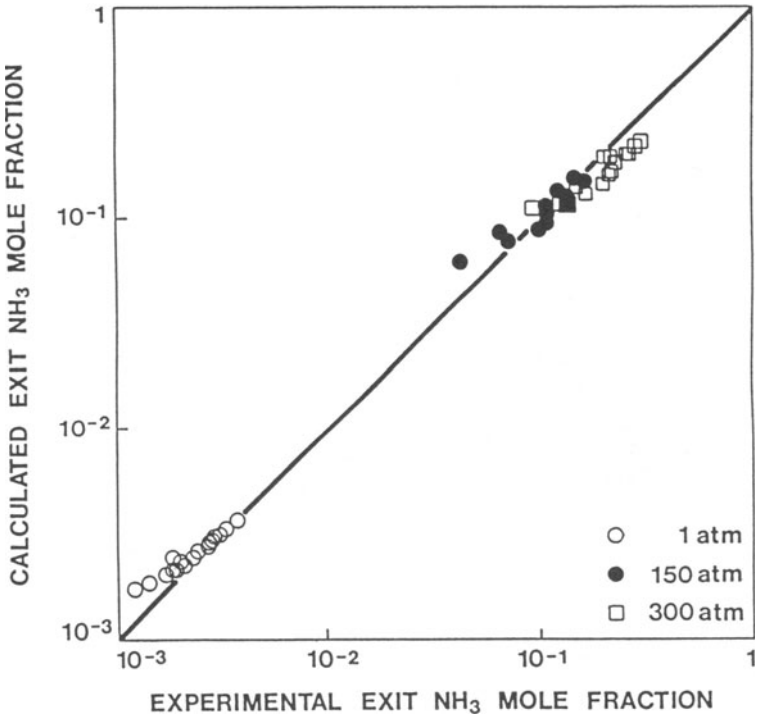

Figure 3.14. Comparison of ammonia production with a commercial catalyst measured under varying conditions of pressures, temperature, and gas flow, against the corresponding data calculated with the quoted kinetic model based on single-crystal, low-pressure data.[64,65]

and water content in the gas phase. For example, the net activation energy for ammonia synthesis can be interpreted as the activation energy for dissociative nitrogen adsorption plus the energy required for the creation of two free adsorption sites, which depends on temperature and pressure. The agreement between $E^* = 46$ kJ mol^{-1} measured around 723 K and 47 kJ mol^{-1} calculated for the same conditions is again excellent.[65] Most recently, the conclusions reached by Stoltze and Nørskov were confirmed by the results of calculations performed by yet another independent group.[68]

A general conclusion from these models based on single-crystal data is that the most abundant surface species under practical synthesis conditions will be adsorbed atomic nitrogen (>90%), despite the fact that its formation is the rate-limiting step of the overall reaction.

3.5. CONCLUSION

The editors of *Catalysis. Science and Technology*, J. R. Anderson and M. Boudart, stated a few years ago in the preface to Vol. 4 of their series[66]: "In a way, surface science studies provide standards by which the quality of work done

by catalytic scientists can be assessed." It is felt that the catalytic synthesis of ammonia is a particular fine example confirming this conclusion. One should keep in mind, however, that this—despite its complexity—is still one of the most simple catalytic reactions.

REFERENCES

1. P. H. Emmett, in: *The Physical Basis for Heterogeneous Catalysis* (E. Drauglis and R. I. Jaffee, eds.), p. 3, Plenum Press, New York (1975).
2. a. A. Ozaki and K. Aika, in: *Catalysis. Science and Technology* (J. R. Anderson and M. Boudart, eds), Vol. 1, p. 88, Springer-Verlag, Berlin (1981). b. G. Ertl, in: *Catalysis. Science and Technology* (J. R. Anderson and M. Boudart, eds.), Vol. 4, p. 209, Springer-Verlag, Berlin (1983). c. M. Grunze, in: *The Chemistry and Physics of Solid Surfaces and Heterogeneous Catalysis* (D. A. King and D. P. Woodruff, eds), Vol. 4, p. 413, Elsevier, Amsterdam (1982). d. G. Ertl, *Catal. Rev. Sci. Eng.* **21**, 201 (1980). e. G. Ertl, *J. Vac. Sci. Technol.* **A1**, 1247 (1983). f. G. Ertl, *CRC Crit. Rev. Solid State Mater. Sci.* **3**, 349 (1982).
3. G. Ertl, D. Prigge, R. Schloegl, and M. Weiss, *J. Catal.* **79**, 359 (1983).
4. Z. Páal, G. Ertl, and S. B. Lee, *Appl. Surf. Sci.* **8**, 231 (1981).
5. a. R. Brill, *Ber. Bunsenges. Phys. Chem.* **15**, 455 (1971). b. R. Brill, E. L. Richter, and E. Ruch, *Angew. Chem.* **6**, 882 (1967).
6. a. J. A. Dumesic, H. Topsoe, S. Khammouma, and M. Boudart, *J. Catal.* **37**, 503 (1975). b. J. A. Dumesic, H. Topsoe, and M. Boudart, *J. Catal.* **37**, 513 (1975).
7. N. D. Spencer, R. C. Schoonmaker, and G. A. Somorjai, *J. Catal.* **74**, 129 (1982).
8. D. D. Strongin, J. Carrazza, S. R. Bare, and G. A. Somorjai, *J. Catal.* **103**, 213 (1987).
9. a. D. R. Strongin, S. R. Bare, and G. A. Somorjai, *J. Catal.* **103**, 289 (1987). b. S. R. Bare, D. R. Strongin, and G. A. Somorjai, *J. Phys. Chem.* **90**, 4726 (1986). c. D. R. Strongin and G. A. Somorjai, *Catal. Lett.* **1**, 61 (1988).
10. G. Ertl, M. Huber, S. B. Lee, Z. Páal, and M. Weiss, *Appl. Surf. Sci.* **8**, 373 (1981).
11. a. G. A. Somorjai, *Chemistry in Two Dimensions: Surfaces*', Cornell University Press, Ithaca (1981). b. G. Ertl and J. Küppers, *Low Energy Electrons and Surface Chemistry*, 2nd edn., Verlag Chemie, Weinheim (1985).
12. K. Christmann, *Surf. Sci. Rep.* **9**, 1 (1988). Provides a general extensive review on the interaction of hydrogen with solid surfaces.
13. E. A. Kurz and J. B. Hudson, *Surf. Sci.* **195**, 15, 31 (1988).
14. F. Bozso, G. Ertl, M. Grunze, and M. Weiss, *Appl. Surf. Sci.* **1**, 103 (1977).
15. G. Wedler, K. P. Geuss, K. G. Colb, and G. McElhiney, *Appl. Surf. Sci.* **1**, 471 (1978).
16. J. P. Muscat, *Surf. Sci.* **110**, 389 (1981); **118**, 321 (1982).
17. R. Imbihl, R. J. Behm, K. Christmann, G. Ertl, and T. Matsushima, *Surf. Sci.* **117**, 257 (1982).
18. a. W. Kinzel, W. Selke, and K. Binder, *Surf. Sci.* **121**, 13 (1982). b. W. Selke, W. Kinzel, and K. Binder, *Surf. Sci.* **125**, 74 (1983).
19. W. Moritz, R. Imbihl, R. J. Behm, G. Ertl, and T. Matsushima, *J. Chem. Phys.* **83**, 1959 (1985).
20. a. E. Shustorovich, *Surf. Sci. Rep.* **6**, 1 (1986). b. P. Nordlander, S. Holloway, and J. K. Nørskov, *Surf. Sci.* **136**, 59 (1984).
21. A. M. Baro and W. Erley, *Surf. Sci.* **112**, L759 (1981).
22. a. G. Ertl, S. B. Lee, and M. Weiss, *Surf. Sci.* **111**, L711 (1981). b. J. Benzinger and R. J. Madix, *Surf. Sci.* **94**, 119 (1980).
23. M. Grunze, M. Golze, J. Fuhler, M. Neumann, and E. Schwarz, Proc. 8th Int. Cong. on Catalysis, p. IV-133, Verlag Chemie, Weinheim (1984).
24. M. Grunze, G. Strasser, and M. Golze, *Appl. Phys.* **A44**, 19 (1987).
25. M. Grunze, M. Golze, W. Hirschwald, H. J. Freund, H. Pulm, U. Seip, M. C. Tsai, G. Ertl, and J. Küppers, *Phys. Rev. Lett.* **53**, 850 (1984).

26. L. J. Whitman, C. E. Bartosch, W. Ho, G. Strasser, and M. Grunze, *Phys. Rev. Lett.* **56**, 1984 (1986).
27. D. Tomanek and K. H. Bennemann, *Phys. Rev.* **B31**, 2488 (1985).
28. H. J. Freund, B. Bartos, R. P. Messmer, M. Grunze, H. Kuhlenbeck, and M. Neumann, *Surf. Sci.* **185**, 187 (1987).
29. G. Ertl, S. B. Lee, and M. Weiss, *Surf. Sci.* **114**, 515 (1982).
30. M. C. Tsai, U. Seip, I. C. Bassignana, J. Küppers, and G. Ertl, *Surf. Sci.* **155**, 387 (1985).
31. G. Wedler, D. Borgmann, and K. P. Geuss, *Surf. Sci.* **47**, 592 (1975).
32. F. Boszo, G. Ertl, M. Grunze, and M. Weiss, *J. Catal.* **49**, 18 (1977).
33. F. Boszo, G. Ertl and M. Weiss, *J. Catal.* **50**, 519 (1977).
34. R. Imbihl, R. J. Behm, G. Ertl, and W. Mortiz, *Surf. Sci.* **123**, 129 (1982).
35. P. A. Dowben, M. Grunze, and R. G. Jones, *Surf. Sci.* **109**, L519 (1981).
36. P. H. Emmett and S. Brunauer, *J. Am. Chem. Soc.* **56**, 35 (1934).
37. J. J. Scholten, P. Zwietering, J. A. Konvalinka, and J. H. de Boer, *Trans. Faraday Soc.* **55**, 2166 (1959).
38. J. Böheim, W. Brenig, T. Engel, and U. Leuthäusser, *Surf. Sci.* **131**, 258 (1983).
39. L. J. Whitman, C. E. Bartosch, and W. Ho, *J. Chem. Phys.* **85**, 3688 (1986).
40. C. T. Rettner and H. Stein, *Phys. Rev. Lett.* **59**, 2768 (1987).
41. G. Haase, M. Asscher, and R. Kosloff, *J. Chem. Phys.* **90**, 3346 (1989).
42. G. Ertl, M. Weiss, and S. B. Lee, *Chem. Phys. Lett.* **60**, 391 (1979).
43. G. Ertl, S. B. Lee, and M. Weiss, *Surf. Sci.* **114**, 527 (1982).
44. a. S. Holloway, B. I. Lundqvist, and J. K. Nørskov, Proc. 8th Int. Cong. on Catalysis, p. IV-85, Verlag Chemie, Weinheim. b. J. K. Nørskov, S. Holloway, and N. D. Lang, *Surf. Sci.* **137**, 65 (1984). c. N. D. Lang, S. Holloway, and J. K. Nørskov, *Surf. Sci.* **150**, 24 (1985).
45. M. Grunze, F. Bozso, G. Ertl, and M. Weiss, *Appl. Surf. Sci.* **1**, 241 (1978).
46. M. Weiss, G. Ertl, and F. Nitschke, *Appl. Surf. Sci.* **2**, 614 (1979).
47. W. Erley and H. Ibach, *J. Electron Spectrosc.* **31**, 61 (1983); *Surf. Sci.* **119**, L357 (1982).
48. a. K. Hermann, Proc. 4th Int. Conf. on Solid Surfaces, p. 196, Suppl. Le Vide, Cannes (1980). b. H. Itoh, G. Ertl, and A. B. Kunz, *Z. Naturforsch.* **36a**, 347 (1981).
49. M. Grunze, *Surf. Sci.* **81**, 217 (1979).
50. I. C. Bassignana, K. Wagemann, J. Küppers, and G. Ertl, *Surf. Sci.* **175**, 22 (1986).
51. K. Yoshida and G. A. Somorjai, *Surf. Sci.* **75**, 46 (1978).
52. W. Reimer, Diploma thesis, Univ. München (1986).
53. M. Drechsler, H. Hoinkes, H. Kaarmann, H. Wilsch, G. Ertl, and M. Weiss, *Appl. Surf. Sci.* **3**, 217 (1979).
54. D. G. Löffler and L. D. Schmidt, *J. Catal.* **44**, 244 (1976).
55. G. Ertl and M. Huber, *J. Catal.* **61**, 537 (1980).
56. G. Ertl, M. Huber, and N. Thiele, *Z. Naturforsch.* **34a**, 30 (1979).
57. M. Boudart, *Catal. Rev. Sci. Eng.* **23**, 1 (1981).
58. M. I. Temkin and V. Pyzhev, *Acta Physicochim. USSR* **12**, 489 (1940).
59. M. Boudart and G. Djéga-Mariadassou, *Kinetics of Heterogeneous Catalytic Reactions.* Princeton University Press, Princeton, N.J. (1984) provides a detailed discussion of the Temkin formalism.
60. M. Boudart, *Ind. Chim. Belge* **19**, 489 (1954).
61. M. Boudart, *Catal. Lett.* **1**, 21 (1988).
62. M. Bowker, I. Parker, and K. Waugh, *Appl. Catal.* **14**, 101 (1985).
63. M. Bowker, I. Parker, and K. Waugh, *Surf. Sci.* **97**, L223 (1988).
64. P. Stoltze and J. K. Nørskov, *Phys. Rev. Lett.* **55**, 2502 (1985); *Surf. Sci.* **189/190**, 91 (1987); *Surf. Sci.* **197**, L230 (1988); *J. Catal.* **110**, 1 (1988).
65. P. Stoltze, *Phys. Scr.* **36**, 824 (1987).
66. J. R. Anderson and M. Boudart (eds.), *Catalysis, Science and Technology*, Vol. 4, p. VIII, Springer-Verlag, Berlin (1983).
67. R. Schloegl, R. C. Schoonmaker, M. Muhler, and G. Ertl, *Catal. Lett.* **1**, 237 (1988).
68. J. A. Dumesic and A. A. Trevino, *J. Catal.* **116**, 119 (1989).

4

A SURFACE SCIENCE AND CATALYTIC STUDY OF THE EFFECTS OF ALUMINUM OXIDE AND POTASSIUM ON THE AMMONIA SYNTHESIS OVER IRON SINGLE-CRYSTAL SURFACES

D. R. Strongin and G. A. Somorjai

4.1. INTRODUCTION

The status of present-day ammonia synthesis is the product of research spanning almost a century. Much of the effort has been directed toward elucidating the mechanism of the promoter effects of potassium and aluminum oxide on the rate of ammonia synthesis. Out of this work has evolved a multitude of techniques, concepts, and ideas which have profoundly affected catalytic chemistry. Many reviews have been written on this subject,[1-3] but it becomes evident from them that an understanding at the molecular level of the promoters is still lacking. A principal reason for this deficiency is that the bulk of this early work could only use indirect methods to study the catalyst. For example, a large amount of kinetic data relating the gas phase ammonia concentration to the surface concentration of promoters has been obtained.[4,5] This type of information is important for optimizing the concentration of promoters but it fails to reveal the effects at the atomic level of the promoters within the working catalyst. With the advent of combined surface-science/high-pressure systems, high-pressure reaction data (>1

D. R. Strongin and G. A. Somorjai • Department of Chemistry, University of California-Berkeley, and Center for Advanced Materials, Lawrence Berkeley Laboratory, Berkeley, California 94720. *Present address of D. R. Strongin*: Department of Chemistry, State University of New York at Stony Brook, Stony Brook, New York 11794.

atmosphere) can now be correlated to the structure of the catalyst surface at the atomic level, which is determined in the ultrahigh vacuum environment ($<10^{-8}$ torr). The combination of surface science and high-pressure catalysis provides powerful tools in the study of the reactivity and structure of surfaces. This chapter will be devoted to describing how surface science work, combined with high-pressure data, has elucidated the structure sensitivity and the role of potassium and aluminum oxide in ammonia synthesis. The structure sensitivity of ammonia synthesis will be presented first, since it serves as necessary background when explaining potassium and aluminum oxide promotion in ammonia synthesis.

Composition of the Industrial Catalyst

Since the realization of ammonia synthesis on the industrial scale in 1916 there have been no fundamental changes in the composition of the iron synthesis catalyst.[2,6] Essentially, potassium carbonate, aluminum oxide, and small amounts of other promoters are fused with magnetite, followed by reduction in situ as described fully in Chapter 2.

The reduction procedure involves treating the catalyst in the oxide state with a stoichiometric mixture of nitrogen and hydrogen.[1,7] The temperature and extent to which this is carried out is dependent on the concentration of potassium, aluminum oxide, and particularly calcium oxide in the catalyst formation. About 1% to 3% of K_2O and Al_2O_3 are usually used and, following reduction, somewhere between 40% and 60% of the iron surface is covered by the promoters.[7-10] Previous work has determined that the presence of aluminum in the catalyst results in an increase of the surface area of the catalyst on reduction, from a value of 1 m^2 per g cat for unpromoted iron to 20 m^2 per g cat[2] (so-called structural promotion). The presence of potassium decreases the surface area to about 10 m^2 per g cat, but the overall activity of the catalyst increased by a factor between three and six (so-called electronic promotion).[2]

4.2. EXPERIMENTAL

4.2.1. The Need for a Model System

It is apparent that the reduced ammonia synthesis catalyst is a complex mixture of iron, potassium, aluminum, and oxygen, and that the promotion by alumina and potash comes through complex interactions with the active iron component.[7] If a complex system such as this is to be understood, it is advisable to simplify the interactions and study each one separately in model systems. In this case iron single crystals prepared and characterized under UHV conditions were used to model the active component of the industrial catalyst. By adding potassium, aluminum, and oxygen quantitatively to the single-crystal surface in UHV and then carrying out high-pressure ammonia synthesis (20 atm of nitrogen and hydrogen), direct correlation can be made between reactivity and surface structure of the catalyst.

4.2.2. Preparation and Characterization of Well-Defined Single-Crystal Surfaces in Ultrahigh Vacuum

The single-crystal samples used in this work typically have an area of about 1 cm^2 with a thickness of 1 mm. They are polished on both sides by standard metallurgical techniques to provide a surface smooth on the micron scale. The crystal can be heated resistively and the temperature of the sample is measured by a chromel-alumel thermocouple which is spot-welded to the crystal edge. In the case of iron crystals, bulk impurities such as sulfur and carbon are common, and before the sample is mounted in the UHV equipment, the crystal must be heated to about 873 K in a hydrogen furnace to help deplete the bulk of the sulfur. The cleaning procedure is continued in UHV where a combination of argon ion sputtering and chemical treatment is used.

Sputtering the iron at 873 K for a prolonged period of time removes the sulfur, but treatment of the sample in about 1×10^{-7} torr of oxygen at 673 K is needed to rid the sample of carbon. The iron surface is considered clean if Auger electron spectroscopy (AES) shows no impurities and if a low-energy electron diffraction pattern (LEED) is obtained which is representative of the bulk crystal orientation.

Aluminum can be evaporated onto the iron crystal surface by heating a ceramic crucible containing aluminum wire which can subsequently be oxidized on the iron surface by leaking about 1×10^{-8} torr of water vapor into the UHV chamber. Oxidation of the aluminum is confirmed by the shift of the 67 eV LVV Auger transition, representative of elemental aluminum, to 54 eV characteristic of the oxide.[11] The extent of the coverage of aluminum oxide on the iron surface is determined by titrating the surface with carbon monoxide, since at room temperature carbon monoxide chemisorbs on metallic iron but not on aluminum oxide.[2,12] By adsorbing and desorbing carbon monoxide from both clean iron and Al_xO_y/Fe surfaces, the relative amount of free iron can be calculated (aluminum oxide is denoted by Al_xO_y because of uncertainty in the aluminum and oxygen stoichiometry). The Auger spectrum can then be calibrated using this data so that coverages of aluminum oxide can be alternatively determined by AES. In such work, one monolayer is defined as the point at which carbon monoxide can no longer adsorb to the surface. Thus, one monolayer might correspond to more than one atomic layer since aluminum oxide grows in three-dimensional islands on the iron surface.[13] The deposition of potassium is accomplished by using a SAES getter source. Coverages of potassium are determined by a potassium uptake curve.

4.2.3. Combined UHV/High-Pressure Apparatus

After the sample has been prepared and characterized in UHV it must be transferred to a different environment if ammonia synthesis is to be studied, since the rate of amonia production from its elements would be negligible in UHV. Having a UHV chamber equipped with a high-pressure cell[14] provides the necessary environment while avoiding exposure of the sample to the ambient atmosphere. The interior of the UHV chamber is shown in Fig. 4.1. The high-pressure cell is shown in the open position in the center of the chamber. An iron

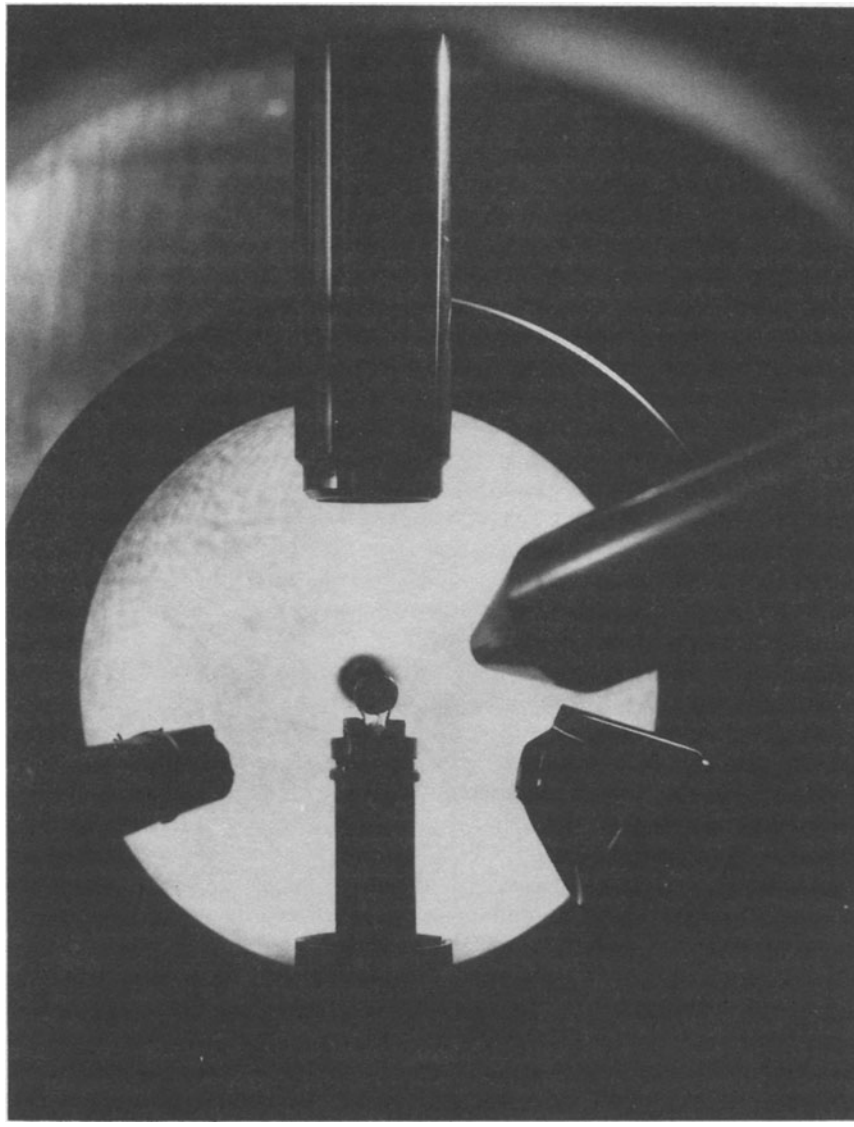

Figure 4.1. The interior of the combined/UHV chamber.

single-crystal sample is shown in the center supported on two copper feedthroughs, which allow the iron sample to be resistively heated. The retarding field analyzer is shown in the background and it allows low-energy electron diffraction and Auger electron spectroscopy to be performed. The aluminum source is in the lower left corner of the chamber and the potassium source is shown in the lower right corner. A typical experiment would proceed as follows. The sample is cleaned and potassium and aluminum oxide are added in the desired concentrations to the

iron surface. The single crystal is enclosed in a high-pressure cell which constitutes part of a microbatch reactor, isolating the sample from the UHV environment. High pressures of gases (15 atm of hydrogen and 5 atm of nitrogen) are introduced and the sample is resistively heated to reaction temperature (673 K unless otherwise noted). Ammonia production is monitored by periodically taking samples from the reaction loop and passing them through a photoionization detector with a 10.2 eV lamp. This photon energy ionizes ammonia but not nitrogen and hydrogen. Thus the PID signal is only proportional to the ammonia partial pressure in the loop. By taking these samples at known times, rates of ammonia synthesis are determined. After the reaction is completed, the reaction loop is evacuated and the cell opened, returning the sample to the UHV environment where surface characterization is performed by AES, LEED, and temperature-programmed desorption (TPD).

4.3. STRUCTURE SENSITIVITY OF THE AMMONIA SYNTHESIS

Since single crystals have a surface with a well-defined geometry, the structure sensitivity of a chemical reaction can be probed directly. This approach has proved effective in many systems[15] where it has been found that surface geometries influence catalytic reactions. This is best exemplified in ammonia synthesis where differences of up to two orders of magnitude are found between different crystallographic planes.[16] The rates of ammonia synthesis are shown over five iron crystal orientations in Fig. 4.2. The Fe(111) and Fe(211) surfaces are by far the most active in ammonia synthesis, and they are followed in reactivity by Fe(100), Fe(210), and Fe(110).[17] Schematic representations of the idealized unit cells for these surfaces, shown in Fig. 4.3, suggest two possible reasons for the high activity of the (111) and (211) faces compared to the (210), (100), and (110) orientations: surface roughness or active sites.

The (111) surface can be considered a rough surface, since it exposes second- and third-layer atoms to reactant gases in contrast to the (110) surface which only exposes first-layer atoms. Work functions are related to the roughness of a surface[18] and it is useful to quantify the corrugation of a plane in this way. The work functions of all the iron faces are not currently available but they are for tungsten,[19] another bcc metal which also shows structure sensitivity for ammonia decomposition.[20] The order of decreasing work function (ϕ) is as follows: $\phi_{110} > \phi_{211} > \phi_{100} > \phi_{111} > \phi_{210}$. Open faces, like the (111) surface, have lower work functions than close-packed faces such as the (110) surface. The significance of this for ammonia synthesis might be that the dissociation of nitrogen (the rate-limiting step[21,22]) proceeds faster on a surface with a low work function. This is supported by theory,[21] which calls for transfer of electronic charge from the *d*-band of iron into the $2\pi^*$ antibonding orbitals of nitrogen for dissociation, a process which might be aided by a low work function.

The second possible explanation for the structure sensitivity involves the nature of the active sites. The (111) and (211) faces of iron are the only surfaces which expose C_7 sites (iron atoms with seven nearest neighbors) to the reactant

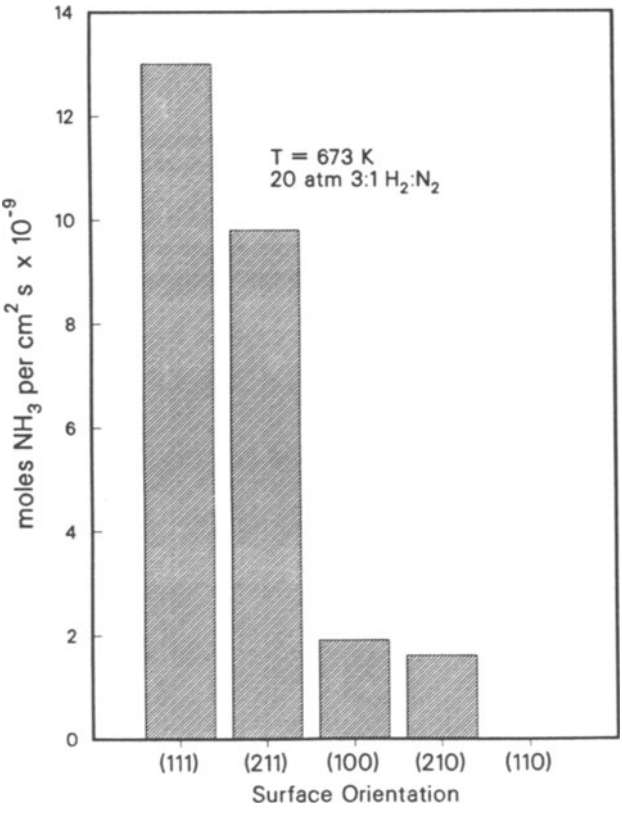

Figure 4.2. The rate of ammonia synthesis over the five iron surfaces studied exhibiting the structure sensitivity of ammonia synthesis.[17]

gases. Theoretical work by Falicov *et al.*[23] has suggested that highly coordinated surface atoms would show increased catalytic activity due to low-energy charge fluctuations in the *d*-bands of highly coordinated surface atoms. Examination of the results suggest that the latter argument of active sites is the key to the structure sensitivity of ammonia synthesis over iron.

The reaction rates, in Fig. 4.2, show that the (211) face is almost as active as the (111) plane of iron, while Fe(210) is less active than Fe(100). The Fe(210) and Fe(111) faces are open faces which expose second- and third-layer atoms. The Fe(211) face is more close packed, but it exposes C_7 sites. If either surface roughness or a low work function were the important consideration for an active ammonia synthesis catalyst, then the Fe(210) would be expected to be the most active face. However, in marked contrast, Fe(111) and Fe(211) faces are much more active, indicating that the presence of C_7 sites is more important than surface roughness in an ammonia synthesis catalyst.

The idea of C_7 sites being the most active site in ammonia synthesis on iron has been suggested in the past. Dumesic *et al.*[24] found that the turnover number

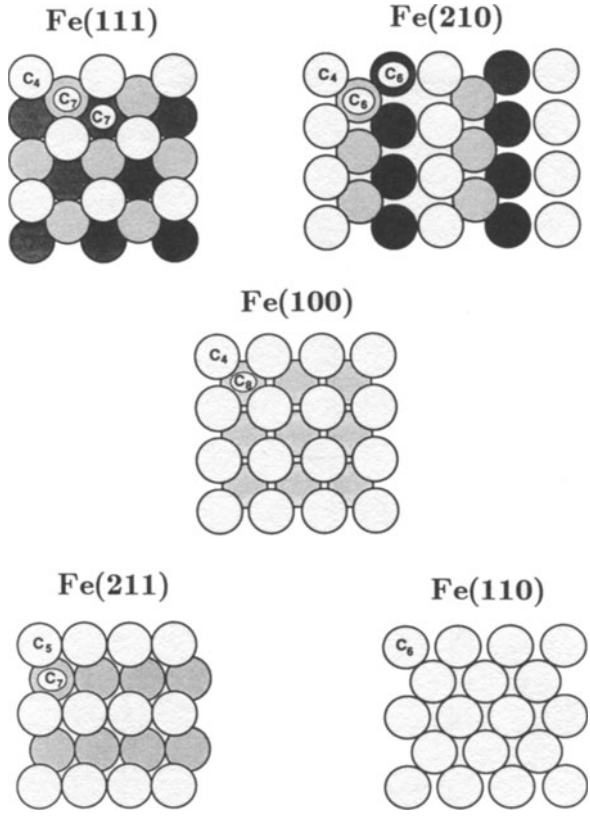

Figure 4.3. Schematic representations of the (111), (210), (100), (211), and (110) orientations of iron.[17] The coordination for each surface atom is indicated.

for ammonia synthesis was lower on small iron particles than larger ones. Pretreatment of an Fe/MgO catalyst with ammonia enhanced the turnover number over small iron particles, but did not affect the larger particles. This result was explained by noting that the concentration of C_7 sites would be expected to be higher on the smaller iron particles and that restructuring induced by ammonia enhanced the number of these sites on the catalyst. This was supported by the fact that the restructured catalyst chemisorbed 10% less carbon monoxide than the unrestructured catalyst. Highly coordinated sites, such as C_7, would chemisorb less carbon monoxide than less coordinated sites because of steric considerations. Thus, it was concluded that C_7 sites are the most active iron atoms for ammonia synthesis.

Additional research, which supports the contention that highly coordinated surface sites are most active for ammonia synthesis, has been carried out on rhenium.[25] In this study the rate of ammonia synthesis over the (0001), (10$\bar{1}$0), (11$\bar{2}$0), and (11$\bar{2}$1) faces were determined (Fig. 4.4). Here, as in the case of iron the face with the highest activity, the (11$\bar{2}$1) plane, is the surface which exposes the most highly coordinated sites. It is also shown in Fig. 4.4 that the (11$\bar{2}$1) face

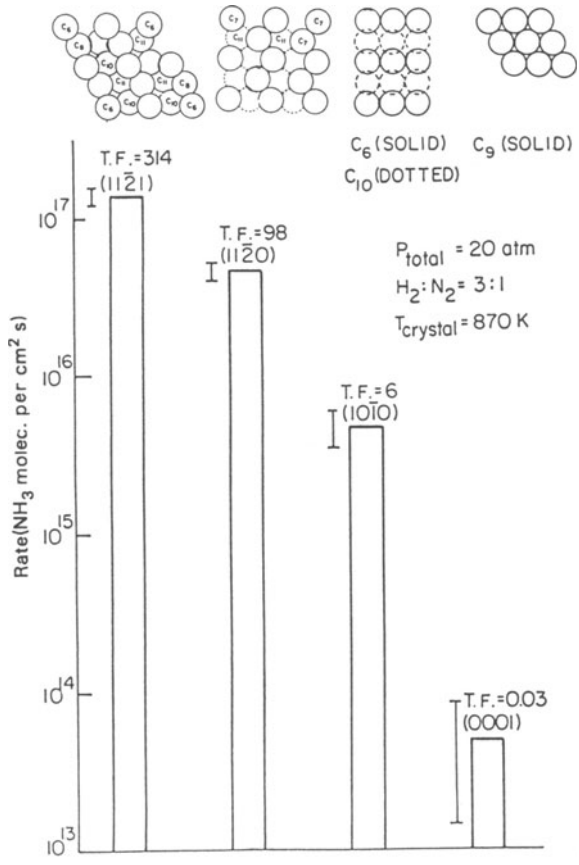

Figure 4.4. The structure sensitivity of ammonia synthesis over rhenium single-crystal surfaces.[25] Schematics of the atomic structure of each surface is given above each bar.

exposes C_{11} and C_{10} sites while the next active (11$\bar{2}$0) face exposes C_{11} and C_7 sites. This work, taken along with the work on the iron crystal faces, supports the contention that highly coordinated sites are those which are most active for ammonia synthesis and that surface roughness is only important to the extent that it can expose these active surface atoms to the gas-phase nitrogen and hydrogen.

4.4. SURFACE-SCIENCE STUDIES OF K/Fe, K/N_2/Fe, AND K/NH_3/Fe SYSTEMS

In this section a large amount of work which has been performed outside the Lawrence Berkeley Laboratory (except for Section 4.4.4) is summarized. The structure and bonding strength of potassium will be discussed along with the effect of potassium on the dissociative chemisorption of nitrogen on iron single-crystal surfaces.

4.4.1. The Structure of Potassium on Iron Single-Crystal Surfaces

The structure of potassium overlayers on well-defined single-crystal surfaces[26,27] has been investigated. Potassium does not show ordered structures on the (100) face of iron at any level of surface coverage. Ordered overlayers have, however, been observed for potassium adsorbed on Fe(110) and Fe(111).

At a saturation coverage of potassium, a hexagonal close-packed ordered overlayer has been observed on the (110) face of iron. A lack of ordering by potassium is found at lower coverages and this is usually explained by noting that the mobility of the alkali metal on the iron surface is high. This allows only small ordered domains to exist which cannot be observed by LEED. At higher coverages lateral interactions between neighboring adsorbed potassium atoms result, and hence the potassium resides in the energetically favorable surface sites which consequently form an ordered structure.

In contrast, the (111) surface of iron exhibits an ordered potassium structure only at low potassium coverages where a (3×3) structure is observed. At higher coverages of potassium, the diffraction pattern corresponding to the (3×3) structure deteriorates and a (1×1) structure results, with a high background that indicates the presence of disordered potassium.

4.4.2. The Stability of Potassium on Iron in UHV

The strength of the interaction between iron and potassium has been studied by temperature-programmed desorption.[26,27] Potassium TPD spectra from the (111), (100), and (110) faces of iron show the same qualitative features. At low coverages of potassium ($\theta_K = 0.07$, where θ_K is equal to the number of potassium atoms divided by the number of surface Fe atoms), desorption occurs at temperatures greater than 800 K, but at higher coverages ($\theta_K = 0.8$) of potassium; the temperature for the maximum rate of desorption decreases to about 550 K (Fig. 4.5). This type of behavior is common for alkali metals deposited on the surface of transition metals. Reneutralization of the alkali metal begins to occur[28] as higher coverages of potassium are achieved, resulting in a lower iron-potassium interaction, and hence a reduction in the desorption energy. Using the Redhead analysis,[29] the desorption energies of potassium on the various iron crystal faces are as follows: Fe(110), 57 ± 2 kcal mol^{-1}; Fe(100), 54 ± 2 kcal mol^{-1}; Fe(111), 52 ± 2 kcal mol^{-1}. These values are obtained by extrapolating to zero coverage, so they are upper limits for the strength of the potassium–iron bond. Desorption energies will become lower at higher coverages of potassium, but the detailed data necessary to determine the potassium desorption energy as a function of coverage are not available.

Coadsorption of oxygen thermally stabilizes the potassium on the iron surface as exhibited in Fig. 4.6. These TPD spectra show that, for high coverages of potassium, the coadsorption of oxygen results in an appreciable increase in the desorption temperature. For a potassium adlayer without oxygen, the maximum desorption rate occurs at 550 K and all the potassium desorbs by 900 K. By contrast, when oxygen is present, the temperature for the maximum rate of desorption is

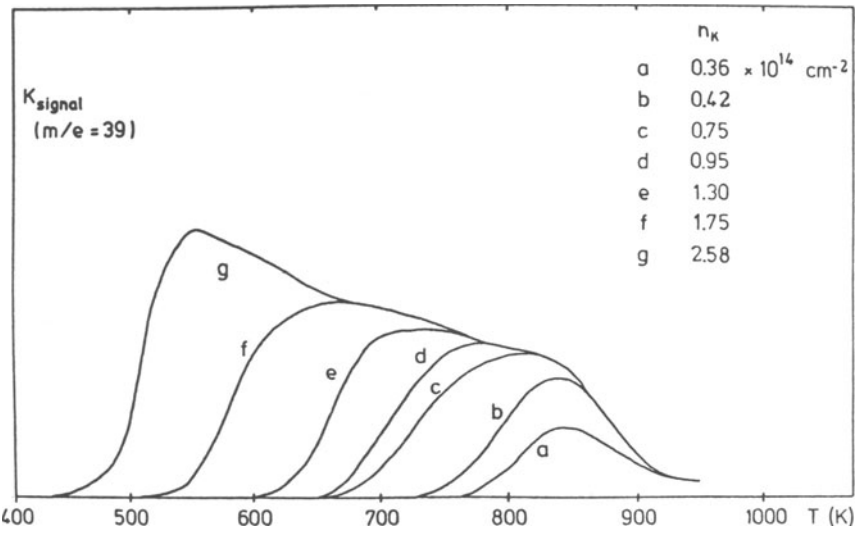

Figure 4.5. TPD spectra[33] for potassium adsorbed on a polycrystalline Fe surface suggest that potassium will not be stable under stationary ammonia synthesis conditions (T = 673 K).

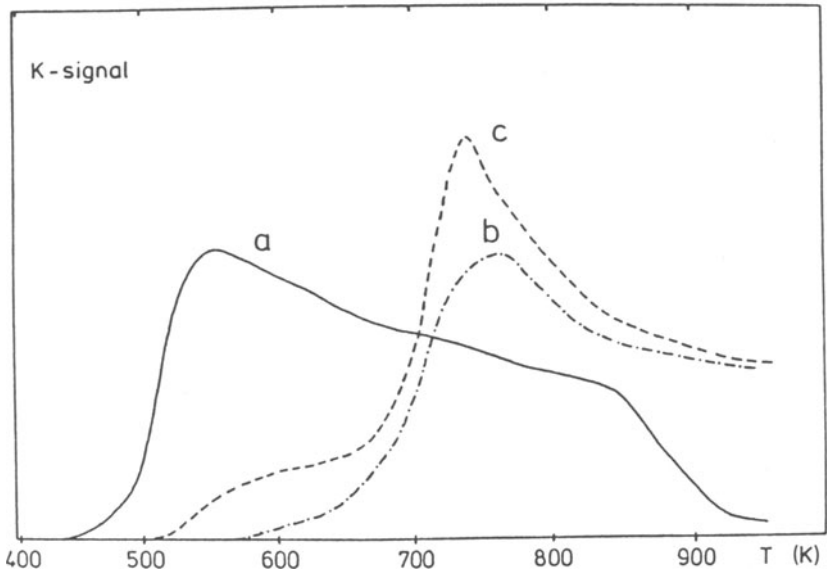

Figure 4.6. The presence of oxygen thermally stabilizes potassium[33]: (a) $n_K = 2.45 \times 10^{14}$ cm^{-2}; (b) $n_K = 2.06 \times 10^{14}$ cm^{-2}, $Y_0 = 0.90$ (O adsorbed first); (c) $n_K = 2.61 \times 10^{14}$ cm^{-2}, $Y_0 = 0.62$ (K adsorbed first). Y_0 is defined as the ratio between the oxygen Auger intensity and iron Auger intensity ($Y_0 = I_{O(510\,eV)} \diagdown I_{FE(650\,eV)}$).

increased to 750 K and, even at 1000 K, part of the potassium-oxygen adlayer remains thermally stable on the iron surface. It is also evident from Fig. 4.6 that the order of adsorption of potassium and oxygen does not significantly change the thermal stability of the adlayer at high coverages of both components. However, at lower coverages of potassium and oxygen, the order of adsorption of the additives does change the thermal stability of the layer. If oxygen is predosed ($Y_0 = 0.48$, Y_0 = Auger intensity of O 510 eV peak/Auger intensity of Fe 650 eV peak) on a polycrystalline iron followed by the addition of potassium ($n_K = 1.48 \times 10^{14}$ cm^{-2}), then the maximum rate of potassium desorption occurs at 750 K, while on a surface where potassium is added first ($n_K = 1.55 \times 10^{14}$ cm^{-2}), followed by oxygen addition ($Y_0 = 0.89$), the maximum rate of potassium desorption occurs at about 800 K. In addition, a much larger fraction of the potassium desorbs above 1000 K when potassium is present on the surface before the addition of oxygen.

The nature of the K + O adlayer is uncertain, but research[30] on Fe(110), using XPS and UPS, has shown that oxygen is directly bound to the iron surface. The interaction between the potassium and the oxygen, probably responsible for the thermal stability of the layer, was observed as a shift in the potassium 2*p* level in the XPS studies. These results suggest that the potassium and oxygen exist as an adlayer in which the potassium and oxygen are both chemisorbed directly to the iron surface or in a configuration where the potassium sits on top of an oxygen layer. The fact that the adlayer is more stable when potassium is adsorbed on the iron before the addition of oxygen is strong evidence for the former case. The formation of a bulk potassium compound, such as K_2O, is extremely unlikely since this compound is known to decompose at about 620 K. This decomposition temperature is well below 1000 K, where the potassium-oxygen layer is stable in the TPD experiments.

4.4.3. The Effect of Potassium on the Dissociative Chemisorption of Nitrogen on Iron Single-Crystal Surfaces in UHV

The rate-determining step in the ammonia synthesis reaction is widely accepted to be the dissociation of nitrogen.[3,5,21] Consequently the direct interaction between nitrogen and iron has been studied[31,32] together with the addition of submonolayer amounts of potassium.[21,33,34] All the work that will be referred to in this section was carried out in a UHV chamber, which therefore limits the pressure range to lie between 10^{-4} torr and 10^{-10} torr.

Using both iron single crystals and polycrystalline foils, the sticking probability of molecular nitrogen on iron was found to be of the order of 10^{-7}. This result reveals why, in addition to thermodynamic considerations, ammonia synthesis from the elements is favored at high reactant gas pressures. Since the sticking probability of dissociating nitrogen is so low on iron, higher pressures of nitrogen enhance the kinetics of the rate-limiting step in ammonia synthesis. The structure sensitivity of the reaction (see Section 4.3) is also revealed in the nitrogen chemisorption studies. It was found that the Fe(111) surface dissociatively chemisorbed nitrogen 20 times faster than the Fe(100) surface and 60 times faster than the Fe(110) surface. This agrees well with the structure sensitivity of ammonia

synthesis and adds more credence to dissociative chemisorption being the rate-limiting step. The addition of submonolayer amounts of elemental potassium has dramatic effects on the nitrogen chemisorption properties of the (110), (100), and (111) faces of iron.

The effect of potassium on the initial sticking coefficient (σ_0) of nitrogen on a Fe(100) surface is shown in Fig. 4.7. For clean Fe(100), $\sigma_0 = 1.4 \times 10^{-7}$, but with the addition of potassium σ_0 increases almost linearly, until a potassium concentration of 1.5×10^{14} K atoms per cm^2, where σ_0 maximizes at a value of 3.9×10^{-5}, a factor of 280 enhancement. Higher coverages of potassium start to decrease σ_0, presumably due to the blocking of iron sites by potassium which would otherwise dissociatively chemisorb nitrogen. The maximum increase in σ_0, due to potassium adsorption, on Fe(111) is about a factor of 8 ($\sigma_0 = 4 \times 10^{-5}$) at a potassium concentration of 2×10^{14} K atoms per cm^2 (Fig. 4.8). The potassium-induced enhancement of σ_0 on the Fe(110) surface is greater than that observed on either Fe(111) or Fe(100), so that the differences in activities for nitrogen dissociation seen on the clean surfaces is eliminated in the presence of potassium.

The mechanism by which potassium promotes nitrogen chemisorption is usually attributed to the lowering of the surface work function in the vicinity of a potassium ion. This effect is greatest at sufficiently low coverages (<0.15) where the potassium-iron bond has strong ionic character, so that the local ionization potential of the surface iron atoms is greatest. This allows for more electron density to be transferrred to the nitrogen $2\pi^*$ antibonding orbitals from the surface. This phenomenon increases the adsorption energy of molecular nitrogen and simultaneously lowers the activation energy for dissociation. For example, on the Fe(100) surface the addition of 1.5×10^{14} K atoms per cm^2 decreases the work function by about 1.8 eV and increases the rate of nitrogen dissociation by more than a factor

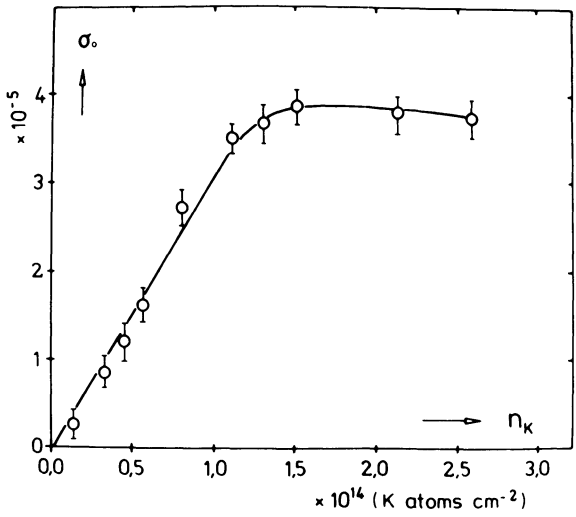

Figure 4.7. The variation in σ_0 with the addition of potassium[34] to Fe(100) at 430 K. σ_0 can be enhanced by a factor of 280 relative to clean Fe(100).

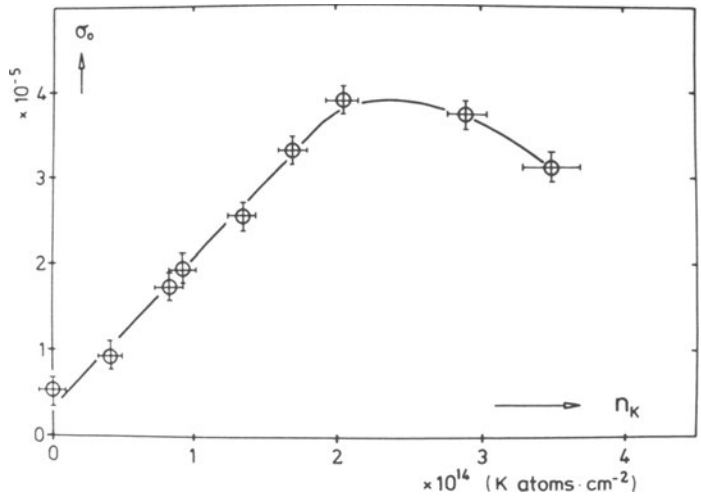

Figure 4.8. σ_0 as a function of potassium coverage on Fe(111) at 430 K.[34] σ_0 can be enhanced by a factor of 8 in the presence of potassium.

of 200. This enhancement in rate is accompanied by an increase in the adsorption energy of nitrogen on Fe(100) by 11.5 kcal mol^{-1}, which decreases the activation barrier for dissociation, in the presence of potassium, from 2.5 kcal mol^{-1} to about 0 kcal mol^{-1}.

The coadsorption of oxygen has been found to decrease the promotional effect of potassium on the rate of nitrogen dissociation over iron. It is shown in Fig. 4.9

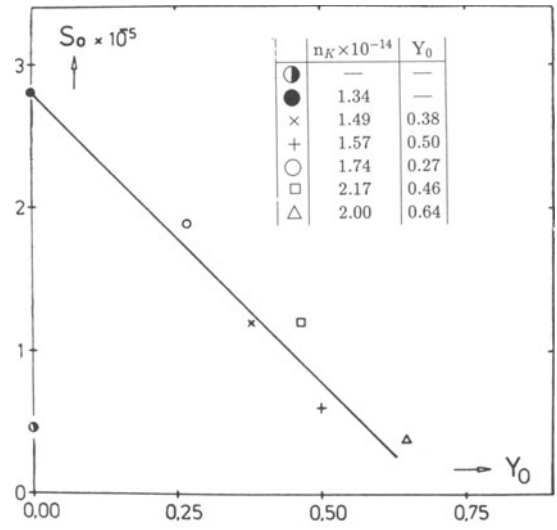

Figure 4.9. The effect of oxygen on σ_0 ($=S_0/10^5$) for a K/Fe(polycrystalline) surface.[33] The decrease in σ_0 is attributed to the physical blockage of surface sites by oxygen. Y_0 is defined as the ratio between the oxygen Auger intensity and iron Auger intensity ($Y_0 = I_{O(510\,eV)}/I_{Fe(650\,eV)}$).

that σ_0 decreases continuously with increasing oxygen coverage on a polycrystalline iron sample. The effect of the oxygen on nitrogen adsorption, in this study, is attributed to the physical blockage of the iron surface, since if σ_0 is normalized to the amount of iron surface which is accessible to nitrogen, then σ_0 remains fairly constant as oxygen coverages are increased. This result implies that the promoter effect of potassium is not significantly affected by the presence of oxygen. It is also strong evidence for an adlayer where both potassium and oxygen interact directly with the iron surface, since potassium sitting on top of oxygen would not be expected to exert the same promotion as potassium adsorbed alone.

4.4.4. Ammonia Temperature-Programmed Desorption Studies on K/Fe

The temperature-programmed desorption of ammonia from clean Fe(111) and K/Fe(111) is shown in Fig. 4.10.[35] Ammonia desorbs through a wide temperature range, resulting in a broad peak with a maximum rate of desorption occurring at around 300 K. With the addition of 0.1 ML of potassium, the peak maximum is reduced by about 40 K. Using the Redhead analysis[29] and assuming first-order desorption for ammonia, the 40 K decrease corresponds to a 2.4 kcal mol^{-1} drop in the adsorption energy of ammonia on iron in the presence of 0.1 ML potassium. The peak maximum continuously shifts to lower temperature with increasing amounts of coadsorbed potassium. At a coverage of 0.25 ML a new desorption peak appears at about 189 K. Increasing coverages of potassium now increase the intensity of the new peak (it also shifts to lower temperatures) and decreases the intensity of the original ammonia desorption peak. At a potassium coverage of about 1.0 ML, only a weakly bound ammonia species is present with a maximum rate of desorption occurring at 164 K. This observation of ammonia adsorption energy decreasing with the coadsorption of potassium on iron is similar to what is found for ammonia desorption from nickel and ruthenium with adsorbed sodium.[36,37]

4.4.5. Summary of Surface-Science Results

Many conjectures on the chemical state and role of potassium in ammonia synthesis can be made from the surface-science results. The potassium TPD results show clearly that elemental potassium will not be stable at the temperatures necessary to perform the synthesis of ammonia. The industrial reaction is usually run between 673 K and 748 K and the TPD results show that elemental potassium would rapidly desorb at these temperatures. However, with the coadsorption of oxygen, potassium can be thermally stabilized, and it desorbs at temperatures greater than 1000 K. Bulk potassium compounds such as K_2O or KOH would not be stable under ammonia synthesis conditions.[38] This suggests that the formation of potassium ferrites in the industrial catalyst results in a chemisorbed potassium and oxygen adlayer, stable under industrial ammonia synthesis conditions.

The (111) face of iron has been shown to chemisorb nitrogen dissociatively 20 times faster than Fe(100) and 60 times faster than Fe(110). The addition of

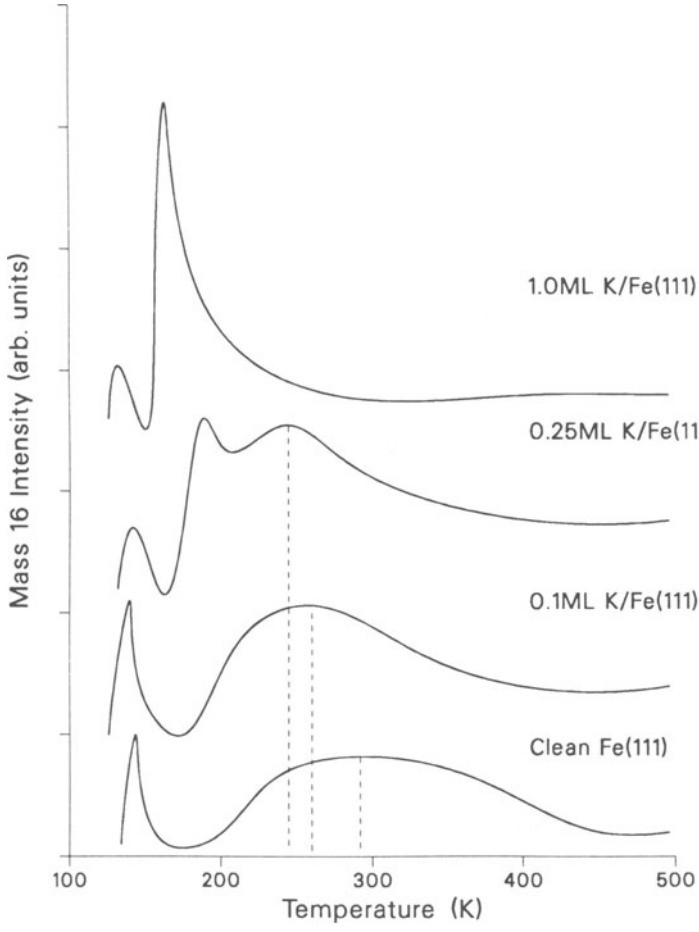

Figure 4.10. Ammonia temperature-programmed desorption from clean Fe(111) and K/Fe(111) surfaces.[35] The desorption temperature of ammonia from Fe(111) is lowered in the presence of potassium. Thus potassium lowers the adsorption energy of ammonia on the iron surface.

potassium increases the rate of nitrogen dissociation over Fe(100) and Fe(110) by more than an order of magnitude. The effect over Fe(111) is much less pronounced, so that the differences in activities, observed over the clean surfaces, is eliminated in the presence of potassium.

Although essential for the thermal stabilization of potassium, the presence of oxygen decreases the rate of nitrogen dissociation on iron because it physically blocks part of the iron surface. A rough inverse proportionality is observed between σ_0, the initial sticking coefficient of nitrogen on K/Fe, and the coverage of oxygen. The K + O adlayer is expected to promote ammonia synthesis by enhancing the rate-limiting step. The high-pressure studies presented next suggest that a more important promoter effect of potassium involves lowering the concentration of

adsorbed ammonia on the iron catalyst, thus making more sites available for the dissociation of nitrogen. This is supported by the ammonia TPD results, which show that potassium substantially decreases the adsorption energy of ammonia on iron. As shown earlier, even in the presence of only 0.1 ML of potassium, the adsorption energy of ammonia is reduced by 2.4 kcal mol^{-1}.

4.5. COMBINED SURFACE-SCIENCE AND CATALYTIC STUDY OF THE EFFECTS OF POTASSIUM ON THE AMMONIA SYNTHESIS REACTION

4.5.1. Effects of Potassium on Ammonia Synthesis Kinetics

Extensive research has been completed in which the effects of potassium on ammonia synthesis over iron single-crystal surfaces of (111), (100), and (110) orientations[35] have been determined. The apparent order of ammonia and hydrogen for ammonia synthesis over iron and K/Fe surfaces has been determined in addition to the effect of potassium on the apparent activation energy (E_a) for the reaction. In all the experiments which will be mentioned, potassium was coadsorbed with oxygen since, as shown before, elemental potassium is not stable and only about 0.15 ML of potassium coadsorbed with oxygen is stable under ammonia synthesis conditions (20 atm 3 to 1 H_2 to N_2 $T = 673$ K)[35,39,40]. It has been shown that the addition of 0.15 ML of potassium to Fe(111) and Fe(100) increases the ammonia partial dependence from -0.60 for the clean iron surfaces to -0.35 for the 0.15 ML K/Fe(111) and 0.15 ML K/Fe(100) surfaces under high-pressure ammonia synthesis conditions (Fig. 4.11). The apparent order in hydrogen has been found to decrease from 0.76 for clean Fe(111) to 0.44 for the 0.15 ML K/Fe(111) surface (Fig. 4.12). The Fe(110) is inactive for ammonia synthesis under these conditions with or without potassium. These changes in both the apparent order of hydrogen and ammonia occur while there is no change in the activation energy suggesting that potassium does not change the elementary steps of ammonia synthesis (Fig. 4.13). The data shows that the promotional effect of potassium is enhanced as the reaction conversion increases (i.e. increasing ammonia partial pressure).

These results are consistent with earlier literature[41] in which the effects of potassium on doubly promoted (aluminum oxide and potassium) catalysts were studied. It was shown that the turnover number for ammonia synthesis is roughly the same over singly (aluminum oxide) and double promoted iron when one atmosphere reactant pressure of nitrogen and hydrogen is used.[12] This implies that at low-pressure conditions, the gas-phase ammonia concentration is not high enough for potassium to exert a promoter effect. As higher reactant pressures are achieved (5–200 atm), the promoter effect of potassium becomes significant. It was found that doubly promoted catalysts became increasingly more active than catalysts without potassium when the concentration of ammonia in the gas phase increased.[41] This implies that potassium makes the apparent order in ammonia less negative over commercial catalysts, in agreement with the single-crystal work.

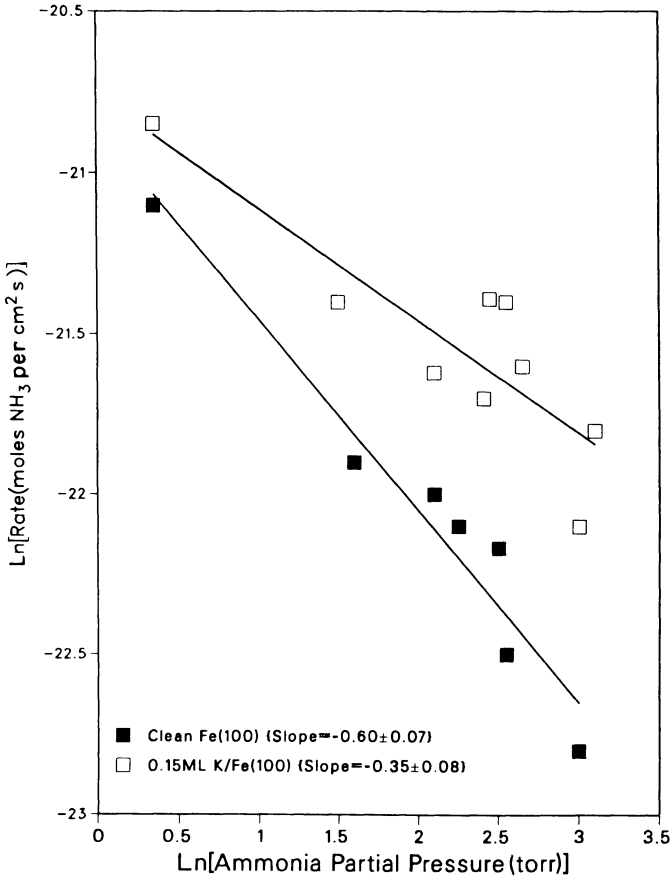

Figure 4.11. The apparent order in ammonia for ammonia synthesis over Fe(100) and K/Fe(100) surfaces.[35] The order in ammonia becomes less negative when potassium is present. The same values, within experimental error, are found for the Fe(111) and K/Fe(111) surfaces.

4.5.2. The Effects of Potassium on the Adsorption of Ammonia on Iron under Ammonia Synthesis Conditions

The changes in the apparent order of ammonia suggest that to elucidate the effects of potassium on both iron single crystals and the industrial catalyst, it is necessary to understand the readsorption of gas-phase ammonia on the catalyst surface during ammonia synthesis. The fact that the rate of ammonia synthesis is negative order in ammonia implies that the adsorption of gas-phase ammonia product decreases the rate of ammonia synthesis. Once adsorbed, the ammonia has a certain residence time (τ) on the catalyst which is determined by its adsorption energy (ΔH_{ad}) on iron [$\tau \propto e(\Delta H_{ad}/RT)$].[15] During this residence on the catalyst, ammonia can either diffuse on the surface or decompose to atomic nitrogen and hydrogen.[21,4,5] In both cases the species produced by ammonia might reside on

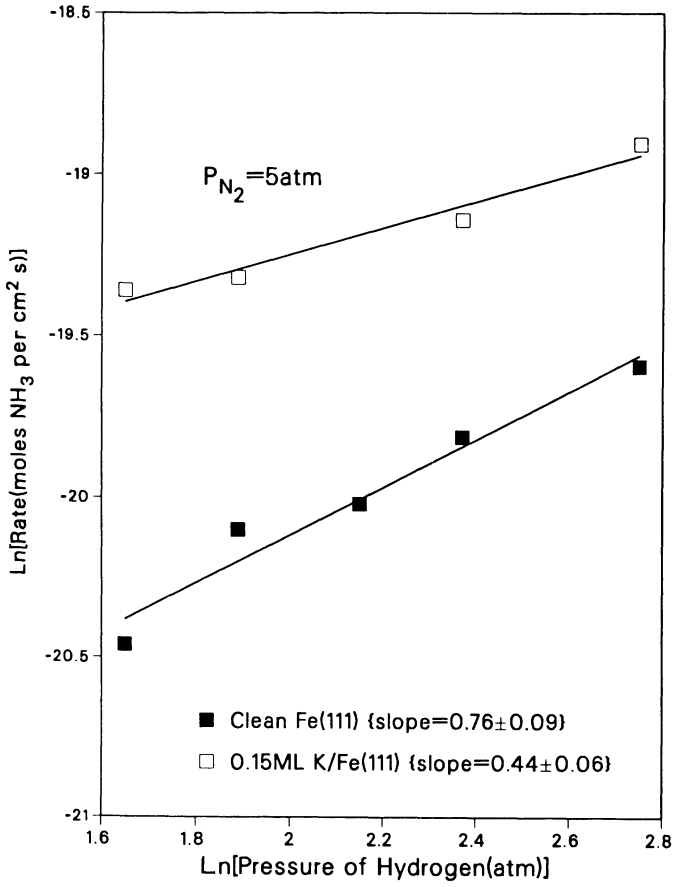

Figure 4.12. The apparent reaction order in hydrogen for ammonia synthesis over Fe(111) and K/Fe(111) surfaces.[35] The order in hydrogen decreases in the presence of potassium.

surface sites that would otherwise dissociatively chemisorb gas-phase nitrogen, and thus decreases the rate of ammonia synthesis.[2,4,5] The promoter effect of potassium then involves lowering the adsorption energy of the adsorbed ammonia so that the concentration of adsorbed ammonia is decreased. This is supported by the temperature programmed desorption results, which show that ammonia desorption from Fe(111) shifts to lower temperatures when potassium is adsorbed on the surface. Even at a 0.1 ML coverage of potassium (coverage roughly equivalent to that stable under ammonia synthesis conditions), the adsorption energy of ammonia is decreased by 2.4 kcal mol^{-1}. Thus, the residence time for the adsorbed ammonia is reduced and more of the active sites are available for the dissociation of nitrogen. At higher coverages of potassium, the adsorption energy of ammonia decreases to an even greater extent, but these coverages could not be maintained under ammonia synthesis conditions. There also seems to be an additional adsorption site for ammonia when adsorbed on iron at high coverages of potassium as indicated

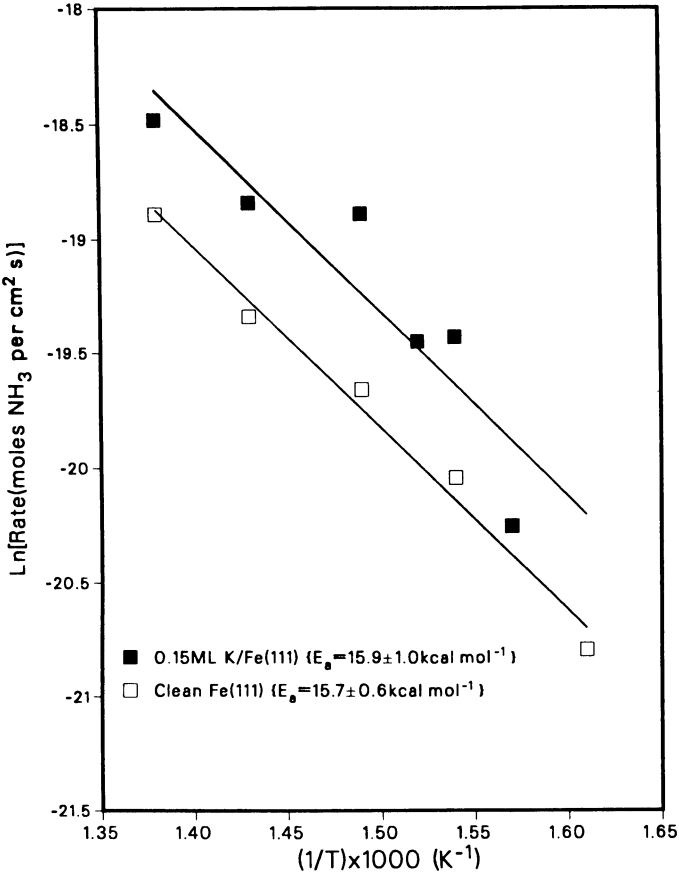

Figure 4.13. The activation energy (E_a) for Fe(111) and K/Fe(111).[35] Within experimental error there is no change in E_a, suggesting that potassium does not change the fundamental reaction steps of ammonia synthesis.

by the TPD results. The development of a new desorption peak with coverages of potassium greater than 0.25 ML might result from ammonia molecules interacting directly with potassium atoms, the negative end of the ammonia dipole interacting with the potassium ion on the iron surface.[36] This interaction appears to be weak, since at a potassium coverage of 1 ML, ammonia desorbs from the surface at 164 K.

Additional experimental evidence supporting the notion that ammonia blocks active sites comes from the post-reaction Auger data. Within experimental error, there is no change in the intensity of the nitrogen Auger peak between a Fe surface and a K/Fe surface after a high-pressure ammonia synthesis reaction. This suggests that potassium does not change the coverage of atomic nitrogen, but instead the presence of potassium helps to inhibit the readsorption or promote the desorption of molecular ammonia on the catalyst. High-pressure reaction conditions are probably needed to stabilize this ammonia product on the iron surface at 673 K,

so it will not be present in the ultrahigh vacuum environment. Thus, only the more strongly bound atomic nitrogen will be detected by AES in UHV.

4.5.3. Modeling the Kinetic Data with a Rate Equation

To model a catalytic reaction, some knowledge of the elementary reaction steps must be assumed. For ammonia synthesis it is usually accepted that the dissociative chemisorption of nitrogen is the rate-limiting step, a process which requires two adjacent open sites on the catalyst surface.[4,5] Using Langmuir-Hinshelwood kinetics the rate of ammonia synthesis (denoted by r) can be written as

$$r = k_1 P_{N_2} \theta_v^2 \tag{4.1}$$

where k_1 is the rate constant for nitrogen dissociative chemisorption and θ_v is the fraction of vacant sites on the surface. It is usually assumed that atomic nitrogen is the majority species on the surface, so that $\theta_v = 1 - \theta_N$ where θ_N is the fraction of surface covered by nitrogen atoms determined by the equilibrium (4.4);

$$N_{ad} + 1.5H_{2(g)} \overset{K_e}{=} NH_{3(g)} \tag{4.2}$$

where K_e is the equilibrium constant. Following the method of Langmuir, θ_N can be determined and substituted into equation (4.1) so that

$$r = \frac{k_1 P_{N_2}}{[1 + (K_e^{-1})(P_{NH_3}/P_{H_2}^{1.5})]^2} \tag{4.3}$$

However, the kinetic and surface science results suggest that adsorbed ammonia blocks catalytically active sites, in addition to atomic nitrogen. In this case $\theta_v = 1 - \theta_N - \theta_{NH_3}$ where θ_N and θ_{NH_3} are determined by the equilibria

$$N_{ad} + 1.5H_{2(g)} \overset{K_2}{=} NH_{3ad} \tag{4.4}$$

and

$$NH_{3ad} \overset{K_3}{=} NH_{3(g)} \tag{4.5}$$

where K_2 and K_3 are equilibrium constants (note $K_e = K_2 K_3$). Now the rate of ammonia synthesis is given by

$$r = \frac{k_1 P_{N_2} P_{H_2}^3}{[P_{H_2}^{1.5} + (P_{NH_3} K_3^{-1})(K_2^{-1} + P_{H_2}^{1.5})]^2} \tag{6}$$

The constants K_3 and K_2 can now be obtained by fitting equation (4.6) to the experimental data. For the clean surface, $K_3 = 0.19$ and $K_2 = 2.6 \times 10^{-3}$. When potassium is present, $K_3 = 0.37$ and $K_2 = 2.6 \times 10^{-3}$. This model, which accounts for adsorbed ammonia blocking active sites, suggests that the enhancement in ammonia synthesis rate seen over the K/Fe surfaces is due to an increase in the equilibrium constant K_3 or a shift in the equilibrium from adsorbed to gas-phase ammonia. The increase in K_3 might be due to the decreased adsorption energy of ammonia when potassium is present, as evidenced by the temperature-programmed desorption results. The decrease in the apparent order in hydrogen is also consistent with the increase in K_3 induced by potassium. Since the rate-limiting step in ammonia synthesis is the dissociation of nitrogen, the only role of hydrogen in the rate expression (4.6) is to create available sites for this step. In the presence of potassium, K_3 increases making more sites available as shown by the equilibria expressions (4.4) and (4.5). This is reflected in the lowering of the apparent order in hydrogen when potassium is added to the iron surface.

4.5.4. The Effect of Potassium on the Dissociation of Nitrogen under Ammonia Synthesis Conditions

The experimentally determined ratio of the rate over clean iron to the rate over K/Fe surfaces as a function of ammonia partial pressure is plotted in Fig. 4.14. The ratio continuously increases as more ammonia is present in the gas phase (i.e., the promoter effect of potassium is enhanced). If the only role of potassium was to keep ammonia off the catalyst surface, then in the limit of zero ammonia partial pressure, the ratio should be unity. Instead, the best fit of the model to the experimental data occurs when the ratio is 1.3 at zero ammonia partial pressure. This implies that potassium increases k_1 (the rate constant for dissociative nitrogen chemisorption) by 30% on both Fe(111) and Fe(100). If the preexponential factor for k_1 is assumed to be the same for clean iron and K/Fe surfaces, then a 30% increase in rate corresponds to a 0.35 kcal mol^{-1} decrease in the activation energy (E_a) for this step. This change in E_a is too small to be resolved in our experiments. A small change in E_a such as this might also explain work, which was carried out on the industrial catalyst, that found the activation energy for ammonia synthesis to be only slightly higher on singly promoted (aluminum oxide) iron than it was on doubly promoted (aluminum oxide and potassium oxide) catalysts.[42.12]

Enhancement of the rate-limiting step in high-pressure ammonia synthesis by potassium is predicted by the surface science research[43,33,27] presented earlier. It was found that elemental potassium on iron increased the rate of nitrogen chemisorption (k_1) by more than two orders of magnitude while the greatest enhancement in k_1 on Fe(111) was found to be a factor of eight.[7] The high-pressure ammonia synthesis results (20 atm reactant pressure and a catalyst temperature of 673 K),[35] carried out on iron single crystals of (110), (100), and (110) orientations, suggest that potassium causes only about a 30% increase in k_1 on Fe(111) and Fe(100). The Fe(110) surface was found to be inactive, with or without adsorbed potassium. Under the synthesis conditions used in these studies, oxygen is needed to stabilize the potassium with respect to thermal desorption. The presence of the

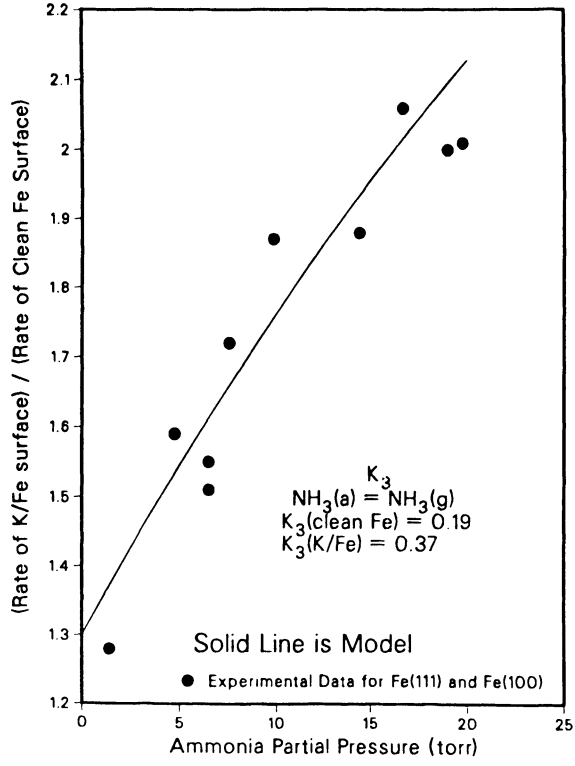

Figure 4.14. The experimental fit of reaction rates over Fe and K/Fe surfaces to a model which allows for the blocking of catalytic sites by adsorbed ammonia as well as atomic nitrogen.[35] In the presence of potassium K_3 is increased.

oxygen might account for the small effect of potassium on k_1 in the high-pressure studies since oxygen has been shown to decrease the promoter effect of potassium, at least in part, by blocking iron sites which are able to chemisorb nitrogen dissociatively.[33] A similar effect might be expected on the industrial catalyst, because it is well known that the potassium is in intimate contact with oxygen.[33,38]

4.6. COMBINED SURFACE-SCIENCE AND HIGH-PRESSURE STUDIES OF THE EFFECT OF ALUMINUM OXIDE ON THE AMMONIA SYNTHESIS REACTION

Most of the early work on aluminum oxide, in relation to ammonia synthesis, suggests that the role of aluminum oxide in the ammonia synthesis catalyst was simply to increase the surface area of the iron catalyst and to inhibit sintering which usually occurs with high surface area metallic particles.[2,44] This belief is supported by BET measurements, which showed that the surface of the industrial

ammonia synthesis catalyst increased tenfold when aluminum oxide was added in the preparation phase.[2] Other workers have asserted that aluminum oxide, in addition to increasing surface area, prevents the conversion of active planes, such as Fe(111), to less active surfaces [i.e., Fe(100) and Fe(110)] during ammonia synthesis,[2] but this, until recently, could not be shown owing to the lack of surface structure probes in this work. Recent surface-science and high-pressure results will now be presented that were obtained directly from an investigated iron–aluminum oxide system for ammonia synthesis over Fe(110), Fe(100), and Fe(111) model single-crystal catalysts.[13]

4.6.1. Effects of Aluminum Oxide in Restructuring Iron Single-Crystal Surfaces for Ammonia Synthesis

The initial rate of ammonia synthesis has been determined over the clean Fe(111), Fe(100), and Fe(110) surfaces with and without aluminum oxide. The addition of aluminum oxide to the (110), (100), and (111) faces of iron decreases the rate of ammonia synthesis in direct proportion to the amount of surface covered.[39] This suggests that the promoter effect of aluminum oxide involves intimate contact with the iron which cannot be achieved by simply depositing aluminum oxide on an iron catalyst.

Remembering that the industrial catalyst is prepared by fusion of 2% to 3% by weight of aluminum oxide and potassium with iron oxide (Fe_3O_4), experiments were performed in which Al_xO_y/Fe single-crystal surfaces were pretreated in an oxidizing environment prior to ammonia synthesis. These experiments were carried out by depositing about 2 ML of Al_xO_y on Fe(111), Fe(100), and Fe(110) surfaces and then treating them in varying amounts of water vapor at 723 K in order to oxidize the iron and to induce an interaction between iron oxide and aluminum oxide. After removal of the water vapor, high pressures of nitrogen and hydrogen were added to determine the rates of ammonia synthesis. The rate of ammonia synthesis over Al_xO_y/Fe surfaces pretreated with water vapor prior to ammonia synthesis is shown in Fig. 4.15. The initially inactive Al_xO_y/Fe(110) surface restructures and becomes as active as the Fe(100) surface after a 0.05 torr water-vapor treatment and as active as the Fe(111) surface after a 20 torr water-vapor pretreatment. This is about a 400-fold increase in the rate of ammonia synthesis compared with clean Fe(110).[16] The activity of the Al_xO_y/Fe(100) surface can also be enhanced to that of the highly active Fe(111) surface by utilizing a 20 torr water-vapor pretreatment and this high activity is maintained for over four hours as in the case for the restructured Al_xO_y/Fe(110). Little change in the activity of the Fe(111) surface is seen experimentally when it is treated in water vapor in the presence of Al_xO_y.

The activity of the Fe(110) and Fe(100) surfaces for ammonia synthesis can also be enhanced to the level of Fe(111) by water-vapor pretreatments in the absence of aluminum oxide, but in this circumstance the enhancement in activity is only transient. Figure 4.16 shows the rate of ammonia synthesis as a function of reaction time for restructured Fe(110) and Al_xO_y/Fe(110) surfaces. Both surfaces have an initial activity similar to the clean Fe(111) surface. The restructured

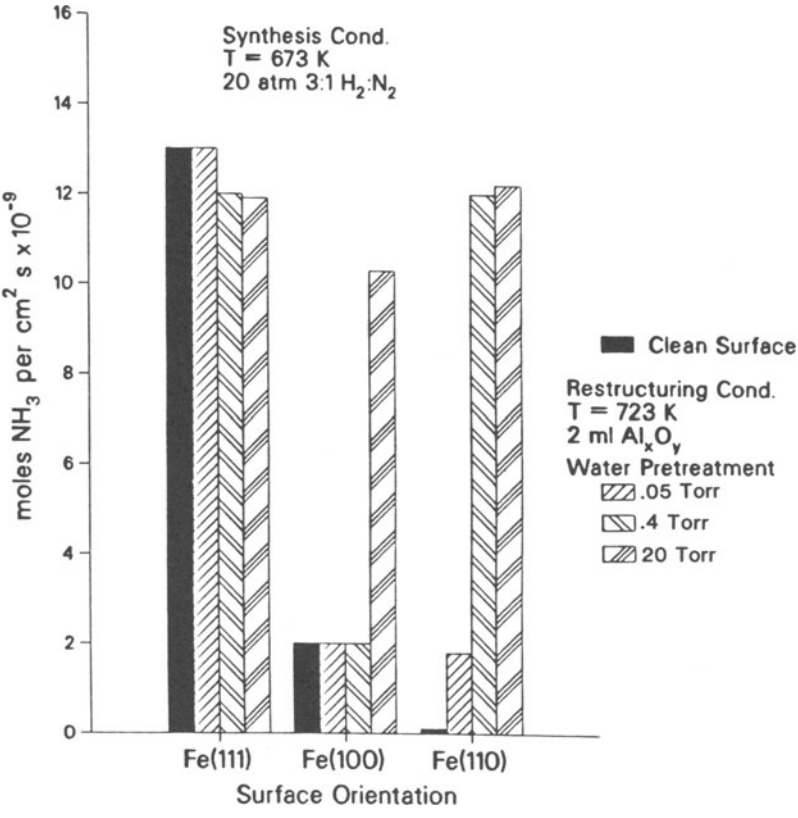

Figure 4.15. Rates of ammonia synthesis over clean iron single crystals and water-induced restructured Al_xO_y/Fe surfaces.[13] Restructuring conditions are given in the figure.

Al_xO_y/Fe(110) surface maintains this activity for over four hours while the restructured Fe(110) surface loses its activity for ammonia synthesis within one hour of reaction.

4.6.2. Characterization of the Restructured Surfaces

The observation that the Al_xO_y/Fe(110) and Al_xO_y/Fe(100) becomes as active as the Fe(111) surface for ammonia synthesis suggests that new crystal orientations are being created upon restructuring the Al_xO_y/Fe(110) and Al_xO_y/Fe(100) surfaces in water vapor. A suggested increase in the surface area cannot account for the enhancement in rate, since it has been shown that about 40% less carbon monoxide adsorbs on restructured Al_xO_y/Fe(110) and Al_xO_y/Fe(100) relative to the clean respective surfaces[13] (i.e., the iron surface area actually decreases).

Auger electron spectroscopy, low-energy electron diffraction, temperature-programmed desorption, and scanning electron microscopy (SEM) have been used

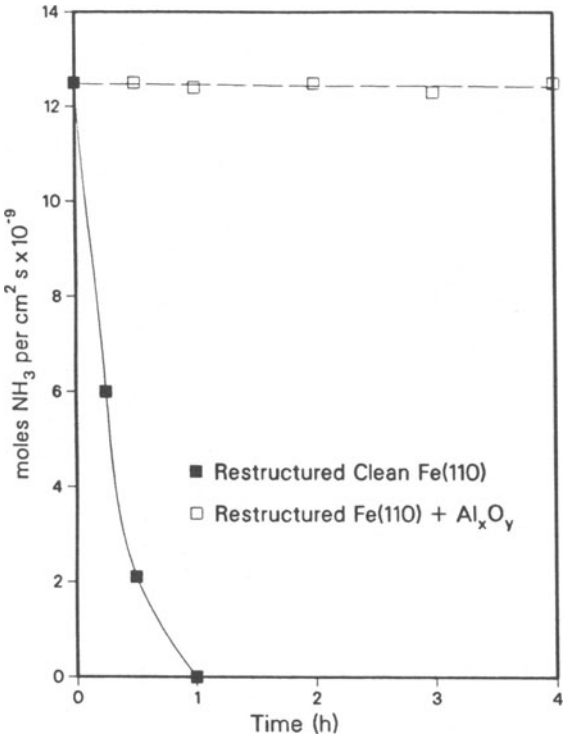

Figure 4.16. Deactivation of the restructured Fe(110) surface occurs within one hour while the restructured Al_xO_y/Fe(110) surface maintains its activity for more than four hours under ammonia synthesis conditions.[13]

to characterize the restructured surfaces. SEM micrographs for restructured Fe(110) and Al_xO_y/Fe(110) surfaces are shown in Figs. 4.17 and 4.18, respectively. The Al_xO_y/Fe(110) surface, restructured with 0.05 torr of water vapor (Fig. 4.17a), shows features about 1 μm across growing on the Fe(110) substrate [the clean Fe(100) surface is smooth and featureless]. After a 20 torr water-vapor pretreatment the surface seems to be completely restructured with features covering the whole surface (Fig. 4.17b). Auger electron spectroscopy finds that only about 5% of the iron surface is covered by aluminum oxide, and sputtering the surface with argon ions reveals aluminum oxide beneath the iron surface.

SEM micrographs of restructured Fe(110) shows none of the features associated with the restructured Al_xO_y/Fe(110) surface. Figure 4.18a shows a (110) surface which has been restructured with 20 torr of water vapor. No LEED pattern is obtainable from this surface. Its appearance is different than the restructured iron single crystals which had aluminum oxide present. None of the crystallite structures associated with the restructured Al_xO_y/Fe(110) surface are present. Figure 4.18b shows the restructured Fe(110) surface after one hour of ammonia synthesis. The features are now gone and the surface has no activity toward

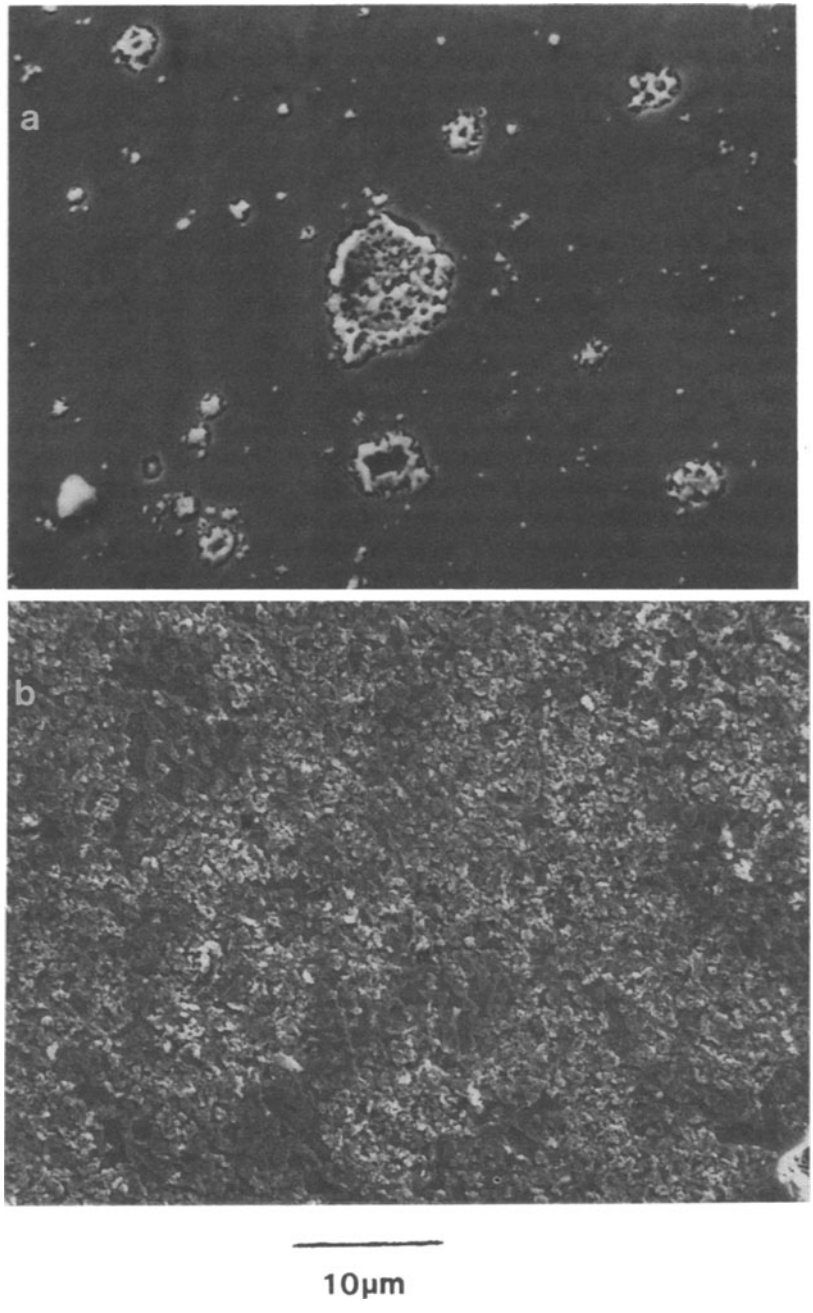

Figure 4.17. SEM of the restructured $Al_xO_y/Fe(110)$ surface[13]: (a) after a 0.05 torr water-vapor treatment and reduction in nitrogen and hydrogen; (b) after a 20 torr water-vapor pretreatment followed by reduction. The aluminum oxide is located underneath the iron surface, so it does not block active catalytic iron sites.

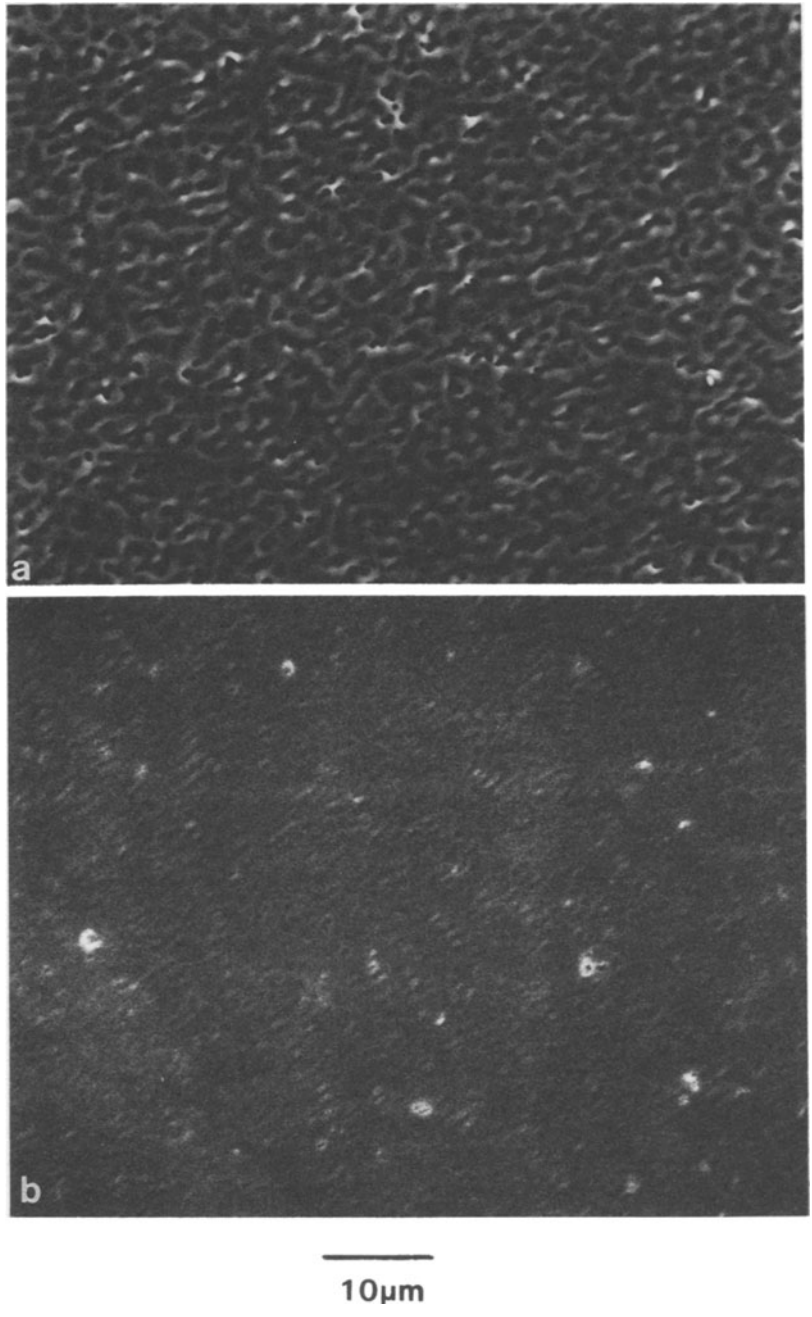

Figure 4.18. SEM of the restructured Fe(110) surface[13]: (a) after a 20 torr pretreatment in water vapor; (b) after one hour of ammonia synthesis. Note that the features smooth out under ammonia synthesis conditions.

ammonia synthesis. In addition, it exhibits a (1 × 1) LEED pattern representative of clean Fe(110).

Temperature-programmed desorption of ammonia from iron single-crystal surfaces after high-pressure ammonia synthesis proves to be a sensitive probe of the new surface binding sites formed upon restructuring. Ammonia TPD spectra for the four clean surfaces are shown in Fig. 4.19. Each surface shows distinct desorption sites. The Fe(110) surface displays one desorption peak (β_3) with a peak maximum at 658 K. Two desorption peaks are seen for the Fe(100) surface (β_2 and β_3) at 556 K and 661 K. The Fe(111) surface exhibits three desorption peaks (β_1, β_2, and β_3) with peak maxima at 495 K, 568 K, and 676 K, and the Fe(211) plane has two desorption peaks (β_2 and β_3) at 570 K and 676 K. Temperature-programmed desorption spectra for the Al_xO_y/Fe(110), Al_xO_y/Fe(100), and Al_xO_y/Fe(111) surfaces restructured in 20 torr of water vapor are shown in Fig. 4.20. A new desorption peak, β_2, develops on the restructured Al_xO_y/Fe(110)

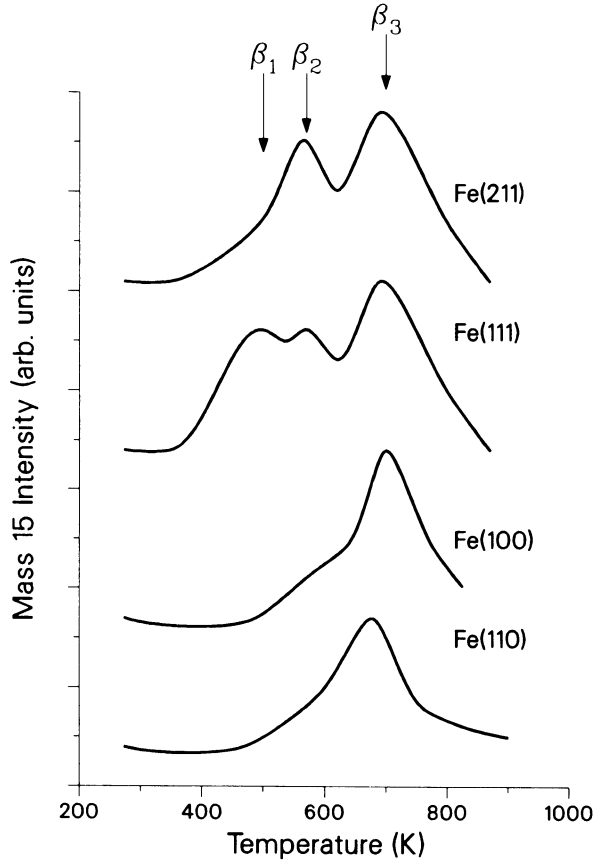

Figure 4.19. Ammonia TPD after high-pressure ammonia synthesis.[13] The low-temperature peaks exhibited by Fe(111) and Fe(211) (β_1 and β_2) are attributed to the presence of C_7 sites.

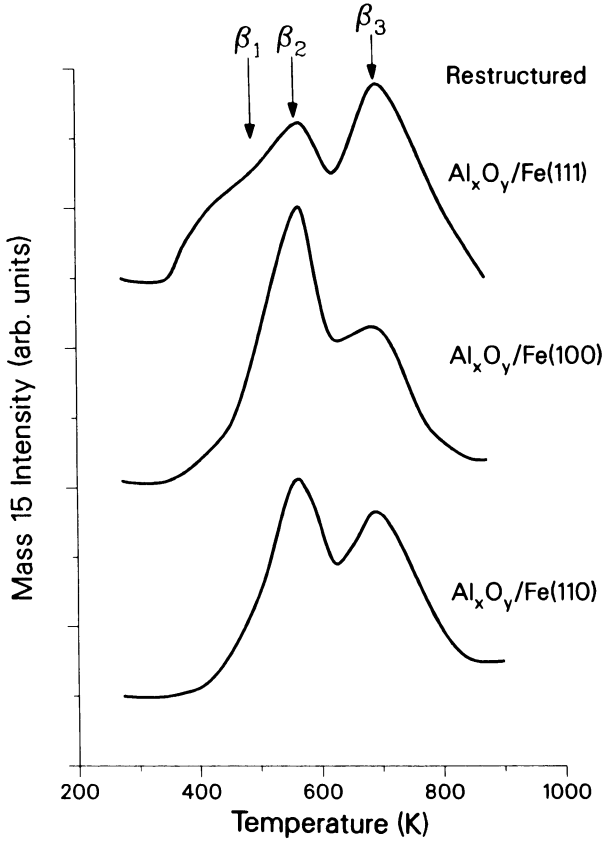

Figure 4.20. Ammonia TPD after ammonia synthesis from restructured Al_xO_y/Fe surfaces.[13] The restructured Al_xO_y/Fe(110) and Al_xO_y/Fe(100) surfaces exhibit low-temperature peaks similar to Fe(111) and Fe(211). Thus, restructuring by water vapor creates active C_7 sites.

surface, and an increase in the β_2 peak occurs on the restructured Al_xO_y/Fe(100) surface. The β_2 peaks from the restructured Al_xO_y/Fe(110) and Al_xO_y/Fe(100) surfaces grow in the same temperature range as the Fe(111) and Fe(211) β_2 peaks. Deactivation of the restructured surfaces by prolonged sputtering at 832 K reduces the intensity of the β_2 peaks on the restructured Al_xO_y/Fe(110) and Al_xO_y/Fe(100) surfaces to the same level as the respective clean surfaces.

The clean Fe(110), Fe(100), and Fe(111) surfaces restructured with 20 torr of water vapor produce the same TPD spectra as the Al_xO_y restructured surfaces. Deactivation of the (100) and (110) clean restructured iron surfaces is rapid under the conditions of ammonia synthesis, and the β_2 peaks become equivalent in intensity to those on the respective clean surfaces within one hour of ammonia synthesis.

The nature of restructuring of the Al_xO_y/Fe surfaces is indicated by the kinetic and TPD results. Kinetic data show that, through restructuring, the activity toward

ammonia synthesis of the Fe(110) and Fe(100) planes approaches that of the clean Fe(111) or Fe(211) planes, while the Fe(111) plane is not affected greatly by restructuring. As described earlier in Section 4.3, the activity of the clean Fe(111) and Fe(211) planes is usually attributed to the presence of C_7 sites. The clean Fe(100) and Fe(110) planes lack these sites. This suggests that restructuring of the surface by water vapor produces highly coordinated C_7 sites on the restructured Fe(110) and Fe(100) surfaces. The increase in rates over the restructured Fe(110) and Fe(100) planes is not attributable to an increase in surface area, since less carbon monoxide is adsorbed on these surfaces when compared to the respective clean surfaces. A similar decrease in carbon monoxide adsorption has also been observed on MgO/Fe ammonia synthesis catalysts that have also been restructured with ammonia[45] (see Section 4.3). These results were interpreted as due to the formation of C_7 sites which are not able to adsorb as much carbon monoxide as lower coordinated sites because of steric reasons. This explanation is applicable to the present study and it further supports the idea of the generation of C_7 sites on restructuring of the surface by the action of water vapor.

The ammonia TPD results point toward the formation of surface orientations which contain C_7 sites during water-vapor-induced restructuring. The growth of the β_2 peaks upon restructuring of the Fe(110) and Fe(100) surfaces suggests that the surfaces change orientation upon water-vapor treatment. The β_2 peaks also reside in the same temperature range as the Fe(111) β_2 peak. It seems likely that the TPD peaks in this temperature range act as a signature for the C_7 site since the Fe(211) surface (Fig. 4.20), which contains C_7 sites and is highly active in the ammonia synthesis reaction, also exhibits a β_2 peak after ammonia synthesis with a peak maximum at 570 K. These results suggest that surface orientations which contain C_7 sites, such as the Fe(111) and Fe(211) planes, are being formed during the reconstruction of clean and Al_xO_y-treated iron surfaces, but only in the presence of Al_xO_y does the active restructured surface remain stable under the ammonia synthesis conditions.

4.6.3. The Restructuring of Iron by Aluminum Oxide

The process by which iron restructures seems to involve both oxidation and reduction. Initial oxidation by water vapor destroys the original morphology of the iron surface. On reduction with nitrogen and hydrogen, the oxygen is removed and the resulting metallic iron is left in orientations active for the ammonia synthesis, such as Fe(111) and Fe(211). The presence of an amorphous surface after water-vapor pretreatment cannot be ruled out, since by using the industrial catalyst[46] it was shown by in situ X-ray diffraction at high pressures that the catalyst surface, after reduction, can be amorphous with no discernible crystal structure. Even if the surface is amorphous, the important point is that C_7 sites should be present and, if no support phase is present (i.e., Al_xO_y), reconversion of the iron into less active orientations is rapid under ammonia synthesis conditions. The idea of aluminum oxide stabilizing active planes for ammonia synthesis can be seen in the literature,[2] but this work is the first direct experimental proof substantiating this claim.

With the addition of Al_xO_y, the mobility of the iron is increased and restructuring can occur at lower pressure of water vapor. The SEM micrographs suggest that iron forms crystallites on top of the restructured Al_xO_y/Fe(110) surface [opposed to the uniform appearance of the restructured clean Fe(110) surface]. AES finds little Al_xO_y on the surface, suggesting that the iron has diffused through the Al_xO_y islands, covering them. These findings can be explained by considering wetting properties and the minimization of the free energy for the iron oxide-aluminum oxide system.

In vacuum or in a reducing environment (i.e., ammonia synthesis conditions), metallic iron will not spread over aluminum oxide (metallic iron has a higher surface tension than aluminum oxide[47]). Conversely, in an oxidizing environment (i.e., the water-vapor treatments) iron oxide forms (the surface tension of the oxide will be lower than the metal[47,48] and possibly similar to Al_xO_y). A chemical interaction between iron and aluminum oxide might then result as inferred from the AES results[13] shown in Fig. 4.21. It is shown that the 42 eV Auger peak representative of iron oxide[49,50] is shifted to about 38 eV in the presence of aluminum oxide and water vapor, indicating that an interaction results between aluminum oxide and iron oxide. Both these considerations favor the concept of iron wetting the aluminum oxide. Using transmission electron microscopy, it has been shown that iron can wet alumina (Al_2O_3) in an oxidizing environment or even in the presence of hydrogen which contains trace amounts of water vapor.[51]

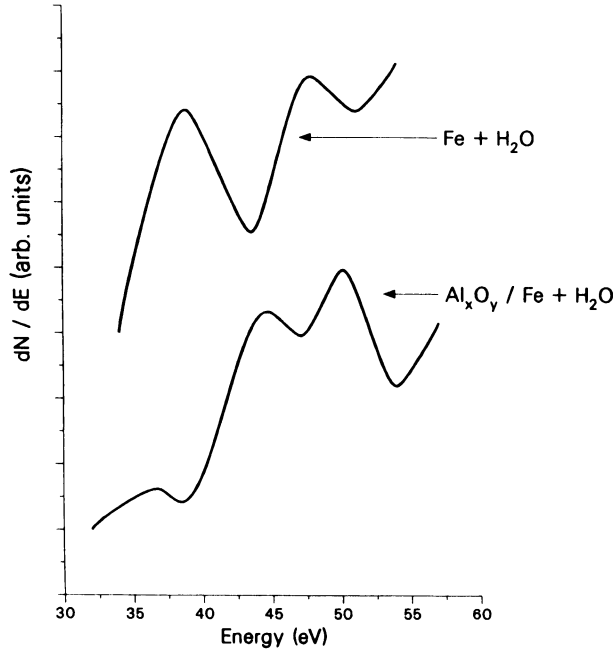

Figure 4.21. AES spectra of oxidized iron and a partially oxidized iron-aluminum oxide surface.[13] The 42 eV iron peak shifts to 39 eV in the presence of aluminum oxide.

The formation of iron aluminate (i.e., $FeAl_2O_4$) in the presence of an oxygen source was also postulated[51] on the basis of microelectron diffraction data.

While 20 torr of water vapor was needed to restructure clean iron single crystals, only 0.4 torr of water vapor is needed to restructure an Al_xO_y/Fe surface. It therefore seems that Al_xO_y provides an alternate and apparently more facile mechanism for the migration of iron. Upon reduction, metallic iron is left in a highly active orientation [such as Fe(111) and Fe(211)] for the ammonia synthesis reaction, and the Al_xO_y stabilizes the active iron, since if the Al_xO_y were not present the iron would move to positions coincident with the bulk periodicity (see Fig. 4.22 for a schematic representation of the restructuring).

The formation of an iron aluminate during reconstruction of the iron surface may be responsible for the stability of the restructured Al_xO_y/Fe surfaces. The presence of iron aluminate has been postulated from XPS studies on $Fe\text{-}Al_2O_3$ and $Fe_3O_4\text{-}Al_2O_3$ systems[52,53] as well as in numerous studies on the industrial ammonia synthesis catalyst.[54-56] The volume of an $FeAl_2O_4$ molecule is approximately equal to the volume of seven iron atoms in a bcc lattice[54] so that $FeAl_2O_4$ can exist as a skeleton in the iron lattice with little distortion. The low coverages of Al_xO_y on the restructured surfaces suggest that the support effect might be coming through inclusions of $FeAl_2O_4$ in the near-surface region. This is supported by the fact that ions sputtering the restructured surfaces reveal subsurface Al_xO_y.

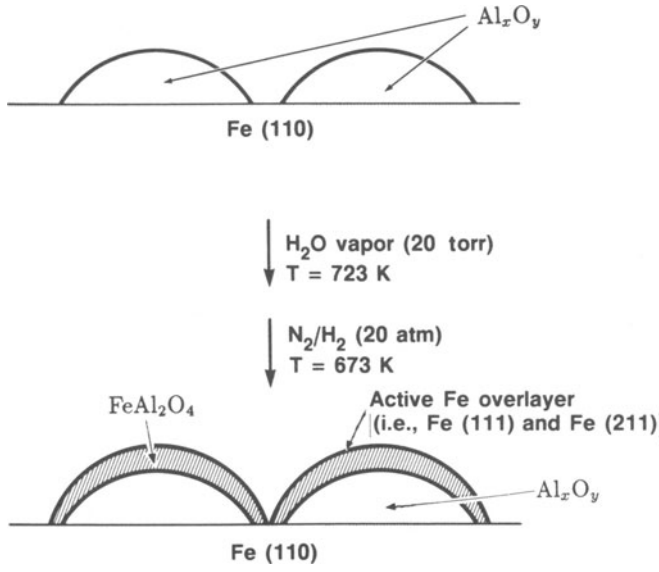

Figure 4.22. A schematic depicting the restructuring process of iron, induced by water vapor, and in the presence of aluminum oxide. The oxidation of the iron allows iron oxide to migrate on top of aluminum oxide. An interaction between the aluminum oxide and iron oxide might enhance this step. Upon reduction in nitrogen and hydrogen the iron is left in active and stable orientations for ammonia synthesis. The formation of iron aluminate might be responsible for this stability.

4.7. COMBINED UHV/HIGH-PRESSURE STUDIES ON THE INTERACTION BETWEEN ALUMINUM OXIDE AND POTASSIUM COADSORBED ON IRON

The industrial catalysts employed for use in ammonia synthesis always contain both aluminum oxide and potassium, often in conjunction with other promoters. Surface-science and catalytic studies will be presented that study the interactions between the two principal promoters.[40]

4.7.1. The Stability of Potassium on Iron when Coadsorbed with Aluminum Oxide

The Auger spectra of a K/Fe(100) surface prepared prior to carrying out ammonia synthesis, a K/Fe(100) surface after reaction, and a postreaction K/40% Al_xO_y/Fe(100) surface are shown in Fig. 4.23. It is apparent that a surface which contains aluminum oxide can retain more potassium during ammonia synthesis conditions than the equivalent surface without aluminum oxide. This suggests that aluminum oxide binds directly to potassium or that there is an interaction mediated through the iron surface. To probe these interactions experiments were performed in which a known amount of Al_xO_y was deposited on a Fe(100) surface. About 1 ML of potassium was evaporated on the crystal and the sample was heated to 673 K in UHV. The Auger signal from the potassium was monitored periodically. A rapid decrease occurred in the potassium Auger signal initially which was due to the low desorption energy of potassium at high surface coverages. After about 20 minutes a steady-state concentration of potassium was established, with the final coverage of potassium approximately equal to the initial coverage of aluminum oxide. This result is represented in Fig. 4.24, where the relative concentration of stabilized potassium is plotted against the relative concentration of stabilized potassium. An approximate 1:1 ratio is found between the surface concentration of potassium and aluminum oxide, and this is suggestive of compound formation between the two additives (i.e., $KAlO_2$), as opposed to a nonstoichiometric Al_xO_y-K surface layer.[39]

4.7.2. The Effects of Coadsorbed Potassium and Aluminum Oxide on the Ammonia Synthesis over Unrestructured Fe(100)

In Fig. 4.25, the rate of ammonia synthesis versus % free iron surface, as determined by carbon monoxide TPD (see experimental section), is shown graphically. The rate of ammonia synthesis decreases roughly in proportion to the amount of iron covered by the aluminum oxide and potassium.[39] The only mechanism for this reduction in rate is site-blocking, which occurs during initial reaction conversions (P_{NH_3} ranges from 0 torr to 3 torr during this measurement).

As the reaction conversion increases, the effects of coadsorbed potassium and aluminum oxide become apparent.[40] The partial pressure of ammonia in the reactor loop versus time for the 0.15 ML K/Fe(100), clean Fe(100), 0.25 ML K/25%

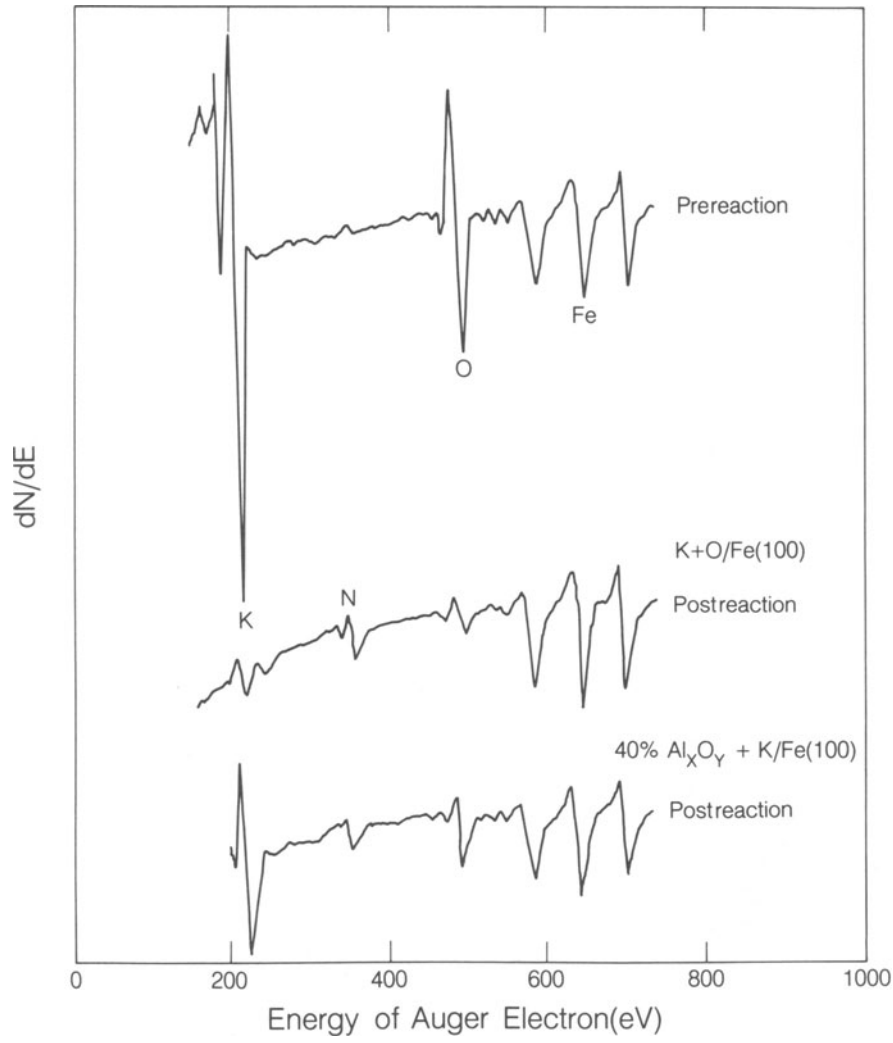

Figure 4.23. AES spectra of promoted Fe(100) surfaces before and after ammonia synthesis.[39] The prereaction potassium signal corresponds to 1 ML.

Al_xO_y/Fe(100) and for the 25% Al_xO_y surfaces is plotted in Fig. 4.26. In these experiments about 10 torr to 13 torr of ammonia was introduced into the reactor loop prior to ammonia synthesis. The 0.25 ML K/25% Al_xO_y/Fe(100) surface becomes increasingly more active than the 25% Al_xO_y/Fe(100) surface as the reaction conversion increases. This is the same behavior observed when the activity of 0.15 ML K/Fe(100) is compared to Fe(100), as described in Section 4.5. The presence of potassium on the iron surface results in a reduction of the adsorption energy of the ammonia product. Thus, the concentration of surface ammonia is

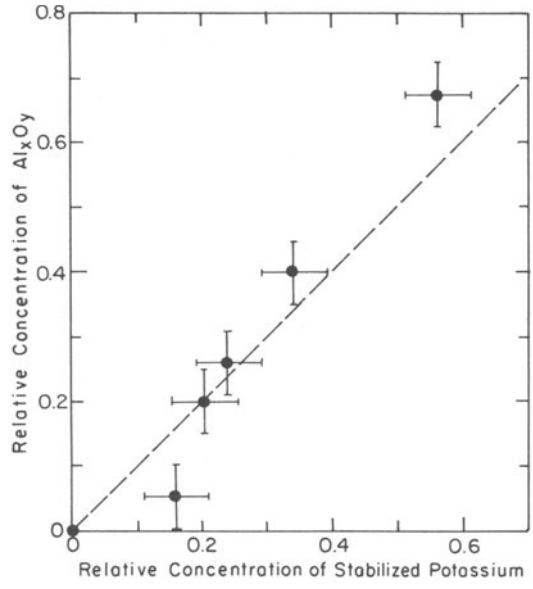

Figure 4.24. The relative concentration of stabilized potassium plotted against the relative concentration of aluminum oxide present.[39] The dotted line corresponds to a 1:1 ratio of potassium to aluminum oxide.

lowered and more catalytic sites are available for the dissociation of nitrogen. Frankenburg[3] has suggested that on the industrial catalyst, potassium neutralizes weak acidic sites which would otherwise bind ammonia and ammonia synthesis or decomposition intermediates. This type of promotion might be an additional effect of potassium when coadsorbed with aluminum oxide, although detailed experiments have not been carried out to address this possibility.

Even though more potassium can be stabilized on the iron surface when aluminum oxide is coadsorbed, an enhancement in the promoter effect was not

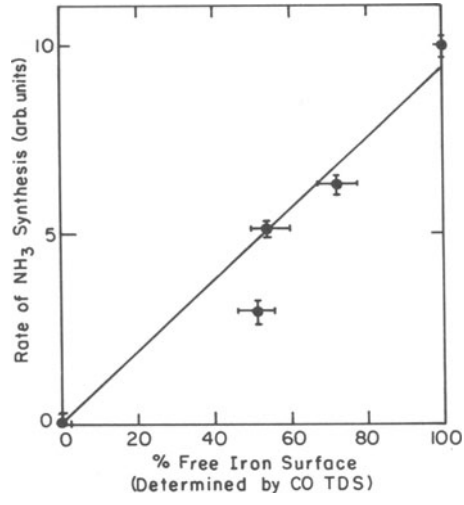

Figure 4.25. The rate of ammonia synthesis decreases roughly in proportion to the amount of iron covered by potassium and aluminum oxide at initial reaction conversions.[39]

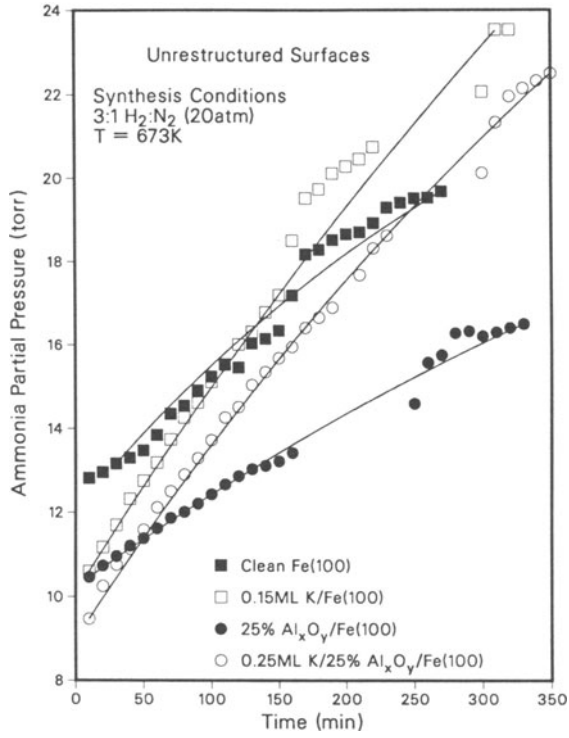

Figure 4.26. The amount of ammonia produced in the reaction loop is plotted against time of ammonia synthesis for the 0.15 ML K/Fe(100), clean Fe(100), 0.25 ML K/25% Al_xO_y/Fe(100), and 25% Al_xO_y/Fe(100) surfaces.[40] The nonlinearity of the curves is due to gas-phase ammonia readsorbing on the catalyst and blocking catalytic sites for the dissociation of nitrogen.

found when these surfaces were compared to the activity of 0.15 ML K/Fe(100). The 0.25 ML K/25% Al_xO_y/Fe(100) surfaces exhibits roughly the same rate as the 0.15 ML K/Fe(100) surface, as indicated by the slopes of the curves in Fig. 4.26. The surface area of the single crystal and the fraction of surface covered by the additive is taken into account when the rates of ammonia synthesis are determined. Thus the potassium, which interacts with the aluminum oxide, seems to be rendered catalytically inactive. Stabilization of more than 0.25 ML of potassium actually results in a decrease in the promoter effect of potassium. This decrease is probably due to high coverages of potassium blocking catalytic sites which dissociate nitrogen,[39] and is paralleled by a reduction in the activity of commercial catalysts should excessive potassium be used in the formulation.

4.7.3. Water-Vapor Pretreatment of Clean and Al_xO_y/Fe Single-Crystal Surfaces in the Presence of Coadsorbed Potassium

Coverages of 0.1 ML to 1.0 ML of potassium adsorbed alone on the (111), (100), and (110) faces of iron failed to produce any promotional effects after

pretreatments with 0.05 torr, 0.4 torr, and 20 torr of water vapor. Subsequent to the water-vapor treatments the coverage of potassium was never greater than 0.4 ML, and it did not exceed 0.1 ML after the ammonia synthesis reaction, in agreement with previous work.[39]

The same coverages of potassium coadsorbed with two monolayers of aluminum oxide on the Fe(110), Fe(100), and Fe(111) surfaces hindered the restructuring process in water vapor (see Section 4.6). As increasing amounts of potassium were coadsorbed, more aluminum oxide was detected by AES after water pretreatments of 20 torr, and less restructuring of the iron occurred (rates of ammonia synthesis over these surfaces were less than the rates on those surfaces which were restructured with aluminum oxide alone). There is a one-to-one ratio between aluminum oxide and potassium on the surface and, in the case where one monolayer of potassium was deposited on two monolayers of aluminum oxide, AES showed that no aluminum oxide or potassium migrated from the iron surface after a 20 torr water-vapor pretreatment and restructuring of the surface failed to occur.

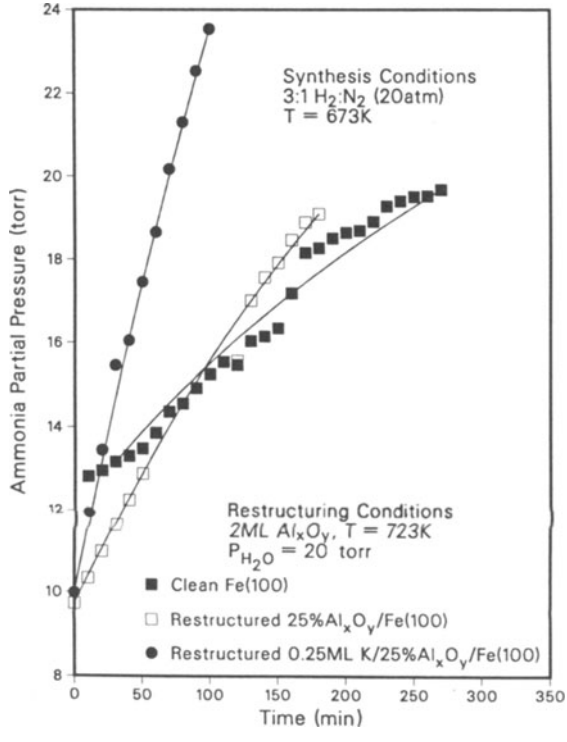

Figure 4.27. Ammonia accumulation in the reaction loop is plotted against time for the clean Fe(100), restructured Al_xO_y/Fe(100), and for a 0.25 ML K/Al_xO_y/Fe(100) which had been restructured before the addition of potassium.[57]

4.7.4. The Effects of Coadsorbed Potassium and Aluminum Oxide on the Ammonia Synthesis over Restructured Fe(100)

It has been shown that inactive Fe(110) and the slightly active Fe(100) surface can be restructured with water vapor in the presence of aluminum oxide to produce new surfaces with activities equivalent to Fe(111) and Fe(211). The coadsorption of potassium with the aluminum oxide inhibits this restructuring. It seems likely that the formation of a potassium aluminate retards the interaction between aluminum oxide and the oxidized iron surface which is needed to change the morphology of the iron surface. Thus, the promotional effect of both aluminum oxide and potassium is eliminated if they are added together prior to the restructuring process on single-crystal catalysts.

To realize fully the promotional effects of potassium and aluminum oxide, the promoters must be added at different times during the preparation of the active catalyst.[40] In Fig. 4.27, the partial pressure of ammonia in the reaction loop versus the time of reaction for clean Fe(100), restructured Al_xO_y/Fe(100), and restructured 0.25 ML K/25% Al_xO_y/Fe(100) where the potassium was added after the restructuring procedure is plotted (see the figure for conditions). The restructured Al_xO_y/Fe(100) surface with 0.25% Al_xO_y is about one order of magnitude more active than the clean Fe(100) surface when the surface areas of the samples are taken into account. The addition of 0.25 ML K to a restructured Al_xO_y/Fe(100) surface increases the activity of the restructured surface twofold at an ammonia partial pressure of 20 torr. Thus the restructured 0.25 ML K/25% Al_xO_y/Fe(100) surface is now 20 times more active than the clean Fe(100) surface. The only way to achieve this level of enhancement is to restructure the surface in the presence of aluminum oxide alone, and then to add the potassium.

4.8. AMMONIA-INDUCED RESTRUCTURING OF IRON SINGLE-CRYSTAL SURFACES

It has been shown throughout this chapter that ammonia synthesis from its elements over iron is an extremely structure-sensitive reaction, and hence a major concern in the preparation of an industrial catalyst is to preferentially create and stabilize active surface orientations [i.e., Fe(111) and Fe(211)]. This objective is uaually accomplished in the chemical technology by combining magnetite (Fe_3O_4) with about two percent by weight of potassium oxide (K_2O) and aluminum oxide (Al_2O_3) and then reducing the catalyst precursor in a stoichiometric mixture of hydrogen and nitrogen or in an ammonia-hydrogen flow.[6] Catalytic studies have found that the industrial iron catalyst is more active when reduced in a stoichiometric mixture of nitrogen and hydrogen than in pure hydrogen.[7] Also, by treating the catalyst with ammonia so as to achieve a higher partial pressure of nitrogen (through the complete dissociation of ammonia), a nitrogen-induced restructuring results in an enhancement in ammonia synthesis activity.[2]

This section presents research[58] which studied the effects of ammonia inducing restructuring on the ammonia synthesis activity of Fe(110), Fe(100), and

Fe(111) surfaces. Also, the effects of the ammonia pretreatment on iron surfaces with coadsorbed potassium and aluminum oxide are presented.

4.8.1. Clean Iron Single Crystals Pretreated with Ammonia Prior to Ammonia Synthesis

Rates of ammonia synthesis over initially clean (110), (100), and (111) faces of iron are shown in Fig. 4.28, along with the rates obtained after the treatment of the Fe(110), Fe(100), and Fe(111) crystals with 5 torr of ammonia at 723 K for 30 minutes prior to the ammonia synthesis reaction. The Fe(110) and Fe(100) surfaces show large increases in activity for ammonia synthesis (Fig. 4.28) after ammonia pretreatment. The initially inactive Fe(110) face becomes about half as active as the clean Fe(111) surface. The activity of the Fe(100) surface, for ammonia synthesis, increases by a factor of four and the Fe(111) surface shows only a small decrease in activity after ammonia pretreatment. Scanning electron micrographs of the ammonia pretreated iron single-crystal surfaces are shown in Fig. 4.29. They clearly show that ammonia pretreatment drastically changes the surface structure of the (110), (100), and (111) faces of iron.

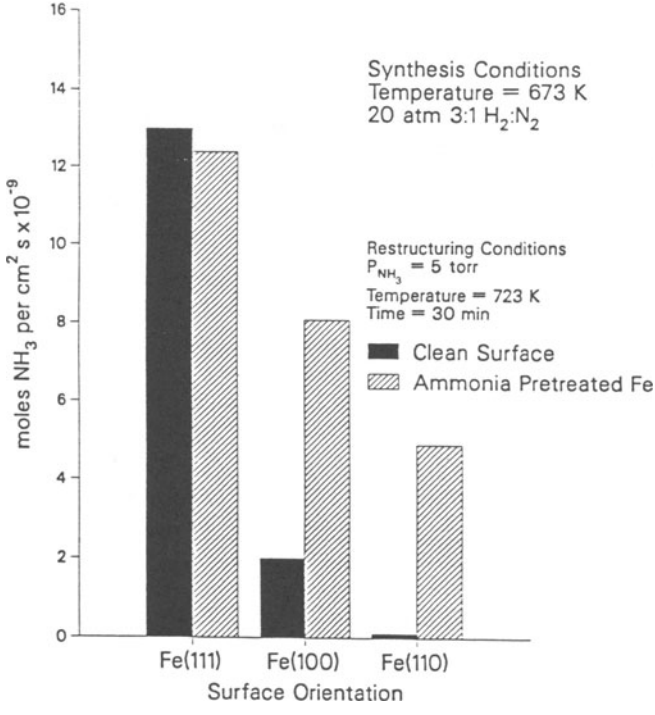

Figure 4.28. Rates of ammonia synthesis over clean Fe single crystals of (111), (100), and (110) orientation and ones pretreated in ammonia prior to ammonia synthesis.[58]

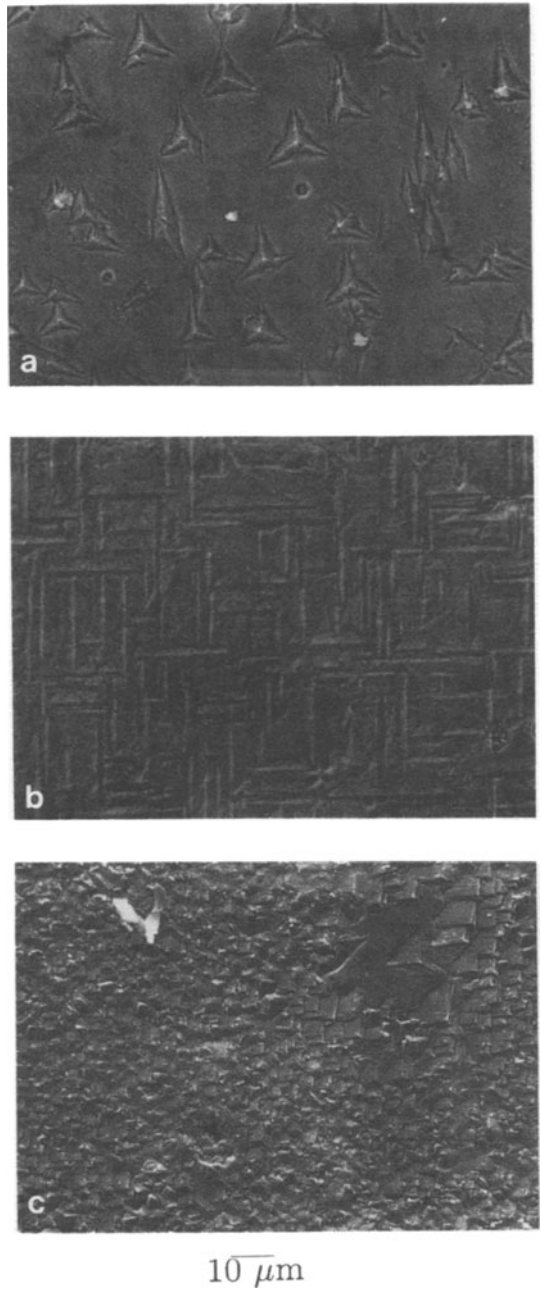

Figure 4.29. Scanning electron micrographs of the (a) Fe(111), (b) Fe(100), and (c) Fe(110) surfaces after they were treated in 5 torr of ammonia at 723 K for 30 minutes indicating the restructuring of all three crystal orientations.[58]

4.8.2. Structural Characterization of the Restructured Surfaces

It was shown in Section 4.6 that the desorption of ammonia after ammonia synthesis is a sensitive probe of surface structure. It is found that Fe(110) and Fe(100) surfaces restructured in ammonia exhibit the β_2 peak which is characteristic of a surface containing the C_7 site. The restructured Fe(111) surface shows little change in its temperature-programmed desorption profile in agreement with the observation of the absence of any significant change in ammonia synthesis activity after restructuring. This suggests that the (111) plane, along with Fe(110) and Fe(100), is restructured to a surface which also contains C_7 sites. This contention is directly confirmed by an SEM analysis of the restructured (111) surface (the details of the analysis are presented in detail elsewhere) which shows that the new surface planes formed after ammonia treatment are (211) planes,[58] shown in Section 4.3 to have a similar activity to the Fe(111) surface.

4.8.3. The Effect of Adsorbed and Dissolved Nitrogen on Iron during Ammonia Synthesis

The presence of adsorbed nitrogen, present during ammonia synthesis, seems not to affect ammonia synthesis activity under the conditions used in this study. Surfaces, restructured in ammonia, produce high near-surface concentrations of nitrogen. The ratio (C_N) of the nitrogen 381 eV AES peak to the iron 652 eV peak is close to unity after ammonia pretreatment of the (110), (100), and (111) iron surfaces. This corresponds to a surface coverage, θ_N, of about 0.6.[31,58] This is in contrast to a C_N value of 0.17 ($\theta_N = 0.09$), which is the surface nitrogen coverage of an iron surface after ammonia synthesis without ammonia pretreatment. However, the surfaces with the high surface concentration of nitrogen have identical ammonia synthesis activity to those surfaces with a lower θ_N. This result suggests that the nitrogen detected in UHV does not reside on catalytic sites during ammonia synthesis, since rates are the same over nitrogen-free and nitrided Fe surfaces after ammonia pretreatment.

4.8.4. The Effects of Aluminum Oxide and Potassium on the Restructuring of Iron by Ammonia

The presence of Al_xO_y on the iron surface inhibits the restructuring process induced by ammonia and the presence of potassium shows no observable effects on the process.

Aluminum oxide is found to block the iron surface which could otherwise dissociate ammonia. This blocking of the restructuring process by Al_xO_y is in sharp contrast to the case where aluminum oxide catalyzes the restructuring of iron in the presence of water vapor prior to ammonia synthesis (Section 4.6). In this circumstance iron oxide is found to migrate on top of the aluminum oxide overlayer as a result of the oxidizing environment (water vapor). The major driving force for this structural transformation is most likely compound formation between iron oxide and aluminum oxide.

When nitrogen is the restructuring agent it is not thermodynamically favorable for iron nitride to cover aluminum oxide, probably because of the absence of a strong chemical interaction between iron nitride and aluminum oxide. Hence, AES finds aluminum oxide on the iron surface after Al_xO_y/Fe surfaces have been pretreated in ammonia. Contrary to this, in the case of restructuring in water vapor, AES finds that Al_xO_y leaves the iron surface region, residing underneath the active iron surface.

The presence of potassium on iron during ammonia pretreatment has no additional effect on the restructuring process when adsorbed alone or when coadsorbed with Al_xO_y. Thus, potassium does not seem to affect the structural promotion of ammonia synthesis catalyst either during ammonia or water-vapor pretreatment. However, the presence of potassium on a Al_xO_y/Fe surface, during water-vapor pretreatment (Section 4.6), inhibits restructuring. A likely explanation for this observation is that the formation of potassium aluminate blocks the interaction between iron oxide and aluminum oxide.[16]

The effects of water-vapor and ammonia pretreatment on the initial rate of ammonia synthesis over Fe, Al_xO_y/Fe, and K/Al_xO_y/Fe surfaces can be summarized as follows. The presence of aluminum oxide promotes the restructuring of iron during the water-vapor pretreatment, but it inhibits the ammonia-induced restructuring. The presence of potassium shows no effect in the ammonia pretreatment and it inhibits water-vapor-induced restructuring of iron. These results suggest that to form the most active ammonia synthesis catalyst, the iron should first be restructured in ammonia before aluminum oxide is added. After aluminum oxide is added the surface should be treated in water vapor, and finally potassium should be added to serve as a promoter at high ammonia synthesis reaction conversions.

4.9. SUMMARY OF THE PROMOTER EFFECTS OF POTASSIUM AND ALUMINUM OXIDE

In this section, the surface-science and catalytic data on the promotional effects of both aluminum oxide and potassium for ammonia synthesis over iron single-crystal surfaces is summarized. The promotional effects of potassium on ammonia synthesis have been investigated over the Fe(110), Fe(100), and Fe(111) surfaces under high-pressure conditions. A coverage of 0.15 ML is the maximum amount of potassium that can be stabilized on the iron single crystals under ammonia synthesis conditions, and adsorbed potassium has no promotional effect on the inactive Fe(110) surface. However, adsorbed potassium increases the rate of ammonia synthesis markedly over the Fe(111) and Fe(100) crystal faces. The promotional effect becomes more significant as the reaction conversion increases. For example, at an ammonia partial pressure of 20 torr there is a twofold increase in the rate of ammonia synthesis over Fe(111) and Fe(100) in the presence of potassium. In the presence of potassium the ammonia reaction order from -0.6 to -0.35 on the (100) and (111) faces of iron is changed, and adsorbed potassium also decreases the reaction order in hydrogen from 0.76 to 0.44 on Fe(111). However, within experimental error, there is no change in the activation energy,

when potassium is present, suggesting that the mechanism for ammonia synthesis is not being changed.

The kinetic data can be explained by a model which accounts for the blocking of catalytic sites which have the ability to dissociate nitrogen, by adsorbed ammonia and atomic nitrogen. The presence of potassium results in lowering the concentration of adsorbed ammonia on the surface, thus making more sites available to chemisorb nitrogen dissociatively and further increasing the rate of ammonia synthesis. The model suggests that an additional promotional effect of potassium is a 30% enhancement in the rate of nitrogen dissociation on Fe(111) and Fe(100), which increases the rate of ammonia synthesis still further. This is in qualitative agreement with nitrogen chemisorption studies on iron and K/Fe surfaces in UHV (Section 4.4).

Treatment of the (110), (100), and (111) faces of iron with 20 torr of water vapor causes surface restructuring. The restructured Fe(110) and Fe(100) surfaces become as active as the clean Fe(111) surface for ammonia synthesis. The restructured Fe(111), however, exhibits a slight decrease (about 5%) in activity when compared to the clean Fe(111) surface. The restructured (110), (100), and (111) surfaces reconvert to their unrestructured orientations within one hour of ammonia synthesis and lose their increase in activity.

The same restructuring on the Fe(110), Fe(100), and Fe(111) surfaces can be performed with water vapor in the presence of aluminum oxide. In this case, 20 torr of water vapor restructures the Al_xO_y/Fe(100) and only 0.4 torr of water vapor is needed to restructure the Al_xO_y/Fe(110) surface so that they become as active as the Fe(111) face in ammonia synthesis. The restructured Al_xO_y/Fe(110) and Al_xO_y/Fe(100) surfaces maintain their activity for longer than four hours in the ammonia synthesis conditions in contrast to the Al_xO_y-free surface. The formation of iron aluminate in the region near to the iron surface is invoked to explain the stability of the restructured Al_xO_y/Fe surfaces.

The studies on reaction rates and ammonia temperature-programmed desorption suggest that planes containing C_7 sites, such as the Fe(211) and Fe(111) surfaces, are being created during the water-vapor pretreatments whether aluminum oxide is present or not. However, only when aluminum oxide is present will these active surfaces remain stable and not reconvert to less active surfaces [i.e., Fe(110) and Fe(100) planes].

The coadsorption of potassium with aluminum oxide inhibits the restructuring process. Thus, to realize the full promotional effects of both aluminum oxide and potassium, the surfaces should first be restructured with aluminum oxide alone and potassium should be added afterward. Using this procedure, the activity of the Fe(110) surface can be increased by a factor of about 800 at an ammonia partial pressure of 20 torr (P_{N_2} = 5 atm and P_{H_2} = 15 atm). Restructuring leads to about a 400-fold increase in the activity of Fe(110), and the addition of potassium contributes a further twofold increase.

The application of these results to industrial catalysts seems to be warranted. Industrial catalysts are prepared by fusion of 1% to 3% by weight of aluminum oxide and potassium to iron oxide with subsequent reduction to the active catalyst in a stoichiometric mixture of nitrogen and hydrogen. This procedure has been

reproduced in the combined UHV/high-pressure studies presented in this chapter. The promotional effects of aluminum oxide in the industrial catalyst probably result from its interaction with the iron oxide during the preparation stage. This interaction results in the formation of solid solutions which could prevent planes such as Fe(111) and Fe(211) formed during reduction from converting to more thermodynamically stable planes, such as the low-activity Fe(110) and Fe(100) surfaces. The presence of potassium seems to have little to do with this structural promotion. Its presence during this step might even inhibit the full promotional effect of aluminum oxide from being realized. Its interaction with aluminum oxide is seen to result in the formation of a potassium aluminate which retards the interaction between iron oxide and aluminum oxide during the restructuring process.

Pretreating iron single crystals in high pressures of ammonia prior to ammonia synthesis have been shown to induce a surface restructuring. Both the Fe(110) and Fe(100) surfaces are found to approach the Fe(111) activity after ammonia pretreatment. Treatment of the Fe(111) surface in ammonia causes a surface transformation to Fe(211). The presence of aluminum oxide on the iron surface inhibits ammonia-induced restructuring and potassium shows no observable effect.

ACKNOWLEDGMENT

This work was supported by the Director, Office of Energy Research, Office of Basic Energy Sciences, Materials Science Division of the U.S. Department of Energy under contract number DE-AC03-76SF00098. The authors gratefully acknowledge partial support for this research by I.C.I. The authors also thank Sabrina Fu for carefully proofreading the manuscript.

REFERENCES

1. A. Nielsen, *An Investigation on Promoted Iron Catalysts for the Synthesis of Ammonia*, 3rd edn., Jul. Gjellerups Forlag, Copenhagen (1968).
2. A. Ozaki, *Catalysis, Science and Technology*, Vol. 1, Chapter 3, Springer-Verlag, Berlin (1981).
3. W. G. Frankenburg, *Catalysis*, p. 171, Reinhold, New York (1955).
4. M. Temkin and V. Pyzhev, *Acta Phys. Chim. URSS* **12**, 327 (1940).
5. A. Ozaki, H. S. Taylor, and M. Boudart, *Proc. R. Soc. London* **47**, 258 (1960).
6. S. A. Topham, *Catalysis, Science and Technology*, Vol. 7, Springer-Verlag, Berlin (1985).
7. G. Ertl, *J. Vac. Sci. Technol.* **A1**(2), 1247 (1983).
8. S. Brunauer and P. H. Emmett, *J. Am. Chem. Soc.* **62** 1732 (1940).
9. R. Krabetz and C. Peters, *J. Am. Chem. Soc.* **77**, 333 (1965).
10. P. H. Emmett and S. Brunauer, *J. Am. Chem. Soc.* **59**, 310 (1937).
11. H. H. Madden and W. Goodman, *Surf. Sci.* **150**, 39 (1985).
12. S. Khammouma, PhD thesis, Stanford University (1972).
13. D. R. Strongin, S. R. Bare, and G. A. Somorjai, *J. Catal.* **103**, 289 (1987).
14. D. W. Blakely, C. I. Kozak, B. A. Sexton, and G. A. Somorjai, *J. Vac. Sci. Technol.* **13**, 1091 (1976).

15. G. A. Somorjai, *Chemistry in Two Dimensions: Surfaces,* Cornell University Press, Ithaca (1981).
16. N. D. Spencer, R. C. Schoonmaker, and G. A. Somorjai, *J. Catal.* **74**, 129 (1982).
17. D. R. Strongin, J. Carrazza, S. R. Bare, and G. A. Somorjai, *J. Catal.* **103**, 213 (1987).
18. R. Smoluchoswki, *Phys. Rev.* **60**, 661 (1941).
19. J. Hoelzl and F. K. Schulte, *Solid Surface Physics*, Springer-Verlag, Berlin (1979).
20. J. McAllister and R. S. Hansen, *J. Chem. Phys.* **59**, 414 (1973).
21. G. Ertl, S. B. Lee, and M. Weiss, *Surf. Sci.* **114**, 527 (1982).
22. A. Nielsen, *Catal. Rev.* **4**, 1 (1970).
23. L. Falicov and G. A. Somorjai, *Proc. Natl. Acad. Sci. USA* **82**, 2207 (1985).
24. J. A. Dumesic, H. Topsøe, and M. Boudart, *J. Catal.* **37**, 513 (1975).
25. M. Asscher, J. Carrazza, M. M. Khan, K. B. Lewis, and G. A. Somorjai, *J. Catal.* **98**, 227 (1986).
26. G. Broden and H. P. Bonzel, *Surf. Sci.* **84**, 106 (1979).
27. S. B. Lee, M. Weiss, and G. Ertl, *Surf. Sci.* **108**, 357 (1981).
28. R. L. Gerlach and T. N. Rhodin, *Surf. Sci.* **19**, 403 (1970).
29. P. H. Redhead, *Vacuum* **12**, 203 (1962).
30. G. Pirug, G. Broden, and H. P. Bonzel, *Surf. Sci.* **94**, 323 (1980).
31. F. Bozso, G. Ertl, M. Grunze, and M. Weiss, *J. Catal.* **49**, 18 (1977).
32. F. Bozso, G. Ertl, and M. Weiss, *J. Catal.* **50**, 519 (1977).
33. Z. Paal, G. Ertl, and S. B. Lee, *Appl. Surf. Sci.* **8**, 231 (1981).
34. G. Ertl, S. B. Lee, and M. Weiss, *Surf. Sci.* **114**, 527 (1982).
35. D. R. Strongin and G. A. Somorjai, *J. Catal.* **109**, 51 (1988).
36. T. E. Madey and C. Benndorf, *Surf. Sci.* **152/153**, 587 (1985).
37. C. Benndorf and T. E. Madey, *Chem. Phys. Lett.* **101**, L277 (1983).
38. J. G. van Ommen, W. J. Bolink, J. Prasad, and P. Mars, *J. Catal.* **38**, 120 (1975).
39. S. R. Bare, D. R. Strongin, and G. A. Somorjai, *J. Phys. Chem.* **90**, 4726 (1986).
40. D. R. Strongin and G. A. Somorjai, *Catal. Lett.* **1**, 98 (1988).
41. K. Altenburg, H. Bosch, J. G. Ommen, and P. J. Gellings, *J. Catal.* **66**, 326 (1980).
42. R. Brill, *J. Polym. Sci.* **12**, 353 (1962).
43. G. Ertl, M. Weiss, and S. B. Lee, *Chem. Phys. Lett.* **60**, 391 (1979).
44. W. D. Mross, *Catal. Rev. Sci. Eng.* **25**(4), 591 (1983).
45. J. A. Dumesic, H. Topsøe, and M. Boudart, *J. Catal.* **37**, 513 (1975).
46. T. Rayment, R. Schlogl, J. M. Thomas, and G. Ertl, *Nature* **315**, 311 (1985).
47. S. H. Overbury, P. A. Bertrand, and G. A. Somorjai, *Chem. Rev.* **75**(5), 547 (1975).
48. D. Beruta, L. Baro, and A. Passerone, in *Oxides and Oxide Films* (A. K. Vijh, ed.), Vol. 6. Dekker, New York (1981).
49. M. Langell and G. A. Somorjai, *J. Vac. Sci. Technol.* **21**, 858 (1982).
50. G. Ertl and K. Wandelt, *Surf. Sci.* **50**, 479 (1975).
51. I. Sushumna and E. Ruckenstein, *J. Catal.* **94**, 239 (1985).
52. E. Paparazzo, J. L. Dormann, and D. Fiorani, *Phys. Rev. B* **28**, 1154 (1983).
53. E. Paparazzo, *Appl. Surf. Sci.* **25**, 1 (1986).
54. W. S. Borghard and M. Boudart, *J. Catal.* **80**, 194 (1983).
55. H. Ludwiczek, A. Preisinger, A. Fischer, R. Hosemann, A. Schonfeld, and W. Vogel, *J. Catal.* **51**, 326 (1978).
56. G. Fagherazzi, F. Galante, F. Garbassi, and N. Pernicone, *J. Catal.* **26**, 344 (1972).
57. Z. Paal, G. Ertl, and S. B. Lee, *Appl. Surf. Sci.* **8**, 231 (1981).
58. D. R. Strongin and G. A. Somorjai, *J. Catal.* **109** 51 (1988).

5

CHEMISORPTION AT MORE ELEVATED PRESSURES ON INDUSTRIAL AMMONIA SYNTHESIS CATALYSTS

J. W. Geus and K. C. Waugh

5.1. INTRODUCTION

This chapter is concerned with the adsorption of hydrogen, nitrogen, and carbon monoxide on promoted iron catalysts in the reduced state at pressures up to about 1 atm. In Chapter 3, Ertl discusses adsorption of hydrogen and nitrogen on iron single crystals with and without added potassium. Schlögl, in Chapter 2, deals with adsorption of nitrogen on industrial ammonia synthesis catalysts. Both Ertl and Schlögl consider only measurements in which the surface coverage is determined by modern surface analytical techniques, such as XPS, UPS, and Auger electron spectroscopy. Since these modern techniques can only be operated at low gas pressures, coverages at higher pressures are not discussed. It is relevant therefore to compare the data described by Ertl and Schlögl with older results measured at higher pressure on reduced iron catalysts. In this older work, the extent of adsorption has been measured both volumetrically and gravimetrically. The properties of hydrogen are particularly interesting. Adsorption of hydrogen on reduced catalysts is generally an activated process, while adsorption on sputter-cleaned single crystals and vapor-deposited iron films is not activated even at low temperatures.

The reactivity of oxygen adsorbed on iron surfaces or present in the surface layer of iron toward hydrogen is highly important in the case of industrial ammonia

J. W. Geus • Department of Inorganic Chemistry, Debije Institute, University of Utrecht, 3522 AD Utrecht, The Netherlands. K. C. Waugh • Catalysis Research Centre, ICI Chemicals and Polymers Ltd., Billingham, Cleveland TS23 1LB, England.

synthesis catalysts. To activate the catalysts, hydrogen reduction of the iron oxide phases present in the fresh catalysts must first be carried out. The efficiency of removal of oxygen from the iron surface by reaction with hydrogen has a major influence upon the subsequent activity in the ammonia synthesis reaction. Furthermore, it has been found that oxygen-containing compounds, such as carbon dioxide, carbon monoxide, and water, poison reversibly the subsequent activity of iron catalysts at concentration ratios far below those at which bulk iron oxides are in thermodynamic equilibrium with bulk metallic iron.

Calculations relating adsorption properties measured on clean single-crystal surfaces at (very) low pressure with actual rates of ammonia synthesis at high pressures described later in this chapter require some measurement of the free metallic iron surface area of the reduced synthesis catalysts. The free metallic iron surface area is generally calculated from the extent of chemisorption of carbon monoxide. In view of the importance of the free metallic iron surface area in work dealing with the mechanism of ammonia synthesis, it is important to review the adsorption of carbon monoxide on different iron surfaces reduced under different conditions.

Finally, the chapters by Schlögl and Somorjai deal with the effects of water on the action of the promoters, in particular alumina, with an oxidized iron surface. The structure and catalytic properties obtained by the iron surface after reduction appear to be affected significantly by previous exposure to water vapor (and hydrogen) at high temperatures. The small amount of alumina present in industrial synthesis catalysts renders assessment of the interaction of the excess oxidized iron with the alumina difficult. We therefore will review some results obtained on iron catalysts supported on alumina at a much lower iron content.

Since the properties of iron catalysts depend strongly on the detailed reduction procedure, the chapter will begin with a discussion of the reduction of alumina-supported iron catalysts. The interaction of alumina with iron(II) formed during the reduction will be evident.

Subsequently, the reactivity of oxygen present on reduced iron surfaces toward hydrogen will be considered. Experiments on single crystals of iron have demonstrated that the reactivity of the monolayer of oxygen atoms toward hydrogen is strongly dependent upon the structure of the iron metal surface. The results of the experiments on single crystals can rationalize a number of the experimental observations detailed in the other chapters.

The literature on the interaction of iron surfaces with carbon monoxide will then be reviewed. It will become apparent that the interaction of iron with carbon monoxide is much more complicated than the interaction of carbon monoxide with metals such as platinum or nickel.

Interaction of iron surfaces with molecular hydrogen will be the subject of the next section. The considerable differences in the interaction of molecular hydrogen with reduced and unreduced iron surfaces will be discussed, followed by a section devoted to a discussion of the interaction of reduced catalysis with molecular nitrogen.

Finally, rates of ammonia synthesis at industrially relevant conditions of temperature (450 °C) and pressure (100 bar) predicted by models based on the kinetics of adsorption and desorption derived both from the single-crystal studies

of Ertl and co-workers and from studies of singly and doubly promoted catalysts by Brunauer and Emmett and also by Scholten and co-workers will be compared with those obtained in practice.

5.2. REDUCTION OF ALUMINA-SUPPORTED IRON CATALYSTS

In contrast to nickel and copper, the reduction of iron oxide to the metallic state calls for a fairly high hydrogen-to-water ratio to become thermodynamically viable. At lower hydrogen-to-water ratios, reduction of bulk iron(III) oxide (alfa-Fe_2O_3 or alfa-FeOOH) proceeds only to magnetite (Fe_3O_4). At temperatures below about 570 °C, magnetite should react with hydrogen to give metallic iron and water. According to the phase diagram, bulk FeO (wustite) is stable only at temperatures above about 570 °C, and should not be formed during mild reduction.[1]

Both Schlögl and Somorjai report on the interaction between oxidized iron and the promoters, mainly alumina and potassium oxide. In particular, the interaction with the structural promoter, alumina, can alter significantly the crystallography of the metallic iron surfaces formed during reduction. Since supported iron catalysts can contain much more alumina than normal for the industrial ammonia synthesis catalyst, any interaction between the iron oxide being reduced and the alumina support is much more easily observed. Some results, indicating unambiguously the effect of the interaction of iron with the alumina, will therefore be reviewed.

Wielers and co-workers[2] have investigated the reduction of alfa-FeOOH (goethite) deposited (25 wt% Fe) on alumina (Degussa) BRD, with a surface area of 100 $m^2\,g^{-1}$, by Mossbauer spectroscopy. To ascertain that neither slow transport of water through the highly porous alumina nor the small size of the supported iron oxide particles determined the course of reduction, the authors measured also a physical mixture of small goethite particles and the same alumina support. The surface area of the unsupported goethite was 403 $m^2\,g^{-1}$, which corresponds to a particle size of 3.5 nm (density 4.28 $g\,ml^{-1}$). In Fig. 5.1 the Mossbauer spectra of the fresh catalyst and the fresh physical mixture of goethite and alumina measured at temperatures of 300, 77, and 4.2 K are shown. At 4.2 K the spectrum of goethite was exhibited. Since the small goethite particles are superparamagnetic at 300 K, a doublet characteristic of high-spin Fe(III) was measured at this temperature. At 77 K, the spectra of goethite and of the high-spin Fe(III) were superimposed. From the temperature dependence of the resonant absorption spectrum, the size of the goethite particle can be estimated. For the alumina-supported goethite, a particle size of 8.5 nm was calculated. In the case of the unsupported goethite particles, a size of 2 to 3 nm was calculated, in excellent agreement with values derived from the surface area measurement.

The Mossbauer spectra of the supported goethite and the goethite in the physical mixture measured at 300 K after successively more severe reduction treatments with hydrogen are shown in Fig. 5.2. The unsupported goethite reacted at 673 K readily to form magnetite. The Mossbauer spectrum is consistent with the presence of large magnetite particles, which indicates severe sintering of the small goethite particles during reduction. Simple dehydration of the goethite had

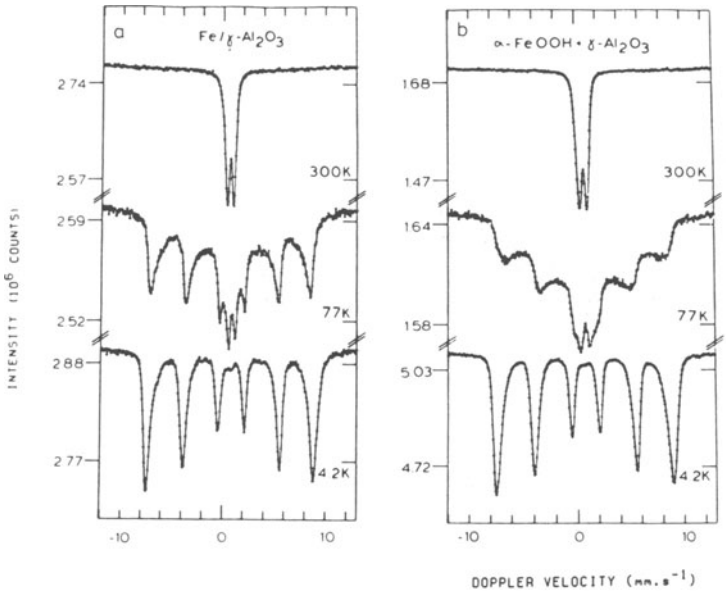

Figure 5.1. Mossbauer spectra of fresh alumina-supported iron catalyst and a physical mixture of geothite and alumina; spectra were measured at 300, 77, and 4.2 K.

led already to substantial sintering and calcination at 573 K caused the surface area to fall to 48 $m^2 g^{-1}$ (particle size 24 nm; density 5.24 g ml^{-1}). Reduction for 9 h at 873 K completed the reduction to metallic iron.

From Fig. 5.2 it is apparent that the reduction of goethite deposited on alumina proceeded in a rather different manner to that of unsupported goethite. Reduction at 673 K led to a strongly broadened spectrum of magnetite together with the spectrum consistent with a significant amount of residual Fe(III). Raising the reduction temperature led remarkably to a strong decrease of the spectrum due to magnetite. An intense Fe(II) spectrum was exhibited. Under conditions where, thermodynamically, the magnetite should be reduced to metallic iron, as shown in the case of the unsupported goethite, the supported magnetite reacted in the first instance to give Fe(II). Further reduction for 9 h at 873 K resulted slowly in the formation of metallic iron, though a significant amount of Fe(II) was still present.

The results of Wielers and co-workers[2] have shown that Fe(II) is stabilized by some interaction with alumina. The stabilization may be due to the formation of $FeAl_2O_4$ or, more probably, to an interaction between ferrous oxide and an alumina or iron(II) aluminate surface. Kock and co-workers[3] demonstrated the stabilization of Fe(II) by alumina using magnetic measurements. The authors studied the reduction of goethite (FeOOH), hematite (Fe_2O_3), a physical mix of FeOOH and alumina, and FeOOH deposited on alumina with carbon monoxide. They raised the temperature of their samples held in a flow of 5% carbon monoxide in helium, with a heating rate of 4.8 K min^{-1} up to a temperature of 770 K and

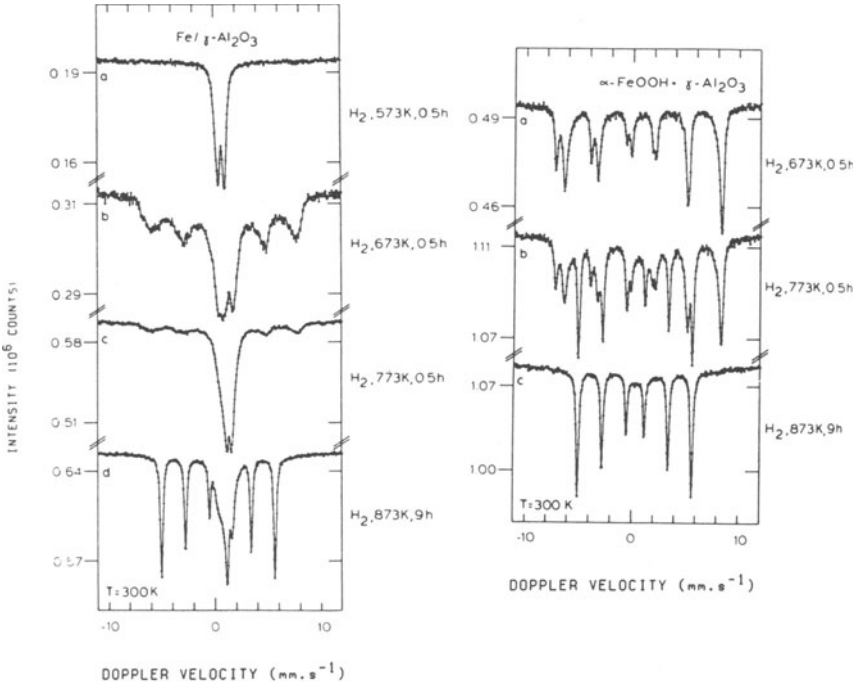

Figure 5.2. Mossbauer spectra of alumina-supported iron and physical mixture of goethite and alumina after increasingly severe thermal treatments.

subsequently decreased the temperature to 300 K at the same rate. Simultaneously the magnetization of the samples at a field strength of 0.52 MA m^{-1} (6500 Oe) was recorded. The Curie temperatures of the reduced samples were evaluated from the magnetization curves measured at decreasing temperatures. The Curie temperatures indicated that a considerable fraction of the unsupported iron oxides had been converted to iron carbide. The freshly reduced iron catalyzed the Boudouard reaction, namely, the disproportionation of carbon monoxide to carbon and carbon dioxide. The resulting carbon was responsible for the formation of iron carbide. A particularly high fraction of carbide was found in reduction of the physical mixture of goethite and alumina. Surprisingly, the supported iron oxide was reduced initially to a ferromagnetic compound (Fe_3O_4, magnetite), which subsequently was further reduced to a nonferromagnetic compound, FeO. Since the carbon monoxide was shown by analysis to be converted completely to carbon dioxide, no iron carbide was formed, in agreement with the magnetization-versus-temperature plot, which indicated the presence of mainly nonferromagnetic compounds.

In the first instance, the results of Kock and co-workers[3] have demonstrated the stability of iron(II) oxide (FeO) supported on alumina. Moreover, the formation of FeO on alumina apparently prevents further reaction to give iron carbide, even with carbon monoxide, which in the absence of alumina leads readily to carbide

formation. Graphite layers, which cover partially the surface of metal particles such as nickel and iron, are susceptible to rapid hydrogenation giving methane and some higher hydrocarbons.[4,5] However, when the metal surfaces are completely encapsulated by graphitic carbon, dissociation of hydrogen cannot proceed readily and the carbon skin is stable to hydrogenation. When small metal particles interact strongly with a support such as alumina, complete encapsulation by carbon does not proceed readily. Even a small fraction of bare metal surface is sufficient to bring about rapid removal of carbon by hydrogenation. The appreciable interaction between iron and the structural promoter, alumina, is therefore consistent with the observation that ammonia synthesis catalysts are not readily poisoned by carbon in contrast to unsupported iron specimens. Furthermore, iron catalysts, in which the iron particles are not bonded significantly to the alumina support, are not stable toward carbon poisoning.

Kock and co-workers[3] have also studied the effect of deposition of hydrated iron oxide onto magnesia. Earlier Boudart and co-workers[6-8] had studied extensively iron particles supported on magnesia; the catalysts investigated by Kock, however, had a much higher loading of iron, viz., 20 wt%. Kock and co-workers studied both magnesium hydroxycarbonate and magnesium oxide as a support to assess the effects of the evolution of carbon dioxide and water from the magnesium hydroxycarbonate supports. The magnetic properties were measured after increasingly severe reduction treatments on both catalysts. The reduction was performed with hydrogen. The magnetization first increased and subsequently decreased to a low value, which then rose slowly to the value expected for metallic iron. The intermediate fall in magnetization indicates unambiguously the formation of an FeO species before the final reaction to metallic iron proceeded. The FeO was stabilized by the magnesia support. It could not be established whether formation of a mixed (Fe, Mg) oxide, or the interaction of FeO with the magnesia surface, was the reason for the stabilization.

Strongin and Somorjai, in Chapter 4, described the effect of water on the interaction between iron oxide and alumina in the presence of hydrogen. Boellaard, Geus, and van der Kraan[9] used an alternative procedure to prepare alumina-supported iron catalysts to investigate the effect of water on the interaction of iron oxide with alumina. Finally divided $Fe(II)_2[Fe(III)(CN)_6]$ was deposited on the alumina by injection of an iron(II) acetate solution into a suspension of alumina (Degussa-C, BRD $100\,m^2\,g^{-1}$) in a solution of ammonium iron(III) cyanide. Oxidation of the product at about 400 °C resulted in decomposition of the cyanide complex with the formation of small iron(III) oxide (Fe_2O_3) particles on the alumina support. The size of the iron(III) oxide particles was about 30 nm. Since reduction of the anhydrous iron oxide releases much less water than that of the alumina-supported hydrated iron oxide investigated by Wielers and co-workers,[2] reduction of the catalyst prepared from the Fe(III) cyanide complex proceeded in the presence of a much lower partial pressure of water vapor. The Mossbauer spectra shown in Fig. 5.3 indicate that reduction of the iron oxide in the catalysts derived from ferric cyanide also led initially to magnetite that subsequently formed FeO, wustite, which in turn was reduced slowly to metallic iron. However, all of the reduction steps from ferric oxide to magnetite, wustite, and finally to metallic

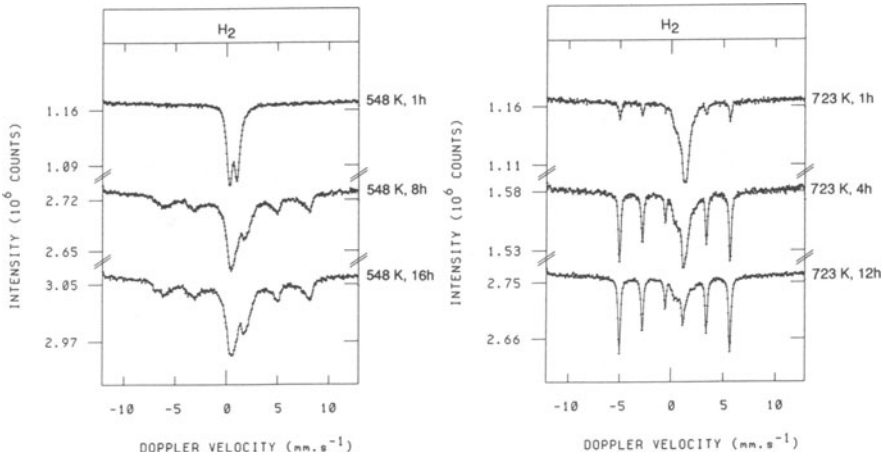

Figure 5.3. Mossbauer spectra of an alumina-supported iron oxide catalyst prepared from Fe(III) cyanide after different reduction treatments; during reduction the amount of water present is relatively small.

iron, are now seen at lower temperatures. The smaller effect imposed by the support will also be apparent in the infrared spectra of adsorbed carbon monoxide which will be presented later in the chapter.

It can be concluded from the above experimental results that the interaction of hydrated iron oxides with supports such as alumina greatly affects the course of the reduction process. An intermediate wustite (FeO) species is stabilized by the support. It is difficult to assess the extent to which stabilization depends on the formation of ferrous compounds, such as $Fe(II)Al_2O_4$ and [Mg, Fe(II)] oxide. However, the results obtained in the presence of relatively small amounts of water vapor suggest that wustite (FeO) species are strongly stabilized without the simultaneous formation of an appreciable amount of $Fe(II)Al_2O_4$.

Industrial ammonia synthesis catalysts are activated by hydrogen reduction of the oxide precursor, which contains a very high proportion of iron oxide and which is prepared by a fusion process. During the reduction process the water vapor content of the process gas is kept below 3000 ppm as mentioned by Gramatica and Pernicone in Chapter 6. To keep the water vapor content low, high gas hourly space velocities of the reduction gas are required. Scholten[9] investigated the effect of the space velocity by monitoring the weight loss of a 150 g sample of a singly promoted catalyst was reduced at 450 °C for 170 h and subsequently at 535 °C for 240 h, but at a higher space velocity of 2000 h^{-1}. The rate of weight loss after of 100 h^{-1}. At the end of the final reduction treatment, the catalyst was still losing weight at a rate of 0.1 mg oxygen per hour. A second identical sample of singly promoted catalyst was reduced at 450 °C for 170 h and subbsequently at 535 °C for 240 h, but at a higher space velocity of 2000 h^{-1}. The rate of weight loss after this second treatment indicated a release of oxygen of 0.01 mg oxygen per hour. The rate of adsorption of nitrogen at 200 °C was no less than a factor of 1000 higher for the catalyst reduced at the higher space velocity. The effect of the

removal of the last traces of oxygen on the adsorption of nitrogen is in complete agreement with Vink's observation[10,11] on the Fe(100) surface, to be discussed in the next section.

Usually, supported metal catalysts are produced by deposition of hydrated precursors onto the support. During calcination, the water is evolved and this can cause reaction between the active precursor and the support, which can lead to severe inhibition of the subsequent reduction. Moreover, the surface area of the support is generally much larger than that of the final active metal in the case of typical supported catalysts. Adsorbed water is fairly strongly bonded by the support and transport of water out of the pore system of typical supported catalysts will therefore be much more difficult than out of an industrial ammonia synthesis catalyst. The iron surface area per unit volume of a conventional ammonia synthesis catalyst is also large; the high iron content easily compensates for the relatively large size of the iron particles, i.e., about 40 nm in diameter. It is therefore difficult to produce supported catalysts that can compete with the overall activity of the conventional ammonia synthesis catalyst prepared by fusion. Nevertheless, Scholten[9] obtained results which suggested the presence of a considerable amount of water adsorbed onto the surface of his catalysts. The amount of water was estimated from the weight loss observed during evacuation of catalysts, which had been reduced for a prolonged period of time with highly pure hydrogen.

5.3. REACTIVITY OF OXYGEN ADSORBED ON IRON TOWARDS HYDROGEN

A model for the reduction procedure of the iron oxide component of the ammonia synthesis catalyst can be obtained using iron single crystals by exposing the clean iron surfaces to molecular oxygen, which thus establishes a layer of oxidized iron on the surface. Subsequently, the oxidized iron surface can be exposed to reducing gases, such as hydrogen or carbon monoxide at different temperatures. The decrease in the amount of oxygen at the iron surface during reduction can be established by Auger electron spectroscopy (AES) or by a combination of ellipsometry and Auger electron spectroscopy.

The sticking coefficient of oxygen is high with all of the crystallographic surfaces of the iron. Furthermore, even after the take-up of a monolayer of oxygen, the sticking coefficient still remains high. After low exposures to oxygen, LEED studies suggest the presence of a number of surface structures exhibiting a multiple mesh of the clean surface, which indicates ordered arrays of adsorbed oxygen atoms. After high exposures and at higher temperatures, formation of FeO can be seen. Vink and co-workers[11,12] studied the effect of thermal treatment on iron (100) surfaces, which had taken up more than a monolayer of oxygen atoms at 298 K and which displayed a disordered surface layer. The authors observed that iron oxide nucleates at 573 K and migrates into the bulk iron. A large proportion of the oxygen present at the surface is thus transported to the iron oxide crystallites, which extend into the metal (Fig. 5.4).

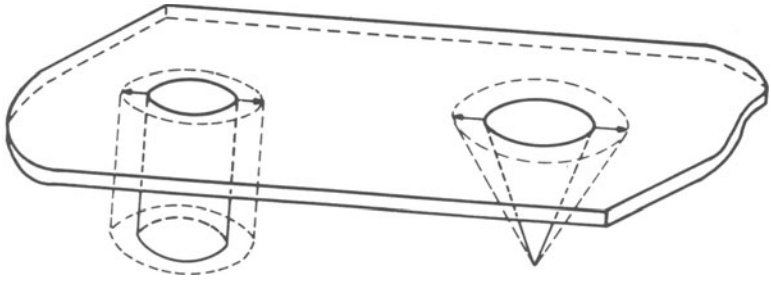

Figure 5.5. Effect of adsorption of oxygen on the electrical resistance of a vapor-deposited metallic iron film. Oxygen admitted at 77 K. Electrical resistance measured at 77 K both before (○) and after heating to 273 K (•) and also at 273 K (×).

This formation of iron oxide nuclei still leaves a monolayer of oxygen atoms at the surface. It is remarkable that the surface covered by the remaining monolayer of oxygen exhibits a very sharp (1 × 1) LEED pattern. The pattern is the same as that displayed by the clean surface. The ordering of the surface, however, seems to be more perfect as the LEED pattern is sharper than that of the clean surface. The presence of the monolayer of oxygen is evident from studies using AES. The remaining monolayer of oxygen atoms is indicative of high stability of the oxygen present at the surface. On subsequent exposure, the surface takes up further oxygen at 298 K, which again migrates to the iron oxide crystallites at 573 K, still leaving behind a monolayer of adsorbed oxygen atoms. The effect caused by nucleation of the iron oxide is evident from the fact that transport of oxygen from the surface proceeds more rapidly after the initial nucleation of the iron oxide.

Vink and co-workers made a highly important observation with the Fe(100) surface that has not been published. When the iron surface was completely free from oxygen, adsorption of nitrogen was observed to proceed readily at room temperature. In marked contrast, adsorption of molecular nitrogen at temperatures up to about 473 K is completely suppressed by only about 10% of a monolayer of oxygen atoms at the surface. The effect of oxygen therefore certainly does not arise through a simple site-blocking mechanism. It appears that the presence of some adsorbed oxygen atoms renders the (100) surface more rigid and thus prevents accommodation of nitrogen atoms between the iron surface atoms. A sharp LEED pattern is observed and is consistent with a higher rigidity of the surface. The strong poisoning effect of oxygen is also apparent in results obtained from commercial ammonia synthesis catalysts.

The extent of oxygen adsorption can be determined more accurately with vapor-deposited metal films, since multilayer adsorption is difficult to measure using AES. The interaction of a vapor-deposited iron film with oxygen after exposure to a dose of oxygen at 77 K and subsequently raising the temperature to 273 K is presented in Fig. 5.5.[15-17] The effect on the electrical resistance of the iron film indicates whether (1) chemisorption, (2) physical adsorption onto a chemisorbed layer, or (3) diffusion of oxygen into the bulk, is proceeding. It can be seen that at 77 K, about 2.5 monolayers of oxygen are taken up, and at room

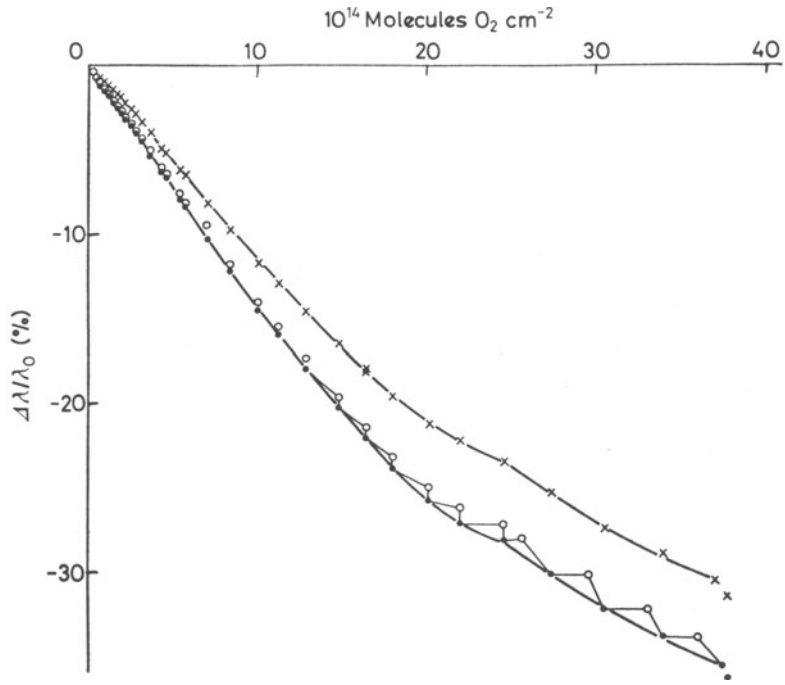

Figure 5.5. Effect of adsorption of oxygen on the electrical resistance of a vapor-deposited metallic iron film. Oxygen admitted at 77 K. Electrical resistance measured at 77 K both before (◦) and after heating to 273 K (•) and also at 273 K (×).

temperature this increases to a value of about 5 monolayers. The surface area of the iron film had been measured previously by physical adsorption of xenon. LEED measurements[13,14] are consistent with the presence of ferrous oxide on the oxidized iron surface. Apparently, not only is ferrous oxide stabilized by interaction with alumina, but metallic iron is also effective.

One of the main impurities in ammonia synthesis gas is water. Moreover, water is produced during reduction of the catalyst. Interaction of iron surfaces with water at temperatures from 150 to 250 K leads to the presence of adsorbed hydroxyl groups and hydrogen atoms on the surface. At higher temperatures, hydrogen desorbs leaving a monolayer of oxygen atoms at the surface. The interaction of defect-free iron surfaces with water is limited to the formation of a single monolayer of oxygen atoms. Disordered iron surfaces interact much more extensively with water. Simultaneous exposure to both water vapor and oxygen leads to a severe attack of the iron surface. The oxide layer recrystallizes readily at room temperature to form an iron oxide hydrate, FeOOH, which does not cover completely the underlying iron. This crystallization process leads to further exposure of bare iron and continuous oxidation results.

The experiments described by Vink and co-workers[10,16] on the reduction of iron surfaces covered by several monolayers of oxygen are very relevant to the

behavior of the industrial ammonia synthesis catalyst. It was observed that the reduction process was highly structure-sensitive. Oxygen present on the most closely packed iron surface, the iron (110) surface, could be removed smoothly and completely by reaction with hydrogen at fairly low pressures and at temperatures in excess of 430 K.[18] Though the (110) surface can be reduced very readily, its activity in the dissociative adsorption dinitrogen, which is the rate-determining step of the ammonia synthesis reaction, is the lowest of all the crystallographic surfaces of iron. The iron (100) surface is much more active in the dissociative adsorption of nitrogen. However, Vink and co-workers[10] observed that the monolayer of oxygen which remains after crystallization of iron oxide cannot be removed by treatment with hydrogen at pressures up to about 1 torr. Though the oxygen of the iron oxide crystallites contained within the bulk of the iron can easily be removed by reaction with hydrogen, the surface monolayer of oxygen remains. The rapid reaction of the oxygen of the iron oxide with hydrogen indicates that the dissociation of hydrogen on the surface must be a rapid process. The fact that the monolayer of oxygen atoms does not react readily with hydrogen must therefore be due to the thermodynamic stability of oxygen atoms adsorbed on the Fe(100) plane. It can therefore be expected that higher hydrogen pressures and elevated temperatures would lead ultimately to reduction of the adsorbed oxygen. However, the adsorbed oxygen could not be removed even at high temperatures at the limited pressures of hydrogen that could be established in the ultrahigh vacuum equipment employed for this work.

The experiments of Vink and co-workers which suggest high thermodynamic stability of a monolayer of oxygen on the Fe(100) surface are convincing, since the Fe(110) surface in the same apparatus was reduced readily by hydrogen. Nevertheless, the implications of the stability of the monolayer of oxygen atoms on the Fe(100) surface are so important, that Van Zoest *et al.*[11] repeated the experiment in another apparatus. They established the position of the adsorbed oxygen atoms accurately using low-energy ion scattering (LEIS) and the previous observations[10] were thus confirmed. The exact location of the oxygen adatoms was determined to be in the fourfold symmetrical sites of the (100) surface at a distance of 560 pm above the surface.

The thermodynamic stability of the monolayer of oxygen atoms on an iron surface fairly active in the adsorption of nitrogen is consistent with the observation that the presence of water at ppm levels in ammonia synthesis gas has a very severe effect on the activity of the technical catalyst. Nielsen, in Chapter 8, deals with the effect of water present in the synthesis gas at concentrations far below the thermodynamic level to bring about oxidation of bulk iron to magnetite. For example, at 700 K a H_2O/H_2 ratio of 0.15 is required to oxidize metallic iron to magnetite while water at a level of just 50 ppm is sufficient to decrease substantially the activity of the promoted iron catalyst. At low partial pressures of water, an adsorbed monolayer of oxygen atoms at those iron surfaces active in the dissociative adsorption of nitrogen is stable, and this accounts for the decrease in activity of the ammonia synthesis catalyst. Schlögl (Chapter 2) mentions that the iron-to-oxygen ratio at the surface of an industrial ammonia synthesis catalyst is 1.85 in dry hydrogen and 1.75 in wet hydrogen. Studies by XPS have indicated the presence

of a stable Fe(II) species in the presence of wet hydrogen. Scholten[9] reports that the free metallic iron surface area of ammonia synthesis catalysts increases at higher degrees of reduction. This also indicates that removal of oxygen present as a monolayer on iron surfaces, such as the Fe(100), proceeds only at very low partial pressures of water vapor.

5.4. ADSORPTION OF CARBON MONOXIDE ON IRON SURFACES

The most common method for the estimation of the surface area of a metallic phase in a supported catalyst is by measuring the extent of the hydrogen adsorption. With iron surfaces, however, the adsorption of hydrogen often does not proceed consistently. The free iron surface area is therefore usually calculated from the extent of adsorption of carbon monoxide, measured at 90 K. In contrast to adsorption of hydrogen, which has a low boiling point, physical adsorption of carbon monoxide by oxidic surfaces present in the catalysts is appreciable at 90 K. The extent of the adsorption is therefore measured twice; after the first measurement, the catalyst is evacuated at 195 K and the extent of adsorption is determined again. The amount of carbon monoxide chemisorbed by the iron surface is assumed to be the difference between the values obtained from the two adsorption isotherms.[19,20]

The amount of carbon monoxide that can be desorbed at 195 K is dependent upon the period of time of the evacuation and the rate of evacuation of the sample. Consequently, Scholten[9] used the value obtained from the adsorption isotherm of physically adsorbed nitrogen for subtraction from the isotherm representing the total adsorption of carbon monoxide. On different inert adsorbants, he determined the ratio of adsorption isotherms of physically adsorbed carbon monoxide and nitrogen to be 1.05.

Brunauer and Emmett determined the ratio of the chemisorbed carbon monoxide, calculated by a similar method to that described above, and the total nitrogen physically adsorbed in a monolayer on a reduced, nonpromoted, pure iron catalyst.[19,21,22] The ratio varied with the reduction treatment, especially the reduction temperature. Values ranging from 1.25 to 0.13 were observed. The lower ratios were found for catalysts reduced at higher temperatures. Zwietering and Westrik[23] measured similar ratios which were in good agreement with the values found by Emmett and co-workers, namely, 1.20 to 0.78. Again, the ratio was lowered when the reduction temperature was raised from 300 to 400 °C. The number of molecules of carbon monoxide adsorbed per cm^2 of iron surface is about 0.7×10^{15}. The number of surface atoms in the different crystallographic planes of iron is: Fe(110), 1.7×10^{15} cm^{-2}; Fe(100), 1.2×10^{15} cm^{-2}; Fe(111), 0.7×10^{15} cm^{-2}.

The number of iron atoms at the surface suggests a level of chemisorption of about one carbon monoxide molecule per two iron surface atoms. Taking into account the size of an adsorbed carbon monoxide molecule, which exhibits a diameter of about 0.3 nm, a coverage of about 1.0×10^{15} molecules per cm^2 is reasonable.

Experimental results on single crystals show that at temperatures below about 250 K, dissociative adsorption of carbon monoxide on the surface does not proceed. Molecular adsorption of carbon monoxide occurs on different sites, each showing different heats of adsorption.

Experiments on vapor-deposited iron films[15] also point to an extent of adsorption of carbon monoxide of about 1.0×10^{15} molecules per cm^2. For example, the effect of carbon monoxide on the electrical conductance of an iron film is represented in Fig. 5.6. When the level of adsorption reaches 0.7 to 1.0×10^{15} molecules per cm^2, the conductance is unaffected by further addition of carbon monoxide. It appears that the smaller ratios measured on iron catalysts after more severe reduction treatments arise from segregation of oxides to the iron surface. The oxides are present initially within the iron and migrate to the iron surface at high temperatures.

Scholten[9] determined the surface area of the alumina present in reduced ammonia synthesis catalysts. He established that alumina accounted for an appreciable fraction of the total surface area of the catalyst, approaching about 60%. Earlier in the chapter evidence was presented that Fe(II) can react with alumina to form iron (II) aluminate or it can dissolve into the alumina. There is evidence that carbon monoxide can be adsorbed onto the Fe(II) component present within the oxide surface. If this adsorption is strong, the determination of the free iron metallic surface may be inaccurate since a fraction of the oxidic surface may be responsible for adsorption of some of the carbon monoxide included in the calculation. Adsorption of carbon monoxide on the Fe(II) surface ions has indeed been demonstrated by infrared spectroscopy, but the adsorption is weak. Carbon monoxide adsorbed on Fe(II) ions can be removed readily, simply by evacuation at room temperature.

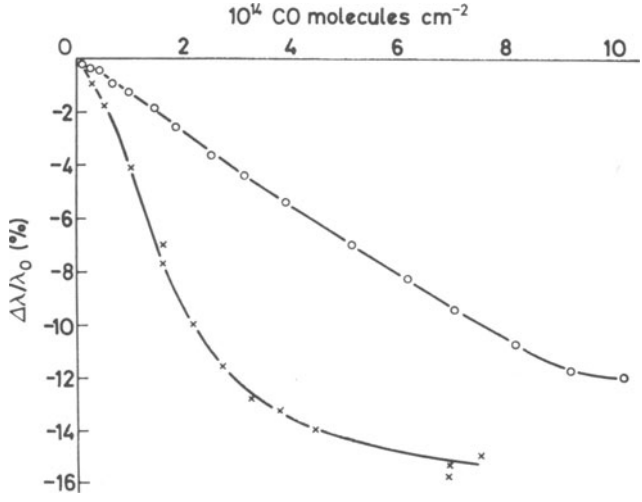

Figure 5.6. Effect of adsorption of carbon monoxide on the electrical conductance at 77 K of vapor-deposited iron films: (×) CO admitted at 273 K; (○) CO admitted at 77 K.

Wielers and co-workers[2] have investigated the infrared spectra of carbon monoxide adsorbed onto alumina-supported iron catalysts. The infrared adsorption spectrum of carbon monoxide adsorbed on an alumina-supported iron catalyst is represented in Fig. 5.7. In addition to maxima lying between 2010 and 2050 cm^{-1}, a peak at 2155 cm^{-1} is also seen. The effect of evacuation on the sample is shown in Fig. 5.8. It can be seen that the carbon monoxide adsorbed on the Fe(II) ions was removed by evacuation for 0.5 h at room temperature.

It is probable that evacuation at 195 K would also remove the carbon monoxide adsorbed on Fe(II) ions within the oxidic surface. However, in Scholten's procedure, the amount of carbon monoxide adsorbed physically on the catalyst is calculated from the extent of nitrogen adsorption at 90 K. The result is that the amount of carbon monoxide adsorbed on Fe(II) ions is also included in the calculation for the free metallic iron surface.

The strong inhibiting effect of water during the reduction of well-dispersed iron oxide phases on alumina surfaces is also apparent from the infrared spectrum of carbon monoxide adsorbed onto the reduced catalyst prepared from complex iron cyanides according to the above procedure of Boellaard and co-workers[9]. Despite the support, the size of the iron particles, and the loading of iron on the support all being essentially the same, the infrared spectrum of the adsorbed carbon monoxide is completely different. The absorption band at 2155 cm^{-1} is not seen, which indicates that Fe(II) is not present at the alumina surface when reduced in the presence of low partial pressures of water vapor. Rather than bands with frequencies above about 2000 cm^{-1}, bands at 1806, 1884, and 1984 cm^{-1} are observed (Fig. 5.9). Even at room temperature, disproportionation of carbon monoxide to carbon dioxide and carbon occurs, which is demonstrated by the presence of carbon dioxide adsorbed onto the alumina support. The infrared bands peaking at 1348 and 1598 cm^{-1} arise from carbon dioxide adsorbed on alumina.

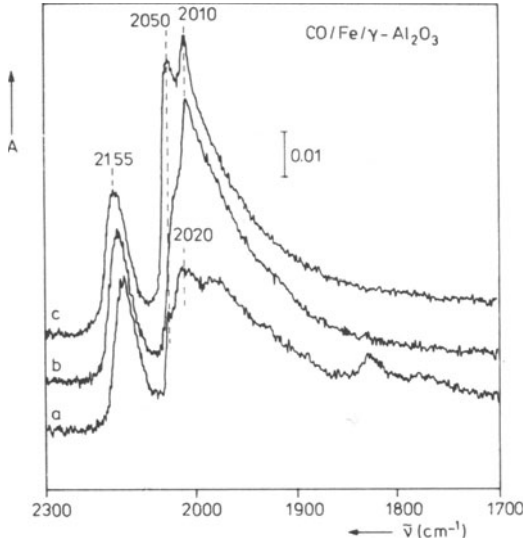

Figure 5.7. Infrared adsorption spectra of carbon monoxide adsorbed on an alumina-supported iron catalyst reduced under increasingly severe conditions: (a) reduced for 0.5 h at 773 K; (b) reduced for 0.5 h at 873 K; (c) reduced for 2 h at 873 K.

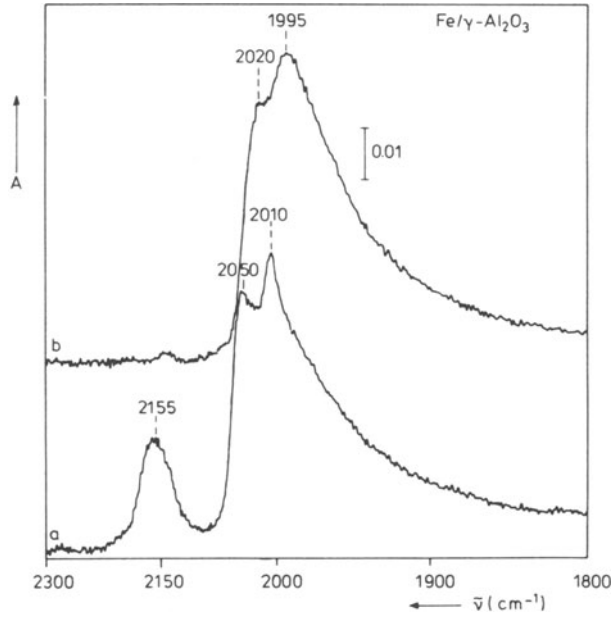

Figure 5.8. Infrared adsorption spectra of carbon monoxide on alumina-supported iron catalysts: (a) 13.3 kPa carbon monoxide dosed after reduction for 15 h at 873 K; (b) subsequently evacuated for 0.5 h at room temperature.

Interaction with the support is much stronger than the Fe(11) present in the alumina at the boundary layer, and this leads to a different shape and surface structure of the iron particles.

5.5. ADSORPTION OF HYDROGEN

Adsorption of hydrogen on supported iron catalysts still remains a controversial subject. Vapor-deposited films and single crystals with sputter-cleaned surfaces take up about half a monolayer of hydrogen readily at low pressures and temperatures well below 293 K. Supported catalysts, on the other hand, only adsorb hydrogen at temperatures above about 473 K. With an iron catalyst, singly promoted by alumina, Scholten[9] observed that the extent of hydrogen adsorption was about 0.7×10^{15} molecules per cm^2, a level which decreased continuously with increasing temperature. The extent of hydrogen adsorption is of the same order of magnitude as that of adsorption of carbon monoxide. With vapor-deposited metal films the extent of adsorption of hydrogen is slightly smaller than that of carbon monoxide. At 273 K and pressures of about 0.6 kPa, about 5×10^{14} molecules of hydrogen per cm^2 are adsorbed, as compared to about 7×10^{14} molecules of carbon monoxide per cm^2.

Topsoe and co-workers[24] have reported that for two ammonia synthesis catalysts containing iron particles of 6 and 40–60 nm, an equal extent of adsorption

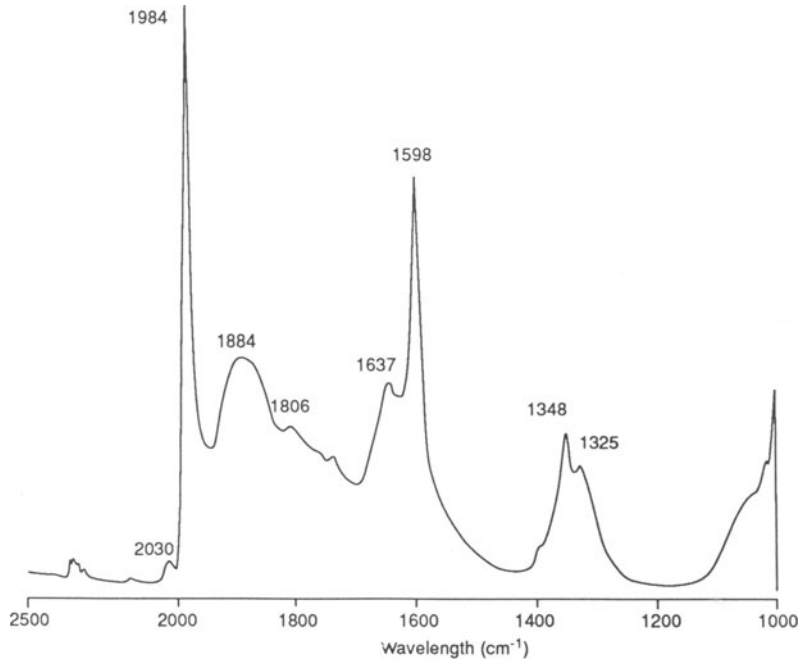

Figure 5.9. Infrared spectra of carbon monoxide adsorbed on alumina-supported iron catalysts prepared from complex iron cyanides. Catalysts reduced at 723 K. 13.3 KPa carbon monoxide dosed at room temperature. Spectra measured immediately after dosing with carbon monoxide.

of hydrogen and of carbon monoxide at 195 and 300 K was also observed. However, magnesia-supported iron particles, with dimensions from 1 to 12 nm, exhibited an adsorption of hydrogen at 195 and 300 K which was at most only 10% of the extent of carbon monoxide adsorption. At 473 K, iron particles larger than about 4 nm supported on magnesia exhibited an adsorption of hydrogen about equal to that of carbon monoxide. Extensive unpublished data from one of the authors (JWG) on small iron particles supported on silica and alumina also demonstrated the small extent of adsorption of hydrogen molecules at room temperature and a considerable increase in the level of hydrogen adsorption at the higher temperature of 473 K.

The low extent of hydrogen adsorption is attributed to the stability of a monolayer of oxygen atoms on most of the crystallographic surfaces of iron. The only oxygen atoms which can be removed easily by hydrogen reduction are those adsorbed on the closely packed Fe(110) surface. The reaction of oxygen adsorbed on most of the other crystallographic surfaces of iron requires extremely low H_2O/H_2 ratios. In the particular case of supported catalysts containing narrow pores and a relatively large surface area of support, a sufficiently low water-vapor pressure cannot be established within a reasonable period of time. It is therefore assumed that hydrogen adsorption on an iron surface covered by a monolayer of oxygen atoms is an activated process. The increase in the extent of hydrogen

adsorption with the size of the iron particles is due to the presence of more Fe(110) surface from which the oxygen can be removed more easily.

5.6. ADSORPTION OF NITROGEN ON IRON CATALYSTS

Emmett and co-workers[25] determined the activation energy of the adsorption of nitrogen on differently promoted iron catalysts, viz., a doubly promoted, a singly promoted, and a catalyst which did not contain promoters. The doubly promoted catalyst showed activation energies ranging from 60 to 67 kJ mol^{-1}. From adsorption isotherms measured at different temperatures, a heat of adsorption of nitrogen of about 150 kJ mol^{-1} was calculated for both the singly and doubly promoted catalysts. The authors also measured the rate of ammonia synthesis over the three catalysts. The authors were able to show that the rate of ammonia synthesis over the three catalysts was roughly equal to that of the rate of nitrogen chemisorption. The activities of the three catalysts at 400 °C and 1 atm pressure showed the same order as the initial rates of nitrogen adsorption at 300–450 °C and the same order as the extent of nitrogen adsorption at both 300–450 °C and 184 K. The authors made the important observation that the doubly promoted catalyst was much more active at a pressure of 100 atm than the singly promoted catalyst.

In later work Scholten[9] performed measurements on highly reduced, singly promoted iron catalysts using a gravimetric procedure. This author observed an activation energy rising with surface coverage from about 41 to 96 kJ mol^{-1}. At surface coverages from 0.25 to 0.70 of a monolayer the activation energy was 96 kJ mol^{-1}. From the rate of desorption measured at different temperatures, an activation energy for the desorption of nitrogen of about 210 to 125 kJ mol^{-1} was calculated. The activation energy for the desorption of nitrogen fell with increasing nitrogen coverage. The heat of adsorption of nitrogen calculated from the activation energies of adsorption and desorption fell from 188 kJ mol^{-1} at low coverages to 46 kJ mol^{-1} at high coverages. With catalysts that had been reduced less extensively, the activation energy for adsorption rose more rapidly with nitrogen coverage and did not show the "steady state" level of 96 kJ mol^{-1}. The final value was about 121 kJ mol^{-1}. The heat of adsorption was also calculated from the activation energies of adsorption and desorption and ranged from about 210 to about 21 kJ mol^{-1}.

In Chapter 3, Ertl reported values for the activation energies of adsorption of atomic nitrogen on iron single-crystalline surfaces. In the limit of zero coverage, the activation energy was 27 kJ mol^{-1} for the Fe(110) surface, 21 kJ mol^{-1} for the Fe(100) surface, and essentially zero for the Fe(111) surfaces. The activation energies for the single crystals also increased with the surface coverage in a similar manner to the polycrystalline catalysts. The initial adsorption energies were 109, 100, and 88 kJ mol^{-1} for Fe(110), Fe(100), and Fe(111) surfaces, respectively. While the activation energies of adsorption at low coverages on the single crystals are within the same range as those measured on actual ammonia synthesis catalysts, the initial heats of adsorption are considerably lower than observed with the catalysts.

The uptake of nitrogen at 273 K by vapor-deposited iron films proceeds fairly rapidly.[15] The final extent of adsorption is 1.3×10^{14} molecules per cm^2 as can be seen from Fig. 5.10. A coverage of up to 20% can be calculated from the extent of adsorption of carbon monoxide. Scholten[9] obtained a final coverage of about 8% at 300 K on a singly promoted catalyst which had been reduced extensively. Adsorption of nitrogen proceeds much more readily on atomically rough surfaces. Since these surfaces are much less abundant with catalysts reduced extensively at high temperatures, the difference in the final coverage by nitrogen is reasonable.

5.7. REACTION MODELING ON THE BASIS OF THE PUBLISHED ADSORPTION/DESORPTION KINETICS OBTAINED BOTH ON SINGLE CRYSTALS AND ON SINGLY AND DOUBLY PROMOTED CATALYSTS

5.7.1. The Energetics

The potential energy diagram shown in Fig. 5.11 is the compilation of a series of experiments conducted by Ertl and co-workers for the determination of the detailed energetics of adsorption, desorption, and surface reaction in ammonia synthesis.[26] The energetics have been determined under ultrahigh vacuum by the techniques of temperature-programmed desorption and by temperature-dependent Auger electron spectroscopy on iron (111), (110), and (100) single crystals at, or near, the limit of zero coverage, conditions which are probably considerably different from those obtaining during ammonia synthesis. It is reasonable therefore to question their relevance to the industrial process, which is carried out at 100 bar and 720 K on a doubly promoted (K_2O/Al_2O_3) polycrystalline iron catalyst; the extrapolation in pressure alone is roughly 14–15 orders of magnitude.

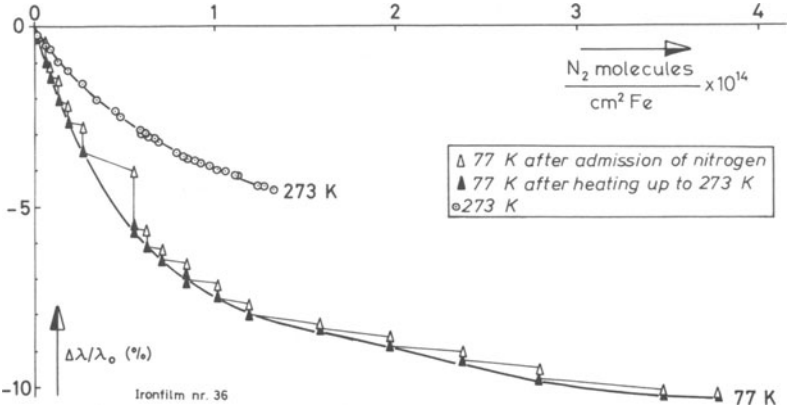

Figure 5.10. Adsorption of nitrogen on vapor-deposited iron film. Effect on the electrical conductance measured at 77 and 273 K. Nitrogen admitted at 77 K. Conductance and extent of adsorption measured at 77 K both before and after heating to 273 K.

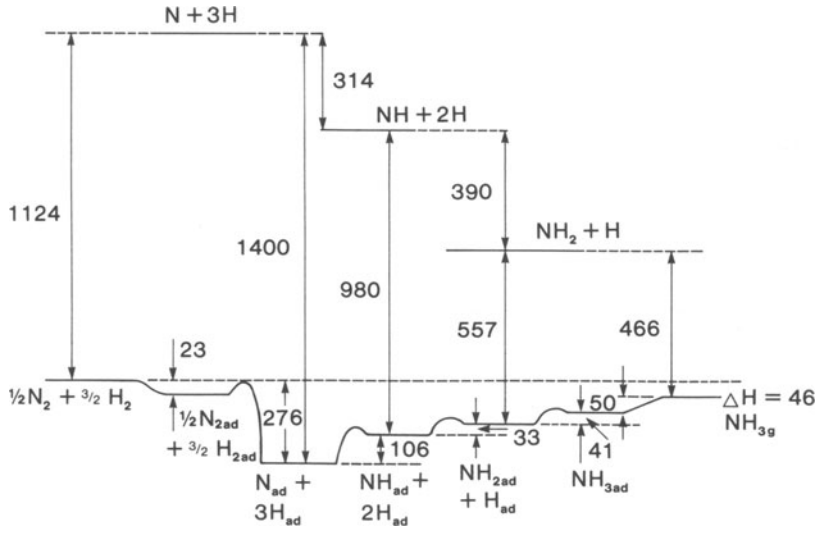

Figure 5.11. Potential energy diagram for ammonia synthesis on a promoted iron catalyst.

This extrapolation has been carried out, by calculation, using a computer program.[27] The program solves the sets of nonlinear equations which are implied in a statement of the elementary reactions of which the potential energy diagram is comprised, the rate constants of the elementary reactions necessarily being expressed in Arrhenius terms. The eight reversible elementary reactions which constitute the mechanism of ammonia synthesis are listed in Table 5.1. The activation energies of each of the forward and reverse reactions listed in Table 5.1 are a re-expression of the potential energy diagram of Fig. 5.11 in elementary reaction terms for the synthesis of ammonia on a doubly promoted (K_2O/Al_2O_3) iron catalyst. This statement will be verified below.

TABLE 5.1. Energetics of the Elementary Reactions Derived from the Potential Energy Diagram (Fig. 5.1) of Ammonia Synthesis[a]

E_f (kJ mol^{-1})		E_r (kJ mol^{-1})	Eq.
0	$N_2 + Fe \rightleftarrows N_{2(a)}$	46	(5.1)
46	$N_{2(a)} + Fe \rightleftarrows N_{(a)} + N_{(a)}$	226	(5.2)
0	$H_2 + Fe \rightleftarrows H_{2(a)}$	0	(5.3)
0	$H_{2(a)} + Fe \rightleftarrows H_{(a)} + H_{(a)}$	109	(5.4)
126	$H_{(a)} + N_{(a)} \rightleftarrows NH_{(a)} + Fe$	20.9	(5.5)
54	$H_{(a)} + NH_{(a)} \rightleftarrows NH_{2(a)} + Fe$	20.9	(5.6)
62.7	$H_{(a)} + NH_{2(a)} \rightleftarrows NH_{3(a)} + Fe$	20.9	(5.7)
50.2	$NH_{3(a)} \rightleftarrows NH_3 + Fe$	0	(5.8)

[a] The subscript (a) refers to an adsorbed component; E_f and E_r are the activation energies of the forward and reverse reactions.

The activation energy ($E_{-5.1}$) for the desorption of the nitrogen held in the molecular precursor state is set at 46 kJ mol^{-1}, the value determined by Ertl and co-workers for the desorption of molecular nitrogen from potassium-promoted Fe(111)[28] and potassium-promoted Fe(100).[29] The activation energy for the dissociation of the molecularly held nitrogen precursor state ($E_{5.2}$) is also set at 46 kJ mol^{-1}, producing a net activation energy of zero for dissociative adsorption of nitrogen—the value found for nitrogen adsorption for the three low-index faces of iron promoted by potassium.[30] The activation energy for the desorption of atomically held nitrogen has been determined by Ertl and co-workers[31] using temperature-programmed desorption and was found to be 226 kJ mol^{-1}. This value is therefore assigned to $E_{-5.2}$.

Reactions (5.3) and (5.4) describe the overall dissociative adsorption of hydrogen. The activation energy for desorption of atomic hydrogen ($E_{-5.4}$) is 109 kJ mol^{-1}, (32) having zero activation energy to dissociative adsorption ($E_{5.3}E_{5.4}$).

From the energetics of reactions (5.1)-(5.4) listed in Table 5.1, the potential energy minimum for one adsorbed nitrogen atom (113 kJ mol^{-1}) and three hydrogen atoms (163 kJ mol^{-1}) is 276 mol^{-1}. This is the energy minimum shown in Fig. 5.11, and also corresponds to the value reported by Ertl.[26,30]

The subsequent activation energies of the surface hydrogenation steps [reactions (5.5), (5.6), and (5.7)] are predetermined by the shape of the reactant and product parts of the potential energy diagram. At the product end of the potential, the overall reaction is exothermic by 46 kJ mol^{-1},[33] and the desorption activation energy of ammonia from Fe(111) is 50 kJ mol^{-1},[34] which is the activation energy for reaction (5.8) ($E_{5.8}$) of Table 5.1.

Adsorbed ammonia therefore has a potential energy of 96 kJ mol^{-1} below zero and this state has to be linked to that of the adsorbed nitrogen and three hydrogen atoms with an energy of 276 kJ mol^{-1} below zero. The reactions (5.6) and (5.7) are endothermic by 33 and 41 kJ mol^{-1}, respectively ($E_{5.6}$-$E_{-5.6}$ and $E_{5.7}$-$E_{-5.7}$ of Table 5.1), values which are identical to those published by Ertl in his potential energy diagram.[26] The reverse reactions—the dehydrogenation steps, $E_{-5.6}$, $E_{-5.7}$ (and $E_{-5.5}$)—are all given nominal activation energies of 21 kJ mol^{-1}, a value which has not been specified by Ertl even though indicated in the published potential energy diagram.[26] Since the activation energy of the dehydrogenation reaction of the adsorbed NH species has been given a value of 21 kJ mol^{-1} ($E_{-5.5}$), the activation energy for the addition of an adsorbed hydrogen atom to an adsorbed nitrogen atom ($E_{5.5}$) must be 126 kJ mol^{-1} to complete the potential energy diagram.

Therefore the energetics listed in Table 5.1 are the exact re-expression, in elementary reaction terms, of the potential energy diagram published by Ertl[26] for ammonia synthesis.

5.7.2. The Values of the Preexponential Terms

Although it appears to be a statement of the obvious, it is important to note that the rates and the net activation energies predicted by the energetics listed in Table 5.1 depend critically on the values assigned to the preexponential terms of the forward and reverse rate constants of the eight reversible reactions. Transition

state theory provides an extremely useful formalism for the evaluation of preexponential terms, allowing an explicit statement to be made of the assumptions involved in the calculation. This will now be outlined.

5.7.2.1. The Desorption Reaction Preexponential

The reactions listed in Table 5.1 (adsorption, surface reaction, and desorption) are bimolecular (adsorption and surface reaction) or unimolecular (desorption). In transition state theory the rate of a gas-phase unimolecular reaction

$$AS \rightarrow A + S \tag{5.9}$$

is given by

$$\text{Rate} = \frac{kT}{h}\frac{q^{\circ *}_{AS}}{q^{\circ}_{AS}} C_{AS}\, e^{-E^*/RT} \tag{5.10}$$

The units of the rate in Eq. (5.10) are number of species per unit volume per second, since the partition functions ($q^{\circ *}_{AS}$ and q°_{AS}) and the concentrations (C_{AS}) are in units of number per unit volume; h (Planck's constant) has units of erg seconds, k (Boltzmann's constant) has units of ergs per degree, and T is the absolute temperature.

The same equation applies for a unimolecular surface reaction (desorption), except that now the units of rate are number of species per cm^2 per second since both the partition functions and the surface concentrations are in units of number per cm^2. Changing to molar units, the C and q quantities are divided by Avogadro's number, N, so that the rate of desorption is now given by

$$\text{Rate of desorption} = \frac{kT}{h}\frac{q^{\circ *}_{AS}}{q^{\circ}_{AS}} \rho_{AS}\, e^{-E^*/RT} \qquad (\text{mol cm}^{-2}\,\text{s}^{-1}) \tag{5.11}$$

where ρ_{AS} is the surface density in units of mol cm^{-2}. The partition functions $q^{\circ *}_{AS}$ and q°_{AS} differ only in respect of one vibrational degree of freedom which, in the activated complex AS^*, is assumed to be a translation in the reaction coordinate. They therefore cancel, so that the preexponential term for a desorption is given by kT/h ($\sim 10^{13}\,s^{-1}$) except in the specific circumstance where it has been determined to be otherwise (*vide infra*).

5.7.2.2. The Bimolecular Surface Reaction Preexponential

Calculation of the preexponential term of a bimolecular surface reaction is also carried out by analogy with the gas-phase reaction. The rate of the bimolecular gas-phase reaction

$$A + B \rightleftarrows AB \tag{5.12}$$

is given by

$$\text{Rate} = \frac{kT}{h}\frac{q^{\circ *}_{AB}}{q^{\circ}_{A} q^{\circ}_{B}} C_A C_B\, e^{-E^*/RT} \qquad (\text{number of species per unit volume per second}) \tag{5.13}$$

[The units of the partition functions and concentrations are number of species per unit volume in Eq. (5.13).] For a surface bimolecular reaction these units became number of species per cm^2, so that converting Eq. (5.13) to molar units yields

$$\text{Rate} = N\frac{kT}{h}\frac{q^{\circ *}_{AB}}{q^{\circ}_{A}q^{\circ}_{B}}\rho_A\rho_B\, e^{-E^*/RT} \qquad (\text{mol cm}^{-2}\,\text{s}^{-1}) \tag{5.14}$$

the ρ terms again being surface densities with units of mol cm^{-2}. The surface partition functions can be factored into their translational, vibrational, and rotational components such that

$$q^{\circ}_i = q^{\circ}_{i\,(\text{trans})}q^{\circ}_{i\,(\text{vib})}q^{\circ}_{i\,(\text{rot})}$$

since $q^{\circ}_{i\,(\text{trans})} = \sum_i g_i \exp(-E_{i\,(\text{trans})}/kT)$ where g_i is the degeneracy of the ith state.

5.7.2.2a. Bimolecular Surface Reaction between Fixed Adsorbates Producing a Fixed Transition State. For the reaction between fixed adsorbates leading to a fixed intermediate, $E^{\circ}_{i\,(\text{trans})}$ is zero and $q_{i\,(\text{trans})}$ reduces to its degeneracy, i.e.,

$$q_{i\,(\text{trans})} = \sum_i g_i \text{ (the degeneracy of the } i\text{th state)}$$

$$= N_s \text{ [the number of surface sites cm}^{-2}\ (\sim 10^{15} \text{ sites cm}^{-2})]$$

The rate of a bimolecular surface reaction can now be expressed in the form

$$\text{Rate} = \frac{N}{N_s}\frac{kT}{h}\left(\frac{q^{\circ *}_{AB\,(\text{vib})}q^{\circ *}_{AB\,(\text{rot})}}{q^{\circ}_{A\,(\text{vib})}q^{\circ}_{A\,(\text{rot})}q^{\circ}_{B\,(\text{vib})}q^{\circ}_{B\,(\text{rot})}}\right)\rho_A\rho_B\, e^{-E^*/RT} \tag{5.15}$$

Since the vibrational and rotational partition functions of the transition state complex and of the reactants are approximately the same, they can be cancelled, so the bimolecular surface A-factor (A_{BS}) now becomes

$$A_{BS} = \frac{N}{N_s}\frac{kT}{h} \cong 10^{21}$$

The reactions in Table 5.1 which probably involve a fixed adsorbate and intermediate are:

1. The recombination of the nitrogen atoms [reaction (−5.2)].
2. The dehydrogenation of the NH species [reaction (−5.5)], the NH species probably being immobile due to its high heat of adsorption.

5.7.2.2b. Bimolecular Surface Reaction between Mobile Adsorbates Producing a Mobile Transition State. For reactions involving mobile adsorbates and intermediates, such as the hydrogen atom recombination [reaction (−5.4)] and the hydrogenation of the NH_2 species [reaction (5.7)], the rate of the bimolecular surface reaction is given by

$$\text{Rate} = \frac{NkT}{h}\left\{\frac{q^{\circ *2}_{AB\,(\text{trans})}q^{\circ *}_{AB\,(\text{vib})}q^{\circ *}_{AB\,(\text{rot})}}{q^{\circ 2}_{A\,(\text{trans})}q^{\circ 2}_{B\,(\text{trans})}q^{\circ}_{A\,(\text{vib})}q^{\circ}_{A\,(\text{rot})}q^{\circ}_{B\,(\text{vib})}q^{\circ}_{B\,(\text{rot})}}\right\}\rho_A\rho_B\, e^{-E^*/RT} \tag{5.16}$$

in which $q^2_{\text{trans}} = 2\pi mkT/h^2 \cong 10^{16}$.

Again, cancelling the contributions of the vibrational and rotational partition functions, the bimolecular surface reaction A-factor A_{BS} now becomes

$$A_{BS} = N\frac{kT}{h(2\pi mkT/h^2)} \cong 10^{21}$$

5.7.2.2c. Bimolecular Surface Reaction between One Fixed and One Mobile Adsorbate Producing Either a Mobile or Fixed Transition State. Two other types of bimolecular surface reaction can occur in the elementary reactions listed in Table 5.1. These are:

1. Reaction between a mobile adsorbate and a fixed adsorbate leading to a fixed intermediate, e.g., reaction (5.2) ($N_{2(a)} + Fe \rightarrow N_{(a)} + N_{(a)}$) and reaction (5.5) ($H_{(a)} + N_{(a)} \rightarrow NH_{(a)} + Fe$).
2. Reaction between a mobile adsorbate and a fixed adsorbate leading to a mobile intermediate, e.g., reaction (5.4) ($H_{2(a)} + Fe \rightarrow H_{(a)} + H_{(a)}$). For the former the bimolecular surface A-factor is given by

$$A_{BS} = N\frac{kT}{hq^{\circ 2}_{A\,(trans)}} \tag{5.17}$$

$$= N\frac{kT}{h(2\pi mkT/h^2)} \tag{5.18}$$

$$\cong 10^{21}$$

and for the latter case the A-factor is given by

$$A_{BS} = N\frac{kT}{h}\frac{q^{\circ *2}_{AB\,(trans)}}{N_s q^{\circ 2}_{A\,(trans)}} \tag{5.19}$$

$$= \frac{N}{N_s}\frac{kT}{h} \tag{5.20}$$

$$\cong 10^{21}$$

5.7.2.3. The Values of the Preexponential Terms of the Eight Elementary Reactions Involved in Ammonia Synthesis (Table 5.2)

Therefore, as a result of the derivations outlined in Sections 5.7.2.2a to 5.7.2.2c the values of all the bimolecular surface reaction A-factors listed in Table 5.2 are 10^{21}, with the exception of the specific instances where they have been determined experimentally to be otherwise. The A-factor values listed in Table 5.2 are those used in the calculation of the rates of ammonia synthesis at both 100 and 107 bar.

The A-factors which differ significantly from the predicted values are those for dissociative nitrogen adsorption [reactions (5.1) and (5.2)] and for ammonia desorption. The initial sticking probability for nitrogen adsorbed into the molecularly held precursor state was determined by Ertl and co-workers to be

TABLE 5.2. Values of the A-Factors for the Elementary Reactions Involved in Ammonia Synthesis

$\log_{10}[A$-factor (forward)]	Reaction	$\log_{10}[A$-factor (reverse)]	
11.0	$N_2 + Fe \rightleftarrows N_{2(a)}$	10.0	(5.1)
15.0	$N_{2(a)} + Fe \rightleftarrows N_{(a)} + N_{(a)}$	21.0	(5.2)
13.0	$H_2 + Fe \rightleftarrows H_{2(a)}$	13.0	(5.3)
21.0	$H_{2(a)} + Fe \rightleftarrows H_{(a)} + H_{(a)}$	21.0	(5.4)
20.8	$H_{(a)} + N_{(a)} \rightleftarrows NH_{(a)} + Fe$	21.0	(5.5)
20.7	$H_{(a)} + NH_{(a)} \rightleftarrows NH_{2(a)} + Fe$	21.0	(5.6)
21.6	$H_{(a)} + NH_{2(a)} \rightleftarrows NH_{3(a)} + Fe$	21.0	(5.7)
13.0	$NH_{3(a)} \rightleftarrows NH_3 + Fe$	12.0	(5.8)

10^{-2} [28] (a value derived from the adsorption isotherms recorded via the work function change), and so $A_{5.1}$ has a value of 10^{11} and not 10^{13}. The desorption A-factor from this molecularly held state is given the value of $10^{10}\ s^{-1}$, a value assigned to it by Ertl and co-workers[35] on the assumption that the value of the preexponential term for desorption from the promoted state would be the same as that determined for the unpromoted state.[28].

The preexponential term for the dissociation of nitrogen held in the molecular precursor state ($A_{5.2}$) is 10^{-6} below the "theoretical" value of 10^{21}. This is in accord with the measured, extremely low sticking probability of atomic nitrogen.[28,35] The initial sticking probability of ammonia on an Fe(111) surface has been measured by Ertl and co-workers[34] to be 0.1, and so the A-factor for the adsorption of ammonia ($A_{-5.8}$) has been given a value of 10^{12}.

The preexponential terms $A_{5.5}$, $A_{5.6}$, and $A_{5.7}$ have all been given values which differ slightly from 10^{21}, so that the model accurately reflects the overall entropy change of the reaction.

Taken in combination, the values shown for the activation energies and A-factors in Tables 5.1 and 5.2 are the exact expression of the kinetics and mechanism of ammonia synthesis on a potassium-promoted Fe(111) surface derived in a considerable body of work by Ertl and co-workers.[26,28-32,34-37] It has been suggested that this system is an exact model for the synthesis of ammonia on a doubly promoted (K_2O/Al_2O_3) iron catalyst. If this is true, the kinetics therefore ought to be able to predict the actual rates of ammonia synthesis under conditions of temperature (~720 K) and pressure (~100 bar) at which ammonia is synthesized industrially. As outlined previously, the accuracy of this prediction (and necessarily the validity of the thesis) has been evaluated using a computer program in which sets of the nonlinear equations implied in the elementary reactions of Tables 5.1 and 5.2 are solved. The program accepts, as input, statements of these elementary reactions together with their Arrhenius parameters, from which it then sets up mass balance equations for each of the components (gas phase and surface). It then solves these equations by Newton–Raphson iteration, a convergent solution being deemed to have occurred when the sum of the squares of the residuals is less than a preset, very small value (usually taken to be 10^{-20}).

The program also requires additional inputs, namely, the reaction pressure, the inlet gas composition, flow rates at given reaction temperatures, the free gas volume, the weight of catalyst, and the surface area of the catalyst. This latter was taken to be $10\,m^2\,g^{-1}$, a value typical of doubly promoted iron catalysts in the active state. The total area of the catalyst is subdivided in sites of 10 $Å^2$ dimension of which 15% are taken to be clean iron on which the hydrogen and nitrogen are assumed to adsorb competitively.

The reasons for the selection of the value of 15% of the total number of surface sites being clean iron and for the concept of competitive adsorption of hydrogen and nitrogen are again to be found in the work of Ertl and co-workers.[36,37] Using X-ray photoelectron spectroscopy Ertl and co-workers[36] showed that on a reduced commercial catalyst from BASF, 15 at% of the surface consisted of free metallic iron on which the presence of atomic hydrogen inhibited the rate of dissociative nitrogen chemisorption. The ultimate steady-state coverage of the surface by hydrogen and nitrogen atoms predicted by the program, however, depends solely on the kinetics of their chemisorption and of their removal by reaction.

5.7.3. The Prediction

5.7.3.1. Predicted Reaction Rates

Under the conditions of 720 K, 107 bar, and with a gas hourly space velocity (GHSV) of 16,000 h^{-1}, the exit concentration of ammonia predicted by the kinetics of the potential energy diagram of Fig. 5.11 is 1.7%. The experimentally determined value is 13.2%.[38] This agreement is remarkably good, considering all the parameters involved and the assumptions made. A minor adjustment of one of the preexponential terms or activation energies could well result in complete agreement.

5.7.3.2. Predicted Overall Activation Energy

A further test of the model is in its prediction of the value of the net activation energy of the ammonia synthesis reaction. This is done simply by increasing the value of the GHSV by a factor of 10^2 and repeating the calculation at temperatures of 720 and 680 K. The predicted exit concentrations of ammonia become 0.145% and 0.079%, from which an overall activation energy of 62 kJ mol^{-1} is obtained. This value is reasonably close to that (76 kJ mol^{-1}) determined by Nielsen[39] from analysis of his rate data obtained near equilibrium using the Temkin–Pyzhev equation,[40] and to that (81 kJ mol^{-1}) obtained by Somorjai and co-workers[41] on an iron single crystal [Fe(111)] at 20 bar. Again the agreement is remarkable.

5.7.3.3. Predicted Surface Coverages

Since the program calculates the steady-state concentrations of all the species involved (gas phase and surface) it can therefore be used to predict the surface composition of the operating catalyst. The predicted surface composition at 720 K, 107 bar, and a GHSV of 16,000 h^{-1} is shown in Table 5.3.

TABLE 5.3. Surface Composition

Adsorbed Hydrogen Atoms ($H_{(a)}$) 1.8×10^{13} atom cm^{-2}	Adsorbed Nitrogen Molecules ($N_{2(a)}$) 2.3×10^{12} molecule cm^{-2}
Adsorbed Nitrogen Atoms ($N_{(a)}$) 1.3×10^{14} atom cm^{-2}	Adsorbed Nitrogen Hydride ($NH_{(a)}$) 2.7×10^{12} species cm^{-2}

The predicted nitrogen atom coverages (1.3×10^{14} atom cm^{-2}) are, again, in remarkably good agreement with those determined experimentally.[37] At 580 K, under partial pressure of 150 torr N_2, 450 torr H_2, and 6 torr NH_3 (equilibrium conditions), the nitrogen atom coverage of an iron single crystal [Fe(111)] was 7×10^{13} atom cm^{-2}.

5.7.4. Alternative Models

5.7.4.1. Lowered Nitrogen Atom Recombination Activation Energy and Preexponential

In a series of papers[42-44] Stoltze and Norskov have propounded an alternative model to the one described by the combination of Tables 5.1 and 5.2 above, differing in the values of only one of the parameters in each of the tables. The only parameters which are changed are the preexponential term and the activation energy for the desorption of nitrogen atoms to give nitrogen molecules. The rationale for changing these parameters is that, since the sticking coefficient for the adsorption of nitrogen atoms is very low ($\sim 10^{-6}$), the preexponential for the desorption reaction must also be equally low.[42] The nitrogen atom desorption activation energy had been determined by Ertl and co-workers[31] by temperature-programmed desorption. This was done by solving the Redhead equation[45,46] at the peak maximum temperature for an assumed value of 10^{13} s^{-1} for the desorption preexponential. The lowering of the value of the desorption preexponential by Stoltze and co-workers[42] requires a concomitant lowering of the desorption activation energy, so that the value of the desorption rate constant at the peak maximum temperature (880 K) is maintained.

The value of the desorption activation energy used by Stoltze and Norskov was 161 kJ mol^{-1} (cf. 226 kJ mol^{-1} of Table 5.2), from which a value of 7.9×10^9 for the desorption preexponential term can be derived. This is a lowering of the normal desorption A-factor by 4.9×10^{-4}, considerably less than the value of 10^{-6} found for the sticking probability. Nevertheless, using this combination of values, Stoltze and Norskov predict ammonia synthesis rates which are in exact agreement with those found experimentally.

Several points can be made about this treatment. First, one is no longer dealing with the published potential energy diagram. Because the desorption activation energy of nitrogen atoms has been raised by 64 kJ mol^{-1}, the energy minimum of a nitrogen atom plus three hydrogen atoms is now raised by 32 kJ mol^{-1}.

Second, there is no need to lower the desorption A-factor commensurate with the lowered adsorption A-factor. It is at this point that the application of transition state theory is particularly helpful. The preexponential term for the dissociation of the nitrogen molecule precursor state, which is mobile, through an intermediate that is fixed and exists on only a small fraction (10^{-3}, say) of the total number of surface sites, is given by

$$A_{\text{diss}} = N\frac{kT}{h}\frac{N_s \times 10^{-3}}{q^{\circ 2}_{N_2\,(\text{trans})}\, q^{\circ}_{N_2\,(\text{rot})}\, q^{\circ}_{N_2\,(\text{vib})}\, N_s} \tag{5.21}$$

The recombination of the fixed adsorbed nitrogen atoms to a fixed intermediate, the latter again being adsorbed on a small fraction of the surface, results in the A-factor given by

$$A_{\text{recom}} = N\frac{kT}{h}\frac{N_s \times 10^{-3}}{(N_s \times 10^{-3})} \tag{5.22}$$

The ratio of the adsorptive and recombinative A-factors is expressed in the form

$$\frac{A_{\text{diss}}}{A_{\text{recom}}} = \frac{N_s \times 10^{-6}}{q^{\circ 2}_{N_2\,(\text{trans})}\, q^{\circ}_{N_2\,(\text{vib})}\, q^{\circ}_{N_2\,(\text{rot})}} \tag{5.23}$$

and ranges in value from 10^{-6} to 10^{-7}, depending on the degree of rotational freedom accorded to the mobile precursor. The use of A-factors for forward and reverse reactions that differ by a factor of 10^6 is therefore not a violation of the principle of microscopic reversibility, as has been suggested.[43]

Finally, the overall activation energy for ammonia synthesis predicted by this potential energy diagram is 17 kJ mol^{-1}, which is considerably lower than the experimental values of 45 kJ mol^{-1} of Nielsen[39] or the 81 kJ mol^{-1} of Somorjai *et al.*[41]

5.7.4.2. Activated Dissociation of the Molecular Nitrogen Precursor State

Several authors have reported that the dissociative adsorption of nitrogen on iron requires the surmounting of an activation energy barrier. In other words, it is an "activated process." Ertl and co-workers[31] have reported that on clean Fe(100) the adsorption of nitrogen atoms has an activation energy which increases from 20 kJ mol^{-1} at a coverage of 0.05 monolayer (ML) to 45 kJ mol^{-1} at 0.2 ML. This result is in good accord with the coverage-dependent activation energy reported by Scholten and co-workers[47] for the adsorption of nitrogen atoms on an iron catalyst promoted by alumina. The activation energy was found to increase in a linear fashion with coverage from 40 kJ mol^{-1} at a coverage of 0.05 ML to 96 kJ mol^{-1} at a coverage of 0.25 ML, remaining constant at that value up to a coverage of 0.7 ML. Baiker and co-workers[48] have calculated an activation energy of nitrogen atom adsorption of 85 kJ mol^{-1} from a kinetic analysis of the rates of ammonia synthesis over amorphous $Fe_{91}Zr_9$ (temperature range 623 to 723 K at 4 bar). Finally, Emmett and Brunauer[25] employed a volumetric technique to measure amounts adsorbed, and obtained activation energies for the adsorption of nitrogen

atoms of 58.6, 60.6, 64.4, 71.5, 75.3, and 66.9 kJ mol^{-1} for the adsorption of 1.7, 2.0, 2.3, 2.8, 3.2, and 3.6 ml of nitrogen on 16.46 g of a doubly promoted (K_2O/Al_2O_3) iron catalyst in the temperature range 546 to 723 K. Taking a nominal value of 10 $m^2 g^{-1}$ for the surface area of the catalyst, those volumes adsorbed correspond to a coverage range of 0.026 ML to 0.055 ML, and so the activation energies to nitrogen adsorption accord reasonably well with those found by Scholten and co-workers.[47] Indeed, in the same paper[25] Emmett and Brunauer found that the rate of ammonia synthesis and nitrogen atom uptake on the catalyst were the same (ammonia synthesis rate 0.21 ml min^{-1}, nitrogen atom uptake in first minute 0.26 ml). They concluded tentatively from this that nitrogen atom adsorption might be the rate-determining step in ammonia synthesis. Furthermore, it is an important tenet of the Temkin–Pyzhev equation (an equation which accurately reflects the rate of ammonia synthesis and decomposition on doubly promoted iron catalysts) that nitrogen adsorption (as atoms) has an activation energy which is dependent on coverage.

It is therefore important that the consequences (in terms of predicted rates) of the activated adsorption of atomic nitrogen be examined. The potential energy diagram of Fig. 5.12 has been constructed using the high-coverage (80% nitrogen atom coverage) adsorption/desorption kinetics of Scholten and co-workers.[47] The activation energy for dissociation of the nitrogen held in the molecular precursor state has been given the value of 96 kJ mol^{-1}, while the reverse reaction (nitrogen atom recombination) has been given the value of 134 kJ mol^{-1}. The activation energy for the desorption of hydrogen ($E_{-5.4}$) has been lowered from 109 kJ mol^{-1} (the low-coverage value[32]) to 62.7 kJ mol^{-1} (the high-coverage model[32]) so that the potential accurately reflects a high-coverage model. A complete listing of the energies involved is given in Table 5.4.

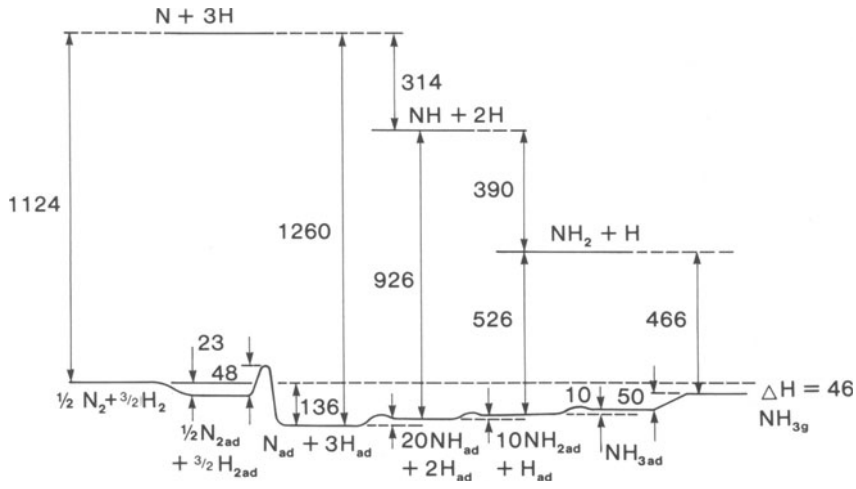

Figure 5.12. Potential energy diagram for ammonia synthesis on a promoted iron catalyst with activated absorption.

TABLE 5.4. Energetics of the Elementary Reactions of a High-Coverage, Activated Nitrogen Adsorption Model of Ammonia Synthesis Used to Construct the Potential Energy Diagram of Fig. 5.12

E_f (kJ mol^{-1})	Reaction	E_r (kJ mol^{-1})	Eq.
0	$N_2 + Fe \rightleftarrows N_{2(a)}$	46	(5.1)
96	$N_{2(a)} + Fe \rightleftarrows N_{(a)} + N_{(a)}$	134	(5.2)
0	$H_2 + Fe \rightleftarrows H_{2(a)}$	0	(5.3)
0	$H_{2(a)} + Fe \rightleftarrows H_{(a)} + H_{(a)}$	62.7	(5.4)
40.9	$H_{(a)} + N_{(a)} \rightleftarrows NH_{(a)} + Fe$	20.9	(5.5)
30.9	$H_{(a)} + NH_{(a)} \rightleftarrows NH_{2(a)} + Fe$	20.9	(5.6)
30.9	$H_{(a)} + NH_{2(a)} \rightleftarrows NH_{3(a)} + Fe$	20.9	(5.7)
50.2	$NH_{3(a)} \rightleftarrows NH_3 + Fe$	0	(5.8)

The striking feature of the potential energy diagram so produced (Fig. 5.12) is the shallowness of the well (136 kJ mol^{-1}) for one nitrogen atom (42 kJ mol^{-1}) and three hydrogen atoms (94 kJ mol^{-1}) adsorbed on the surface. From this point now only 90 kJ mol^{-1} is required to produce ammonia in the gas phase.

5.7.4.2a. The Prediction. Standard values for the preexponential terms (10^{13} for adsorption and unimolecular desorption reactions and 10^{21} for bimolecular surface reactions) at 107 bar and 723 K are employed in this model, which predicts an ammonia concentration in the exit gas of 14.2% (cf 13.2% experimental[38]) for a GHSV of 16,000 h^{-1}.

The surface coverages corresponding to that rate are as follows: $N_{2(a)} = 4.4 \times 10^{12}$ molecule cm^{-2}, $N_{(a)} = 8.1 \times 10^{13}$ atom cm^{-2}, $NH_{(a)} = 1.2 \times 10^{13}$ species cm^{-2}, $NH_{2(a)} = 8.4 \times 10^{12}$ species cm^{-2}, $NH_{3(a)} = 5.7 \times 10^{12}$ molecule cm^{-2}, $H_{(a)} = 3.3 \times 10^{13}$ atom cm^{-2}, Fe = 5.3×10^{12} site cm^{-2}.

The coverage of the surface by nitrogen atoms predicted by this model accords very well with that found by Ertl and co-workers (7×10^{13} atom cm^{-2}).[37]

Although the overall activation energy predicted by the model at 117 kJ mol^{-1} is higher than the value of 81 kJ mol^{-1} found by Somorjai and co-workers,[41] the model is remarkably good.

5.7.5. Conclusions

1. The potential energy diagram (Fig. 5.11), derived from the detailed kinetics of ammonia synthesis obtained from a considerable body of work by Ertl and co-workers[26,28-32,34-37] in combination with experimentally derived *A*-factors, predicts rates of ammonia synthesis within a factor of 10 of those found experimentally when the kinetics are extrapolated by calculation to pressures (107 bar) and temperatures (723 K) used in the industrial manufacture of ammonia. Furthermore, the overall activation energy predicted by the model (62 kJ mol^{-1}) is also in good agreement with that (81 kJ mol^{-1}) found by Somorjai and co-workers[41] at 20 bar.

2. The potential energy diagram constructed on the premise, that the adsorption of nitrogen into the atomic state on a doubly promoted (K_2O/Al_2O_3) iron catalyst requires the surmounting of an activation energy barrier, also predicts rates of ammonia synthesis at 107 bar and 723 K which are in good agreement with those found experimentally, but with an overall activation energy higher than that found experimentally.
3. The combination of the fact that more than one set of the energetics are able to predict rates of ammonia synthesis with reasonable accuracy, and the uncertainty as to whether the adsorption of nitrogen on a doubly promoted iron catalyst is activated, suggests that the detailed kinetics of nitrogen adsorption on a doubly promoted catalyst should be determined using modern surface-science techniques.

REFERENCES

1. I. Barin, and O. Knacke, *Thermochemical Properties of Inorganic Substances* (Supplement), Springer-Verlag, Berlin, 1977.
2. A. F. H. Wielers, A. J. H. M. Kock, C. E. C. A. Hopp, J. W. Geus, and A. M. van der Kraan, *J. Catal.* **117**, 1 (1989).
3. A. J. H. M. Kock, K. F. Fortuin, and J. W. Geus, *J. Catal.* **96**, 261 (1985).
4. J. G. McCarty, P. Y. Hou, D. Sheridan, and H. Wise, in: *Coke Formation on Metal Surfaces* (L. F. Albright and R. T. K. Baker, eds.), ACS Symposium Series No. 202, American Chemical Society, Washington, D.C. (1982).
5. P. K. de Bokx, A. J. H. M. Kock, E. Boelliaard, W. Kiop, and J. W. Geus, *J. Catal.* **96**, 454 (1985).
6. M. Boudart, A. Deiboulile, J. A. Dumesic, S. Khammouma, and H. Topsoe, *J. Catal.* **37**, 486, 503, 513 (1975).
7. M. Boudart, H. Topsoe, and J. A. Dumesic, in: *The Physical Basis for Heterogeneous Catalysis* (E. Drauglis and R. I. Jaffee, eds.), p. 377, Plenum Press, New York (1975).
8. M. Boudart, J. A. Dumesic, and H. Topsoe, *Proc. Natl. Acad. Sci. U.S.A.* **74**, 806 (1977).
9. J. J. F. Scholten, Chemisorption of Nitrogen on Iron Catalysts in Connection with Ammonia Synthesis, Thesis, Technical University of Delft, The Netherlands (1959).
10. T. J. Vink, J. M. der Kinderen, O. L. J. Gitzeman, and J. W. Geus, *Appl. Surf. Sci.* **26**, 367 (1986).
11. J. M. van Zoest, J. M. Fluit, T. J. Vink, and B. A. van Hassel, *Surf. Sci.* **182**, 179 (1987).
12. T. J. Vink, J. M. der Kinderen, O. L. J. Gitzeman, J. W. Geus, and J. M. van Zoest, *Appl. Surf. Sci.* **26**, 357 (1986).
13. M. W. Roberts and C. S. McKee, *Chemistry of the Metal-Gas Interface*, p. 474, Clarendon Press, Oxford (1978).
14. G. A. Somorjai, *Chemistry in Two Dimensions: Surfaces*, p. 264, Cornell University Press, Ithaca and London (1981).
15. J. W. Geus, in: *Chemisorption and Reactions on Metallic Films*, Volume I (J. R. Anderson ed.), p. 432, Academic Press, London and New York (1971).
16. R. Suhrmann, J. M. Heras, L. Viscido de Heras, and G. Wedier, *Ber. Bunsenges. Phys. Chem.* **68**, 511, 590 (1964).
17. R. Suhrmann, J. M. Heras, L. Viscido de Heras, and G. Wedler, *Ber. Bunsenges. Phys. Chem.* **72**, 854 (1968).
18. T. J. Vink, S. J. M. Sas, O. L. J. Gitzeman, and J. W. Geus, *J. Vac. Sci. Technol.* **A54**, 718 (1987).
19. S. Brunauer and P. H. Emmett, *J. Am. Chem. Soc.* **59**, 310 (1937).
20. S. Brunauer and P. H. Emmett, *J. Am. Chem. Soc.* **62**, 1732 (1940).
21. J. T. Kummer and P. H. Emmett, *Phys. Colloid Chem.* **55**, 342 (1961).

22. H. H. Podgurski and P. H. Emmett, *J. Am. Chem. Soc.* **57**, 159 (1953).
23. P. Zwietering and R. Westrik, *Proc. K. Ned. Akad. Wet.* **56**, 492 (1953).
24. H. Topsoe, N. Topsoe, H. Bohibro, and J. A. Dumesic, in: *Proceedings of the 7th International Congress on Catalysis Tokyo 1980* (T. Seiyama and K. Tanabe, eds.), p. 247, Elsevier, Amsterdam (1981).
25. P. H. Emmett and S. Brunauer, *J. Am. Chem. Soc.* **56**, 35 (1934).
26. G. Ertl, *Catalysis, Science and Technology* **4**, 273 (1983).
27. M. Bowker, I. B. Parker, and K. C. Waugh, *Appl. Catal.* **14**, 101 (1985).
28. G. Ertl, S. B. Lee, and M. Weiss, *Surf. Sci.* **114**, 527 (1982).
29. G. Ertl, M. Weiss, and S. B. Lee, *Chem. Phys. Lett.* **60**, 391 (1979).
30. G. Ertl, *Catal. Rev. Sci. Eng.* **21(2)**, 201 (1980).
31. F. Bozso, G. Ertl, M. Grunze, and M. Weiss, *J. Catal.* **49**, 18 (1977).
32. F. Bozso, G. Ertl, M. Grunze, and M. Weiss, *Appl. Surf. Sci.* **1**, 103 (1977).
33. A. Nielsen, *An Investigation on Promoted Iron Catalysts for the Synthesis of Ammonia*, 3rd edn., p. 21, Jul. Gjellerups Forlag (1968).
34. M. Grunze, F. Bozso, G. Ertl, and M. Weiss, *Appl. Surf. Sci.* **1**, 241 (1978).
35. G. Ertl, S. B. Lee, and M. Weiss, *Surf. Sci.* **114**, 515 (1982).
36. G. Ertl and N. Thiele, *Appl. Surf. Sci.* **3**, 99 (1979).
37. G. Ertl, M. Huber, S. B. Lee, Z. Paal, and M. Weiss, *Appl. Surf. Sci.* **8**, 373 (1981).
38. A. Nielsen, *An Investigation on Promoted Iron Catalysts for the Synthesis of Ammonia*, 3rd edn., p. 51, Jul. Gjellerups Forlag (1968).
39. A. Nielsen, *An Investigation on Promoted Iron Catalysts for the Synthesis of Ammonia*, 3rd edn., p. 115, Jul. Gjellerups Forlag (1968).
40. M. I. Temkin and V. Pyzhev. *J. Phys. Chem. (USSR)* **13**, 851 (1939).
41. N. D. Spencer, R. C. Schoonmaker, and G. A. Somorjai, *J. Catal.* **74**, 129 (1982).
42. P. Stoltze and J. K. Norskov, *Phys. Rev. Lett.* **55**, 2502 (1985).
43. P. Stoltze, *Phys. Scr.* **36**, 824 (1987).
44. P. Stoltze and J. K. Norskov. *J. Catal.* **110**, 1 (1988).
45. P. A. Redhead, *Trans. Faraday Soc.* **57**, 641 (1961).
46. P. A. Redhead, *Vacuum* **12**, 203 (1962).
47. J. J. F. Scholten, P. Zwietering, J. A. Konvalinka, and J. H. de Boer, *Trans. Faraday Soc.* **55**, 2166 (1959).
48. A. Baiker, H. Baris, and R. Schlögl, *J. Catal.* **108**, 467 (1987).

6

KINETICS OF AMMONIA SYNTHESIS AND INFLUENCE ON CONVERTER DESIGN

Giorgio Gramatica† and Nicola Pernicone

6.1. CLASSICAL AMMONIA SYNTHESIS KINETICS

6.1.1. Introduction

Ammonia synthesis is one of the most important processes operated by the chemical industry. Modern ammonia synthesis plants can produce up to 1800 tons of ammonia per day. Clearly, the design of the large reactors requires powerful and reliable calculation methods and the availability of a sound kinetic equation is an essential requirement. It is not only necessary for reactor design, but is also required to express catalyst performances generated from either laboratory or pilot plant experiments.

From a practical point of view the kinetic equation can be derived in any way, provided that it fits accurately the experimental data. A theoretical derivation is clearly preferable, since this allows assignment of a physical meaning to the various constants, but entirely empirical equations can be safely used as well.

Ammonia synthesis is a relatively simple reaction without the complication of any secondary reaction product, and is especially suitable for a theoretical approach to its kinetics. In fact, the most used kinetic equation for ammonia synthesis was developed by Temkin on the basis of theoretical assumptions about 50 years ago and is still used successfully by chemists and engineers.

Very recently the major developments in both adsorption and reaction rate studies on well-defined surfaces under high vacuum conditions have been extrapolated to industrial conditions, so that interesting comparisons can now be done with the traditional high-pressure experimentation.

Giorgio Gramatica† • Agrimont S.p.A., Enimont Group, 20138 Milano, Italy—Deceased. Nicola Pernicone • Ausimont Catalizzatori S.z.l., Montedison Group, 28100 Novara, Italy. *Present address for Nicola Pernicone*: Via Pansa 7, 28100 Novara, Italy.

6.1.2. Development of the Temkin Equation

It was demonstrated[1] in the early days that nitrogen adsorption is the rate-determining step in ammonia synthesis, and this was the basic assumption used in the development of the Temkin equation. It was also assumed that hydrogen and ammonia have no significant influence on nitrogen adsorption, and that the kinetics of nitrogen adsorption and desorption can be described adequately by Elovich-type expressions,[2] namely,

$$r_A = K_A P_N e^{-g\theta} \tag{6.1}$$

$$r_D = K_D e^{h\theta} \tag{6.2}$$

where r_A and r_D are the adsorption and desorption rates, P_N is the partial pressure of nitrogen in the gas phase, θ is the degree of coverage, while K_A, K_D, g, and h are constants. The ammonia synthesis rate r_S is therefore given by the expression

$$r_S = K_A P_N e^{-g\theta} - K_D e^{h\theta} \tag{6.3}$$

According to Temkin,[2] the degree of coverage is given by

$$\theta = \frac{1}{f} \ln(bP_N^*) \tag{6.4}$$

where $f = g + h$, $b = K_A/K_D$, and P_N^* is the virtual pressure of nitrogen in equilibrium with the degree of coverage θ. It was assumed by Temkin that this virtual pressure is given by

$$P_N^* = \frac{1}{K_{eq}} \frac{P_A^2}{P_H^3} \tag{6.5}$$

where K_{eq} is the equilibrium constant of the reaction $N_2 + 3H_2 = 2NH_3$ while P_A and P_H are the partial pressures of ammonia and hydrogen in the gas phase.

Therefore, by substitution of these values for f, b, and P_N^* in Eq. (6.4), the degree of coverage becomes

$$\theta = \frac{1}{g+h} \ln\left(\frac{K_A}{K_D} \frac{P_A^2}{K_{eq} P_H^3}\right) \tag{6.6}$$

and further substitution of these values for θ in expression (6.3) for r_S yields, after suitable rearrangements,

$$r_S = K_1 P_N \left(\frac{P_H^3}{P_A^2}\right)^{\alpha} - K_2 \left(\frac{P_A^2}{P_H^3}\right)^{1-\alpha} \tag{6.7}$$

where $K_1 = K_A(K_A/K_D)^{-g/(g+h)}K_{eq}^{g/(g+h)}$, $K_2 = K_D(K_A/K_D)^{h/(g+h)}K_{eq}^{-h/(g+h)}$, with $\alpha = g/(g+h)$ and $1-\alpha = h/(g+h)$.

This equation is the well-known Temkin or Temkin-Pyzhev equation, which can be easily integrated[3] for practical applications.

6.1.3. Problems in the Application of the Temkin Equation

The first problem that arose in the early attempts to use the Temkin equation was the dependence of the constants on pressure. This was later overcome by using fugacities.[4]

More seriously, however, simple inspection of the Temkin equation reveals that it gives an infinite rate at very low partial pressures of ammonia. This does not give rise to problems in the interpretation of plant data where, due to the recycle nature of the process, appreciable amounts of ammonia are present in the feed gas. However, for catalyst testing in laboratory equipment, where pure synthesis gas is commonly used, the Temkin equation should be employed with much caution. Suitable modifications which overcome this inconvenience are available, and these are shown in Section 6.1.4.

The value to be given to the α parameter has been debated at length in the scientific literature. While Temkin himself assigned to it a value of 0.5, other workers found that higher values gave a better fit with their experimental data. For instance, Nielsen[5] preferred the value of 0.75. Irrespective of the chosen value, the α parameter should be kept constant in the interpretation of kinetic data from different catalysts for their comparative evaluation.[6]

6.1.4. Other Kinetic Equations for Ammonia Synthesis

While the Temkin equation has found wide application during the last fifty years, many other kinetic equations have also been developed using both theoretical and practical approaches.

An important modification of the Temkin equation was made by Temkin himself[7] by the incorporation of hydrogen addition to adsorbed nitrogen as a second rate-determining step. The following equation was obtained:

$$r_S = \frac{K' P_N^{1-\alpha}[1 - (1/K_{eq})(P_A^2/P_N P_H^3)]}{[(K''/P_H) + (1/K_{eq})(P_A^2/P_N P_H^3)]^{\alpha}[(K''/P_H) + 1]^{1-\alpha}} \tag{6.8}$$

It was established by ICI workers[8] that this equation gives a better description of the experimental data than the classical Temkin equation.

The latter was further modified by Temkin and co-workers[9] to take into account the effect of small amounts of water in the feed gas. In this case the following equation gives satisfactory results:

$$r_w = \frac{k_1 P_N - k_2(P_A^2/P_H^3)}{[(P_A^2/P_H^3) + C(P_w/P_H)]^{\alpha}} \tag{6.9}$$

where P_w is the partial pressure of water vapor.

Other equations have been developed starting from the Langmuir isotherm. Brunauer and co-workers[10] obtained the following equation, which is especially useful at low concentrations of ammonia:

$$r_S = K_A P_N / (1 + bK_{eq} P_A / P_H^{1.5})^{2\alpha} \tag{6.10}$$

An equation valid for low temperature and pressure operation was derived by Ozaki, Taylor and Boudart[11]:

$$r_S = K_A P_N / (1 + K_A P_A / P_H)^2 \tag{6.11}$$

They assumed, quite reasonably, that the surface is mainly covered by NH species, at the low temperature and pressure ranges under consideration.

Starting from the results reported in Ref. 11, Nielsen and co-workers[12] derived the following equation:

$$r_S = \frac{K_2(K_{eq} P_N - P_A^2 / P_H^3)}{(1 + k_3 P_A / P_H^{1.5})^{2\alpha}} \tag{6.12}$$

They found that the best value for α is 0.75.

It was proposed by Brill[13] that the rate-determining step in ammonia synthesis was molecular rather than dissociative nitrogen chemisorption. On this basis, the following equation was derived for the kinetics of ammonia synthesis:

$$r_S = K_A P_N / (1 + K_A P_A^2 / P_H^3) \tag{6.13}$$

and should be applied to the low conversion range.

The well-known Hougen-Watson procedure has also been applied to derive kinetic equations for ammonia synthesis. A comprehensive discussion of this subject was given by Buzzi Ferraris and co-workers.[14] They built 23 different kinetic models and evaluated them using data generated by Nielsen and reported in Ref. 12. Most of the models gave a better fit than the classical Temkin equation. Though this is clearly due to the many constants introduced by such models, two important statements have been confirmed. Kinetic studies alone are not sufficient for the elucidation of reaction mechanisms and, second, the Hougen-Watson approach is very suitable for engineering purposes. On this point, it is worthy of mention that the best fit reported in Ref. 14 was given by the equation

$$r_S = \frac{P_N P_H^2 - K_{eq}^2 P_A^2 / P_H}{C_1 P_N^2 + C_2 P_A^2 / P_H + C_3 P_H P_A} \tag{6.14}$$

where C_1, C_2, and C_3 are constants.

6.1.5. Derivation of Ammonia Synthesis Kinetics from UHV Adsorption Studies

During the last few years, a tremendous effort has been devoted to bridging the gap between the surface-science approach to catalytic phenomena and real catalysis under practical conditions. A significant proportion of this effort has been applied to ammonia synthesis.

The large amount of available data on nitrogen and hydrogen adsorption on clean iron surfaces prompted some research groups to try to generate kinetic data for ammonia synthesis at high pressure and temperature, starting from adsorption data obtained under UHV conditions.

The first attempt was by ICI scientists,[15] who tried to extrapolate to real synthesis conditions (450 °C, 100 atm) the low-coverage potential energy diagram[16] obtained by Ertl from TPD and AES experiments. No hypothesis about the rate-determining step was adopted. The set of elementary steps considered is shown in Table 6.1, together with the pertinent energy data. The input to the computer program also included reaction pressure, stoichiometric feed gas composition, flow rate, free gas volume, catalyst weight, catalyst surface area (taken as $10\ m^2\ g^{-1}$), and surface free iron percent (assumed 15). Nitrogen and hydrogen were assumed to adsorb competitively. The result of the calculations was that the ammonia content of the exit gas was more than 10^5 times lower than the real value. It was recognized by the authors that the energy "well" of the adsorbed nitrogen atoms was too deep, so that the first hydrogenation step appeared to be rate-determining rather than dissociative nitrogen adsorption.

The potential energy diagram was therefore modified following suggestions by Ertl, on the basis that, under the conditions of temperature and pressure required for industrial ammonia synthesis, the dissociative adsorption of nitrogen becomes an activated process. The potential energy diagram is reported in Fig. 4.13. While there is no direct experimental evidence for this postulate, it is noteworthy that the same basic assumption was taken by Temkin for the development of his kinetic equation.[2]

Recalculation of the ammonia content in the exit gases showed that they lay within 10% of the experimental values. Thus nitrogen dissociative adsorption does appear to be rate-determining, as widely accepted.

TABLE 6.1. Elementary Reaction Steps of Ammonia and Related Arrhenius Data[15]

Reaction step	$\text{Log}_{10} A_F$	E_F^*	$\text{Log}_{10} A_R$	E_R^*
$N_2 + Fe = N_2(a)$	13.0	0	13.0	46 000
$N_2(a) + Fe = 2N(a)$	21.0	46 000	21.0	225 804
$H_2 + Fe = H_2(a)$	13.0	0	13.0	0
$H_2(a) + Fe = 2H(a)$	21.0	0	21.0	108 732
$H(a) + N(a) = NH(a) + Fe$	20.8	125 910	21.0	20 910
$H(a) + NH(a) = NH_2(a) + Fe$	20.8	53 910	21.0	20 910
$H(a) + NH_2(a) = NH_3(a) + Fe$	20.7	62 730	21.0	20 910
$NH_3(a) = NH_3 + Fe$	13.0	50 184	13.0	0

The authors conclude correctly that factors other than those accounted for in the UHV studies also play an important role in real synthesis conditions. However, it was possible to make a satisfactory fit to the experimental data by introducing simple assumptions. While they are not based on direct experimental evidence, they do not appear to be unreasonable.

The same problem was also approached at the same time by scientists from Topsøe,[17] starting from the same set of reaction steps shown in Table 6.1. The following main assumptions were taken:

1. Dissociative adsorption of nitrogen as the rate-determining step under all reaction conditions.
2. No adsorbate-adsorbate interaction (the most risky assumption according to the authors).
3. Energetically homogeneous surface.
4. Ideal gases.

The statistical thermodymamic Fowler-Guggenheim treatment of adsorption was applied, and the equilibrium constant of each reaction step in terms of partition functions was calculated, after the introduction of various additional assumptions. The experimental data of Ertl[18] for a potassium-covered iron surface (at optimum potassium coverage) were used, but a much lower value for the nitrogen atom chemisorption energy than quoted by Ertl was adopted. This value and the sticking coefficient of nitrogen were recognized as the parameters on which the results depend most sensitively.

The ammonia synthesis rate per iron surface area was calculated in this way. The iron surface area of the commercial Topsøe KM1R catalyst was determined by the carbon monoxide chemisorption method, assuming that each carbon monoxide molecule titrates two iron atoms (this method gives a rather higher iron surface area than usually accepted). After integration of the rate equation for a piston-flow reactor, values for the ammonia concentration in the exit gas were obtained in very good agreement with the experimental values as shown in Fig. 4.14. However, the authors themselves prefer not to stress such agreement, in view of the approximations introduced and because of the uncertainties in some of the input data.

While such approaches to the kinetics of catalytic reactions are still in the pioneering stage, it is anticipated that chemisorption data obtained under well-controlled low-pressure conditions will, in the near future, help to bridge the so-called "pressure gap" between UHV adsorption studies and real catalytic behavior.

6.2. RATE-LIMITING PHENOMENA ON THE INDUSTRIAL SCALE

The rate expressions described in the preceding section were derived on the assumption that surface processes are the only steps that can limit the reaction rate. In order to obtain the "intrinsic" or surface rate equation, the primary requirement in kinetic measurements is the collection of experimental data under

conditions that are free of any deviating effects, such as flow maldistribution, mass and heat transfer, and catalyst poisoning. Considerable effort is spent in the laboratory to eliminate, as far as possible, the influence of any other rate-limiting phenomenon on the "intrinsic" activity of the catalyst. Kinetic data are thus obtained in the laboratory using experimental reactors with specific features operating under "idealized" conditions.

The isothermal integral reactor is commonly used. Crushed catalysts of very small size, in the range between 0.5 mm and 1.5 mm, are commonly used to avoid pore-diffusion restrictions and heat-transfer resistance in the catalyst particles. To avoid flow maldistribution and back-mixing of product ammonia, very high ratios of bed length to bed diameter are chosen. Longitudinal and lateral temperature gradients in the catalyst bed are avoided by maintaining the reactor at constant temperature by external heating. The catalyst is often diluted with considerable amounts of inert materials and, sometimes, experimental reactors are operated under differential conditions. A particular very fast reduction procedure is usually adopted, and very pure reactants, often obtained by cracking of anhydrous ammonia, are employed.

These conditions are not achieved at the industrial scale. Therefore, when laboratory data are translated to industrial conditions, any deviating effect and nonideal condition pertaining to the converter under consideration must be identified and quantified. In other words, the intrinsic rate constants determined in the laboratory must be combined with appropriate corrective factors for proper scale-up, design, and simulation of any industrial converter. In this section an attempt will be made to summarize the concepts and calculations that are necessary to perform this translation successfully.

6.2.1. Physical Factors

6.2.1.1. Intrabed Phenomena

6.2.1.1a. Flow Maldistribution in Catalyst Beds. Deviations from the ideal piston-flow assumption will be discussed in this section. The piston-flow assumption requires that temperature, concentrations, reaction rate, and mass flow rate are uniform over any cross section of the catalyst bed.

Before discussing the rate-limiting phenomena occurring in the catalyst bed as a whole, it is appropriate to mention the different types of bed and flow arrangements which are commonly used in industrial converters.

In some of the early designs for the synthesis converters, the catalyst mass was contained in a single continuous bed which was cooled continuously by cold reaction gas that passed through a "tube bundle," and which was consequently preheated to the reaction temperature. This type of converter was referred to as a "tube-cooled" converter. In any converter provided with a heat exchanger, whether of counter-current or co-current type, through the catalyst bed, the catalyst particles which are located far from the cooling walls work at higher temperatures and with different reaction rates and ammonia concentrations than those lying near the walls in the same cross section. This gives rise to all sorts of lateral gradients in

the bed. In this instance, it is very difficult to make a correct calculation of both lateral and longitudinal temperature gradients and, due to the extreme sensitivity of reaction rate to temperature, of their effects on converter performance. In practice, because of these difficulties, the design of these converters was carried out by empirical methods. Since heat transfer depends on surface area while heat generation by chemical reaction is proportional to catalyst volume, and since these parameters do not vary in the same ratio, tube-cooled converters were scaled-up by simply increasing the shell diameter, leaving the diameter and the length of the cooling tubes unchanged. As expected, it became increasingly more difficult, as capacity increased, to charge catalyst to the converter uniformly. In particular, filling the shell side of an increasingly large heat-exchanger bundle often led to voidage. From an operational point of view, the only means of control for the converter was by inlet temperature. Owing to these difficulties, and with the advent of increasingly larger ammonia plants in the early 1960s, the tube-cooled converter design was abandoned, and will not be considered here.

All modern ammonia converters are based on adiabatic catalyst beds with intermediate cooling. The various flow arrangements that have most frequently been used or proposed for adiabatic beds of ammonia converters are illustrated in Fig. 6.1. In each case, the catalyst volume must be accommodated within a cylinder, usually referred to as a cartridge.

The simple axial flow model, which undoubtedly represents the best utilization of the internal volume of the converter, has two drawbacks. To contain pressure drops, it is imperative to use relatively large-size catalysts, which are less efficient due to pore diffusion limitation, and this results in an increase in the specific volume of the converter. Despite this technical concession, low bed-height to bed-diameter ratios are also required, leading to large diameters and consequent wall thicknesses of the vessel. Such converters become relatively expensive, and heavy. Several alternative flow models, taking advantage of a larger bed cross-sectional area in proportion to the vessel cross-section, have been found to overcome this problem.

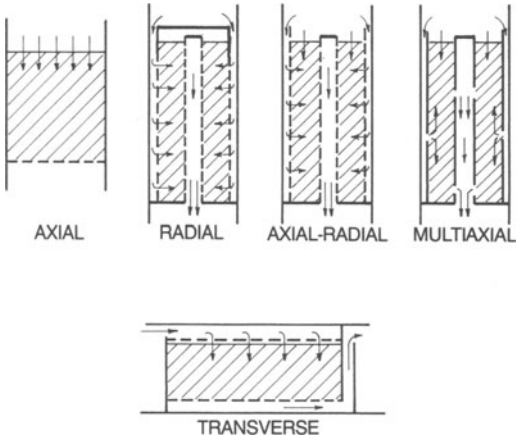

Figure 6.1. Flow models in adiabatic catalyst beds. Besides the simple axial-flow model, several alternative flow-models have been proposed to contain the pressure drop when relatively small-size catalysts, which are more active, are used.

In the radial-flow model,[19] pressure drop is extremely low, even when using catalysts of small particle size. For this reason, a gas distribution problem arises with this bed arrangement and additional concentrated pressure drops, obtained by special devices, are needed at the inlet and outlet walls of the bed. Furthermore, a sealed compensation chamber filled with catalyst must be provided at the top of the bed so that, in the event of bed shrinkage on operation, it is not possible for some gas to bypass the bed altogether.

The recovery of this dead volume of catalyst is the main purpose of the axial-radial concept.[20] The bed is open at the top thus allowing part of the gas to flow axially, while the remaining part flows radially through the lower portion of the bed. Since the axial flow zone acts as a sealing pad for the gas flow, sealing at the top of the bed is unnecessary.

In the multiaxial flow model,[21] the pressure drop through the bed can be easily adjusted by changing the number of modules in parallel and their dimensions. This greatly simplifies the gas-distribution problem, requiring no additional concentrated pressure drop.

The transverse-flow model,[22] in horizontal converters, has also been used in extremely large-capacity converters.

The gas flow distribution through the catalyst is the most critical feature in the design of an adiabatic bed. Obviously, when the residence times of equal amounts of synthesis gas in contact with the catalyst are significantly different, they pass through different profiles of conversion and temperature along the bed. Those portions of gas that spend a shorter time in contact with the catalyst than the optimum cannot be compensated, in terms of total conversion, by the other portions which stay longer, because of equilibrium constraints.

The distribution of contact times in a catalyst bed is governed by localized area of pressure drop. Inaccurate calculations of the pressure drop through the ammonia converter can result in severe bottlenecking of the whole plant. Since the literature dealing with this matter is often vague and unreliable, it is appropriate at this point to discuss briefly this subject and also to give a method for calculation.

When a fluid flows steadily in a nonuniform empty duct, the overall mechanical energy balance of the mass unit of fluid in its differential form is given by the equation

$$dx + \frac{dP}{\rho} + d\left(\frac{v^2}{2g}\right) = -\frac{f}{R_H}\frac{v^2}{2g}\,dL = 4\frac{f}{D}\frac{v^2}{2g}\,dL \tag{6.15}$$

where dx is the vertical distance through which the fluid is raised when it moves a distance dL along the duct, dP is the drop in static pressure, ρ is the fluid density, which may be considered constant along dL, v is the mean linear velocity in any cross section of the duct, g is the gravitational constant, and R_H is the hydraulic radius of the duct (by definition, the ratio of the cross-sectional area to wetted perimeter of the duct); f is a dimensionless friction factor, to be evaluated from experimental data and which is a function of the Reynolds number

$$R_e = \frac{4R_H\rho v}{\mu} = \frac{D\rho v}{\mu} \tag{6.16}$$

in which μ is the dynamic viscosity of the fluid and $D = 4R_H$ is the equivalent diameter of the duct. The friction factor f also depends upon the relative roughness of the wetted wall, but this parameter cannot in practice be evaluated in geometrical terms.

When the duct is fully occupied by a fixed bed of material which packs uniformly or of irregular-shaped catalyst particles, flow equations (6.15) and (6.16) are still valid provided the geometry-dependent variables, v and R_H, are relative to the actual dimensions of the channels between the particles in the bed. These channels, however, are of different size and shape and change randomly from point to point within the same bed in any direction, so that they cannot be represented by precise mathematical formulation; a semi-empirical approach is the only method available.

What is known, or what can easily be calculated about a catalyst bed as a whole, is as follows:

1. The superficial gas velocity V through the empty duct which contains the catalyst bed, i.e., based on the empty cross section of the bed, A.
2. The length L of the bed, i.e., the bed thickness in the flow direction.
3. A range of particle linear dimensions defined by sieve analysis; d_1 is the mesh size of a sieve through which particles pass, and d_2 is the mesh size through which they do not.

In addition, although it is less easy to estimate, we may utilize the bed external void fraction ε_e, which is defined as the quotient of the external void space that surrounds the catalyst particles in the bed, and the total bed volume according to the equation

$$\varepsilon_e = 1 - \rho_B/\rho_P \tag{6.17}$$

where ρ_B is the bulk density of the bed and ρ_P is the apparent particle density.

If we consider ε_e to be a characteristic parameter of the bed in any dimension, it then follows that (1) the free cross-sectional area of the bed is equal to $\varepsilon_e A$, (2) the linear velocity v is equal to V/ε_e, and (3) the wetted perimeter of the bed is the ratio of the total geometric surface area of the solid in the bed, S_t, and the bed thickness, L. Rather than the total solid surface S_t, however, it is more practical to use the specific geometric surface area of the solid, S_v, i.e., the geometric surface per unit volume of solid, defined as

$$S_v = S_t/[AL(1 - \varepsilon_e)] \tag{6.18}$$

The hydraulic radius then becomes

$$R_H = \frac{\varepsilon_e AL}{S_t} = \frac{\varepsilon_e}{S_v(1 - \varepsilon_e)} \tag{6.19}$$

in which

$$S_v = \frac{a_P}{v_P} = \frac{6}{\psi D_S} \tag{6.20}$$

and a_P is the external geometric surface of the average particle, v_P is its external geometric volume, ψ is its sphericity, i.e., the ratio of the surface area of a sphere having the same volume of the average particle and the effective external surface area of the average particle, and D_S is the diameter of the equivalent sphere, i.e., the diameter of a sphere having the same volume of the average particle.

Substitution of Eqs. (6.19) and (6.20) into Eqs. (6.15) and (6.16) leads to the following general equations for fluid flow through packed beds:

$$\rho\, dx + dP + \frac{G}{\rho g \varepsilon_e^2}\, dG = -\frac{3f}{\psi D_S} \frac{(1-\varepsilon_e)}{\varepsilon_e^3} \frac{G^2}{\rho g}\, dL \tag{6.21}$$

$$R'_e = \frac{\psi D_S}{1.5(1-\varepsilon_e)} \frac{G}{\mu} \tag{6.22}$$

where ρV has been replaced by the mass velocity G, which is the mass flow rate of fluid relative to the unit area of the empty cross section of the bed.

The relationship

$$f_K = 3f = \frac{100}{R'_e} + 1.75 \tag{6.23}$$

proposed by Ergun,[23] for the evaluation of the bed friction factor f, is preferred to others because:

1. It has been tested extensively and found to be satisfactory for many solids which pack in different ways, including granular and crushed materials.
2. Since it contains a viscosity term and an inertia term, it is applicable to all types of flow (laminar, transitional, and turbulent).
3. Equations are more convenient than tables or graphical correlations in computer-aided design and operation.

In the case of gases flowing through a catalyst bed in which a nonequimolar and nonisothermal reaction is taking place, the exact integration of Eq. (6.21) would be very complicated. However, a good approximation may be achieved when the bed parameters D_S, ψ, and ε_e are uniform, and when the bed pressure drop does not exceed 5% of the inlet pressure, by substitution of the gas mixture properties, ρ and μ, with their mean values, which may be calculated for adiabatic catalyst beds using the equation

$$\rho = \frac{\rho_{in} - \rho_{out}}{\ln(\rho_{in}/\rho_{out})} \tag{6.24}$$

where

$$\rho_{\text{in,out}} = (B \sum y_i M_i)_{\text{in,out}} \qquad \text{and} \qquad B = \frac{P}{\delta RT} \tag{6.25}$$

Subscripts "in" and "out" refer to bed inlet and outlet conditions, y_i and M_i are the molar fraction and the molecular weight of each component in the gas mixture, R is the gas constant, equal to 0.082 atm m^3 $kmol^{-1}$ K^{-1}, and δ is the compressibility factor of the gas mixture. The average viscosity may be calculated similarly.

With the limitations mentioned above, integration of Eq. (6.21) then leads to

$$\frac{\Delta P}{L} = \frac{P_{\text{out}} - P_{\text{in}}}{L} = -\left[\frac{100}{R'_{\text{e,in}}} + 1.75\right] \frac{(1-\varepsilon_e)}{\varepsilon_e^3} \frac{G_{\text{in}}^2}{\psi D_S g \rho} \mp \rho \tag{6.26}$$

for axial flow in vertical beds, along which the cross-sectional area does not vary (i.e., $dG/dL = 0$ and $dx = \pm dL$), and where the plus sign refers to downward flow and the negative sign to upward flow.

In the case of radial flow in vertical cylindrical beds (i.e., $dx = 0$ and $dL = \pm dD/2$), the expression becomes

$$\Delta P = P_{\text{out}} - P_{\text{in}} = \pm \frac{G_{\text{in}}^2}{2g\rho} \left\{ \frac{D_{\text{in}}}{\psi D_S} \frac{(1-\varepsilon_e)}{\varepsilon_e^3} \times \left[\frac{100}{R'_{\text{e,in}}} \ln \frac{D_{\text{out}}}{D_{\text{in}}} + 1.75\left(1 - \frac{D_{\text{in}}}{D_{\text{out}}}\right)\right] \pm \frac{1}{\varepsilon_e^2}\left[1 - \left(\frac{D_{\text{in}}}{D_{\text{out}}}\right)^2\right]\right\} \tag{6.27}$$

where the plus sign refers to inward flow and the negative sign to outward flow; D is the bed diameter and subscripts "in" and "out" refer again to bed inlet and outlet conditions, respectively.

Generally, in the case of gas flow through a catalyst bed, the energy-loss term on the right of Eq. (6.21) is predominant when compared to the geodetic term dx and to the velocity-head term dG. The last term on the right of Eqs. (6.26) and (6.27) is negligible. In each case, consistent measurement units must of course be used.

To apply Eqs. (6.26) and (6.27), a knowledge of bed parameters ψ, D_S, and ε_e is required in addition to data pertaining to flow rate, gas properties, and overall bed dimensions.

For particles of regular geometric shape, values of D_S and ψ can be calculated readily from the equivalent sphere definition and by Eq. (6.20), as listed in Table 6.2 for a number of geometric solids. However, the catalyst most commonly used in ammonia synthesis is a crushed and classified material which consists of a mixture of irregular particles having linear dimensions defined by the sieves used in the classification. The surface area of individual catalyst particles is very irregular and complex, and does not permit direct measurement or calculation. Consequently, a nominal sphericity factor of 0.65, as reported in the literature for

TABLE 6.2. Particle Parameters of Regular Geometric Bodies

Shape	Dimensions	v_p	a_p	D_S	ψ
Sphere	D_S	$\pi D_S^3/6$	πD_S^2	D_S	1
Cube	a	a^3	$6a^2$	$1.241a$	0.806
Square Prism	$h = 2a$	$2a^3$	$10a^2$	$1.563a$	0.767
Square Cylinder	$h = d$	$\pi d^3/4$	$3\pi d^2/2$	$1.145d$	0.873
Rectangular Cylinder	$h = 2d$	$\pi d^3/2$	$5\pi d^2/2$	$1.442d$	0.832
Hollow Cylinder	$d_o = d$ $d_i = d/2$ $h = d$	$3\pi d^3/16$	$15\pi d^2/8$	$1.040d$	0.577

similar crushed materials, is often adopted for all particle sizes. The equivalent diameter of the average particle, D_S, can again be calculated on the basis of the equivalent sphere definition:

$$D_S = \left(\frac{6W_S}{\pi \rho_P N_S}\right)^{1/3} \tag{6.28}$$

where W_S and N_S are respectively the weight and the number of particles of a representative catalyst sample. Besides this simple but rather tedious procedure, D_S can also be estimated by the Sauter equation when the catalyst size distribution is known from screen analysis:

$$D_S = \frac{\sum (D_{S,i}^3 W_i)}{\sum (D_{S,i}^2 W_i)} \tag{6.29}$$

where W_i is the fractional weight of particles having size $D_{S,i}$, and $D_{S,i} = (d_1 d_2)^{0.5}$, where d_1 and d_2 are the dimensions defining the sieve fraction.

Within a given catalyst size classification, differences in particle size distribution and in equivalent particle diameter are possible, particularly for wide classification ranges. This is shown in Table 6.3, which collates D_S values obtained by application of Eq. (6.29) to the screen analysis of two catalyst samples, both classified in the range 6–10 mm. When particle size-distribution data are not available, bed parameters for the most commonly used catalyst sizes can be taken from Table 6.4, where ranges of values are given and which allow a satisfactory approximation for use in pressure-drop calculations in industrial converters.

Attention is drawn to the significance of the void fraction values reported in Table 6.4. Inspection of expressions (6.26) and (6.27) shows that the most critical factor in pressure-drop calculation is the estimate of the bed void fraction ε_e, since it occurs in the equations as square and cubic power terms. Besides being dependent upon catalyst size, shape, and roughness, it is also dependent on the bed type and

TABLE 6.3. 6-10 mm Ammonia Synthesis Catalyst Average-Particle Equivalent Diameter

Screen opening (mm)	$D_{S,i}$ (mm)	X_i (weight % on the screen)	
11.10	—	0	0
9.51	10.27	0.04	0.12
8.00	8.72	0.35	0.40
6.35	7.13	0.42	0.40
5.00	5.63	0.15	0.05
3.18	3.99	0.03	0.02
<3.18	3.18	0.01	0.01
	D_S	7.94	8.42

dimensions, and on the mode and rate with which the catalyst is charged into the bed. Pouring the catalyst onto the bed surface followed by raking level results in loose loading with poor homogeneity. Catalyst beds filled by such methods can be expected to shrink after a short time on line, even when it is believed that individual catalyst particles do not shrink during their reduction *in situ*. Due to differences in the coefficients of thermal expansion of the catalyst and the cartridge material, temperature changes during both start-up and continuing operation cause reorientation of the individual catalyst particles giving denser packing, thus leading to a shrinkage of the whole bed with a corresponding increase in the pressure drop. For this reason, catalyst vibration or other techniques for high density loading,

TABLE 6.4. Ammonia Synthesis Catalyst—Bed Parameters

Catalyst size classification (mm)	ψ	D_S (mm)	ρ_P unreduced cat. (g cm^{-3})	ρ_P prereduced cat. (g cm^{-3})
1.5-3	0.65	1.8-2.2	4.85	3.80
3-6	0.65	4.0-4.5	4.75	3.75
4.5-8	0.65	5.5-6.5	4.75	3.75
6-10	0.65	7.5-8.5	4.70	3.70
8-12	0.65	9.5-10.5	4.70	3.70
		ε_e fresh catalyst loose loading	ε_e fresh catalyst dense loading	ε_e aged catalyst
1.5-3		0.46-0.48	0.41-0.43	0.40-0.41
3-6		0.45-0.47	0.40-0.42	0.39-0.40
4.5-8		0.44-0.46	0.40-0.42	0.39-0.40
6-10		0.42-0.44	0.39-0.41	0.38-0.39
8-12		0.42-0.44	0.39-0.41	0.38-0.39

and which consequently allow more catalyst to be charged into the bed, are recommended. This applies particularly to those catalyst beds in which the direction of loading is perpendicular to the direction of gas flow. Even when vibrated during charging, a catalyst bed will still undergo further shrinkage during its lifetime. The values listed in the last column of Table 6.4 are those that may be expected at the end of life, in the case of gradual catalyst aging. They do not include any component arising from malfunctions such as, for instance, crust formation or dust accumulation in the catalyst bed due to breakdown of the catalyst particles by attrition, arising from impingement of the gas entering the bed at high velocity. Such events usually develop quickly, often resulting in a severe and dramatic increase in pressure drop, and uneven flow distribution.

If a longitudinal part of the bed volume is loaded so that the void fraction ε_L is higher than that ε_A assumed in the design equation, the quantity of catalyst in the whole bed is lower than that required to obtain the expected conversion. Furthermore, in operation, a comparatively higher gas flow rate will pass through such a portion of the bed. The two mass velocities, G_L and G_A, are then correlated through the equation $G_L = (1 - \varphi)G_A$, where

$$\varphi = 1 - \left[\frac{1 - \varepsilon_A}{1 - \varepsilon_L}\left(\frac{\varepsilon_L}{\varepsilon_A}\right)^3\right]^{0.5} \tag{6.30}$$

The corresponding fractional flow rates are given in the equations

$$w_L = \frac{a_L(1 - \varphi)}{1 - \varphi a_L} \quad \text{and} \quad w_A = \frac{1 - a_L}{1 - \varphi a_L} \tag{6.31}$$

where a_L is the fractional cross-sectional area with void fraction ε_L.

If the contact time s is defined as the volume of solid in the bed (m^3) divided by the actual flow rate of gas entering the bed ($m^3\,s^{-1}$), the resulting contact time distribution is given by

$$t_L = t_{id}\frac{1 - \varepsilon_L}{1 - \varepsilon_A}\frac{1 - \varphi a_L}{1 - \varphi} \quad \text{and} \quad t_A = t_{id}(1 - \varphi a_L) \tag{6.32}$$

The ideal contact time t_{id} is that pertaining to the whole bed in accordance with the ideal piston-flow assumption,

$$t_{id} = \frac{3600(1 - \varepsilon_A)}{SV_{in}}\,22.414B_{in} \tag{6.33}$$

where the space-velocity, SV, is defined as the ratio of the inlet gas flow rate at standard conditions and the volume of the catalyst bed, $Nm^3\,m^{-3}\,h^{-1}$.

To evaluate the effect resulting from a spread of contact times accurately, the relationship between fractional conversion and contact time of each individual catalyst bed under specific operating conditions must be known. In Fig. 6.2, two

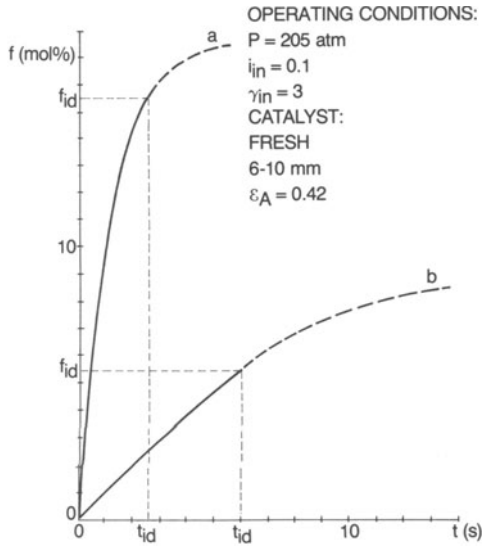

Figure 6.2. Fractional-conversion profiles in adiabatic catalyst beds vs contact time. Curve a represents the behavior of the first catalyst bed of an ammonia converter. Curve b refers to the third catalyst bed, which operates in a range of comparatively low reaction rates, of the same converter.

typical curves giving fractional conversion vs contact time in adiabatic beds are known, and the relevant operating conditions are also given. Curve a refers to an adiabatic bed running at high reaction rates, and shows the behavior of the first catalyst bed of an ammonia converter. Curve b refers to the last catalyst bed, where the inlet ammonia concentration is high, and consequently operating in a range of comparatively low reaction rates. The slope of the tangent to the curve at each point represents the local value of the reaction rate. Dealing with adiabatic catalyst beds, the corresponding temperature profile along each bed shows a similar trend.

If the effectiveness factor EF_{IL} for incorrect loading of the catalyst in the bed is defined as the ratio of the actual weighted-average conversion and the ideal one,

$$EF_{IL} = \frac{\sum_i (f_i w_i)}{f_{id}} \tag{6.34}$$

and the numerical values pertaining to curves a and b are inserted into Eq. (6.34), the values of EF_{IL} reported in Fig. 6.3 are different values of a_L and $\varepsilon_L/\varepsilon_A$ are obtained. In Table 6.5 conversion and temperature profiles along the two parallel bed sectors for $a_L = 0.5$ and $\varepsilon_L = 1.15\varepsilon_A$ are given.

These examples show the order of magnitude of the deviations from the ideal condition that may arise because of incorrect loading. Axial beds always show a similar behavior, since the region adjacent to the wall is always affected by a higher void fraction than that of the central core of the bed. This so-called wall effect has been thoroughly investigated by Schwartz and Smith.[24] They found that when a bed is filled by a method which leads to loose packing, the catalyst particles which settle against the wall tend to generate a zone of considerably higher than

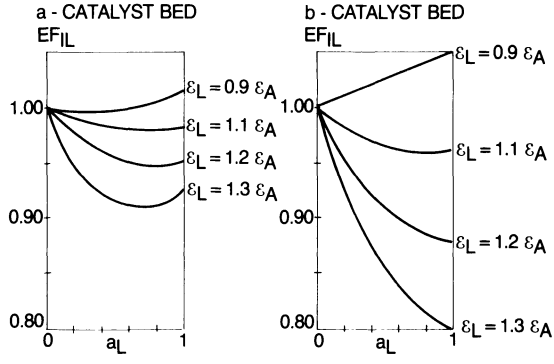

Figure 6.3. Effect of differentiated loading density on the conversion degree of the two catalyst beds of Fig. 6.2. Quantity a_L is the fractional cross-section area of the catalyst bed which has been loaded with a void fraction ε_L higher than that, ε_A, assumed in the design equation (6.81). The operating conditions are as reported in Fig. 6.2.

average voidage, and this effect extends to a depth of a few particle diameters into the bed. In large adiabatic axial beds, the fraction of the cross-sectional area that can be affected by this wall effect is very small. Furthermore, since their height-to-diameter ratios are usually low, differences in loading density are unlikely to occur and to be in the same longitudinal sector for the entire height of the bed. This is not the case for small pilot reactors and, particularly at low linear gas velocity, care must be taken in the assessment and scale-up of the relevant experimental data. In multiaxial and radial beds, which are nearly always rather narrow, differentiated loading densities are more likely to take place, even on an industrial scale converter, and in this case the importance of achieving a catalyst loading as dense and homogeneous as possible is paramount.

It is appropriate at this point to note that the maldistribution component of the bed effectiveness factor can be largely corrected, and the flow distribution improved by insertion in the bed of high-resistance gas redistributors. The maldistribution factor φ then becomes

$$\varphi = 1 - \left[\left(\frac{1-\varepsilon_A}{\varepsilon_A^3} + K\right) \Big/ \left(\frac{1-\varepsilon_L}{\varepsilon_L^3} + K\right)\right]^{0.5} \tag{6.35}$$

TABLE 6.5. Incorrect Catalyst Loading: Conversion and Temperature Profiles Along Adiabatic Beds

Position in the bed (vol% from inlet)	Curve a (first cat. bed) NH$_3$(mol%)		Curve a (first cat. bed) Temperature (°C)		Curve b (third cat. bed) NH$_3$(mol%)		Curve b (third cat. bed) Temperature (°C)	
	z_L	z_A	T_L	T_A	z_L	z_A	T_L	T_A
0	2.50	2.50	400.0	400.0	15.30	15.30	412.0	412.0
20	3.84	4.46	422.4	432.3	15.84	16.08	419.7	423.1
40	5.21	6.50	444.0	463.8	16.39	16.84	427.0	433.3
60	6.60	8.47	465.3	493.3	16.88	17.53	433.9	442.4
80	7.98	10.25	486.1	519.2	17.36	18.13	440.2	450.1
100	9.29	11.00	505.1	529.9	17.80	18.59	445.8	456.0

which approaches zero if the redistributor pressure drop is high in comparison with that of the catalyst bed overall.

High-resistance redistributors are usually placed at the inlet and exit of radial beds, which are frequently characterized by a very low pressure drop even when the smallest grade of catalyst is used. This very low pressure drop, by itself, cannot compensate for dynamic effects developing upstream and downstream of the catalyst bed. The two basic types of flow configuration in radial beds are shown in Fig. 6.4. The gas enters the cartridge parallel to the bed axis, either through the central pipe or the external annulus. It then flows in a radial manner through the catalyst bed and finally passes axially into the exit duct. To facilitate analysis, the following assumptions are made:

1. Since the inlet and exit ducts are uniform, the gas velocity v is the same at any point of the inlet cross section of the duct; this also means that the gas pressure at the inlet of the entrance duct (point A) is uniform.
2. The catalyst bed is uniform with no axial gas mixing in the catalyst bed; any axial flow in the bed would introduce a back-mixing effect and decrease overall conversion, since mixing of gases having different contact time would result.
3. The axial profile of the radial velocity is of the type

$$u(x) = \left[1 + \varphi - 3\varphi\left(\frac{x}{H}\right)^2\right]\bar{u} = \bar{u}\mathrm{N} \tag{6.36}$$

where $\bar{u}$ is the radial velocity with perfect distribution and φ is the maldistribution factor.

Equation (6.36) represents the first-order approximation of the deviation from uniformity ($\varphi = 0$). Along the inlet and exit ducts, the fluid behavior is then governed by a modified form of Eq. (6.15), to which at least one additional term

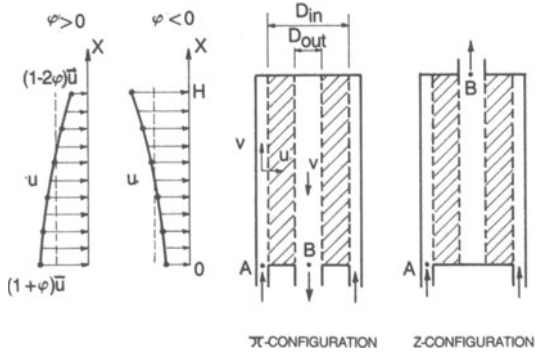

Figure 6.4. Basic flow configurations in radial beds. On the left: the two different axial profiles of the radial velocity for a maldistribution factor φ positive and negative.

must be included to take account of the velocity head of the gas, radially shifted to any level x of the duct height:

$$dx + \frac{dP}{\rho} + d\left(\frac{v^2}{2g}\right) \pm \frac{\pi D}{A}\frac{vu}{2g}\,dx = -\frac{4f}{D_{eq}}\frac{v^2}{2g}\,dx \tag{6.37}$$

where u is the radial superficial velocity, A and D_{eq} are the cross-section area and the equivalent diameter of the duct, while D is the bed diameter at the corresponding duct. The positive sign refers to the exit duct while the negative sign refers to the entrance duct. At any level x, radial velocity is related to axial velocity in the duct through the continuity equation

$$dv = \pm\frac{\pi D}{A}\,u\,dx \tag{6.38}$$

where the plus sign refers to downflow in the inlet and to upflow in the exit ducts, while the negative sign represents the opposite flows. Inserting Eq. (6.38) into Eq. (6.37), rearranging, and integrating between 0 and H yields

$$\Delta P_{out} - \Delta P_{in} = \pm\rho_{out}\frac{\bar{v}_{out}^2}{2g}\left[\tfrac{3}{2}(1 \mp a) + b\left(f_{out} \pm a f_{in}\frac{D_{eq,out}}{D_{eq,in}}\right)\right] + (\rho_{in} - \rho_{out})H \tag{6.39}$$

where

$$a = \frac{\rho_{out}}{\rho_{in}}\left(\frac{A_{out}}{A_{in}}\right)^2 \qquad \text{and} \qquad b = \frac{4}{3}\frac{H}{D_{eq,out}}(1 - \tfrac{7}{10}\varphi + \tfrac{8}{35}\varphi^2)$$

In Eq. (6.39), $\bar{v}_{out}$ is the maximum gas velocity in the exit duct, while the upper sign refers to the π-configuration and the lower sign to the Z-configuration of Fig. 6.4. For downflow in the inlet duct, the sign in front of the last term must be reversed. On the other hand, since the total pressure drop through the system between points A and B is independent of the flow pattern in the middle ($\Delta P_{AB} = \Delta P_{in} + \Delta P_{cat} + \Delta P_{out}$ = constant), this results in

$$\varphi = 1 - \left[1 + \frac{\Delta P_{out} - \Delta P_{in}}{3\Delta P_{cat}(\bar{u})}\right]^{0.5} \tag{6.40}$$

where $\Delta P_{cat}(\bar{u})$ is the pressure drop in the catalyst bed and through its inlet and outlet walls, for perfect gas distribution.

Equations (6.27), (6.39), and (6.40) allow calculation of the maldistribution factor φ and of the distribution of the contact times,

$$t = \frac{V_{cat}}{\pi H D_{in}}\frac{(1 - \varepsilon_e)}{\bar{u}N} = \frac{t_{id}}{N} \tag{6.41}$$

The fraction of the flow rate which spends time t in contact with the catalyst is thus

$$dw = \frac{N}{H}\,dx \tag{6.42}$$

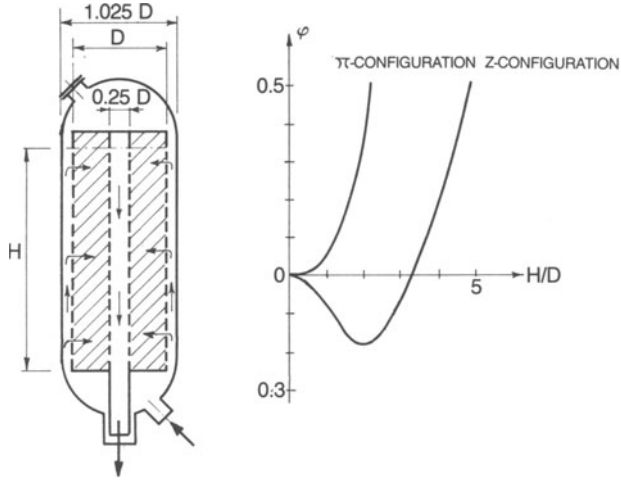

Figure 6.5. Relationship between the maldistribution factor φ and the height-to-diameter ratio of the third catalyst bed of Fig. 6.2 in the π- and Z-configuration. Operating conditions are as reported in Fig. 6.2b.

and the maldistribution effectiveness factor of the bed becomes

$$\mathrm{EF_{MD}} = \frac{\int_0^H f\,dw}{f_{id}} = \frac{\int_0^H fN\,dx}{f_{id}H} \tag{6.43}$$

In Fig. 6.5 the maldistribution factor is shown as a function of the height-to-diameter radio for the previously considered (Fig. 6.2*b*) catalyst bed, in the π- and Z-configuration, and for the sizing indicated in the sketch on the left of the same figure. The corresponding effectiveness factors of the full bed may be seen in Fig. 6.6. These values, of course, refer to a specific example, and the result may be considerably different in other cases. It should be kept in mind that, while the

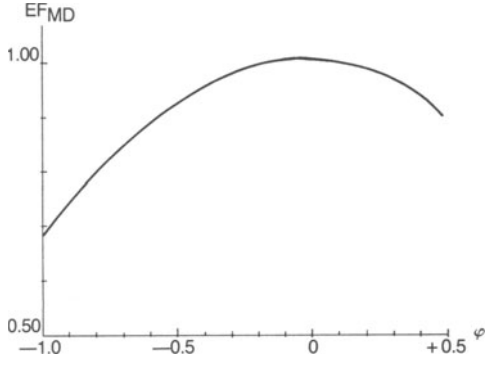

Figure 6.6. Effect of the maldistribution factor φ on the conversion degree for the radial beds considered in Fig. 6.5. Operating conditions are as reported in Fig. 6.2b.

maldistribution factor φ and the flow distribution function N depend only upon the geometric parameters of the bed and do not vary with the total gas flow rate, the maldistribution effectiveness factor EF_{MD} does vary with process conditions, particularly the bed space-velocity, and has to be individually calculated case by case.

Since Eqs. (6.27) and (6.39) do not allow us to distinguish the radial flow direction in the bed, one can state that the centripetal and centrifugal flows are equivalent. Equation (6.39) also shows that, in principle, the π-configuration is preferred when frictional losses in the duct are negligible compared to momentum losses; in contrast, when losses due to friction are predominant, the Z-configuration will give better flow profiles, particularly for slim beds.

It is evident from Eq. (6.40) that flow distribution in radial beds can be improved simply by increasing the pressure drop through the bed and placing high-resistance redistributors at the walls containing the bed. This remedy, however, is not so straightforward as it seems. Perforated plates are commonly employed as redistribution devices. Since the redistributors must produce a higher pressure drop than that generated by the entire bed, through a much lower thickness, their void fraction will be much lower than that of the catalyst in the bed. Considering that the lowest practicable diameter for the distribution holes is in the order of magnitude of the plate thickness, the resulting number of holes will be low and their pitch high. If such a single-wall distributor were put in direct contact with the catalyst, it would generate gas jets and shade zones in the catalyst bed, as illustrated in Fig. 6.7a, thus leaving considerable portions of catalyst unused. The arrangement which proves to be most suitable is thus the double-wall distributor, illustrated in Fig. 6.7b, or something equivalent. Whatever the design, it is important to equalize the pressure after distribution and before the gas enters the catalyst bed.

Finally, it should be remembered that flow maldistribution in radial beds can be even worse than that considered here whenever the favorable assumptions under points (1) and (2) are not fulfilled. In the situation depicted in Fig. 6.5, for instance, the impact of the radial component of the gas jet coming out of the entrance

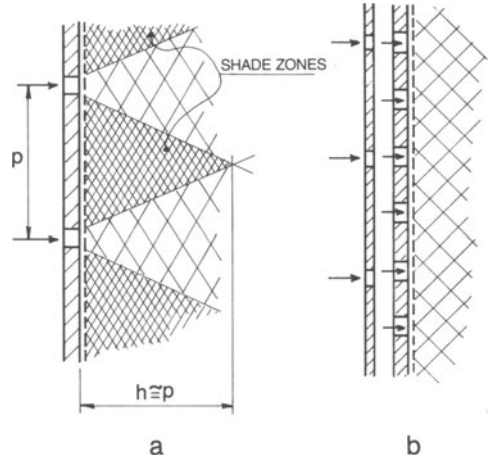

Figure 6.7. Flow redistributors in catalyst beds.

nozzle, against the central pipe and the corresponding wake, generates zones of compression and suction at the inlet to the bed inlet duct that may be much higher than the bed pressure drop. Therefore, care should be exercised during investigations and calculations on fluid flow whenever the pressure drop through a catalyst bed appears too low, and corrective measures are strongly recommended in this case.

Flow redistributors are also usually installed at the top of each transverse bed in horizontal converters, to which a calculation procedure, similar to that presented above for radial beds, is applicable.

An additional distribution problem arises with axial–radial beds. In the upper part of these beds, a certain spread of flow lines occurs, but since this generally involves only a minor portion of the catalyst bed, corrections are not required.

6.2.1.1b. Back-Mixing of Ammonia in Catalyst Beds. Severe temperature and concentration gradients, a direct consequence of the exothermic synthesis reaction, will develop longitudinally in a catalyst bed operating in a steady-state condition. Temperature and concentration gradients could also arise laterally between the center of the bed and the periphery. The conductive heat transfer and the diffusive mass transfer generated through the bed by these gradients affect the ideal displacement conditions and represent deviations from the ideal piston-flow model. The intensity of these dispersion phenomena depends upon the local values of the reaction rate, its derivatives, the specific flow rate, and on the geometric parameters of the catalyst bed. When significant, they must be superimposed on the piston-flow model and the relevant mass- and heat-balance equations become a set of second-order partial differential equations. These can be quite difficult to solve numerically, even when a fairly large computer is available.

The catalyst beds of industrial converters are in most cases thermally insulated. If any uneven flow distribution has been adequately corrected in large adiabatic beds, then there is no driving force for long-range temperature and concentration gradients to exist in lateral directions. Should partial cooling occur at the periphery of an adiabatic bed, this would tend to increase the total conversion and the overall performance of the bed.

In the case of longitudinal mass transfer, we will take into consideration only the back-mixing of product ammonia since, of the concentration gradients developed along the bed by the reaction, those of ammonia are always the most significant. By considering a differential section of a catalyst bed, containing a differential mass of catalyst (dw_B, ton), the ammonia- and heat-balance equations according to the longitudinally dispersed piston-flow model are

$$D_L \rho_B A^2 \frac{P}{\delta RT} \frac{d^2 z}{dw_B^2} dw_B + r\, dw_B = F \frac{dz}{(1+z)} = F_{in} \frac{(1+z_{in})}{(1+z)^2} dz \qquad (6.44)$$

and

$$\lambda_L \rho_B A^2 \frac{d^2 T}{dw_B^2} dw_B + r H_r\, dw_B = F c_p\, dT = F_{in} \frac{(1+z_{in})}{1+z)} c_p\, dT \qquad (6.45)$$

where r is the reaction rate (kmoles of ammonia h^{-1} ton^{-1}), z is the current ammonia mole fraction in the bulk gas, F is the total gas flow rate (kmol h^{-1}), H_r is the reaction heat, defined as positive for exothermic reactions (kcal $kmol^{-1}$), R is the gas constant ($=0.082$ m^3 atm K^{-1} $kmol^{-1}$), c_p is the mean specific heat of the reacting gas (kcal $kmol^{-1}$ K^{-1}), D_L is the apparent diffusion coefficient (m^2 h^{-1}), and λ_L ($=12.5$) is the thermal conductivity of the bed (kcal m^{-1} h^{-1} K^{-1}).

The difference between these equations and those for the ideal piston-flow model is the inclusion of the first term on the left side in each of them. These terms represent the rate of accumulation of ammonia and heat in the bed element, due to mass dispersion and heat conduction, respectively. For small deviations from the ideal piston-flow model, these terms can be omitted in obtaining the second-order derivatives:

$$\frac{d^2z}{dw_B^2} = \frac{r}{F_{in}^2}\frac{(1+z)^3}{(1+z_{in})^2}\left[2r + (1+z)\frac{dr}{dz}\right] \tag{6.46}$$

$$\frac{d^2T}{dw_B^2} = \frac{rH_r}{c_pF_{in}^2}\frac{(1+z)^2}{(1+z_{in})^2}\left[r + (1+z)\frac{dr}{dz}\right] \tag{6.47}$$

We can then evaluate the relative importance of the two terms on the left side of Eqs. (6.44) and (6.45). It can also be shown that longitudinal dispersion effects may be ignored as long as the following conditions are satisfied:

$$\text{MDT} = \left|\frac{\psi D_S}{(P_e)_m}\rho_P\frac{1-\varepsilon_e}{\varepsilon_e}\frac{A}{F_{in}}\frac{(1+z)^2}{(1+z_{in})}\left[2r + (1+z)\frac{dr}{dz}\right]\right| \ll 1 \tag{6.48}$$

$$\text{HDT} = \left|\frac{\psi D_S}{(P_e)_h}\rho_P\frac{1-\varepsilon_e}{\varepsilon_e}\frac{A}{F_{in}}\frac{(1+z)}{(1+z_{in})}\left[r + (1+z)\frac{dr}{dz}\right]\right| \ll 1 \tag{6.49}$$

where $(P_e)_m$ and $(P_e)_h$ are the Peclet numbers for the longitudinal mass and heat transfer, respectively given by

$$(P_e)_m = \frac{\psi D_S V}{\varepsilon_e D_L} \tag{6.50}$$

and

$$(P_e)_h = \frac{\psi D_S V c_p}{\varepsilon_e \lambda_L} B \tag{6.51}$$

For $R_e' \geq 10$, experimental evidence[25] indicates that $(P_e)_m$ and $(P_e)_h$ are constant with respect to the Reynolds number, in particular $(P_e)_m = 2$.

Values of the MDT and HDT terms have been calculated for the two above-mentioned catalyst beds, for axial, centrifugal radial and centripetal radial flow, and are reported in Table 6.6. Some effect of back-mixing of ammonia arises at

TABLE 6.6. Longitudinal Dispersion Effects in Catalyst Beds[a]

Position in the bed (vol% from inlet)	Axial		Radial centrifugal		Radial centripetal	
	MDT 10^3	HDT 10^3	MDT 10^3	HDT 10^3	MDT 10^3	HDT 10^3
	Curve a (first catalyst bed)					
0	4.07	0.17	10.95	1.22	26.10	6.90
20	3.27	0.14	12.24	1.92	19.16	4.71
40	2.17	0.13	14.47	2.98	16.67	3.69
60	3.61	0.15	18.94	4.14	16.44	3.12
80	4.62	0.19	27.05	6.44	16.29	2.63
100	5.95	0.24	28.35	9.71	16.01	1.71
	Curve b (third catalyst bed)					
0	0.83	0.04	4.68	1.12	11.85	7.21
20	0.89	0.04	7.26	2.51	11.66	6.46
40	0.97	0.04	9.69	4.11	11.23	5.52
60	1.04	0.04	12.15	5.93	10.49	4.42
80	1.14	0.05	14.79	8.02	9.21	3.11
100	1.23	0.05	17.47	10.27	6.90	1.60

[a] $H/D = 2$ for the first catalyst bed in radial flow; $H/D = 4$ for the third catalyst bed in radial flow.

the outlet of the first catalyst bed in radial flow and, from this point of view, centripetal flow results in less dispersion than centrifugal. However, since this does not mean a penalty in term of conversion, we may conclude that dispersion phenomena can be disregarded when the continuity equations (6.44) and (6.45) are applied to industrial conditions.

6.2.1.2. Interparticle and Intraparticle Phenomena

Ammonia synthesis catalysts, after reduction, have a very porous structure. By comparing the particle density of prereduced catalysts (3.70 g cm^{-3}) with that of pure iron (7.86 g cm^{-3}) we can estimate an internal void fraction, ε_i, of 0.47. What is more important, however, the average pore radius is normally in the range of 300–400 Å with a very narrow pore-size distribution. This means that activated catalysts have a surface area in the range between 10 and 20 $m^2 g^{-1}$ and that nearly all of their active surface is therefore located within the particles. The intrinsic reaction rate must then be related to the ability of the reactants to gain access to the inner catalyst surface and of ammonia to escape to the external surface of the catalyst particle by diffusion through the pores. Similarly, the heat of reaction, which is released inside the catalyst particles, is transferred to their external surfaces by conduction.

Other factors that could play a role are the mass and heat transfer through the stagnant film which surrounds each catalyst particle. Since these mass- and heat-transfer phenomena are developed by driving forces, temperature and concentration gradients, which would affect the reaction rate, can arise between the

bulk of the flowing gas and the external surface of the catalyst particles, and also within the particles.

At the high linear gas velocities usually encountered in industrial converters, a well-developed turbulence exists in the circulation gas and the film thickness is very small compared to the particle dimensions. Consequently, the largest concentration gradient resides within the catalyst particles. Since the thermal conductivity of iron catalysts, $\lambda_c = 3\ \text{kcal m}^{-1}\ \text{h}^{-1}\ \text{K}^{-1}$, is much higher than that of the synthesis gas, $\lambda_g = 0.12\ \text{kcal m}^{-1}\ \text{h}^{-1}\ \text{K}^{-1}$, the major temperature difference will reside in the external gas film, while catalyst particles themselves will operate under nearly isothermal conditions.

With the aid of Eq. (6.20), and equating the rates of removal through the film with the rates of generation by reaction within the particles, we find

$$z_S - z = \frac{\psi D_S \rho_P}{6 k_g P} r \tag{6.52}$$

and

$$T_S - T = \frac{\psi D_S \rho_P}{6h} r H_r \tag{6.53}$$

where z_S and T_S are ammonia mole fraction and temperature at the catalyst external surface; k_g (kmol $\text{h}^{-1}\ \text{m}^{-2}\ \text{atm}^{-1}$) and h (kcal $\text{h}^{-1}\ \text{m}^{-2}\ \text{K}^{-1}$) are the mass- and heat-transfer coefficients through the film, respectively. Mass transfer through the stagnant film occurs by free molecular diffusion, while heat transfer takes place by conduction. For the evaluation of the corresponding coefficients the well-known analogy developed by Chilton and Colburn will be followed. Their dimensionless factors, J_D and J_H, are numerically similar and have the advantage of correlating the relevant parameters as unique functions of the Reynolds number:

$$J_D \cong J_H \tag{6.54}$$

$$J_D = \frac{k_g M P}{G}(1 + z)\left(\frac{\mu}{\rho D_B}\right)^{2/3} \tag{6.55}$$

$$J_H = \frac{hM}{c_p G}\left(\frac{\mu c_p}{\lambda_g}\right)^{2/3} \tag{6.56}$$

where M is the mean molecular weight of the gas mixture (kg kmol^{-1}) and D_B is the bulk diffusion coefficient of ammonia ($\text{m}^2\ \text{h}^{-1}$).

Dwivedi and Upadhyay[26] have analyzed the experimental data on mass transfer between fluid and particles in fixed and fluidized beds, previously obtained by many authors. From their collection of data referring to gas flow in fixed beds we have found the following correlation, valid for $R'_e \geqslant 10$:

$$J_D = 1.13 R'^{-0.425}_e \tag{6.57}$$

which, upon insertion in Eqs. (6.55) and (6.56), leads to

$$h = 1.13 \frac{c_p G}{M} R_e'^{-0.425} \left(\frac{\mu c_p}{\lambda_g} \right)^{-2/3} \tag{6.58}$$

and

$$k_g P = 1.13 \frac{G}{(1+z)M} R_e'^{-0.425} \left(\frac{\mu}{\rho D_B} \right)^{-2/3} \tag{6.59}$$

The calculated values of temperature and ammonia concentration in the bulk gas and at the catalyst external surface are reported in Table 6.7 for the first catalyst bed of Fig. 6.2 in both axial and radial centrifugal flow. Since radial flow converters are usually filled with smaller-size catalyst particles than the catalyst considered here, from this point of view they are equivalent to axial converters, which are always filled with large-size catalysts to contain pressure drops. It also appears that the effects of mass and heat transfer at the external surface of the catalyst particle are oppositely directed so that they partly compensate for each other. We may conclude that in industrial converters their combined influence on the reaction rate is negligible compared to the inaccuracies inherent in the experimental determination of the intrinsic activity of the catalyst. In any case, interparticle phenomena can be readily incorporated as boundary conditions in the intraparticle problem:

$$y_{A,S} = z_s, \qquad y_{H,S} = y_H - \frac{3}{2} \frac{k_{g,A}}{k_{g,H}} (z_S - z), \qquad y_{N,S} = y_N - \frac{1}{2} \frac{k_{g,A}}{k_{g,N}} (z_S - z) \tag{6.60}$$

TABLE 6.7. Mass- and Heat-Transfer Effects at the Particle External Surface

Position in the bed (vol% from inlet)	z NH_3 (mol%)	z NH_3 (mol%)	T (°C)	T_S (°C)
	Curve a (first catalyst bed) axial			
0	2.500	2.592	400.0	401.4
20	4.200	4.288	428.1	429.5
40	5.960	6.045	455.1	456.5
60	7.700	7.778	481.9	483.2
80	9.300	9.361	505.5	506.6
100	10.500	10.536	522.7	523.3
	Curve a (first catalyst bed) radial centrifugal $H/D = 2$			
0	2.500	2.662	400.0	402.5
20	4.200	4.389	428.1	431.2
40	5.960	6.163	455.1	458.5
60	7.700	7.902	481.9	485.4
80	9.300	9.469	505.5	508.3
100	10.500	10.606	522.7	524.6

The overall reaction rate may be considerably limited by ammonia diffusion through the pores within the catalyst particles. It is generally accepted that under the usual high-pressure conditions adopted on the industrial scale, surface migration and Knudsen diffusion do not contribute significantly to the diffusion rate. A consequence of the high gas density is that the mean free path between intermolecular collisions is small compared to the pore diameter and diffusion takes place almost completely by ordinary gaseous diffusion or bulk diffusion. As a result of this simplifying and conservative assumption, the intraparticle mass transfer only depends upon the partial-pressure gradients along the pores. Considering, then, an isothermal and uniform spherical particle of radius $R_S = \psi D_S/2$, the ammonia molar balance in the radial direction at any internal spherical surface of radius R leads, under steady-state conditions, to

$$\frac{1}{R^2}\frac{d}{dR}(R^2 F_A) = r\rho_P \tag{6.61}$$

By taking into consideration the gaseous volume decrease as the reaction proceeds, resulting in a net molar flow directed toward the center of the particle, the molar flux of ammonia within the particle (kmol m^{-2} h^{-1}) is given by

$$F_A = -\frac{BD_A}{(1+z_i)}\frac{dz_i}{dR} \tag{6.62}$$

where $z_i = y_{A,i}$ is the instantaneous ammonia mole fraction within the pores, and D_A is the effective diffusion coefficient of ammonia through the pores (m^2 h^{-1}). On combining Eqs. (6.61) and (6.62), differentiating, and rearranging we obtain

$$\frac{d^2 z_i}{dR^2} - \frac{1}{(1+z_i)}\left(\frac{dz_i}{dR}\right)^2 + \frac{2}{R}\frac{dz_i}{dR} = -(1+z_i)\frac{r\rho_P}{BD_A} \tag{6.63}$$

which should be solved subject to the following boundary conditions:

$$\frac{dz_i}{dR} = 0 \qquad \text{at } R = 0$$

$$z_i = y_{A,S} \qquad \text{at } R = R_S \tag{6.64}$$

The value at the pore mouth ($R = R_S$) of the first-order derivative of the solution to Eq. (6.63) would allow calculation of the total flow of ammonia coming out of the catalyst particle and, consequently, of the intraparticle effectiveness factor:

$$EF_{IP} = \frac{a_P F_A}{v_P r_S \rho_P} = \frac{3}{R_S}\frac{BD_A}{r_S\rho_P}\left[-\frac{1}{(1+z_i)}\frac{dz_i}{dR}\right]_{R_S} \tag{6.65}$$

where r_S is the reaction rate (kmol of ammonia h^{-1} ton^{-1}) at the particle external surface conditions.

The analytical solution to Eq. (6.63) is not known. On the other hand, the exact numerical integration procedure adopted by Dyson and Simon[27] and Singh and Saraf[28] is rather troublesome and time-consuming even for a fast computer.

A simplified procedure has therefore been proposed by Cappelli and Collina.[29] When the volume contraction due to reaction is ignored and only the ammonia diffusion in a stagnant gas is considered, Eqs. (6.62) and (6.63) are reduced to

$$F_A = -BD_A \frac{dz_i}{dR} \tag{6.66}$$

and

$$\frac{d^2 z_i}{dR^2} + \frac{2}{R}\frac{dz_i}{dR} = -\frac{r\rho_P}{BD_A} \tag{6.67}$$

In Eq. (6.67) two terms of Eq. (6.63), which are numerically similar, have been eliminated. Despite this simplification, Eq. (6.67) can be integrated analytically only when r is a straightforward function of z_i, i.e., for a first-order reaction. This is not true for the ammonia synthesis reaction. As a first approximation, however, we can consider the factor

$$\left|\frac{dr_S}{dz_S}\right| = k^* \tag{6.68}$$

to be equivalent to the constant of a first-order kinetics. We can then express the intraparticle effectiveness factor as a function of the Thiele modulus by the following well-known equation:

$$EF_{IP} = \frac{3}{m}\left[\frac{1}{tghm} - \frac{1}{m}\right] \tag{6.69}$$

where

$$m = \frac{\psi D_S}{2}\left(\frac{k^*}{D_A}\right)^{0.5} \tag{6.70}$$

The effective diffusivity takes into account the facts that not all of the area normal to the direction of the flux within the particle is free for diffusion and that the paths are tortuous. An equation that relates D_A in the pore to the bulk diffusivity is

$$D_A = \frac{\varepsilon_i}{\tau} D_{B,A} \tag{6.71}$$

where ε_i is the internal void fraction of the catalyst particle ($\varepsilon_i = 0.55$), and τ is the tortuosity, defined as the ratio of the actual distance between two points along the pore and the shortest distance between those two points ($\tau = 2.2$).

The diffusion coefficient can be converted from its normal value by the relation

$$D_{B,A} = D_A^0 \left(\frac{T}{273}\right)^{1.75} \frac{1}{P} \tag{6.72}$$

The normal diffusivity of ammonia in a mixture of hydrogen and nitrogen can, in turn, be calculated from the respective binary diffusion coefficients through the following relation proposed by Fairbanks and Wilke[30]:

$$D_A^0 = (1 - z_S) \Big/ \left(\frac{y_{H,S}}{D_{A,H}^0} + \frac{y_{N,S}}{D_{A,N}^0}\right) \tag{6.73}$$

The values of normal diffusivities used in our calculation are $D_{A,H}^0 = 0.257$ and $D_{A,N}^0 = 0.0788$ ($m^2\,h^{-1}$).

Similar considerations apply to the thermal effects in catalyst particles. An energy balance in the spherical particle leads to a differential equation which is identical to Eq. (6.63), if the following relation holds:

$$T_i - T_S = \frac{BD_A H_r}{\lambda_c}(z_i - z_S) \tag{6.74}$$

where z_i is the mole fraction of ammonia at any point within the particle and T_i is the local temperature. Equation (6.74) can be used to estimate the maximum possible temperature difference between the interior of the particle and the surface. Since the mole fraction of ammonia, z_{eq}, at equilibrium depends only upon the total pressure and on the hydrogen-to-nitrogen molar ratio γ and is maximum for $\gamma = 3$, we can state that the maximum possible temperature inside the particle is

$$T_M = T_S + \frac{BD_A H_r}{\lambda_c}(z_{eq} - z_s) \tag{6.75}$$

Values of the intraparticle effectiveness factors, calculated according to Eq. (6.69), and of maximum temperature gradients within the catalyst particles for the two beds of Fig. 6.2 are reported in Table 6.8.

6.2.2. Chemical Factors

Other factors that must be taken into consideration in converter design and simulation are the presence of catalyst poisons in the circulation gas in contact with the catalyst and progressive catalyst aging. It is well known that, even with the best of care, a catalyst charge deactivates in industrial service through sintering or poisoning. This subject is dealt with in detail in Chapters 7 and 8. In this chapter, only the effect of oxygen-containing compounds on intrinsic catalyst activity and reaction rate will be examined.

TABLE 6.8. Intraparticle Effectiveness Factors and Temperature Gradients

Position in the bed (vol% from inlet)	EF_{IP}	$T_M - T_S$ (°C)
Curve a (first catalyst bed)		
0	0.218	4.86
20	0.332	3.27
40	0.409	2.11
60	0.465	1.35
80	0.498	0.90
100	0.511	0.59
Curve b (third catalyst bed)		
0	0.905	2.77
20	0.903	2.47
40	0.901	2.15
60	0.898	1.79
80	0.895	1.45
100	0.893	1.15

6.2.2.1. Temporary Poisoning of the Ammonia Catalyst by Oxygen-Containing Compounds

The oxygen-containing compounds most frequently present in the make-up gas of an ammonia plant are water vapor, traces of carbon monoxide, and carbon dioxide. Water and carbon dioxide are usually almost completely removed in the last ammonia condensation stage of the synthesis loop before reaching the converter. To save energy in a few recent ammonia plants, the fresh make-up gas is dried by molecular sieves, which can also adsorb carbon dioxide, and is then introduced into the synthesis loop at the converter inlet. Whichever method is used, traces of carbon monoxide reach the converter continuously and affect the catalyst activity adversely. However, poisoning by oxygenated compounds may be considered to be only a temporary effect because they lower the catalyst activity only as long as they are present in the synthesis gas. In old plants where the final gas purification step was a copper-liquor wash to remove carbon monoxide, the leakage of considerable amounts of carbon monoxide toward the synthesis loop was not rare. When this occurred, the catalyst activity was gradually restored when operation with pure gas was resumed.

It is also known that catalysts characterized by a high thermal stability are less sensitive to the action of oxygen-containing poisons.

There is general agreement that equivalent concentrations, on an oxygen atom basis, of water, carbon monoxide, carbon dioxide, and oxygen give rise to the same extent of deactivation. On the other hand, it is also well known to operators of high-pressure methanol plants that activated iron is a very good methanation catalyst:

$$CO + 3H_2 = CH_4 + H_2O$$

$$CO_2 + 4H_2 = CH_4 + 2H_2O$$

For example, the conversion of carbon monoxide to methane is reported to be complete, for concentrations of carbon monoxide up to 0.7%.[31]

Assuming that atomic oxygen competes with molecular nitrogen for adsorption sites on the catalyst surface, Temkin and co-workers[9] determined the rate equation (6.9), which gives the reaction rate r_w during water-vapor poisoning. In the case where $P_w = 0$, Eq. (6.9) simplifies to the original well-known Temkin equation. The ratio of the reaction rate during temporary poisoning to the rate with pure gas may be regarded as a correction factor which accounts for temporary poisoning:

$$\begin{aligned} EF_{TP} = \frac{r_w}{r} &= [1 + CP_w(P_H/P_A)^2]^{-0.5} \\ &= \left\{1 + CPy_{w,in}\frac{(1+z)}{(1+z_{in})z^2} \right. \\ &\quad \left. \times \left[\frac{\gamma_{in}}{(1+\gamma_{in})}(1 - i_{in} - z_{in})\frac{(1+z)}{(1+z_{in})} - \frac{3}{2}\frac{(z - z_{in})}{(1+z_{in})}\right]^2\right\}^{-0.5} \end{aligned} \tag{6.76}$$

where $y_{w,in}$, z_{in}, and i_{in} are molar fractions of equivalent water ($y_w = y_{H_2O} + y_{CO} + 2y_{O_2} + \cdots$), ammonia, and inert compounds in the gas entering the converter or the catalyst bed; γ_{in} is the hydrogen-to-nitrogen molar ratio in the inlet gas, z is the current ammonia molar fraction in the reacting gas, and P is the total pressure (atm).

Using the experimental data of I. A. Smirnof reported by Nielsen,[31] we find the temperature dependence of C given by the following relation:

$$C = A_w \exp(8700/T) \tag{6.77}$$

with $A_w = 1.5 \times 10^{-6}$ for a singly promoted iron catalyst and $A_w = 1.78 \times 10^{-6}$ for a doubly promoted catalyst.

Values of the correction factor for temporary poisoning, calculated by Eq. (6.76) for different operating conditions and different contents of equivalent water, are reported in Tables 6.9 and 6.10. The mean value of the correction factor is the ratio between the amount of catalyst that would be necessary for operation with pure gas and that required to obtain the same conversion with oxygenated compounds in the feed gas. These values suggest that it should be advantageous to move the addition point of the make-up gas into the synthesis loop, and thus use the make-up gas as a quench gas for the last catalyst bed of the ammonia converter. How long a catalyst charge can operate under these conditions without showing further deactivation is not known. It is possible that the last catalyst bed of the ammonia converter, with a suitable catalyst under mild operating conditions, could be a substitute for the methanation step in the gas-preparation section. This appears to be feasible provided that a carbon monoxide selective oxidation plant followed by molecular sieves or an equivalent purification treatment is placed upstream the synthesis unit.

TABLE 6.9 Correction Factors for Temporary Poisoning

NH_3 (mol%)	Temperature (°C)	Equivalent water content in the gas entering the bed		
		5 ppmv	40 ppmv	400 ppmv
	Curve a (first catalyst bed)			
2.50	400.0	0.815	0.446	0.156
4.20	428.1	0.952	0.739	0.328
5.96	455.5	0.985	0.894	0.534
7.70	481.9	0.994	0.955	0.715
9.30	505.5	0.997	0.978	0.830
10.50	522.7	0.998	0.987	0.887
	Mean Value	0.997	0.972	0.775
	Curve b (third catalyst bed)			
15.30	412.0	0.996	0.971	0.789
15.97	421.6	0.997	0.978	0.828
16.64	430.7	0.997	0.983	0.859
17.27	438.9	0.998	0.986	0.883
17.83	446.2	0.998	0.989	0.902
18.30	452.3	0.999	0.990	0.915
	Mean Value	0.998	0.986	0.883

6.2.2.2. Self-Poisoning of the Ammonia Catalyst during Reduction

Water vapor is always in contact with any catalyst charge while it is being reduced from magnetite to active iron. The process conditions for catalyst reduction in industrial installations are selected to minimize the partial pressure of water vapor in the reducing gas and hence its adverse effect on the initial activity of the

TABLE 6.10 Correction Factors for Temporary Poisoning

Bed inlet conditions: pressure = 85 atm, $\gamma_{in} = 2.5$, $i_{in} =$ 12 mol%, $y_{w,in} = 400$ ppmv)		
NH_3 (mol%)	Temperature (°C)	EF_{TP}
9.00	390.0	0.674
10.00	405.2	0.765
11.00	419.6	0.834
12.00	433.7	0.884
	Mean Value	0.820

TABLE 6.11. Self-Poisoning Corrective Factors

Catalyst size classification (mm)	Catalyst type	ψD_S (mm)	EF_{SP}
Crushed	Unreduced	0.5	1
1.5-3	Prereduced	1.4	0.90-0.95
3-6	Prereduced	2.9	0.78-0.85
6-10	Prereduced	5.4	0.70-0.80
8-12	Prereduced	6.5	0.65-0.75

catalyst. Thus, while pressure is maintained below 100 atm, a gas circulation rate as high as possible is used throughout the reduction procedure and, once water begins to form, the temperature increase is carefully controlled so that water concentration in the gas leaving the converter never exceeds 3000 ppm. Therefore, even when reduction on the industrial scale is carried out using the most favorable conditions, thousands of ppm of water are present in the gas flowing between the catalyst particles. Since the transfer of water vapor, from inside each catalyst particle to the bulk gas, takes place by diffusion along the porous structure as it is being formed, even higher concentrations of water are in direct contact with the internal surface of the catalyst during the most critical moments. Indeed, it is apparent that reduction, which usually lasts five or six days, is the first challenge that a catalyst charge must face in its life.

It seems reasonable to assume that an oxidation-reduction dynamic equilibrium is established on the catalyst surface during the reduction step and that appreciable restructuring of the catalyst surface can take place. Since the kinetics of the process are controlled by pore diffusion, particle size and shape once again play an important role in determining the initial activity of the catalyst. In fact, rate measurements conducted by the authors in the laboratory with prereduced catalysts of various particle sizes show that the initial activity of the larger catalyst particles is considerably lower than that of the smaller particles. Consequently, another corrective factor, EF_{SP}, which takes into account the influence of the catalyst particle size on this inherent self-poisoning effect, must be included in the rate equation for use in converter calculations. Values of EF_{SP} for various catalyst size ranges are reported in Table 6.11.

6.3. APPLICATION TO CONVERTER DESIGN AND OPERATION

In the previous sections, the fundamental kinetic equations that can be used to correlate experimental data and to calculate ammonia production under given operating conditions have been discussed. Chemical and physical factors, such as mass, heat, and momentum transfer, which could limit the available active surface of the catalyst and the reaction rate in industrial service, have also been mentioned and evaluated. In the following section, we shall consider the basic design criteria

of industrial converters and develop a mathematical model suitable for calculating their performances on the basis of known rate constants.

The first requirement is that the process design of an ammonia synthesis converter must be consistent with the thermodynamic restrictions on reaction rates, and with the catalyst properties. These limitations are indicated qualitatively in Fig. 6.8, in which temperatures are plotted as functions of ammonia concentrations for a given total pressure and given inert level i_{in}, at a hydrogen-to-nitrogen ratio γ_{in}, for the gas entering the converter. Pressure and inlet gas composition are basic design parameters derived from complex economic considerations and do not vary significantly in a synthesis loop operating at steady-state conditions.

The principal limitation to the overall performance of an ammonia converter is generated by the reaction equilibrium. Since the reaction is exothermic, the equilibrium concentration of ammonia falls as the reaction temperature increases. Since the number of moles of gas decreases as the reaction proceeds, the equilibrium line moves from left to right in the figure and the concentrations of ammonia at equilibrium rise when the pressure increases, or the inert level decreases, and *vice versa.* Although the highest equilibrium concentrations of ammonia are obtainable with $\gamma_{in} = 3$, the highest production rate was found at $\gamma_{in} < 3$, as noted by Nielsen.[31] Moreover, since hydrogen is considerably more expensive than nitrogen, operations at $\gamma_{in} > 3$ are not of practical interest.

Other limitations to the industrial operating conditions are imposed by the intrinsic activity of the catalyst and its resistance to thermal sintering. When the catalyst is kept at a temperature higher than its maximum allowable temperature (540 °C for common commercial catalysts when operated on pure synthesis gas) it quickly loses its activity due to a surface reorganization of its structure. The limitations imposed by the materials of construction are a further reason why temperatures above this value must not be allowed in industrial converters.

The minimum allowable temperature is determined by the minimum industrially acceptable reaction rate. Under normal operating conditions, the exothermic reaction is self-substaining. Whenever the catalyst temperature is lowered, the

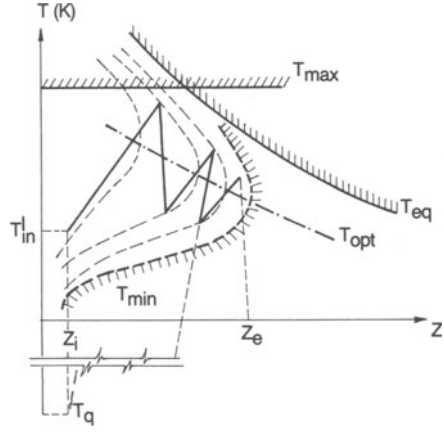

Figure 6.8. Reaction-rate curves in the field temperature (T)-ammonia mole fraction (z). The region of industrial interest is limited by the equilibrium line (T_{eq}), the intrinsic activity of the catalyst (T_{min}), and its resistance to thermal sintering (T_{max}).

reaction rate falls with a consequent fall in the amount of heat generated. Below a certain limit the heat of reaction is unable to sustain the process and stability is lost. In this way industrial converters are usually shut down and cooled. A further consequence is that external heating is necessary at the start-up of the converter before the autothermal reaction process can be established. In other words, the synthesis loop must be equipped with a start-up heater. For a freshly charged very active catalyst, the minimum temperature at low ammonia concentrations is approximately 350–360 °C and the T_{min} line moves upward to 390–400 °C for less active or aged catalysts. When a more active catalyst becomes commercially available, the T_{min} line will move toward lower temperatures. The same degree of conversion for a given quantity of catalyst would then be obtained at a lower pressure and temperatures which will certainly be the future trend in catalyst development.

Only the region within the above-mentioned boundaries is therefore of current industrial relevance. At any given point within this region, the reaction rate depends only on the actual activity of the catalyst. The rate varies from point to point determined by two opposing factors: temperature and isothermal distance from the equilibrium line. Thus, at any fixed ammonia concentration the reaction rate at first rises with the increasing temperature, reaches a maximum, and then falls rapidly as the equilibrium line is approached. In Fig. 6.8, broken lines connect identical values of reaction rate for a catalyst of given intrinsic activity. It should be noted that each line has a maximum at a certain temperature, which is a function of the ammonia concentration. The locus of these maxima (dotted line) represents the optimum temperature profile. This "ideal" temperature sequence along the converter minimizes the quantity of catalyst required for a given total conversion, $z_e - z_i$, at a given circulation rate. Below the T_{opt} line, the system is too far from equilibrium and the reaction speeds up when the temperature is raised; above the T_{opt} line, the reaction becomes equilibrium limited and it is advantageous to lower the temperature to increase the conversion. The position of the T_{opt} line may be determined by successive approximation or by differentiating the rate equation $r_S = r_S(z, T)$ with respect to T and setting $\delta r_S / \delta T = 0$.

The reaction rate decreases continuously along the ideal temperature profile line, and a continuous decrease in the heat removed from the system as the reaction proceeds should therefore be necessary for following the optimal sequence. Since, in practice, it is impossible to achieve this target precisely, the ideal converter is not realizable. Nevertheless, the best approximation to the T_{opt} line should be the aim both in converter design and in converter operation.

It has already been mentioned that modern ammonia synthesis converters have been designed with the catalyst charge arranged in adiabatic beds. Contrary to the ideal temperature profile, the temperature in each of them rises from inlet to outlet following a nearly straight line, in the T–z field, the slope of which depends only upon the ratio between the heat of reaction and the specific heat of the reacting gas. The adiabatic temperature rise of the ammonia synthesis reaction (approximately 14–15 °C/1% increase in ammonia concentration) is such that high temperatures are reached for rather low conversions. This means that high conversions cannot be achieved with a single adiabatic catalyst bed and that the converter

design must include means for lowering the temperature of the reacted gas after it leaves each catalyst bed. A series of sawtooth movements around the optimum line is the result. The larger the number of beds with interbed cooling, the closer the converter performance approaches the optimum line. The total quantity of catalyst required to reach the expected total conversion is therefore minimized.

Interstage coolings are achieved in practice either by means of heat-exchange surfaces, which are more efficient but more difficult to be arranged within the converter, or alternatively by injection of a portion of cold synthesis gas to the gas leaving each catalyst bed. When cooling by means of quenching, the ammonia concentration of the gas leaving each catalyst bed is lowered by the injection of cold, unreacted synthesis gas. A significant proportion of the circulation gas does not therefore pass through all the catalyst beds. A consequence of the effects of dilution and bypass is a penalty in converter size: for a given total conversion, a quench-type converter requires some 10–15% more catalyst than a converter with indirect cooling and with the same number of beds. Moreover, the quench converter must also be provided with very efficient gas distribution and mixing devices. In either case, easily operable, precise temperature-control systems are necessary to ensure reaction stability and optimal operation.

Superimposed on the graphs in Fig. 6.8 is the reaction profile occurring in a typical three-bed converter. The first intermediate cooling is performed by a heat exchanger, in which the gas temperature decreases without any dilution, while the second cooling is performed by direct quench with cold gas.

In accordance with the piston flow and the steady-state assumptions, and in the absence of significative diffusion phenomena, the ammonia molar balance equation for a differential mass of catalyst, dw_B, is thus given by

$$r\,dw_B = \frac{F}{(1+z)}\,dz = \frac{F_{in}(1+z_{in})}{(1+z)^2}\,dz \tag{6.78}$$

In the case where the reaction takes place adiabatically and heat conduction is not significant, the heat balance equation simplifies to

$$rH_r\,dw_B = Fc_p\,dT \tag{6.79}$$

or

$$dT = \frac{H_r}{c_p(1+z)}\,dz \tag{6.80}$$

Finally, by integration of Eq. (6.78) from inlet to outlet conditions, the volume v_B of each catalyst bed can be obtained (m^3):

$$v_B = \frac{w_B}{\rho_p(1-\varepsilon_A)} = \frac{F_{in}(1+z_{in})}{\rho_p(1-\varepsilon_A)} \int_{z_{in}}^{z_{out}} \frac{1}{(1+z)^2}\,\frac{dz}{r} \tag{6.81}$$

The rate of ammonia formation (kmol h^{-1} ton^{-1}) derived from the classical rate equation of Temkin-Pyzhev, slightly modified by introducing activities instead of partial pressures, becomes

$$r = k_{act}[K_{eq}^2 a_N (a_H^3/a_A^2)^{\alpha} - (a_A^2/a_H^3)^{(1-\alpha)}] \tag{6.82}$$

where the activities can be expressed in terms of molar fractions and fugacity coefficients of each pure component at the temperature and pressure of the system:

$$a_i = \nu_i y_{i,S} P \tag{6.83}$$

The terms $y_{i,S}$ are given by Eqs. (6.60) in which

$$\begin{aligned} y_H &= [\gamma_{in} b_{in} + \tfrac{3}{2} z_{in} - z(\tfrac{3}{2} - \gamma_{in} b_{in})]/(1 + z_{in}) \\ y_N &= [b_{in} + z_{in}/2 - z(\tfrac{1}{2} - b_{in})]/(1 + z_{in}) \\ y_A &= z \end{aligned} \tag{6.84}$$

with

$$b_{in} = (1 - i_{in} - z_{in})/(1 + \gamma_{in})$$

A consistent set of the thermodynamic data required for calculations was originally given by Beattie[32] and by Gillespie and Beattie.[33] The equilibrium constant, fugacity coefficients, and heat of reaction can be obtained from the following sources:

1. The equilibrium constant K_{eq} as a function of temperature: Gillespie and Beattie,[33] also reported by other authors.[6,27,31,34,35]
2. The fugacity coefficients of pure components, ν_i: Cooper,[36] Newton,[37] and others.[6,27,31,34]
3. The heat of reaction, H_r, corrected by the heat of mixing: Kazarnovskii,[38] and Gaines.[34]

The specific heat of each component, corrected for the departure from ideality, is given by Hougen *et al.*[39] More accurate estimations of the temperature rise from Eq. (6.80) are obtainable by using enthalpy rather than specific heat. In this case, the value of the heat of reaction at the standard conditions for the enthalpies must be used (e.g., $H_r^0 = 11{,}040$ kcal $kmol^{-1}$ at 1 atm and 298 K).

The mole fractions of ammonia at equilibrium, $(y_A)_{eq}$, can be calculated through the equilibrium constant by the mass-action law:

$$\frac{\nu_A}{\nu_N^{0.5} \nu_H^{1.5}} \frac{(y_A)_{eq}}{(y_N)_{eq}^{0.5} (y_H)_{eq}^{1.5}} \frac{1}{P} = K_{eq} \tag{6.85}$$

In Eq. (6.82), the factor k_{act} includes the kinetic constant of the reverse reaction, k_2, and the effectiveness factors, EF_{ij}, for the rate-limiting phenomena as discussed in the previous section, namely,

$$k_{act} = (k_2 EF_{SP} EF_{TP} EF_{AG})_S EF_{IP} \tag{6.86}$$

where EF_{AG} is the catalyst aging factor, which can be defined as the ratio between the current activity of the catalyst and its initial value. The kinetic constant represents the temperature-dependent term of the rate equation as given by the Arrhenius expression,

$$k_2 = k_{20} \exp\left[-\frac{E_2}{R}\left(\frac{1}{T} - \frac{1}{T_0}\right)\right] \tag{6.87}$$

where E_2 is the activation energy for the ammonia decomposition reaction (kcal kmol^{-1}), $R = 1.987$ is the gas constant (kcal kmol^{-1} K^{-1}), T_0 is a reference absolute temperature (K), and k_{20} is the frequency factor (kmol of NH_3 atm$^{(1-\alpha)}$ h^{-1} ton of catalyst^{-1}).

The numerical values of E_2 and k_{20} represent the intrinsic activity of the catalyst measured on crushed catalyst at a normal particle size of 0.5 mm and which must be determined from experimental data worked out using the same rate expression. Kinetic measurements must be obtained in standard testing equipment on a sample of fresh catalyst as commercially available. The experimental conditions should cover the range representative of the industrial conditions as closely as possible. When the rate equation (6.82) with $\alpha = 0.75$ is used, a typical value of the kinetic constant E_2 is 40,500. The constant k_{20} varies from (70–80) for unreduced catalysts and (80–90) for prereduced catalysts, when $T_0 =$ 7.23.2 K (450 °C).

The rate expression is complex, so the mass- and energy-balance differential equations (6.78) and (6.80) must be solved numerically using a step-by-step procedure from given initial values corresponding to the known conditions at the inlet of each catalyst bed. A graphical integration procedure is illustrated in the upper section of Fig. 6.9.

Equations (6.81), (6.80), and (6.82) are essential components for building a mathematical model of the converter, which may then serve the following purposes:

1. Determining the current activity of a catalyst charge in service and estimating its residual life from a standard die-off program.
2. Optimization of the control of an operating converter, and optimization of the design of the converter type and size.

When the model is used to determine the catalyst activity relative to a particular converter using a consistent set of operational data, the aim is reached simply by letting the program find the catalyst aging factors which reproduce the measured catalyst temperatures as accurately as possible. With this method, the numerical integration procedure recycles until, with a suitable integration step, the actual volume of each catalyst bed is reached and the outlet temperature of each bed is equal to the measured value.

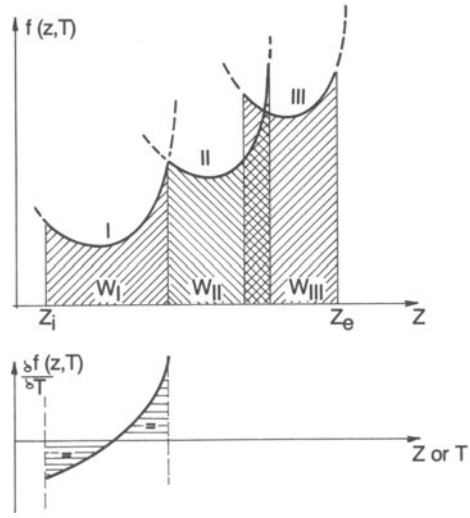

Figure 6.9. Graphical calculation of catalyst volumes. The volume of each bed is proportional to the area under the curve relating the function $f(z, T) = 1/(1 + z)^2/r$ to z.

Since each converter is designed for the catalyst activity and the operating conditions normally expected at the end of the useful life of a catalyst (typically two-thirds of the initial activity after five years of operation at 250 atm and after ten years at 150 atm), in the early stages of a new charge, the catalyst is not working to its limits. Throughout much of the catalyst life, the plant operator can therefore then take advantage of this situation in several ways, such as:

1. By increasing the load of the plant, provided the corresponding additional make-up gas is available.
2. By allowing the loop pressure to decrease, thus saving energy in the make-up gas compressor.
3. Increasing the level of inert gas in the loop by reducing the purge rate, thus increasing the overall conversion yield.
4. Increasing the conversion per pass by reducing the circulation rate, provided the design temperature at the converter outlet is not exceeded, leading to an increase in the recovery of the heat of reaction and saving energy in the circulation and refrigeration compressors.

The opportunity for optimizing control of the converter arises, and the operator should then be able to select from the available operating conditions those which will maximize profits or minimize variable production costs. The performance-optimization program must therefore include an economic objective function which involves factors such as market, sales, product price, raw materials, and energy costs. So far as kinetic aspects are concerned, for any set of operating conditions considered by the model, the maximization of the total conversion obtainable with a given quantity of catalyst is then achieved using the method of Horn,[40] by determining the inlet temperature for each catalyst bed that satisfies the following condition:

$$\int_{\text{in}}^{\text{out}} \frac{\delta f_S(z, T)}{\delta T}\, dz = 0 \tag{6.88}$$

The meaning of Eq. (6.88) is easily interpreted by looking at the graphical solution plotted in the lower section of Fig. 6.9. The "best" set of operating conditions varies throughout the life of the catalyst as its activity decreases. When all the options mentioned above for operating the converter are completely exhausted, the catalyst charge will have to be replaced.

The minimum total quantity of catalyst for a given pressure and a given inlet gas composition is obtainable by including in the design program the equation

$$\underset{\text{previous bed}}{f(z, T)_{\text{out}}} = \underset{\text{next bed}}{f(z, T)_{\text{in}}} \tag{6.89}$$

in addition to Eq. (6.88). Independent of the number of beds, Eqs. (6.88) and (6.89) reduce the problem of optimum design to a one-dimensional search, where only the best inlet temperature at the first catalyst bed needs to be found. Nevertheless, the catalyst temperatures leading to the minimum quantity of catalyst do not correspond to the optimum converter design and optimization should be carried out at a level which involves the entire synthesis loop. In principle, the program for optimum design should include all the parameters which determine the economics of the system and the economic objective should be formulated in terms of total investment, production costs, or return on investment.

In practice, the design parameters of a synthesis loop are often dictated by engineering considerations such as the maximum allowable delivery pressure, the minimum allowable efficiency for centrifugal compressors, and the maximum weight for vessels and heat exchangers. Thus, the design pressure, which rarely exceeded 300 atm in the recent past, is presently limited to the range 90–160 atm and the inert gas level at the converter inlet lies in the range 10–15 mol%, when the make-up gas contains about 1 mol% of inerts.

For a given production capacity, the total quantity of catalyst and the converter size are approximately proportional to the total conversion per pass. However, the converter should be designed for a high conversion, because this will mean savings in energy consumptions due to:

1. A lower circulation rate.
2. Lower energy requirements in the refrigeration section.
3. More efficient recovery of the heat of reaction.
4. Lower investment costs, since low recycle rates require smaller equipment and piping in the remaining part of the synthesis loop.

The optimum conversion should therefore be found by balancing the increase in the capital cost of the plant with the increased energy saving.

In any case, an important task of the designer is to arrange the reaction system in such a way that it is possible to recover the maximum heat of reaction at the maximum temperature, in addition to preheating of the gas entering the converter

up to the reaction temperature. It is then necessary to transfer this heat to the high-pressure steam system of the plant either through boilers or boiler feed water preheaters. When a converter is designed for a high conversion per pass, it is necessary to arrange the converter layout so that part of the heat of reaction is recovered before the conversion has been completed. In this case, the boiler not only generates high-pressure steam but also controls the interbed temperature.

In its most common configuration, an ammonia converter consists of an external heavy vessel in carbon or low-alloyed steel and an internal apparatus, the cartridge which is comparatively light, fabricated in stainless steel, and which contains both the catalyst and the interbed-cooling devices. Thermal insulation is provided between the two. Most of the designers in the past have avoided putting the materials of construction under the combined action of both high pressure and high temperature, thus avoiding the problem of embrittlement arising from hydrogen attack and nitriding. For this reason, the ammonia converter also usually contains at least one gas–gas heat exchanger. The cold inlet gas flows through the annular space between the vessel and the insulated internal apparatus before entering the heat exchanger. Such an arrangement also allows a higher design stress for the construction materials of the vessel and eliminates the cost of a high-pressure shell for the heat exchangers. In a particular nonadiabatic converter type, namely the Fauser–Montecatini converter, in which the heat of reaction was completely recovered inside the converter, the entire high-temperature area of the synthesis loop was confined within the internal structure of the ammonia converter.

To avoid overstress and failure, the internal apparatus within the converter must be designed to allow free thermal expansion for all components and the catalyst beds must have a low pressure drop. Precautions must be taken to prevent the gas from bypassing the catalyst beds, the heat exchangers, and cooling devices by fitting high-integrity, long-lived internal couplings. The converter design must also provide easy access for maintenance. A satisfactory means of charging and discharging the catalyst is also required. If the cartridge is not removable because the vessel is not provided with a full closure, the design and fabrication must also ensure that the vessel can be heat-treated after welding and hydraulically tested with the cartridge in place. Obviously, safety and reliability are essential when in operation.

It is comparatively rare to find such a number of features combined together within one single item of equipment. That is why the synthesis converter is still considered a key item in the ammonia plant and a distinguishing feature of the various options available in the technology of ammonia production.

Reviews of the different converter types most frequently used in industrial applications are available in the literature.[41-44]

REFERENCES

1. C. Bokhoven, C. Van Heerden, R. Westrik, and P. Zwietering, in: *Catalysis* (P. H. Emmett, ed.), Vol. 3, p. 318, Reinhold, New York (1955).

2. M. Temkin and V. Pyzhev, *Acta Physicochim. USSR* **12**, 327 (1940).
3. Ref. 1, p. 321.
4. M. Temkin, *J. Phys. Chem. USSR* **24**, 1312 (1950).
5. A. Nielsen, J. Kjaer, and B. Hansen, *J. Catal.* **3**, 68 (1964).
6. U. Guacci, F. Traina, G. Buzzi Ferraris, and R. Barisone, *Ind. Eng. Chem., Prod. Des. Dev.* **16**, 166 (1977).
7. M. I. Temkin, N. M. Morozov, and E. N. Shapatina, *Kinet. Catal. (Engl. Transl.)* **4**, 565 (1963).
8. G. W. Bridger and C. B. Snowdon, in: *Catalyst Handbook*, p. 141, Wolfe Scientific Books, London (1970).
9. I. A. Smirnof, N. M. Morozov, and M. I. Temkin, *Dokl. Akad. Nauk SSSR* **153**, 386 (1963).
10. S. Brunauer, K. S. Love, and R. G. Keenan, *J. Am. Chem. Soc.* **64**, 751 (1942).
11. A. Ozaki, H. S. Taylor, and M. Boudart, *Proc. R. Soc. London, Ser. A* **258**, 47 (1960).
12. A. Nielsen, J. Kjaer, and B. Hansen, *J. Catal.* **3**, 68 (1964).
13. R. Brill, *J. Catal.* **16**, 16 (1970).
14. G. Buzzi Ferraris, G. Donati, F. Rejna, and S. Carrà, *Chem. Eng. Sci.* **29**, 1621 (1974).
15. M. Bowker, I. B. Parker, and K. C. Waugh, *Appl. Catal.* **14**, 101 (1985).
16. G. Ertl, in: *Catalysis Science* and *Technology* (J. R. Anderson and M. Boudart, eds.), Vol. 4, p. 273, Springer-Verlag, Berlin (1983).
17. P. Stoltze and J. K. Norskov, *Phys. Rev. Lett.* **55**, 2502 (1985).
18. G. Ertl, *Critical Reviews in Solid State and Materials Science*, p. 349, CRC Press, Boca Raton (1982).
19. *Nitrogen* **31**(9), 22 (1964).
20. U. Zardi, Ammonia Casale A.S., U.S. Patent No. 4,372,920 (1983).
21. G. Gramatica, Tecnimont S.p.A., U.S. Patent No. 4,205,044 (1980).
22. O. J. Quartulli and G. A. Wagner, *Hydrocarbon Process.* **12**, 115 (1978).
23. S. Ergun, *Chem. Eng. Prog.* **48**(2), 89 (1952).
24. C. E. Schwartz and J. M. Smith, *Ind. Eng. Chem.* **45**(6), 1209 (1953).
25. O. Levenspiel and K. B. Bischoff, *Advances in Chemical Engineering*, Vol. 4, Academic Press, New York (1963).
26. P. N. Dwivedi and S. N. Upadhyay, *Ind. Eng. Chem., Process Des. Dev.* **16**(2), 157 (1977).
27. D. C. Dyson and J. M. Simon, *Ind. Eng. Chem., Fundam.* **7**(4), 605 (1968).
28. C. P. P. Singh and D. N. Saraf, *Ind. Eng. Chem., Process Des. Dev.* **18**(3), 364 (1979).
29. A. Cappelli and A. Collina, *Inst. Chem. Eng., Symp. Ser.* **35**(5), 10 (1972).
30. D. F. Fairbanks and C. R. Wilke, *Ind. Eng. Chem.* **42**(3), 471 (1950).
31. A. Nielsen, *An Investigation on Promoted Iron Catalysts for the Synthesis of Ammonia*, 3rd ed., Jul. Gjellerups Forlag, Copenhagen (1968).
32. J. A. Beattie, *Proc. Natl. Acad. Sci. U.S.A.* **16**, 14 (1930).
33. L. J. Gillespie and J. A. Beattie, *Phys. Rev.* **36**, 743 (1930).
34. L. D. Gaines, *Ind. Eng. Chem., Process Des. Dev.* **16**(3), 381 (1977).
35. B. Mansson and B. Andersen, *Ind. Eng. Chem., Process Des. Dev.* **25**, 59 (1986).
36. H. W. Cooper, *Hydr. Proc., Pet. Ref.* **46**(2), 159 (1967).
37. R. H. Newton, *Ind. Eng. Chem.* **27**, 302 (1935).
38. Ya. S. Kazarnovskii, *Zh. Fiz. Khim.* **19**, 392 (1945).
39. O. A. Hougen, K. M. Watson, and R. R. Ragatz, *Chemical Process Principles*, Part II, Wiley, New York (1947).
40. F. Horn, *Z. Elektrochem.* **65**, 295 (1961).
41. S. Strelzoff, *Technology and Manufacture of Ammonia*, Wiley, New York (1981).
42. U. Zardi, *Hydr. Proc.* **8**, 129 (1982).
43. *Nitrogen* **140**(6), 30 (1982).
44. A. V. Slack and G. R. James, *Ammonia*, Vol. III, Marcel Dekker, New York (1977).

7

AMMONIA SYNTHESIS: COMMERCIAL PRACTICE

C. W. Hooper

7.1. AMMONIA PRODUCTION TECHNOLOGY

7.1.1. Introduction

The aim of this chapter is to relate the detailed analysis of the ammonia synthesis reaction, as examined in other sections of this book, to the commercial operation of one of the major processes of the worldwide chemical industry. The present annual production of ammonia is in excess of 120 million tons per year and virtually all of this ammonia is produced from a mixture of hydrogen and nitrogen over a promoted iron catalyst operating at elevated temperature and pressure. Over 90% of ammonia produced is used as a fertilizer, principally in the form of urea or ammonium nitrate.

The main emphasis in this chapter will be placed on the industrial application of the reaction between hydrogen and nitrogen to form ammonia.

However, this reaction must also be considered in the context of the overall process, beginning with primary raw materials. An introduction to the overall process routes is essential for several reasons. First, the purity of the ammonia synthesis gas depends on the gas production process. Second, commercially available processes are usually complete packages, where the synthesis section is an integral part of the overall process. A more detailed treatment of the other sections of the ammonia process can be found elsewhere.[1,2]

Modern, commercially important ammonia processes are basically of two types characterized by the method of hydrogen production; i.e., the steam-reforming route and the partial oxidation route.

C. W. Hooper • ICI Katalco, Billingham, Cleveland TS23 1LB, England.

7.1.2. The Steam-Reforming Route

The feedback in this process route to ammonia is a light hydrocarbon stream such as natural gas, liquified petroleum gas, or naphtha. The following example is based on methane, the principal constituent of natural gas, although the process is essentially the same when naphtha is the feedstock. The process follows a series of catalytic steps. The steam-reforming route to ammonia is shown diagrammatically in Fig. 7.1.

The first step is hydrodesulfurization, where sulfur is removed from the feedstock to prevent poisoning of downstream catalysts. A small amount of hydrogen is added to the feedstock, which is then heated to about 400 °C and passed over a catalyst containing either cobalt oxide or nickel oxide plus molybdenum oxide on an alumina support. The catalyst converts nonreactive organic sulfur compounds to hydrogen sulfide. A bed of zinc oxide particles is then used to remove hydrogen sulfide and reactive organic sulfur compounds, such as mercaptans, from the feed gas. The zinc oxide is not a catalyst, but an absorbent, because it is converted stoichiometrically to zinc sulfide during the process:

$$ZnO + H_2S = ZnS + H_2O$$

Desulfurized natural gas or naphtha is then mixed with process steam and preheated before passing to the primary reformer. The steam ratio, which is the molar ratio of steam to carbon, is typically between 3.0 and 4.0 moles of steam per atom of carbon in the hydrocarbon feedstock. An excess of steam over the stoichiometric quantity is required to suppress carbon-forming reactions and to provide a favorable equilibrium composition for the reaction of methane. The primary reformer consists of a large number of tubes packed with supported nickel oxide catalyst and contained in a furnace.[3] The purpose of the furnace is to heat the reactants to

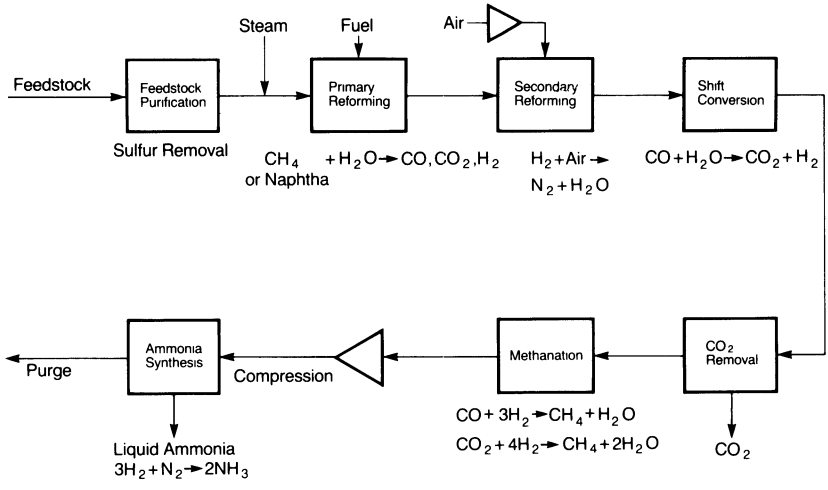

Figure 7.1. The steam-reforming route to ammonia.

between 750 °C and 850 °C and provide the endothermic heat of reaction. Before the catalyst can be used, the nickel oxide must be reduced to nickel. The typical reformer operating pressure in modern ammonia plants is between 25 and 40 bar (1 bar = 10^5 Nm^{-2}). In the primary reformer, the hydrocarbon feedstock is largely converted to carbon oxides and hydrogen by the following reactions, which proceed very close to the equilibrium state;

Methane-steam reaction $$CH_4 + H_2O \rightleftharpoons CO + 3H_2$$

CO shift reaction $$CO + H_2O \rightleftharpoons CO_2 + H_2$$

The next unit of the process is the secondary reformer, which consists of an adiabatic bed of supported nickel oxide catalyst. The secondary reformer satisfies two purposes; it introduces nitrogen to the process gas, and it provides the very high temperature required to reduce the methane content of the gas to an acceptable level, as determined by the methane-steam reaction equilibrium. Both objectives are achieved by mixing compressed and preheated air with the reformer gas. The oxygen in the air is consumed in a combustion zone above the catalyst bed. The amount of air is usually controlled to give a 3:1 hydrogen:nitrogen ratio in the subsequent synthesis gas, although in some processes an excess of air is used. The typical exit condition from a secondary reformer is a temperature of 1000 °C and a methane content of 0.3% on a dry basis.

From the secondary reformer, the gas is cooled with the simultaneous generation of high-pressure steam and flows to the carbon monoxide conversion stage. Carbon monoxide is converted to carbon dioxide in an exothermic reaction often known as the shift reaction:

$$CO + H_2O \rightleftharpoons CO_2 + H_2$$

The usual modern practice is to use a two-stage process. In the first stage, high-temperature shift conversion, an iron oxide/chromium oxide catalyst operates in the range 350–500 °C. The carbon monoxide concentration can be reduced to about 3% (dry basis) in a single adiabatic bed. The second stage, low-temperature shift conversion, uses a bed of copper oxide/zinc oxide/alumina operating at 200–250 °C to reduce the carbon monoxide content to between 0.2 and 0.4% (dry basis).

After shift conversion, the gas passes to the carbon dioxide removal stage. Carbon dioxide is removed from the gas to a residual level of 0.1% or less by solvent scrubbing. There is a range of proprietary processes available, e.g., the Benfield process[4] which is based on hot potassium carbonate solution, the Selexol process[5] which uses an organic solvent, and the MDEA process.[6] A discussion of carbon dioxide removal processes is beyond the scope of this chapter.[4–7] In recent years there has been considerable progress in reducing the energy requirement for the carbon dioxide removal process and thereby improving the efficiency of the overall ammonia process.

Following carbon dioxide removal a typical composition of the "make gas" on a dry basis is as follows:

	mol%
H_2	74.6
N_2	24.4
CH_4	0.3 (ex secondary reformer)
CO	0.3 (ex low-temperature shift)
CO_2	0.1 (ex CO_2 removal)
Ar	0.3 (atmospheric air addition)

The final stage of synthesis gas preparation is to remove the remaining carbon oxides by methanation. This occurs over a supported nickel oxide catalyst at a temperature of 250–350 °C. The nickel oxide must be reduced to the metallic state before use.

$$CO + 3H_2 \rightleftharpoons CH_4 + H_2O$$

$$CO_2 + 4H_2 \rightleftharpoons CH_4 + 2H_2O$$

In the methanation stage the residual carbon oxide content is lowered to less than 5 ppm. This is most important because of the poisoning effect of oxygen-containing compounds on the ammonia synthesis catalyst as described in Chapter 6. Methanated gas consists of a 3 : 1 stoichiometric mixture of hydrogen and nitrogen containing about 0.6–1.0% methane and 0.3% argon. This gas is cooled to recover heat and also to condense water, and then compressed and passed to the ammonia synthesis section of the plant.

7.1.3. The Partial Oxidation Route

This process route is used for heavy hydrocarbon feedstocks which are not suitable for steam reforming. The range of fuels includes naphtha, heavy fuel oil, crude oil, asphalt, and tar. In the partial oxidation reactor, or gasifier, the feedstock is burnt with a limited supply of oxygen in the presence of steam.[8] The basic reaction is

$$CxHy + (x/2)O_2 \rightarrow xCO + (y/2)H_2$$

The product from the gasifier consists mainly of hydrogen and carbon monoxide with some carbon dioxide and water, with small amounts of methane and sulfur-containing gases such as hydrogen sulfide. There is also some soot which must be removed by scrubbing with water and then recycled to the gasifier. Modern partial oxidation processes operate at pressures up to 80 bar and at a typical temperature of 1250 °C. On leaving the gasifier, the gas is cooled rapidly to "freeze" the equilibrium composition of the high-temperature reaction (i.e., to retain a low methane content). The cooling can be done either by a water quench or in a waste heat boiler. This cooled gas is then scrubbed to remove carbon particles. Carbon

is recovered from the scrubbing water and can either be recycled to the gasifier or used elsewhere as fuel.

There are two well-known commercial processes for partial oxidation, the Shell process[9] and the Texaco[10] process. These processes are broadly similar, but differ in areas such as the carbon recovery system and the reactor gas cooling system.

The clean gas available after soot removal requires further processing to produce ammonia synthesis gas. The overall process route is shown in Fig. 7.2. After gasification, the next stage is conversion of carbon monoxide to carbon dioxide over an iron oxide high-temperature shift catalyst. The gas is then treated for removal of acid gases, residual carbon dioxide, and hydrogen sulfide. A process based on the physical solubility of carbon dioxide (e.g., Rectisol[11]) is usually used, because the gas has a high carbon dioxide content. Such a gas mixture would require a very large input of heat when used in processes based on chemical solution, such as hot potassium carbonate.

The gas is next purified by a nitrogen wash. This involves contacting the gas with liquid nitrogen at very low temperature. The liquid nitrogen is obtained from the air separation plant, an essential component of the overall process which is required to supply oxygen to the gasifier. The nitrogen wash is controlled in order to add the stoichiometric amount of nitrogen to the hydrogen-rich gas. Other components consisting of carbon monoxide, carbon dioxide, and the bulk of the methane and argon are removed in the liquid nitrogen stream. The purified synthesis gas is then compressed and fed to the ammonia synthesis loop. As far as ammonia synthesis is concerned, the nitrogen wash is a key feature of the partial oxidation route, as it produces a 3 : 1 stoichiometric mixture of hydrogen and nitrogen with very low inerts levels (typically less than 5 ppm methane and 50 ppm argon) and virtually complete removal of oxygen-containing poisons.

Processes based on coal feedstock are similar to the partial oxidation process for heavy oil, and usually include a nitrogen wash stage to produce a similar

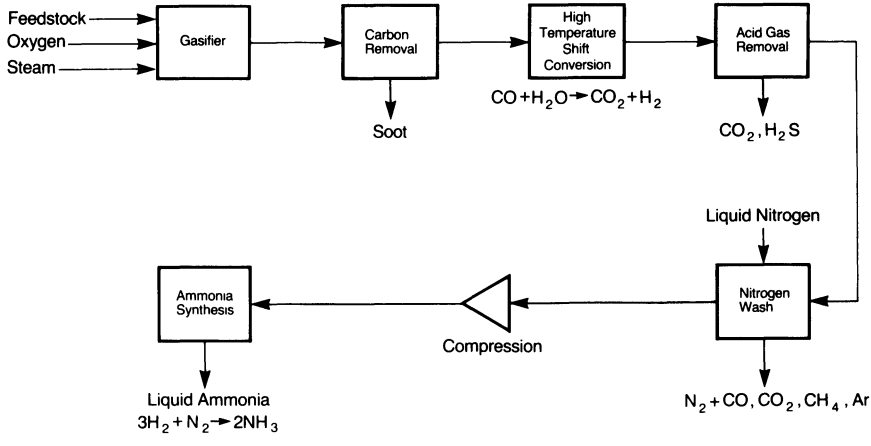

Figure 7.2. The partial oxidation route to ammonia.

synthesis gas with low inerts content and very low levels of poisons. In the late 1970s and early 1980s there was considerable interest in coal-based ammonia plants, as reviewed for example by Nurse,[12] but very few were actually built because of the very high capital cost.

7.1.4. The Ammonia Synthesis Loop

Having introduced the two main processes for the production of ammonia synthesis gas, the commercial application of the synthesis reaction can now be considered.

Because of constraints imposed by the thermodynamic equilibrium of the ammonia synthesis reaction under normal operating conditions, only a fraction of the hydrogen and nitrogen in the synthesis gas can be converted to ammonia in a single-pass converter. In developing the ammonia synthesis process it was soon realized that an economic process would only be possible if unreacted hydrogen and nitrogen were recycled after removal of the ammonia product. This recycle arrangement is known as the ammonia synthesis loop and is a fundamental feature of all commercial ammonia plants. A considerable variety of synthesis loop designs have been developed over the years. The best introduction to the design problems that have led to these varied solutions is to examine the simplest possible loop design. The essential features are:

1. Ammonia converter—the catalyst-containing reaction vessel.
2. Cooler—to remove the exothermic heat of the synthesis reaction and to condense the ammonia product.
3. Purge—a facility for removing nonreactants.
4. Synthesis gas addition—addition of fresh compressed synthesis gas to the loop.
5. Ammonia catchpot (or separator)—for removal of product ammonia as a liquid.
6. Circulator—a means of circulating gas through the loop equipment.

This basic synthesis loop flowsheet is shown in Fig. 7.3.

The function of each of these items will be explained and, by this means, some of the interrelated design criteria for ammonia synthesis loops will become apparent.

7.1.4.1. Ammonia Converter

The ammonia converter must be designed to contain a large volume of catalyst operating at temperatures up to 530 °C at pressures typically in the range 100–350 bar. Under these conditions with high partial pressures of hydrogen and ammonia, high-grade materials (usually stainless steels) are required to resist hydrogen attack and nitriding. The solution commonly adopted to this vessel design problem is the use of two concentric vessels.

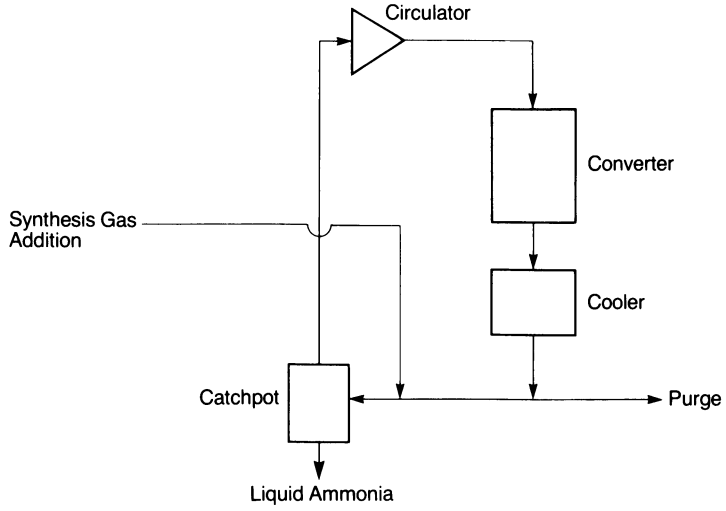

Figure 7.3. Basic ammonia synthesis loop.

The inner shell (the "cartridge") is made of stainless steel and operates at catalyst temperature, but is only designed for the differential pressure across the converter (typically 5–10 bar). The outer shell (the pressure shell) only experiences low temperatures at which both hydrogen attack and nitriding are much less significant and consequently less expensive steels can be used. The pressure shell is kept cool primarily by a flow of cool gas between the pressure shell and the cartridge, and also by thermal insulation of the cartridge.

The other basic feature of converter design is a means of temperature control for the catalyst beds. First, a feed gas heat exchanger is required to heat the circulating synthesis gas to the catalyst operating temperature. The feed gas temperature is initially low, as this gas keeps the pressure shell at the required low temperature. Consequently the gas must be heated to 370–420 °C before contacting the catalyst. Second, the reacting gas must be cooled to control the converter temperature, which increases due to the heat of reaction. This cooling is necessary because the operating temperature range of commercially available catalyst is limited, and also because lower temperatures give a more favorable ammonia concentration at equilibrium. The cooling can be done either directly by adding further cold feed gas or indirectly via heat exchange surfaces. The details of specific converter designs will be considered in Section 7.3, although a useful review is given in Ref. 13.

7.1.4.2. Cooler

Ammonia synthesis is exothermic and the heat of reaction is 46.22 MJ $kmol^{-1}$ NH_3 (at 25 °C, 1 atm). For a typical pass in which the concentration of ammonia is increased from 2 to 15%, this is equivalent to an increase in the temperature of the circulating gas of about 150 °C. In early plants this heat was largely wasted to

cooling water, but with modern designs the optimization of heat recovery from the synthesis loop is an important element of the overall process design. The heat of reaction represents about 8% of the total energy input to a modern ammonia process, and is usually utilized for steam raising or boiler feed water heating.

7.1.4.3. Purge

In an ammonia plant based on the steam-reforming route, the fresh synthesis gas contains about 0.3% argon and 0.8% methane in addition to the 3:1 stoichiometric hydrogen:nitrogen mixture. The concentration of argon and methane builds up in the loop and consequently reduces the partial pressures of the reactants. Hence, a purge from the loop is required. The optimum purge rate is derived from an economic balance between the cost of additional compression power at a higher loop pressure and the wastage of purified hydrogen as fuel. As an approximate guide, the inerts level (argon and methane at the inlet to the converter) is usually between 10 and 20%. The purge is usually taken where the concentration of inerts is at its highest, i.e., at a point between the converter exit and the synthesis gas addition.

There is also an "involuntary purge" caused by inert gases dissolving in the liquid ammonia product. Some plants with low levels of inerts rely only on this involuntary purge and a voluntary purge is not required. For example, in a partial oxidation based plant the purified make-up gas may contain only 50 ppm argon and no methane. This will build up to between 2% and 5% argon in the synthesis loop, the exact level depending on loop pressure and ammonia separator temperature.

7.1.4.4. Synthesis Gas Addition

The pressure of the synthesis gas from the gas preparation stages is too low for synthesis, and further compression is required prior to addition to the synthesis loop. Until the early 1960s, reciprocating compressors were used for this duty but modern practice, except for a few small scale plants, is to use centrifugal compressors. Compression will be considered in more detail in Section 7.2.2. The location of the synthesis gas addition point is important. Conventionally this is upstream of the ammonia separator, to prevent some catalyst poisons reaching the ammonia converter by dissolution in the liquid ammonia product. Synthesis gas generated by a process based on steam reforming contains water, carbon dioxide, carbon monoxide, and traces of oil from the compressor. The bulk of the water is removed in the compressor interstage catchpots to give a final level in the range 200–400 ppm depending on loop pressure. Typical carbon oxide levels are 2–5 ppm carbon dioxide and 1–2 ppm carbon monoxide. Both water and carbon dioxide will enter the liquid phase in the ammonia separator provided that there is adequate vapor–liquid contacting between the fresh synthesis gas and the product ammonia. The carbon dioxide is removed as ammonium carbamate, as shown in the equation

$$CO_2 + 2NH_3 \rightarrow NH_4COONH_2$$

Traces of oil will also remain in the liquid phase; this prevents poisoning of the catalyst but may result in contamination of the product. In the case where reciprocating compressors are used, filters are normally required to remove any oil.

The only catalyst poison that enters the synthesis loop during normal operation is the small amount of residual carbon monoxide from the methanator.

7.1.4.5. The Ammonia Separator

The simplest way to recover the product from an ammonia plant is by condensation followed by separation of liquid ammonia from the circulating gas. The optimum temperature for the separator is a function of the synthesis pressure. At high pressure, such as 300–350 bar, simple water cooling can be utilized with a separator temperature just above ambient. At lower pressures, however, the dewpoint of the converter effluent is reduced significantly and refrigeration must be used to condense the product ammonia. Typical separator temperatures in modern plants are in the range −10 °C to −25 °C.

7.1.4.6. Circulator

The circulator is a simple compressor which is employed to recycle gas through the synthesis loop equipment. Although the circulation rate is typically four times greater than the fresh synthesis gas rate, the circulation power is relatively small compared with the compressor power because of the relatively low pressure differential around the synthesis loop. The circulator is usually, but not always, integrated with the synthesis gas compressor.

An alternative to the circulator is to use an ejector. In this case the synthesis gas is compressed to a pressure higher than the loop pressure and is let down in an ejector to provide the driving force for gas circulation. Although this arrangement has worked successfully in the past, it is not used in modern practice because of low energy efficiency.

7.1.5. High-Pressure Ammonia Synthesis

Since the first commercial application of the Haber process for ammonia production in 1913, a wide variety of synthesis loop designs have been developed. A history of the early developments is given in Chapter 1, and has also been reviewed elsewhere.[14,15] However, by the 1950s and early 1960s, a broad consensus about the optimum design conditions for an ammonia synthesis loop had been reached. A typical design from this period will be described. This will be used to demonstrate how the elements of the synthesis loop are applied to produce a practical design, and will also serve as a base case for the discussion of modern developments. A flowsheet for this type of synthesis loop is shown in Fig. 7.4.

In a plant of this type, synthesis gas was produced by the steam reforming of naphtha or natural gas at a pressure of 10–20 bar followed by shift conversion and removal of carbon dioxide and carbon monoxide. This gas was then compressed to a pressure of 300–350 bar using multistage reciprocating compressors. It was

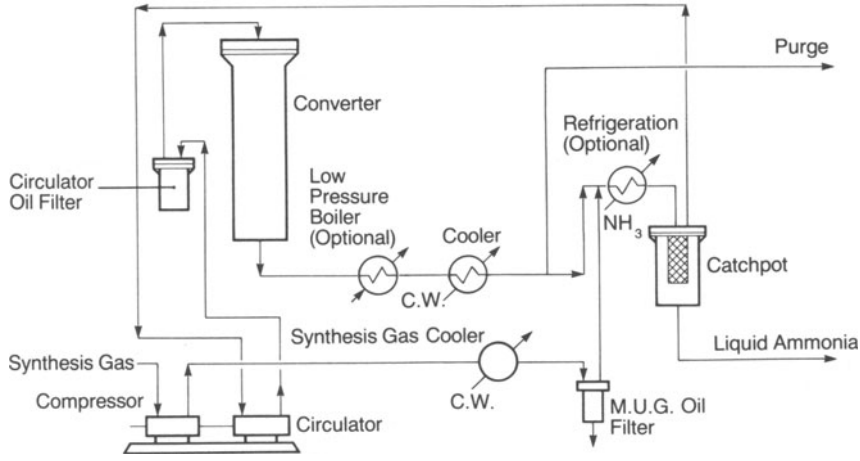

Figure 7.4. High-pressure ammonia synthesis loop.

normal practice to use two compressors in parallel. This was partly due to limits on the maximum compressor and motor sizes available, but also principally to maintain ammonia production during the frequent routine maintenance periods required with this type of machine. The compressed gas was cooled, filtered to remove oil, and added to the synthesis loop downstream of the loop cooler. The mixed gas stream flowed to the ammonia separator where the liquid ammonia product was removed, and then to the circulator. On some plants, depending on ambient temperature, there was further cooling by refrigeration upstream of the separator. The circulator increased the gas pressure by 15–20 bar to overcome the pressure drop around the loop.

From the circulator, the gas passed directly to the ammonia converter. A converter design widely used at this time was the "TVA" converter (Fig. 7.5), originally developed by the Tennessee Valley Authority. This consisted of a single catalyst bed with a heat exchanger below, inside the usual stainless steel cartridge. The circulating gas flowed upward through the heat exchanger, upward again through the cooling tubes within the catalyst bed, then downward through the bed and finally through the other side of the exchanger. This tube-cooled design gave a good approximation to the optimum converter temperature profile (see Chapter 6). Gas left the converter at about 180 °C with a typical ammonia concentration of 18%. After some heat recovery to raise low-pressure steam, the circulating gas was cooled with cooling water. The purge gas stream was taken off at this point (i.e., where the concentration of inerts is greatest) before mixing with fresh synthesis gas.

This simple design of synthesis loop was widely used until the 1960s. The main limitation was that it could not be scaled up to the large capacities required to meet the demand for fertilizers in the late 1960s and 1970s. The maximum throughput of a reciprocating synthesis gas compressor is equivalent only to approximately 300 tons per day of ammonia. Hence, multiple compressors would

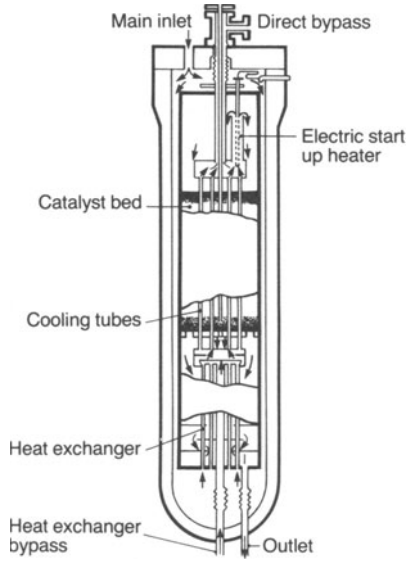

Figure 7.5. TVA ammonia converter.

be needed for large-capacity plants and this would result in high maintenance costs, poor reliability, and high capital cost.

7.1.6. Energy Considerations

One of the major objectives of ammonia process development in recent years has been to reduce the energy consumption of the process. As ammonia is produced from feedstocks such as natural gas or naphtha which are fuels, energy consumption is expressed in terms of the fuel value (or calorific value) of the materials consumed. Energy consumption may be stated as either Gross Calorific Value (Higher Heating Value) which assumes that the water formed in the combustion process is condensed to the liquid state, or Net Calorific Value (Lower Heating Value) which assumes the combustion products contain water vapor. The difference between GCV and NCV is the latent heat of evaporation of the water formed. Gross Calorific Value will be used throughout this chapter. The units for energy consumption per unit of ammonia are $J\,kg^{-1}$, although it is more usual to use GJ per ton of ammonia when considering commercial processes.

The improvement in ammonia process efficiency with time is shown in Fig. 7.6. The efficiency of modern processes is in the range 32–35 $GJ\,ton^{-1}$ GCV depending on the process and the application. Factors such as plant scale and ambient temperature have a significant effect. It is noteworthy that the minimum theoretical energy consumption is the calorific value of ammonia itself. This is

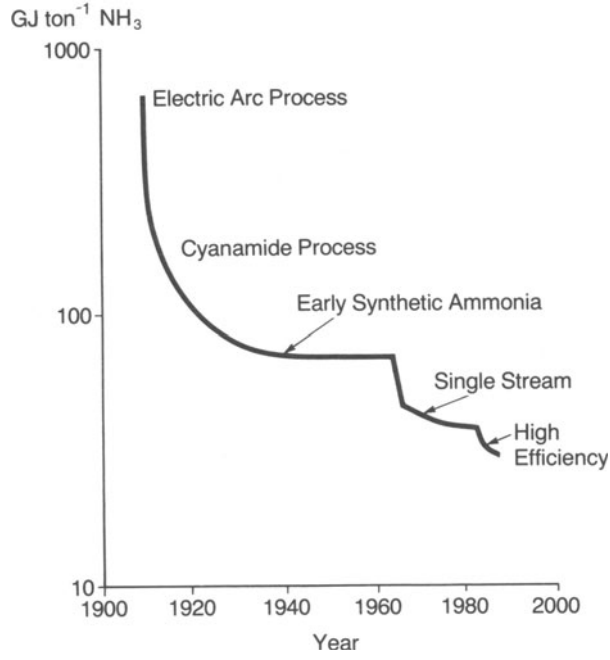

Figure 7.6. Energy consumption of the ammonia process.

22.48 GJ ton^{-1} for gaseous ammonia at 25 °C and 21.32 GJ ton^{-1} for liquid ammonia at 25 °C.

Energy flows in the synthesis loop will now be considered to examine how the synthesis area relates to the overall plant in terms of energy consumption. The heat of reaction for ammonia synthesis is the first consideration. This is 46.22 MJ kmol^{-1} NH_3 (at 25 °C, 1 atm, gaseous NH_3) or 2.71 GJ ton^{-1}. This is approximately 8% of the total energy consumption and hence there is a strong incentive to recover as much as possible of this heat output. Modern processes can recover up to 90% of the reaction heat, usually for preheating boiler feed water or for raising high-pressure steam.

The other energy flows in a practical process are associated with the material balance and with gas-compression requirements.

The material efficiency of modern synthesis loops is very high; hydrogen efficiencies of 98% can be achieved when hydrogen recovery from purge gas is included in the process. The remaining 2% of the feed hydrogen which is not converted to ammonia is utilized as fuel.

The final energy input is power for the three gas-compression duties: synthesis gas compression, synthesis loop circulation, and ammonia refrigeration. The power required for these duties depends, for example, on synthesis pressure and on converter design. Refrigeration power is strongly dependent on ambient temperature. However, typical figures for a modern 1000 ton per day low-pressure

ammonia plant are as follows:

Syn gas compression and circulation	10.0 MW
Refrigeration	6.0 MW
Total	16.0 MW

This power requirement can be converted to equivalent natural gas by using a typical efficiency of 30% for a high-pressure steam power cycle. The natural gas input is $16.0/0.30 = 53.3$ MW, which can be expressed as 4.6 GJ per ton of ammonia. Hence, even with modern technology the compression requirements in the synthesis area are a significant part of the total energy consumption of the process.

7.2. MODERN DEVELOPMENTS IN AMMONIA SYNTHESIS TECHNOLOGY

In recent years there have been major advances in ammonia synthesis technology. These changes have resulted in increased plant capacity, improved reliability, higher efficiency, and lower capital cost. These developments came about in two stages: first by the introduction of the large single-stream ammonia plant, and second as a result of the search for maximum plant efficiency.

The large-capacity single-stream ammonia plant resulted from the successful integration of a range of improvements in the technology. The use of centrifugal instead of reciprocating compressors for the main duties, especially synthesis gas compression, is one important advance. The application of the "total energy concept" is another significant feature. Waste heat from the process is used to generate high-pressure steam, which then drives the centrifugal compressors with process steam requirements satisfied by pass-out at the appropriate pressure.

The second stage, consisting of further improvements in efficiency, is really a refinement and optimization of the single-stream process concept. These developments followed as a consequence of the rises in the price of oil during the 1970s.

The last 25 years has seen an increase in maximum single-stream capacity from 500 to over 2000 ton per day (although in recent years there has been renewed interest in smaller capacity plants), with a reduction in energy consumption from over 45 MJ kg^{-1} ammonia to less than 32 MJ kg^{-1}.

To examine how this has been achieved, the following aspects of ammonia plant design will be examined:

1. Synthesis gas quality.
2. Synthesis gas compression.
3. Ammonia converter and synthesis loop design.

Section 7.3 of this chapter will describe now these general trends are reflected in the specific process conditions of some of the leading, commercially available ammonia processes.

7.2.1. Synthesis Gas Quality

There have been many improvements in synthesis gas production technology in recent years brought about by developments in process engineering, mechanical engineering, and catalysis. A detailed discussion of the whole ammonia plant is beyond the scope of this chapter, and this discussion will concentrate on those changes which have a direct effect on the ammonia synthesis operation.

A significant improvement in gas quality was achieved in the 1960s by the introduction of two new catalysts for gas purification, namely, the low-temperature shift and methanation catalysts. These catalysts led to a significant improvement in the level of oxygen-containing compounds in the synthesis gas, and low-temperature shift in conjunction with methanation is now the standard method of gas purification in processes based on steam reforming.

The earlier technology consisted of shift conversion using iron-oxide-based high-temperature shift catalyst followed by carbon dioxide removal (e.g., using hot potassium carbonate or an amine solution), and the ammoniacal cuprous formate process for removal of residual carbon monoxide and dioxide. Total residual levels of the oxides of carbon from this process were typically around 10 ppm, and this level could be reduced to 2–3 ppm using the low-temperature shift and methanation route. The other catalyst poisons in the synthesis gas are water and machine oil, which may also contain small amounts of sulfur and other poisons. Bulk water is generally removed to as low a level as possible by condensation between the stages of compression. Residual water is then removed by contacting the fresh synthesis gas with liquid ammonia. This also removes carbon dioxide by formation of ammonium carbamate. Carry-over of oil to the synthesis loop has been significantly reduced by the modern practice of using centrifugal compressors.

A recent trend in gas purification has been to use dryers containing a molecular sieve to remove water from the synthesis gas before addition to the loop.[16] This has the advantage that the water level can be reduced to a very low level (0.1 ppm v/v) and this enables the synthesis gas to be added to the loop downstream of the ammonia separator. This has a process advantage in that the concentration of ammonia in the gas returning to the converter is lower, because the concentration of ammonia at equilibrium at the separator temperature is diluted by the fresh synthesis gas which is, of course, free from ammonia.

7.2.2. Synthesis Gas Compression

One of the major changes in ammonia technology that occurred in the 1960s was the adoption of centrifugal instead of reciprocating compressors for the major duties, particularly synthesis gas compression.[17,18] The main advantages are high stream capacity, with production rates of 2000 tons per day or more possible with a single compressor, and improved reliability. More specifically, the reliability advantage comes about because centrifugal compressors do not need to be shut-down for frequent routine maintenance. Another important feature is that centrifugal machines operate at high speed and can be driven directly by high-pressure

steam turbines. Utilization of waste heat to generate steam at high pressure (typically 100–120 bar) greatly improves both the capital cost and operating cost. The major operating costs in an ammonia synthesis unit are synthesis gas compression power, circulator power, refrigeration power, and the credit for heat recovery from the synthesis loop. As the synthesis pressure increases, the gas compression power obviously increases. The other factors tend to compensate for this effect. For example, at pressures in excess of 300 bar, no refrigeration power is necessary as ammonia can be condensed to a level suitable for return to the converter at ambient temperature. However, the calculation of the operating cost variation with pressure is complex because it depends on the assumptions made for such variables as converter design, equipment pressure drop, ammonia conversion per pass, and ammonia separator temperature. Hence the pressure of the ammonia loop is related to features of specific commercial processes and it is not possible to calculate a generally applicable optimum. There is, however, a tendency to use higher synthesis pressure in large-capacity plants. There are two reasons for this. First, in smaller plants (approximately 400–600 tons per day) low pressure is favored because the efficiency of centrifugal compressors is lower when the actual volume flow is small. Second, at very high plant capacities (1500 tons per day or more) a higher pressure is generally favored to limit the physical size of the equipment, particularly the ammonia converter, for both ease of transport and erection.

7.2.3. Ammonia Converter and Synthesis Loop Design

This section will consider modern trends in converter design, and discuss how these relate to the design of the synthesis loop. Two general trends are apparent in modern converter design: the use of a radial flow pattern instead of axial flow, and the use of heat exchange instead of quench gas between the catalyst beds.

7.2.3.1. Radial Fow

By changing the flow pattern in a catalyst bed from the conventional axial flow to radial flow, the catalyst pressure drop can be greatly reduced. This is simply a result of the bed geometry with radial flow giving a larger flow area and a shorter flow path. The obvious alternative is to make an axial flow bed wider and shallower, but this is not economic with current pressure vessel technology. Catalyst pressure drop is inversely proportional to particle size. As catalyst pressure drop is no longer a constraint, radial flow beds can utilize the smallest catalyst particles that can be retained in a catalyst "basket" with permeable walls. The practical catalyst size for radial flow is normally 1.5 to 3 mm. At this size, there is virtually no diffusional limitation and the intrinsic activity of the catalyst can be utilized. Hence, radial flow converters have the advantages of lower pressure drop and smaller catalyst volumes than axial flow converters.

The pioneers in the application of radial flow to ammonia synthesis were Topsoe[19] with their well-known S-100 and S-200 designs, and Chemoprojekt in Czechoslovakia.[20,21] More recently, other companies have developed their own radial flow designs, such as Ammonia Casale[22] and Uhde.[23] The Ammonia

Casale designs actually use a mixed flow pattern known as axial-radial flow, where some gas enters the top of the catalyst in axial flow but the majority of the gas enters the bed radially. This design also achieves the radial flow objectives of low pressure drop with small catalyst particles.

The implications for the catalyst are that there are several areas of research and development that are less important than formerly. First, diffusional resistance in the catalyst particles is not significant with the size grades used for radial flow. Second, optimization of particle shape and size to minimize pressure drop is no longer required because catalyst pressure drop becomes very small compared with the total pressure drop through the loop equipment. Third, the requirement for mechanical strength is less because the catalyst is not subjected to high dynamic loads caused by pressure drop. Catalyst development for radial flow applications can concentrate on achieving high activity and long-term stability.

7.2.3.2. Heat Exchange Between Beds

Almost all modern ammonia converters utilize a series of adiabatic catalyst beds with cooling between the beds to contain the temperature increase produced by the reaction. This cooling can be either by addition of cool converter feed gas (quench gas) or by use of a heat exchanger (intercooling). Although quench converters are mechanically simpler, intercooled converters have the advantage that the ammonia content of the converter gas leaving a catalyst bed is not diluted by mixing with feed gas. In this way an intercooled converter can achieve a higher ammonia concentration (higher conversion per pass) than a quench converter with the same number of catalyst beds. Higher conversion per pass in the converter has beneficial effects on the design of the synthesis loop. The loop equipment can be smaller because of the lower circulation rate, and the circulator power requirement is reduced. Furthermore, a higher ammonia concentration increases the dewpoint of the converter exit gas. In high-pressure loop designs this enables more ammonia to be condensed by cooling with cooling water rather than by refrigeration, which reduces both capital cost and operating cost. For these reasons the modern trend is to use intercooled converters rather than quench converters.

7.3. COMMERCIAL AMMONIA PROCESSES

7.3.1. The Kellogg Ammonia Process

The ammonia process introduced by Kellogg in the mid-1960s[27] incorporated a number of innovations which were integrated to produce overall a highly efficient process. By using centrifugal compressors for the major compression duties, very high production rates could be achieved from a single-stream plant. The operating conditions and particular features of the Kellogg process will now be described briefly.[28]

The naphtha or natural gas feedstock is desulfurized using any suitable process, e.g., activated carbon or catalytic hydrodesulfurization, and then mixed with superheated 40-bar steam to give a steam-to-carbon ratio of 3.5 mol water vapor

per atom of carbon in the hydrocarbon feedstock. The mixed reactants are preheated to about 450 °C and enter the primary reformer, which consists of a number of tubes containing a nickel-based catalyst heated in a radiant furnace. The reformer exit condition is typically 800 °C and 32.0 bar. This was a relatively high pressure for steam reforming when the process was first introduced, although high-pressure reforming is now standard practice for modern ammonia plants. High pressure has the advantage of reducing downstream compression requirements. Reformed gas flows to the secondary reformer, where it reacts with compressed and preheated air in an adiabatic reactor also containing a nickel-based catalyst. The exit temperature from the secondary reformer is typically 1000 °C and the methane content of the gas is about 0.3% on a dry basis. The gas is cooled by raising high-pressure steam prior to carbon monoxide shift conversion using high-temperature and low-temperature shift catalysts. This reduces the carbon monoxide content to 0.3% (dry basis). Removal of carbon dioxide to a residual level of about 0.1% is accomplished by contacting the gas with a liquid solvent using any one of a number of proprietary processes. The final stage of synthesis gas preparation is methanation of the residual carbon monoxide and dioxide over a nickel-based catalyst at a temperature of 300–350 °C. The resulting synthesis gas at a pressure of 25 bar is then cooled and flows to the synthesis gas compressor. A typical analysis of the synthesis gas is:

H_2	74.2
N_2	24.7
CH_4	0.8
Ar	0.3
	100.0

This gas is compressed to the synthesis pressure in a multistage centrifugal compressor driven by a high-pressure steam turbine. In the final stage of compression, the fresh synthesis gas mixes with recycle gas (cooled converter effluent gas) within the compressor casing before the final compressor wheel. This is the recycle wheel or circulator which circulates synthesis gas around the ammonia loop. The pressure at the recycle wheel delivery is typically 150 bar for plants in the range of 600–1100 tons per day. Higher pressures are used for larger capacity plants; this is mainly to limit the size of the loop equipment, particularly the ammonia converter.

Gas leaving the compressor is cooled to −25 °C (using ammonia as the refrigerant) to condense the product ammonia, which is then removed in a separator. The gas stream containing about 2% ammonia is preheated to 140 °C by interchange with converter exit gas and then enters the ammonia converter. In Kellogg plants with a capacity of around 1000 tons per day, the converter consists of four axial-flow catalyst beds with an interchanger positioned above the top bed (see Fig. 7.7). The main gas flow is into the bottom of the converter, between the high-pressure shell and the cartridge, then up to the top-mounted interchanger. Gas is heated in the interchanger and then enters the first catalyst bed. A heat

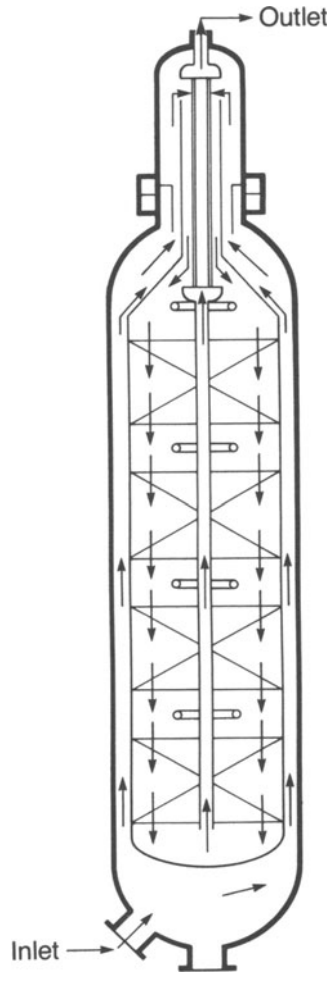

Figure 7.7. Kellogg ammonia converter. Courtesy of British Sulphur Corporation.

exchanger bypass controls the bed inlet temperature. Quench gas, that is cool loop gas which has not been heated by the exotherm, is mixed with the gas leaving each bed to control the temperature of subsequent beds. Gas leaving the final bed contains 10–12% ammonia. This gas flows up the converter through a central pipe to the interchanger and then leaves the converter at the top. The synthesis catalyst is a conventional, commercially available iron-based catalyst in the size range of 6–10 mm. Gas leaving the converter is cooled with simultaneous heat recovery by heating boiler feed water and by interchange with the converter feed. A purge stream is taken at this point to control the level of inerts in the loop and the remaining gas returns to the recycle stage of the compressor. The purge gas, after recovery of ammonia, is utilized as fuel.

A major feature of the Kellogg process is the integrated heat recovery system to utilize the otherwise waste heat from various process streams and from the reformer flue gas, which is used to raise 100-bar superheated steam. The steam is let down in a turbine, which drives the synthesis gas compressor. Passout steam at 40 bar is used for process steam and for other machine drives. Passout steam from some of the smaller turbines at 4.5 bar is used for minor process heating duties. This "total energy" concept is largely responsible for the efficiency improvement over earlier processes.

Many of the features of the Kellogg process, for example, centrifugal compressors, high-pressure steam systems, and high-pressure reforming, have subsequently been widely adopted by the ammonia industry.

In recent years, the Kellogg process has been developed to improve its efficiency still further.[29,30] The process improvements fall into five areas:

1. Primary and secondary reforming.
2. Carbon dioxide removal.
3. Synthesis gas purification.
4. Ammonia converter design.
5. Purge gas recovery.

7.3.1.1. Primary and Secondary Reforming

The pressure of the primary reformer has been increased in order to reduce the synthesis gas compression power. The radiant heat load of the reformer has been reduced by increasing the preheat temperatures for both process air and reformer reactants. This in turn reduces the fuel requirement of the reformer.

7.3.1.2. CO_2 Removal

In line with other modern processes, the Kellogg process can utilize one of the latest low-energy consumption carbon dioxide removal processes, such as Selexol or Lo-heat Benfield.

7.3.1.3. Synthesis Gas Purification

Final purification of the synthesis gas uses molecular sieve dryers. This enables the synthesis gas to be added to the synthesis loop at converter inlet instead of upstream of the ammonia separator.

7.3.1.4. Ammonia Converter Design

The synthesis loop uses a horizontal converter[31,32] in which the catalyst beds are arranged as horizontal slabs (Fig. 7.8). This configuration results in a very small catalyst pressure drop, and this enables small catalyst particles to be used with a subsequent increase in the effectiveness factor of the catalyst. In this way the process effect is very similar to a radial flow converter.

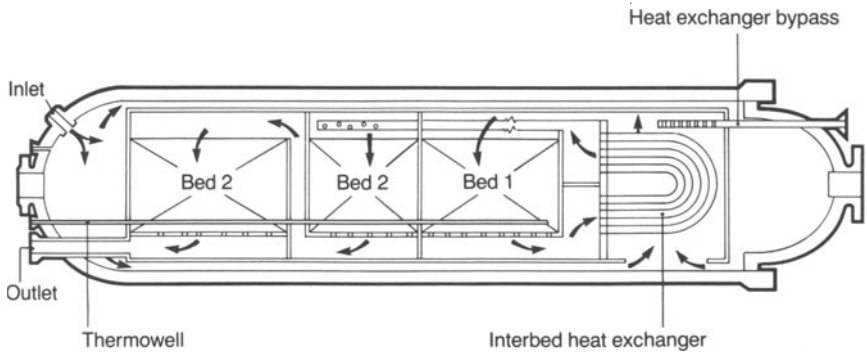

Figure 7.8. Kellogg horizontal intercooled ammonia converter. Courtesy of British Sulphur Corporation.

7.3.1.5. Purge Gas Recovery

In common with other processes, the overall efficiency can be improved by recovery of hydrogen from the purge gas instead of using it as fuel. Either of the two general types of hydrogen recovery unit may be used: cryogenic recovery[24,25] or membrane separation.[26]

7.3.2. The Braun Purifier Process

The Braun purifier process is based on the steam-reforming route but differs from other processes in the method of purifying the synthesis gas upstream of the synthesis loop.[33–36] Synthesis gas production includes the essential process steps of desulfurization, primary and secondary reforming, shift conversion, carbon dioxide removal, and methanation. However, the process is characterized by the use of a large excess of process air in the secondary reformer coupled with removal of the resultant excess nitrogen in a cryogenic separation unit downstream of the methanator. The main advantages of this arrangement are a reduction in the size and cost of the primary reformer and a reduction in the fuel requirement, because the primary reformer heat load is relatively small. The principal features of the process are as follows.

Following desulfurization of the natural gas or naphtha feedstock, primary reforming takes place at conventional pressure and steam ratio (typically 30 bar and 3.5 mol steam per atom of carbon) but at lower temperature, generally less than 700 °C at the outlet of the primary reformer. Process air is compressed and preheated before addition to the secondary reformer. An excess of air is used, equivalent to about 50% more than the stoichiometric nitrogen requirement. This generates more heat than usual in the secondary reformer and thereby allows an equivalent reduction in the primary reformer duty. The exit temperature from the secondary reformer is relatively low at about 900 °C. This gives a relatively high methane content at the secondary outlet, but this is acceptable as methane is removed in the purifier before entering the synthesis loop. Gas leaving the secondary

reformer follows the normal process steps of high-temperature and low-temperature carbon monoxide shift conversion, carbon dioxide removal, and methanation. After methanation, the gas is cooled before entering the purifier.

The purifier is the key process step which differentiates the Braun process from other processes. The purifier removes essentially all the impurities from the synthesis gas before entering the synthesis loop. First of all, water is removed by molecular sieve dryers to prevent freezing in the purifier. The dried gas then enters a cryogenic purifier which consists of a multistream heat exchanger, a gas expander, and a rectifier column. Feed gas is cooled partially, then passed through a turbo-expander to provide the required refrigeration, and further cooled to about −175 °C. The cooled stream enters the rectifier, which includes an integral reflux condenser. The top product from the rectifier is pure synthesis gas and the bottom product is a waste stream that is used as fuel. Both streams are used to cool the feed gas in the multistream heat exchanger. The product gas is a 3 : 1 stoichiometric mixture of hydrogen and nitrogen containing about 0.2% argon and a trace of methane. The overall pressure drop in the purifier is two to three bars, most of which falls across the turbo-expander to provide the net refrigeration requirement.

This low level of inerts coupled with the low level of oxygen-containing poisons influences the design of the ammonia synthesis loop.

Synthesis gas from the purifier is compressed to a pressure in the range 140 to 200 bar before addition to the synthesis loop. In the synthesis loop, recycle gas is mixed with fresh synthesis gas before the final compressor wheel (recycle wheel) and, because this gas is pure, it can be fed directly to the converter. Gas leaving the converter is cooled, ammonia is condensed and separated, and the remaining gas is recycled to the converter. A small purge stream is necessary to control the level of argon in the loop. This purge gas is scrubbed with water to recover ammonia and recycled to the purifier.

Waste heat from various stages of the process is recovered to generate high-pressure steam which is utilized in steam turbines. The use of a large excess of process air reduces the heat load on the primary reformer to such an extent that there is no longer sufficient waste heat to satisfy the total plant compression power requirements by means of a high-pressure steam system. Therefore a gas turbine is usually integrated into the power cycle as this provides an efficient means of balancing the steam and power requirements of the process. The gas turbine drives the process air compressor, and exhaust gas from the turbine at about 500 °C provides combustion air for the primary reformer furnace.

The ammonia converter in the purifier process is the Braun 2-stage adiabatic synthesis converter.[37] In process engineering terms this is a two-bed, axial-flow converter with heat exchange between the beds. However, the mechanical design differs from the majority of modern converters in that each catalyst bed is enclosed in its own separate pressure shell (see Fig. 7.9).

The gas flow path in each converter is as follows. Gas enters at the bottom of the vessel and flows upward between the pressure shell and the stainless steel catalyst container, then downward through the catalyst bed in axial flow to the outlet nozzle. A catalyst loading port is provided at the top of the vessel. When a change of catalyst is due, the old catalyst is discharged by gravity at the bottom

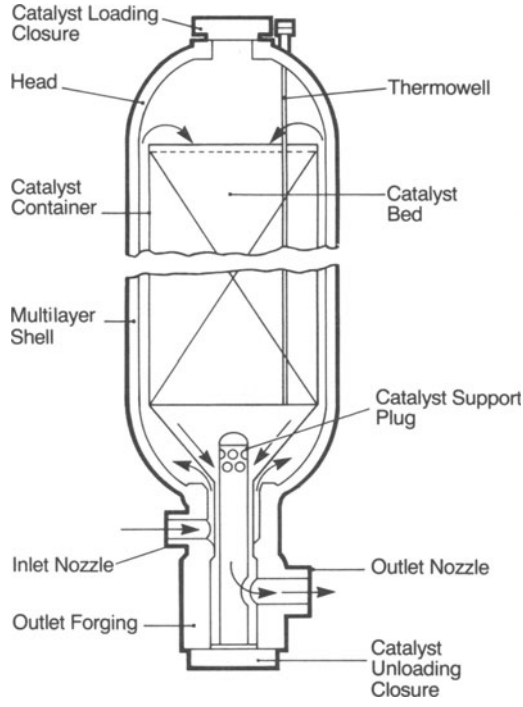

Figure 7.9. Braun ammonia converter. Courtesy of British Sulphur Corporation.

of the vessel after removing the unloading closure and a catalyst support plug. The support plug provides a path for gas flow to the outlet nozzle. This converter design has the advantages of simplicity and easy catalyst loading and unloading. Each pressure vessel is relatively small and this ensures easier fabrication, transport, and erection. However, the separate vessel approach also presents significant engineering problems. These arise because the pressure vessels have to be designed for higher temperatures and higher concentrations of ammonia than other converters. The pressure vessel is in contact with gas at the catalyst bed inlet temperature, typically 400 °C, rather than the converter inlet temperature which is normally in the range 50–250 °C depending on converter design. This increased temperature requires that the thickness of the pressure shell is also increased. The outlet nozzles and the inlet nozzle to the interbed heat exchanger must be designed for the maximum bed exit temperature, approximately 530 °C, and a high concentration of ammonia, both of which increase the rate of nitriding.[38] These problems have been successfully solved by the choice of appropriate materials of construction.

Two recent developments have been made to the synthesis loop of the purifier process, in line with the general trend of modern ammonia synthesis technology.[39] First, a third ammonia converter has been added to increase the conversion per pass. Heat recovery between the second and third converters is used for the generation of high-pressure steam. Second, the design of the converter internals

has been modified to provide radial flow instead of axial flow. This leads to a reduction in pressure drop, which thus enables smaller catalyst particles to be used.

7.3.3. The Topsoe Ammonia Process

The production of synthesis gas in the modern Topsoe process follows the normal process steps of the steam-reforming route. For a natural gas or naphtha feedstock, these steps are desulfurization, primary reforming, secondary reforming, shift conversion, carbon dioxide removal, and methanation. The Topsoe process is characterized by equipment design and catalysts rather than by the process sequence or operating conditions. The most notable engineering feature in the gas preparation area is the primary reformer furnace. This is a side-fired design in which a large number of burners are set in the furnace walls. This is in contrast to the top-fired design used in most other processes. Topsoe produce their own range of catalysts for all the duties in the ammonia process.

The synthesis gas produced by this process has the conventional composition of a 3:1 stoichiometric hydrogen/nitrogen mixture, containing 0.3% argon and approximately 0.8% methane. Topsoe's current synthesis technology is the S-200 Ammonia Synthesis Process[40] and the heart of this process is the radial-flow S-200 converter.[40-42] This design was first used commercially in 1979, although Topsoe's experience of radial-flow ammonia converters dates from the introduction of the S-100 converter in the mid-1960s.[19] A description of the modern Topsoe synthesis loop is as follows.

Fresh synthesis gas produced by the steam-reforming route is compressed to synthesis pressure in a two-stage centrifugal compressor. The compressor is usually driven by a steam turbine. The compressed make-up gas is chilled and added to the loop before the final loop chiller. After the chiller, the ammonia product is removed in the ammonia separator which operates at a typical temperature of −5 °C. Traces of carbon dioxide and water in the incoming gas are removed with the product ammonia. Topsoe have calculated that with their synthesis conditions, the saving in energy obtained by the alternative system of molecular sieves for carbon dioxide and water removal is small and does not justify either the extra investment or the risk of dust carryover from the molecular sieves.

Gas from the separator is reheated in two gas-gas interchangers, upstream of each loop chiller, and passes to the circulator which forms part of the high-pressure stage of the compressor. The gas is then heated in a feed-effluent exchanger and enters the synthesis converter. Gas exiting the converter is cooled initially with simultaneous recovery of waste heat by raising high-pressure steam and successively by the feed-effluent exchanger, by cooling water, and finally by two levels of chilling involving gas-gas exchange. Purge gas is taken off after the final interchanger, just before addition of fresh synthesis gas. In modern plants, a purge gas recovery unit is usually used to recover hydrogen.

The ammonia converter in the Topsoe process features radial flow and usually contains two catalyst beds. As explained earlier, the principal advantage of radial flow is the very low pressure drop. This enables small catalyst particles to be used (typically 1.5-3 mm), and hence the diffusional limitation associated with larger

catalyst particles is overcome. This in turn results in a smaller catalyst volume required to achieve a given conversion.

Topsoe's first radial-flow converter (the S-100) consisted of two radial-flow catalyst beds, with quench gas added between them and a feed effluent exchanger installed beneath the second bed. In the S-200 design, heat exchange instead of quench gas is used to control the temperature of the second bed (see Fig. 7.10). Indirect cooling results in higher conversion per pass for a given volume of catalyst. The second heat exchanger is located in the centre of the first (upper) catalyst bed. On the feed side, the two heat exchangers operate in parallel. A further variation is the S-200 without a lower heat exchanger. In this case, converted gas leaving the second bed exits the converter and flows directly to heat recovery at high temperature, e.g., for raising high-pressure steam. A similar arrangement is used in other modern processes where high-temperature heat recovery is required. The advantages are improved process efficiency and a simpler converter layout. The disadvantage is a higher converter inlet temperature, which results in a higher design temperature and a larger external feed-effluent exchanger.

With a two-bed converter, and assuming conventional catalyst temperatures, the conversion to ammonia per pass is limited by the thermodynamic reaction

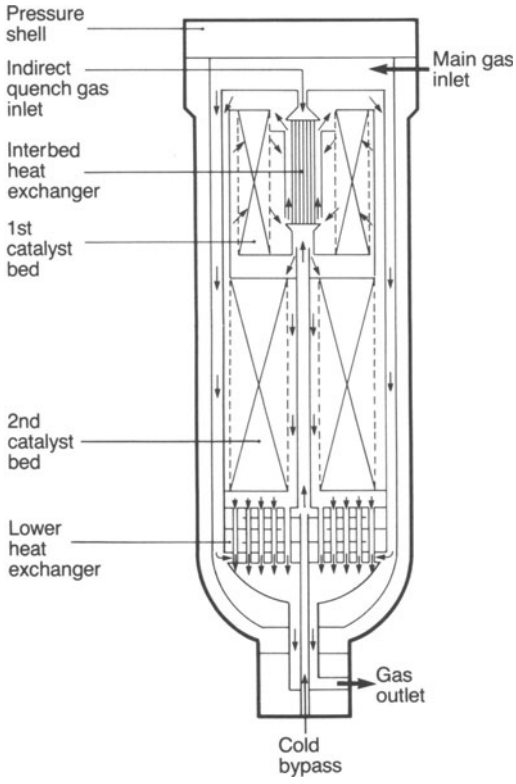

Figure 7.10. Topsoe S-200 ammonia converter. Courtesy of British Sulphur Corporation.

equilibrium. If three intercooled beds are used, then a higher conversion per pass can be obtained. The principal advantage of higher conversion per pass is that the dew point of the converted gas is higher and hence more ammonia can be condensed simply using cooling water, rather than a need for refrigeration. Topsoe have a three-bed converter design[43] which consists of a two-bed S-200 converter followed by a boiler and an additional single-bed radial-flow converter. Heat recovery before the final bed enables the heat of reaction to be recovered at a higher temperature. This is an advantage when the overall heat recovery scheme for the plant requires the ammonia loop heat recovery to be used for a high-pressure boiler rather than for boiler feed water heating.

7.3.4. The ICI AMV Ammonia Process

As with the processes already discussed, the ICI AMV process is based on steam reforming of either natural gas or naphtha. It uses the same basic process steps as the Kellogg or Topsoe processes, but the operating conditions are significantly different.[44-47]

In essence, the ICI AMV Process comprises the following steps. Primary reforming is carried out at mild temperatures and followed by secondary reforming using a substantial excess of process air. The subsequent steps of shift reforming, carbon dioxide removal, and methanation use conventional modern technology with appropriate heat recovery. The methanated gas contains an excess of nitrogen and a relatively high level of methane. This gas is subjected to a limited amount of compression and enters the synthesis loop where ammonia is formed. The inert components (methane and argon) and the excess nitrogen are all removed by cryogenic treatment. The low synthesis pressure enables the cryogenic unit to operate at synthesis loop pressure with the recovered hydrogen returned to the circulator suction.

The ICI AMV design is an overall process in which the operating conditions of the individual process steps have been optimized to complement each other. This can be demonstrated by describing a typical AMV flowsheet.

Natural gas feed is mixed with recycle hydrogen, heated, and desulfurized. It is then cooled by preheating the feed to the desulfurizer, before passing to a feed gas saturator where it is contacted with circulating hot process condensate. The feed gas from the saturator is mixed with a further quantity of steam to give a steam : carbon ratio of about 2.8 : 1 and preheated in the reformer flue gas duct. The reactants enter the primary reformer, which operates with an exit temperature of 750–800 °C and a pressure of 30–40 bar. The gas mixture is then fed to a secondary reformer for further reforming with an excess of unheated process air. The secondary reformer operates at an exit temperature of 900–950 °C. The design methane slip from the secondary reformer is about 1% (dry gas basis). The reformed gas is cooled by generating high-pressure steam and then shifted in high-temperature (HT) and low-temperature (LT) shift converters. Between the HT and LT shift converters, the gas is cooled by heating the circulating water for the feed gas saturator. The heat in the gas leaving the LT shift converter is used to preheat high-pressure boiler feed water.

After shift conversion, the gas is taken to a low-energy carbon dioxide removal plant and then compressed to 80–110 bar.

The compressed gas is methanated and then cooled and dried by a molecular sieve. The catalysts used in the production of synthesis gas are all conventional.

The dried gas enters the ammonia synthesis loop at the circulator suction point. In the synthesis loop, gas from the circulator is heated and passed over an optimized low-pressure ammonia synthesis catalyst to produce ammonia.

The hot gas leaving the ammonia converter is cooled by further heating boiler feed water and by heating the feed gas to the converter. Ammonia is separated from the partially cooled gas using mechanical refrigeration. Gas leaving the ammonia catchpot is returned to the circulator.

Inerts and excess nitrogen from the synthesis loop are removed by taking a purge from the circulator delivery and treating it in a cryogenic hydrogen recovery unit. The recovered hydrogen is recycled to the circulator suction.

7.3.5. Other Processes

The four processes described above account for the majority of plants that have been commissioned in recent years, although this is not intended to be an exhaustive survey of current ammonia technology. Many other companies are also active in ammonia technology including, for example, KTI[48] and Uhde.[49] The processes described also cover the major technical options, although the recently developed ICI LCA process[52] includes a number of significant technical improvements. Two plants using this technology were commissioned in 1988. This process is considered in more detail in Section 7.5.

As far as ammonia converter design is concerned, Ammonia Casale's technology has already been introduced in Section 7.2.3. Ammonia Casale converter designs using the axial–radial flow concept have achieved considerable success in recent years, particularly for modification of existing axial-flow converters.[50] These converter retrofits can be achieved by *in situ* changes to the converter internals in the case of converters where the catalyst basket cannot be removed from the pressure shell.

7.4. SYNTHESIS LOOP OPERATION

7.4.1. Catalyst Reduction

A commercially available ammonia synthesis catalyst is usually supplied with the iron phase in the form of magnetite, which first must be reduced to metallic iron before the catalyst is used. The reduction time is typically from three to five days, although the actual time required is dependent on the plant design and on limitations of equipment, such as the start-up heater. The general principles of reduction are outlined below. More detailed information to suit a specific plant can be obtained from catalyst suppliers. The principal factors governing a plant reduction are the water content of the circulating gas, the gas flowrate, the reduction pressure, and the reduction temperature.

7.4.1.1. Water Content

The water content of the circulating gas returning to the converter must be kept to a minimum, e.g., less than 100 ppm. This is to prevent re-oxidation of catalyst which has already been reduced. The concentration of water may be minimized by commissioning the synthesis loop refrigeration system as soon as the ammonia content of the reduction water is sufficiently high to avoid freezing (20% ammonia in the water is adequate). On some plants, ammonia can be injected into the loop to prevent freezing of reduction water before significant amounts of ammonia are produced on the partially reduced catalyst bed.

The water content of the gas leaving the catalyst bed during reduction influences the final activity of the reduced catalyst. In general, the lower the water concentration the better. In practice, an exit water concentration of 5000 ppm is a good operating limit and 10,000 ppm should be regarded as a maximum. In a multibed converter, the beds must be reduced in sequence to avoid the reduction water re-oxidizing catalyst that has already been reduced.

7.4.1.2. Gas Flowrate

Reduction should be conducted at the highest possible gas flowrate to speed the reduction and to ensure adequate gas distribution. Initially, the gas rate is limited by the capacity of the start-up heater. Start-up heaters are usually fired heaters external to the ammonia converter using natural gas, naphtha, or synthesis gas as fuel. Alternatively, some designs incorporate electric heating elements within the ammonia converter vessel. In either case, the sizing of the heater is an economic balance between capital cost of a larger heater and the operating cost of a prolonged start-up and reduction. With a multibed converter, ammonia synthesis commences as the first catalyst bed is reduced, and the heat of reaction supplements the start-up heater input. This enables the gas rate to be increased for subsequent stages of the reduction.

Good gas distribution is important during reduction as uneven flows can lead to uneven reduction of the catalyst. This can result in local high concentrations of water and high local temperatures when the synthesis reaction starts. This could lead to some loss of activity.

Uneven distribution can be overcome by increasing the flowrate through the converter.

7.4.1.3. Reduction Pressure

As far as the catalyst is concerned, the reduction pressure is not critical. Higher pressure increases the rate of the ammonia reaction and hence increases the evolution of heat once the first part of the catalyst is reduced. This heat liberation enables the flowrate to be increased as explained above. On the other hand, a high rate of ammonia production can make temperature control more difficult. The practical solution to these conflicting effects is to perform the reduction at a pressure rather lower than the normal operating pressure, for example, using a reduction pressure of 100 bar in a loop with a normal operating pressure of 150 bar.

7.4.1.4. Reduction Temperature

A typical procedure is to heat the catalyst so that the temperature rises at about 50 °C per hour to a level of 320–330 °C and then to reduce the rate of heating to about 10 °C per hour until reduction commences in the temperature range 370–380 °C. The reduction rate is strongly dependent on temperature and the recommended exit concentrations of water are achieved by controlling the reduction temperature. As reduction proceeds, the synthesis reaction will commence and careful temperature control is required as bed temperatures can then increase rapidly. Peak catalyst temperatures should be kept below 500 °C until reduction is complete. Unreduced beds should be kept below 350 °C to avoid simultaneous reduction of two or more catalyst beds.

7.4.2. Pre-Reduced Catalyst

Although ammonia synthesis catalyst is normally supplied in the oxidized form, it may also be reduced and stabilized by the manufacturer and supplied as pre-reduced catalyst. The stabilization consists of a controlled partial re-oxidation to allow handling of the catalyst and charging to the converter. Stabilized pre-reduced catalyst is usually less than 10% oxidized.

The principal advantage of using pre-reduced catalyst is that it requires only a short activation period and the converter can be commissioned more quickly.

7.4.3. Operation and Optimization

Although ammonia converters and synthesis loops vary considerably in design, there are a number of general operating principles which can be applied to most commercial plants:

1. Increasing the catalyst temperature increases the reaction rate when far away from equilibrium, but higher temperature gives a less favorable equilibrium; the optimum temperature is a balance between reaction rate and equilibrium.
2. Methane and inert gases, mainly argon, accumulate in the loop and suppress the partial pressure of the reactants. The optimum inerts level is a balance between increased power consumption with a high inerts concentration and reduced feedstock efficiency if the inerts level is lowered by increasing the purge rate.
3. Increasing the loop pressure gives a higher equilibrium concentration of ammonia and also increases the rate of reaction. Hence, the maximum production capacity is attained at the maximum operating pressure of the equipment. On the other hand, the synthesis gas compression power is also increased.
4. Increasing the circulation rate through the converter increases the ammonia production rate but also requires more power for circulation and refrigeration.

Optimum loop operation must take account of all these factors, and relate them to the mechanical features of each particular plant.

7.5. FUTURE TRENDS

For many years into the future there will be a continuing requirement for the large-scale production of ammonia, principally for fertilizer use. The main objectives for commercially sized plants are high efficiency, low capital cost, and high reliability. The trends in plant design to achieve these objectives can be considered on a number of different levels, ranging from broad issues such as choice of feedstock to details of the ammonia converter design.

7.5.1. Feedstock

Present-day proposals for ammonia plants are predominantly based on natural gas feedstock, although a few plants are naphtha-based. A small minority of current projects are based on partial oxidation of heavy fuel oil, for example, in China. This pattern is likely to continue for the foreseeable future. A changeover to coal-based technology is unlikely in the near future because of the very high capital cost involved.

7.5.2. Plant Scale

Two trends in plant scale are apparent. The first is a continuation of present plant capacities in the range 1000–1750 tons per day. There is unlikely to be a trend to build larger plants as envisaged a few years ago. Although single-stream plants with capacities of over 2000 tons per day are feasible, such large projects are more difficult to finance, and are likely to encounter constraints of feedstock availability and product marketing.

The second trend in plant scale is to invest in medium-scale plants, typically in the range 400–600 tons per day.[51] Plants of this scale can be more easily matched to limited feedstock supplies or to local markets. Alternatively, they are useful for incremental increases in production capacity.

7.5.3. Reforming Technology

In the development of the steam-reforming route to ammonia, for many years there has been a desire to eliminate the steam-reforming furnace for reasons of capital cost, efficiency, and reliability. This technology has now been demonstrated on a commercial scale by ICI with the LCA process.[52] With this process the plant is simplified by the use of a Gas Heated Reformer (GHR) in which the primary reformer receives heat directly from the process gas leaving the secondary reformer. This compact pressurized reformer eliminates the massive furnace structure and the high-pressure steam system of a conventional plant. A pressure swing adsorption

system removes carbon dioxide and some of the nitrogen arising from the excess air required for the reforming heat load.

This technology is particularly suitable for medium-scale plants as envisaged above.

Elimination of the reforming furnace is likely to be a significant trend in future ammonia plants. Similar technology is also under development by Uhde with their Combined Autothermal Reformer or CAR,[53] although this process requires the use of oxygen rather than air in the secondary reformer.

7.5.4. Ammonia Converter

The present trends in ammonia converter technology are likely to continue into the future. In summary, these are the use of small catalyst particles, particularly in radial-flow converters, and the use of intercooling between catalyst beds rather than quench gas. The present trend of modifying existing converters to incorporate these improvements is also likely to continue.

Despite all these improvements to the modern ammonia process, the heart of the process, namely, the reaction of hydrogen and nitrogen over a promoted iron catalyst at elevated temperature and pressure, is likely to remain essentially the same for many years to come.

REFERENCES

1. A. V. Slack and G. Russell James, *Ammonia*, Parts I to IV, Marcel Dekker, New York (1977).
2. M. V. Twigg, *Catalyst Handbook*, Wolfe Publishing, London (1989).
3. *Nitrogen* **174**, 23 (1988).
4. R. L. Baker and D. H. McCrea, The Benfield LoHeat Process: An Improved HPC Absorption Process, *AIChE National Meeting* Houston, Texas (April 1981).
5. V. A. Shah and J. McFarland, *Hydrocarbon Process.* **67**(3), 43 (1988).
6. W. Gerhardt and W. Hefner, BASF's Activated MDEA—A Flexible Process to Meet Specific Plant Conditions, *AIChE Ammonia Safety Symposium* (1988).
7. F. C. Brown and C. L. Leci, Criteria for Selecting CO2 Removal Processes, Paper read before *The Fertiliser Society*, London (21 October 1982).
8. S. Strelzoff, *Hydrocarbon Process.* **53**(12), 79 (1974).
9. L. W. ter Haar, *2nd Symposium on Large Chemical Plants*, Antwerp, Belgium (November 1973).
10. C. P. Marien and W. L. Slater, Manufacture of Tonnage Hydrogen by Partial Combustion—The Texaco Process, *6th World Petroleum Congress*, Frankfurt, Sect 111, paper 22 (June 1963).
11. G. Hochgesand, *Ind. Eng. Chem.* **62**(7), 37 (1971).
12. T. W. Nurse, Ammonia From Coal; Choosing a Design. *Proc.—Int. Symp. Large Chem. Plants*: Energy, Feedstocks, Processes, 5th, p. 131 (1982).
13. *Nitrogen* **140**, 30 (1982).
14. S. A. Topham, *Catalysis Sci. Technol.* **7**, 1 (1985).
15. S. D. Lyon, Development of the Modern Ammonia Industry, Tenth Brotherton Memorial Lecture, *Chem. Ind. (London)*, **17**, 731 (1975).
16. W. Toering, *Plant/Oper. Prog.* **4**(3), 127 (1985).
17. W. A. Zech, Centrifugal Compressors for Ammonia Plant Design and Operation Considerations, Proc. Meet. UNIDO-FAI *Saf. Des. Oper. Ammonia Plants*, Paper V (1976).
18. K. J. Stokes, *Chem. Eng. Prog.* **75**(7), 88 (1979).

19. *Nitrogen* **31**, 22 (1964).
20. V. Vek and P. Kyril, Second Generation of Radial Flow Converters in Ammonia Synthesis, *Fertiliser Industry Annual Review*, X1, p. 89 (1988).
21. V. Vek, *Ind. Eng. Chem., Process Des. Dev.* **16**(3), 412 (1977).
22. U. Zardi, E. Commandini, and C. Gallazzi, 4th Fer. Nitrogen Proce. Br. Sulphur. Corp. *Int. Conf. Fert. Technol.* **1**, 173 (1981).
23. R. Weicken, Ammonia Plants. High Performance Reactor Reduces Energy Consumption, *Chem. Ind.* (*Dusseldorf*) No. 8, p. 674 (1986). (In German.)
24. T. R. Tomlinson and W. H. Isalski, Developments in Hydrogen Recovery Processes, *XV International Congress of Refrigeration*, Venice (Sept. 1979).
25. A. Finn, *Nitrogen* **175**, 25 (1988).
26. E. Perry, UK Patent 2017071A "Ammonia Synthesis Process," Monsanto Company (1978).
27. J. A. Finneran and H. C. Mayo, US Patent No. 3441393 "Process for the Production of Hydrogen-Rich Gas," Pullman Incorporated (1966).
28. A. V. Slack and G. Russell James, *Ammonia*, Part III, p. 293, Marcel Dekker, New York (1977).
29. J. R. Le Blanc, *Energy Prog.* **5**(1), 4 (1985).
30. A. Hickman, *Fertilizer Focus* **4**(9), 24 (1987).
31. O. J. Quartulli and G. A. Wagner, *Hydrocarbon Process.* **57**(12), 115 (1978).
32. S. E. Handman and J. R. Le Blanc, *Chem. Eng. Prog.* **79**(5), 56 (1983).
33. B. J. Grotz, US Patent No 3442613 "Hydrocarbon Reforming for Production of a Synthesis Gas from which Ammonia can be Prepared," C. F. Braun & Company (1965).
34. B. J. Grotz, *Nitrogen* **100**, 71 (1976).
35. K. C. Wilson, B. J. Grotz, M. L. Bhakta, and J. H. Gosnell, *Nitrogen* **151**, 31 (1984).
36. J. H. Gosnell, B. J. Grotz, and L. Grisolia, *Ammonia Plant Saf.* **25**, 38 (1985).
37. W. A. Glover and J. P. Yoars, Two-Stage Adiabatic Ammonia Synthesis Converter, *AIChE Safety Symposium*, Minneapolis (Aug 29, 1972).
38. G. R. Prescott, *Plant/Oper. Prog.* **1**(2), 94 (1982).
39. J. S. Uschold, *Fertilizer Focus* **4**(9), 47 (1987).
40. I. B. Dybkjaer and E. A. Gam, *Chem. Econ. Eng. Rev.* **16**(9), 29 (1984).
41. I. B. Dybkjaer, *Ammonia Plant Saf.* **25**, 15 (1985).
42. I. B. Dybkjaer, *NATO Adv. Study Inst. Ser., Ser. E* **110**, 795 (1986).
43. P. Pederson, *Fertilizer Focus* **4**(9), 38 (1987).
44. J. G. Livingstone and A. Pinto, *Chem. Eng. Prog.* **79**(5), 62 (1983).
45. *Nitrogen* **162**, 27 (1986).
46. W. K. Taylor and A. Pinto, *Plant/Oper. Prog.* **6**(2), 106 (1987).
47. C. W. Hooper and A. Pinto, Development and Operation of the ICI AMV Ammonia Process, *Fertilizer Industry Annual Review*, XI, p. 61 (1988).
48. W. F. Van Weenen and J. Tielrooy, *Chem. Age India* **31**(12), 2 (1980).
49. P. Kalthoff *Fertilizer Focus* **4**(9), 32 (1987).
50. *Nitrogen* **163**, 41 (1986).
51. K. I. Arkley and A. Pinto, Expansion of Ammonia Capacity by Smaller Modern Plants, *FAI Seminar*, New Delhi (Dec. 1986).
52. J. M. Halstead, A. M. Haslett, and A. Pinto, Design and Operating Experience of the ICI LCA Ammonia Process, *FAI Seminar*, New Delhi (Dec. 1988).
53. H. D. Marsch and N. Thiagarajan, CAR, A New Reformer Technology, *AIChE Ammonia Safety Symposium*, Denver, Colorado (1988).

8

DEACTIVATION OF SYNTHESIS CATALYST

P. E. Højlund Nielsen

8.1. INTRODUCTION

The catalytic synthesis of ammonia from hydrogen and nitrogen was invented around 1910. Already by that time it had been established that a reduced, promoted magnetite was superior to all other catalysts, except osmium. Since that time, reduced magnetite has continued to provide the basis for ammonia synthesis, even though numerous attempts have been made to make better catalysts.

The phenomenon of deactivation of the synthesis catalyst has been recognized since the beginning of the industrial synthesis. Quite early on, compounds such as water and hydrogen sulfide were recognized as poisons, and short lifetimes, in the order of years, were usual. In modern plants, lifetimes of 10–20 years are not uncommon. This has been achieved largely by an improved purification system for the synthesis gas and an optimization of the catalyst production procedure, yielding a more stable and active magnetite, which is still the ammonia catalyst used exclusively in the industry today.

Previous and Present Industrial Practice

Reference is made to the preceding chapter and the monographs in the field, notably by Slack.[1] In general, the synthesis of ammonia takes place at temperatures above 625 K and pressures above 8 MPa. The upper values for temperatures are most often determined by the adiabatic approach to equilibrium, and are dependent on pressure. However, temperatures above 825 K are rarely encountered, except in older plants toward the end of the catalyst life. With respect to pressure, older plants have operated at pressures above 50 MPa, but in modern plants the pressure is most often below 20 MPa.

P. E. Højlund Nielsen • Haldor Topsøe A/S, Nymøllevej 55, DK-2800 Lyngby, Denmark.

A consequence of the current trend to lower pressure and temperature is that the reaction rate decreases, and thus the demand on the activity and lifetime of the synthesis catalysts has been increased.

As described in Chapter 7, synthesis of ammonia takes place in a circulatory system commonly known as a loop. Only a fraction of the synthesis gas is converted per pass, as limited by the equilibrium concentration of ammonia at the exit conditions of the converter. The relevant part of the loop is shown in Fig. 8.1.

In general, the make-up gas fed to the loop will contain about 99% of nitrogen and hydrogen in the molar ratio $H_2/N_2 \simeq 3.0$ with about 1% methane and argon, besides minor amounts of other molecules, some of which may be poisons. In plants using a liquid nitrogen wash, methane and argon are absent. However, in these plants, oxygen may be present in small amounts, and this would be detrimental to activity.

The deactivation of the ammonia catalyst is dependent on the operating conditions, i.e., pressure and temperature, but more significantly on the small amounts of gaseous compounds contained in the feed gas.

In the early days of ammonia manufacture, the average lifetime of the ammonia synthesis catalyst was limited to a few years, while today, lifetimes in excess of 10 years are common. This dramatic increase arises from a number of improvements. Most noteworthy are the introduction of centrifugal compressors and the application of lubrication oils with low sulfur content as outlined by Nielsen.[2] Another significant improvement is the incorporation of a secondary ammonia condensation system, in which the make-up gas together with the recirculating gas is "washed" in liquid ammonia before entering the ammonia synthesis converter (see Fig. 8.1).

The result of the ammonia wash is to prevent water and carbon dioxide from entering the loop, except in the case of a malfunction leading to carry-over from

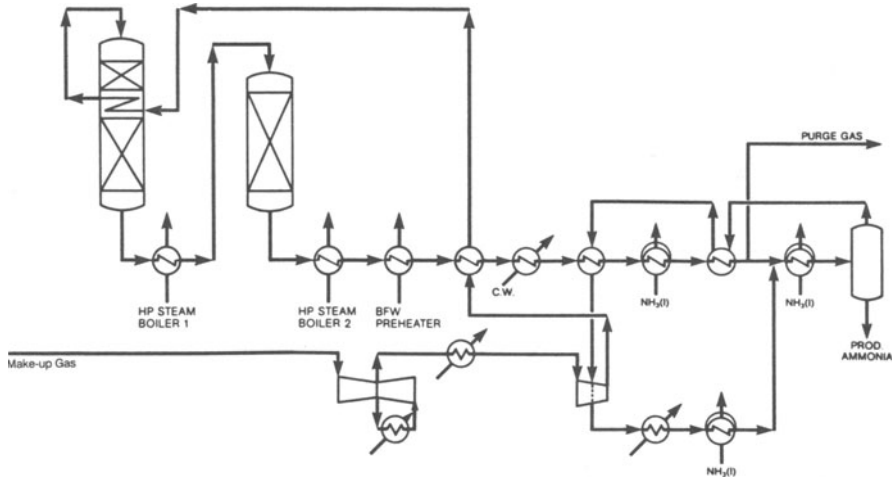

Figure 8.1. A synthesis loop with the Haldor Topsøe S-250 three-bed reactor. Note that the make-up gas is compressed and that water from the clean-up methanation is separated. Furthermore, the make-up gas is washed in liquid ammonia as it enters the synthesis loop.

the ammonia separator. Carbon monoxide is not removed by the ammonia wash, but is converted instead to methane and water in the loop. Thus the two major sources of poisons have been almost eliminated by design changes. Removal of the oxygenic impurities results in a higher catalyst activity, whereby operation at lower temperatures and pressures becomes possible as outlined by Dybkjær.[3]

8.2. FUNDAMENTAL DEACTIVATION PROCESSES

Promoted magnetite in its reduced state, used as an ammonia synthesis catalyst, undergoes deactivation for a number of reasons. Like other high-surface area structures, it may sinter. Species present in the gas stream may chemisorp upon the catalytic surface and thereby poison it, and furthermore, access to the pore system may be blocked by deposits. These processes of sintering, poisoning, and fouling are discussed below.

8.2.1. Sintering

In its active state, an ammonia synthesis catalyst is a high-density, medium-surface area composite, which is produced by the reduction of promoted magnetite (see Chapter 2). With a resulting surface area of about 10 $m^2 g^{-1}$ and a bulk density around 2.8 g cm^{-3}, an approximate surface area of 2–3 $\times$ 10^7 m^2 per m^3 is available. On a microscopic scale this corresponds to an average crystallite size of about 20–30 nm.

Such small particles are generally not thermodynamically favored due to their excess surface energy. The sintering process results in an irreversible increase in average crystallite size. Mass transport is involved, and this may occur through diffusion (surface or bulk) or the formation of volatile intermediaries. Sintering is discussed in more detail later in the chapter and by Hughes.[4]

8.2.2. Poisoning

The catalytic activity of an ammonia catalyst may be reduced in the presence of certain chemical compounds, referred to as poisons. These may be gaseous, occurring as minor components of the synthesis gas, or as solids introduced to the catalyst during the manufacturing process, as impurities in the natural magnetite from which the catalyst is made. The latter will not be dealt with here, since they are already covered in Chapter 2.

In the case of gaseous catalyst poisons, a distinction can be made between permanent poisons causing an irreversible loss of catalytic activity and temporary poisons which lower the activity only while present in the synthesis gas. This distinction is fully discussed in the book by Nielsen.[2] Permanent poisons such as sulfur accumulate upon the catalyst surface and may be detected by chemical and spectroscopic analysis, while temporary poisons do not interact nearly as strongly with the catalyst. It is very difficult to detect temporary poisons by means of post-analytical methods. The principal temporary poisons are oxygen, carbon oxides, and water. Since the catalyst also contains percent amounts of oxygen

associated with the promotors, differentiation between the two types is extremely difficult.

8.2.3. Fouling

The term fouling describes the mode of catalyst deactivation, in which deposition of solid residues causes part of the porous structure of the catalyst to be blocked, preventing access to the reacting gases. This is a common mode of deactivation in a number of catalytic reactions such as reforming and desulfurization of heavy oils, as described by Hughes.[4] However, it is extremely rarely encountered in the case of ammonia synthesis, being limited to cases where large amounts of compressor oil enter the catalytic bed.

8.3. PERMANENT POISONS

Permanent poisoning is caused by compounds, the presence of which in the synthesis gas results in an activity decline. The activity is not regained when the compound is removed from the synthesis gas. The poisoning action is frequently due to the irreversible formation of surface and/or bulk compounds with iron or with one of the promotors, in particular potassium. The deposition of solid material, as discussed briefly in Section 8.2.3, can also lead to permanent poisoning.

In the case of temporary poisoning, the activity loss depends on the surface coverage of the chemisorbed poison, which under steady-state conditions is in equilibrium with the gas phase, in contrast to the effect of permanent poisons. An isotherm can be used to describe the extent of coverage as a function of the poison concentration in the gas phase. In the situation where the catalytic reaction takes place at a considerably higher temperature than normal, the surface coverage for a given poison concentration will be much reduced and the activity loss negligible. On the other hand, the surface coverage and consequent activity loss at much lower temperatures seem to be irreversible and a case of permanent poisoning exists. Thus the operating conditions affect the distinction between temporary and permanent poisons. If the operating temperature of ammonia converters had been above, say, 1200 K, sulfur may well have been a temporary poison.

8.3.1. Sulfur

Sulfur is the most common of the permanent poisons. In plants based on gasification of sulfur-containing feedstocks, in particular coal, traces of carbonyl sulfide and hydrogen sulfide may reach the synthesis converter. In plants based on natural gas, the sulfur content of the feed is very low, and furthermore the copper-based low-temperature shift catalyst and the nickel-based clean-up methanation catalyst act as efficient guards by irreversibly absorbing these traces of sulfur. In the earlier days of ammonia synthesis, the lubrication oil for the compressors was a common source of sulfur,[2] but today this problem is widely recognized and examples of sulfur poisoning in the industry are rare.

Sulfur is chemisorbed very strongly by the iron crystal surface. Benard *et al.*[5] suggest a value of $-190\,\mathrm{kJ\,mol^{-1}}$ for the enthalpy for formation of a sulfide

monolayer, while bulk FeS has a ΔHf on $-100\,kJ\,mol^{-1}$.[6] Grabke *et al.*[7] found that the rate of carburization of iron according to $CH_4 \rightleftarrows C(dissolved) + 2H_2$ and the nitrogenation and denitrogenation according to $N_2 \rightleftarrows 2N(dissolved)$ became appreciably affected at an H_2S/H_2 ratio of 10^{-7} at 1073 K. Using the enthalpy for monolayer formation suggested by Benard *et al.*,[5] an H_2S/H_2 ratio of 10^{-12} at 700 K would cause a similar effect.

Studies of sulfur poisoning of ammonia synthesis catalysts have been carried out by a number of authors. More recent work by Enikeev and Krylova[8] has shown that chemisorption of hydrogen sulfide adsorption leads to an increase in the work function, as is also the case for carbon monoxide, carbon dioxide, and water. Contrary to the latter, however, heating in hydrogen did not lower the work function to its unpoisoned level, which is indicative of permanent poisoning. Brill and Tauster,[9] Tauster,[10] and Brill *et al.*[11] have carried out experimental studies on iron metal and singly (Al_2O_3) promoted catalysts. They found that approximately $0.2\,mg\,S\,m^{-2}$ iron surface resulted in complete deactivation, and the maximum uptake of sulfur was found to be $0.4–0.5\,mg\,m^{-2}$ iron surface. There are about 1.2×10^{19} Fe in $1\,m^2$ of Fe(100) surface, while there are only 3.8×10^{18} sulfur atoms in 0.2 mg of sulfur. Thus in the limiting case of complete poisoning, there are about three iron atoms per sulfur atom. Brill *et al.*[11] found that the chemisorbed sulfur was very strongly held and could not be removed by heating up to 900 K.

Analysis of spent industrial catalysts discharged from the inlet layer of the catalyst bed has revealed sulfur in concentrations ranging from 1000 to 5000 ppm.[2] If all the sulfur is present as a monolayer, this would correspond to an iron metal surface area from 2 to $10\,m^2\,g^{-1}$. It may also indicate that the major part of the catalyst surface is the iron surface and not, as often suggested by Emmett (see Section 8.4), made up by promoter phases.

8.3.2. Other Permanent Poisons

In general, any compound that lowers the surface tension of iron may exert a poisoning reaction. Thus most chemical species may be regarded as potential poisons for the ammonia synthesis catalyst. Phosphorus and arsenic compounds, for example, are known to be permanent poisons.[2] However, in natural-gas-based plants they are present only in exceedingly low amounts. Their poisoning action is thought to resemble sulfur mechanistically,[2] since both phosphorus and arsenic form well-defined stable binary compounds with iron, as can be seen from their phase diagrams detailed by Hansen.[12]

Chlorine is also a serious poison for the synthesis catalyst, particularly for ammonia plants using hydrogen produced by electrolysis plants. Chlorine reacts with the potassium promoter[2,13] and forms potassium chloride, which may migrate in the catalyst particle or diffuse into the gas stream, depending on the temperature.

8.3.3. Admissible Level of Permanent Poisons

As implied in Section 8.3.2 above, a permanent poison is characterized by the fact that it is difficult to remove under normal process conditions once it has

reacted with the catalyst. Depending on the nature of the poison, one can calculate the amount of poisons sufficient to reduce the catalyst activity by a given fraction per year from the catalyst bed volume, gas rate, and surface area.

As an example let us consider the first bed in the Haldor Topsøe S-200 radial flow converter in a 1000 metric ton per day (MTPD) ammonia plant. At a design pressure of 18 MPa, the weight of reduced catalyst is 20 t, corresponding to a volume of about 9 m^3. The second bed is much bigger, containing about 25 m^3. The make-up gas is added before the ammonia condensation system, and all the synthesis gas passes through the first and second bed, respectively. Thus the first bed is subjected to all the permanent poisons, and it is a matter of rate velocity how fast the poisons become absorbed. Usually, the chemisorption is fast in the case of sulfur. If we allow 2% of the catalyst in the first bed to be poisoned per year and we consider the 5000 ppm of sulfur mentioned earlier as the maximum poison capacity, the following calculation can be carried out:

Active surface area $\sim (5000)/32 = 156\ \mu\text{mol g}^{-1} \sim 3120$ mol per first bed

2% of the above ≈ 60 mol per year

Make-up gas ($1000\ \text{t NH}_3\ \text{d}^{-1}$) $\sim 1.2 \times 10^8\ \text{mol d}^{-1} \sim 4 \times 10^{10}$ mol per year

Concentration of permanent poisons $\sim (60)/4 \times 10^{10} = 1.5 \times 10^{-9}$ V/V

This model is based upon the assumption that all irreversible poisons undergo a chemisorption process and do not form bulk compounds with the catalyst.

Furthermore, it has been assumed that the chemisorption front is sharp, i.e., the separation between the unpoisoned and completely poisoned region containing 156 μmol poison per g catalyst is very narrow.

In the case of chlorine, the mechanism of poisoning does not proceed by a surface chemisorption reaction but by a bulk chemical reaction with the potassium promoter. A similar calculation to that shown above, but with respect to the maximum chlorine content, may also be carried out. Let us assume that the catalyst has a potassium content of 1 wt%.

1% of $20 \times 10^3 \sim 200$ kg.

2% of this ≈ 4 kg ~ 100 mol, yielding $(100)/4 \times 10^{10} = \underline{2.5 \times 10^{-9}\ \text{V/V}}$

which is the maximum permissible chlorine content in the make-up gas, if only 2% of the catalyst is allowed to become poisoned per year.

Lifetimes in excess of 10 years are not uncommon in the ammonia industry, and there are other causes of permanent deactivation such as sintering. Furthermore, the estimates shown above are on the optimistic side with respect to catalyst surface area. It may therefore be concluded that the average content of permanent poisons in the make-up gas is usually well below 10^{-9} v/v.

8.4. TEMPORARY POISONS

A temporary poison lowers the activity of an ammonia synthesis catalyst by reversible adsorption onto the catalyst surface. Unsaturated hydrocarbons like ethylene may also react as a temporary poison according to studies by Nielsen,[2] but generally, it is the oxygenic compounds that constitute the single most important poison for ammonia synthesis.

The most common oxygenic compounds encountered in ammonia synthesis are carbon monoxide, carbon dioxide, and molecular oxygen. The equivalence per oxygen atom of these compounds has been established by Larson and Tour[14] and Almquist and Black.[15] This is due to the methanation activity of the ammonia synthesis catalyst:

$$3H_2 + CO \rightarrow CH_4 + H_2O$$

Carbon dioxide will undergo a similar reaction, though more slowly, and molecular oxygen will be hydrogenated too. Thus in the major part of the catalytic reactor, the sole oxygen-containing compound will be water.

With respect to the interaction between water and iron surfaces, reference is made to the preceding chapters, in particular Chapters 3–5.

From thermodynamical data it may be shown that, in ammonia synthesis gas, water is required in percent amounts in order to oxidize bulk metallic iron to the oxide (magnetite or wustite). On the other hand, it is very clear from the poisoning studies to be discussed later in this chapter that water in the low ppm range exerts a definite poisoning action.

The reason for this observation is a key question in catalysis and reference is made to Chapters 3–5. However, it should be mentioned here that there seems to be a general rule that compounds formed by interaction between a gas and a metal surface are generally more thermodynamically stable than the bulk ones. The increase in stability is gained from two contributions. Firstly, metal atoms on the crystallite surface are highly reactive due to their high surface tension (i.e., low coordination), and secondly, the fact that the two-dimensional structure formed by chemisorption possesses a higher degree of freedom than the corresponding three-dimensional compound, which results in a more stable configuration. This is illustrated clearly by the sulfur poisoning example.

It can be calculated that a H_2S/H_2 ratio of 4.7×10^{-5} is required to establish the Fe/FeS equilibrium at 700 K, using data from Barin *et al.*,[6] but a H_2S/H_2 ratio of only 10^{-12} to affect the surface properties as extrapolated from Grabke's data.[7] Similarly, a H_2O/H_2 ratio of 0.15 is required to establish the equilibrium between magnetite and iron at 700 K, but only ppm levels of water are required to affect the catalytic activity of an ammonia synthesis catalyst.

8.4.1. Oxygen and Oxygenic Compounds—Old Studies

Studies of the poisoning of the ammonia catalyst by oxygenic compounds date back to 1922, when Larson and Tour[14] carried out experiments with 0.04–0.1% of water vapor at pressures up to 100 atm. Experiments were also carried out with carbon monoxide, and the equivalence of the various oxygenic compounds was recognized. Almquist and Black[15] conducted experiments with up to 0.16% oxygen in the synthesis gas at ambient pressure. Almquist[16] evaluated the stability of the surface oxide and suggested that its free energy of formation was about 50 kJ per gram atom of iron lower than a gram atom of iron in magnetite.

Emmett and Brunauer[17] extended the measurements of Almquist and Black[15] to include higher pressures.

One of Emmett and Brunauer's conclusions has survived to this day and is cited even in modern reviews, such as that of Hughes,[4] namely, that the amount of oxygen absorbed by a catalyst is proportional to $(H_2O/H_2)^{1/2}$ as shown in Fig. 8.2a. This is, however, a questionable conclusion since according to Emmett and Brunauer[17] the pure synthesis gas contained "only a few thousandths of a percent of water vapor."

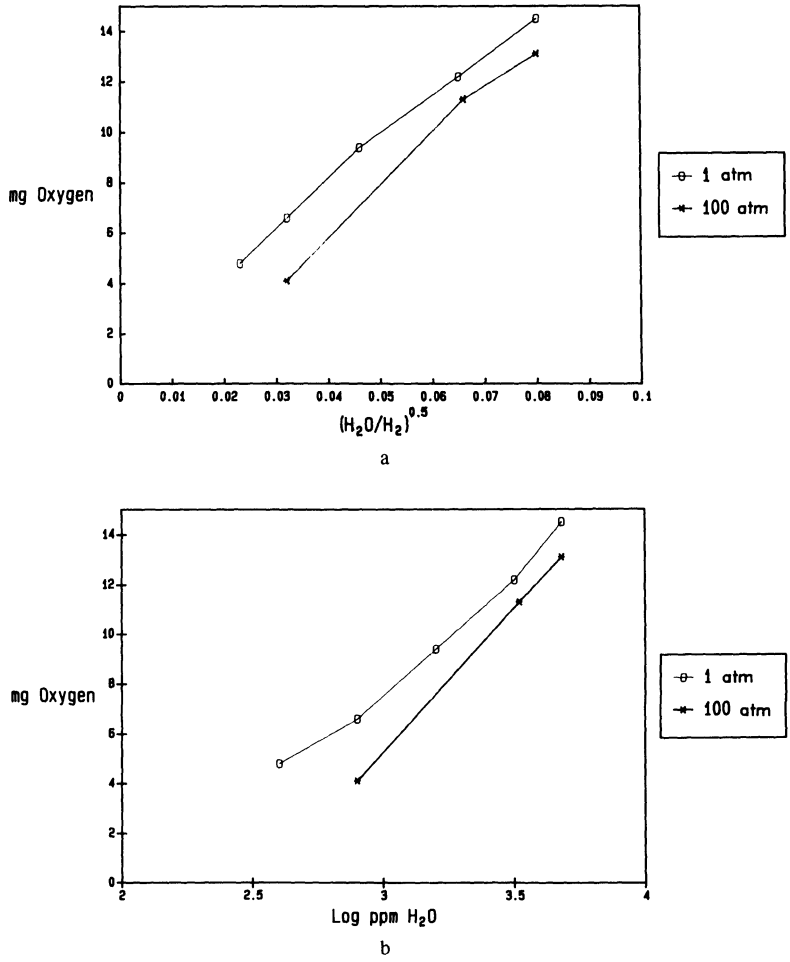

Figure 8.2. Uptake of oxygen upon an ammonia synthesis catalyst (921). × refers to 10 MPa data from Emmett and Brunauer[17] and ○ to 0.1 MPa data from Almquist and Black.[15] Note the different abscissa, suggesting a straight line through the origin, while a straight line intersects at log ppm $H_2O \sim 2$, indicates a base level around 100 ppm H_2O in the "pure" gas.

However, in Fig. 8.2b a plot of oxygen uptake versus log [H_2O] is shown, and suggests that a water content of at least 100 ppm was present in the "pure" gas. This is consistent with the low catalytic activities obtained. With a similar catalyst in pure synthesis gas and under the same conditions, one would today record activities approximately 1–2 order(s) of magnitude higher.

It can safely be concluded that a major part of the studies of ammonia synthesis catalysts has taken place using a "pure" synthesis gas contaminated by ppm amounts of oxygen compounds. In a recent paper, Stoltze[18] has demonstrated that a good interpretation of Nielsen's[2] low-temperature data can be made, assuming a water content of 10 ppm. This has made it even more difficult to obtain reliable kinetics. The early surface studies are characterized by the same problems, and it was not until recent times that studies using modern surface techniques have provided reliable data for the iron surface, as discussed in Chapter 4.

8.4.2. Selected Older Studies of Oxygen Poisoning

The use of relatively impure synthesis gas, characteristic of most older studies, does not invalidate many interesting studies on ammonia synthesis catalysts that were carried out. One of the most remarkable studies was carried out by Ussatschew *et al.*[19] A sort of pulse experiment was performed, where predetermined volumes of carbon monoxide, carbon dioxide, oxygen, and sulfur dioxide were injected into the feed gas stream at ambient pressure and at temperatures of 600–800 K. This resulted in an immediate release of ammonia to values exceeding the thermodynamic equilibrium followed by an activity loss, which in the case of sulfur dioxide was irreversible. An 80 cm^3 of volume of carbon monoxide resulted in an almost complete poisoning of 10 cm^3 of catalyst, and about 10 cm^3 of ammonia was released during the initial poisoning; 5 cm^3 of carbon monoxide resulted in a desorption of 4.6 cm^3 of ammonia. It was suggested that the release of ammonia was due to a replacement of chemisorbed nitrogen species (N, NH, NH_2) with oxygen. In the present context this is consistent with a nitrogen coverage of approximately 1/8 of the available surface sites. A large proportion of the remaining sites had probably been occupied by oxygen, judging from the activity of the catalyst. The observation to the effect that a substantial part of the catalyst surface is covered by nitrogenous species is consistent with modern interpretations of the mechanism of ammonia synthesis as proposed by Ertl (see Chapter 5) and Stoltze[18] and Stoltze and Nørskov.[20]

A similar interference by oxygen may also have affected the pioneering chemisorption studies by Brunauer and Emmett.[21] Studies using hydrogen, carbon monoxide, and carbon dioxide were carried out in order to determine active surface areas, which were all found to be much smaller than the total (BET) surface area determined by nitrogen physisorption.

8.4.3. Later Studies

High-pressure studies were carried out by Bokhoven,[22] Uchida and Todo,[23] and Nielsen.[2] Bokhoven made use of an isotope tracer technique, demonstrating

the reversibility of the poisoning as illustrated in Fig. 8.3, and the equivalence between carbon monoxide and dioxide, although a small amount of carbon dioxide was found to be irreversibly adsorbed. Uchida and Todo[23] carried out studies on carbon monoxide with a number of promoted catalysts at temperatures of 300–450 °C and 100 kg cm^{-2} pressure. At lower temperatures, the rate of methanation was low and some of the carbon monoxide was not converted to methane. At higher temperatures, the resulting poisoning was found to be reversible, while at lower temperature, complete reversibility was not observed and the experiments were not continued long enough to establish the true steady state.

Nielsen[2] also demonstrated the equivalence of the various oxygenic compounds. Furthermore, he showed that a six-day exposure to 100 ppm carbon monoxide at 450 °C and 330 kg cm^{-2} did not harm the catalyst permanently.

Studies at ambient pressure and 723K were carried out by Royen and Langhans[24] using a singly promoted catalyst (Al_2O_3) with water as a poisoning agent. Between 1.2–32.3 mg of oxygen was found to be chemisorbed on the catalyst, which had a BET surface area of 250 m^2, and a specific surface area of 4.22 $m^2\,g^{-1}$. From 0.008 to 4.16 vol% of water vapor was applied. The duration of the experiments does, however, not seem sufficient for the establishment of a steady state.

Smirnov *et al.*[25] conducted experiments at ambient pressure and suggested a modification of the conventional "Temkin" rate equation of ammonia synthesis (see Chapter 7). This equation was later generalized by Smirnov[26] to cover higher pressures. The expression was

$$\omega = (k_+ P_{N_2} - k_- P^2_{NH_3}/P^3_{H_2})/(P^2_{NH_3}/P^3_{H_2} + C \cdot P_{H_2O}/P_{H_2})^{0.5} \qquad (8.1)$$

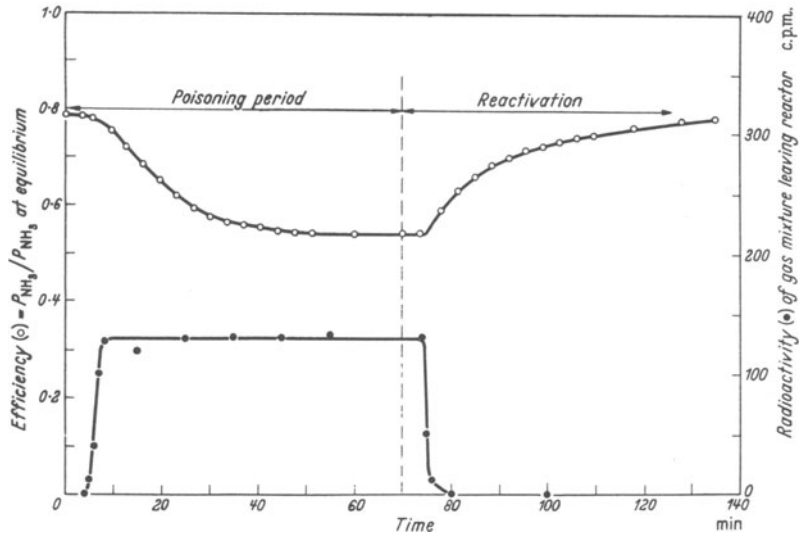

Figure 8.3. Poisoning experiments with 0.0025% CO at 450 °C and 3 MPa. Data from Bokhoven.[22] By permission of Butterworth Co. (Publishers) Ltd.

where ω is the reaction rate, k_+ and k_- are the rate constants for the forward and reverse reaction, while $k_+/k_- = k_e$ is the equilibrium constant for the ammonia synthesis. The reaction mechanism requires a displacement stage:

$$N_2(ads) + H_2O + 2H_2 \rightleftarrows O(ads) + 2NH_3$$

and C is the equilibrium constant for this reaction.

Earlier work by Ussatschew *et al.*[19] is consistent with such a displacement reaction. The values of C depend upon temperature and upon the promoters present within the catalyst. Smirnov has found that values of C for both singly and doubly promoted catalysts can be derived from the following equations, respectively.

$$C_1(\text{Fe, } Al_2O_3, K_2O \text{ catalyst}) = 1.3 \times 10^{-6} \exp(8930/T) \tag{8.2}$$

$$C_2(\text{Fe, } Al_2O_3 \text{ catalyst}) = 1.15 \times 10^{-6} \exp(8930/T) \tag{8.3}$$

Using these equations Smirnov obtained a satisfactory rationalization of earlier results, including the early work by Larson and Tour,[14] Almquist and Black,[15] and Emmett and Brunauer.[17] There remains, however, considerable uncertainty, since these earlier studies were carried out under partially poisoned conditions as already mentioned.

Brill *et al.*[27] examined the water poisoning of an unpromoted iron catalyst at ambient pressure, where water levels up to 95.8 ppm were applied. The activation energy of ammonia synthesis was found to be independent of the degree of poisoning, which is shown in Fig. 8.4, using results from a backmix reactor. Neither

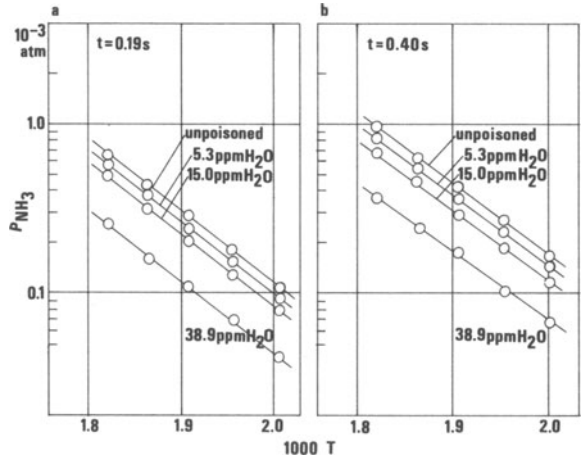

Figure 8.4. Plot of R_{NH_3} versus $1/T$ (K^{-1}) at various water poisoning levels. The catalyst has been poisoned at 350 °C and ambient pressure in an internal recirculation reactor at H_2O levels from 5.3 to 38.9 ppm. At steady state the temperature is quenched to 200 °C and the H_2O supply is interrupted simultaneously. The rate is then measured at temperatures of 225–275 °C. Note that the lines are parallel, indicating an unchanged activation energy. Data from Brill *et al.*[27] By permission of Verlag Chimie GmbH.

the model by Smirnov[26] nor the rate expression by Ozaki, Taylor, and Boudart[28] modified with a Langmuir isotherm for water adsorption gives a satisfactory description of Brill's data.

The experiment in the backmix reactor was conducted in an interesting manner. First, the catalyst was poisoned at a certain water level at 350 °C. At steady state the water addition was interrupted and the temperature was reduced. Thereupon the conversion was measured at temperatures between 225 and 275 °C (see Fig. 8.4). At these low temperatures, oxygen poisoning is effectively permanent. Since the activation energy does not change with the degree of poisoning, this suggests that a part of the catalyst is totally inactive, while the remaining unpoisoned part has an unchanged activity. The amount of active surface decreases with increasing partial pressures of water, and *vice versa.* In other words, temporary poisoning is a thermodynamic phenomenon rather than a kinetic one.

In recent work, Smirnov's theory was discussed by Boreskova *et al.*[29] They carried out isotopic exchange studies of nitrogen on reduced catalyst surfaces. They found that adsorption of 150 μmol of water onto an industrial catalyst of a total surface area of 173 m^2, which with reference to Eq. (8.3) may contain around 3000 μmol of iron surface atoms, resulted in a twofold (approximately) decrease in the amount of adsorbed nitrogen. However, the initial rate of adsorption as well as the rate of exchange were reduced by more than a factor of 10. Boreskova *et al.* were unable to explain these data by applying the theory of Smirnov.[26] It seems more likely, however, that adsorbed oxygen not only poisons the iron atom on which it lies, but also limits adsorption of nitrogen on neighboring sites, as suggested by Stoltze[18] and Stoltze and Nørskov.[20] If two neighboring sites are required for exchange of molecular nitrogen, even a partial coverage of the surface with oxygen would be sufficient to cause a major decrease in the rate of exchange. It is also significant that Boreskova *et al.*[29] found that addition of hydrogen to the partially poisoned catalyst increased the exchange rate dramatically.

8.4.4. Recent High-Pressure Studies

Højlund Nielsen[30] and S. Andersen[31] carried out studies of poisoning at 100 kg cm^{-2} pressure, and temperatures from 620 to 730 K. Their results may be described by means of a thermodynamic isotherm of the type

$$\theta = \frac{1}{k}(\Delta H_0 - T\Delta S - RT \ln(P_{H_2O})/P_{H_2} \tag{8.4}$$

or

$$\theta = a + bT + cT \ln(H_2O)/H_2 \tag{8.5}$$

S. Andersen[31] found, by varying the H_2/N_2 ratio, that the expression $\theta = a + bT + cT \ln X H_2O$ gave an overall better fit to the experimental results (Fig. 8.5), where X is the mole fraction.

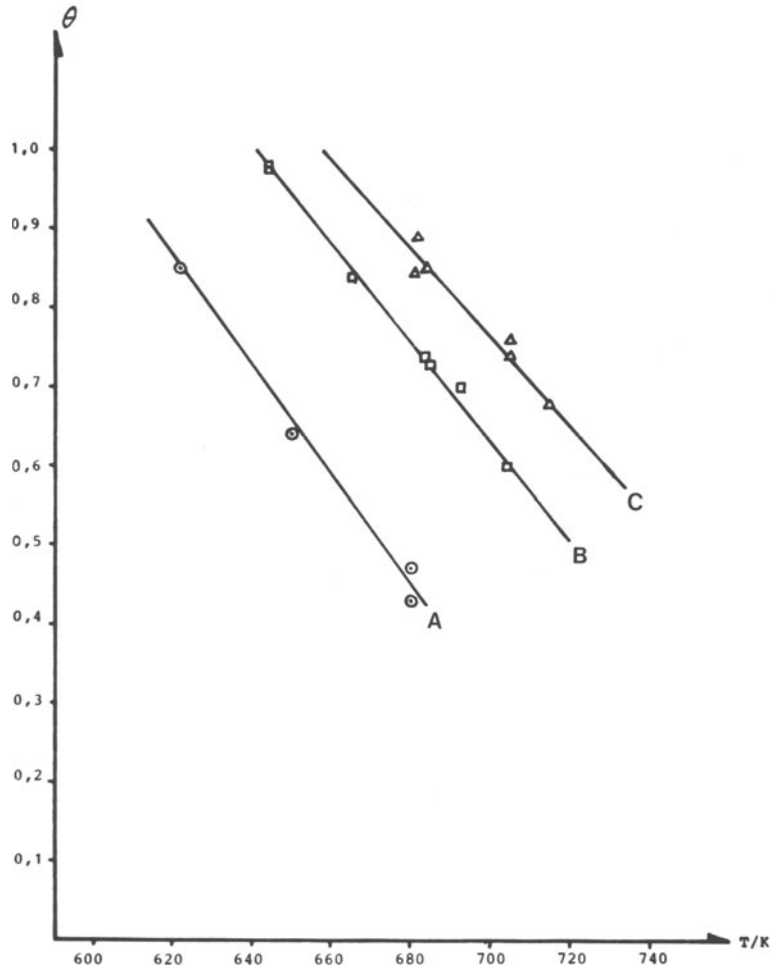

Figure 8.5. Degree of poisoning, θ, *vs.* T for a K-promoted synthesis catalyst. Tests conducted mainly at 10 MPa. Note that the data points fall in a straight line at constant poison level. A corresponds to an oxygen content of about 10 ppm, B to about 30 ppm, and C to about 40 ppm, respectively. Data from P. E. Højlund Nielsen.[30]

A possible interpretation of these data is that the main effect of exposure of the catalyst to water vapor is a reduction of the amount of chemisorbed nitrogen upon the surface. Since the surface coverage by hydrogen is very low according to Stoltze and Nørskov,[20] the hydrogen dependence is negligible.

The term θ in the previous expression is not determined by direct experiment. It is calculated from the rates of ammonia synthesis, assuming that $R_{NH_3} = f(P_{N_2}, P_{H_2}, P_{NH_3}, P_{inert}, T, t, \text{pois})$, where P_i represents partial pressures, t designates catalyst age, and pois is the amount of poisons. The expression may then be

simplified to

$$R_{NH_3} \cong f^1(P_i, T) \times \text{pois} \qquad \text{where pois} = 1 - \theta$$

Reference should here be made to the earlier discussion of the data by Brill *et al.*[27]

The value of θ may then be determined without the need to assume a particular rate equation, by measuring the conversion in an isothermal reactor without diffusion limitations. The quantity $1 - \theta$ then arises as the ratio of the flow necessary to yield the same exit concentration of ammonia in the poisoned and unpoisoned cases. In practice, diffusional limitations may be greatly reduced by using preconverted synthesis gas in order to reduce the reaction rates. Low reaction rates would make it easier to control the temperature increase associated with an exothermic reaction. Diffusional limitations may also be reduced by using small-size catalyst particles. The overall effect is that the effectiveness factor comes very close to 1. See Chapter 7 of this book and Chapter 5 in the book by Nielsen.[2]

Stoltze and Nørskov[20] used a different approach in their kinetic model by assuming the equilibrium reaction

$$H_2O(g) + 3^* \rightleftarrows 2H - * + O - *$$

where $*$ denotes a surface site.

Assuming that the adsorbed oxygen blocks the nearest-neighbor unit cell and using the experimental data of S. Andersen,[31] they obtained the fit seen in Fig. 8.6, which shows that poisoning may be accounted for even when using a one-parameter model.

The effect of oxygen poisoning in their model is that the activation energy for the rate-limiting step in the synthesis of ammonia will be increased. The reason for this is that the adsorption enthalpy for oxygen is high. Stoltze and Nørskov[20]

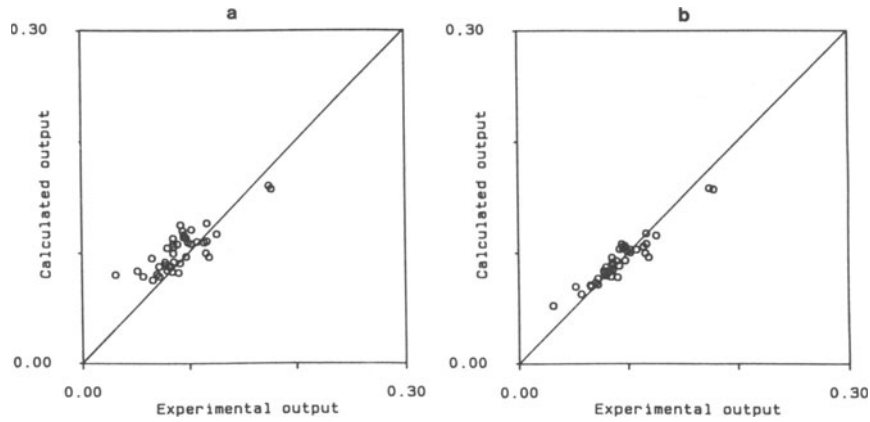

Figure 8.6. The relation between calculated and experimental NH_3 concentration for a K-promoted catalyst operating at 7–20 MPa, 573–723 K, 0–25 ppm H_2O. (a) The effect of H_2O has been neglected. (b) The effect of H_2O has been treated by including the $H_2O + 3^* \rightarrow 2H^* + O^*$ reaction in their ammonia synthesis rate expression. Data from Stoltze and Nørskov.[20] By permission of the American Institute of Physics.

found a value of $-112\,kJ\,mol^{-1}$, while Smirnov found $-74\,kJ\,mol^{-1}$, and the adsorption enthalpy obtained by Højlund Nielsen[30] and S. Andersen[31] was a median value of $-97\,kJ\,mol^{-1}$. The inhibition of adsorption on neighboring sites is also supported by the data of Boreskova *et al.*[29] A comparison between Figs. 8.5 and 8.6 seems to indicate that the kinetic approach of Stoltze and Nørskov has not yet reached a high degree of precision in describing poisoning by water. On the other hand, it should be noted that S. Andersen[31] and Højlund Nielsen[30] used a three-parameter expression in contrast to the one-parameter model of Stoltze and Nørskov.

As seen before in scientific discussion, these different views are complimentary in their description of the same phenomena, however different as they may seem. kinetic approach starts with a model of the fundamental reaction events. The key feature in the experiment by Brill *et al.*[27] was that the conversion experiment was carried out at the very low temperature of 225–275 °C. In practice, this will result in both the surface equilibrium suggested by Smirnov[25,26]

$$N_2(ads) + H_2O + 2H_2 \rightarrow O(ads) + 2NH_3$$

as well as the one suggested by Stoltze and Nørskov[20]

$$H_2O(g) + 3^* \rightarrow 2H - ^* + O^*$$

being completely displaced toward the right, while the data are consistent with both models.

8.5. SINTERING OF AMMONIA SYNTHESIS CATALYSTS

Whether operated in pure or impure synthesis gas, the catalyst may lose activity irreversibly due to a mass transfer process in which the catalytically active material loses surface area due to crystal growth. Such a process is usually known as sintering.[4] The sintering process is very temperature-dependent, but may, as suggested above, also be promoted by impurities in the gas phase.

In Chapter 2 the reduction of the synthesis catalyst and the development of the active phase are described. The reduced catalyst contains more than 90% iron in the metallic state. The iron is present as small (20–30 nm) crystals imbedded in a promoter matrix with some potassium at the surface. A number of crystalline compounds has been identified in the promoter phases. Their main function is to keep the iron crystals separated from each other.

The active catalyst is obtained by the reduction of promoted magnetite. On reduction, a weight loss of about 25%, the crystal density of the iron phase increases from 5.1 to $7.9\,g\,cm^{-3}$, but the overall particle dimensions are unchanged. The result is a porosity of approximately 50% and a catalyst consisting of iron crystallites, which have an internal surface area typically above $10\,m^2\,g^{-1}$ when measured with the BET method.

Metallic iron has a fairly high surface tension. Miedema[32] suggests a value of 2.42 J m^{-2} at 700 K for the (100) surface of iron that corresponds to 119 kJ mol^{-1} of iron surface atoms.

There is, therefore, a substantial chemical potential for reducing the iron metal surface by crystal growth. However, since the iron crystallites are physically separated, the growth mechanism has to take place across the boundaries of the structural promoter phases.

In a well-formulated catalyst, the small—less than 10 wt%—amount of structural promoters is sufficient to block crystal growth at normal operating conditions in an ammonia synthesis reactor.

A high degree of oxygen poisoning may reduce the lifetime of the catalyst. Since oxygen poisoning greatly reduces the reaction rate, the temperatures and pressures must be increased in order to maintain the level of production. The resulting high temperatures accelerate the sintering process, but it also seems as though the combined effect of water and temperature lead to an accelerated crystal growth of iron. This is also illustrated by the effect of high water partial pressure during reduction, as outlined by Nielsen[2] and the series of reduction experiments by Sidorov and Istomina.[33] In the latter experiments, catalyst situated in five reactors in series was reduced under such conditions that a water vapor level of 7500 ppm was reached at the exit of the last reactor. The activity upon reduction decreased from reactor one to reactor five. However, at very high space velocities and a low exit concentration of water, no difference was found.

It is still unclear which mechanism causes the ammonia synthesis catalyst to sinter in the presence of water vapor at high temperature. In the new edition of *Catalyst Handbook*[34] it is argued that when the reduced catalyst is exposed to moderate partial pressures of water vapor, partial and reversible surface oxidation takes place rather than bulk oxidation. The latter would incidentally require several orders of magnitude higher water vapor concentration. In contrast to fresh catalyst, the transient oxidic phases probably do not contain alumina in solid solution. Thus no structural promoter is present in the oxide structure to prevent sintering during re-reduction. This continuous oxidation/reduction mechanism for chemical sintering is progressively enhanced at high partial pressures, particularly as the temperature is increased. Another possibility could be that water increases the mobility of the structural promoter, whereby the antisintering function is reduced.

The adverse effect caused by a high concentration of water has also been demonstrated on an industrial scale. In a partial oxidation plant with a liquid nitrogen wash, about 100 ppm of oxygen leaked into the synthesis loop, giving an [0] content in the inlet gas of about 20–30 ppm. This resulted in an immediate activity decline. The pressure was increased as well as the temperature. However, the production declined somewhat. After some months of operation, the oxygen contaminant was removed and the catalyst regained its former activity.

Under normal operating conditions the sintering is almost negligible, and the deactivation rates are in the order of a few percent per year, if at all perceivable. If also the presence of poisons can be eliminated, the catalyst may very well outlast the converter. Thus lifetimes in excess of 10 years are not unusual, and lifetimes above 20 years have been registered in several cases. Generally, replacement of

the catalyst takes place when the converter has to be opened for inspection of the pressure shell, or when the synthesis loop is upgraded by taking a new type of converter into service.

REFERENCES

1. A. V. Slack and G. Russell James, *Ammonia*, Marcel Dekker Inc., New York and Basel (1977).
2. A. Nielsen, *An Investigation on Promoted Iron Catalysts for the Synthesis of Ammonia*, Jul. Gjellerup, Copenhagen (1968).
3. I. Dybkjær, in *Fertilizer Nitrogen*, Vol. 2 (A. I. Liöre, ed.), British Sulfur Corp., London, p. 503 (1982).
4. R. Hughes, *Deactivation of Catalysts*, Academic Press, London (1984).
5. J. Benard, J. Oudar, N. Barbouth, E. Margot, and Y. Berthier, *Surf. Sci.* **88**, L35 (1979).
6. I. Barin, O. Knacke, and O. Kubaschewski, *Thermochemical Properties of Inorganic Substances* (Supplement), p. 251, Springer-Verlag, Berlin (1977).
7. H. J. Grabke, W. Paulitschke, G. Tauber, and H. Viefhaus, *Surf. Sci.* **63**, 377 (1977).
8. E. Enikeev and A. V. Krylova, *Kinet. Catal.* **3**, 116 (1962).
9. R. Brill and S. Tauster, *Ber. Bunsenges. Phys. Chem.* **67**, 390 (1963).
10. S. Tauster, Poisoning Experiment with Iron-Type Ammonia Synthesis Catalysts, Doctoral Thesis, Polytechnic Institute of Brooklyn, June 1964 (available university microfilms, 64-10, 728).
11. R. Brill, H. Schaefer, and G. Zimmerman, *Ber. Bunsenges. Phys. Chem.* **72**, 1218 (1968).
12. M. Hansen and K. Anderko, *Constitution of Binary Alloys*, McGraw-Hill, New York (1958).
13. H. J. Hansen, in: *Fertilizer Nitrogen* (V. Sauchelli, ed.), p. 89, Reinhold, New York (1964).
14. A. T. Larson and R. S. Tour, *Chem. Met. Eng.* **26**, 647 (1922).
15. J. A. Almquist and C. A. Black, *J. Am. Chem. Soc.* **48**, 2814 (1926).
16. J. A. Almquist, *J. Am. Chem. Soc.* **48**, 2820 (1926).
17. P. H. Emmett and S. Brunauer, *J. Am. Chem. Soc.* **52**, 2682 (1930).
18. P. Stoltze, *Phys. Scr.* **36**, 824 (1987).
19. P. W. Ussatschew, W. J. Tarakanowa, and W. A. Komarov, *Z. Elektrochem.* **40**, 647 (1934).
20. P. Stoltze and J. K. Nørskov, *J. Vac. Sci. Technol. A5* **4**, 581 (1987).
21. S. Brunauer and P. H. Emmett, *J. Am. Chem. Soc.* **62**, 1732 (1940).
22. C. Bokhoven, *Proceedings of the Second Radioisotope Conference, Oxford* 1954, p. 53, Butterworths Scientific Publications, London (1954).
23. H. Uchida and N. Todo, *Report of the Tokyo Industrial Research Institute Laboratory* **46**, 213-224 (1951).
24. P. Royen and G. H. Langhans, *Z. Anorg. Allg. Chem.* **315**, 1 (1962).
25. I. A. Smirnov, N. M. Morozov, and M. I. Temkin, *Kinet. Catal.* **6**, 351 (1965).
26. I. A. Smirnov, *Kinet. Catal.* **7**, 93 (1966).
27. R. Brill, J. Hensel, and H. Schaefer, *Ber. Bunsenges. Phys. Chem.* **73**, 1003 (1969).
28. A. Ozaki, H. Taylor, and M. Boudart, *Proc. R. Soc. London, Ser. A* **258**, 47 (1960).
29. E. G. Goreskova, V. L. Kuchaev, and M. I. Temkin, *Kinet. Catal.* **25**, 116 (1984).
30. P. E. Højlund Nielsen, The Poisoning of Ammonia Synthesis Catalysts by Oxygenic Compounds Lecture given at ACS Meeting, Washington D.C. (Sept. 1983).
31. S. Andersen, Haldor Topsøe A/S, unpublished results (1983-85).
32. A. R. Miedema, *Z. Metallkd.* **69**, 287 (1978).
33. I. P. Sidorov and K. E. Istomina, *Chem. Abstr.* **54**, 6049 (1960).
34. J. R. Jennings and S. A. Ward, *Catalyst Handbook* (M. V. Twigg, ed.), Wolfe Publishing Ltd., London (1989).

9

ALTERNATIVE NONIRON CATALYSTS

S. R. Tennison

9.1. INTRODUCTION

It has been shown in the previous chapters that metallic iron, derived from triply promoted magnetite, is the only ammonia catalyst in general use today. This does not represent a step in a long evolutionary process. The catalyst is not very different in either form or performance from that first used commercially at Oppau in 1913. Despite dramatic improvements in process efficiencies the magnetite catalyst still demands what are relatively high pressures (typically in excess of 130 Bar), high temperatures (up to 823 K), and very large catalyst volumes (in excess of 60 m^3) to achieve good process economics, although pressures down to around 80 bar are used in the most recent processes.

The absence of any substantial increase in the catalyst performance since the 1920s does not imply there is no scope for improvement. While the magnetite TON (turnover number), under normal commercial synthesis conditions, is quite reasonable (approximately 1 mol $site^{-1}$ s^{-1}), this is only achieved at high pressures and temperatures. Potential still exists to make improvements to the current magnetite system, but major increases in catalyst activity will be necessary to bring about substantial further changes in the commerical process. For instance, it has already been shown that simply reducing the synthesis loop pressure does not improve the process economics.[4] To achieve substantial improvements also requires a significant reduction in operating temperature and an increase in conversion per pass. This will require a catalyst with a volumetric efficiency some two orders of magnitude greater than magnetite.

In the search for improved catalysts most of the metals in the periodic table have been investigated, either as the primary components or as promoters. Much of this work took place during the early, pioneering studies in the BASF

S. R. Tennison • New Technology Division, BP International Limited, Sunbury Research Centre, Sunbury on Thames, Middlesex TW16 7LN, England.

laboratories. In the period up to 1908 Haber had demonstrated that, even under equilibrium limited conditions, a viable process was possible at low conversions by removing the product ammonia and recycling the unconverted feed gas.[1] This was demonstrated in 1909 at 175–200 bar and 500–600 °C using osmium, the most active catalyst then available. However, it was clear from the outset that this was not a practical proposition—at that time the entire world supply only amounted to a few kilograms. The only other system that demonstrated reasonable activity and stability was uranium, but it was far too sensitive to water contamination.[2] A major program was therefore initiated by BASF to search for an alternative.

From Mittasch's record of these studies at BASF[3] it is clear that the hypotheses upon which much of their early work was based were badly misplaced. The "mixed systems" and "flux promoter" concepts from earlier inorganic synthesis studies led to the inclusion of many components that were actually detrimental to the catalysts under investigation. In addition, the impact of poisons such as sulfur and chlorine and the effect of contaminants such as oxygen and water were not realized. The probability of finding a viable catalyst was therefore small. Consequently, during the period up to November 1909, a vast number of materials were evaluated but none gave the required activity and stability.[3] Iron in both a very pure or sulfur-contaminated state was tested several times and discarded. The breakthrough, using iron "contaminated" with alumina and potash and the subsequent optimization program, are well documented[3] and have also been reviewed in Chapter 1.

The drive to improved process efficiency in the wake of the increases in energy costs since the mid-sixties has given new priority to the production of improved catalysts, and these are now beginning to reach the marketplace. The first to achieve commercial status was a cobalt-modified magnetite introduced in 1985.[5] However, with similar kinetic characteristics to its parent magnetite and at best a twofold increase in volumetric efficiency, major process modifications seem unlikely. The only other catalyst system to have received significant attention in recent years has been based on ruthenium. The latest catalysts, supported on specially prepared carbons and promoted with cesium and barium,[6] represent a far more significant advance in activity (Fig. 9.1a) combined with a greater tolerance for higher ammonia partial pressures (Fig. 9.1b). This should allow more flexibility in process design but is unlikely to permit any dramatic decrease in pressure. The catalysts have a similar sensitivity to oxygen-containing impurities (although they are less sensitive to permanent poisons such as sulfur) and therefore have similar feed gas purity requirements to magnetite.

What then are the chances of finding still better catalysts? In Section 9.2 the factors influencing the ammonia synthesis reaction will be considered. This will concentrate on the factors influencing nitrogen adsorption and dissociation and their impact on the kinetics. The key factors have been identified from the detailed investigations carried out on iron. It is now apparent that the "low" reactivity of magnetite can be attributed to two main factors:

1. The structure sensitivity of molecular nitrogen adsorption.[8] In addition to iron this is also shown by rhenium,[9] while there is indirect evidence

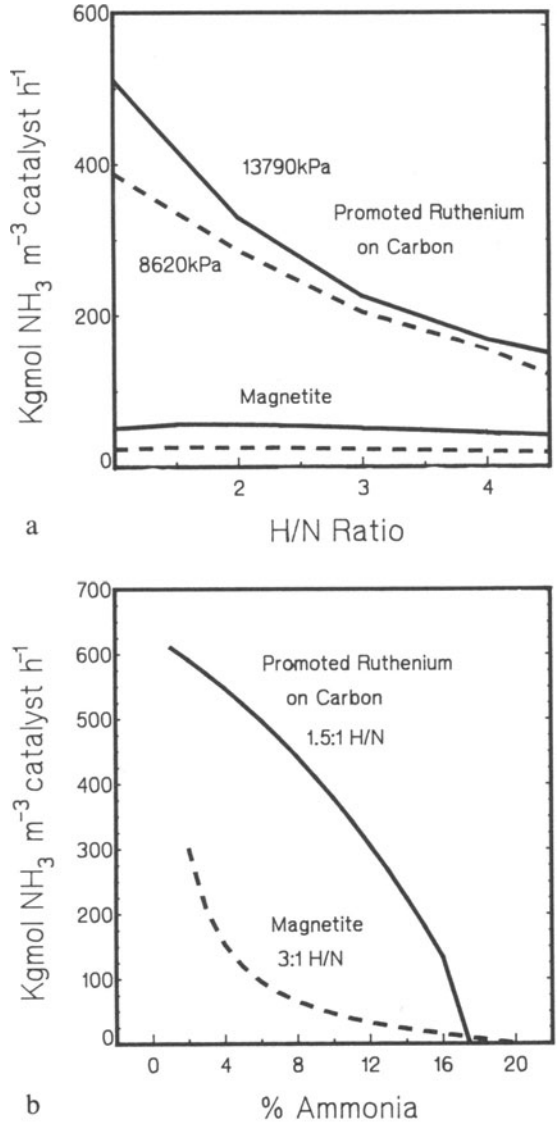

Figure 9.1. Comparison of the performance characteristics of alkali-promoted ruthenium on carbon and triple promoted magnetite: a. Pressure and H/N ratio response (data at 6 vol% ammonia, 673 K); b. Ammonia inhibition (data at 13,790 kPa, 703 K).

for similar effects on nickel,[10] iridium,[11] ruthenium,[12] cobalt,[13] and nitrides such as MoN_2.[14] This growing body of evidence suggests that this may be a general phenomenon in nitrogen adsorption and therefore central to an understanding of ammonia synthesis.

2. The nature of the nitrogen adsorption and dissociation steps.[15] The rate-limiting step in the synthesis reaction is the dissociation of adsorbed molecular nitrogen. This is controlled by both the activation energy for the $N_{2\,(ads)}$ transition and the surface coverage of $N_{2\,(ads)}$.

TABLE 9.1. Heats of Formation of the Nitrides (kJ mol^{-1})

3A	4A	5A	6A	7A	8A	8B	8C
ScN	TiN	VN	CrN	Mn	Fe_4N	Co_3N	Ni_3N
−285	−337	−173	−118	?	−48	?	+0
YN	ZrN	NbN	MoN	TcN	Ru	Rh	Pd
−300	−365	−247	−69	?			
LaN	HfN	TaN	W_2N	Re_2N	Os	Ir	Pt
−297	−326	−242	−71	?			
CeN	UN			Unstable	No nitrides		
−326	−334			nitrides			

Other factors that also influence the ultimate performance of a catalyst are the more practical problems such as the number of active sites, physical form, and porosity which will also be examined in Section 9.2.

In Section 9.3 the characteristics of those materials that have been investigated as synthesis catalysts will be examined and compared. These are subdivided into three main groups based on the ease with which the metals form nitrides. They are shown, along with the heat of formation of the most common nitrides, in Table 9.1. The divisions highlight some key characteristics of the groups:

Group 1. No stable nitrides: Ru, Rh, Pd, Os, Ir, Pt.
These metals are used in supported form, reflecting both their cost and their stability when highly dispersed. They also require the presence of alkali promoters to bring about nitrogen dissociation.

Group 2. Stable nitrides not formed under reaction conditions: Re, Tc, Mn, Fe, Co, Ni, and the alloys of iron.
These metals can form nitrides, but it is unlikely that bulk nitrides are present under ammonia synthesis conditions. Alkali promoters are generally required although their role is uncertain, perhaps influencing both nitrogen dissociation and ammonia inhibition. This group also includes the alloys of iron.

Group 3. Present as nitrides under reaction conditions: Groups 3A to 6A.
These all exist as the nitride under synthesis conditions, irrespective of the precursor composition. A major problem, as shown by uranium, is increased sensitivity to oxygen.

9.2. FACTORS INFLUENCING CATALYST PERFORMANCE

9.2.1. Theoretical Aspects of Gas Adsorption

The nature of the adsorption of the reactant, intermediates, and products is central to whether a given system has any probability of functioning as an ammonia synthesis catalyst. The Langmuir expression (9.2.5) derived in the section on kinetics

provides a simple framework from which to consider the implications of the adsorption characteristics of the various components. In principle, if the heat of adsorption of each of the reactants, intermediates, and products was known, along with the activation energies and frequency factors for each elementary reaction step, the performance of a particular catalyst system could be estimated. Unfortunately, such detailed adsorption data are not readily available. The question arises as to whether it is possible to determine such values from a theoretical basis. It has been recognized for a long time that the heats of adsorption of gases follow broad trends. The bond energies for M—N and M—H fall from left to right along the periodic table and down the groups (Table 9.2). Early attempts to estimate these bond energies based on correlations with heats of formation of compounds were only able to reproduce the trends in the broadest of fashions.[29] A slightly more rigorous determination, based on the bond energy bond order (BEBO) approach, gave somewhat better estimates for hydrogen but still very poor correlation with the observed data for nitrogen.[30] Substantially better correlations are now being achieved by use of more rigorous theoretical calculations, based on either extended surface or local cluster models,[31] although the errors are still unacceptably large from a kinetics standpoint.[32] They also leave aside variations in bond energies with coverage, surface geometry, and the presence of promoters.

The preexponential factors for each of the reaction steps can, in principle, be estimated using either gas kinetics or transition state theory. Desorption occurs when the adsorbate-adsorbent bond acquires the required activation energy for desorption in the form of vibrational energy. To a first approximation the vibrational frequency can be assumed to be approximately 10^{13} s^{-1} for the temperature at which desorption proceeds at a significant rate. The frequency of bond rupture is given by

$$f = \nu_1 \exp(-E_d/kT) \qquad s^{-1} \tag{9.1}$$

TABLE 9.2. Bond Energies (kJ mol^{-1}) for M—N and M—H on Close-Packed Faces[a]

Cr	Mn[b]	Fe	Co	Ni	Cu
bcc		bcc	fcc	fcc	
		(110)		(111)	(111)
		585/267		564/263	−/234
Mo	Tc	Ru	Rh	Pd	Ag
bcc	hcp	hcp	fcc	fcc	
(110)		(001)		(111)	(111)
644[61]/299[60]		566[58]/259[56]		543/259	
W	Re	Os	Ir	Pt	Au
bcc	hcp	hcp	fcc	fcc	
(110)	(001)		(111)	(111)	
640/284	604[59]/—		530/263	530/238	

[a] Most data are taken from Ref. 57. Other sources are indicated by the superscript.
[b] Molybdenum exhibits variable structure.

where E_d is the desorption activation energy. The rate of desorption in a first-order process is then given by

$$-dn_a/dt = n_a \nu_1 \exp(E_d/RT) \qquad \text{mol s}^{-1}\,\text{cm}^{-2} \tag{9.2}$$

where n_a is the surface adsorbate concentration in mol cm^{-2}. In first-order processes, where the vibrational frequency ν_1 is taken to be about 10^{13}, and assuming approximately monolayer coverage, the overall preexponential becomes 10^{28} mol s^{-1} cm^{-2}.

For molecules such as hydrogen, that dissociate on adsorption, the rate of desorption is controlled by atom recombination followed by molecular desorption. The rate of desorption is given by

$$-\tfrac{1}{2}(dn_a/dt) = n_a^2 \nu_2 \exp(-E_d/RT) \tag{9.3}$$

$$= (\pi kTm)^{1/2} d \approx 10^{-2}\,\text{s}^{-1} \tag{9.4}$$

where the frequency ν_2 is the number of collisions per second in a two-dimensional gas, m is the mass of the adatom, and d is the collision diameter. The result is again an overall preexponential for the second-order process of $\approx 10^{28}$ mol cm^{-2} s^{-1}. Very similar preexponentials can be calculated via transition state theory.

In practice, values for the desorption frequency ν_n for hydrogen on various metals vary between 10^6 and 10^{14} s^{-1}, while for nitrogen at low coverage, values as high as 10^{16} s^{-1} have been reported. In addition, although ν_n is usually assumed to be coverage-independent, it can increase, decrease, or show a complex variation with coverage.[33] This frequently manifests itself as a compensation effect, whereby if E_d rises then ν_n also rises, and *vice versa*. In transition state terms this can be attributed to changes in the number of degrees of freedom between the adsorbed molecule and the transition state complex. At present, there is no way of predicting in advance the nature of the TSC and therefore the preexponential.

Under these circumstances the use of calculated preexponentials in kinetic model development is likely to lead to significant errors, in addition to those inherent in the use of calculated heats of adsorption. These problems are reflected in the attempt to model magnetite kinetics using observed heats of adsorption and estimated frequency factors,[81] which gave rise to a calculated reaction rate a factor of $\sim 10^5$ too low. The development of mechanistically sound, kinetic models will therefore remain dependent on the direct determination of the heats of adsorption, activation energies, and frequency factors for the forseeable future.

However, even practical data are subject to significant errors and uncertainties. Much of the early data obtained using metal films were compromised by poor vacuum and the resulting surface contamination. Improved data were subsequently obtained with metal wires which could be outgassed at higher temperatures,[35] and improved vacuum systems that allowed clean surfaces to be maintained for longer periods of time. The surfaces were, however, poorly defined, and marked variations between studies and with coverage reflected the presence of a wide variety of crystal faces and high concentrations of defects.

The twin problems of cleanliness and structure can now be overcome by the use of single crystals, where both the chemical and physical states of the surface can be monitored using a range of surface spectroscopic techniques. However, single-crystal studies introduce other limitations. In particular the measurements must be carried out under UHV and it is only possible to measure the heats of adsorption indirectly. The most common methods involve either isotherm data and the use of the Clausius–Clapeyron equation or direct analysis of the temperature programmed desorption (TPD) peaks.

TPD data, while the most widely used, are prone to the greatest inaccuracy,[36] Two key adsorption parameters, ν_i and E_i, are contained in the Polyani–Wigler expression describing thermal desorption:

$$dN_i/dT = \nu_i N_i^{x_i} \exp(-E_i/RT) \tag{9.5}$$

where E_i is the desorption energy (kJ mol^{-1}), X_i the reaction order, ν_i the frequency factor (s^{-1}), and N_i is the surface population (mol cm^{-2}).

If both E_i and ν_i were constant, then they could be obtained directly from TPD peak shape analysis:

$$E_i = RT_{pi}[\ln(\nu_i \cdot T_{pi}/\beta) - 3.46] \tag{9.6}$$

where T_{pi} is the temperature at the desorption peak maxima and β is the heating rate (in K s^{-1}). The early practice of assuming a frequency factor of 10^{13} s^{-1} and then deriving E_d directly from the TPD peak maximum is clearly inadvisable[36] as both E_d and ν can be strongely coverage-dependent. Under these circumstances it is impossible to derive unequivocal values for either parameter without an independent measurement of the other. These problems are reflected in the large variations of the desorption activation energies that can be found in the literature even for such simple systems as hydrogen on Pt(111), where values ranging from 43 to 67 kJ mol^{-1} have been reported.[37,38]

The use of the low-pressure experimental conditions also impacts on the observed adsorption characteristics. For surface states with low heats of adsorption, it follows from the Clausius–Clapeyron equation that very low temperatures are required to achieve reasonable coverages at the pressures used in most single-crystal studies ($<10^{-5}$ torr). In the case of hydrogen, for instance, where the heat of adsorption is very low (43–67 kJ mol^{-1}),[37–40] temperatures of around 160 to 280 K are required. The even less strongly bound molecular precursor states, which can have heats of adsorption below 20 kJ mol^{-1}, require experimental temperatures as low as 20 K[41] Clearly, if adsorption studies are carried out at ambient temperature then these states will not be observed.

Such low temperatures cause additional problems when the adsorption process is activated, as is the case with nitrogen and sometimes hydrogen and ammonia. The formation of the surface species that would be dominant at normal pressure and temperatures can be missed, as has been demonstrated in competitive adsorption studies using nitrogen and hydrogen on iron. In the case of nitrogen, it is well established that at high temperatures the major surface species is atomic nitrogen,[164] which has a heat of adsorption of between 213 and 242 kJ mol^{-1}.[26]

Conversely, at low temperatures it is the molecular state, with a heat of adsorption of approximately 21 kJ mol^{-1}, that predominates. In contrast, hydrogen is only present in a dissociated state with a heat of adsorption of 75 to 96 kJ mol^{-1}. It can therefore be seen that a low temperatures (<400 K) hydrogen will displace the molecular nitrogen, while at higher temperatures, when nitrogen dissociation occurs, the nitrogen will inhibit hydrogen adsorption.[41,42]

Real catalysts also comprise a wide range of crystallographic planes, edges, defects, etc., which influence the adsorption characteristics of both nitrogen and hydrogen. In the case of the more open crystallographic planes, where sites of different structure are present, several distinct adsorption states are observed as can be seen from the heat of adsorption vs coverage curves for tungsten (Fig. 9.2).[166] The impact of steps, kinks, defects, etc. on the heat of adsorption is frequently even more marked. To provide a realistic description of a particular system it will be necessary to examine single-crystal surfaces representative of all the structural features. However, Lombardo and Bell[169] have now shown that all of the observed features in complex desorption spectra can be reproduced by using Monte Carlo simulation techniques that take account of adsorbate–adsorbate and metal–adsorbate interactions on single-geometry sites. The simulation also reproduces the observed changes in desorption energy with coverage. This may lead to a further reappraisal of the interpretation of TPD spectra.

While the results discussed above are of obvious relevance to catalysts such as iron, where the metal is in the bulk state, many catalysts comprise very small metal particles on supports. There is evidence that for particle sizes below about 3 nm the heat of adsorption increases quite markedly. This has been demonstrated

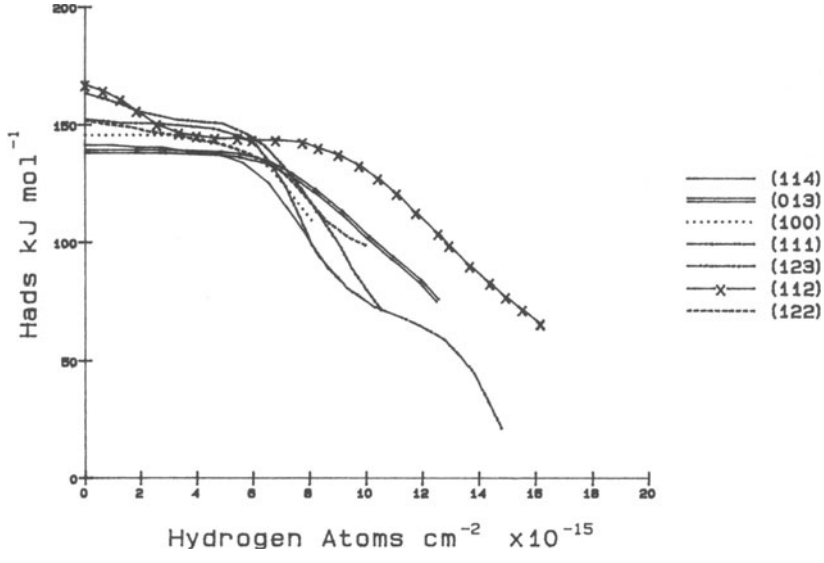

Figure 9.2. Variation in the heat of adsorption of hydrogen on tungsten with coverage and surface structure. Data from Ref. 166.

by a direct calorimetric method for hydrogen[43] and carbon monoxide[44] on palladium and, indirectly, from TPD measurements for hydrogen on platinum.[45] As the particle size for many supported catalysts falls into this range, extrapolation from measurements on single crystals may be inadequate.

9.2.2. The Impact of Structure on Gas Adsorption

This will be examined primarily from the standpoint of the major gaseous components: nitrogen, hydrogen, and ammonia.

9.2.2.1. Nitrogen

9.2.2.1a. Iron. Much of the work on iron, in the context of nitrogen adsorption, has been carried either on pure iron, in the form of crystals, wires, or films, or on conventional promoted magnetite catalysts. It has been one of the unusual characteristics of iron catalysts that, unlike most metallic catalysts, they cannot be made to work satisfactorily on supports. Part of the reason for this is the problem of achieving stable high dispersions. However, using magnesia and titania these can be achieved, but they do not give ammonia synthesis activities per unit surface area of iron of the same magnitude as promoted magnetite.[46]

The first study using magnesia-supported iron indicated that it was not simply free iron surface that was important for the dissociation of nitrogen but a very specific surface site.[46] Further analysis of these results led to the suggestion that this was the C_7 site (Fig. 9.3a) that occurred with the greatest frequency on the Fe(111) planes and particularly on intermediate-size crystallites.[48] This change in specific activity of a metal with crystallite size, or "structure sensitivity," was by no means new. What was unusual was the apparent requirement for an intermediate-size crystallite rather than a high or low dispersion. This has been attributed by Van Hardeveld *et al.* to the presence of highly coordinated sites at the edges of incomplete atomic layers at the surfaces of intermediate-size crystallites[161] (Fig. 9.3b). The concentration of such defects reached a maximum in crystallites of 2–6 nm diameter.

Low energy electron diffraction (LEED) studies have since provided direct evidence for this structure sensitivity. Studies by Ertl's group[26,49] have shown that the activation energy for nitrogen dissociation is small on the Fe(111) plane and hardly varies with coverage (0 to 4.2 kJ mol^{-1}) while on the Fe(100) face it increases from approximately 20 kJ mol^{-1} to 45 kJ mol^{-1} at 20% coverage. These high activation energies for dissociation seem at first sight to provide a simple explanation for the extremely low sticking probabilities observed for dissociative adsorption and the synthesis activity of the single crystals at pressures up to 2000 kPa and temperatures approaching real synthesis conditions.[8]

However, even at low coverages on the Fe(111) face, where the most recent studies show an activation energy for the dissociation process of -3.4 kJ mol^{-1}, the dissociative sticking probability is still only 2×10^{-6} s^{-1}.[50] This reflects, in the first instance, the low sticking probability of the molecularly adsorbed species, N_2^*, which at approximately 10^{-2} is considerably lower than that observed for

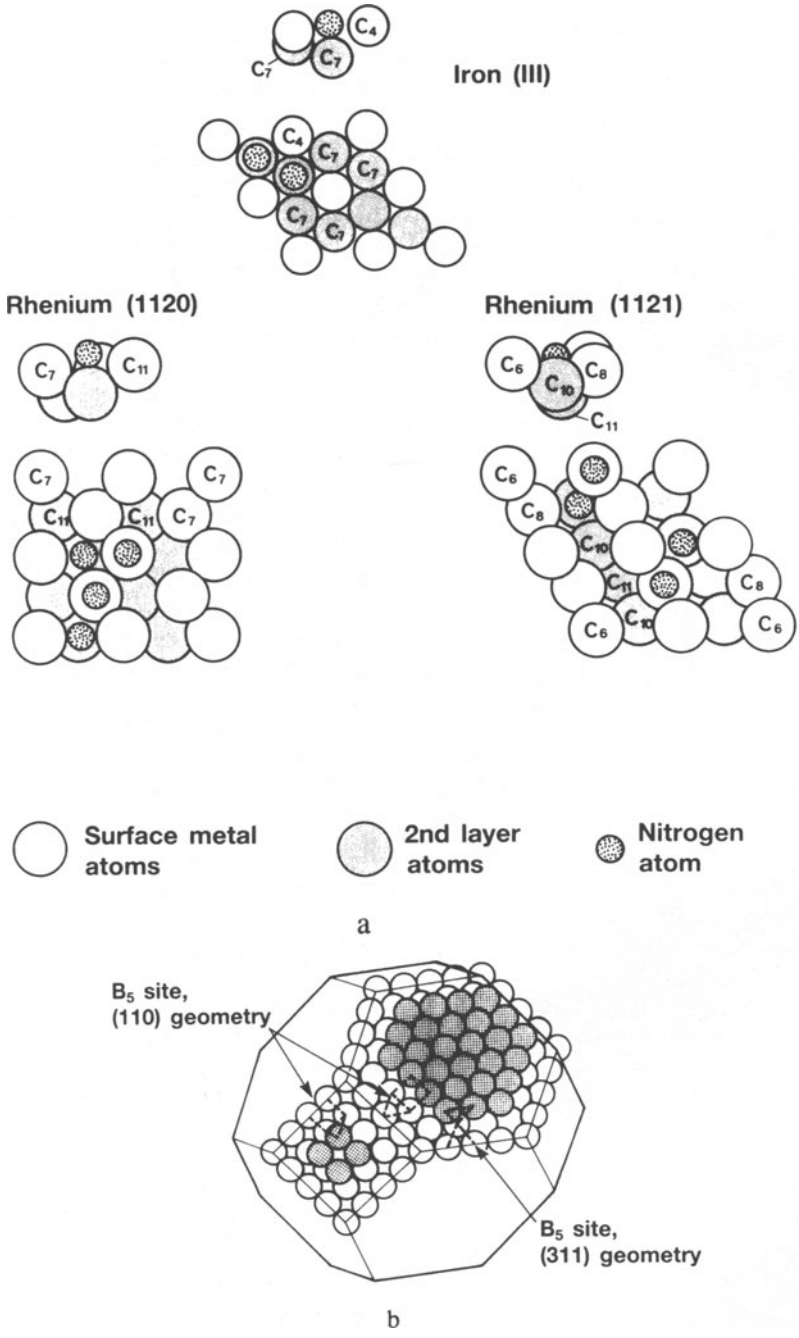

Figure 9.3. Metal crystallite and surface structures: (a) Nitrogen adsorption sites on iron and rhenium.[9] (b) Formation of highly coordinated sites on a small fcc cubo octahedral crystallite.[161].

most other gases. More recent studies have shown that the dissociation precursor state of nitrogen, N_2-α, is preceded by a less strongly bound, N_2-γ, state that desorbs at 95 K (H_{ads} = 23.8 kJ mol^{-1}) and that this state exhibits a relatively normal sticking probability of about 0.7.[15] These are shown in the one-dimensional potential energy diagrams in Fig. 9.4. The overall kinetics of adsorption/dissociation then reflect a balance between the various states with only one pathway leading to dissociative adsorption.

9.2.2.1b. Other Metals. Structure sensitivity is not limited to iron. Similar face sensitivities are also exhibited by rhenium,[9] while there is indirect evidence on ruthenium[12] and molybdenum nitride.[14] For both rhenium and ruthenium it is clear that, as in the case of iron, the close-packed surfaces are the least active. It has also been shown that molecular nitrogen adsorbs on supported nickel,[10] iridium,[11] and, to a lesser extent, platinum and palladium[51] catalysts when the metal crystallites are of an intermediate size. In the case of nickel and iridium very small sticking probabilities for dissociative adsorption have been measured, ca 10^{-7}, although these are associated with high sticking probabilities for molecular nitrogen adsorption (Ni, 0.7; Ir, about 1.0[52]). This high molecular sticking probability was at first thought to differentiate nickel and iridium from iron, although

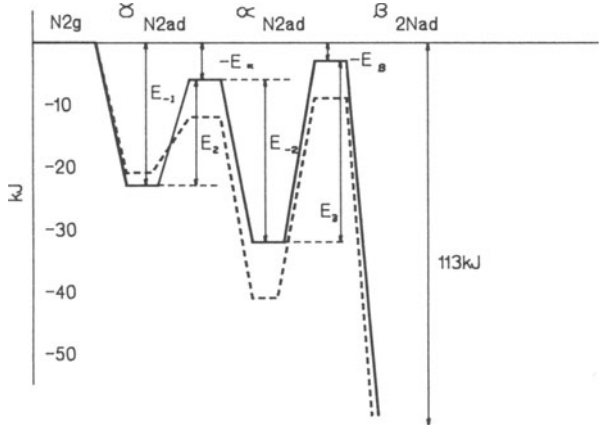

Figure 9.4. One-dimensional potential energy diagram for nitrogen adsorption and dissociation on promoted and unpromoted Fe(111).[15]

	K Free	K Promoted
S_o^{γ}	0.70	
ν_{-1} (s^{-1})	1.0×10^{13}	
ν_2 (s^{-1})	7.0×10^{7}	
ν_3 (s^{-1})	1.0×10^{8}	
E_{-1} (kJ mol^{-1})	23.8	22.2
E_2 (kJ mol^{-1})	17.6	10.0
E_{-2} (kJ mol^{-1})	25.2	28.4
E_3 (kJ mol^{-1})	28.1	31.3
E_α (kJ mol^{-1})	−6.2	−12.0
E_β (kJ mol^{-1})	−3.35	−9.14

it is now known that a similar molecular state, with high sticking probability, exists on iron as well.

Even the metals with a high affinity for nitrogen, such as tungsten, show a high face specificity for nitrogen adsorption that is associated with a high initial sticking probability for molecular dissociation on the more open faces[53] (Table 9.3). It was at first thought that the high sticking probability could be directly correlated with the number of four coordinate sites on each surface.[54] More detailed studies on a variety of high index faces [W(310), W(320), and W(411)] have since demonstrated that neither the initial sticking probability nor the saturation coverage can be directly correlated with the (100) site density. It has been suggested that although the (100) sites are probably critical for the initial adsorption and dissociation, the nitrogen atoms subsequently diffuse onto the terraces.[55] This is similar to the situation on rhenium, where the initial studies indicated a requirement for C_7 sites although subsequent studies demonstrated that the synthesis rate was only dependent on the presence of a very open structure.[9]

While concrete evidence for a very specific site for nitrogen adsorption may no longer be present, it is apparent that the formation of the molecular state requires, at the least, a nonclose-packed surface. The similarities across a wide range of disparate metals tend to suggest that this is structural rather than electronic, and may imply that a very specific orientation of the nitrogen molecule relative to the surface is required. The transition to the atomic state is then primarily a function of the activation energy for dissociation.

9.2.2.2. Hydrogen

For the close-packed surfaces the M—H bond strength shows a monotonic small decrease across and down the periodic table (Table 9.2). While it might be expected that the heat of adsorption should be higher on the more open surfaces, there is only slight evidence for such systematic changes. Typical values for tungsten, nickel, platinum, and palladium are shown in Table 9.4. The variations are in general small and of the same order as the changes in the heat of adsorption

TABLE 9.3. Nitrogen Sticking Probabilities on W at 300 K

Plane	S_0	Ref.
(110)	$<10^{-3}$	53
(211)	$<10^{-2}$	156
(321)	$<10^{-2}$	54
(111)	$\sim 10^{-2}$	155
(310)	0.28	155
(411)	0.31	54
(210)	0.25	155
(311)	0.29	54
(100)	0.4	156

TABLE 9.4. Effect of Surface Structure on Heat of Adsorption of Hydrogen (kJ mol^{-1})

	Ref.		(110)	(100)	(211)	(210)	(111)	(013)	(122)	(123)	(114)
W	48	bcc	138	146	167		153	138	153	163	142
	62		137	135			147				
	44				146						
Ni	63	fcc	90	96			96				
Pt	39	fcc	50		61	82	66				
	37						43				
	40						52				
	38						67				
Pd	64	fcc	96.1				99				
	65			102							

between similar metals and between studies on the same crystal face. This can be seen for Pt(111) in Table 9.4, where values ranging from 43 to 72 kJ mol^{-1} have been obtained. A similar variability is found with ruthenium, where the heat of adsorption varies between 72 and 120 kJ mol^{-1}[56] for the most strongly bound state and between 35 and 90 kJ mol^{-1} for the weaker state. Some of this variability is due to the use of TPD methods. Many of the earlier studies quote values for the heat of adsorption derived directly from TPD peak maxima assuming a value of $\nu_{des} = 10^{13}\ s^{-1}$. In the more recent studies, peak-shape analysis techniques have allowed direct determination of ν_{des}, which lies between 10^9 and $10^{13}\ s^{-1}$.

These results at first sight indicate that hydrogen adsorption is largely structure-insensitive. However, on stepped Pt surfaces, Pt [6(111) × (111)], the heat of adsorption is significantly increased at low coverages from around 39 to 50 kJ mol^{-1} along with a marked increase in the sticking probability. The presence of defects also has a major impact with an increase from 42 to 67 kJ mol^{-1} on Pt(111).[37] This shows that while there may be little difference between crystal faces, adsorption at edges and defects is strongly modified. Further evidence for this has come from studies into hydrogen adsorption on supported palladium, where the heat of adsorption is very sensitive to the dispersion. The integral heat of adsorption increases from approximately 63 to in excess of 105 kJ mol^{-1} at crystallite sizes below 2.5 nm. This increase is far larger than has been observed between crystal faces, and led the authors to speculate on the presence of electronic effects in the small crystals. However, the observation of increases of similar magnitudes at single-crystal defects implies that it is predominantly a local environment effect rather than due to crystallite size. A similar effect can also be inferred from the TPD characteristics of supported platinum catalysts.[45]

9.2.2.3. Ammonia

Much of the data on the adsorption characteristics of ammonia have come from ammonia decomposition studies. The decomposition reaction profile on

platinum demonstrates a factor common to many transition metals: the activated nature of the initial NH_3* to NH_2* reaction step (Fig. 9.5a). On Ru(0001) only molecular adsorption occurs below 200 K with dissociative adsorption only commencing at above 300 K.[12] Similarly, rhenium exhibits a very low sticking probability for ammonia adsorption, characteristic of activated adsorption.[24] In the case of tungsten the adsorption of ammonia does not appear to be activated and NH_2* is readily formed, although the subsequent decomposition step, $NH_2^* \Rightarrow NH^*$, does appear to be strongly activated due primarily to the high binding energy for NH_2*.[25] Iron appears to occupy a middle position with no evidence of any significant activation energies for interconversion between any of the NH_x* species. This can be seen from the energy diagram in Fig. 9.5b and is also apparent from

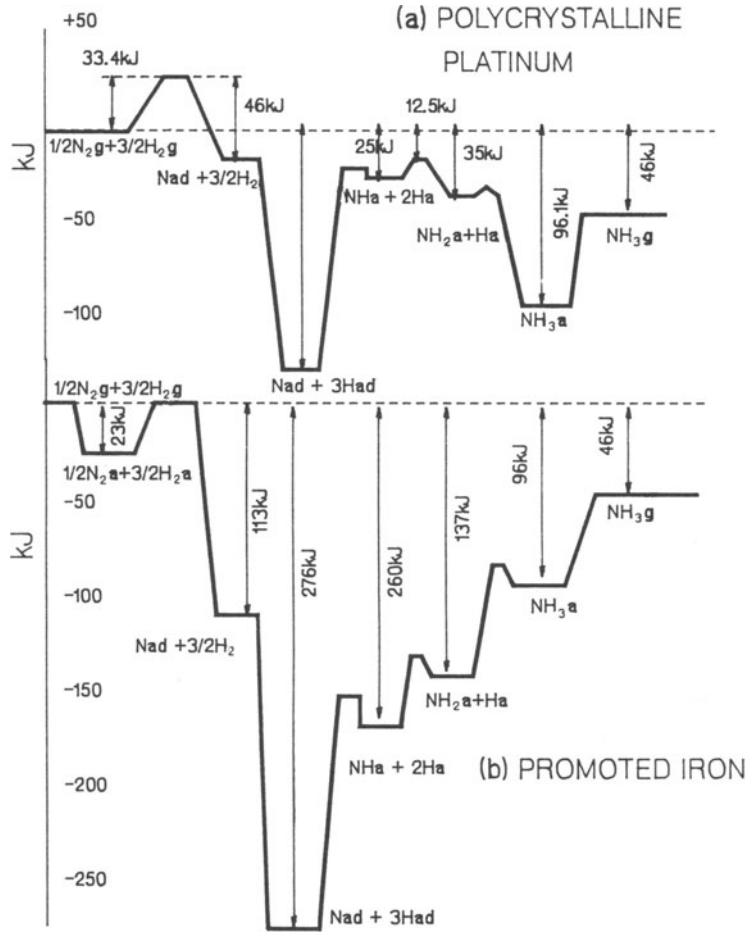

Figure 9.5. One-dimensional potential energy diagrams for ammonia synthesis and decomposition on platinum and iron: (a) Polycrystalline platinum[12]; (b) iron.[81]

the fact that some ammonia decomposition occurs on Fe(111) at temperatures as low as 160 K while all N—H bonds are lost by 320 K.[163]

Ammonia adsorption and decomposition is also structure-sensitive, although this can manifest itself in two ways. There is evidence that, following activated adsorption of ammonia, the breaking of N—H bonds to give NH_2* and NH* occurs more readily at terrace sites on stepped single crystals. Evidence for this has been found on both ruthenium[28] and nickel.[66] On the Ru(1110) terraced surface both NH* and NH_2* were observed under ammonia flow conditions at 380 K while on the Ru(0001) surface only atomic nitrogen is detected, but at significantly higher temperatures. Indirect evidence for structure sensitivity has also been obtained on metal films of nickel, tungsten, and iron where the rate of decomposition drops significantly when the films are annealed.[25]

9.2.3. The Impact of Promoters on Gas Adsorption

Promoters can influence the adsorption characteristics of catalysts in two, quite distinct ways:

1. Electronic, whereby the site adsorption characteristics are altered.
2. Structural, where the number and stability of surface sites is modified.

The first group comprises predominantly group 1A, and possibly group 2A metals, while the structural promoters are normally nonreducible oxides such as alumina. The chemical state of the promoters is in most cases poorly understood and the nature, location, and mode of action of potassium in classical Haber catalysts has yet to be determined unequivocally after 80 years of research.

In the case of Haber-type catalysts the potassium is present in the unreduced catalyst, predominantly in a compound form associated with both the iron oxide and alumina phases, while in supported platinum group metal catalysts the alkali may be added in salt form (nitrate, carbonate, hydroxide, etc.) or as the metal. In single-crystal studies the alkali may be "fired" at the crystal surface from molecular sieve ion sources or evaporated onto the surface as the metals.

Under reaction conditions, it can be shown from free-energy considerations that the alkali salts will reduce readily to the hydroxide or to an adsorbed complex of the type

$$X^- — M^+$$

where X is either the transition metal or the support. The free energies for the reactions to the oxide, hydroxide, or metal complex, at 600 K, assuming that the heat of formation of the complex is 84 kJ mol^{-1}, are summarized in Table 9.10a (below in Section 9.3.1.3). It can be seen that the reduction to either the hydroxide or the complex is strongly favored. At lower alkali metal coverages, where the heat of adsorption is considerably higher (Fig. 9.6), the thermodynamic driving force to the formation of the complex will be considerably enhanced. It is also possible to calculate the water vapor pressure below which the adsorbed complex becomes

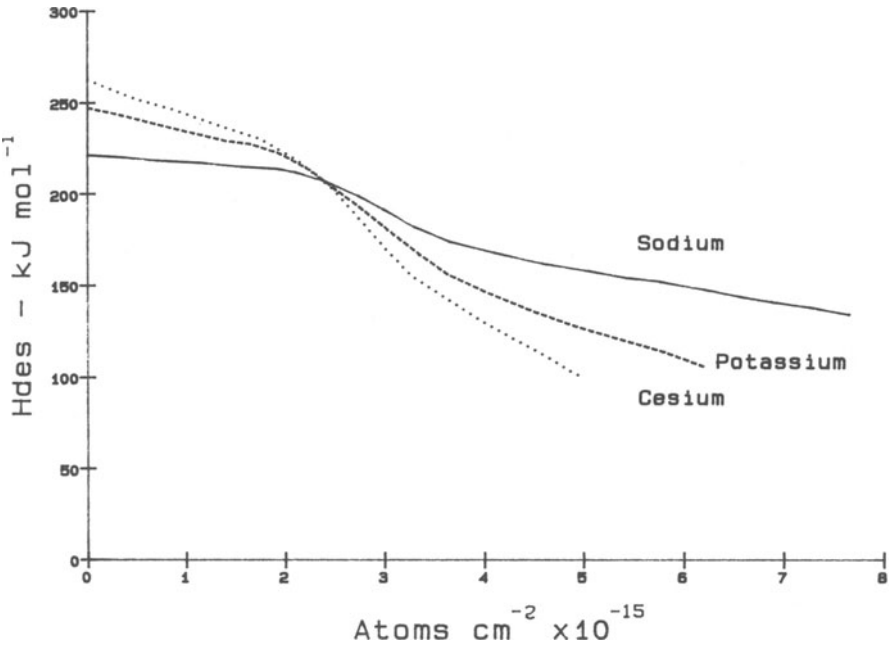

Figure 9.6. Desorption energy vs coverage for sodium, potassium, and cesium on Ni(110). Data from Ref. 67 (assumed desorption frequency $\nu = 10^{13}\,s^{-1}$).

the thermodynamically favored species relative to the hydroxide. These are shown in Table 9.10b for the group 1A metals over a range of temperatures. It can be seen that, even assuming a high coverage heat of adsorption of 84 kJ mol^{-1}, the potassium complex should be stable, relative to the hydroxide, at up to approximately 340,000 ppm water at 800 K.

However, while this shows that the complex is likely to be produced during catalyst reduction, it is unlikely to remain on the catalyst surface at the temperatures where ammonia synthesis catalysts operate (>623 K). The rate of desorption of the alkali is strongly dependent on the heat of adsorption which, on carbon supports or single-crystal metal surfaces, decreases markedly with coverage, as shown for nickel in Fig 9.6.[67] Similarly, for potassium on ruthenium the heat of desorption decreases from 272 ($\theta = 0\%$) to 105 kJ mol^{-1} ($\theta = 40\%$)[68] while only a 5% potassium surface coverage remains after flash desorption of Ru(0001) at 1000 K.[69] A simple calculation, based on a desorption frequency of $\nu = 10^{13}\,s^{-1}$, implies that for a heat of adsorption of 270 kJ mol^{-1} the residence time on the surface at 773 K would only be

$$\tau = \tau_0 \exp(H_{ads}/RT) \approx 24\,\text{h} \qquad (\text{where } \tau_0 = 5 \times 10^{-14}\,s^{-1}) \qquad (9.7)$$

or 1.4 years at 673 K. Similar rates of desorption would also be expected under normal, high-pressure synthesis conditions. The hydroxides, which have high vapor pressures under synthesis conditions, would also desorb rapidly.

Several possibilities can be proposed to explain the retention of the alkali on a working catalyst. Leaving aside the formation of stable compounds such as potassium aluminate, which are unlikely to function as promoters, there is evidence that co-adsorption of the alkali metal and oxygen, as against the formation of the alkali compound, significantly stabilizes the adsorbed alkali. The studies, covered in detail in Chapter 5, have shown that at low coverages the oxygen is not adsorbed onto the alkali metal but adjacent to it on iron surfaces.[70] This stabilizes both the iron-alkali metal and iron-oxygen bonds.

This effect has also been observed on ruthenium[154] at 5% potassium coverage, where the thermal desorption peak shifted from about 970 K to 1200 K after saturation with oxygen. It is apparent that the presence of alkali metal enhances both the extent and strength of oxygen adsorption. Similar co-stabilization effects have also been observed with nitrogen, but they are not sufficiently marked to significantly modify the alkali stability. However, while the presence of oxygen stabilizes the alkali on the transition metal surface, it is not yet clear whether the resultant complex still functions as an electronic promoter. There is some evidence that the presence of the oxygen substantially reduces the ability of the alkali to influence the transition metal-nitrogen bond strength in the Fe-α state and therefore its electronic promotional capability.[170,171] This would be consistent with the known sensitivity of all ammonia synthesis catalysts to oxygen-containing poisons. This has also been demonstrated in the single-crystal studies, reported in Chapter 5, where some enhancement of the ammonia synthesis rate was observed in the presence of potassium and oxygen relative to the clean surface, although it was reduced relative to potassium in the absence of oxygen. It is possible that in the latter case the effect was due to stabilization of the Fe(111) structure rather than to electronic promotion. However, ESCA studies have shown that the addition of alkali salts to silica-supported ruthenium significantly modifies the binding energy of the ruthenium,[85] although it was not possible to determine whether this was due to charge transfer to the ruthenium. This was then reflected in the hydrogen adsorption and Fischer Tropsch conversion characteristics, similar effects being observed for nitrates, carbonates, and chlorides. This is in marked contrast to ammonia synthesis over ruthenium on carbon catalysts, where alkali chlorides show no promoting capability (Fig. 9.7). This suggests that, while the presence of alkali compounds (KCl, KO, etc.) can influence the transition metal, the effect is small and unlikely to modify nitrogen dissociation in ammonia synthesis to any significant extent.

An alternative, high-stability alkali complex has been observed on alkali-promoted supported transition metals. Infrared studies into nitrogen adsorbed on $M/X/Al_2O_3$, where M was ruthenium, rhodium, or rhenium and X sodium or potassium, all gave adsorption bands in the 2020 cm^{-1} region which is associated with σ-bonded nitrogen on unpromoted iron (Table 9.5). For these metals, the band only appears when the catalysts are exposed to nitrogen at above approximately 573 K—very substantially higher than the 90 K where the Fe-γ state is formed. The band is also stable to hydrogen at 430 K and 218 torr and can only be eliminated by treatment in hydrogen at 620 K.[71] Subsequent studies have shown that the formation of the IR band is associated with incorporation of both potassium

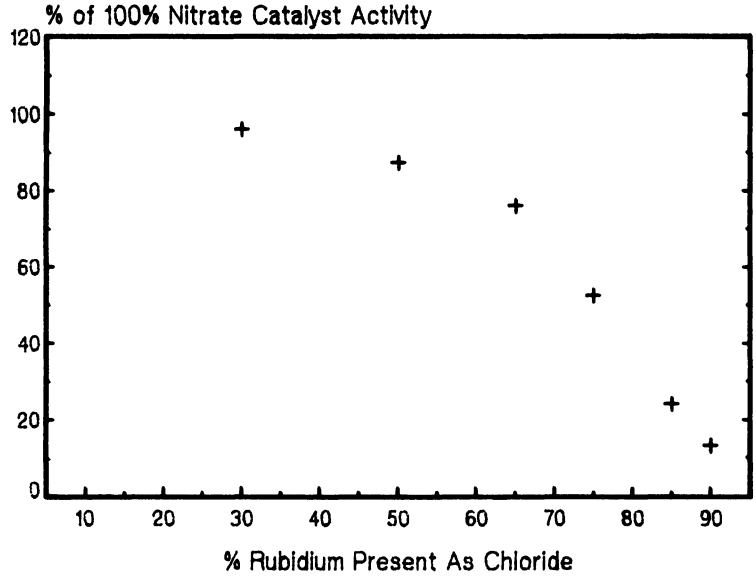

Figure 9.7. Relative promotional capability of rubidium chloride and nitrate. Relative activity of 10 parts ruthenium/20 parts rubidium on carbon catalysts at 7.2 bar in 3:1 H/N ratio syngas.

and nitrogen into the bulk of the ruthenium with a stoichiometry that suggests the formation of

$$K—Ru—N_2$$

where the nitrogen is held in the molecular form. There is additional evidence for the formation of such complexes on several transition metals, including iron.[34] Its apparent absence in single-crystal studies may reflect either the low-temperature and pressure conditions, both of which would inhibit its formation, or the difficulty

TABLE 9.5. Infrared Adsorption Frequencies (cm^{-1}) for M···N—N

	Ref.	γ	α_1	α_2
Single-Crystal Systems				
Fe(111)	86	2194	1490	
K/Fe(111)	86			1370
Pt(1111)	87	2238		
Promoted-Alumina Supported Metals				
Ru/K	71		2020	
Ru/Na	71		2028	
Rh/K	71		2040	
Re/K	71		2024	

of detecting it in the bulk of the single crystal compared to the highly dispersed, supported metals where it has been observed. The formation of this species in supported ruthenium catalysts is discussed in more detail in Section 9.3.

There is also evidence for structural stabilization of the adsorbed alkali metal. Although it has been shown that alkali desorption is largely independent of the crystal face,[67] LEED studies have demonstrated that though Ba^{2+} is not adsorbed on the Ru(0001) basal surface, it does adsorb on the more open Ru(1010) surface[72] giving a clearly defined and stable structure. This may imply that defect or step structures are significant in stabilizing alkali ion adsorption and are worthy of more detailed investigation. During thermal desorption studies of alkali overlayers it is also apparent that a significant proportion of the alkali is not desorbed, but diffuses into the bulk of the crystal and can then only be removed by sequential oxidation and thermal treatment. It is possible that such absorbed alkali could have a sufficiently enhanced heat of adsorption to be stable under ammonia synthesis conditions.

Recent work on ruthenium single crystals has also shown the presence of a more strongly bonded low-coverage species.[170] If potassium is adsorbed on Ru(0001) at above 450 K, several additional high-temperature TPD peaks (>1370 K), due to the desorption of K^+, are formed with desorption energies of >330 kJ mol^{-1}. The results also indicated the presence of neutral potassium species with similar binding energies. This would increase the residence time on the surface to in excess of 30 years at 773 K, compared to the 24 h estimated for an energy of desorption of 270 kJ mol^{-1}.

The various mechanisms for the stabilization of M^+, in conjunction with their thermodynamic stability, suggest that the charge transfer complex is the more likely source of electronic promotion.

9.2.3.1. Electronic Promotion

This has been examined in detail in an earlier chapter but will be briefly reviewed here. As indicated above there is still no definitive evidence for the chemical state of the alkali on magnetite-derived catalysts. However, in the case of supported ruthenium catalysts it is reasonably clear that the alkali metal is responsible for the observed enhancement in performance. Such promotion proceeds via electron transfer from the alkali to the transition metal. The extent of charge transfer can be monitored by the changes in the work function of the transition metal/alkali metal complex.

The free alkali metals have work functions (θ) considerably below those of the transition metals (Table 9.6).[167] At low coverage, this leads to charge transfer and the development of an ionic double layer, which gives rise to the observed decrease in the work function. At low surface coverage, charge transfer is complete. As the coverage increases the work function continues to decrease, reaching a minimum that depends on the alkali metal, the substrate, and the substrate geometry. After this, lateral interactions between the adsorbed ions become significant and the work function starts to rise, eventually reaching the value for a

TABLE 9.6. Work Functions (ϕ) of the Elements (eV)[a]

Sodium	2.75	Vanadium	4.3
Potassium	2.30	Manganese	4.1
Cesium	2.14	Iron	4.67 (100)
Calcium	2.87		4.81 (111)
Barium	2.70	Cobalt	5.0
		Nickel	5.22 (100)
			5.04 (110)
			5.35 (111)
			5.35 (111)
Molybdenum	4.53 (100)	Cerium	2.9
	4.95 (100)	Tungsten	4.63 (100)
	4.55 (111)		5.25 (100)
	4.36 (112)		4.47 (111)
Ruthenium	4.71		4.18 (113)
Rhodium	4.98	Rhenium	5.75 (1011)
Palladium	5.12	Osmium	(4.83)
	5.60 (111)	Iridium	5.42 (110)
			5.76 (111)
Uranium	3.73 (100)		5.67 (100)
	3.90 (110)		5.0 (211)
		Platinum	5.7 (111)

[a] Values are shown for the different crystal faces, where available.

simple alkali metal surface. These effects are well accounted for by the "jellium" model of Lang *et al.* at low coverages but tend to break down at higher coverages, where interactions between the adsorbed atoms become more significant. The lower heat of adsorption that results from lateral interactions at higher coverage almost certainly restricts alkali coverage on a working catalysts to around 10%. The high-coverage regions are therefore of little significance for catalysis.

Typical results for sodium, potassium, and cesium on Ni(110) in Fig. 9.8[67] show that the minimum value of the work functions falls in the order Na < K < Cs, as does the surface coverage at which the minimum occurs. The transition metal structure has a discernible, though less marked, effect on the work function, the minima being most pronounced for the close-packed surfaces, Ni(111) and Ni(100), and almost absent on the more open Ni(110) face.

Calculations have shown[165,73] that the transferred charge is localized close to the adsorption site and is screened from surrounding atoms in the metal matrix. This significantly modifies the local density of states in the immediate vicinity of the adsorbed alkali. Enhanced charge transfer to the $2\pi^*$ state of an adsorbing molecule can then occur, resulting in a strengthened metal-adsorbate bond and a weakened bond between the atoms of the adsorbed molecule. This is shown clearly by changes in vibrational frequency of N-α_2 on iron, where the N—N stretching frequency is shifted downward by approximately 100 cm^{-1}.

The consequence of the localization of the charge is that the strength of the adsorbate-adsorbent bond will only be significantly modified if adsorption occurs

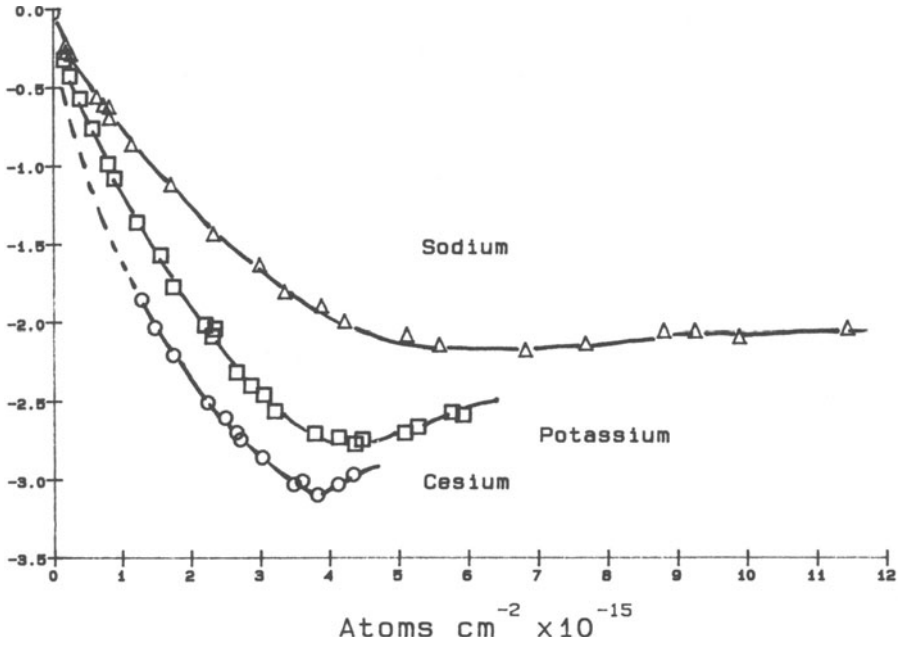

Figure 9.8. Work function *vs.* coverage for sodium, potassium, and cesium on Ni(110). Data from Ref. 67.

in the immediate vicinity of the alkali promoter. This strict localization has been directly confirmed for potassium on Ni(111) from the Penning spectrum of adsorbed xenon and the quenching of metastable helium atoms,[74] and also by PAX for potassium on Ru(0001).[69] In both cases, at low alkali metal coverages it is possible to detect two different adsorption sites associated with the free and the promoter-modified transition metal. As the alkali coverage increases, the free metal surface sites progressively disappear.

While it has been shown that on iron the presence of low levels of potassium increases the heat of adsorption of the nitrogen, leading to the presence of two distinct α states, α_1 on the free iron and α_2 adjacent to the potassium atoms,[15] recent data suggest that it is *not* this strongly bonded α_2 state that is responsible for the observed improvement in the synthesis rate. On the unpromoted surface the coverage of the weakly bound α_1 state is unusually low, *ca* 0.06 ML. In the presence of 0.16 ML of potassium this increases by up to a factor of 4.8 ± 2.1. It is believed that this large increase in the concentration of the α_1 state, along with smaller changes in the dissociation activation energy from the α_1 state, influences the rate, rather than the larger changes in the dissociation activation energy from the Fe-α_2 state. More interesting is that the promotion must then be via long-range, possibly electrostatic, effects rather than the expected short-range changes in the local density of states.

The impact of alkali promoters on hydrogen adsorption is quite different. Although there is no conclusive evidence for the mechanism, it is clear that their presence can severely inhibit hydrogen uptake. In the case of W(100) the presence of cesium on the surface dramatically reduces the hydrogen sticking probability due to an increase in the activation energy for dissociation (from 0 on the clean surface to about 20 kJ mol^{-1} at 20% coverage and 85 kJ mol^{-1} for a cesium-saturated surface). Chlorine also increases the activation energy for adsorption to as high as 67 kJ mol^{-1} on ruthenium.[123] The presence of one chlorine atom influences up to 6 surrounding ruthenium atoms and almost totally suppresses hydrogen chemisorption, on these metal atoms, at the usual titration temperatures (298 K). Saturation coverage could only be achieved after extended exposure at temperatures above 373 K.

Alkali promoters can also inhibit ammonia adsorption. In the case of magnetite catalysts there is indirect evidence that this is caused by neutralization of the acidic alumina phase. A similar effect is also observed on alumina-supported transition metals. ESCA evaluation of ruthenium catalysts demonstrated a significant increase in the ammonia bonding on alumina supports that could be reversed in the presence of alkali promoters. This is also apparent from the marked changes in the reaction order in ammonia for ruthenium on a variety of acidic and basic supports (Table 9.7). However, recent surface-science studies (discussed in detail in Chapter 5)

TABLE 9.7. Performance Characteristics of Promoted Ruthenium Catalysts

Support[a]	% Disp	E_a (kJ mol^{-1})	Reaction orders			TON (s^{-1})[b]		Ref.
			$M(N_2)$	$M(H_2)$	$M(NH_3)$	(1)	(2)	
BeO	8.6	75				1.6	11.3	91
MgO	2.9	41.8				14.3	42.3	91
CaO	2.5	33.0				18.7	44.1	91
Al_2O_3	5.0	71.0				0.7	44.0	91
BeO/K	8.6	100.3				204	2756	91
MgO/K	2.9	66.9				197	1118	91
CaO/K	2.5	46.0				75	247	91
Al/K	5.0	112.9				100	1870	91
AC/K	10.3	92.0				205	2230	91
Al/CsOH	42	108.7				2.4	40	113
Al/KOH	21	117.0				3.8	79	113
Al	19	62.7	1.06	0.3	0.74			127
Al/CsOH	43	112.9	1.00	0.55	0			127
CsOH	1.1	92	0.95	0.90	0.07			127
MgO	12	—	0.99	0.66	0.78			127
MgO/CsOH	—	112.9	0.99	0.43	0.12			127
SiO_2			1	1.25	1			126

[a] Al = alumina, AC = active carbon.
[b] 1. TON × 10^4 measured at 588 K, 600 torr H/N (3:1); 2. Estimated TON × 10^4 at 673 K based on observed activation energy.

have shown that the presence of the alkali also lowers the heat of adsorption of ammonia on the iron.

9.2.3.2. Structural

Structural promotion can take two main forms, although both are concerned with maintaining the effective surface area of the catalyst active component. The use of alumina to generate the pore structure of iron catalysts has been investigated extensively and is discussed fully in an earlier chapter. In the absence of alumina, iron sinters on reduction, giving low surface areas. In the presence of the optimum level of alumina (approximately 2%) surface areas as high as $25\ m^2\ g^{-1}$ can be obtained although, in the presence of potassium, this is reduced to $10\text{–}15\ m^2\ g^{-1}$.

In addition to the impact on the available surface there is also evidence for a second effect. Single-crystal studies have shown that in the presence of water vapor the less active iron faces, Fe(110) and Fe(100), reorient to the more active Fe(111) face. In the absence of alumina and under reaction conditions (20 bar syngas) these rapidly revert to the original structure. In the presence of low levels of alumina on the iron surface, lower levels of water (<20 torr) are required to bring about the transformation and the reoriented structure remains stable under reaction conditions.[75] This may partly explain the specific requirement for alumina. There is evidence that alumina can also induce reorientation in platinum[76] which may indicate that the promotion of reorientation is a more general phenomenon.

The second type of structural stabilization is inhibition of sintering in supported metals. This is primarily associated with barium,[77] although the lanthanides and other metals capable of forming perovskites or pyrochlores may also have beneficial effects.[78] Most of the evidence has come from studies into barium-promoted ruthenium, auto exhaust catalysts. In these systems the barium is apparently present as the oxide and $BaRuO_4$, and it is this compound form of the oxide that is thought to prevent oxide volatilization. However, there is also clear evidence that barium has beneficial effects in the strongly reducing ammonia synthesis environment.[79,80] It is possible that the presence of barium at the low coordination sites inhibits sintering by maintaining the defects in the small crystallites during the reduction/activation phase.

9.2.4. Support Effects

In this section the benefits and drawbacks to using supported as against bulk metal systems will be reviewed. This is followed by a more detailed discussion of the properties of the two main classes of supports: oxides and high surface area carbons.

The commercial ammonia synthesis process is unusual in that it uses an unsupported metal catalyst. There are two main reasons. In the first instance the major component, iron, is cheap enough that the cost of the large amount of metal used (up to 350 t) is not a restriction. Clearly, in the case of the platinum group metals this would not be a viable option. Second, by the addition of alumina, a

high surface area ($>3\ m^2\ cm^{-3}$), similar to those attained in highly dispersed supported catalysts ($1-5\ m^2\ g^{-1}$ of catalyst; around $100\ m^2\ g^{-1}$ of metal at 50% dispersion), is achieved and, more importantly, maintained at the ammonia synthesis temperatures.

In most cases the use of supported metals is essential and the properties of these supported catalysts will be influenced by several factors:

1. *Metal Dispersion.* To achieve a high dispersion at a reasonable metal loading it is necessary that the support has an adequate surface area. The area required will vary with the metal loading, the required dispersion, and the type of support.
2. *Dispersion Stability.* Sintering can be inhibited by using a more "active" support phase, where a strong interaction can occur between the metal precursor and the support.[82-84] However, this can lead to problems during the preparation and difficulties in reducing the metal.
3. *Promoter Location.* It might be expected that promotion of supported catalysts would be difficult because the promoter localizes on the support. However, ESCA studies[85] have shown that, in the case of silica-supported ruthenium promoted with alkali carbonates, the promoter preferentially associates with the ruthenium. Conversely, the high heat of adsorption of the alkali on carbon supports (up to $450\ kJ\ mol^{-1}$) leads to preferential association of the alkali with the carbon.
4. *Gas Transport Effects.* While small pores are essential to give high surface areas, larger transport pores are necessary to minimize diffusional inhibition although, as the porosity increases, both the support crush strength and attrition resistance decrease.

   Diffusion can also be minimized by reducing the catalyst particle size. While a viable option in experimental studies, it is of limited use in a commercial reactor because of the increase in pressure drop caused by the decrease in bed void volume. However, by careful design (radial flow, horizontal converters, etc.) most modern reactors now use considerably smaller particle sizes (1-2 mm) in the high activity/high temperature beds. The voidage can also be uncoupled from the particle size by the use of shaped supports, such as Rachig rings, trilobes, etc.
5. *Anion Retention.* Transition metal chlorides are often favored as catalyst precursors because of their ready availability, high solubility, and their ease of reduction. However, residual chloride anions (from incomplete catalyst reduction) can have a very marked effect on the properties of the catalysts. While the platinum group metal chlorides are, from a thermodynamic standpoint, very easy to reduce (Pt > Ru > Ir > Rh), residual chloride ions on the metal surface can be tenaciously bonded. The severity necessary to remove all the surface chloride reflects the surface energy of the metal (Ru, Mo, Ir > Rh > Pt > Pd). In the case of ruthenium, although bulk reduction apparently occurs at around 470 K, extended reduction above 700 K can be necessary to remove all chloride anions. The presence

of residual chloride can substantially modify both the ammonia synthesis[88] and hydrogen chemisorption[123] characteristics of the catalyst.

When the promoters are added to the catalysts, some of this residual chloride is converted to macrocrystalline alkali chlorides. While this lowers the amount of active alkali present, it also provides a facile way of reducing chloride poisoning. This is the probable cause of reported increases in hydrogen chemisorption, and therefore apparent catalyst dispersion, following the addition of alkali promoters.

9.2.4.1. Oxides

One of the first effects encountered in the use of oxides as supports is the influence of the surface acidity, or basicity, on the chemical state of the precipitating metal. A detailed review of the effects lies beyond the scope of this chapter, but a few key points will be highlighted. A more wide-ranging overview can be found in the papers contained in Ref. 104. Metals are typically added to supports via impregnation, coprecipitation, or ion exchange. In all cases the form of the metal in the impregnation solution is strongly influenced by the solution pH. Iron, for instance, is present at pH = 0 primarily as the hexaquo ion, $[Fe(H_2O)_6]^{3+}$, while above pH 2–3 multi-nuclear complexes form, resulting eventually in the deposition of colloidal Fe—O—Fe systems. The pH in the pores of a catalyst may differ significantly from that in the bulk solution. Relatively little change will occur in an essentially neutral support such as silica, but a drastic acceleration of the above reactions, resulting in very poor dispersions, can occur in aluminas. Similar precipitation problems are also encountered with the metal chlorides, i.e., ruthenium trichloride.[87]

The ease of reduction and subsequent performance of the catalyst will be strongly influenced by the extent and nature of the interaction between the metal and the oxide support. In ammonia synthesis studies the most commonly used oxides have been alumina[90] and magnesia.[46] Some work has also been carried out with basic materials such as calcia, etc., although they have little commercial potential due to their low surface areas. In the case of magnesia and alumina, high and reasonably stable dispersions can be produced but complete reduction is sometimes very difficult to achieve. In the case of coprecipitated iron/alumina the spinels formed can only be reduced at temperatures above 1073 K.[92] The reducibility of the supported systems also tends to be retarded to a greater extent by low vapor pressures of water than less highly dispersed catalysts.[90]

Even more pronounced changes in chemisorption properties are observed using the oxides of titanium, vanadium, tantalum, and niobium[93] as supports. The "Strong Metal Support Interaction" (SMSI)[94] occurs when the catalyst is reduced at high temperatures (about 773 K) and is believed to be due to a combination of effects:

1. Slight reduction of the titania support and subsequent migration of the titanium onto the catalytic metal surface.
2. A change in the form of the metal crystallites from hemispherical to rafts.[95]

In the SMSI state, hydrogen chemisorption is drastically reduced while there is little impact on carbon monoxide adsorption. It is not clear whether the inhibition of hydrogen chemisorption is due to site blocking, electronic effects, or a combination of the two. The observed reduction in ammonia synthesis rate on iron–titania catalysts may be due to either a change in the structure of the iron crystallites, influencing the nitrogen adsorption properties, or a significant reduction in hydrogen chemisorption.[96]

The retention of chloride can also cause problems when using supports such as alumina.[88] It is unclear whether this modifies the interaction between the metal crystallites and the support, or migrates onto the metal crystallite during reduction. There are, however, subtle differences between chlorine added directly to the support or via the transition metal precursor. These effects are not observed with more neutral supports such as silica, which retains no chlorine.

9.2.4.2. Carbon

Active carbons have surfaces that can range from slightly basic to fairly acidic (pH 3) depending on the preparative route. Normal commercial production routes, that involve oxidative activation, tend to give rise to acidic surfaces. The acidity is due to relatively labile surface species which can be modified by relatively mild heat treatment in inert or reducing atmospheres. Heating to 1273 K and cooling in nitrogen or hydrogen will usually change an acidic carbon to a basic with little effect on the pore structure. The pore structure of carbons is very complex and depends not only on the production route, but also on the precursor. Most active carbons tend to be highly microporous with the majority of the available surface area in pores of less than 2 nm diameter. Reported BET surface areas can range from 500 to as high as 3000 $m^2 g^{-1}$ although areas above about 700 $m^2 g^{-1}$ should be regarded with considerable caution. The pore structures are in most cases difficult to characterize and poorly understood.

One of the main advantages of carbon is its ability to stabilize high loadings of alkali metals. Early claims that the resulting benefits were due to the formation of intercalates[97] or charge transfer from the alkali metal to the transition metal via the graphite have been discounted. The heat of formation of the intercalates is low (143 to 180 kJ mol^{-1} for various cesium/graphite stages) and they decompose well below synthesis temperature.[98] Claims that catalysts prepared by the reduction of intercalates were active, because atomic dispersions of the reduced metals were held between the layer planes,[99] have also been discounted.[100] It is more likely that the activity was due to the presence of small metal crystallites formed on the graphite edge planes as metal atoms diffused out of the lattice during reduction.

The key to the nature of the carbon–alkali interaction has come from studies into nuclear isotope trapping using active carbons. These have demonstrated that metallic cesium is very strongly adsorbed onto active carbons with a heat of adsorption which reaches 500 kJ mol^{-1} at low surface coverages[101,102] (Fig. 9.9) due to charge transfer to the carbon. Calculations have shown that for the ideal graphite adsorption site (a six-atom hole) the heat of adsorption should be approximately 850 kJ mol^{-1}.[103] A secondary result of this high heat of adsorption is to

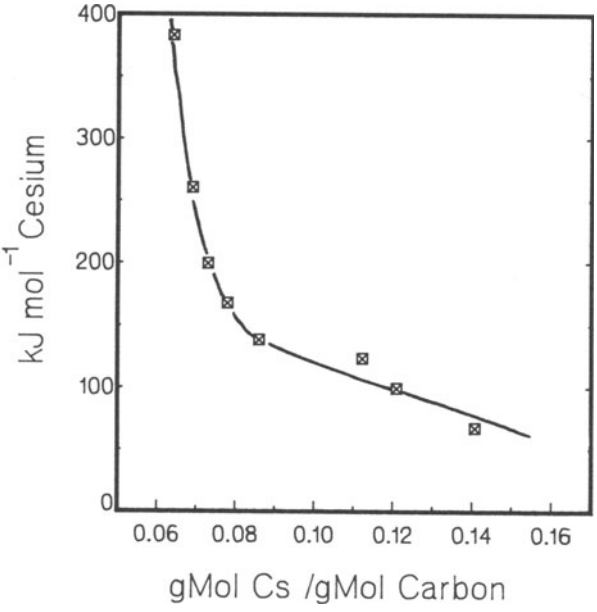

Figure 9.9. Heat of desorption *vs.* coverage for cesium on activated carbon. Data from Ref. 101.

provide a driving force for the reduction of promoter precursors. While under normal circumstances reduction of a salt such as potassium nitrate should not proceed past the hydroxide, the additional energy derived from the graphite/alkali interaction is sufficient to push the reduction through to the metal. Values of quantities ΔG, ΔH, and ΔS for formation of the alkali metal-carbon complex[102] demonstrate that the reaction should proceed readily even at fairly high water-vapor pressures.

A major limitation on the use of active carbon has, until recently, been its reactivity—carbons are by their very nature reactive and can be oxidized or reduced readily. In a typical ammonia synthesis environment, at high temperatures and hydrogen pressures, and in the presence of materials that are generally also methanation catalysts, severe support methanation has been shown to occur.[104] However, this can be almost entirely suppressed by careful heat treatment of the support to temperatures in excess of around 1800 K.[105] Using these modified carbons lifetimes of at least 6 years can be expected under high-pressure synthesis conditions.

9.2.4.3. Diffusion and Gas Transport Effects

The other major factor influencing catalyst performance, common to both supported and unsupported catalysts, is diffusional inhibition. In general, the use of the small particles (0.1–0.5 mm) will minimize the effect except at high temperatures and in the region close to equilibrium. Early attempts to allow for

diffusion were constrained by the problems involved in solving the differential diffusion equations

$$\frac{d^2X_i}{dZ^2} - \frac{2(dX_i/dZ)}{(S_i + 2X_i)} + \frac{2(dX_i/dZ)}{Z} = \frac{-R^2(S_i + 2X_i)V_i}{CD_{ie}S_i} \tag{9.8}$$

where X_i is the molar concentration of i, C the total concentration, D_{ie} the effective diffusion constant for i, R the equivalent particle spherical radius, S_i the stoichiometric coefficient of i, and V_i is the rate of formation of i; quantity Z is the dimensionless radial coordinate (0 denotes the center and 1 the surface) for the boundary conditions

$$dX_i/dZ = 0 \qquad \text{at} \qquad Z = 0 \tag{9.9}$$

and

$$X_i = X_{i\ \text{bulk}} \qquad \text{at} \qquad Z = 1 \tag{9.10}$$

as analytical solution is only possible for integral-order nonreversible reactions.[106] Assumptions of simple integral-order[107] nonreversible kinetics[108] has led in many cases to a marked underestimation of the extent of inhibition and to erroneous conclusions, such as increases in effectiveness with pressure.[109] Modern computational techniques now make it possible to solve the diffusion expressions for any form of kinetic expression and the method has been applied to ammonia synthesis using Temkin kinetics.[110]

Some key assumptions are, however, still implicit in this approach. Solution of the equations requires knowledge of the diffusion coefficients for each of the components, which is in turn influenced by the nature of the support pore structure. In the case of wide-pore, magnetite-based catalysts at high pressures, bulk diffusion will predominate, while in more microporous supported catalysts there will be contributions from Knudsen diffusion. Under low-pressure conditions (1 bar) Knudsen diffusion will probably predominate.

The effective Knudsen diffusion coefficient is given by

$$D_{\text{k eff}} = \frac{19{,}400\ \theta^2\,(T/M)^{0.5}}{S\tau\rho} \tag{9.11}$$

while the effective bulk diffusivity is given by

$$D_{\text{b eff}} = \frac{D_{12}\theta}{\tau} \tag{9.12}$$

where θ is the particle porosity (cm^3/cm^3), S the pore surface area ($\text{cm}^2\,\text{g}^{-1}$), and ρ the pellet density (g cm^{-3}). The factor τ, the tortuosity, allows for nonlinearity, varying pore cross sections, etc. To a first approximation the use of bulk diffusion is acceptable, although it should be remembered that the temperature and pressure

responses of bulk and Knudsen diffusion are different. For bulk diffusion, they can be estimated from the Lennard-Jones expression for intermolecular forces:

$$D_{12} = \frac{0.001858T^{3/2}[(M_1 + M_2)/M_1M_2]^{1/2}}{P\sigma_{12}^2\Omega_D} \tag{9.13}$$

In applying these expressions it can be seen that, in the case of bulk diffusion, the only structural parameter is total porosity while for Knudsen diffusion it is also necessary to know the pore diameter (this is implicit in the surface area/pore volume ratio). However, in practice all of the structural factors (S, ρ, and θ) can be included in the tortuosity τ if it is determined experimentally. The latter quantity is frequently determined from gas transport measurements through porous plugs at atmospheric pressure. This inevitably leads to an underestimate as it only measures the flow in the main transport pores, while the active catalyst sites are almost certainly in smaller, possibly dead-end, pores. This can be overcome by nonsteady-state pulse methods, although these tend to overcompensate by including even the smallest micropores. The best method is to determine the detailed kinetic response of the catalyst for a range of particle sizes. A combination of the kinetics obtained from the smallest particles and the differential diffusion equations then enables one to determine a "reaction" tortuosity. Some of the literature values for τ are summarized in Table 9.8 and range from around 0.1 to as high as 5. The higher values almost always arise from reaction-type measurements rather than low-pressure flow methods. This demonstrates that, unless a realistic value for τ is available, it is unwise to utilize values determined from low-pressure flow methods.

9.2.5. Catalyst Kinetics

In the previous sections the factors that influence gas adsorption on the catalyst surface have been discussed in detail. If the adsorption energies, frequency factors, and the variations with coverage, discussed in these sections, were known for each individual step in the reaction pathway, the catalyst activity and response to operating conditions could be calculated explicitly. As has been shown, the accurate

TABLE 9.8. Tortuosity (τ) Values for Various Porous Materials[a]

Material	Technique	T (K)	r_p (nm)	θ	τ
Alumina	Diffusion	303	9.6	0.812	0.85
Magnetite	Diffusion	298	17.7	0.52	2.7
Vycor glass	Flow	298	5.0	0.28	5.9
SiO_2/Al_2O_3	Flow	273-323	1.6-2.4	0.4-0.53	0.28-0.73
SiO_2/Al_2O_3	Reaction	420	2.4	0.5	5.6
SiO_2/Al_2O_3	Reaction	755	2.8-7.1	—	3-10
Carbon	Reaction	673	3.5	0.45	6.0

[a] r_p is the pore radius and θ the porosity.

determination of all of these factors would be extremely time-consuming and would still require experimental confirmation from the high-pressure evaluation of the catalyst in question. Most applied catalyst research has therefore concentrated on the examination of a catalyst under higher-pressure test conditions, and the subsequent development of a mathematical description of the catalyst's response to the various operating variables (pressure, temperature, reactant/product partial pressures).

For the purposes of plant design the "kinetic model" need not have any mechanistic pretensions and could take the form of a simple power rate law expression:

$$\text{rate} = P_{N_2}^X P_{H_2}^Y P_{NH_3}^Z$$

However, it is essential that this type of expression is never extrapolated outside the range of the variables from which it was developed. Consequently, and as a result of the inherent requirement for a very comprehensive data base, most kinetic models have been derived from mechanistic assumptions. While these provide a better basis for limited extrapolation, it should be remembered that a good fit of the observed data to the model does not "prove" that the underlying model is correct. In the following sections the two forms of kinetic model most commonly applied to ammonia synthesis will be examined, along with a brief examination of the more rigorous, surface-science-based models that are now beginning to emerge.

9.2.5.1. Temkin Kinetics

The most widely used expression for ammonia synthesis kinetics is the Temkin equation, introduced in 1939[7]:

$$dNH_3/dT = 2k_b\left[K_a^2 a_{N_2}\left(\frac{a_{H_2}}{a_{NH_3}^2}\right)^{\alpha} - \left(\frac{a_{NH_3}^2}{a_{H_2}^3}\right)^{1-\alpha}\right] \tag{9.14}$$

The background to this model has been discussed in an earlier chapter and will not be considered here in detail. However, the two basic assumptions are that dissociation of nitrogen is rate limiting and that the heat of adsorption of the nitrogen (Q_{ads}) decreases linearly with coverage:

$$Q_{ads} = Q_0(1 - a\theta) \tag{9.15}$$

This gives rise to the *Temkin* adsorption isotherm:

$$\theta = \frac{RT}{\theta_0} a \ln\left[K/b \exp\frac{(\theta_0)}{RT}\right]P \tag{9.16}$$

where a and b are constants.

In the *Temkin* kinetic equation α can usually be assumed to be 0.5, although values as high as 0.67 have been reported for magnetite, while for metals such as nickel and cobalt it may drop to as low as 0.1.

This expression provides an adequate fit for magnetite, but the results for other metals are generally unsatisfactory. This is particularly apparent in the early attempts to apply the *Temkin* equation to metals as diverse as cerium and ruthenium[16] where the rate constants show marked residual variations. This reflects both the scanty nature of the data used and, in the earlier studies, errors due to poor experimental conditions, inadequate allowance for diffusional effects, and the use of pressure rather than fugacity in the high-pressure studies. Significant residual errors are also apparent in some of the reported magnetite studies. These suggest that the general applicability of this model, claimed in some of the earlier papers, is more an artifact of the poor data.

9.2.5.2. Langmuir-Hinshelwood Kinetics

The most widely encountered mechanistic model in general kinetic studies is the Langmuir-Hinshelwood (LH) equation and its derivatives. Although this has not been extensively used for ammonia synthesis over iron-based catalysts, largely due to the success of the *Temkin* model, it has been widely applied to other ammonia synthesis catalyst systems. In contrast to the *Temkin* equation this assumes that the heats of adsorption of the reacting species on the surface of the catalyst are independent of coverage. The surface coverage is then related to the pressure, or, preferably at high pressures, the fugacity, of the reacting species via the Langmuir isotherm:

$$P = \frac{k_r K \theta}{(1 - \theta)} \tag{9.17}$$

The other assumptions in the derivation of the LH rate expression are:

1. Absorption equilibrium is established for all reactions except the rate-limiting step.
2. All components compete for the same surface sites.
3. Only one step is rate-limiting.

The apparent inability to apply this approach to many ammonia synthesis systems could, at first sight, be attributed to the clear deviation of all synthesis catalysts from the main Langmuir assumption that the heat of adsorption of the reacting species is independent of coverage. However, it can also be attributed to the use of simplified LH expressions that do not take adequate account of all the intermediate species. To derive the complete rate expression it is necessary to postulate a full mechanistic pathway with one rate-limiting step. In the case of ammonia

synthesis, if the steps are assumed to be

$$1. \quad N_{2\,(g)} + S \Leftrightarrow N_2^* \tag{9.18}$$

$$2. \quad N_2^* + S \Leftrightarrow 2N^* \tag{9.19}$$

$$3. \quad H_{2\,(g)} + S \Leftrightarrow H_2^* \tag{9.20}$$

$$4. \quad H_2^* + S \Leftrightarrow 2H^* \tag{9.21}$$

$$5. \quad N^* + H^* \Leftrightarrow NH^* + S \tag{9.22}$$

$$6. \quad NH^* + H^* \Leftrightarrow NH_2^* + S \tag{9.23}$$

$$7. \quad NH_2^* + H^* \Leftrightarrow NH_3^* + S \tag{9.24}$$

$$8. \quad NH_3^* \Leftrightarrow NH_{3\,(g)} \tag{9.25}$$

where S is a free site and step 2, the dissociation of adsorbed molecular nitrogen, is assumed to be rate-limiting, the overall rate expression is given by

$$d[NH_3]/dt = \text{rate of forward reaction} - \text{rate of back reaction} \tag{9.26}$$

$$= k_f \theta N_2 - k_b(\theta N)^2 \tag{9.27}$$

All of the other steps are then assumed to be in equilibrium and can be expressed in the following form using the Langmuir isotherm:

$$K_1 = \frac{\theta N_2}{a_{N2} \cdot S} \tag{9.28}$$

$$3. \quad K_3 = \frac{\theta H_2}{a_{H2} \cdot S} \tag{9.29}$$

and so on.

Stepwise substitution then gives the following expressions for the surface coverages of each component:

$$\theta H = (K_3 K_4 a_{H_2})^{0.5} S \tag{9.30}$$

$$\theta H_2 = K_3 a_{H_2} S \tag{9.31}$$

$$\theta N_2 = K_1 a_{N_2} S \tag{9.32}$$

$$\theta N = \frac{a_{NH_3} S}{K_5 K_6 K_7 K_8 (K_3 K_4 a_{H_2})^{1.5}} \tag{9.33}$$

$$\theta NH = \frac{a_{NH_3} S}{K_6 K_7 K_8 (K_3 K_4 a_{H_2})} \tag{9.34}$$

$$\theta NH_2 = \frac{a_{NH_3} S}{K_7 K_8 (K_3 K_4 a_{H_2})^{0.5}} \tag{9.35}$$

$$\theta NH_3 = a_{NH_3} \frac{S}{K_8} \tag{9.36}$$

Elimination of S from these expressions and substitution back into the overall rate expression (9.27) then yields

$$\frac{d(NH_3)}{dt} = \frac{A \exp(-E_a/RT) \cdot a_{N_2}}{[1 + \kappa_H + \kappa_{H_2} + \kappa_{N_2} + \kappa_N + \kappa_{NH} + \kappa_{NH_2} + \kappa_{NH_3}]^2} \left(1 - \frac{a_{NH_3}{}^2}{K_a{}^2 a_{H_2}{}^3 a_{N_2}}\right) \tag{9.37}$$

where

$$\kappa_H = (K_3 K_4 a_{H_2})^{0.5} \tag{9.38}$$

$$\kappa_{H_2} = K_3 a_{H_2} \qquad \text{etc.} \tag{9.39}$$

from expressions (9.30)-(9.36) and

$$a_i = f_i / f_i^* = f_i^0 X_i = \gamma_i X_i P \tag{9.40}$$

The values of the fugacity coefficients γ_i and the equilibrium constant K_p for use in this expression can be found elsewhere.[110]

This rate expression provides an excellent description of the operating characteristics of alkali-promoted ruthenium on carbon catalysts over a wide range of pressure, temperature, and gas composition[19] based on kinetic constants derived directly from pilot plant studies.

It is interesting to note that an expression of identical form has also been derived without direct recourse to the assumptions inherent in the Langmuir approach, although the presence of a single type of site was assumed. The constants were then obtained from experimentally determined adsorption characteristics (H_{ads}, ν, etc.). The resulting expression was shown to be valid for magnetite catalysts over a wide range of ammonia synthesis conditions (pressure 1-30,000 kPa, temperature 648-773 K).[17,164] This is examined in more detail in the chapter on catalyst kinetics. However, the assumption in this work of a single reactive site raises interesting questions as to the nature of the magnetite surface. Other studies using isotopically enriched nitrogen have demonstrated that, at 100 kPa pressure and temperatures as low as 573 K, all nitrogen on the surface of a conventional magnetite catalyst has an equivalent reaction probability[18] despite the known variations in the heat of adsorption with both coverage and structure. This indicates that while nitrogen may adsorb preferentially at certain sites, it then possesses sufficient mobility to diffuse to sites where the reaction occurs.

9.2.5.3. Surface-Science-Based Kinetic Models

The ability to model a reaction with a reasonable degree of precision does not "prove" that the underlying model is correct. Such an assumption is particularly dangerous in the LH approach, where there are usually sufficient terms to insure that the model fits the data. It is also apparent that the use of a single homogeneous surface, as implied in the LH kinetics, or a simple change in heat of adsorption with coverage, as implied in the *Temkin* kinetics, are at best gross oversimplifications. It has also been shown that, in ammonia decomposition reactions where LH kinetics provide an excellent description of the catalyst response over a wide range of conditions, the heats of adsorption implicit in the LH constants bear little relation to independently determined values. In applying the LH equation it should also be remembered that, although the values of K_i are generally assumed to be temperature-independent, they actually include the heats of adsorption and surface reaction activation energies. It may be necessary to include these variations if the underlying database is both accurate and large enough.

With the increased availability of extensive data on the adsorption of reactants and products on well-defined surfaces it is now possible to contemplate the development of more mechanistically based kinetic models. Two approaches have been adopted: the one described in the previous section, which has much in common with the LH approach, and the more general approach that requires a rate expression, incorporating heats of adsorption, frequency factors etc., for each of the individual synthesis reaction steps [Eqs. (9.18–9.25)]. These rate expressions are then solved simultaneously to give the overall reaction rate.

The first attempt to use the simultaneous solution approach for ammonia synthesis over iron catalysts[81] gave estimated reaction rates several orders of magnitude lower than those found in practice. This is discussed in the chapter on iron kinetics, but can be attributed to inadequacies in the underlying database, in particular the use of low-coverage adsorption data. The closest approach to a mechanistically acceptable model has come from studies into ammonia decomposition on platinum.[20–22] The characteristics of this reaction over many transition metals are:

1. The reaction tends toward zero-order kinetics at low temperature and/or high pressure where the surface is largely N* saturated, the rate being controlled by nitrogen recombination. Under these conditions the overall activation energy for the reaction is high, typically $>150\ \text{kJ mol}^{-1}$.
2. At high temperatures and/or low pressures where the N* surface coverage is low, the rate is controlled by N—H bond cleavage and the reaction becomes first order in ammonia with an almost zero activity energy.

The rate-limiting step in the decomposition reaction is a very sensitive function of the surface coverages of the various components and, in particular, of atomic nitrogen. Studies using both single-crystal and polycrystalline platinum[20–22] and several other transition metals (tungsten,[27] nickel,[23] rhenium,[159] and ruthenium[28]) have confirmed that the reaction follows the same pathway as the ammonia synthesis reaction on iron. All of the transition metals show broadly

similar ammonia decomposition characteristics. The temperature at which the transition from nitrogen desorption to N—H bond breaking as the rate-determining step occurs depends on the surface coverages of all the components, and therefore on the heats of adsorption as well as the reaction conditions. The various adsorption energies for platinum are summarized in the one-dimensional potential energy diagram derived by Vajo *et al.*[21] (Fig. 9.5a). In this case the low adsorption energy of the atomic nitrogen makes desorption of nitrogen (92 Kj mol^{-1}) more favorable than the hydrogenation of surface nitrogen for which the activation energy is 117 kJ mol^{-1}. This can be compared with the situation on iron (Fig. 9.5b)[81] where the activation energy for nitrogen desorption and ammonia formation are 225.8 and 230 kJ mol^{-1}, respectively. The temperature at which the rate-limiting step switches from N* recombination to N—H bond breaking should also increase as the heat of adsorption of atomic nitrogen increases, reflecting the ease with which higher surface coverages can be maintained. This is evident on moving from platinum (600 K) to nickel (approximately 900 K)[23] to tungsten (1200 K).[27]

While a reasonable fit to the observed reaction characteristics can be obtained using Langmuir-Hinshelwood kinetics,[168] this leads to a marked overestimate of the heat of adsorption of ammonia, an effect also observed with nickel catalysts.[23] This has been attributed to adsorption equilibrium not being established between gaseous and adsorbed ammonia. The simultaneous solution of the rate expressions for the individual steps has provided an improved fit to the observed reaction characteristics over a very wide range of operating conditions, as it avoids any assumptions pertaining to the rate-limiting step, establishment of equilibrium, etc. However, it still fails to account for all the observed characteristics. This can only be achieved by assuming that the heat of adsorption of hydrogen varies with coverage.[20] For the step

$$H_{2\,(g)} \Leftrightarrow 2H^* \tag{9.41}$$

the rate of desorption is given by

$$R_{d\,H_2} = 2k^0_{d\,H_2}(\theta)(n_s\theta_h)^2 \exp[-E_d(\theta)/kT] \tag{9.42}$$

where

$$k^0_{d\,H_2}(\theta) = k^0_{d\,H_2} \exp(-\alpha\theta) \tag{9.43}$$

and

$$E_d(\theta) = E_d - \beta\theta \tag{9.44}$$

while α and β are constants. This is a manifestation of the compensation effect between the activation energy for desorption, E_d, and the desorption frequency, ν_{des}, that is observed for many adsorbents and adsorbates. It is still necessary to determine the constants in these coverage expressions from the experimental data.

The similarity of the ammonia decomposition mechanism over a variety of metals suggests that, while the LH expression should provide a reasonable first approximation to the synthesis kinetics of a wide variety of catalysts, the simultaneous-solution approach will provide a more mechanistically rigorous solution

where the relevant adsorption data are available. However, the complexity of the approach and the requirement for a very extensive and accurate database will limit its use to fundamental rather than applied (process design) catalyst studies for most systems.

9.3. SPECIFIC CATALYST SYSTEMS

In the previous sections most of the factors that control whether or not a particular system has potential in ammonia synthesis have been examined. In this section the characteristics of those materials that show significant synthesis activity will be examined in more detail. These are split into three groups based on the nature of their nitrides (Table 9.1):

1. Platinum group metals: no bulk nitrides (Ru, Os, Ir, Pt, etc.).
2. Those metals where nitrides are unlikely to be present under synthesis conditions (Mn, Fe, Co, Ni, Tc, Re), including alloys of these metals.
3. Metals probably present as nitrides under synthesis conditions (Groups 3a to 6a).

9.3.1. Platinum Group Metals

9.3.1.1. General overview

Of the platinum group metals only ruthenium and osmium show significant ammonia synthesis activity, though only in the presence of alkali promoters. This can be seen from the performance of the potassium metal promoted carbon-supported catalysts in Table 9.9.[117] Although osmium was one of the earliest and most active synthesis catalysts,[111] interest has largely shifted to ruthenium because of the dangers associated with osmium, the very small quantities available, and the improved performance of promoted ruthenium.

Although none of these metals form bulk nitrides, the transition metal–nitrogen bond energies are still significant. For ruthenium the surface bond strength (566 kJ mol^{-1}) is not markedly lower than on iron (585 kJ mol^{-1}) (Table 9.2) and even the inactive metals such as palladium have bond strengths of around

TABLE 9.9. Ammonia Synthesis Activity of Metals Supported on Active Carbon and Promoted with Potassium Metal (ml NH_3/ml Catalyst/573 K, 600 torr, 3:1 H/N)[a]

		Fe	Co	Ni
		0.72	0.40	0.04
Mo		Ru	Rh	Pd
0.6		22.4	0.52	0
	Re	Os	Ir	Pt
	0.36	5.6	0.68	0.008

[a] Data are taken from Ref. 117.

543 kJ mol^{-1}. However, it is not the strength of the M—N bond that is critical, but the ability of the catalysts to adsorb molecular nitrogen and the size of the subsequent dissociation activation energy barrier.

9.3.1.2. Adsorption Characteristics

9.3.1.2a. Nitrogen Adsorption. Molecular nitrogen adsorbs to a limited extent on all of the platinum group metals. On polycrystalline platinum two molecular states are formed, α_1 and α_2, with a dissociation activation energy for the α_1 state of 31 kJ mol^{-1}. These convert very slowly to the atomic state at room temperature, confirming the presence of the appreciable activation energy for nitrogen dissociation[112] found in ammonia decomposition studies. In a separate study, using (111) oriented Pt ribbon, molecular adsorption at low temperatures (<120 K) gave rise to an IR reflectance band at 2239 cm^{-1} [37] similar to bands found on several other transition metals that can be attributed to the adsorption of nitrogen at sites with a very specific structure.[10]

The furrowed iridium(110) surface demonstrates similar adsorption characteristics[52] with two molecular states giving rise to TPD peaks at very similar temperatures to those found for platinum (approximately 140 K and 210 K). First-order desorption kinetics give a value for the heat of desorption of around 33.6 kJ mol^{-1} with ν_{des} somewhat low at between 10^8 and 10^{11} s^{-1}. A relatively low saturation coverage of 4.8×10^{14} mol cm^{-2} was also observed on this face, in reasonable accord with the requirement for the presence of special sites. The formation of IR active states has also been observed on supported iridium and, as in the case of nickel, this was restricted to catalysts where the crystallite size was in the range 2–4 nm.

In all of these studies the sticking probability for molecular nitrogen was in the range 0.2 to 1.0, in marked contrast to iron where low probabilities are observed in the α states that populate at similar temperatures (on iron sticking probability only exceeds 0.1 at lower temperatures, about 70 K) where the σ-bonded γ-state forms, the higher-temperature Fe-α states being attributed to a π-bridge bonded dissociation precursor state not observed on the platinum group metals. The higher sticking probability for the molecular state on the platinum group metals does not, however, result in any significant increase in the dissociative sticking probability which, in the case of platinum, is still only 10^{-4} s^{-1}.

Dissociative adsorption only occurs to any significant extent on ruthenium, although there is direct evidence that, as on most transition metals, it does not occur on the close-packed Ru(0001) face[12,115] or even on the open faces in the absence of promoters. The heat of adsorption of dissociated nitrogen is, however, high on the Ru(0001) surface (184 kJ mol^{-1} with ν_{des} of 1.3×10^{-3} [58]). The coverage of N*, derived from the decomposition of ammonia, is approximately 100% at 600 K falling slowly to 10% at 800 K in 2×10^{-6} torr ammonia.

Similar results are obtained for Pt(110) although the N* surface coverage falls to 10% at around 600 K, reflecting the lower heat of adsorption (102 kJ mol^{-1}) (ν_{des} was very low for a second-order process, 4×10^{-8} s^{-1}). Ammonia decomposition data implies an activation energy for nitrogen dissociation of 67 kJ mol^{-1}, far

in excess of the small activation energies found on unpromoted iron and probably sufficient to account for the absence of any ammonia synthesis activity over platinum catalysts.

The impact of promoters on nitrogen adsorption has only been studied in any depth on ruthenium, and then from reaction rather than gas adsorption experiments. The only data for the other metals is shown in Table 9.9,[117] where all the metals exhibit essentially zero activity in the absence of the potassium metal promoter. On unpromoted ruthenium powder, nitrogen uptake, even after 40 h at 623 K, is very low and only detectable from thermal desorption rather than uptake measurements, although the desorption peak, at around 700 K, is consistent with the TPD from ruthenium single crystals.[116] In the presence of potassium, nitrogen uptake is substantial (0.62–0.75 mmol g^{-1}) and considerably exceeds the hydrogen uptake (0.27 mmol g^{-1}). This indicates that absorption of some of the nitrogen into the bulk of the ruthenium must be occurring.

In the absence of promoters while negligible nitrogen adsorption occurs, three atomic nitrogen TPD peaks are observed at 480, 600, and 700 K, the lower two peaks being consistent with those found on stepped single crystals following ammonia decomposition. In the presence of potassium the higher peak shifts to approximately 800 K, consistent with an increase in the transition metal–nitrogen bond strength.[28]

9.3.1.2b. Ammonia Adsorption and Decomposition. On Ru(0001) TPD shows the presence of three molecular states with desorption temperatures of 133, 186, and 330 K (heats of desorption of 30, 44.3, and 96 kJ mol^{-1}, respectively). Dissociation of the adsorbed ammonia is activated and only occurs to any extent above 300 K. This is followed by the loss of hydrogen, implying the formation of stable NH_2* fragments.[12] The sticking probability for dissociative adsorption is also low (2×10^{-5}), as expected for an activated process (the activation energy for dissociation is 50 kJ mol^{-1}). On stepped ruthenium surfaces Ru(1110), ammonia dissociation occurs readily at 300 K, again leading to the formation of stable NH* and NH_2^* fragments. Nitrogen desorption from the stepped surface is also more facile with a second TPD peak at 560 K in addition to the normal desorption peak at 760 K.[28] Similar characteristics are shown by platinum, although the activation energy for both ammonia (67 kJ mol^{-1}) and nitrogen dissociation[22] are considerably higher.

9.3.1.2c. Hydrogen Adsorption. There are wide variations in the measured heats of adsorption. In the case of ruthenium, TPD studies have given low coverage values varying between 72 and 120 kJ mol^{-1}.[118] The lower values were obtained from TPD data using both the Redhead formula and peak shape analysis,[39] which gave a value $\nu_{des} = 10^{-3}\ s^{-1}$, in reasonable agreement with theory. This was also in agreement with the earlier data of Danielson *et al.*,[12] but in marked contrast to the later and rather more detailed data of Feulner and Menzel[118] who gave a heat of desorption between 120 and 90 kJ mol^{-1} with corresponding values for ν_{des} from 3.0 to $5 \times 10^{-2}\ cm^2\ s^{-1}$ at 0 to 50% coverage. The value of ν at low coverage

is very high compared to the theoretical value for a second-order reaction and was attributed by the authors to localized adsorption. The most recent data[119] give a value for the heat of desorption and ν_{des} of 92.4 kJ mol^{-1} and 1×10^{-3} s^{-1}, respectively. The marked variation in the assigned values for the heat of desorption and ν_{des} demonstrate clearly the problems of deriving unequivocal values from TPD data.

Heats of adsorption on the other metals in the group show equally large variations. Some of the values obtained for various platinum and palladium faces are summarized in Table 9.4 with typical transition metal–hydrogen bond energies in Table 9.2. Although the variation in the heat of adsorption between faces is of the same order as the variation between similar faces on adjacent metals, there is evidence to suggest that hydrogen adsorption is structure-sensitive. In many TPD studies on either less than perfect single crystals or deliberately roughened crystals, significant high-temperature tailing occurs (on platinum from 34–42 kJ mol^{-1} to 67 kJ mol^{-1} [37], indicative of a significant increase in the heat of desorption. A similar, though smaller, effect is found with stepped vs planar palladium[64] and iridium[114] crystals. This also extends to supported catalysts. In the case of platinum, an extended tail is observed during TPD while direct DSC measurements on supported palladium catalysts show a marked increase in the integral heat of adsorption from 63 to 105 kJ mol^{-1} at particle sizes below 2.5 nm.[43] These results indicate that where ammonia synthesis is inhibited by hydrogen, the effect will become more severe as the dispersion of the metal is increased.

The impact of promoters is markedly different to the effects found with nitrogen. All adatoms, alkali metals, copper, sulfur, chlorine, etc. *inhibit* hydrogen adsorption to similar extents. On ruthenium, the presence of one sulfur adatom inhibits hydrogen adsorption on four adjacent ruthenium atoms, a copper adatom on five adjacent ruthenium atoms,[120] and a chlorine atom on six ruthenium atoms.[123] Inhibition by alkalis has also been observed on rhodium/silica and rhodium/titania,[121] rhodium/alumina,[122] and ruthenium/silica.[85] One explanation is a significant increase in the activation energy for hydrogen dissociation. This has been shown to increase from 0 to 60 kJ mol^{-1} in the presence of chlorine[123] and has also been claimed to increase in the presence of alkalis.[85] Under the relatively low temperature conditions in which most hydrogen adsorption studies have been carried out, such an increase would result in the observed reduction in adsorption. This effect should also be borne in mind when using hydrogen chemisorption to determine catalyst dispersion. The presence of residual chlorine from the catalyst preparation[124] may give rise to a significant apparent decrease in the dispersion. Effective neutralization of the chlorine by the addition of alkali promoters is probably responsible for the reported increases in dispersion following catalyst promotion.[125]

9.3.1.3. Catalyst Characteristics

From the limited data available it is clear that the activation energy for nitrogen dissociation increases both along and down the group 8 metals such that significant synthesis activity for metals other than ruthenium and osmium is unlikely (Table

9.9). The relatively high activation energy for nitrogen dissociation on ruthenium and osmium will also make them considerably more dependent on the presence of promoters than metals such as iron.

The early studies into promoted ruthenium were restricted to the use of alkali metals as promoters. These were added in the gas phase to supported ruthenium by circulation at a temperature sufficient to maintain an adequate vapor pressure. They showed a correlation between catalyst activity and the ionization potential of the alkali promoter used (Cs > K > Na) and provided clear evidence that charge transfer from the alkali to the ruthenium was responsible for the observed increase in synthesis rate (Fig. 9.10a).[117] The interaction between ruthenium loading, promoter loading, and activity on the carbon supports is, however, complex. The early studies showed that catalyst activity increases from zero in the absence of the alkali metals to a plateau at around 4 mg-atom alkali g^{-1} catalyst (Fig. 9.10b) for cesium, potassium, and sodium.[47] Rather surprisingly, a very similar effect is also found with alkali salt promoted ruthenium/carbon catalysts.[129] The data from Fig. 9.10a, normalized to 593 K using the observed activation energy of 83.6 kJ mol^{-1} and per gram of ruthenium, is compared with the results from Ref. 129 in Fig. 9.11. This shows that the intrinsic performance of the catalysts is primarily dependent on the alkali concentration. The latter situation appears to reflect the variation in the heat of adsorption of the alkalis on the carbon supports which, as can be seen from Fig. 9.9, starts to increase dramatically as the molar loading of alkali falls below around 0.07 g mol alkali per g-mol carbon.

The results in Refs. 91 and 127 (Table 9.7) also demonstrate that some alkali salts (nitrate, carbonate, hydroxide) give rise to efficiencies similar to the alkali metals as promoters, while others (chlorides)[129] are almost totally inactive, which is in marked contrast to alumina-supported catalysts where the addition of alkali salts has little promoting effect.[113] The active state of the promoter on ruthenium/carbon catalysts is unlikely to be metallic, as the high vapor pressure of the alkali metals would give rise to substantial losses under synthesis conditions. The more probable state is a $M^{+}\cdot\cdot C^{-}$ charge transfer complex with the graphite support, where the reduction of the promoter salts is driven by the high heat of formation of the carbon–alkali complex. The high heat of adsorption of the alkali metals on carbon would also suppress the alkali vapor pressure to a level where vaporization and loss from the catalyst would not occur under synthesis conditions. Support for this comes from the thermodynamics of the alkali salt reduction reactions. It can be seen from Table 9.10 that, even assuming a relatively low heat of adsorption for the alkali on the graphite, the reduction of the nitrates and carbonates is highly exothermic and will occur even at quite high water-vapor pressures.

Promotion must then take place by one of the following three routes (Fig. 9.12) as longer-range interactions will be shielded by the carbon support:

1. Promotion occurs at contact points between the ruthenium crystallite and the alkali metals adsorbed onto the graphite (the "hot ring" picture).
2. The heat of adsorption of the alkali on the ruthenium is sufficient to maintain a limited coverage in equilibrium with the alkali on the graphite.

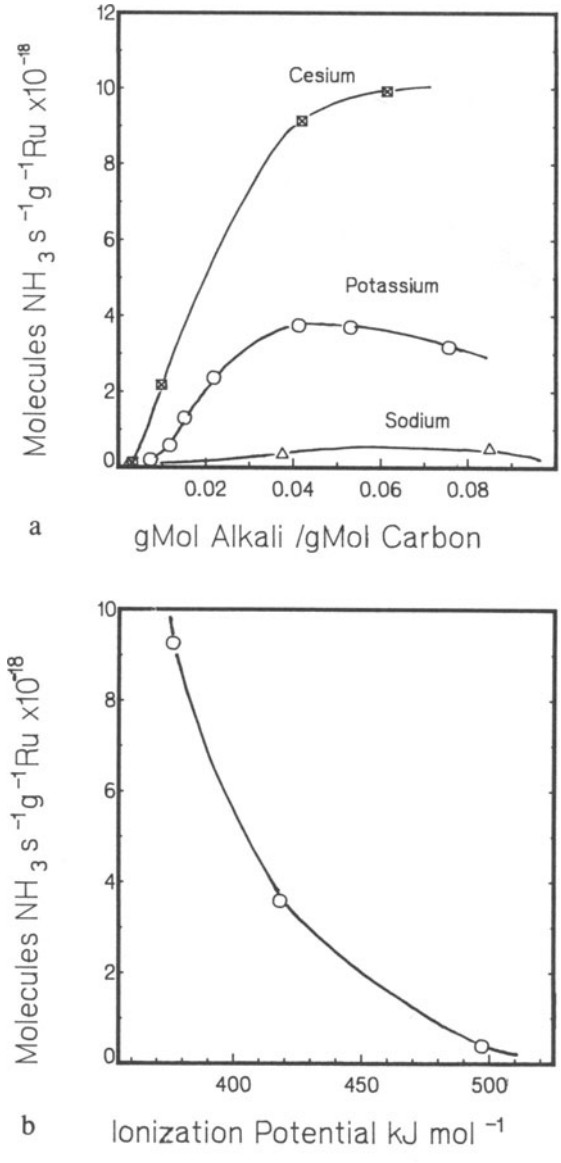

Figure 9.10. Effect of alkali metals on the activity of ruthenium-carbon catalysts: (a) Activity *vs.* alkali loading for Cs, K, and Na promoted 2.5 %wt Ru/C catalysts; (b) Activity *vs.* ionization potential for alkali promoted 2.5 %Ru/C catalysts (data from Ref. 47).

3. The alkali is stabilized by absorption into the bulk of the crystal, either as the metal or the M—Ru—N_2 complex.

It is not possible to distinguish between these options from the available data, but it is clear that the first should lead to a significant increase in activity with dispersion while (2) will be sensitive to the relative support and ruthenium surface

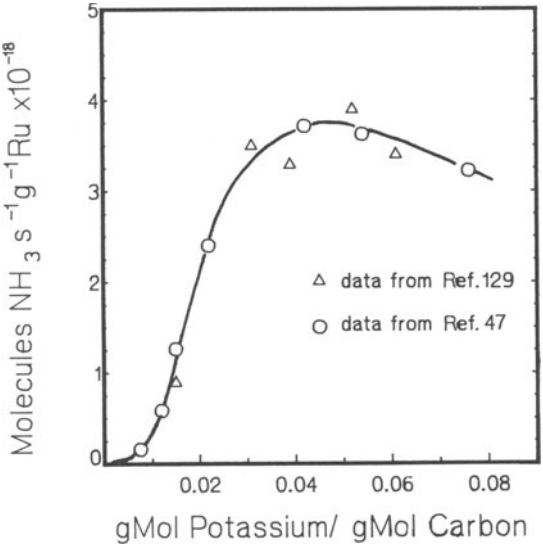

Figure 9.11. Comparison of alkali metal (Ref. 47) and alkali salt promoted (Ref. 129) ruthenium-carbon catalysts.

TABLE 9.10. Thermodynamics of Alkali Nitrate Reduction

a. *Free Energies of Reduction Reactions*

Reaction (600 K)	ΔG (kJ mol^{-1})				
	Li	Na	K	Rb	Cs
$MNO_3 + X \Rightarrow XM + NH_3 + 3H_2O$	−388	−451	−418	−389	−422
$MNO_3 \Rightarrow MOH + NH_3 + 2H_2O$	−530	−489	−447	−405	−434
$MNO_3 \Rightarrow 0.5M_2O + NH_3 + 2.5H_2O$	−456	−426	−368	−313	−342

b. *Hydrolysis of Adsorbed Alkali Metal*

$$X_s \cdot M_s + H_2O_{(g)} \cdot \Leftrightarrow X_s + MOH_{(s)} + 0.5\ H_{2\,(g)}$$

$$K_p = \frac{P_{H_2}^{0.5}}{P_{H_2O}} = \exp(-\Delta G^\circ / RT)$$

where X = transition metal or support

Temperature (K)	Equilibrium water content (ppm) (below this level the metal is favored)				
	Li	Na	K	Rb	Cs
500	2.4×10^{-6}	7.4	33	310	2,300
600	1.4×10^{-3}	370	1,800	6400	34,000
700	0.16	6000	36,000	5.6×10^4	2.4×10^5
800	5.1	4.8×10^4	3.4×10^5	2.8×10^5	5.0×10^5

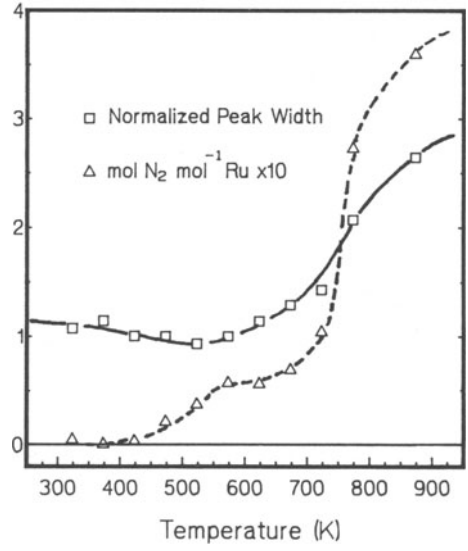

Figure 9.12. Pulsed nitrogen adsorption on potassium nitrate promoted ruthenium–carbon catalysts. □ denotes normalized peak width. This is a function of the heat of adsorption of the more weakly bonded species. The increase in peak width above 520 K indicates the onset of an activated adsorption/desorption process. Δ denotes moles of irreversibly adsorbed nitrogen. The rapid increase above 700 K is possibly due to the formation of the N_2—Ru—K bulk complex.

areas because the heats of adsorption on both are strongly coverage-dependent. Option (3) would probably be sensitive to dispersion, as smaller crystallites would favor the presence of the promoting metal close to the surface of the crystallite. The observed heats of adsorption for potassium on Ru(0001) (105 to 272 kJ mol^{-1} at 0 to 40% coverage[68]) relative to those on graphite (up to 400 kJ mol^{-1}) suggest that, if the latter explanation is correct, the surface coverage of the alkali on the ruthenium will be relatively small.

Nitrogen uptake studies on potassium-promoted Raney ruthenium have shown the presence of a form of absorbed nitrogen that correlates with the level of the potassium promoter but is 6–9 times greater than the total number of surface ruthenium atoms. Absorption of nitrogen into this state is very slow and activated[158] and subsequent desorption is negligible, even after 38 hours at 623 K in vacuo. Additional evidence has also been obtained from pulse nitrogen adsorption studies.[157] This irreversible absorption of nitrogen is significantly in excess of the number of surface ruthenium atoms once the adsorption temperature is above about 723 K (Fig. 9.13). The change in the amount of reversibly adsorbed nitrogen with temperature can be seen from the normalized peak width. For a nonactivated adsorption process this would decrease continuously with temperature, while it can be seen that it remains constant to around 623 K and then increases rapidly as the absorption of nitrogen into the bulk commences. This suggests that alkali metal on the surface of the ruthenium is responsible for strong, irreversible, nitrogen adsorption. Furthermore, it is the absorbed alkali that, by increasing the extent of reversible nitrogen adsorption, promotes the ammonia synthesis reaction.

Analysis of Raney ruthenium and alumina-supported ruthenium by IR spectroscopy has shown the presence of a band at 2020 cm^{-1} attributed to the N—N

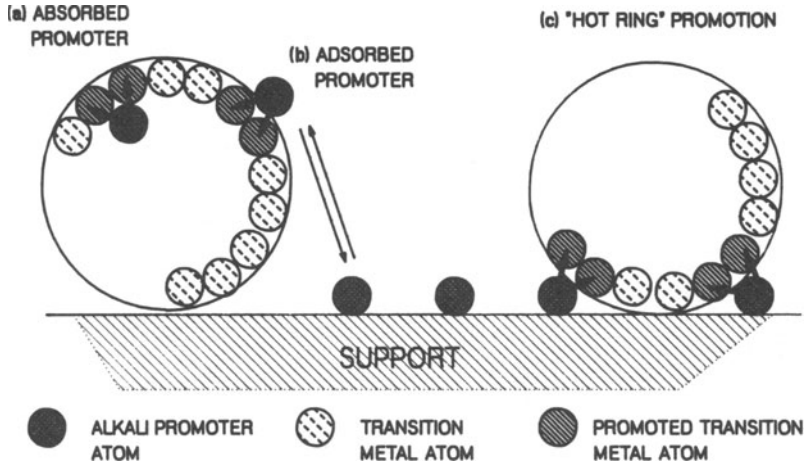

Figure 9.13. Alternative routes for alkali metal promotion. Three proposed locations for alkali metals in supported transition metal catalysts: (a) is absorbed within the transition metal crystallite, possibly as a complex with nitrogen; (b) is on the surface of the crystallite at a concentration fixed by the relative heats of adsorption on the metal and support; (c) is adsorbed on the support, but in contact with the transition metal.

stretch frequency in a compound of the form

$$K—Ru—N_2$$

Similar bands are also formed with rhenium and rhodium on alumina (Table 9.5) with the intensity of the band decreasing in the order K > Na and Ru > Rh > Re.[71] It is possible that similar complexes are formed on other active metals, such as iron, and could be responsible for the stabilization of the potassium in the commerical magnetite catalyst. The high activation energy for formation of the complex and the requirement for significant partial pressures of nitrogen may explain why it has not been observed in single-crystal studies. The complex will not, however, play any direct part in the ammonia synthesis reaction as both its rate of formation and hydrogenation are far too slow.

The effectiveness of the promoter in the nitrogen exchange reaction can be further extended by supporting ruthenium/potassium on basic oxides such as BeO, CaO, and MgO in place of the more usual acidic and neutral oxides. A steady increase in the nitrogen exchange TON with support basicity is seen but, surprisingly, there is no effect on the ammonia synthesis TON relative to that observed on the carbon-supported catalysts.[91] This may reflect a marked shift in the overall synthesis kinetics, which are strongly dependent on both the support and the promoter.

The values for the orders in hydrogen, nitrogen, and ammonia, along with the apparent activation energies and TONs, where available, are summarized in Table 9.7. The synthesis reaction on these metals is approximately first order in nitrogen, irrespective of the support and the presence or absence of promoters. In contrast, the reaction order for both hydrogen and ammonia is strongly influenced

by both. In the case of ammonia the value shifts from around −0.8 on alumina and magnesia to around −0.56 on silica[126] and approaches zero on cesium hydroxide, cesium hydroxide doped alumina,[127] celite,[128] and unsupported ruthenium.[172] These results show a tendency toward decreased inhibition by ammonia as the electronegativity of the system decreases. The converse was observed in XPS studies where the addition of chlorine to ruthenium/silica caused the ruthenium to become more electronegative, leading to an increase in the strength of the NH_3—Ru bond.[88] This would suggest that a low value for the ammonia order should be expected on carbon and alkali-promoted carbon. Some evidence for this is seen in the space velocity response.[129]

The order in hydrogen over ruthenium catalysts is even more strongly influenced by the support, changing from +0.78 on magnesia to around −1.0 on unsupported ruthenium[127] and cesium hydroxide supported ruthenium. As in the case of ammonia, extended reduction of the cesium hydroxide doped magnesia also caused a major shift from +0.43 to −0.43, which could be due to either the removal of residual chloride from the catalyst or reduction of the cesium hydroxide to metallic cesium. The absence of any pressure response on ruthenium/alkali/carbon catalysts[129] provides further evidence that hydrogen inhibition must be significant. As the order in nitrogen is usually +1.0, this must imply approximately −1.0 for the hydrogen order. There is also evidence that hydrogen inhibition is very severe on unsupported osmium.[130] It should also be remembered that the dispersion of the metal is likely to influence the reaction orders for both hydrogen and nitrogen.

The marked variations observed in the reaction orders for hydrogen and ammonia make the determination of apparent activation energies of limited value unless changes in ammonia and hydrogen partial pressure are minimized. The values in Table 9.7 do, however, show a clear trend with values of >90 kJ mol^{-1} when the order in ammonia approaches zero, and significantly lower values where the order is negative. This would imply a negative order in ammonia for all of the oxide supports and, in particular, calcia and magnesia. Even in the presence of potassium metal these effects are not entirely neutralized.

These results show the marked impact of the support and promoter on the overall kinetic response. The results in Table 9.10 also demonstrate that high TONs for ammonia synthesis are only obtained under these low-pressure (80 kPa) test conditions in the presence of potassium metal as the promoter. Addition of the alkali salts causes only a marginal improvement. The high TONs at low pressure and the apparently marked inhibition by hydrogen have led to the suggestion that alkali metal promoted ruthenium catalysts, while superior to iron at low pressures, are unlikely to be of any great benefit at higher pressures. This is not borne out by the work in Ref. 79 or 80, where alkali/alkaline earth promoted catalysts both demonstrated high activities. This can be seen from Fig. 9.1, where the alkali salt promoted catalyst demonstrates exceptionally high activity relative to a conventional magnetite catalyst at pressures up to 13,500 KPa. At approximately 0.1 s^{-1} (588 K) the turnover number is noticeably higher than found in the low-pressure, alkali metal promoted studies (maximum value 0.02), which may indicate that the low values obtained with the salt-promoted systems in Table 9.7 are due to incomplete promoter reduction under the reaction conditions employed. The

overall performance characteristics of promoted ruthenium catalysts are also shown in Fig. 9.1. The lower heat of adsorption of nitrogen and the resulting increase in the impact of hydrogen are reflected both in the pressure and the H/N ratio response, which demonstrate the marked inhibition of the ruthenium catalysts by hydrogen and the relatively limited degree of ammonia inhibition.

9.3.1.4. Summary

The platinum group metals demonstrate clearly the impact of the key parameters that influence the efficiency of ammonia synthesis catalysts: structure sensitivity, the heat of adsorption of reactants and products, and the roles of promoters and supports. The key requirement to minimize the activation energy for nitrogen dissociation limits the active metals to alkali-promoted ruthenium and osmium. Similar activities are then obtained, irrespective of the genesis of the alkali metal promoter (salt or metal), indicating that both convert to a similar state, probably a charge transfer complex of the form $Ru^- - - M^+$. There is evidence that this can be stabilized by absorption into the ruthenium ($M-Ru-N_2$ complex), adsorption on the ruthenium, or co-adsorption on the support. The promoter requirements also dictate the possible supports with carbon or basic oxides giving the best results. The promoter/support combination also influences the hydrogen and ammonia surface coverages on the metal leading to significant variations in reaction orders for ammonia and hydrogen.

The alkali-promoted, supported ruthenium catalyst is the only system currently capable of achieving volumetric efficiencies significantly higher than those attainable with magnetite. The ability to adjust the promoters and supports also offers the prospect of "tuning" the catalyst kinetics.

9.3.2. Metals Forming Weak or Unstable Nitrides

The second group of metals to be considered are those that form weak or unstable nitrides (Table 9.1) including Mn, Fe, Co, Ni, Tc, and Re. The exclusion of molybdenum and tungsten from this group is based on the premise that the metals of the current group are probably in the metallic state while the metals of groups 3 to 6 probably exist as the nitrides. All members of the current group do form nitrides, but the stabilities and heats of formation vary greatly. The nitrides of nickel and cobalt, for instance, have a very narrow range of stability under ammonia decomposition conditions (710–724 K and 723–753 K, respectively).[131] The principal characteristic of this group that distinguishes it from the platinum group metals is that all of the metals show significant synthesis activity in the absence of alkali promoters. The role of the alkali, when present in the catalyst, is still very much open to question.

9.3.2.1. Rhenium

As in the case of iron, there is clear evidence for severe structure sensitivity and conflicting evidence as to the role of promoters. Nitrogen adsorbs at low

temperatures with a high sticking probability (0.9) on the close-packed Re(0001) surface to give a single state (Re-α_1 desorbing at 120 K) and on the more open Re(1120) face to give two states (α_1 and α_2 desorbing at 129 and 155 K), in contrast to iron where only the Fe-γ state, desorbing at 95 K, shows a high sticking probability (0.70). The sticking probability for the Fe-α state on iron which desorbs at 160 K is only $10^{-2}\,s^{-1}$. Desorption occurs from the rhenium molecular states with a preexponential of $10^{11}\,s^{-1}$, very similar to that observed on both iron and other transition metals.

The nitrogen adsorption and ammonia synthesis characteristics of the different rhenium crystal faces are summarized in Table 9.11.[9] As in the case of iron the low dissociative sticking probabilities on rhenium (9×10^{-6} and 4×10^{-4} on the 0001 and 1120 faces, respectively) reflect significant dissociation activation energy barriers (14 and 6 kJ mol^{-1}, respectively). In marked contrast to these low values, polycrystalline rhenium has a dissociative sticking probability of 0.25 at low coverage decreasing to 0.025 at saturation. This indicates the presence of sites on the polycrystalline rhenium that do not exist on the single crystals studied. The ammonia synthesis rates shown in Table 9.11 mirror the dissociative sticking probabilities. The polycrystalline Re TON at 673 K ($20\,s^{-1}$) is the highest value yet observed while the Re(1120) TON at 588 K ($0.2\,s^{-1}$) is higher than that found on the best carbon-supported ruthenium catalyst. This high activity does not, however, extend to more normal operating conditions where, even in the presence of potassium, the activity is lower than iron and significantly lower than ruthenium (Table 9.9).[117] The likely reason for this is the marked inhibition of ammonia synthesis on the polycrystalline rhenium by ammonia detectable at pressures as low as 130–260 Pa[162] ammonia in 2000 KPa syngas. This may also explain the greater benefit observed from promoters under normal, as against low-pressure, synthesis conditions as they are known to inhibit ammonia adsorption (see Chapter 5).

Evidence for stable NH_x^* species on the rhenium surface has been obtained from ammonia decomposition studies over rhenium wires[132] and ammonia adsorption on polycrystalline rhenium.[24] In both cases, although ammonia adsorption was activated, there was evidence that dissociation proceeded to an NH_x^* species which decomposed, evolving nitrogen and hydrogen at above about 600 K. The presence of similar species has also been proposed on tungsten. Inhibition by

TABLE 9.11. Performance Characteristics of Rhenium Single Crystals[a]

Rhenium structure	(0001)	(1010)	(1120)	(1121)	Polycrystalline
Rate[b]			4.6	14.1	18.4
TON (s^{-1})	0.03	6.4	98	314	
Activation energy (kJ mol^{-1})			81 ± 5.9		
TON at 673 K[c]	0.01	1.8	29.7	95.3	

[a] Data are taken from Ref. 9; results at 870 K, 2000 kPa, and 3:1 H/N ratio.
[b] Rate = molecules $NH_3\,cm^{-2}\,s^{-1}$ at 870 K.
[c] TON $\times 10^4$ scaled to 673 K based on the observed E_a value of 81 kJ mol^{-1}.

ammonia becomes progressively more severe moving to the left from group 8 and is then one of the main limitations on synthesis performance.

9.3.2.2. Cobalt and Nickel

On both of these metals there is clear evidence that molecular nitrogen adsorption is structure-sensitive. Nitrogen adsorbs on supported nickel catalysts (metal crystallites between 1.5 and 7 nm) giving an IR active state (2331 cm^{-1}) which is similar to that found on several of the platinum group metals. The heat of desorption of nitrogen is strongly coverage-dependent, decreasing from about 50 to about 15 kJ mol^{-1}, while the low-coverage entropy of adsorption on the 1.5 (125 J mol^{-1}) implies immobile adsorption. Similar heats of adsorption have also been found on "channelled" Ni(110) single crystals, which show three γ molecular states with heats of desorption of <30, 25–42, and 38–59 kJ mol^{-1}, respectively. Exposure to nitrogen at 190 K leads to the formation of two atomic states, desorbing at 470 and 783 K, with heats of desorption 110 and 180 kJ mol^{-1}, that suggests a relatively low activation energy for nitrogen dissociation.[133] A similar high-temperature state, with a heat of desorption 211 kJ mol^{-1}, is also produced by ammonia decomposition.[23] The heat of desorption of ammonia, at approximately 78 kJ mol^{-1}, is considerably higher than that found for either iron or platinum (about 50 kJ mol^{-1}).

On cobalt powder the rate of ammonia synthesis decreases significantly as the structure changes from HCP to FCC when the powder is heated above 753 K. The surface area of the powder was significantly larger than the area deduced from hydrogenation of adsorbed nitrogen, implying that adsorption only occurred at specific surface sites. The synthesis activity of cobalt was, however, very poor with a TON of only 8×10^{-4} at 673 K in the higher-activity HCP state.[13] While this could be due to structure sensitivity and the very low dispersion, it is also consistent with earlier data for cobalt supported on high surface alumina which had TONs of around $7 \times 10^{-5}\ s^{-1}$. Similar TONs were also obtained for nickel/chromium oxide, although on a volume basis they were slightly less active than the unsupported cobalt.[135]

The response to hydrogen and nitrogen partial pressure of nickel and cobalt differs from that of iron. Both catalysts exhibit marked increases in synthesis rate with nitrogen partial pressure, although the effect is more marked for cobalt. Nickel also shows a significant increase in rate with hydrogen partial pressure at constant nitrogen pressure. These results can be fitted to the *Temkin* equation with values for α of 0.22 and 0.32 for cobalt and nickel, respectively, compared to 0.5 or more for iron.

9.3.2.3. Iron Alloys

There have been many attempts to improve on the activity of iron. These have been based either on magnetite systems alloyed with a second metal, such as nickel or cobalt, or on intermetallic compounds where the underlying structure of the

iron component is modified. The recently released Fe/Co alloy catalyst[5] represents the only alternative to magnetite currently available for commercial use.

9.3.2.3a. Iron/Cobalt. Most of the early studies into Fe/Co were carried out in Russia. The initial rationale was to investigate the impact of phase changes on synthesis activity. In the range 273–773 K Fe/Co alloys can exist in three forms: (1) ferrite (bcc) at up to 75% cobalt, (2) two-phase ferrite + austenite from 75–89% cobalt, and (3) either austenite (fcc) or the ε form above 89% cobalt. The transition between austenite and the ε form occurs at a temperature that depends strongly on the iron content and varies from 673 K at 100% cobalt to 293 K at 92% cobalt.[136]

One of the main difficulties in determining the effect of added components such as cobalt is that the surface area also varies. Iron/cobalt alloys can be readily prepared via coprecipitation from nitrate solutions, dehydration and ignition of molten nitrates, or oxide fusion. In the absence of alumina as a structural promoter, pure iron catalysts tend to have a very low surface area but this is increased by the addition of cobalt to a maximum of 6–7 $m^2 g^{-1}$ at around 75% cobalt (Table 9.12),[136] compared to normal areas for triply promoted magnetite of 10–15 $m^2 g^{-1}$. From synthesis results obtained at 1 bar pressure, there is no evidence of any significant changes in synthesis characteristics at the break points where phase changes occur. Evaluation of the data using the *Temkin* equation indicates a shift in the constant α from the expected 0.5 for pure iron to a lower value at >75% cobalt, although the synthesis activity changes very little with composition in the range 25–85% cobalt. The inclusion of promoters (K_2O, alumina) and preparation by normal fusion methods makes relatively little difference to the surface area of the alloy catalysts which remain in the 6.5–10 $m^2 g^{-1}$ range, in marked contrast to the pure iron which increases from <1 to >10 $m^2 g^{-1}$.[137]

From these earlier studies there was no real evidence that any significant benefit could be gained by using cobalt alloy catalysts under commercial conditions. They did, however, indicate that a decrease in ammonia inhibition might be attainable, leading to improvements in low-pressure performance. In addition, the

TABLE 9.12. Performance Characteristics of Iron/Cobalt Alloy Catalysts

Composition (% Fe)	Method of preparation	$m^2 g^{-1}$	Rate[a]	E_a (kJ mol^{-1})	Ref.
100	Fusion	0.3			136
50	Ignition of nitrates	1.9			136
25	Fusion	5.0			136
15	Fusion	4.9			136
3	Fusion	2.4			136
100	ppt	3.7	18.9	56.8	138
95	ppt	3.8	36.1	65.5	138
90		4.3	28.7	68.9	138
80		4.3	22.9	79.5	138
60		3.5	22.4	68.7	138

[a] Rate at 673 K, mol $cm^{-2} s^{-1} \times 10^{-11} \equiv$ TON $\times 10^4$ assuming 10^{15} atom cm^{-2}.

benefits were more marked for alumina-modified iron and could then be achieved at lower cobalt content. These points have subsequently been investigated in more detail and form the basis for a recent patent.[5] The primary role of cobalt in these catalysts is not to raise the activity but to increase the stability. The apparent increase in activity, by a factor of around 2 on a weight basis (Table 9.12), appears to be due primarily to the higher surface areas arising from the use of coprecipitation rather than fusion in the formation of the magnetite. A limited amount of data are available on the actual synthesis and nitrogen adsorption/exchange activity of these alloys. At low pressure (100 kPa), in contrast to the patent data, the alloys show a marked improvement when containing low levels of cobalt. The activity at 673 K increases from 18.9×10^{15} mol s^{-1} m^{-2} to 36.1×10^{15} mol s^{-1} m^{-2} in the presence of 5% cobalt, in good agreement with the earlier Russian data.[138]

Cobalt appears to function by interacting with the alumina, giving rise to a surface layer of cobalt spinels that tends to produce smaller iron crystallites on reduction. This results in a higher total surface area (35-38 m^2 g^{-1}), although only 4-6 m^2 g^{-1} of this is active surface (from CO chemisorption).[139] The presence of cobalt also significantly modifies the reduction characteristics of the coprecipitated catalysts and is itself modified by the presence of K_2O, as shown by temperature-programmed reduction.[140] Pure cobalt oxide shows a single narrow reduction peak at approximately 723 K. In the presence of alumina, a doublet forms with a sharp peak at 523 K and a higher temperature peak with a significant tail. This indicates the formation of two distinct states, the higher temperature peak presumably arising from a strong interaction with the alumina support. In the presence of K_2O both peaks are shifted down by 30 and 50 K, respectively, indicating a significant reduction in the CoO/alumina interaction. Similar effects have also been observed for precipitated iron/alumina/K_2O. This may indicate that a role of the potash component is to modify the reduction characteristics of the cobalt or iron spinels. In the presence of at least 20% cobalt Mossbauer spectroscopy shows a substantial depletion in the Fe_2O_3 phase, which was the major component in these precipitated catalysts,[139] with the simultaneous formation of mixed, more easily reducible Fe/Co spinels (the main TPR peak shifts from 1009 K to 915 K and drops still further[140] at higher cobalt levels).

Alloying also affects the rate of nitrogen adsorption. Nitrogen adsorption on the precipitated iron/alumina catalysts is slow at 673 K and 1 bar, requiring in excess of ten hours to reach equilibrium. In the presence of 5% cobalt, the initial adsorption rate is increased from 6 to 210×10^8 mol L^{-1} s^{-1} at 673 K while the coverage is increased from 10 to >19% (based on CO chemisorption). It seems improbable that this dramatic increase can be attributed to electronic promotion, as is usually invoked in the presence of alkali promoters. A more plausible explanation may be that cobalt enhances the reduction of the spinels present on the catalyst surface thereby reducing the extent of oxygen "poisoning." This is supported by the similar improvement in the specific synthesis rate, from about 15 to 22×10 mol s^{-1} m^{-2}, which can be achieved by reducing conventional magnetite catalysts at 1173 K.[92] This may also account partly for the observed differences between the high- and low-pressure synthesis results on cobalt-modified catalysts. Reduction of surface spinels should be enhanced at high pressure and

would narrow the gap between the cobalt-promoted and cobalt-free catalysts. At least part of the benefit of the cobalt may therefore derive from the more facile removal of surface oxygen at more normal reduction temperatures.

9.3.2.3b. Iron/Nickel. The reduction properties of precipitated iron catalysts are also markedly modified by the addition of nickel. As in the case of cobalt, there is a significant lowering of the main iron oxide reduction peak from around 973 K to 873 K, accompanied by the development of a second phase, presumably a spinel, that can only be reduced at temperatures in excess of 1173 K.[140] The addition of the nickel, like cobalt, changes the nitrogen adsorption characteristics of the precipitated iron, increasing the initial rate of nitrogen adsorption from 6 to 21×10^8 mol L^{-1} s^{-1} (with cobalt the increase was from 6 to 210 mol L^{-1} s^{-1}). The ammonia synthesis activity increased from 18.9 to 32.9×10^{15} mol s^{-2} at 15% nickel, a value similar to that obtained with 5% cobalt. The surface areas of the nickel/iron alloys, however, are considerably lower than either the cobalt alloys or the unmodified iron, and the activity on a unit volume basis is therefore low. There is also evidence that nickel alloys are less thermally stable than cobalt alloys. Hydrogen treatment at 1073 K, where reduction of the spinel phase should occur, leads to a reduction in area of the 20% nickel catalyst to 0.1 m^2 g^{-1} while the areas of the iron and iron/5% cobalt alloys decrease to 0.7 and 0.3 m^2 g^{-1}, respectively.[92]

9.3.2.3c. Uhde-Type Alloys (Fe-Cu, Ru, Os). The implication that surface oxygen plays a key role in lowering the activity of iron catalysts has led to the investigation of a variety of oxygen-free systems. Most notable of these are the "Uhde" catalysts based on ferrocyanides of the form

$$KFe[M(CN)_3]_2 \qquad \text{and} \qquad KFe[M(CN)_4]$$

where M may be a metal such as iron, ruthenium, osmium, or copper.[141,142] These systems have the advantage that reduction proceeds at low temperatures (around 573 K) and the reduction products are either ammonia or methane. In the low-temperature regimes, all of these systems show enhanced activity over conventional magnetite catalysts. However, the activity of the copper analog declines rapidly above around 623 K and, after a short treatment at 823 K, falls essentially to zero due to severe sintering. The ruthenium and osmium analogs show improved stability and maintain a significant activity advantage over a standard catalyst at 698 K. However, the benefit is more than outweighed by the potential cost of the catalysts, which contain between 0.5 : 1 and 1 : 1 mol ratio of either osmium or ruthenium to iron. This is clearly impractical, as it would imply the use of the order of 50 t of these rare metals per commercial converter.

9.3.2.3d. Intermetallic Compounds. Several studies over recent years have demonstrated the ability of rare-earth intermetallic compounds to dissociate hydrogen and function as effective hydrogenation catalysts. Subsequent examination of such intermetallics in ammonia synthesis[143] has demonstrated that significantly better activity per unit surface area can be obtained, relative to conventional magnetite catalysts (Table 9.13). The TONs in Table 9.13 have been scaled to

TABLE 9.13. Synthesis Activities of Rare-Earth Intermetallics

Composition	Yield at 723 K (mol NH_3 cm^{-2} s^{-1})	TON[a] (673 K)	E_a (kJ mol^{-1})
416[b]	807	27.8	85.7
$CeCo_3$	7800	4966	36.4
$CeRu_2$	6050	3563	42.6
Ce_2Co_7	4033	—	—
Ce_2Fe_{17}	3000	1980	33.4
$PrCo_5$	2690	—	—
$CeCo_5$	2460	1518	38.9
$CeCo_2$	1930	1428	24.2
$Ce_{24}Co_{11}$	1930	1185	39.3

[a] Estimated TON × 10^4 at 673 K based on observed E_a; data are taken from Ref. 143.
[b] Standard triple promoted magnetite.

673 K using the observed activation energies to allow direct comparison with the TONs for the supported ruthenium catalysts in Table 9.7. Interestingly, in the light of the results obtained with the cyanide-based catalysts in the previous section, by far the most active catalysts were obtained with the cerium intermetallics of cobalt, ruthenium, and iron. Examination of the used catalysts by XRD showed that decomposition of the intermetallic occurred under reaction conditions. The hydrogen adsorption and dissociation efficiency of the intermetallics is therefore unlikely to play any significant role in the synthesis reaction. In the case of the cerium compounds the decomposition was frequently accompanied by the formation of cerium nitride and, presumably, finely divided transition metal. The fact that high activities are only achieved with the cerium compounds may be related to the high nitrogen exchange capability of cerium nitride.[144] The precise nature of the active sites in these catalysts is not known, but the high specific activity of the iron and cobalt systems clearly indicates that the rare earth is exerting a significant influence. It is also apparent from the observed synthesis activation energies that the kinetics change markedly with the composition of the intermetallic. All of the active intermetallics exhibit exceptionally low activation energies, suggesting that they may be subject to severe ammonia inhibition. However, the surface areas of the intermetallics is very poor and, on an activity per unit volume basis, the catalysts are markedly inferior to magnetite.

9.3.2.3e. Metallic Glasses. Metallic glasses are a further category of iron alloys which are produced as ribbons by the rapid quenching of a premixed melt and have very low surface areas in the range 0.02 to 0.07 m^2 g^{-1}. The mechanics of the formation of the glasses and their very low surface areas mean that their use as practical catalysts is very unlikely. One key point to emerge from these studies is that the $Fe_{91}Zr_9$ glass has a very low activity in its initial amorphous form which then increases slowly with time (at 690 K) as the crystallinity increases,[145] taking in excess of 500 hours to reach a steady-state value of approximately 1.8×10^{-3} mol s^{-1} at 693 K, 900 KPa, 1:1 H/N. This demonstrates quite clearly the

requirement for a specific iron crystalline form in the active state. This TON is, however, extremely low compared to the results obtained with, for instance, the intermetallics which were of the order of 1 mol s^{-1} at 700 K and the Ru/C catalysts at 2 mol s^{-1} at 690 K. The FeZr alloy was also approximately an order of magnitude more active than the stabilized pure iron system on an activity per m^2 basis; the activity of the pure iron system was only around 1×10^{-4} mol s^{-1}.

The kinetic response of the iron/zirconia ribbon[146,147] was similar to that of the pure iron ribbon, indicating that the zirconia was not modifying the intrinsic properties of the iron but probably just increasing the number of active sites. The limited kinetics data set could be modeled using the expression proposed by Ozaki:

$$\frac{d\mathrm{NH_3}}{dt} = \frac{kP_{\mathrm{N_2}}}{[1 + K_1(P_{\mathrm{NH_3}}/P_{\mathrm{H_2}})^{1.5}]^2}\left(1 - \frac{K_p \cdot P^2_{\mathrm{NH_3}}}{P^3_{\mathrm{H_2}}P_{\mathrm{N_2}}}\right) \tag{9.45}$$

where nitrogen dissociation on a uniform surface is the rate-limiting step with N* as the most abundant surface species.

9.3.3. Metals Forming Stable Nitrides

The heats of formation of the more common nitrides are shown in Table 9.1. All of the transition metal nitrides are close-packed interstitial structures and in some cases a wide variety of nitrides are formed depending on the number of octahedral holes that are filled. Manganese, for instance, forms

$$\mathrm{MnN},\ \mathrm{Mn_6N_5},\ \mathrm{Mn_3N_2},\ \mathrm{Mn_2N},\ \mathrm{Mn_4N} \quad \text{through to } \mathrm{Mn_xN}$$

The type of nitride structure formed is dictated by the ratio of the metal to the nitrogen hard-sphere radius. For $R_x/R_m < 0.41$ simple systems are formed with a preference for the rock salt structure. Between 0.41 and 0.49 lattice expansion occurs, while above 0.49 extensive structural reorganization will take place. In all of these materials, the different compounds are formed by the removal of nitrogen atoms from the lattice leaving a progressively larger number of vacancies. The stable nitrides come from groups 3 to 6 of the periodic table. Of these, only uranium and molybdenum have received any significant attention as ammonia synthesis catalysts. Molybdenum, tungsten, and to a lesser extent vanadium are also the key metals in the biological fixation of nitrogen. All of the metals in this group will exist as bulk nitrides under normal synthesis conditions, but there is little data available on the adsorption characteristics of the nitrides. A further problem, particularly with metals to the left of the table, are the very high heats of formation of the oxides. This gives rise to a pronounced sensitivity to oxygenates and was the main reason that uranium was not pursued further in the early BASF studies.

All the metals in this group show a high heat of adsorption for nitrogen. Polycrystalline molybdenum gives two TPD peaks at 1050 K and 1150 K, equivalent to desorption activation energies of 255 and 285 kJ mol^{-1}, respectively. On tungsten, the heats of adsorption are even higher with single TDS peaks at 1415, 1425, and

1455 K on the W(100), (310), and (210) planes, respectively (equivalent to desorption activation energies of approximately 314 kJ mol^{-1}), although adsorption does not apparently occur on the close-packed planes such as W(110). The high heats of adsorption are associated with high dissociative sticking probabilities of between 0.24 and 0.37 at low coverages.

Hydrogen adsorbs on both Mo(110) and W(100) to give two β-states (desorption activation energies of 117 and 142, and 109 and 134 kJ mol^{-1}, respectively). In both cases the low-coverage sticking probability was approximately 0.1–0.2. As has been shown previously, the addition of cesium reduces the hydrogen uptake on both metals. On molybdenum, each cesium atom apparently "blocks" up to six molybdenum sites. On tungsten where, in the absence of cesium, there is no activation energy barrier to adsorption and dissociation, the reduction has been attributed to a decrease in sticking probability due to the presence of an activation energy barrier.

Ammonia adsorption on tungsten is distinctly different to that observed in the previous two groups. On W(211) ammonia adsorbs with a high sticking probability at room temperature. Loss of hydrogen to give NH_2^* only occurs above 600 K. Total decomposition of the NH_2^* only occurs at around 1200 K with the simultaneous evolution of both hydrogen and nitrogen, although simple evolution of adsorbed nitrogen only occurs above 1400 K. This implies both a high heat of adsorption and a high activation energy barrier for decomposition of the surface NH_2^* species.

9.3.3.1. Molybdenum

This is the most interesting member of this group as it shows synthesis activity in both biological systems and in air-sensitive Glemser compounds[148] under ambient conditions, and as the nitride under commercial synthesis conditions where it demonstrates the structure sensitivity[14] associated with the metallic catalysts discussed in the previous sections.

9.3.3.1a. Ambient Temperature Systems. Most important are the biological systems which are described in detail in Chapter 10. Briefly, these comprise two groups, those that live in association with roots (e.q., rhizobia in legumes) and those that are free living in soil (e.g., azotobacter). In both cases nitrogen fixation is catalyzed by two oxygen-sensitive proteins working together. The first, with a molecular weight of around 60,000, contains four iron and four sulfur atoms. The second, of molecular weight around 220,000, contains approximately 30 iron and 30 sulfur atoms along with two molybdenum atoms (or, more recently, two vanadium atoms[149]) which are essential for nitrogen fixation. The precise location of the molybdenum is not known, but the nitrogen is thought to be bound to the metal centre of the larger protein while the smaller protein supplies the electrons to maintain the fixation cycle. The type of structure is shown diagramatically in Fig. 9.14. The nitrogen is probably bound in a similar fashion to that found in complexes such as

$$trans - [Mo(N_2)_2(dppe)_2]$$

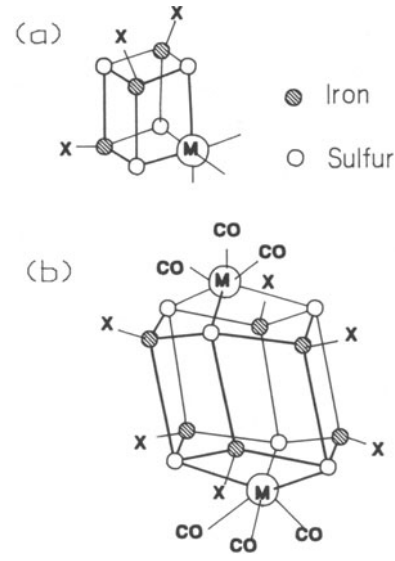

Figure 9.14. Cluster compounds relevant to nitrogenase structure: (a) M = Mo. (CN) ($C_6Cl_6O_2$) or V. (OCHN $(CH_3)_2)_3$; X = SC_2H_5 (for M = Mo) or Cl (for M = V). (b) M = Mo or W; X = p—$CH_3OC_6H_4$ or Cl. Data from Ref. 149.

where dppe is $Ph_2PCH_2CH_2PPh_2$. In nature, each fixation cycle takes approximately 1 second to produce 2 ammonia molecules (Fig. 9.15). Electrochemical reduction of the molybdenum complex[150] shows the same stoichiometry as the biological cycle:

$$N_2 + 8H^+ + 8e \Leftrightarrow 2NH_3 + H_2$$

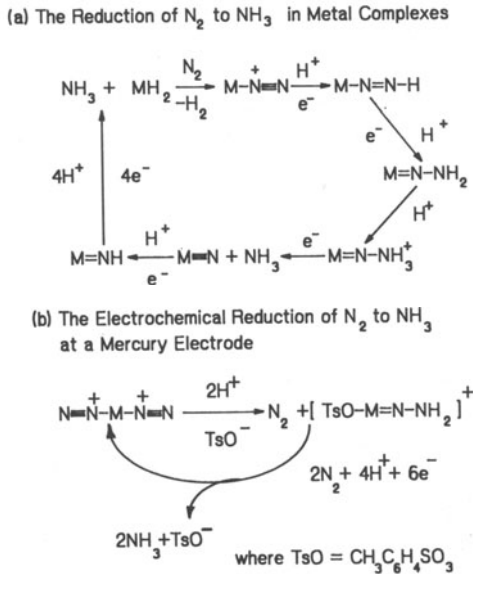

Figure 9.15. Proposed reaction pathways for the reduction of nitrogen: (a) Reduction over metal complexes; (b) Electrochemical reduction. Data from Ref. 150.

The efficiency of both the natural and electrochemical processes are limited as 1 mol of hydrogen is always produced along with the 2 moles of ammonia. The rate-limiting step in these low-temperature fixation processes has been shown to be the hydrogenation of the terminal nitrogen rather than nitrogen dissociation.

Molybdenum, in the form of Glemser compounds, is also claimed to show synthesis activity at ambient temperature. The compound is made by the reduction of MoO_3 with nascent hydrogen to give an air-sensitive compound of formula

$$H_2Mo_5O_7(OH)_8$$

containing two Mo—H bonds. The evidence for catalytic rather than stoichiometric activity using this compound is scanty, based on 3–4 times as much hydrogen in the product ammonia as was present in the original molybdenum compound. The turnover number for these compounds is, however, extremely low ($<5 \times 10^{-5}$)[151] compared to the biological systems, and also significantly lower than the TONs determined for supported ruthenium catalysts at ambient temperature.

9.3.3.1b. Molybdenum Nitride. Conversion of molybdenum to the nitride occurs under synthesis conditions. Metallic molybdenum, formed by the reduction of MoO_3, adsorbs nitrogen slowly at 673 K and rapidly at 773 K and conversion of the metal to the nitride is accelerated by the presence of hydrogen, presumably due to the formation of ammonia. MoN_2 formed in this way has a significantly higher surface area ($13.5\ m^2\ g^{-1}$) than either the oxide ($0.53\ m^2\ g^{-1}$) or metal ($5.3\ m^2\ g^{-1}$) precursors.[134] Direct conversion of the oxide to the nitride by dry ammonia has also been observed, although this requires a higher temperature.

Although there is some disagreement over the kinetics, two expressions are suggested, both consistent with nitrogen dissociation as the rate-limiting step while both also show severe inhibition by ammonia and a high surface coverage of N*:

Ref. 134
$$\frac{d\mathrm{NH_3}}{dt} = \frac{kP_{\mathrm{N_2}}}{(1 + K'P_{\mathrm{NH_3}}/P_{\mathrm{H_2}}^{1.5})^2} \tag{9.46}$$

Ref. 14
$$\frac{d\mathrm{NH_3}}{dt} = \frac{kP_{\mathrm{N_2}}}{(1 + K'P_{\mathrm{NH_3}}/P_{\mathrm{H_2}}^{0.5})^{1.36}} \tag{9.47}$$

The first is a classic Langmuir-Hinshelwood expression while the second is of the *Temkin* form with $\alpha = 0.68$. This discrepancy demonstrates the problems of establishing a kinetic model from a very limited data base. The extent of inhibition by ammonia is considerably greater than that observed with iron catalysts, and is similar to that shown by single-crystal rhenium. This implies that some improvement in the higher-pressure performance could be achieved by the addition of alkali metal promoters, as in supported rhenium catalysts. The latter study also demonstrated the marked structure sensitivity of the synthesis reaction over MoN_2, where the rate decreased by over two orders of magnitude as the particle size decreased from 63 nm to 3 nm. However, even for the largest particle size, and at very low conversions (0.5% of equilibrium) where ammonia inhibition should be minimal, the turnover number was only approximately $5 \times 10^{-4}\ s^{-1}$ at 588 K compared to 0.2 on ruthenium/carbon catalysts.

9.3.3.1c. Other Metals. Ammonia synthesis has been studied over other members of this group, but to a limited extent.[152] The early studies of Haber on uranium nitride have already been mentioned, although there is little detailed data on the physical characteristics of the catalyst. It is claimed that the kinetics are similar to iron with $\alpha = 0.5$. The activity is poor compared with standard magnetite, only achieving 3.4% ammonia in the gas phase at 810 K, 49.6 bar, and 24,750 GHSV. However, different nitrides of uranium exhibit very different synthesis rates, α-U_2N_3 being several orders of magnitude less active than $UN_{1.7}$. This is reflected in the nitrogen exchange activity, which is also very much lower on U_2N_3. The nitrogen exchange and ammonia synthesis rates on $UN_{1.7}$ (22.6 kgmol m^{-3} h^{-1} at 673 K, 10,000 kPa) are similar to those on pure iron, but significantly lower than the conventional magnetite catalyst (62.2 kgmol h^{-1} m^{-3}) under similar test conditions, although on an equivalent surface area basis the difference is smaller (the $UN_{1.7}$ had a surface area of 1.5 compared to 13 m^2 g^{-1} for the magnetite).[153]

The heat of adsorption of nitrogen on these nitrides correlates well with the observed activation energy for nitrogen exchange, indicating that there is no marked activation energy for nitrogen adsorption. The difference in the characteristics of the two nitrides can be attributed directly to the much higher heat of adsorption of nitrogen on U_2N_3 (226 kJ mol^{-1} vs 106 kJ mol^{-1}) which in turn may be attributable to the larger number of lattice vacancies. From the nitrogen exchange properties $UN_{1.7}$ would be expected to show higher synthesis activities than is actually observed. This discrepancy can be attributed to significant inhibition by hydrogen, with an order of about -0.2.[153] Cerium nitride shows a lower nitrogen exchange rate (8×10^{10} mol cm^{-2} s^{-1} at 573 K) than the $UN_{1.7}$ (10×10^{12}) as would be expected from the higher heat of adsorption of nitrogen (approximately 125 kJ mol^{-1}). This is also reflected in the synthesis activity which, at 4.5 kgmol m^{-3} h^{-1} (673 K/10,000 kPa), is considerably lower than $UN_{1.7}$ at 22.6 kgmol m^{-3} h^{-1}.[144]

A large amount of data are available for nitrogen adsorption on tungsten surfaces but very little on its catalytic properties, although *Temkin* has claimed that the kinetics are similar to iron with a value of 0.5 for α. As in the case of molybdenum, it is probable that under synthesis conditions tungsten will be present as the nitride, so that adsorption studies on the clean metal surface will be of little direct significance. Ammonia decomposition studies have shown the formation of stable MH^*/NH_2^* surface species that may imply a significant inhibition by ammonia. Manganese also shows limited synthesis activity.

9.4. CONCLUSIONS

The preceding sections have demonstrated that, irrespective of the catalyst, the rate-limiting step in the ammonia synthesis reaction is the dissociation of the nitrogen molecule and that the limiting catalyst efficiency is dictated primarily by the activation energy of the dissociation reaction. This, at first sight, is surprising given the marked differences in the heats of adsorption of nitrogen, and the adsorption activation energies. In the case of tungsten, for instance, it would appear

that in the absence of any significant dissociation activation energy, and with the high heat of adsorption of N*, hydrogenation of N* should be rate-limiting. This can be attributed to the synthesis reaction for such metals taking place on the nitride rather than the metal. The activated nature of the dissociation process on nitrides, such as those of molybdenum and cerium, is well established.

The other common factor is that molecular nitrogen adsorption is structure-sensitive, even on metals such as tungsten where the heat of N* adsorption is substantial. Extensive studies have failed to link conclusively this sensitivity with any particular surface structure. It seems to require the presence of a very "open" surface which may be linked to high index planes or the presence of surface defects such as steps, kinks, etc. In any event this manifests itself in supported catalysts as an unusual dependence on the metal crystallite size, with the optimum activity occurring in the 2 to 6 nm range.

The attainment of a high synthesis activity is linked to both of these factors. In the absence of appropriate sites, the residence time in the molecular state will be insufficient for the nitrogen to dissociate, even when the activation energy for dissociation is low. With the correct sites, dissociation is unlikely to occur when the activation energy is higher. Only when both of these conditions are satisfied will the impact of other factors such as hydrogen and ammonia inhibition, etc., have any impact on the overall kinetics. The data available have shown that these requirements are achieved only by a very limited range of metals: iron, rhenium, ruthenium, and osmium, and that within this group the potential of rhenium is limited by very strong ammonia inhibition. While it is possible that some of the nitrides of the group 5–7 metals intermediate between cerium and molybdenum may also show significant synthesis activity, it seems probable that their potential will be limited by the trend to increasing ammonia inhibition to the left of group 8.1 (Fe, Ru, and Os).

The main options for the immediate future therefore hinge around catalysts based on ruthenium, iron, and their variants (osmium is not available in sufficient quantities to make commericial exploitation feasible). The potential for ruthenium to displace iron in new plants will depend on whether the benefits it offers are sufficient to overcome the increased cost inherent in the use of a platinum group metal. In addition to their substantially higher volumetric efficiency, the promoted ruthenium catalysts also exhibit quite different kinetic characteristics. Their marked preference for operation at lower H/N ratios, the lower level of ammonia inhibition, and their excellent low-pressure performance are all well tuned to the requirements of modern synthesis plants. However, the catalysts are still sensitive to oxygen-containing contaminants and still require the extensive syngas purification systems found in current technology plants. Some further improvements in performance are probable, but it is unlikely that the ultimate level of activity will be high enough to allow plant pressures to be reduced to the pressure used in the syngas preparation stages (about 3000 kPa). Dramatic changes in plant configuration are therefore unlikely.

The limitations of magnetite-based plants are well known. Operation around 80 bar already requires large catalyst volumes; significant pressure reductions, even with more active catalysts, are highly unlikely. The catalyst is also severely inhibited

by ammonia, preventing any substantial increases in conversion per pass. While some improvements have been achieved by the use of cobalt/iron alloys, further improvements are likely to revolve primarily around increases in available surface area per unit volume of catalyst. These are unlikely to increase the activity by more than a factor of 2–3 and are unlikely to have any impact on the catalyst kinetics. As such, while changes in the converter are still likely, there is no likelihood of any significant changes in the overall plant configuration using iron-based catalysts.

REFERENCES

1. German Patent 235421 (1908).
2. F. Haber and R. Le Rossignol, *Chem. Ber.* **40**, 111 (1907).
3. A. Mittasch, *Adv. Catal.* **2**, 81 (1950).
4. Ib Dybkjaer and E. A. Gamm, *Ammonia Plant Safety* **25**, 15 (1985).
5. European Patent 174,079 (July 1985).
6. US Patent 4,163,775, British Petroleum (1979).
7. M. I. Temkin and V. Pyschev, *Zh. Fiz. Khim.* **13**(7), 851 (1939).
8. D. R. Strongin, J. Carraza, S. R. Bare, and G. Somorjai, *J. Catal.* **103**, 213 (1987).
9. M. Asscher, J. Carrazza, M. M. Khan, K. B. Lewis, and G. Somorjai, *J. Catal.* **98**, 277 (1986).
10. R. Van Hardeveld and A. Van Montfort, *Surf. Sci.* **17**, 90 (1969).
11. R. Van Hardeveld and F. Hartog, *Adv. Catal.* **22**, 75 (1972).
12. I. R. Danielson, M. J. Dresser, E. E. Donaldson, and J. Dickinson, *Surf. Sci.* **71**, 599 (1978).
13. G. Rambeau, A. Jorti, and H. Amoriglio, *J. Catal.* **94**, 155 (1986).
14. L. Volpe and M. Boudart, *J. Phys. Chem.* **90**, 4874 (1986).
15. L. J. Whitman, C. E. Bartosch, and W. Ho, *J. Chem. Phys.* **86**, 3688 (1986).
16. M. I. Temkin and S. Kiperman, *Zh. Fiz. Chem.* **21**(8), 927 (1947).
17. P. Stolze and J. K. Norskov, *Phys. Rev. Lett.* **55**, 2502 (1985).
18. E. G. Boreskova, V. L. Kuchaev, and M. I. Temkin, *Kinet. Katal.* **25**(1), 112 (1984).
19. R. McMurray, private communication.
20. W. Tsai, J. J. Vajo, and W. H. Weinberg, *J. Phys. Chem.* **89**, 4926 (1985).
21. J. J. Vajo, W. Tsai, and W. H. Weinberg, *J. Phys. Chem.* **90**, 6531 (1986).
22. J. J. Vajo, W. Tsai, and W. H. Weinberg, *J. Phys. Chem.* **89**, 3243 (1985).
23. R. W. McCabe, *J. Catal.* **79**, 445 (1983).
24. Y. Fukuda, F. Honda, and J. W. Rabalais, *Surf. Sci.* **99**, 289 (1980).
25. J. R. Anderson (ed), *Chemisorption and Reaction on Metallic Films*, Academic Press, New York (1971).
26. F. Bozso, G. Ertl, M. Grunze, and M. Weiss, *J. Catal.* **49**, 18 (1977).
27. M. Grosman and D. G. Loffler, *J. Catal.* **80**, 188 (1983).
28. C. Egawa, S. Naito, and K. Tamaru, *Surf. Sci.* **138**, 279 (1984).
29. K. Tanaka and K. Tamaru, *J. Catal.* **2**, 366 (1963).
30. E. Miyazaki, *J. Catal.* **65**, 84 (1980).
31. R. P. Messmer, *Surf. Sci.* **158**, 40 (1985).
32. P. Nordlander, S. Holloway, and J. K. Norskov, *Surf. Sci.* **149**, 59 (1985).
33. E. G. Seeabauer, A. C. F. Kong, and L. D. Schmidt, *Surf. Sci.* **193**, 417 (1988).
34. R. Brill, P. Jiru, and G. Schulz, *Z. Phys. Chem.* **64**, 215 (1969).
35. D. D. Eley and P. R. Norton, *Proc. R. Soc. London, Ser. A* **314**, 301 (1970).
36. D. A. King, *Surf. Sci.* **47**, 384 (1975).
37. K. Christmann, G. Ertl, and T. Pignet, *Surf. Sci.* **54**, 365 (1976).
38. B. Lang, R. W. Joyner, and G. Somorjai, *Surf. Sci.* **30**, 454 (1972).

39. R. W. McCabe and L. D. Schmidt, *Proceedings, 7th International Vacuum Congress, Vienna,* 1201 (1977).
40. P. R. Norton, J. A. Davies, and T. E. Jackman, *Surf. Sci.* **121**, 103 (1982).
41. M. J. Grunze, J. Fuhler, M. Neumann, C. R. Brundle, D. J. Auerbac, and R. J. Behm, *Surf. Sci.* **139**, 109 (1984).
42. G. Wedler and D. Borgman, *J. Catal.* **44**, 139 (1976).
43. P. Chou and M. A. Vannice, *J. Catal.* **104**, 1 (1987).
44. P. Chou and A. M. Vannice, *J. Catal.* **104**, 17 (1987).
45. J. R. Anderson, K. Foger, and R. J. Breakspere, *J. Catal.* **57**, 458 (1979).
46. M. Boudart, A. Delbouille, J. A. Dumescic, S. Khammoumma, and H. Topsoe, *J. Catal.* **37**, 486 (1975).
47. K. Aika, H. Hori, and A. Ozaki, *J. Catal.* **27**, 424 (1972).
48. J. A. Dumesic, H. Topsoe, and M. Boudart, *J. Catal.* **37**, 513 (1975).
49. F. Bozso, G. Ertl, and M. Weiss, *J. Catal.* **50**, 519 (1977).
50. G. Ertl, S. B. Lee, and M. Weiss, *Surf. Sci.* **114**, 515 (1982).
51. R. Van Hardeveld and A. Van Montfoort, *Surf. Sci.* **4**, 396 (1966).
52. D. E. Ibbotson, T. S. Wittrig, and H. H. Weinberg, *Surf. Sci.* **110**, 313 (1981).
53. P. W. Tamm and L. D. Schmidt, *Surf. Sci.* **26**, 286 (1971).
54. D. L. Adams and L. H. Germer, *Surf. Sci.* **27**, 21 (1971).
55. S. P. Singh-Boparai, M. Bowker, and D. A. King, *Surf. Sci.* **53**, 55 (1975).
56. J. A. Scharwz, *Surf. Sci.* **87** 525 (1979).
57. G. Ertl, in: *Nature of the Surface Chemical Bond, Conf. Proc. Natl. Surf. Chem. Bond* (T. Rhodin and G. Ertl, eds.), North-Holland, Amsterdam (1979).
58. W. Tsai and W. H. Weinberg, *J. Phys. Chem.* **91**, 5302 (1987).
59. G. Haase and M. Aascher, *Surf. Sci.* **191**, 75 (1987).
60. M. Mahning and L. D. Schmidt, *Z. Phys. Chem.* **80**, 71 (1971).
61. J. Lapujoulade and K. S. Neil, *C. R. Acad. Sci. Paris, Ser. C* **274**, 2125 (1972).
62. R. R. Rye, B. D. Barford, and P. G. Cartier, *J. Chem. Phys.* **59**, 1693 (1973).
63. K. Christmann, O. Schober, G. Ertl, and J. Neumann, *J. Chem. Phys.* **60**, 4528 (1974).
64. H. Conrad, G. Ertl, and E. E. Latta, *Surf. Sci.* **41**, 435 (1974).
65. R. J. Behm, K. Christmann, and G. Ertl, *Surf. Sci.* **99**, 320 (1980).
66. K. Jacobi, F. S. Jensen, T. N. Rhodin, and R. P. Merrill, *Surf. Sci.* **108**, 397 (1981).
67. R. L. Gerlach and T. N. Rhodin, *Surf. Sci.* **19**, 403 (1970).
68. R. A. De Paola, J. Hrbek, and F. M. Hoffman, *J. Chem. Phys.* **82**, 2484 (1985).
69. K. Markert and K. Wandelt, *Surf. Sci.* **159**, 24 (1985).
70. G. Pirug, G. Broden, and H. P. Bonzel, *Surf. Sci.* **94**, 323 (1980).
71. M. Ohkita, A. Aika, K. Urabe, and A. Ozaki, *J. Catal.* **44**, 460 (1976).
72. C. C. A. Riley, private communication.
73. R. W. Joyner, J. B. Pendry, K. Saldin, and S. R. Tennison, *Surf. Sci.* **138**, 84 (1984).
74. J. Lee, C. P. Hanrahan, J. Arias, R. M. Martin, and H. Metiu, *Surf. Sci.* **161**, L543 (1985).
75. D. R. Strongin, S. R. Bare, and G. Somorjai, *J. Catal.* **103**, 289 (1987).
76. J. J. McCarroll, private communication.
77. C. A. Clausen and M. L. Good, *J. Catal.* **46**, 58 (1977).
78. M. Shelef and H. S. Gandhi, *Platinum Met. Rev.* **18**, 2 (1974).
79. European Patent 120,655, British Petroleum (1984).
80. US patent 4,142,993, Research Council of Alberta (1979).
81. M. Bowker, I. B. Parker, and K. C. Waugh, *Appl. Catal.* **14**, 101 (1985).
82. P. W. Selwood, *Adv. Catal.* **3**, 28 (1951).
83. F. Solymosi, *Catal. Rev.* **1** (2), 233 (1967).
84. G.-M. Schwab, *Adv. Catal.* **27**, 1 (1978).
85. J. Z. Shyu, J. G. Goodwin, and D. M. Hercules, *J. Phys. Chem.* **91**, 4983 (1985).
86. M. Grunze, M. Golze, W. Hirchswald, H. J. Freund, H. Pulm, U. Seip, and W. Tsai, *Phys. Rev. Lett.* **53**, 850 (1984).
87. R. A. Shigeishi and D. A. King, *Surf. Sci.* **62**, 379 (1977).

88. W. K. Shiflett and J. A. Dumescic, *Ind. Eng. Chem., Fundam.* **20**, 246 (1981).
89. T. Narita, H. Miura, K. Sugiyama, and T. Matsuda, *J. Catal.* **103**, 492 (1987).
90. I. Sushumna and E. Ruckenstein, *J. Catal.* **94**, 239 (1985).
91. K. Aika, A. Ohya, A. Ozaki, Y. Inoue, and I. Yasumori, *J. Catal.* **92**, 305 (1985).
92. P. J. Smith, D. W. Taylor, D. A. Dowden, C. Kemball, and D. Taylor, *Appl. Catal.* **3**, 303 (1982).
93. S. J. Tauster and S. C. Fung, *J. Catal.* **55**, 29 (1978).
94. S. J. Tauster, S. C. Fung, and R. L. Garten, *J. Am. Chem. Soc.* **100**, 170 (1978).
95. R. T. K. Baker, E. B. Prestridge, and R. L. Garten, *J. Catal.* **59**, 390 (1979).
96. A. Nobile, PhD Thesis, University of South Carolina (1986).
97. Japanese Patent 44509 (1976), Japanese Gasoline Company.
98. F. Salzano and S. Aronson, *J. Chem. Phys.* **45**, 2221 (1966).
99. W. Jones, J. M. Thomas, T. B. Tennakoon, R. Schogl, and P. Diddams, in: *Catalyst Characterisation Science*, p. 472, Aun. Chem. Soc. (1985).
100. S. Parkash, S. K. Chakrabartty, and J. G. Hooley, *Carbon* **16**, 231 (1978).
101. E. E. Anderson, G. L. Wessman, and L. R. Zumwalt, *Nucl. Sci. Eng.* **12**, 106 (1962).
102. C. E. Milstead, A. B. Riedinger, and L. R. Zumwalt, *Carbon* **4**, 99 (1966).
103. B. L. Holian, in: *Conference on Computer Simulation for Materials Applications, Caithersburg, Maryland*, Los Alamos Report LA-UR-76-854 (April 1976).
104. F. F. Gadallah, R. M. Elofson, P. Mohammed, and T. Painter, in: *Preparation of Catalysts III* (G. Poncelet, P. Grange, and P. A. Jacobs, eds.), p. 409, Elsevier Science, Amsterdam (1983).
105. UK Patent 1,468,441 (1977).
106. C. N. Satterfield and T. Sherwood, *Role of Diffusion in Catalysis*, Addison-Wesley, Reading, Mass. (1963).
107. G. W. Roberts and C. N. Satterfield, *Ind. Eng. Chem., Fundam.* **4**, 288 (1965).
108. H. So-Ping Kao and C. N. Satterfield, *Ind. Eng. Chem., Fundam.* **7**, 665 (1968).
109. C. Bokhoven and W. van Raayen, *J. Phys. Chem.* **58**, 471 (1954).
110. D. C. Dyson and J. M. Simon, *Ind. Eng. Chem., Fundam.* **7**, 605 (1968).
111. F. Haber, *Z. Electrochem.* **16**, 244 (1910).
112. M. Wilf and P. T. Dawson, *Surf. Sci.* **60**, 561 (1976).
113. K. Aika, K. Shimazaki, Y. Hattori, A. Ohya, S. Oshima, K. Shiriota, and A. Ozaki, *J. Catal.* **92**, 296 (1985).
114. B. E. Nieuwenhuys, D. I. Hagen, G. Rovida, and G. A. Samorjai, *Surf. Sci.* **59**, 155 (1976).
115. P. D. Reed, C. M. Comrie, and R. M. Lambert, *Surf. Sci.* **72**, 423 (1978).
116. Y. Ogaka, K. Aika, and T. Onishi, *Surf. Sci.* **140**, 285 (1984).
117. A. Ozaki, *Acc. Chem. Res.* **14**, 16 (1981).
118. P. Feulner and D. Menzel, *Surf. Sci.* **154**, 465 (1985).
119. W. Tsai, PhD Thesis, California Institute of Technology (1987).
120. J. H. Sinfelt, Y. L. Lam, J. A. Cusumano, and A. E. Barnett, *J. Catal.* **42**, 227 (1976).
121. G. Marcelin, J. E. Lester, and S. F. Mitchell, *J. Catal.* **102**, 240 (1986).
122. D. G. Blackmond, J. A. Williams, S. Kesraoui, and D. S. Blazewick, *J. Catal.* **101**, 496 (1986).
123. K. Lu and B. J. Tatarchuk, *J. Catal.* **106**, 166 (1987).
124. K. C. Taylor, *J. Catal.* **38**, 299 (1975).
125. S. Parkash, F. F. Gadallah, and S. K. Chakraberty, *Carbon* **17**, 403 (1979).
126. R. Holzman, W. R. Shiflett, and J. A. Dumesic, *J. Catal.* **62**, 173 (1980).
127. K. Aika, M. Kumasaka, T. Oma, O. Kato, H. Matsuda, N. Watanabe, K. Yamazaki, A. Ozaki, and T. Onishi, *Appl. Catal.* **28**, 57 (1986).
128. K. Aika and A. Ozaki, *J. Catal.* **16**, 97 (1970).
129. A. I. Foster, P. J. James, J. J. McCarroll, and S. R. Tennison, US Patent 4163775 (Aug. 1979).
130. G. Rambeau, A. Jorti, and H. Amoriglio, *Appl. Catal.* **3**, 273 (1982).
131. C. R. Lotz and F. Sebba, *Trans. Faraday Soc.* **53**, 1246 (1967).
132. R. P. Gasser and D. P. Green, *Surf. Sci.* **82**, 582 (1979).
133. M. Grunze, R. K. Driscoll, G. N. Burland, J. C. L. Cornish, and J. Pritchard, *Surf. Sci.* **89**, 381 (1979).

134. K. Aika and A. Ozaki, *J. Catal.* **14**, 311 (1969).
135. N. M. Morozov, E. N. Shapatina, L. I. Luk'yanova, and M. I. Temkin, *Kinet. Katal.* **7**(4), 688 (1977).
136. N. Morozov, L. I. Lukyanova, M. I. Temkin, and L. Y. Karpov, *Kinet. Katal.* **6**(1), 82 (1963).
137. Y. N. Artyukh, M. T. Rusov, and N. A. Boldyreva, *Kinet Katal.* **8**(6), 114 (1967).
138. D. W. Taylor, P. J. Smith, D. A. Dowden, C. Kemball, and D. A. Whan, *Appl. Catal.* **3**, 161 (1982).
139. M. J. Tricker, P. P. Vaishnava, and D. A. Whan, *Appl. Catal.* **3**, 283 (1982).
140. R. Brown, M. E. Cooper, and D. A. Whan, *Appl. Catal.* **3**, 177 (1982).
141. F. Uhde, German Patent 493, 793 (1925).
142. Zh. I. Tkachenko, L. I. Palenko, and Yu. A. Lyubchenko, *J. Appl. Chem. USSR* **3**, 1540 (1980).
143. T. Takeshita, W. E. Wallace, and R. S. Craig, *J. Catal.* **44**, 236 (1976).
144. G. I. Panov and A. S. Kharatinov, *React. Kinet, Lett.* **29**, 267 (1985).
145. E. Armbruster, A. Baiker, H. Baris, H. Guntherodt, R. Scholgl, and B. Walz, *J. Chem. Soc., Chem. Commun.*, 2993 (1986).
146. A. Baiker, R. Schlogl, E. Armbruster, and H. J. Guntherod, *J. Catal.* **107**, 221 (1987).
147. A. Baiker, H. Baris, and R. Scholgl, *J. Catal.* **108**, 469 (1987).
148. O. Glemser, *Naturwissenschaften* **37**, 539 (1950).
149. D. J. Lowe, B. E. Smith, and R. N. F. Thorneley, in: *Metalloproteins*, Part 1 (P. M. Harrison, ed.), p. 207, Verlag Chimie (1985).
150. C. J. Pickett and J. Talarmin, *Nature* (London) **317**, 652 (1985).
151. O. Glemser, German Patent 956674 (1957).
152. M. Temkin and S. Kiperman, *Zh. Fiz. Chem.* **21**(8), 927 (1947).
153. G. I. Panov, G. K. Boreskov, A. S. Kharatinov, E. M. Moroz, and V. I. Sobolev, *Kinet Katal.* **25**(1), 123 (1984).
154. L. Surnev, G. Rangelov, and M. Kiskinova, *Surf. Sci.* **179**, 283 (1987).
155. D. L. Adams and L. H. Germer, *Surf. Sci.* **27**, 21 (1971).
156. T. A. Delchar and G. Erlich, *J. Chem. Phys.* **42**, 2686 (1965).
157. A. C. Collins, private communication.
158. A. Ohya, K. Urabe, A. Aika, and A. Ozaki, *J. Catal.* **58**, 313 (1979).
159. N. D. Spencer and G. Somorjai, *J. Catal.* **78**, 142 (1982).
160. K. Aika, J. Yamaguchi, and A. Ozaki, *Chem. Lett.*, 161 (1973).
161. R. Van Hardeveld, and F. Hartog, *Surf. Sci.* **15**, 189 (1969).
162. M. Aascher, J. Carraza, M. M. Khan, K. B. Lewis, and G. A. Somorjai, *J. Catal.* **98**, 227 (1986).
163. M. Grunze, F. Bozso, G. Ertl, and M. Weiss, *Appl. Surf. Sci.* **1**, 241 (1978).
164. P. Stolze, J. K. Norskov, and Nordita, AIChE Annual Mtg, Miami, paper 151 (Nov. 1986).
165. N. D. Lang and W. Kohn, *Phys. Rev. B* **1**, 4555 (1970).
166. M. Domke, G. Jahnig, and M. Dreschler, *Surf. Sci.* **42**, 389 (1974).
167. K. F. Wojchiechowski, *Surf. Sci.* **55**, 246 (1976).
168. D. G. Loffler and L. D. Schmidt, *J. Catal.* **41**, 440 (1976).
169. S. J. Lombardo and A. T. Bell, *Surf. Sci.* **206**, 101 (1988).
170. R. Duszak and R. H. Prince, *Surf. Sci.* **205**, 143 (1988).
171. E. L. Garfunkel, M. H. Farias, and G. A. Somorjai, *J. Am. Chem. Soc.* **107**, 349 (1985).
172. G. Rambeau and H. Amariglio, *J. Catal.* **72**, 1 (1981).

10

WHAT DOES THE FUTURE HOLD?

A Survey of Possible Technical Developments

G. J. Leigh

10.1. INTRODUCTION

Forecasting technical developments is not something to be undertaken lightly. In every case, there is any number of unforeseeable developments which can cause the forecaster to be completely incorrect. Consequently, this chapter is not intended to be an exercise in inexpert crystal gazing. Rather, it will be an attempt to assess the direction and pace of developments which are currently in train, and to suggest the impact they may have, all other things (political and social, especially) being equal.

It is not easy to assess accurately the total world production of fixed nitrogen but an amount of about 60×10^6 tonnes is probably not too far from reality. What is clear is that production patterns are changing and that there is a significant excess of capacity for ammonia production in Western Europe and the United States. According to the *Fertilizer Review*, 1987, in six years in the early 1980s, 9 million tonnes of nitrogen capacity were closed down. The most detailed production statistics to hand are from the United States.[1] These show that ammonia production has fluctuated quite widely in recent years, and it is tempting to see ammonia production as a weathervane of economic activity or even as a predictor (Table 10.1). What is clear is that the overall production in the United States has fallen considerably from its peaks of 1980 and 1985 and, at the same time, the United States has become a significant importer of fixed nitrogen fertilizer. In the meantime nitrogen capacity in the Third World has undoubtedly increased. How long these trends will continue is a matter of speculation.

G. J. Leigh • AFRC Institute of Plant Science Research, Nitrogen Fixation Laboratory, University of Sussex, Brighton BN1 9RQ, England.

TABLE 10.1. Anhydrous Ammonia Production in Various Countries in Recent Years (Thousands of Tons)[1]

	1987	1986	1985	1984	1983	1982
USA	16,161	14,005	17,319	16,692	14,072	15,801
USSR	—	19,590	18,232	17,677	16,904	14,605
Mexico	2121	1949	2261	2156	2355	—
Japan	1784	1794	1981	2021	1881	—

The excess of capacity in the Western World is linked to the fall in agricultural production provoked by the agricultural surpluses, especially of cereals. In fact forecasts of fertilizer consumption have often been overestimated, but even so, world fertilizer consumption is expected to have fallen by more than 10% in the last five years.[2] It is ironic that the application of such fertilizers would undoubtedly increase food production in many Third World countries, could the farmers there pay for it. However, another factor influencing the drop in the use of inorganic nitrogen in Western economies may be the fears about nitrate pollution. It is true the nitrogen in groundwaters is becoming a problem in some countries, but it is a misconception to believe that the use of "organic" nitrogen fertilizers will solve this problem. Indeed, it is now known that nitrate runoff is at its greatest in the UK in fall and early winter when the mineralization of organonitrogen compounds is still rapid and when plants are not taking up that nitrogen for further growth. This is true whether "organic" or "inorganic" nitrogen is used as fertilizer. In addition, nitrate levels in groundwaters would not be expected to change rapidly even if nitrogen application were drastically reduced.[3] This kind of problem is more likely to be solved in many cases by management techniques rather than by reducing the nitrogen inputs necessary to obtain economic yields, and for this a better understanding of the whole nitrogen cycle is required. Future demand for fixed nitrogen fertilizer is likely to depend on many factors, but it is unlikely that an intensive and widespread agriculture using low "inorganic" nitrogen inputs will develop in the near future.

The discussion which follows is divided into three parts: (1) impact of work on biological nitrogen fixation; (2) development of new processes; and (3) developments of current or recent industrial procedures. It is a matter of some doubt whether some or any of these areas will change as proposed below. It is also possible that some will have application only in certain limited circumstances. For example, a peasant-based agriculture on small plots may not be affected very much by changes in the technology arising from precipitated catalysts. The reader should be aware that his own evaluation of the development described below is at least as valid as that of the writer.

10.2. RESEARCH ON NITROGEN FIXATION PROCESSES

10.2.1. Impact of the Work on Biological Nitrogen Fixation

Research on biological nitrogen fixation is just over 100 years old.[4] In 1888

Hellriegel and Wilfarth finally established definitively that leguminous plants can utilize atmospheric nitrogen for growth. Ever since then, scientists have puzzled about how this apparently energy-intensive process (ca 500 kJ are used per mole nitrogen fixed, see below) can be undertaken using air, water, and light energy as the feedstocks. This section contains a summary of our current understanding, but the references cited are solely to provide an introduction to the appropriate literature and are selective rather than comprehensive.

At the turn of the century, of course, it was discovered how to synthesize ammonia from dinitrogen industrially. Currently, the common agricultural practice of broadcasting nitrogen-containing fertilizers is being questioned ever more pointedly because of doubts that the nitrate content of groundwaters is acceptable. The pressure to find acceptable biological ways to supply the large amounts of fixed nitrogen to ensure the high yields of the Western agricultural systems is growing. This leaves us confronted with a dilemma, because the supply of fixed nitrogen is generally the limiting factor in the productivity of agriculture, at least in the United Kingdom.[5]

All the known biological nitrogen-fixing processes are carried out by microorganisms. There are no known nitrogen-fixing plants. To answer the question: "Can we design a nitrogen-fixing plant, such as a wheat, which could fix enough nitrogen to maintain current yields without the nitrate runoff associated with broadcasting nitrogenous fertilizers?" requires answers to an enormous variety of subquestions, some of which are still not defined or definable. However, some of them are these: would it be preferable to fix nitrogen in the leaves where energy is available or in the roots, to which carbohydrate needs to be transported?; if in the leaves, how can one circumvent the problem of molecular oxygen generated by photosynthesis in proximity to the oxygen-sensitive nitrogenase?; and will the gains from producing nitrogen for protein synthesis be offset by loss in yield arising from a deficiency of energy available for growth? The following resumé of the current state of knowledge will show to what extent such questions still remain to be answered.

In 1930, Bortels[6] showed that the nitrogen-fixing systems in *Azotobacter* with which he was working required molybdenum. At the same time, he suggested that vanadium could also support nitrogen fixation, but this observation has been generally ignored. Since 1930 it has become an article of faith that molybdenum is at the active site of nitrogenase, and research has shown that all nitrogenases are very similar.[7] Only in the last two years has it become clear that there is a molybdenum-free vanadium-based nitrogenase,[8] and furthermore there is now firm evidence for a third variety, based neither on molybdenum nor on vanadium.[9] It is tempting to suggest that this variety is iron-based, but definitive evidence is lacking. It is possible that since 1930 biologists have unconsciously selected systems for study which contain molybdenum to the exclusion of any variants. Consequently, the significance of the alternative nitrogenases in Nature cannot yet be assessed. If they are important, the magnitude and significance of, and the long-term implications for, biological nitrogen fixation will have to be reassessed.

Be that as it may, vanadium nitrogenase seems to be very similar in many ways to the classical molybdenum nitrogenase. They both consist of two air-sensitive proteins, a larger one of molecular weight ca 260,000 and a smaller one

of molecular weight ca 60,000. The smaller protein, which contains an Fe_4S_4 cluster, is a specific electron transferase to the larger, which contains the site at which molecular nitrogen is bound and reduced. The larger protein can be broken down to yield a cofactor containing one molybdenum or vanadium atom, about six iron atoms, and four sulfide sulfur atoms, which seems to give rise to the active site. In all, the larger protein contains a maximum of two molybdenum or vanadium atoms, ca 24 iron atoms, and an equivalent amount of inorganic sulfide. The structure is uncertain, although EXAFS studies have allowed a series of educated guesses, which have achieved a rough consensus. Cubane-type metal–sulfur clusters with molybdenum or vanadium atoms in one corner and three iron and four sulfur atoms at each of the others would seem to be implicated.[10]

In the molybdenum systems, the smaller protein transfers eight electrons in eight separate steps to the larger in order to complete one catalytic cycle. This gives the stoichiometry shown in Eq. (10.1):

$$N_2 + 8H^+ + 8e \rightarrow 2NH_3 + H_2 \tag{10.1}$$

The "waste" of two electrons in the generation of molecular hydrogen seems unavoidable, even *in vivo*, though some organisms possess hydrogenases which can recycle some of the dihydrogen:

$$H_2 \rightarrow 2H^+ + 2e \tag{10.2}$$

Each electron transfer requires the hydrolysis of two molecules of ATP, so that one complete cycle consumes 16 ATP molecules which is equivalent to the loss of about 488 kJ. On this basis, biological nitrogen fixation is considered to be an energy-intensive process and, indeed, biological systems possess regulatory mechanisms which prevent even the synthesis of nitrogenase if there is an adequate supply of fixed nitrogen. This is presumably to conserve energy. Other regulatory systems prevent oxygen damage, for example, by stopping nitrogenase synthesis in aerobes if the oxygen tension within the cell rises above a certain critical value.[11]

A mechanism for the mode of action of molybdenum nitrogenase has been established by stopped-flow presteady-state studies, and is represented in Fig. 10.1. This model was obtained by fitting the curves obtained for the rates of, for example, hydrogen production and ammonia formation, upon mixing the nitrogenase proteins, reducing agent, and ATP in the stopped-flow apparatus. These rates refer to the functioning nitrogenase as it commences to turn over and eventually reaches the steady state. The analysis was based upon the assumption that the complete nitrogenase cycle involves eight stages with a common rate-determining step, the transfer of an electron from the smaller nitrogenase protein to the larger. Each electron transfer involves association and dissociation of a complex formed between the two nitrogenase proteins. Figure 10.1 also shows the stages in the cycle at which the chemical transformations indicated are believed to occur, and also other proposed features of the mechanism, such as the participation of metal hydrides. For a fuller discussion, the reader is referred to the original literature.[12]

It is believed that all molybdenum nitrogenases behave in this way. For vanadium-based nitrogenases, little has yet been established unambiguously,

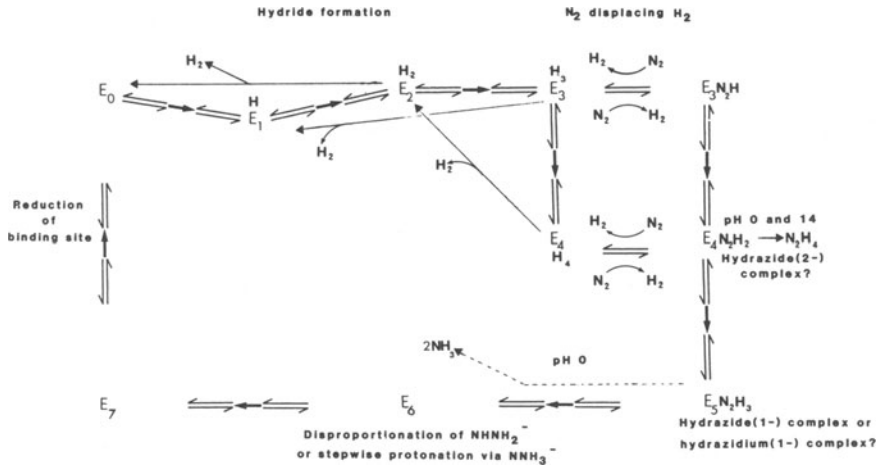

Figure 10.1. A model for the functioning of molybdenum nitrogenase based on stopped-flow kinetic studies.[12] The chemical steps suggested to correspond to the various stages of the cycle are also shown.

though the stoichiometry of the catalytic cycle appears to be different. Currently, experiments show that only 50% of the electrons are used for dinitrogen reduction and the remaining 50% generate dihydrogen, though this [see Eq. (10.3)] has yet to be proved conclusively.

$$N_2 + 12H^+ + 12e \rightarrow 2NH_3 + 3H_2 \qquad (10.3)$$

The genetic control of these complex transformations has largely been unravelled in the organism *Klebsiella pneumoniae*, which possesses a cluster of at least 20 genes which control the synthesis and function of nitrogenase. A current gene map is displayed in Fig. 10.2. The alphabetical designations of these *nif* genes (Q, B, A, L, etc.) in the map represent an international consensus. The letters have no significance with respect to the function of any given gene. There are also at least three regulatory genes (*ntr* genes) and conceivably others.[13]

In other organisms, the arrangements and numbers of copies of these genes are different from those in *Klebsiella*. Nevertheless the genes involved appear to be very similar and, furthermore, both the gene products and their functions would also seem to be similar, even for symbiotic organisms such as *Rhizobia*, for which additional genes such as fixation (*fix*) and nodulation (*nod*) are required.[14] Clearly the situation is complex. The vanadium system is controlled by genes, some of which are common with those of the molybdenum systems and some of which are similar to the molybdenum genes. Molybdenum inhibits formation of the vanadium nitrogenase, implying some kind of close interaction of the two nitrogenase control systems.

Our genetic understanding is developing rapidly and the interpretations change all the time. However, it is far from clear whether the complex of genes responsible

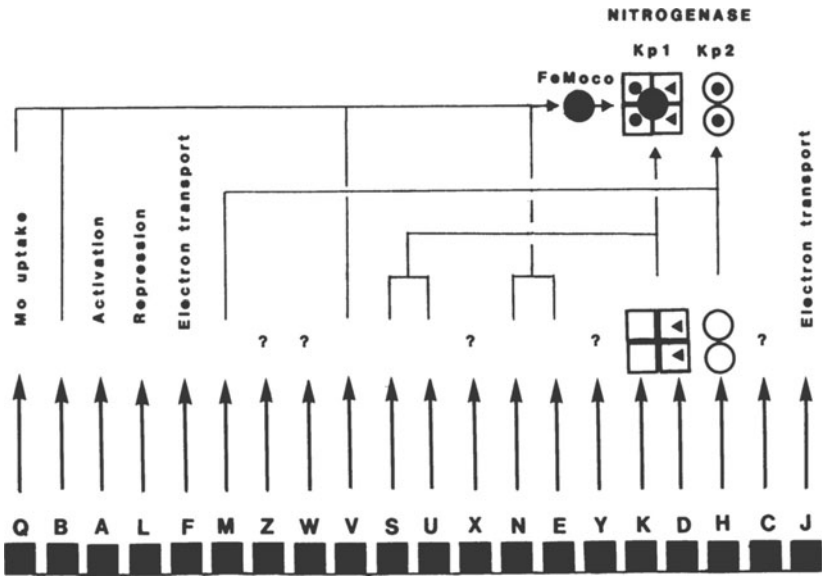

Figure 10.2. Map of the genes responsible for nitrogen fixation in *K. pneumoniae* (see Ref. 13 and related publications).

for nitrogen fixation can survive and be expressed (i.e., function) in the alien environment of, say, a plant chloroplast. In the first place, we need to be able to transfer all the necessary genes with their activators and promoters. Then the environment needs to be such that the genes can function and the nitrogenase produced can fix nitrogen catalytically without being destroyed. For example, nitrogenase is oxygen-sensitive, and nitrogen-fixing organisms adopt various strategies to protect it. *Rhizobia* use leghaemoglobin as an oxygen filter, *Anabaena* fix nitrogen in differentiated heterocysts where photosynthesis does not occur, *Gloeothece* fix nitrogen and photosynthesize at different times, and aerobic bacteria respire at enhanced rates to keep oxygen tension low. The oxygen status in a plant chloroplast, in which a nitrogen-fixing system might be placed, is not known. Maybe there is a niche which an oxygen-sensitive system could occupy, but this has to be determined.

Even if the development of a nitrogen-fixing plant is not achieved, and there is no reason to believe that this will be the case, rhizobial inoculants are already available commercially.[15] These currently available inoculants are still "natural" organisms, but organisms produced by genetic engineering with, for example, the ability to produce fixed nitrogen even in environments containing sufficient fixed nitrogen to switch-off conventional nitrogenase systems, are being tested in the field.[16] Organisms of this kind, or with comparable adaptations, may confidently be expected to be in use agriculturally in the near future.

Assuming that the transfer and expression of nitrogenase in plants can be carried through successfully, the question arises as to whether this will affect the yields of agricultural produce to an unacceptable degree. This judgement has to

be made in the light of the social and political circumstances in which the agricultural system using the engineered plants would operate. For example, within Western Europe, productivity and demand in many areas of agriculture are such that a drop in yield coupled with a drop in the costs of buying and broadcasting fertilizer might well be acceptable. Whether it would be acceptable in a wider, world context is open to question.

The degree to which the consumption of energy by a plant in order to fix nitrogen might affect the overall productivity has been discussed in some detail.[17] Such discussions must include many assumptions and hypotheses which can render their conclusions somewhat questionable. Indeed, if fixation were desirable from the plant's point of view, why have not plants already developed the capacity to fix nitrogen? Recent calculation of the energy cost of fixation in nodules and bacteria is of interest here. Attempts were made[18] to cost, in terms of ATP, the production of ammonia. The standard free energy ($\Delta G°$) for the conversion of molecular nitrogen shown in Eq. (10.4) is 340 kJ mol^{-1} NH_3.

$$N_2 + 3H_2O \rightarrow 2NH_3 + \tfrac{3}{2}O_2 \qquad (10.4)$$

Since the oxidation of glucose generates 3140 kJ mol^{-1}, then, if all systems were functioning at 100% efficiency, only 0.11 mole of glucose would be required to produce one mole of ammonia. However, maximum efficiency is never achieved. The stoichiometry of Eq. (10.2) implies an efficiency in terms of actual fixation of only 75% (25% of the electrons are "wasted" as H_2), and all the other maintenance and respiration functions associated with fixation suggest that the maximum achievable efficiency is between 10 and 20% for the enzyme, and very much less for whole bacteria.[18]

It has been estimated[19] that natural fixation consumes about 2.5% of the total photosynthate generated on land. However, this cannot give us a direct measure of the cost of fixation in terms of yield. Minchin and Pate[20] showed that with rhizobium, in peas, the nodulated roots consume 18.8 g glucose to produce 1 g of fixed nitrogen.[17] Only some of this glucose is used directly in fixation-related processes, and one estimate is about 12.0 g.[17] On this basis the efficiency of nitrogen fixation is about 12% of the theoretical value. If all the fixed nitrogen of legumes (ca 2.8% by weight) came from fixation, then it is calculated that 150 g primary photosynthate (the energy source for the system) might yield only 82 g of final dry weight, compared with 100 g if all the nitrogen had been supplied free, a reduction in yield of about 18%.[17] If light intensity is yield-limiting, as it could be in Northern agricultural systems, this may not be acceptable. In the tropics, where there is more daylight, such constraints would be expected to be less severe.

However, this is not the end of the story, because the primary form of fixed nitrogen absorbed by plant roots is nitrate rather than ammonia. The value of $\Delta G°$ for the conversion of nitrate to ammonia is 331 kJ mol^{-1}, comparable to that for the conversion of dinitrogen to ammonia. It is thus not at all clear that a plant required to fix nitrogen would be at a disadvantage compared to one obtaining its nitrogen from nitrate.[21] Consequently, this discussion can only be concluded definitively when a nitrogen-fixing plant has been constructed.

There are various other stratagems which might conceivably be adopted in the future, including the possibility to influence nitrification and denitrification processes, and applying fertilizers in small pulses or in forms enforcing slow release of nitrogen to the biosphere. Some of these have already been investigated, even in the field, but they are not likely to impinge significantly on developed agricultural systems.

10.2.2. Developments of New Processes

In 1963, Volpin and Shur[22] reported that a mixture of an organotitanium compound and a reducing agent in a nonaqueous anaerobic environment absorbs dinitrogen from the gas phase and that addition of aqueous acid then results in the generation of ammonia. This report was the seminal chemical stimulus to the large effort expended in attempts to understand how these and related reactions occur. In 1965, the first dinitrogen complex was isolated by Allen and Senoff.[23] This material, $[Ru(NH_3)_5(N_2)]^{2+}$, proved of considerable fascination, particularly in its mode of formation by action of molecular nitrogen at atmospheric pressure on aqueous $[Ru(NH_3)_5(H_2O)]^{2+}$. This displacement reaction favors the dinitrogen complex even in the presence of 55.5 molar water![24] However, the complex proved to be of little interest from the standpoint of the reactivity of the coordinated nitrogen molecule, which can act as a Lewis base to various metal ions but does not do much else. In particular, it cannot be reduced to ammonia.

Since then, a wide variety of dinitrogen complexes has been prepared from nearly all of the transition metals.[25] They may be arranged in groups (Table 10.2) on the basis of the bonding mode of the bound dinitrogen. The largest group contains singly-bound end-on dinitrogen, M—N≡N, as in $[Ru(NH_3)_5(N_2)]^{2+}$ (Fig. 10.3). In such compounds, the metal-nitrogen bond is multiple, and the nitrogen-nitrogen bond length is of the order of 1.12 Å, a little longer than that in gaseous

TABLE 10.2. Principal Dinitrogen-Binding Structures of Dinitrogen Complexes

M—N≡N
M—N≡N—M or M—N≡N—M′
M=N—N=M
M—N≡N(M′)(M′)
M—N(N)
M—N≡N—M′ (M″)

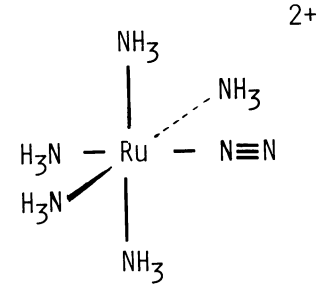

Figure 10.3. Representation of molecular structure of $[Ru(NH_3)_5(N_2)]^{2+}$.

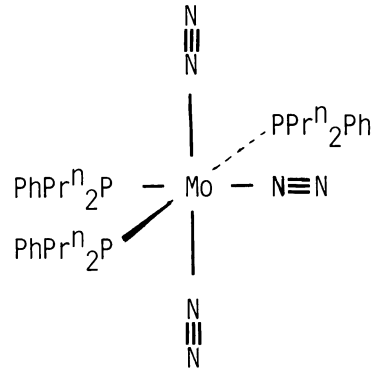

Figure 10.4. Representation of molecular structure of $[Mo(N_2)_3(PPr^n_2Ph)_3]$.

nitrogen (1.098 Å), which does not suggest any dramatic "activation" upon coordination. As many as three nitrogen molecules can be coordinated to a single metal ion in a stable complex, as in $[Mo(N_2)_3(PPr^n_2Ph)_3]$ (Fig. 10.4).[26] The next group consists of bridging nitrogen, and here there are two subclasses. One may be regarded as a Lewis acid/Lewis base adduct, involving a singly-bound terminal dinitrogen and metal acid. An example is $[MoCl_4(OMe)N_2ReCl(PMe_2Ph)_4]$ (Fig. 10.5).[27] In contrast, when the metal ions at either end of the nitrogen are such that they can relatively easily lose two electrons each (i.e., they have accessible oxidation states two units apart), an internal redox reaction can take place, giving a different kind of formulation.

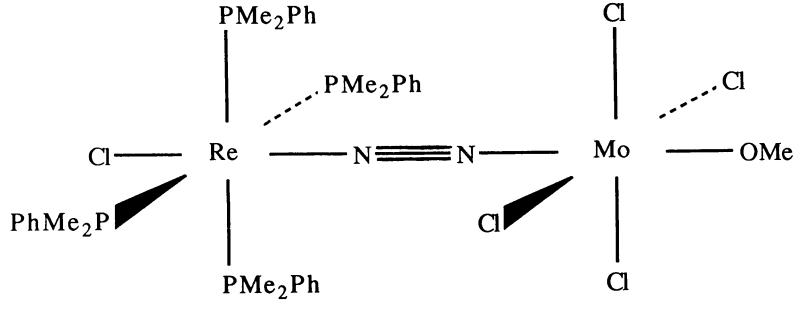

Figure 10.5. Representation of molecular structure of $[\{ReCl(PMe_2Ph)_4\}(N_2)\{MoCl_4(OMe)\}]$.

$$M \leftarrow N{\equiv}N \rightarrow M' \qquad M{=}N{-}N{=}M'$$

(A) (B)

The product (B) is more akin to a hydrazine (N_2^{4-}) derivative than a dinitrogen complex. Typical examples of such compounds are known with M = M′ = Nb^{III}, Ta^{III}, or W^{IV} in (A), acting actually as Nb^{V}, Ta^{V}, and W^{VI} in (B).[28] Such complexes usually (but not invariably) react with proton acids to yield hydrazine.

There are other, more complex bridging arrangements, involving two or more metal atoms, some examples of which are shown, the tungsten and titanium examples being from Refs. 29 and 30, respectively (Figs. 10.6 and 10.7). In general, these are extremely air-sensitive systems, and although they are often reactive with protic materials, producing ammonia and/or hydrazine, they are not well understood.

Finally, the possibility of side-on binding of dinitrogen to transition-metal ions needs to be mentioned. There is only one example in which the bonding of dinitrogen to a metal is thought to be side-on in a mononuclear species, namely $[Zr(C_5H_5)_2\{CH(SiMe_3)_2\}(N_2)]$, and this has yet to be proven by X-ray structural analysis.[31] Side-on nitrogen is, at best, a rather rare animal.

The reactivity of coordinated dinitrogen in mononuclear complexes is still not yet fully understood. The reactive complexes are those at the left-hand end (Groups 4, 5, and 6)[32] of the transition series and the reactions are best developed in the case of complexes of molybdenum and tungsten. The first reaction discovered was an acylation[33] of coordinated nitrogen, but it was quickly recognized that protonation is equally, if not more, facile.[34]

Complexes such as $[W(PMe_2Ph)_4(N_2)_2]$ react with proton acids, even those as weak as methanol, losing at least one mole of nitrogen, with the formation of ammonia hydrazine. In the best cases, one mole of complex yields two moles of ammonia, all the six electrons for the reduction of the dinitrogen coming from the

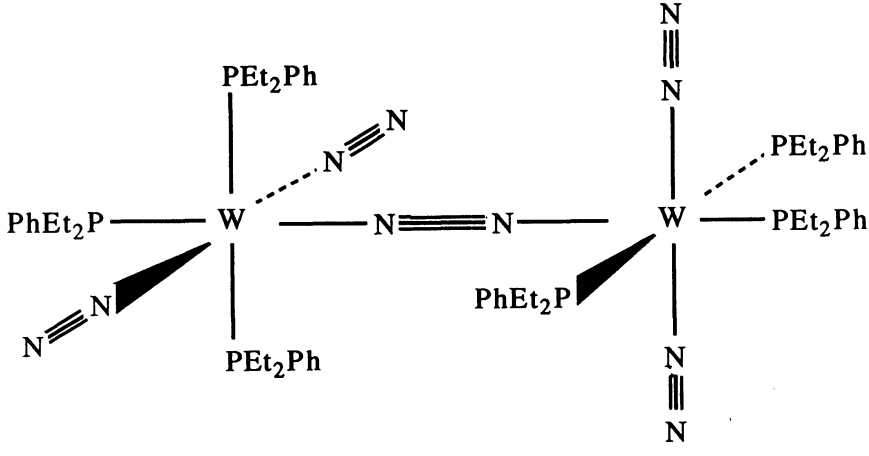

Figure 10.6. Representation of molecular structure of $[\{W(N_2)_2(PEt_2Ph)_3\}_2N_2]$.

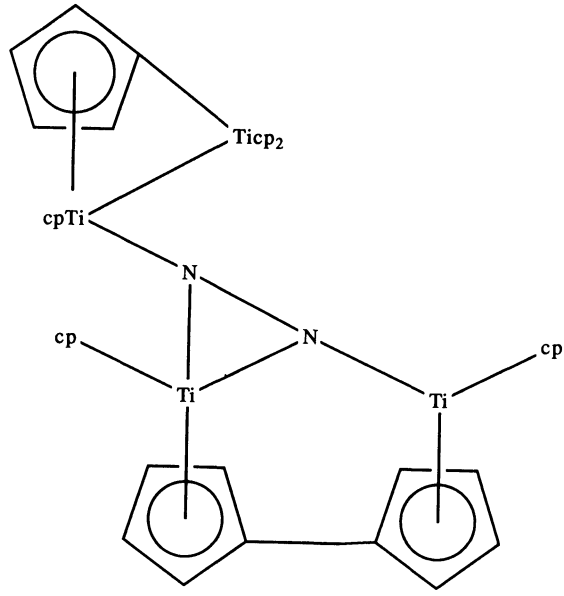

cp = (π-C_5H_5)

Figure 10.7. Representation of molecular structure of $[\mu_3\text{-}N_2\{(\eta^5, \eta^5\text{-}C_{10}H_8)(\eta^5\text{-}C_5H_5)_2Ti_2\}\Delta\{(\eta^1, \eta^5\text{-}C_5H_4)(\eta^5\text{-}C_5H_5)_3Ti_2\}]$. cp = ($\pi$-$C_5H_5$).

tungsten.[35] In the related reaction of similar compounds such as $[W(N_2)_2(Ph_2PCH_2CH_2PPh_2)_2]$, the protonation does not proceed as far, stopping at the stage of a hydrazine derivative, of which the complex $[WCl(NNH_2)(Ph_2PCH_2CH_2PPh_2)_2]^+$ is a typical example.[36] The mechanisms of such protonations have been elucidated in considerable detail,[37] and Schemes 1 and 2 summarize the results of the kinetic studies. The individual reactions are stoichiometric and the overall process is not catalytic. It is unfortunately not practicable to make the systems cyclizable.

Coordinated dinitrogen can also be alkylated by alkyl halides, and the products reduced to yield secondary amines, as shown below.[38] These reactions are also well worked out (Scheme 3).

$$[Mo(N_2)_2(Ph_2PCH_2CH_2PPH_2)_2] + RBr \rightarrow [MoBr(NNR)(Ph_2PCH_2CH_2PPh_2)_2]$$

$$[MoBr(NNR)(Ph_2PCH_2CH_2PPh_2)_2] + RBR \rightarrow [MoBr(NNR_2)(Ph_2PCH_2CH_2PPh_2)_2]Br$$

$$[MoBr(NNR_2)(Ph_2PCH_2CH_2PPh_2)_2]^+ + BH_4^- \rightarrow R_2NH + ?$$

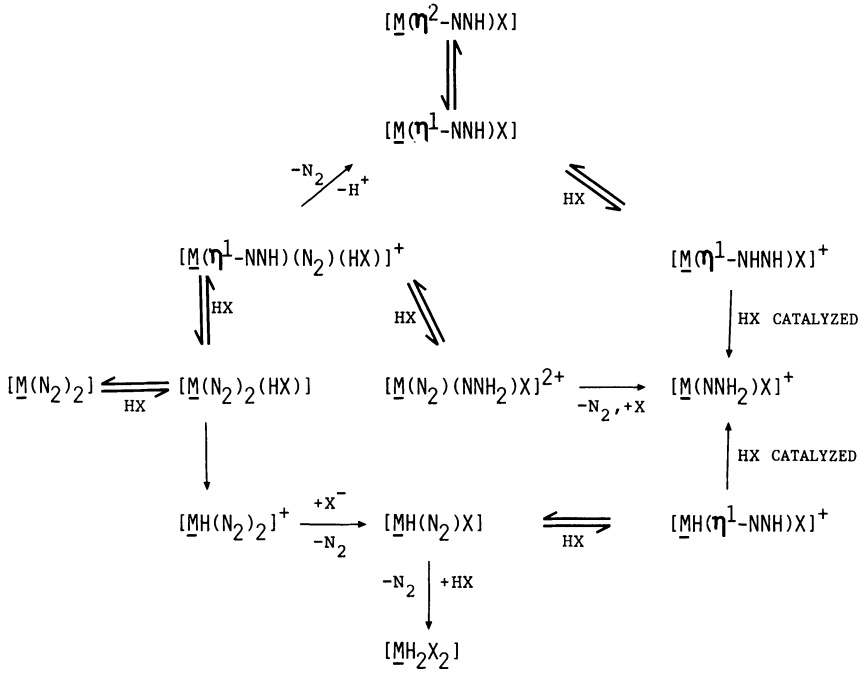

Scheme 1. Protonation mechanisms of $[M(N_2)_2(Ph_2PCH_2CH_2PPh_2)_2]$: M = $M(Ph_2PCH_2CH_2PPh_2)_2$, M = Mo or W.

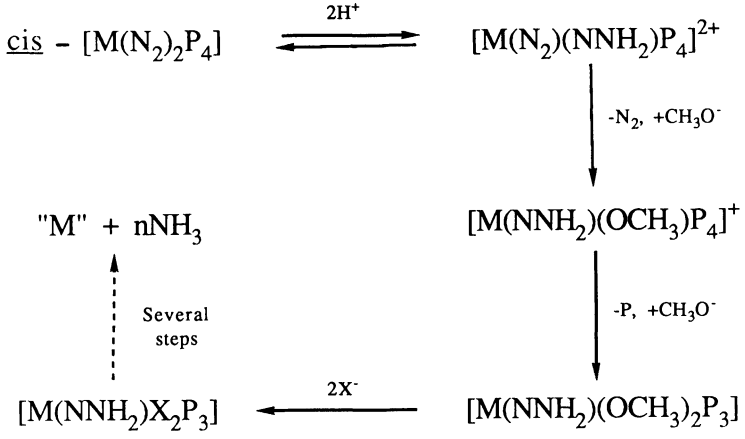

Scheme 2. Initial stages in the protonation of $[M(N_2)_2P_4]$ in methanol: M = Mo or W, P = PMe_2Ph; for M = W in the best cases "M" is a W^{VI} compound and $n = 2$.

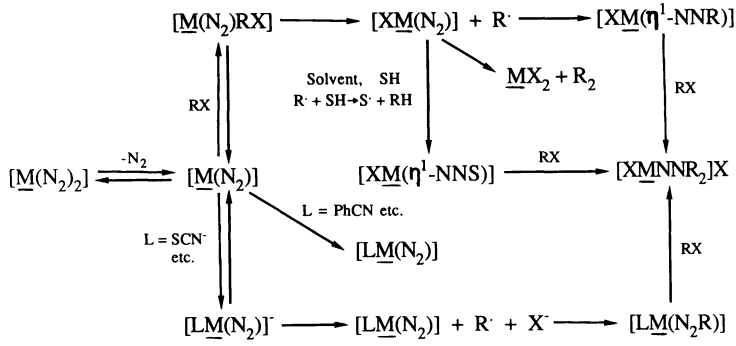

M = M(diphosphine)$_2$ [M = Mo or W]

Scheme 3. Alkylation mechanisms of [M(N$_2$)$_2$].

More recently, electrochemical methods have been used to bring about a controlled reduction of the dialkylhydrazide compounds formulated above, and the whole system has been cyclized, as shown in Scheme 4.[39] This opens the way for the production of amines directly from coordinated dinitrogen, without the intermediacy of ammonia. It suggests a possible electrochemical cycle for the production of ammonia, too, but until recently this has not been a feasible route, because reduction of the hydrazine derivative (=NNH$_2$ stage) always led to the evolution of hydrogen rather than to the reduction of the compound and loss of the bromide, as occurs in the alkylated-nitrogen cycle.

Recently, by using an acid with an anion which is a good leaving group, it has proved possible to produce an electrochemical cycle for the production of ammonia from coordinated dinitrogen.[40] It is based upon the principles expounded above, and can operate in aqueous-type media. The development of a device

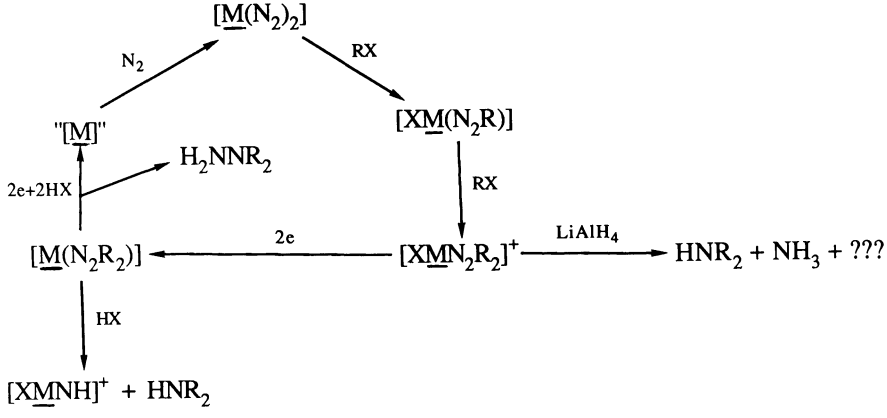

M = M(Ph$_2$PCH$_2$CH$_2$PPh$_2$)$_2$; M = Mo or, more often, W

Scheme 4. Reductive pathways of [M(N$_2$)$_2$].

for producing ammonia based upon the systematic exploitation of hard-won knowledge of the precise details of the chemistry of N_2-protonation is a triumph of inorganic chemistry. Whether it will lead to a device that will actually be used commercially to produce ammonia is still open to question. The full scheme is detailed in Scheme 5.

However, this is not the only system for catalytic or cyclic production of ammonia from dinitrogen. The work of Volpin has spanned a large number of similar systems involving a transition metal compound, a reducing agent, often organometallic, and a nonaqueous anaerobic environment.[41] Some of the systems apparently involve catalytic nitridation, but since all of them require an ultimate irreversible hydrolysis step it is likely that exploitation as a process will prove very difficult. It would appear that these systems actually split the dinitrogen molecule on the surface of finely divided metal (or, at the very least, on metal complexes of low oxidation state) producing nitrido-species, but the evidence for the mechanism is not very strong. On the other hand, the Haber process catalysis would appear to provide a precedent for nitridation.

The research of Shilov also seems to have real commercial potential.[42] He has discovered several new systems, some of which are catalytic and function in protic solvents such as methanol. His most recent system uses sodium amalgam or electrochemical reduction of dinitrogen mediated by molybdenum, probably in the form of a molybdenum(III) complex. Phosphines enhance the reaction, and so does lethicin, which coats the amalgam surface. The reaction rate at room temperature and atmospheric pressure is greater than 0.3 mol N_2 reduced per catalytic center per second, and the turnover number is several hundreds per molybdenum.[43] No firm conclusions have yet been drawn concerning the mechanism of dinitrogen reduction, though it is believed that polynuclear species are

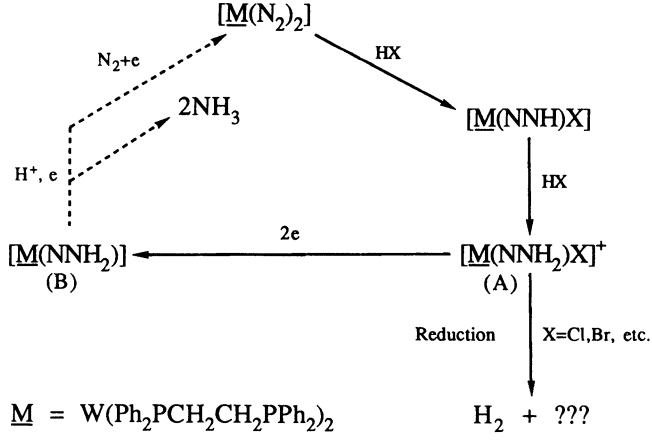

Scheme 5. Cyclic system for production of NH_3 from $[M(N_2)_2]$ and N_2. (Conversion of (A) to (B) and consequent regeneration of $[M(N_2)_2]$ only observed extensively for HX = 4-$MeC_6H_4SO_3H$).

involved. This is true of all the other systems of Shilov, such as those which are based on vanadium(II), but conclusive evidence is not yet available. Whatever the case, the potential of the chemistry has been demonstrated because at least some of the $^{15}N_2H_4$ available commercially from East European sources is apparently manufactured using one of these systems.[44]

There are also hints of alternative systems for the catalysis of the Haber process, though none as yet is so efficient that it can in any way be considered to challenge it. For example, potassium–metal oxide compounds can catalyze N_2/H_2 interaction, to produce ammonia, although the catalysts are exceedingly oxygen- and water-sensitive and the reactions are currently very slow.[45] Similarly, alkali metal compounds with graphite or with metal pthalocyanines can also catalyze the H_2/N_2 reaction.[46] The presence of iron in the graphite–alkali metal matrix increases the yield by more than two orders of magnitude.[47] A potassium–polynaphthoquinone complex converts dinitrogen (15 cm Hg) and hydrogen (45 cm Hg) in a 1.4% yield in 21 h at 300 °C. If iron(III) chloride is incorporated in the catalyst, then the yield increases to 18.4% under the same conditions (24.4 cm^3 NH_3 per g catalyst).[48] The long-term potential of these systems may be considerable.

Perhaps of even greater potential is the demonstration that some materials can catalyze the interaction of nitrogen and methane to form ammonia, among other products.[49] These reactions only operate on a very small scale and have not yet been exploited seriously. The initial publication describes how ruthenium (0.4%) supported on silica reacts with water at 400 °C to yield hydrogen, leaving oxygen on the surface. After evacuation, the catalyst can be reduced with methane to give carbon monoxide and hydrogen (cf. steam reforming). The introduction of dinitrogen and water then produces ammonia. Presumably, methane reacts with water to produce carbon monoxide and dihydrogen and the dihydrogen then reacts with molecular nitrogen. Clearly, were it possible to operate such a system on anything like a commercial scale, the ability to build a plant without a separate hydrogen-generating system would generate significant cost savings.

Photochemistry is now beginning to provide new systems for conversions of nitrogen to ammonia, and these also have long-term potential. For example, it has long been known that TiO_2 (anatase or rutile) doped with transition metals can photocatalyze the homolysis of water to dihydrogen and dioxygen. If this is done with iron-doped titania in the presence of dinitrogen, then ammonia and hydrazine are produced.[50] This represents the use of photoenergy rather than thermal energy to overcome the activation energy obstacle to ammonia synthesis. Presumably hydrogen atoms are able to attack the nitrogen molecule to initiate the process of dinitrogen breakdown. The yields quoted are very low, for example, 1.39 μmol NH_3 and 0.5 μmol N_2H_4 after irradiation by mercury light over 0.2 g catalyst for 3 h, but the significance of the observations is much greater. The detailed mechanism remains something of a conundrum in any given case. It has been argued persuasively that the photocatalysis of the N_2/H_2O reaction over rutile can also occur by an essentially oxidative route[51] in which hydrogen peroxide is formed from water at the surface. Breakdown of the hydrogen peroxide releases oxygen atoms, which generate nitric oxide with dinitrogen.

Clearly, such systems are very complex and the mechanisms have not been elucidated in most cases. In fact, photocatalytic synthesis of ammonia on TiO_2 in soil was suggested as early as 1941 (N. R. Dhar, E. V. Sechacharyubu and S. K. Mukerji, quoted in Ref. 52). The use of $SrTiO_3$ and $BaTiO_3$ doped with RuO_2 and NiO increases the yield considerably, but the system is complicated by the simultaneous photodecomposition of ammonia.[52] Titanium-exchanged zeolites can also act as photocatalysts, and irradiation of catalyst by a 150 watt lamp can produce 0.35 mg NH_e per g catalyst per h[53] from dinitrogen and water. In practice the catalyst as such is not necessary at all. A glow discharge in acidified water can produce ammonia and nitrate, and amino acids are generated in the presence of carboxylic acids.[54] These reaction conditions are reminiscent of the investigations on the origins of biological molecules in primeval soups, and the yields are very low. Nevertheless, these admittedly rather selective citations suggest that there are many potential fixation processes, some of which may be occurring in Nature.

The rates and yields of the reactions discussed above make it unlikely that they can be developed easily into an industrial process. However, nitrogen fixation may have been going on continuously in, say, desert environments even though the ammonia produced is not normally available for use by biological systems. Desert sands have been checked for the ability to catalyze photochemical nitrogen fixation, and some have been found to do so.[55] It has even been suggested that photochemical nitrogen fixation might occur on planets such as Mars.[56] This whole area of fascinating speculation may one day be susceptible to empirical testing on Mars itself.

10.2.3. Developments of Current or Recent Industrial Procedures

There is no doubt that more nitrogen must be persuaded to enter the biological nitrogen cycle if food production is to keep up with the expected doubling of the world's population before a stationary population level is reached. However, in some areas it is clear that a tolerable limit to the amount of fixed nitrogen which can be applied to the soil has been already reached. This implies that more damage is being done in some areas by, for example, nitrate poisoning of groundwaters, than can possibly be justified in the name of increased food production.

Ironically, within the EEC, efforts are now being made to reduce food production, something which one hopes is just a quirk of the current economic and political situation, and one way to do this would be simply to limit the amount of nitrogenous fertilizer which can be applied. A more constructive long-term approach would be to modify fertilizer application (both in its method and its form) so that nitrogen uptake would be more efficient and the runoff of surplus nitrate consequently diminished. Work of this kind is proceeding in several research establishments.

Another possibility is to find nonobligate symbioses (i.e., associations of plants and micoorganisms which are mutually beneficial but are not necessary for nitrogen to be fixed) which could be of agricultural value but would not risk upsetting the current natural nitrogen flows. Symbioses on the leaves of ferns can give rise to usable "green" fertilizer, and there are also symbioses with rice which are also of

considerable agricultural significance.[57] Consequently, it is worthwhile to continue looking for symbiotic systems in Nature which could have applied value.

It is also possible to consider modifying the nitrification and denitrification paths of the natural nitrogen cycle. The enzymes involved, such as nitrate reductase and nitrite reductase, are not yet completely understood. However, the controlled conversion of ammonia to nitrate (nitrification) could be advantageous in that it would limit nitrate concentration at any given time. Commercial nitrification inhibitors such as dicyandiamide have been claimed to be cost-effective for turf but also probably for wheat.[58] Certainly inhibitors can improve the efficiency of uptake of nitrogen fertilizers, but whether such materials can be broadcast for long periods and still be environmentally acceptable is open to question. The immediate preference is not to spread yet more foreign materials into the environment, unless the benefits are immediately and widely acknowledged and the conceivable disadvantages acceptable.

Interference with the natural denitrification process does not seem to be desirable, other than to speed it up to reduce groundwater contamination by nitrate. This is a problem of which we shall probably hear a great deal in the near future.

The aqueous oxidation of dinitrogen to nitric acid [Eq. (10.5)] is a reaction which is very attractive to contemplate from an industrial point of view. Indeed, on thermodynamic grounds, it should have converted all the atmospheric oxygen and nitrogen to dilute nitric acid long ago, because it is exothermic. No catalyst has yet been found.

$$2N_2 + 5O_2 + 2H_2O \rightarrow 4HNO_3 \qquad (10.5)$$

The oxidation process most exploited hitherto is the carbon arc process [Eq. (10.6)], also called the Birkeland–Eyde or the Norwegian process. The thermodynamics of the reaction, represented by Eq. (10.6), are such that there is only 3% NO in equilibrium in the reaction at ca 2500 °C, and at 700 °C the equilibrium amount is close to zero. The high temperatures required were obtained in an electric arc. The process was last applied commercially about 1941, and had by then become unprofitable due to the high cost of electricity for the arc.[59]

$$N_2 + O_2 \rightleftharpoons 2NO \qquad (10.6)$$

Recently, the arc process has been revived by workers from the Kettering Laboratory at Yellow Springs, Ohio, but in a completely different context.[60] They use an arc struck between cast-iron electrodes, apparently in a variety of arrangements. The laboratory system uses a high-voltage electrode in one end of an iron pipe which constitutes the other electrode. The pipe has a diameter of ca 6.5 cm (2.5 inches) and is ca 90 cm (36 inches) long. Air is pumped along the tube while an arc is struck between the electrode and the pipe, which is earthed. A temperature of ca 2000 °C is reached in the arc, at which temperature oxides of nitrogen are formed. The oxides of nitrogen are then absorbed by an aqueous suspension of

limestone. The power source used in field experiments in Nebraska was a photovoltaic array, a solar power generator with a maximum output of 25 kW. The cell used for fixation required only 3 kW, so that there was plenty of power available even admitting the extra power needed to convert the photovoltaic output to a form suitable for use by the arc furnace. The conclusions from the Nebraska field tests were that the arc furnace provides an excellent off-peak use for the excess of power from the photovoltaic array, although it could not compete with commercially available fertilizer.[61] However, this is only a problem of commercial power and feedstocks are the sources of energy and hydrogen.

A modified system has apparently been field tested in Nepal. This consists of two ceramic (sewer) pipes, one of which contains two cast-iron electrodes, and constitutes the furnace. The other is packed with lime, and is the absorber. The subsidiary equipment, selected to be cheap, robust, and reliable, consists of a power source (wind, or falling water, or the sun may be appropriate), a gas pump to circulate air, and an alternator (from a truck or lorry) to provide the spark. Such a system is grossly inefficient, but does produce fertilizer. It also generates a lot of heat, and it has been suggested that this could be used domestically. This is a very imaginative application of what is really rather old technology, and it does appear to be capable of providing fertilizer nitrogen using no commercial energy and feedstock, without being so outrageously expensive that it cannot be envisaged as being used by peasant farmers.

The possibility of oxidation of nitrogen by metal oxides has been explored. For example, dinitrogen reacts with both alumina and zirconia melts to form nitride and oxynitride.[62] It is also possible to obtain nitrogen(II) oxide from such systems,[63] though whether it is actually feasible to develop a commercial process on such a basis appears unlikely at present.

Apart from the cost of the plant, which is probably still the major determinant of the cost of ammonia in Western economies, the other major cost is in the generation of dihydrogen. The possibility of using hydrocarbons directly has already been suggested by the experiments mentioned earlier on the methane–dinitrogen reaction. An alternative supply of clean hydrogen for use in the Haber process is the electrolysis of water.

In 1980, there were at least five commercial ammonia plants in operation based upon water electrolysis.[64] These were in Norway (2); Aswan, Egypt; Reykjavik, Iceland; and Cuzco, Peru. The Norwegian ammonia production using electrolytic hydrogen was greater in the 1960s, but since then some of the capacity has been converted to hydrocarbon feedstock. Clearly, the balance between electrolytic hydrogen and hydrocarbon-derived hydrogen depends very much on the relative costs of the hydrocarbon (not very stable) and electricity (presumably stable if supplied by hydroelectric sources). The advantages of electrolytic hydrogen include the simplicity of production, the lack of pollution, and the availability of raw materials. It is calculated[64] that the energy consumption per tonne of ammonia produced in an electrolysis plant is about the same as on a conventional natural gas plant, and the capital cost is likely to be comparable and, consequently, surprisingly high. For example, in about 1980, the capital cost of an electrolysis-based ammonia plant rated at 300 tonnes per day was stated to be ca $\$80 \times 10^6$.

The cost of a water electrolysis plant increases linearly with capacity, with few economies of scale.[64] Hence, in general, the determinant is going to be the relative costs of energy sources, and this is not readily predictable, at least for smaller plants.

Various other techniques have been suggested for improving the Haber process. It must be borne in mind that modifications in process design and catalyst performance are being made continuously, with the aim of increasing reaction rates, thus allowing reduction in working pressures and temperatures. Cheap electrical power would raise the possibility not only of electrolytic hydrogen, but also of electroreforming and of the direct oxidation of nitrogen. Cheap nuclear energy could lead to the possibility of firing steam reformers with nuclear power. Even if it is feasible to reach the temperatures required for steam reforming using a nuclear source, whether it would be desirable to use nuclear power at all is quite another question.[65]

In the case of electroreforming, a conventional gas-fired 1000 tonne per day plant requires heating power of 400 MW, which is provided by burning hydrocarbon. The efficiency of electroreforming can be such that the hydrocarbon-based energy used in heating can be replaced by less than half of the equivalent of electrical energy.[65] The net result is that the hydrocarbon fuel requirement is reduced to zero and the feedstock requirements by ca 25%. There would also be capital economies, but, again, the decisive factor would appear to be the relative costs of hydrocarbon and of electricity.[65]

There has been an immense amount of research into variations of the original Haber catalyst first used commercially. Current catalysts have been improved so that commercial plants using the ICI AMV process operate at 70–80 atm pressure. The bed exit temperatures are still above 400 °C because of the equilibrium properties of nitrogen/hydrogen mixtures (see Appendix 5) and the reaction-rate requirements. The development of high-activity catalysts could lead to significant reductions in temperature and pressure, and consequent savings on capital and fuel costs.

Several catalyst types have received recent attention, all of which show promise of producing high-activity catalysts for Haber-type systems under mild conditions. These can be classified as supported catalysts, intermetallic catalysts, and precipitated catalysts. These classifications are not rigid, neither are they necessarily absolutely distinct from the current range of promoted catalysts made by fusion, and the references cited below are only exemplary.

Among catalysts derived from intermetallic compounds, titanium–iron systems have received some attention. The precise course of reactions involved is not clear. For example, it is claimed that the catalyst derived from a suitably activated TiFe intermetallic phase is TiN + Fe. The TiN is said to react with molecular hydrogen.[66] On the other hand, in a series of patents on Fe–Ti systems, covering a range of iron-to-titanium ratios, with or without addition transition elements, it is quite clearly regarded that the titanium is capable of forming hydrides. Whatever the mechanism, such systems appear capable of promoting ammonia synthesis in commercial yields at 300 °C, 80 atm, while some are even claimed to be active at 125 °C and 1 atm.[67] Rare earth metals, in combination with iron, ruthenium, or cobalt, can also function as catalysts.[68] Again, the rare earth metals seem to be

hydrided, and specific activities exceeding those of doubly-promoted Haber catalysts are claimed. Amorphous metal alloys such as $Fe_{91}Zr_9$ are also promising catalyst precursors, showing activities an order of magnitude greater than that of polycrystalline iron.[69] The use of such catalysts in industry is speculative because, whatever the activities may be, disintegration during activation and use is not a trivial problem to overcome. However, simply on the basis of activities, these catalysts appear full of potential.

As already described in Chapter 9 very high activities have already been demonstrated using ruthenium supported on modified carbon. If this activity can be retained at lower ruthenium contents, then the resistance of ruthenium catalysts to poisoning and the high activity would lead to significant process changes.

Similarly, precipitation technology applied to iron catalysts has also led to materials of promise.[70] Incorporation of 10–20% cobalt into the catalyst leads to a threefold increase in catalytic activity,[71] but again serviceability in a real system presents problems over and above simple considerations of activity. What is, nevertheless, quite evident, is that the development of Haber catalysts for the commercial process has by far not yet reached its technical limit.

10.3. CONCLUSION

It will be some years before the academic research in biological or chemical aspects of nitrogen fixation makes any impact on current industrial or agricultural practice, at least in highly developed economies. Nevertheless, small-scale nitrogen-fixing processes and novel nitrogen-fixing biological systems have moved from the realm of academic discussion to reality and industrial exploitation seems a possibility. Whether such processes or organisms will eventually earn wide application is still open to question. In the meantime, there are still many improvements which can be made to the conventional Haber process, and these are continually being developed and applied. The large-scale Haber process still has much to offer, whatever the future holds with respect to changes in the cost of hydrocarbons.

REFERENCES

1. *Chemical & Engineering News*, June 20, 1988.
2. K. Windridge, *Fertilisers: A World Industry, Fertiliser Review 1987*, p. 16, Fertiliser Manufacturers Association, London, 1987.
3. Much of the work on the fate of nitrogen in temperate soils has been carried out at Rothamsted Experimental Station, UK. The Station's Annual Reports carry useful summaries of their research.
4. H. Hellriegel, *Landw. Vers. Sta.* **33**, 464 (1887); a good account of this work is given in P. W. Wilson, *The Biochemistry of Symbiotic Nitrogen Fixation*, University of Wisconsin Press, Madison, Wisconsin (1940).
5. A. E. M. Hood, *Phil. Trans. R. Soc. London, Ser. B* **296**, 315 (1982).
6. H. Bortels, *Arch. Mikrobiol.* **1**, 330 (1930).

7. *For a general review of biological nitrogen fixation research, see J. R. Postgate, The Fundamentals of Nitrogen Fixation*, Cambridge University Press, Cambridge (1982).
8. R. Eady, R. Robson, and J. Postgate, Vanadium puts nitrogen in a fix, *New Scientist*, Issue 1565, p. 59, June 18, 1987.
9. R. D. Joerger, R. Premakumar, and P. E. Bishop, *J. Bacteriol.* **168**, 673 (1986); R. Pau, personal communication.
10. J. M. Arber, B. R. Dobson, R. R. Eady, P. Stevens, S. S. Hasnain, C. D. Garner, and B. E. Smith, *Nature* **325**, 372 (1987); M. K. Eidsness, A. M. Flank, B. E. Smith, A. C. Flood, C. D. Garner, and B. E. Smith, *J. Am. Chem. Soc.* **108**, 2746 (1986).
11. R. A. Dixon, M. Buck, M. Drummond, T. Hawkes, H. Khan, S. MacFarlane, M. Merrick, and J. R. Postgate, *Plant Soil* **90**, 225 (1986).
12. D. J. Lowe and R. N. F. Thorneley, *Biochem. J.* **224**, 895 (1984) and references cited therein.
13. A. Toukdarian and C. Kennedy, *EMBO J.* **5**, 399 (1986); M. Drummond, P. Whitty, and J. Wootton, *EMBO J.* **5**, 441 (1986).
14. An overview can be garnered from H. J. Evans, P. J. Bottomley, and W. E. Newton (eds.), *Nitrogen Fixation Research Progress*, Martinus Nijhoff, Dordrecht (1985).
15. For an indication of what the future may hold, see S. Dickman, *Nature* **328**, 568 (1987).
16. For a discussion of general prospects of engineered systems, see R. W. F. Hardy, Applications of nitrogen fixation in agriculture and forestry, in Ref. 14, p. 683.
17. V. P. Gutschick, Long-term strategies for supplying nitrogen to crops, Informal Report LA-6700-19S, Los Alamos Scientific Laboratory, Los Alamos, New Mexico, 87545 (1977).
18. J. S. Pate, C. A. Atkins, and R. M. Rumbird, Theoretical and experimental costing of nitrogen fixation and related processes in nodules of legumes, in: *Current Perspectives in Nitrogen Fixation* (A. H. Gibson and W. E. Newton, eds.), Australian Academy of Sciences, Canberra (1981).
19. V. P. Gutschick, Energy flows in the nitrogen cycle, especially in fixation, in: *Nitrogen Fixation*, Volume 1 (W. E. Newton and W. H. Orme-Johnson, eds.), University Park Press, Baltimore (1980).
20. F. R. Minchin and J. S. Pate, *J. Exp. Bot.* **24**, 259 (1973).
21. M. J. Merrick, *J. R. Agric. Soc. Engl.* **147**, 202 (1986).
22. M. E. Volpin and V. B. Shur, *Dokl. Akad. Nauk SSSR* **156**, 1102 (591 in translation) (1964).
23. A. D. Allen and C. V. Senoff, *Chem. Commun.* **24**, 621 (1965).
24. D. F. Harrison, E. Weissberger, and H. Taube, *Science* **159**, 320 (1968).
25. R. A. Henderson, G. J. Leigh, and C. J. Pickett, *Adv. Inorg. Chem. Radiochem.* **27**, 198 (1983).
26. S. N. Anderson, D. L. Hughes, and R. L. Richards, *J. Chem. Soc., Dalton Trans.*, 1591 (1986).
27. M. Mercer, R. H. Crabtree, and R. L. Richards, *J. Chem. Soc., Chem. Commun.*, 808 (1973).
28. See, for example, R. C. Murray and R. R. Schrock, *J. Am. Chem. Soc.* **107**, 4557 (1985) and references cited therein; J. R. Dilworth, S. J. Harrison, R. A. Henderson, and D. R. M. Walton, *J. Chem. Soc., Chem. Commun.*, 176 (1984).
29. S. N. Anderson, R. L. Richards, and D. L. Hughes, *J. Chem. Soc., Chem. Commun.*, 1291 (1982).
30. G. P. Pez, P. Apgar, and R. K. Crissey, *J. Am. Chem. Soc.* **104**, 482 (1982).
31. J. Jeffrey, M. F. Lappert, and P. I. Riley, *J. Organomet. Chem.* **181**, 25 (1979).
32. We adopt the new IUPAC recommendations for Group numbering.
33. J. Chatt, G. A. Heath, and G. J. Leigh, *J. Chem. Soc., Chem. Commun.*, 444 (1972).
34. J. Chatt, G. A. Heath, and R. L. Richards, *J. Chem. Soc., Chem. Commun.*, 1010 (1972).
35. J. Chatt, A. J. Pearman, and R. L. Richards, *Nature* **253**, 39 (1975).
36. J. Chatt, G. A. Heath, and R. L. Richards, *J. Chem. Soc., Dalton Trans.*, 2074 (1974).
37. R. A. Henderson, *J. Chem. Soc., Dalton Trans.*, 2259 (1984) and references cited therein.
38. W. Hussain, G. J. Leigh, H. Mohd-Ali, and C. J. Pickett, *J. Chem. Soc., Dalton Trans.*, 1473 (1986) and references cited therein.
39. G. J. Leigh and C. J. Pickett, *J. Chem. Soc., Chem. Commun.*, 1033 (1981).
40. C. J. Pickett, K. S. Ryder, and J. Talarmin, *J. Chem. Soc., Dalton Trans.*, 1453 (1986) and references cited therein.

41. M. E. Volpin and V. B. Shur, Nitrogen fixation involving nitride and related intermediates, in: *New Trends in the Chemistry of Nitrogen Fixation* (J. Chatt, L. M. da Camara Pina, and R. L. Richards, eds.), Academic Press, New York (1980).
42. For a review, see. A. E. Shilov, *Energy Resources through Photochemistry and Catalysis*, Academic Press, New York (1983).
43. L. P. Didenko, A. B. Gavrilov, A. K. Shilova, V. V. Strelets, V. N. Tsarev, A. E. Shilov, V. D. Makhaev, A. K. Banerjee, and L. Pospisil, *Nouv. J. Chim.*, 538 (1986).
44. N. T. Denisov, O. N. Efimov, V. F. Shuvalov, N. I. Shuvalova, A. K. Shilova, and A. E. Shilov, U.S. Patent 3 707 354 (1972).
45. See A. Ohaya, K-I. Aika, and A. Ozaki, *J. Chem. Soc., Chem. Commun.*, 321 (1984) and references cited therein.
46. M. Sudo, M. Ichikawa, M. Soma, T. Onishi, and K. Tamaru, *J. Phys. Chem.* **73** 1174 (1969).
47. M. Ichikawa, T. Kondo, K. Kawase, M. Sudo, T. Onishi, and K. Tamaru, *J. Chem. Soc., Chem. Commun.*, 176 (1972).
48. Y. Iwasa, T. Onishi, and K. Tamaru, *J. Chem. Soc., Chem. Commun.*, 1051 (1972).
49. S. Naito and K. Tamaru, *J. Chem. Soc., Chem. Commun.*, 1105 (1978).
50. G. N. Schrauzer and T. D. Guth, *J. Am. Chem. Soc.* **99**, 7189 (1977); G. N. Schrauzer and T. D. Guth, Photoreduction of nitrogen, U.S. Patent 4113590 (1978).
51. R. I. Bickley and V. I. Vishwanathan, *Nature* **280**, 306 (1979); R. K. M. Jayantay, V. Viswanathan, and J. A. Navio, *NATO Adv. Study Inst. Ser., Ser. C* **174**, 555 (1986).
52. Q. Li, K. Domen, and S. Naito, *Chem. Lett.*, 321 (1983).
53. F. Khan, P. Yue, L. Rizzuti, V. Augugliaro, and M. Shiavello, *J. Chem. Soc., Chem. Commun.*, 1049 (1981).
54. K. Harada, S. Igari, M. Takasaki, and A. Shimoyama, *J. Chem. Soc., Chem. Commun.*, 1384 (1986).
55. G. N. Schrauzer, T. D. Guth, M. R. Palmer, and J. Salehi, Nitrogen reducing solar cells, Sol. Energy: Chem. Convers. Storage [Symp.], 1978, 261 (1979).
56. G. N. Schrauzer, personal communication.
57. J. R. Postgate, see Ref. 7, especially Chapter 6.
58. G. Rieder and H. Michaud, Some Aspects of Costs versus Efficiency in the use of the nitrification inhibitor Didin, Paper 20, Proc. Fourth Int. Conf. Fertilizer Technology, p. 413 British Sulphur Corp., London (1981).
59. For a general history and discussion, see S. A. Topham, The history of the catalytic synthesis of ammonia, in: *Catalysis Science and Technology* (J. R. Anderson and M. Boudart, eds.), Vol. 7, p. 1, Springer, Berlin (1985).
60. R. W. Treharne, D. R. Moles, M. R. Bruce, C. K. McKibben, and B. K. Rein, Nitrogen fertilizer production by solar energy, Proc. Int. Solar Energy Meeting, Atlanta, Georgia (1979). An alternative approach has recently been described in the New York Times: Wednesday, August 26, 1987, page D6.
61. B. K. Rein, N. W. Sullivan, and P. E. Eisenbach, Nitrogen fertilizer from solar energy, Paper No. 80-3545, Proc. Am. Soc. Agricultural Engineers, Chicago, Illinois (1980).
62. J. P. Traverse, B. Granier, M. Foex, and F. Pichoir, *Rev. Int. Hautes Temp. Refract.* **11**, 295 (1974).
63. N. D. Parkyns and B. C. Patterson, *Chem. Commun.*, 531 (1965); see also N. D. Parkyns, U.K. Patent 1,149,858 (1965).
64. T. Grundt and K. Christiansen, Hydrogen by water electrolysis as a basis for small-scale ammonia production, Paper 4, Proc. Four Int. Conf. Fertilizer Technology, p. 73, British Sulphur Corp., London (1981).
65. L. Siberring, New technology for reducing ammonia plant feedstock consumption and replacing fuel by other energy forms, Paper 5, Proc. Fourth Int. Conf. Fertilizer Technology, p. 93, British Sulphur Corp., London (1981).
66. E. Schwab and E. Wick, *Z. Phys. Chem. (Wiesbaden)* **122**, 217 (1980).
67. M. N. Ozyagcuilar, U.S. Patents 1604263 (1978),1604264 (1978), and 1604265 (1978).

68. T. Takeshita, W. E. Wallace, and R. S. Craig, *J. Catal.* **44**, 236 (1976).
69. E. Armbruster, A. Baiker, H. Buris, H. J. Guntherodt, R. Schlegl, and B. Walz, *J. Chem. Soc., Chem. Commun.*, 299 (1986).
70. W. J. J. van der Wal and J. W. Geus, U.S. Patent 4459370 (1984).
71. J. R. Jennings, U.K. Patents 758412, 758413, and 758414 (1985).

APPENDIX 1

*Production and Uses of Ammonia**

PRODUCTION

World capacity of ammonia production[1] was 113 million tonne per year (expressed as N) in 1985 and is now (1990) somewhat in excess of this. The forecast[2] for the early 1990s is that world ammonia capacity will reach 125×10^6 t N per year. There are now more than 600 plants in operation, with most modern plants having an output of about 1000–1500 tonne per day, but a substantial amount of ammonia is still produced by plants which have a smaller capacity than this (Table A.1).[1] A census in 1981 gave 40 producers of ammonia in the United States, some with several plants, but many were shut down.[3]

TABLE A.1. World Ammonia Capacity (1984–1985)

Individual plant capacity (10^6 t N per year)	Share of world capacity (%)
<100	17.1
100–200	20.6
201–300	33.5
301–400	23.7
401–501	5.1

World and U.S. production of synthetic ammonia[2,3] is given in Table A.2.

TABLE A.2. Production of Ammonia (10^6 t N per year)

	1970	1975	1979	1980	1981	1984	1988
World	40.8	57.3	74.5	77.4	78.5	85.8	95.9
USA	10.3	12.4	13.9	14.7	14.2	—	—

* Compiled by M. S. Spencer, University of Wales, Cardiff, Wales.

TABLE A.3. U.S. Uses of Ammonia in 1981

Uses—products[3]:	20% Nitric acid
	20% Urea
	15% Ammonium phosphates
Uses—applications[3]:	80% Fertilizers
	20% Plastics and fibers
	5% Commercial and military explosives

TABLE A.4. Production of Major Nitrogen-Containing Industrial Chemicals in the United States (10^6 t N per year)[3]

Compound	1972	1975	1978	1979	1980	1981
Acrylonitrile	506	636	796	917	832	912
Ammonium nitrate	6,255	6,955	6,555	7,539	8,297	7,992
Ammonium sulfate	2,246	2,545	2,636	2,253	2,033	1,919
Ammonium phosphates	5,909	6,727	10,470	10,984	12,162	11,037
Nitric acid	7,255	7,545	7,213	8,105	8,392	8,218
Urea	3,191	3,445	5,703	6,364	7,118	6,918

USES

The production of fertilizers is the major use for synthetic ammonia and the forecast for early 1990s is that world N fertilizer consumption will reach 77×10^6 t N per year.[2] Industrial uses of ammonia now correspond to 20% of world output.[2]

Total consumption of ammonia in the United States exceeded 19×10^6 tonne in 1981.[3] The distribution of uses is given in Table A.3 and the production of major nitrogen-containing industrial chemicals in Table A.4.

REFERENCES

1. J. R. Jennings and S. A. Ward, in: *Catalyst Handbook* (M. V. Twigg, Ed.), 2nd ed., p. 384, Wolfe, London (1989).
2. *Nitrogen*, No. 147, p. 3 (1984).
3. G. T. Austin, *Shreve's Chemical Process Industries*, 5th ed., McGraw-Hill, New York (1984).

APPENDIX 2
*Processes and Catalysts**

Processes available for license are described in Chapter 7, *Ammonia Synthesis: Commercial Practice.* The following catalyst manufacturers are listed[1] as supplying steam reforming and/or ammonia synthesis catalysts:

United States

Haldor Topsøe, Houston, TX
Katalco, Oak Brook, IL
United Catalysts, Louisville, KY

Western Europe

BASF, West Germany
Haldor Topsøe, Denmark
ICI Chemicals & Polymers Ltd., UK

REFERENCE

1. J. T. Richardson, *Principles of Catalyst Development*, Plenum Press, New York (1989).

* Compiled by M. S. Spencer, University of Wales, Cardiff, Wales.

APPENDIX 3

*Properties of Ammonia**

These data have been collated from various standard sources: Kirk Othmer's *Encyclopedia of Chemical Technology*, Ullman's *Encyclopedia of Industrial Chemistry*, *Handbook of Chemistry and Physics*, American Institute of Physics Handbook, JANAF Thermodynamic Tables, L. Haar and J. S. Gallagher [*J. Phys. Chem. Ref. Data* **7**, 635-792] (1978), etc.

Molecular weight	17.03
Freezing point	−77.7 °C
Boiling point	−33.35 °C
Critical temperature	113 °C
Critical pressure	112.5 atm
Critical density	0.235 g cm^{-3}
Critical volume	4.225 cm^3 g^{-1}
Critical compressibility	0.242
Critical thermal conductivity	0.522 kJ K^{-1} h^{-1} m^{-1}
Density of liquid	
at 0 °C, 1 atm	0.6386 g cm^{-3}
at −33.43 °C, 1 atm	0.682 g cm^{-3}
at 40 °C	0.580
Density of gas	
at 0 °C, 1 atm	0.7714 g l^{-1}
at −33.43 °C, 1 atm	0.888 g l^{-1}
Vapor pressure at 25.7 °C	10 atm
at −77.7 °C	6.077 kPa
Van der Waals constants: *a*	4.170 $liter^2$ atm mol^{-2}
b	0.03707 liter mol^{-1}

* Compiled by M. S. Spencer, University of Wales, Cardiff, Wales.

Viscosity of liquid at −33.5 °C	0.255 cp
Viscosity of gas at −78.5 °C	67.2 microp
0 °C	91.8 microp
20 °C	98.2 microp
100 °C	127.9 microp
200 °C	164.6 microp
300 °C	198.7 microp
Surface tension, liq/vap, at 11.1 °C	23.4 dyn cm^{-1}
at 34.1 °C	18.1 dyn cm^{-1}
Thermal conductivity, gas, at −40.0 °C	1.815×10^{-4} J cm^{-1} s^{-1} K^{-1}
−17.8	2.023×10^{-4} J cm^{-1} s^{-1} K^{-1}
4.4	2.230×10^{-4} J cm^{-1} s^{-1} K^{-1}
26.7	2.455×10^{-4} J cm^{-1} s^{-1} K^{-1}
48.9	2.697×10^{-4} J cm^{-1} s^{-1} K^{-1}
Molecular structure	Symmetrical pyramid, N at apex
Point group	C_{3v}
H—N—H bond angle	106.67 °
N—H bond length	1.0124 Å
Vibrational frequencies (degeneracies)	3506 cm^{-1} (1)
	1022 cm^{-1} (1)
	3577 cm^{-1} (2)
	1691 cm^{-1} (2)
Ionization potential	10.2 eV
Molar refraction	5.448 cm^3 g^{-1} mol^{-1}
Refractive index, liq, at 16.5 °C	1.325
Bond dissociation enthalpy,	
$H—NH_2$, at 25 °C	431 kJ mol^{-1}
H—N, at 25 °C	388 kJ mol^{-1}
Dielectric constant of liquid, at −77.7 °C	25
at −33 °C	22.4
at 25 °C	16.9
Dipole moment	1.47 debye
Polarizability volume	2.22×10^{-24} cm^3
Ionization constant in water,	
at 25 °C (pK)	9.25
Electrical conductivity at −35 °C	
very pure	1×10^{-11} ohm^{-1} cm^{-1}
commercial	3×10^{-5} ohm^{-1} cm^{-1}

Ideal gas properties, 25 °C and 1 bar:

Specific heat (C_p)	35.652 J K^{-1} mol^{-1}
Standard entropy	192.774 J K^{-1} mol^{-1}
Standard enthalpy of formation	−45.898 kJ mol^{-1}
Free energy of formation	−16.367 kJ mol^{-1}
Equilibrium constant (log K_f)	2.867

Latent heat of evaporation	1.37 kJ g^{-1}
Standard entropy of evaporation	87.75 J K^{-1} mol^{-1}
Latent heat of fusion	0.3323 kJ g^{-1}
Standard entropy of fusion	28.93 J K^{-1} mol^{-1}
Heat of solution in water	2.180 kJ (g NH_3 gas)$^{-1}$

Properties of Equilibrium Vapor/Liquid System

Property	25 °C	−33.60 °C
Vapor pressure (bar)	10.031	1.000
Specific volume: liquid (cm^3 g^{-1})	1.65842	1.46636
vapor (cm^3 g^{-1})	128.13	1137.99
Free energy (G/RT)	−23.21	−24.33
Internal energy liquid (J g^{-1})	−646.53	−914.98
vapor (J g^{-1})	391.82	341.72
Enthalpy liquid (J g^{-1})	−644.86	−914.84
vapor (J g^{-1})	520.35	455.52
Latent heat (J g^{-1})	1165.2167	1370.3578
Entropy liquid (J g^{-1} K^{-1})	6.1059	5.1043
vapor (J g^{-1} K^{-1})	10.0140	10.8249
C_p liquid (J g^{-1} K^{-1})	4.7990	4.4286
vapor (J g^{-1} K^{-1})	3.1351	2.2325
C_v liquid (J g^{-1} K^{-1})	2.8517	3.1237
vapor (J g^{-1} K^{-1})	2.1345	1.6457

Flammability limits of ammonia in air: 16 & 25%
Flammability limits of ammonia in oxygen: 15 & 79%
Ignition temperature: ca 650 °C

APPENDIX 4
Nomograph of Properties of Ammonia

A copy of Appendix 8 of *Catalyst Handbook* is presented, the nomograph of selected properties of ammonia. Also given are standard free energy of formation, standard enthalpy of formation, and standard state entropy of ammonia. Numerical data are from D. R. Stull, E. F. Westrum Jr., and G. C. Sinke, *The Chemical Thermodynamics of Organic Compounds*, Wiley, New York (1969).

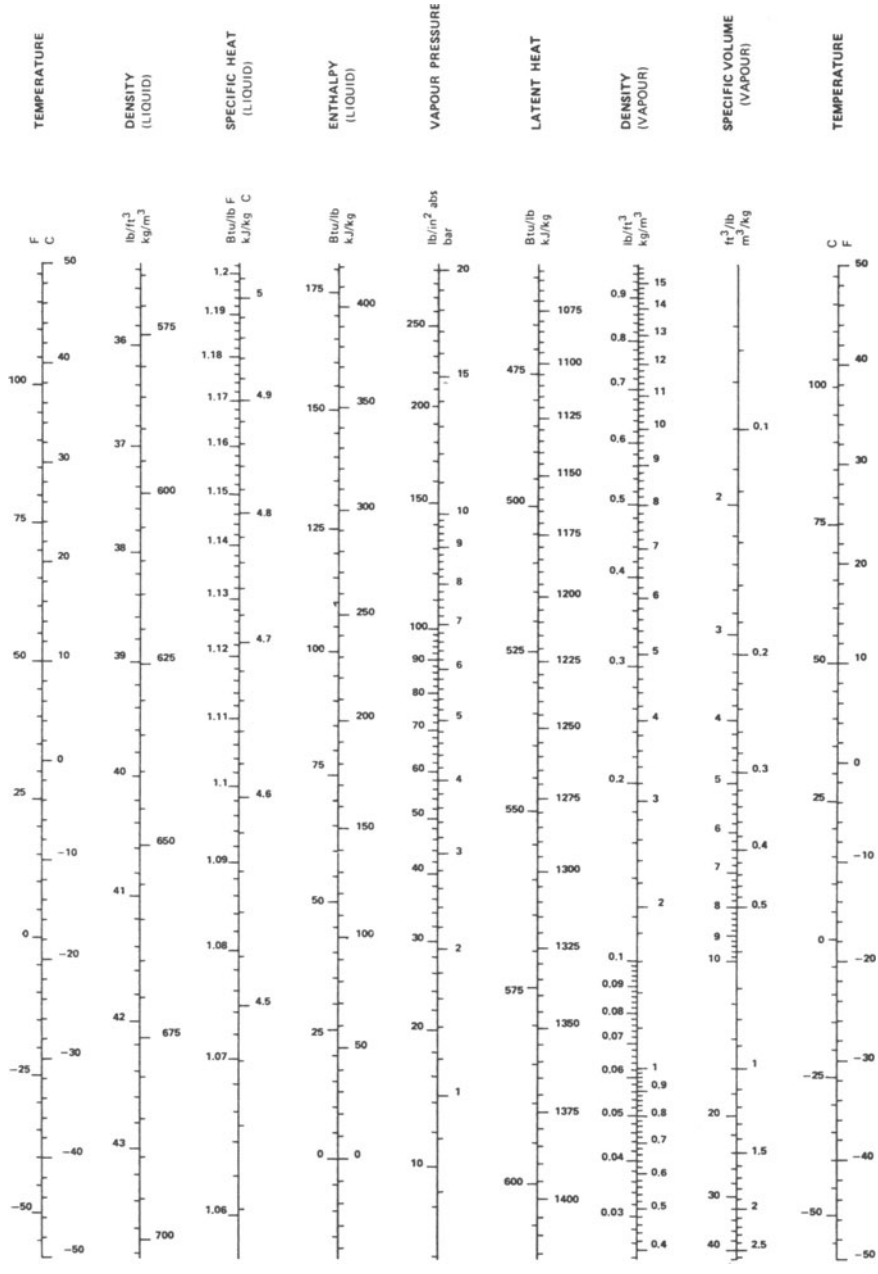
TEMPERATURE
F
C
DENSITY (LIQUID)
lb/ft3
kg/m3
SPECIFIC HEAT (LIQUID)
Btu/lb F
kJ/kg C
ENTHALPY (LIQUID)
Btu/lb
kJ/kg
VAPOUR PRESSURE
lb/in2 abs
bar
LATENT HEAT
Btu/lb
kJ/kg
DENSITY (VAPOUR)
lb/ft3
kg/m3
SPECIFIC VOLUME (VAPOUR)
ft3/lb
m3/kg
TEMPERATURE
C
F

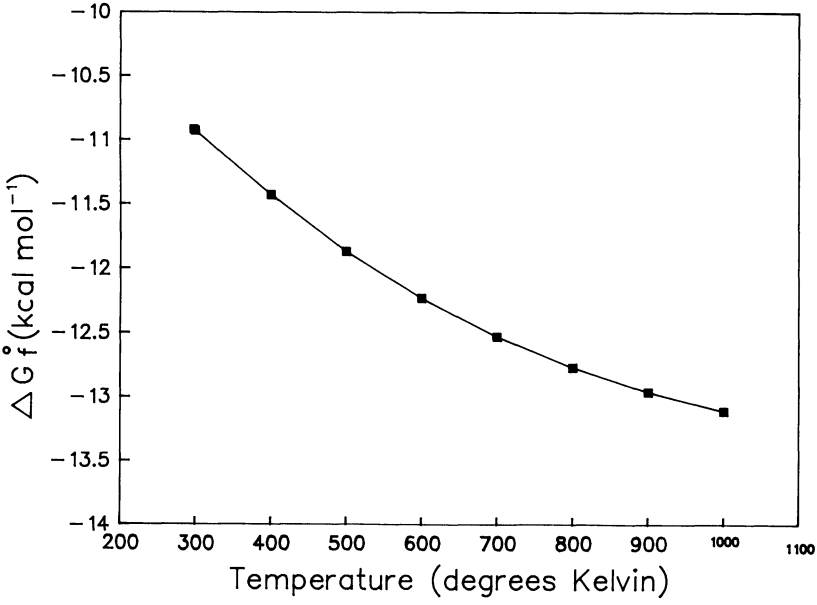

Standard free energy of formation.

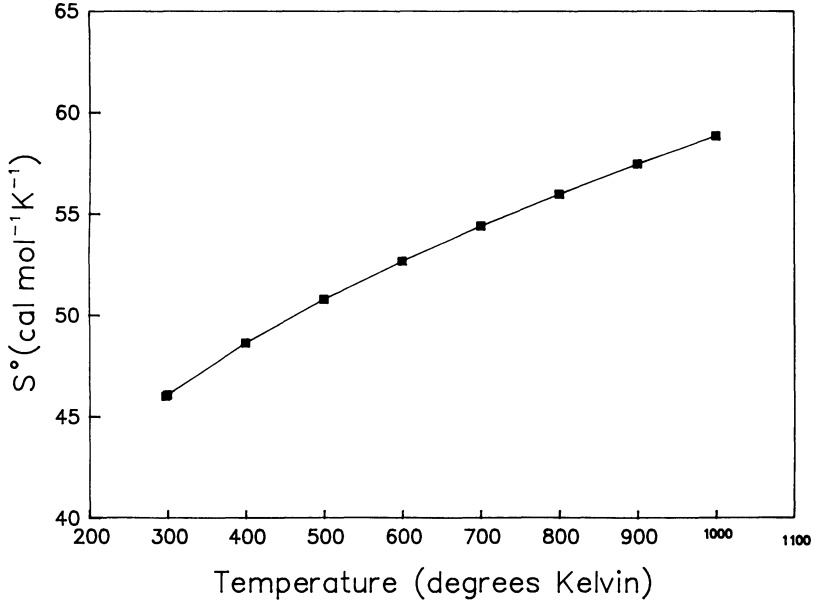

Standard entropy of ammonia.

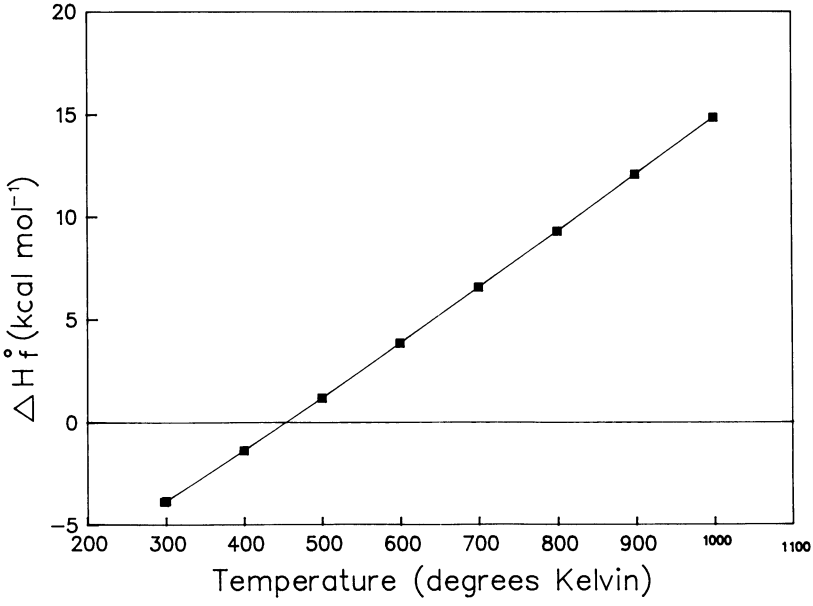

Standard enthalpy of formation.

APPENDIX 5

Equilibrium Data on Ammonia Synthesis Reaction

The tables of data are calculated from standard thermodynamic data, using the method of L. J. Gillespie and J. A. Beattie, *Phys. Rev.* **36**, 743 (1924).

Percent Composition

H_2	N_2	CH_4	A	He	NH_3
75.00	25.00	0.00	0.00	0.00	0.00

Molar Percent NH_3 at Equilibrium

Temp (°C)	Pressure (bar abs) 1	5	10	25	50	75	100	125
150	33.105	60.050	69.875	80.296	86.410	89.399	91.290	92.636
160	28.036	55.196	65.777	77.305	84.190	87.583	89.741	91.282
170	23.492	50.293	61.507	74.095	81.765	85.582	88.022	89.771
180	19.509	45.429	57.118	70.687	79.143	83.397	86.131	88.099
190	16.090	40.685	52.671	67.106	76.332	81.030	84.069	86.266
200	13.204	36.138	48.229	63.387	73.348	78.489	81.838	84.270
210	10.803	31.853	43.855	59.564	70.209	75.784	79.443	82.115
220	8.827	27.879	39.609	55.679	66.936	72.928	76.894	79.806
230	7.214	24.251	35.544	51.774	63.555	69.938	74.201	77.350
240	5.903	20.984	31.705	47.892	60.095	66·834	71.379	74.758
250	4.842	18.080	28.126	44.075	56.585	63.637	68.444	72.042
260	3.984	15.528	24.831	40.361	53.057	60.372	65.414	69.217
270	3.290	13.306	21.831	36.787	49.542	57.065	62.312	66.301
280	2.727	11.387	19.129	33.381	46.074	53.742	59.159	63.312
290	2.270	9.740	16.716	30.168	42.679	50.430	55.979	60.270
300	1.898	8.333	14.580	27.166	39.386	47.155	52.795	57.198
310	1.594	7.135	12.700	24.384	36.218	43.941	49.632	54.115
320	1.344	6.118	11.056	21.827	33.194	40.813	46.511	51.046
330	1.139	5.255	9.625	19.495	30.331	37.789	43.453	48.008
340	0.969	4.524	8.382	17.381	27.639	34.888	40.479	45.023
350	0.828	3.904	7.306	15.476	25.126	32.123	37.605	42.108
360	0.710	3.377	6.377	13.768	22.794	29.505	34.846	39.281
370	0.612	2.930	5.574	12.243	20.643	27.042	32.213	36.555
380	0.529	2.549	4.881	10.886	18.670	24.737	29.716	33.942
390	0.459	2.224	4.283	9.682	16.867	22.592	27.360	31.450
400	0.400	1.946	3.766	8.617	15.228	20.606	25.148	29.088
410	0.350	1.707	3.318	7.675	13.742	18.774	23.083	26.860
420	0.307	1.502	2.931	6.843	12.399	17.091	21.162	24.766
430	0.270	1.326	2.595	6.108	11.188	15.551	19.383	22.809
440	0.238	1.173	2.303	5.460	10.099	14.145	17.741	20.985
450	0.211	1.041	2.048	4.889	9.122	12.865	16.230	19.292
460	0.187	0.926	1.826	4.384	8.244	11.703	14.843	17.726
470	0.167	0.827	1.632	3.938	7.458	10.649	13.574	16.280
480	0.149	0.739	1.462	3.543	6.753	9.694	12.414	14.949
490	0.134	0.663	1.313	3.194	6.122	8.831	11.357	13.727
500	0.120	0.596	1.181	2.884	5.556	8.050	10.393	12.606
510	0.108	0.537	1.066	2.609	5.049	7.345	9.517	11.580
520	0.097	0.485	0.963	2.365	4.595	6.708	8.720	10.641
530	0.088	0.439	0.873	2.147	4.187	6.133	7.996	9.784
540	0.080	0.398	0.792	1.953	3.821	5.613	7.338	9.001
550	0.073	0.362	0.721	1.780	3.492	5.144	6.740	8.287

Percent Composition						
H_2	N_2	CH_4	A	He	NH_3	
75.00	25.00	0.00	0.00	0.00	0.00	

Temp (°C)	Molar Percent NH_3 at Equilibrium Pressure (bar abs)						
	150	175	200	225	250	275	300
150	93.658	94.469	95.131	95.682	96.150	96.551	96.899
160	92.457	93.390	94.156	94.796	95.340	95.808	96.215
170	91.109	92.176	93.053	93.789	94.416	94.958	95.430
180	89.610	90.820	91.817	92.656	93.373	93.994	94.537
190	87.959	89.318	90.442	91.391	92.204	92.911	93.530
200	86.152	87.668	88.926	89.990	90.906	91.703	92.404
210	84.190	85.869	87.265	88.450	89.473	90.365	91.153
220	82.077	83.921	85.460	86.771	87.904	88.897	89.774
230	79.818	81.829	83.512	84.951	86.199	87.295	88.266
240	77.419	79.596	81.425	82.994	84.358	85.560	86.628
250	74.890	77.231	79.205	80.903	82.384	83.693	84.859
260	72.244	74.743	76.858	78.684	80.282	81.697	82.962
270	69.495	72.143	74.394	76.344	78.057	79.579	80.942
280	66.657	69.446	71.826	73.895	75.718	77.342	78.803
290	63.751	66.666	69.166	71.347	73.275	74.999	76.552
300	60.793	63.821	66.428	68.712	70.739	72.557	74.200
310	57.803	60.927	63.630	66.007	68.124	70.028	71.756
320	54.802	58.004	60.787	63.245	65.443	67.427	69.232
330	51.811	55.070	57.919	60.445	62.712	64.766	66.641
340	48.846	52.144	55.041	57.622	59.948	62.061	63.996
350	45.929	49.245	52.173	54.794	57.165	59.327	61.313
360	43.074	46.389	49.332	51.978	54.381	56.581	58.609
370	40.299	43.593	46.533	49.189	51.611	53.837	55.896
380	37.617	40.871	43.792	46.444	48.872	51.112	53.190
390	35.038	38.236	41.123	43.756	46.178	48.420	50.507
400	32.572	35.699	38.537	41.139	43.541	45.774	47.860
410	30.226	33.268	36.045	38.603	40.975	43.187	45.262
420	28.005	30.951	33.655	36.158	38.489	40.671	42.724
430	25.912	28.751	31.374	33.811	36.091	38.235	40.258
440	23.946	26.673	29.205	31.570	33.791	35.886	37.871
450	22.107	24.717	27.152	29.437	31.592	33.633	35.572
460	20.394	22.882	25.215	27.415	29.499	31.478	33.366
470	18.802	21.167	23.396	25.507	27.513	29.427	31.258
480	17.326	19.568	21.691	23.710	25.637	27.481	29.251
490	15.963	18.082	20.099	22.025	23.869	25.640	27.345
500	14.705	16.704	18.616	20.447	22.208	23.905	25.543
510	13.547	15.430	17.237	18.975	20.653	22.274	23.843
520	12.483	14.252	15.958	17.605	19.198	20.744	22.244
530	11.505	13.167	14.774	16.331	17.842	19.312	20.743
540	10.609	12.167	13.679	15.149	16.580	17.975	19.337
550	9.788	11.247	12.668	14.054	15.407	16.729	18.023

Percent Composition

H_2	N_2	CH_4	A	He	NH_3
74.25	24.75	0.75	0.25	0.00	0.00

Molar Percent NH_3 at Equilibrium

Temp (°C)	Pressure (bar abs) 1	5	10	25	50	75	100	125
150	32.448	58.860	68.490	78.705	84.698	87.626	89.480	90.799
160	27.480	54.101	64.474	75.774	82.521	85.847	87.962	89.471
170	23.025	49.296	60.288	72.627	80.144	83.885	86.277	87.990
180	19.122	44.528	55.986	69.286	77.574	81.743	84.423	86.352
190	15.770	39.878	51.627	65.777	74.819	79.424	82.402	84.555
200	12.942	35.422	47.273	62.131	71.895	76.933	80.215	82.599
210	10.588	31.221	42.986	58.384	68.818	74.282	77.869	80.487
220	8.652	27.326	38.824	54.577	65.610	71.483	75.370	78.224
230	7.070	23.770	34.839	50.749	62.296	68.553	72.731	75.817
240	5.786	20.568	31.076	46.944	58.905	65.511	69.965	73.276
250	4.746	17.722	27.569	43.202	55.465	62.378	67.089	70.615
260	3.905	15.220	24.339	39.563	52.007	59.178	64.120	67.847
270	3.224	13.042	21.399	36.059	48.563	55.937	61.079	64.989
280	2.673	11.161	18.750	32.721	45.163	52.680	57.990	62.060
290	2.225	9.546	16.385	29.572	41.836	49.433	54.874	59.079
300	1.860	8.167	14.291	26.628	38.608	46.224	51.753	56.069
310	1.562	6.993	12.448	23.901	35.503	43.074	48.653	53.048
320	1.318	5.996	10.837	21.395	32.539	40.008	45.594	50.039
330	1.116	5.151	9.434	19.109	29.732	37.044	42.597	47.062
340	0.950	4.434	8.216	17.037	27.094	34.201	39.682	44.137
350	0.811	3.826	7.162	15.170	24.630	31.491	36.865	41.280
360	0.696	3.310	6.250	13.495	22.345	28.925	34.160	38.509
370	0.600	2.872	5.463	12.001	20.236	26.510	31.580	35.837
380	0.518	2.498	4.784	10.671	18.302	24.251	29.132	33.275
390	0.450	2.179	4.198	9.491	16.535	22.148	26.822	30.834
400	0.392	1.907	3.691	8.446	14.927	20.200	24.655	28.518
410	0.323	1.673	3.252	7.523	13.471	18.405	22.630	26.333
420	0.301	1.472	2.873	6.707	12.154	16.755	20.747	24.281
430	0.265	1.299	2.543	5.987	10.968	15.245	19.003	22.362
440	0.234	1.150	2.257	5.352	9.900	13.867	17.393	20.574
450	0.207	1.020	2.008	4.792	8.942	12.612	15.912	18.915
460	0.184	0.908	1.790	4.297	8.082	11.473	14.552	17.379
470	0.164	0.810	1.600	3.860	7.311	10.439	13.308	15.962
480	0.146	0.725	1.433	3.473	6.620	9.504	12.171	14.657
490	0.131	0.650	1.287	3.131	6.001	8.657	11.134	13.458
500	0.118	0.584	1.158	2.827	5.447	7.892	10.190	12.359
510	0.106	0.526	1.045	2.558	4.950	7.201	9.330	11.353
520	0.096	0.475	0.944	2.318	4.504	6.576	8.549	10.433
530	0.086	0.430	0.855	2.105	4.105	6.012	7.839	9.592
540	0.078	0.390	0.777	1.915	3.746	5.503	7.194	8.825
550	0.071	0.355	0.706	1.745	3.423	5.043	6.608	8.125

Percent Composition						
H_2	N_2	CH_4	A	He	NH_3	
74.25	24.75	0.75	0.25	0.00	0.00	

Temp	Molar Percent NH_3 at Equilibrium Pressure (bar abs)						
(°C)	150	175	200	225	250	275	300
150	91.801	92.595	93.244	93.785	94.243	94.636	94.977
160	90.622	91.538	92.288	92.915	93.448	93.907	94.306
170	89.301	90.347	91.207	91.928	92.543	93.074	93.536
180	87.833	89.018	89.995	90.817	91.520	92.129	92.661
190	86.213	87.546	88.647	89.577	90.374	91.066	91.647
200	84.443	85.929	87.161	88.204	89.101	89.882	90.569
210	82.520	84.165	85.533	86.895	87.697	88.571	89.343
220	80.450	82.256	83.764	85.048	86.159	87.132	87.991
230	78.235	80.205	81.855	83.265	84.488	85.562	86.514
240	75.884	78.017	79.810	81.347	82.684	83.861	84.907
250	73.406	75.700	77.634	79.298	80.750	82.031	83.174
260	70.813	93.262	75.335	77.123	78.689	80.076	81.316
270	68.119	70.715	72.921	74.831	76.509	78.000	79.336
280	65.338	68.071	70.404	72.431	74.218	75.809	77.240
290	62.491	65.347	67.797	69.934	71.824	73.513	75.035
300	59.592	62.559	65.115	67.353	69.339	71.120	72.730
310	56.663	59.724	62.373	64.702	66.777	68.643	70.336
320	53.722	56.860	59.588	61.997	64.150	66.094	67.863
330	50.790	53.985	56.777	59.253	61.475	63.487	65.324
340	47.885	51.118	53.957	56.487	58.776	60.837	62.733
350	45.025	48.276	51.147	53.716	56.040	58.159	60.105
360	42.228	45.478	48.363	50.956	53.312	55.469	57.455
370	39.508	42.737	45.620	48.224	50.598	52.780	54.797
380	36.879	40.070	42.934	45.534	47.914	50.110	52.147
390	34.351	37.487	40.318	42.900	45.274	47.472	49.518
400	31.934	35.000	37.784	40.334	42.690	44.879	46.924
410	29.635	32.618	35.341	37.849	40.174	42.344	44.378
420	27.458	30.346	32.998	35.452	37.738	39.878	41.891
430	25.405	28.190	30.762	33.152	35.388	37.490	39.474
440	23.478	26.153	28.635	30.955	33.133	35.188	37.135
450	21.676	24.235	26.623	28.864	30.978	32.979	34.881
460	19.996	22.436	24.725	26.882	28.926	30.867	32.719
470	18.435	20.754	22.941	25.011	26.979	28.856	30.652
480	16.988	19.187	21.269	23.250	25.140	26.948	28.684
490	15.651	17.730	19.708	21.597	23.406	25.144	26.816
500	14.418	16.379	18.254	20.051	21.778	23.443	25.049
510	13.283	15.129	16.902	18.607	20.253	21.843	23.383
520	12.239	13.975	15.648	17.263	18.827	20.343	21.814
530	11.281	12.911	14.487	16.014	17.497	18.939	20.343
540	10.402	11.930	13.413	14.855	16.259	17.628	18.964
550	9.597	11.028	12.422	13.782	15.109	16.406	17.676

Percent Composition

H_2	N_2	CH_4	A	He	NH_3
71.25	23.75	3.75	1.25	0.00	0.00

Molar Percent NH_3 at Equilibrium

Temp (°C)	Pressure (bar abs) 1	5	10	25	50	75	100	125
150	29.915	54.299	63.193	72.628	78.162	80.866	82.578	83.795
160	25.331	49.904	59.483	69.920	76.151	79.222	81.174	82.568
170	21.222	45.468	55.618	67.014	73.956	77.410	79.618	81.200
180	17.622	41.066	51.646	63.928	71.583	75.432	77.906	79.686
190	14.531	36.774	47.621	60.688	69.039	73.290	76.039	78.026
200	11.924	32.661	43.602	57.321	66.339	70.990	74.020	76.220
210	9.755	28.785	39.644	53.862	63.498	68.543	71.853	74.270
220	7.970	25.191	35.802	50.347	60.536	65.959	69.547	72.180
230	6.513	21.910	32.125	46.814	57.477	63.254	67.111	69.959
240	5.329	18.957	28.653	43.301	54.346	60.446	64.558	67.614
250	4.371	16.332	25.416	39.848	51.171	57.554	61.903	65.158
260	3.596	14.025	22.437	36.488	47.979	54.601	59.164	62.604
270	2.969	12.017	19.725	33.255	44.801	51.610	56.358	59.967
280	2.461	10.283	17.281	30.174	41.663	48.604	53.508	57.265
290	2.049	8.795	15.101	27.268	38.592	45.608	50.632	54.515
300	1.713	7.524	13.170	24.553	35.613	42.646	47.753	51.737
310	1.439	6.442	11.471	22.037	32.747	39.740	44.892	48.951
320	1.213	5.524	9.986	19.725	30.012	36.910	42.069	46.175
330	1.028	4.745	8.692	17.616	27.423	34.175	39.304	43.428
340	0.874	4.084	7.570	15.705	24.988	31.551	36.614	40.729
350	0.747	3.524	6.598	13.983	22.715	29.050	34.015	38.093
360	0.641	3.049	5.758	12.439	20.606	26.682	31.519	35.536
370	0.552	2.645	5.033	11.061	18.661	24.454	29.137	33.070
380	0.477	2.301	4.407	9.834	16.876	22.369	26.878	30.707
390	0.414	2.007	3.867	8.746	15.246	20.429	24.747	28.453
400	0.361	1.756	3.400	7.783	13.763	18.632	22.747	26.316
410	0.316	1.541	2.996	6.932	12.420	16.975	20.878	24.300
420	0.277	1.356	2.646	6.180	11.205	15.453	19.140	22.406
430	0.244	1.197	2.343	5.517	10.111	14.059	17.531	20.635
440	0.215	1.059	2.079	4.932	9.127	12.788	16.045	18.984
450	0.190	0.940	1.849	4.415	8.242	11.631	14.678	17.453
460	0.169	0.836	1.649	3.959	7.449	10.579	13.423	16.035
470	0.151	0.746	1.474	3.556	6.738	9.626	12.275	14.727
480	0.135	0.667	1.320	3.200	6.102	8.763	11.226	13.523
490	0.121	0.598	1.185	2.884	5.531	7.982	10.269	12.416
500	0.108	0.538	1.067	2.604	5.020	7.276	9.398	11.402
510	0.097	0.485	0.962	2.356	4.562	6.639	8.605	10.473
520	0.088	0.438	0.870	2.136	4.151	6.063	7.884	9.624
530	0.080	0.396	0.788	1.939	3.783	5.543	7.229	8.848
540	0.072	0.359	0.715	1.764	3.452	5.073	6.634	8.140
550	0.066	0.327	0.651	1.607	3.155	4.648	6.093	7.494

Percent Composition

H_2	N_2	CH_4	A	He	NH_3
71.25	23.75	3.75	1.25	0.00	0.00

Molar Percent NH_3 at Equilibrium Pressure (bar abs)

Temp (°C)	150	175	200	225	250	275	300
150	84.720	85.454	86.052	86.552	86.975	87.338	87.653
160	83.631	84.476	85.168	85.747	86.240	86.664	87.032
170	82.410	83.375	84.169	84.834	85.402	85.892	86.319
180	81.053	82.147	83.048	83.807	84.456	85.018	85.509
190	79.557	80.787	81.803	82.661	83.397	84.035	84.596
200	77.922	79.293	80.430	81.392	82.220	82.941	83.574
210	76.147	77.664	78.926	79.998	80.922	81.730	82.441
220	74.235	75.902	77.293	78.478	79.502	80.400	81.193
230	72.190	74.009	75.531	76.831	77.959	78.950	79.828
240	70.021	71.989	73.643	75.061	76.294	77.380	78.345
250	67.734	69.850	71.635	73.169	74.509	75.691	76.744
260	65.342	67.601	69.513	71.163	72.608	73.886	75.029
270	62.856	65.251	67.287	69.049	70.596	71.971	73.203
280	60.291	62.813	64.965	66.835	68.483	69.950	71.270
290	57.664	60.301	62.561	64.533	66.276	67.833	69.237
300	54.990	57.729	60.088	62.153	63.985	65.627	67.112
310	52.288	55.114	57.559	59.708	61.622	63.344	64.904
320	49.576	52.472	54.991	57.214	59.201	60.994	62.625
330	46.871	49.821	52.398	54.684	56.734	58.591	60.285
340	44.191	47.177	49.798	52.134	54.237	56.148	57.897
350	41.553	44.556	47.207	49.579	51.724	53.680	55.476
360	38.972	41.974	44.639	47.034	49.208	51.199	53.033
370	36.463	39.446	42.109	44.514	46.707	48.721	50.583
380	34.036	36.985	39.631	42.032	44.231	46.259	48.140
390	31.704	34.602	37.217	39.603	41.796	43.826	45.716
400	29.473	32.307	34.879	37.236	39.413	41.435	43.324
410	27.351	30.108	32.625	34.943	37.093	39.097	40.977
420	25.341	28.012	30.463	32.732	34.844	36.822	38.683
430	23.447	26.022	28.399	30.609	32.676	34.619	36.453
440	21.668	24.141	26.436	28.581	30.595	32.495	34.295
450	20.004	22.370	24.578	26.651	28.606	30.457	32.215
460	18.454	20.710	22.826	24.822	26.711	28.507	30.220
470	17.013	19.157	21.179	23.094	24.915	26.651	28.312
480	15.677	17.710	19.636	21.468	23.216	24.889	26.495
490	14.443	16.365	18.194	19.942	21.616	23.223	24.771
500	13.305	15.118	16.851	18.514	20.112	21.652	23.139
510	12.257	13.964	15.603	17.181	18.703	20.175	21.600
520	11.293	12.898	14.445	15.940	17.386	18.789	20.151
530	10.409	11.915	13.373	14.786	16.158	17.492	18.792
540	9.598	11.010	12.382	13.716	15.015	16.281	17.518
550	8.854	10.177	11.467	12.724	13.952	15.153	16.328

Percent Composition

H_2	N_2	CH_4	A	He	NH_3
67.50	22.50	7.50	2.50	0.00	0.00

Temp (°C)	Molar Percent NH_3 at Equilibrium Pressure (bar abs) 1	5	10	25	50	75	100	125
150	26.950	49.011	57.070	65.622	70.640	73.091	74.643	75.746
160	22.811	45.032	53.708	63.168	68.816	71.600	73.369	74.633
170	19.102	41.016	50.207	60.534	66.826	69.957	71.958	73.391
180	15.855	37.033	46.610	57.737	64.674	68.163	70.405	72.018
190	13.070	33.151	42.966	54.801	62.369	66.221	68.713	70.513
200	10.721	29.433	39.329	51.752	59.922	64.137	66.882	68.875
210	8.768	25.931	35.748	48.620	57.348	61.919	64.919	67.107
220	7.162	22.686	32.275	45.437	54.666	59.579	62.829	65.215
230	5.852	19.725	28.950	42.239	51.896	57.129	60.623	63.202
240	4.787	17.060	25.813	39.061	49.061	54.586	58.311	61.079
250	3.926	14.694	22.891	35.937	46.187	51.968	55.907	58.855
260	3.230	12.615	20.201	32.899	43.299	49.295	53.428	56.543
270	2.666	10.806	17.754	29.976	40.423	46.588	50.889	54.156
280	2.210	9.245	15.551	27.193	37.585	43.869	48.309	51.711
290	1.840	7.905	13.585	24.568	34.808	41.159	45.707	49.223
300	1.538	6.762	11.845	22.116	32.114	38.480	43.103	46.711
310	1.291	5.789	10.315	19.845	29.524	35.851	40.515	44.190
320	1.089	4.963	8.978	17.759	27.053	33.293	37.963	41.680
330	0.923	4.262	7.813	15.856	24.714	30.821	35.463	39.196
340	0.785	3.669	6.809	14.133	22.515	28.450	33.031	36.756
350	0.671	3.165	5.929	12.581	20.463	26.190	30.681	34.373
360	0.575	2.738	5.174	11.190	18.559	24.051	28.426	32.062
370	0.496	2.375	4.522	9.948	16.804	22.038	26.274	29.833
380	0.429	2.066	3.959	8.844	15.194	20.156	24.233	27.697
390	0.372	1.802	3.473	7.864	13.724	18.405	22.308	25.661
400	0.324	1.577	3.054	6.997	12.387	16.783	20.502	23.731
410	0.283	1.384	2.691	6.231	11.176	15.288	18.815	21.909
420	0.248	1.217	2.376	5.555	10.082	13.915	17.246	20.199
430	0.219	1.074	2.104	4.958	9.096	12.658	15.794	18.600
440	0.193	0.951	1.867	4.432	8.210	11.512	14.453	17.110
450	0.171	0.844	1.660	3.967	7.413	10.469	13.220	15.727
460	0.152	0.751	1.481	3.557	6.699	9.521	12.088	14.448
470	0.135	0.670	1.323	3.195	6.059	8.662	11.053	13.267
480	0.121	0.599	1.185	2.875	5.486	7.884	10.107	12.181
490	0.108	0.537	1.064	2.591	4.973	7.181	9.244	11.183
500	0.097	0.483	0.958	2.340	4.513	6.546	8.459	10.268
510	0.087	0.435	0.864	2.116	4.101	5.971	7.744	9.431
520	0.079	0.393	0.781	1.918	3.731	5.453	7.095	8.665
530	0.071	0.356	0.707	1.742	3.400	4.985	6.504	7.966
540	0.065	0.323	0.642	1.584	3.102	4.562	5.968	7.327
550	0.059	0.293	0.584	1.443	2.835	4.180	5.482	6.745

Percent Composition

H_2	N_2	CH_4	A	He	NH_3
67.50	22.50	7.50	2.50	0.00	0.00

Molar Percent NH_3 at Equilibrium Pressure (bar abs)

Temp (°C)	150	175	200	225	250	275	300
150	76.585	77.250	77.792	78.245	78.629	78.959	79.245
160	75.596	76.362	76.989	77.514	77.960	78.345	78.680
170	74.488	75.363	76.082	76.685	77.200	77.644	78.032
180	73.256	74.248	75.065	75.752	76.340	76.850	77.295
190	71.900	73.014	73.434	74.712	75.379	75.958	76.466
200	70.417	71.659	72.689	73.561	74.310	74.964	75.538
210	68.808	70.182	71.325	72.296	73.133	73.865	74.509
220	67.075	68.585	69.845	70.918	71.845	72.658	73.377
230	65.223	66.870	68.248	69.425	70.447	71.344	72.138
240	63.258	65.040	66.538	67.821	68.938	69.921	70.794
250	61.188	63.104	64.720	66.108	67.321	68.391	69.344
260	59.022	61.067	62.799	64.292	65.599	66.757	67.791
270	56.772	58.941	60.783	62.378	63.779	65.022	66.137
280	54.451	56.735	58.682	60.375	61.866	63.194	64.388
290	52.074	54.462	56.508	58.292	59.869	61.278	62.548
300	49.656	52.135	54.270	56.139	57.797	59.283	60.626
310	47.212	49.771	51.983	53.929	55.661	57.218	58.630
320	44.759	47.381	49.661	51.673	53.471	55.094	56.569
330	42.313	44.984	47.317	49.386	51.242	52.922	54.454
340	39.890	42.593	44.967	47.081	48.984	50.714	52.297
350	37.505	40.224	42.624	44.771	46.712	48.483	50.108
360	35.172	37.890	40.302	42.471	44.440	46.241	47.900
370	32.904	35.605	38.016	40.193	42.178	44.002	45.687
380	30.711	33.380	35.776	37.951	39.941	41.777	43.480
390	28.603	31.226	33.595	35.755	37.741	39.579	41.290
400	26.588	29.153	31.482	33.616	35.587	37.419	39.129
410	24.670	27.166	29.445	31.544	33.490	35.306	37.008
420	22.855	25.271	27.491	29.545	31.459	33.250	34.935
430	21.143	23.474	25.626	27.627	29.500	31.259	32.920
440	19.537	21.775	23.853	25.795	27.619	29.340	30.970
450	18.035	20.175	22.174	24.051	25.821	27.498	29.091
460	16.634	18.675	20.591	22.398	24.109	25.736	27.288
470	15.334	17.273	19.103	20.837	22.486	24.059	25.564
480	14.128	15.967	17.709	19.368	20.951	22.467	23.922
490	13.014	14.752	16.408	17.989	19.505	20.961	22.363
500	11.987	13.626	15.195	16.699	18.146	19.541	20.889
510	11.042	12.585	14.067	15.495	16.874	18.207	19.497
520	10.172	11.623	13.022	14.374	15.684	16.954	18.188
530	9.375	10.736	12.054	13.333	14.574	15.783	16.960
540	8.643	9.919	11.159	12.366	13.542	14.689	15.809
550	7.973	9.168	10.333	11.471	12.582	13.669	14.734

Percent Composition

H_2	N_2	CH_4	A	He	NH_3
63.75	21.25	11.25	3.75	0.00	0.00

Temp (°C)	Molar Percent NH_3 at Equilibrium Pressure (bar abs)							
	1	5	10	25	50	75	100	125
150	24.191	44.136	51.440	59.198	63.752	65.978	67.386	68.387
160	20.460	40.532	48.393	56.971	62.097	64.623	66.229	67.375
170	17.121	36.898	45.220	54.582	60.291	63.131	64.946	66.247
180	14.201	33.296	41.962	52.046	58.338	61.503	63.537	65.001
190	11.699	29.789	38.664	49.385	56.247	59.741	62.001	63.634
200	9.591	26.432	35.374	46.621	54.028	57.851	60.340	62.147
210	7.841	23.273	32.137	43.784	51.695	55.839	58.559	60.544
220	6.402	20.349	28.999	40.903	49.264	53.717	56.664	58.827
230	5.228	17.683	25.999	38.010	46.755	51.497	54.664	57.003
240	4.276	15.286	23.169	35.135	44.188	49.193	52.569	55.078
250	3.506	13.159	20.535	32.312	41.586	46.822	50.392	53.063
260	2.884	11.292	18.113	29.567	38.973	44.402	48.146	50.968
270	2.380	9.669	15.912	26.929	36.372	41.952	45.847	48.807
280	1.973	8.268	13.930	24.417	33.806	39.492	43.513	46.594
290	1.642	7.068	12.164	22.051	31.297	37.041	41.159	44.343
300	1.373	6.044	10.602	19.841	28.865	34.620	38.803	42.069
310	1.152	5.173	9.229	17.796	26.527	32.245	36.464	39.790
320	0.972	4.434	8.030	15.920	24.297	29.934	34.157	37.520
330	0.823	3.807	6.986	14.208	22.188	27.703	31.898	35.276
340	0.700	3.276	6.082	12.660	20.207	25.562	29.702	33.071
350	0.598	2.826	5.299	11.265	18.358	23.524	27.581	30.919
360	0.513	2.445	4.623	10.016	16.645	21.596	25.546	28.832
370	0.442	2.120	4.040	8.902	15.066	19.782	23.605	26.821
380	0.382	1.844	3.536	7.912	13.618	18.087	21.765	24.893
390	0.332	1.609	3.102	7.034	12.296	16.510	20.030	23.057
400	0.289	1.407	2.727	6.257	11.096	15.051	18.403	21.317
410	0.253	1.235	2.403	5.571	10.008	13.076	16.884	19.675
420	0.222	1.087	2.122	4.965	9.026	12.472	15.472	18.134
430	0.195	0.959	1.878	4.431	8.141	11.342	14.165	16.694
440	0.172	0.848	1.666	3.960	7.346	10.313	12.959	15.353
450	0.153	0.753	1.482	3.545	6.632	9.376	11.850	14.108
460	0.135	0.670	1.321	3.178	5.992	8.525	10.833	12.957
470	0.121	0.598	1.181	2.854	5.419	7.754	9.903	11.896
480	0.108	0.534	1.058	2.567	4.905	7.057	9.053	10.919
490	0.097	0.479	0.950	2.314	4.446	6.426	8.279	10.023
500	0.087	0.431	0.855	2.089	4.034	5.856	7.574	9.201
510	0.078	0.388	0.771	1.890	3.665	5.342	6.933	8.449
520	0.070	0.350	0.696	1.713	3.335	4.877	6.350	7.761
530	0.064	0.317	0.631	1.555	3.038	4.458	5.821	7.134
540	0.058	0.288	0.573	1.414	2.772	4.079	5.341	6.561
550	0.052	0.262	0.521	1.289	2.533	3.737	4.904	6.039

Percent Composition

H_2	N_2	CH_4	A	He	NH_3
63.75	21.25	11.25	3.75	0.00	0.00

Molar Percent NH_3 at Equilibrium Pressure (bar abs)

Temp (°C)	150	175	200	225	250	275	300
150	69.148	69.752	70.245	70.656	71.005	71.305	71.564
160	68.249	68.945	69.515	69.991	70.396	70.746	71.050
170	67.243	68.037	68.689	69.237	69.704	70.108	70.460
180	66.124	67.024	67.765	68.389	68.922	69.385	69.790
190	64.892	65.903	66.738	67.443	68.048	68.574	69.035
200	63.546	64.673	65.607	66.397	67.078	67.670	68.192
210	62.085	63.332	64.369	65.249	66.009	66.672	67.257
220	60.514	61.883	63.025	63.998	64.839	65.577	66.228
230	58.835	60.327	61.577	62.644	63.570	64.383	65.103
240	57.053	58.669	60.026	61.189	62.201	63.091	63.884
250	55.177	56.913	58.378	59.636	60.735	61.704	62.569
260	53.215	55.068	56.637	57.990	59.174	60.223	61.160
270	51.177	53.142	54.811	56.256	57.525	58.652	59.661
280	49.076	51.144	52.909	54.442	55.792	56.995	58.076
290	46.925	49.087	50.940	52.556	53.984	55.260	56.410
300	44.736	46.982	48.915	50.607	52.109	53.454	54.670
310	42.525	44.842	46.846	48.607	50.176	51.585	52.863
320	40.307	42.682	44.745	46.567	48.195	49.664	50.999
330	38.096	40.514	42.626	44.499	46.179	47.700	49.087
340	35.906	38.353	40.501	42.415	44.138	45.703	47.136
350	33.752	36.211	38.384	40.327	42.084	43.687	45.158
360	31.645	34.103	36.286	38.249	40.030	41.661	43.163
370	29.596	32.039	34.220	36.191	37.988	39.637	41.163
380	27.617	30.031	32.198	34.166	35.967	37.628	39.168
390	25.715	28.087	30.229	32.183	33.979	35.643	37.191
400	23.897	26.215	28.321	30.252	32.035	33.682	35.239
410	22.168	24.423	26.483	28.381	30.142	31.785	33.324
420	20.531	22.714	24.720	26.578	28.308	29.929	31.453
430	18.989	21.093	23.038	24.847	26.540	28.132	29.634
440	17.542	19.562	21.439	23.194	24.843	26.400	27.874
450	16.189	18.121	19.926	21.621	23.221	24.738	26.179
460	14.928	16.770	18.499	20.131	21.678	23.149	24.552
470	13.758	15.507	17.158	18.724	20.214	21.636	22.996
480	12.673	14.331	15.903	17.400	18.830	20.200	21.516
490	11.672	13.238	14.731	16.158	17.527	18.843	20.110
500	10.748	12.225	13.639	14.996	16.303	17.563	18.781
510	9.898	11.288	12.624	13.912	15.156	16.360	17.526
520	9.117	10.423	11.684	12.903	14.085	15.232	16.347
530	8.401	9.626	10.813	11.966	13.086	14.177	15.240
540	7.744	8.892	10.009	11.096	12.157	13.192	14.203
550	7.142	8.217	9.266	10.291	11.293	12.274	13.234

Percent Composition

H_2	N_2	CH_4	A	He	NH_3
60.00	20.00	15.00	5.00	0.00	0.00

Molar Percent NH_3 at Equilibrium

Temp (°C)	Pressure (bar abs) 1	5	10	25	50	75	100	125
150	21.620	39.628	46.247	53.287	57.423	59.444	60.724	61.634
160	18.266	36.367	43.485	51.265	55.919	58.213	59.672	60.713
170	15.269	33.081	40.610	49.097	54.279	56.858	58.506	59.688
180	12.653	29.828	37.661	46.797	52.506	55.379	57.226	58.555
190	10.414	26.664	34.679	44.385	50.608	53.779	55.831	57.313
200	8.532	23.639	31.705	41.882	48.595	52.063	54.323	55.963
210	6.970	20.796	28.783	39.313	46.481	50.239	52.706	54.508
220	5.687	18.168	25.953	36.706	44.277	48.315	50.987	52.949
230	4.643	15.774	23.250	34.090	42.005	46.302	49.173	51.294
240	3.796	13.626	20.704	31.493	39.681	44.215	47.274	49.549
250	3.111	11.721	18.337	28.944	37.327	42.068	45.302	47.723
260	2.558	10.052	16.162	26.469	34.965	39.878	43.268	45.826
270	2.111	8.602	14.188	24.092	32.615	37.662	41.188	43.869
280	1.749	7.352	12.413	21.831	30.298	35.438	39.076	41.865
290	1.456	6.282	10.833	19.702	28.034	33.224	36.947	39.829
300	1.217	5.369	9.436	17.717	25.842	31.037	34.819	37.773
310	1.021	4.593	8.210	15.881	23.735	28.894	32.706	35.713
320	0.861	3.936	7.140	14.198	21.729	26.810	30.623	33.663
330	0.730	3.379	6.209	12.665	19.831	24.799	28.586	31.636
340	0.621	2.907	5.403	11.279	18.051	22.872	26.606	29.647
350	0.530	2.507	4.706	10.032	16.391	21.038	24.694	27.706
360	0.455	2.168	4.105	8.915	14.853	19.304	22.862	25.825
370	0.392	1.880	3.586	7.920	13.437	17.674	21.115	24.013
380	0.339	1.635	3.139	7.037	12.140	16.152	19.460	22.278
390	0.294	1.426	2.753	6.254	10.958	14.737	17.901	20.626
400	0.256	1.248	2.419	5.561	9.883	13.428	16.439	19.061
410	0.224	1.095	2.131	4.950	8.911	12.223	15.076	17.586
420	0.196	0.963	1.882	4.411	8.034	11.118	13.809	16.202
430	0.173	0.850	1.665	3.935	7.244	10.107	12.638	14.909
440	0.153	0.752	1.478	3.516	6.534	9.186	11.557	13.706
450	0.135	0.667	1.314	3.147	5.898	8.349	10.565	12.590
460	0.120	0.594	1.172	2.821	5.327	7.589	9.655	11.559
470	0.107	0.530	1.047	2.533	4.816	6.901	8.823	10.609
480	0.095	0.474	0.938	2.278	4.359	6.278	8.063	9.734
490	0.086	0.425	0.842	2.053	3.950	5.716	7.371	8.932
500	0.077	0.382	0.758	1.853	3.583	5.208	6.742	8.197
510	0.069	0.344	0.683	1.676	3.255	4.749	6.170	7.525
520	0.062	0.311	0.617	1.519	2.961	4.335	5.650	6.911
530	0.056	0.281	0.559	1.379	2.697	3.962	5.178	6.351
540	0.051	0.255	0.508	1.254	2.461	3.624	4.750	5.839
550	0.046	0.232	0.462	1.143	2.248	3.320	4.361	5.373

Percent Composition

H_2	N_2	CH_4	A	He	NH_3
60.00	20.00	15.00	5.00	0.00	0.00

Molar Percent NH_3 at Equilibrium Pressure (bar abs)

Temp (°C)	150	175	200	225	250	275	300
150	62.325	62.874	63.332	63.696	64.013	64.285	64.522
160	61.507	62.139	62.657	63.090	63.459	63.776	64.053
170	60.592	61.313	61.906	62.404	62.828	63.195	63.515
180	59.575	60.392	61.065	61.632	62.117	62.537	62.905
190	58.455	59.373	60.132	60.772	61.321	61.798	62.218
200	57.232	58.255	59.103	59.821	60.439	60.977	61.451
210	55.906	57.038	57.979	58.777	59.467	60.069	60.600
220	54.480	55.722	56.758	57.641	58.404	59.073	59.665
230	52.956	54.310	55.443	56.411	57.252	57.989	58.643
240	51.340	52.805	54.036	55.091	56.009	56.817	57.535
250	49.639	51.214	52.541	53.683	54.678	55.558	56.342
260	47.861	49.541	50.963	52.190	53.263	54.214	55.064
270	46.016	47.796	49.308	50.618	51.768	52.789	53.705
280	44.114	45.987	47.586	48.975	50.198	51.288	52.268
290	42.167	44.125	45.803	47.267	48.561	49.717	50.759
300	40.187	42.220	43.971	45.503	46.863	48.081	49.183
310	38.188	40.285	42.099	43.693	45.114	46.391	47.548
320	36.184	38.332	40.199	41.849	43.322	44.652	45.861
330	34.186	36.373	38.284	39.979	41.499	42.875	44.131
340	32.209	34.421	36.364	38.095	39.654	41.071	42.367
350	30.265	32.488	34.452	36.210	37.799	39.248	40.579
360	28.365	30.586	32.559	34.333	35.944	37.419	38.777
370	26.518	28.724	30.695	32.476	34.100	35.592	36.971
380	24.735	26.913	28.871	30.648	32.276	33.778	35.171
390	23.022	25.162	27.095	28.860	30.484	31.987	33.386
400	21.386	23.476	25.376	27.120	28.730	30.227	31.626
410	19.830	21.863	23.721	25.434	27.024	28.507	29.899
420	18.359	20.326	22.134	23.810	25.372	26.835	28.212
430	16.973	18.868	20.620	22.252	23.779	25.216	26.573
440	15.674	17.491	19.183	20.764	22.252	23.656	24.988
450	14.459	16.197	17.822	19.350	20.792	22.160	23.460
460	13.329	14.984	16.540	18.010	19.404	20.730	21.996
470	12.279	13.851	15.336	16.745	18.087	19.369	20.596
480	11.308	12.796	14.209	15.556	16.844	18.078	19.264
490	10.410	11.816	13.157	14.441	15.673	16.858	18.001
500	9.584	10.908	12.179	13.398	14.574	15.708	16.805
510	8.823	10.069	11.269	12.426	13.545	14.628	15.678
520	8.125	9.295	10.426	11.521	12.583	13.615	14.619
530	7.484	8.582	9.646	10.681	11.688	12.668	13.625
540	6.897	7.925	8.926	9.902	10.854	11.785	12.694
550	6.360	7.322	8.262	9.181	10.080	10.961	11.825

APPENDIX 6

*Selected Patents on Ammonia Synthesis**

This list of patents is not comprehensive nor does it include some patents of historical importance. The patents selected are predominantly those relevant to the modern processes and to possible new or improved processes and catalysts. They are listed in chronological order of first publication date. A list of assignees and their patents is also given.

Patent Codes: AU—Australia; BE—Belgium; CA—Canada; CH—Switzerland; CN—China; DE—German Federal Republic; EP—European Patent; ES—Spain; FR—France; GB—Great Britain; IT—Italy; JP—Japan; NL—Netherlands; NO—Norway; PL—Poland; SU—USSR; US—United States of America; WO—World Intellectual Property Organisation; ZA—South Africa.

1959

1. Manufacture of catalysts for ammonia synthesis. (Imperial Chemical Industries Ltd). BE 576059 (1959).

1961

2. Manufacture of shaped catalysts for ammonia synthesis by crushing and firing precursor powder, pelleting, and sintering. Examples include beryllium addition. A, Nielson, S. S. Bergh, and H. Topsoe (Wargons Aktiebolag and Haldor Topsoe). GB 989242 (1961); US 3243386 (1966).

1964

3. Manufacture of catalysts for ammonia synthesis. (Kuhlmann). GB 1080838 (1964); CH 434218 (1964).

* Compiled by M. S. Spencer, University of Wales, Cardiff, Wales.

4. Radial flow converter for ammonia synthesis processes. (Haldor Topsoe). ZA 645279 (1964).

5. Catalysts for ammonia synthesis containing caesium. J. L. Carter and C. G. Savini. US 3472794 (1969).

1965

6. Hydrocarbon reforming for the production of synthesis gas for ammonia synthesis process. B. J. Grotz (C. F. Braun Co.). US 3442613 (1965).

1969

7. Improvements in the energy cycle in ammonia synthesis processes. J. A. Finneran, H. C. Mayo, R. H. Multhaup, and R. B. Smith (Pullman Inc.). US 3441393 (1969).

1970

8. Preparation of a reduced ammonia synthesis catalyst which resists oxidation. (Imperial Chemical Industries Ltd.). GB 1191846 (1970); US 3513107 (1970).

1971

9. Ammonia synthesis process using a catalytic reactor with multiple beds and controlled gas entry temperatures. (Chemicke Zavody NP). FR 1603902 (1971); GB 1258410 (1971).

10. Supported ruthenium catalyst for ammonia synthesis. A. Ozaki, K. Aika, and A. Furuta (Okagama). DE 2130732 (1971); US 3770658 (1973).

11. Ammonia synthesis process using a catalyst containing a transitional metal and an alkali metal in the metallic state. (Japan Gasoline Co. Ltd.). BE 768802 (1971); US 3770658 (1973); GB 1361822 (1974).

12. Catalysts for ammonia synthesis consisting of graphite complexes, especially those containing ferric chloride and potassium. (Sagami Chemical Research Center). DE 2114769 (1971).

1972

13. Catalysts for ammonia synthesis consisting of donor-acceptor complexes of alkali metals and transition metal phthalocyanines. (Tokyo University). US 3658721 (1972).

14. Catalysts for ammonia synthesis prepared from graphite/alkali metal compositions. (Tokyo University). US 3660028 (1972).

15. Platinum-containing catalyst for ammonia synthesis. (Chevron Research Co.). US 3653831 (1972).

16. An iron oxide-based ammonia synthesis catalyst with mixed metal promoters of increased alumina content. L. M. Dmitrenko and P. K. Rabina. SU 270702 (1972).

17. Ammonia synthesis catalysts consisting of magnetite containing a small amount of cobalt oxide. (Societe Chimique de la Grande Paroisse). NL 7203559 (1972); US 3839229 (1974).

1973

18. Ammonia synthesis process with decreased ammonium carbamate decomposition in the compressor. (Mitsubishi). JP 48008699 (1973).

1974

19. Pre-reduction with hydrogen of ammonia synthesis catalysts. (American Cyanamid Co.). US 3787335 (1974).

20. Ammonia synthesis catalysts of increased activity prepared from hexacyanoferrate and ruthenium. Y. A. Lyubchenko. SU 422442 (1974).

21. Catalysts for ammonia synthesis consisting of graphite complexes, especially those containing ferric chloride and potassium. (Sagami Chemical Research Center). US 3830753 (1974).

22. Ammonia synthesis catalyst prepared from iron oxide, alumina, and one or more oxide of potassium, calcium, and barium. (Japan Gasoline Co. Ltd.). JP 74034916 (1974).

1975

23. Separation of vent gases from an ammonia synthesis process into hydrogen-rich and argon-rich fractions. (Linde AG). DE 2348329 (1975).

24. Carbon oxides removal from gas streams in ammonia synthesis processes, by catalytic conversion and subsequent absorption of carbon dioxide. T. A. Semenova. SU 436075 (1975).

25. Optimal size and shape of catalyst particles for ammonia synthesis processes. (Chemie Linz). US 3965246 (1975).

26. Strength tester for ammonia synthesis catalysts, consisting of a truncated cone test chamber on a rod with solenoid core reciprocation from below. P. P. Andreichev. SU 448291 (1975).

27. Preparation of iron-oxide-based, ammonia synthesis catalysts which includes a stage of granulation in the turbulent flow of an activating liquid. V. P. Lytkin. SU 476018 (1975).

28. Reactivation of reduced and passivated ammonia synthesis catalysts (containing surface oxygen) by heating in inert gas to avoid the production of water vapor. (Moscow Mendeleev Chemical Institute). SU 484000 (1975).

1976

29. Hydrogen recovery by pressure swing adsorption from the synthesis loop of an ammonia synthesis process. (Union Carbide Corp.). US 4077780 (1976).

30. Production of iron-oxide-based, ammonia synthesis catalysts, including a stage of fusion in the presence of graphite. (Lummus Co.). US 3951862 (1976); GB 1529823 (1978).

31. Preparation of ammonia synthesis catalysts by the treatment of a reduced iron oxide with an aqueous solution of a cerium salt. (Lummus Co.). US 3992328 (1976); GB 1479310 (1977).

32. Ammonia synthesis catalysts prepared by heating an iron-oxide-based mixture containing promoters, and granulation by molding. S. P. Vorontsev. SU 487663 (1976).

1977

33. Manufacture of catalysts for ammonia synthesis. (Imperial Chemical Industries Ltd). GB 1484864 (1977).

34. Ammonia synthesis catalysts containing iron, potassium, and zirconium oxides, and cobalt and magnesium ferrites. P. D. Rabina, V. S. Komarov, and M. D. Efros. SU 539601 (1977).

35. Ammonia synthesis catalyst prepared from a graphite/metal halide compound and an aluminum compound. (Sagami Chemical Research Center). JP 77010833 (1977).

1978

36. Ammonia synthesis catalysts of increased low-temperature activity, prepared from iron and potassium oxides, cobalt ferrite, and calcium aluminate. V. S. Komarov, P. D. Rabina, and L. M. Dmitrenko. SU 598632 (1978).

37. Gas production in and ammonia synthesis process by hydrocarbon reforming, with reaction tubes in a fluidized bed furnace. L. F. Robinson, DE 2815985 (1978); US 4224298 (1980); GB 1579577 (1980).

38. Ammonia synthesis process. E. Perry (Monsanto Co.). GB 2017071A (1978).

39. Process measurement and control system, suitable for processes such as ammonia synthesis. R. W. Rutledge and F. D. Ganaway (Phillips Petroleum Co.). US 4069413 (1978).

40. Design of synthesis loop for an ammonia synthesis plant, with ammonia removal by water. C. L. Becker (Pullman Inc.). DE 2741851 (1978).

41. Production of ammonia synthesis catalysts of increased activity by a specified heat treatment of a mixture of iron oxide(s) and promoters in an electric arc furnace. V. D. Lytkin, D. B. Chistozvon, and V. S. Sobolevski. SU 445230 (1978).

42. Catalysts for ammonia synthesis prepared with an impregnation stage with cerium salts. (The Lummus Corp.). GB 1529823 (1978).

43. Catalysts for ammonia synthesis made from iron-titanium alloys. M. N. Ozyagcilar (The Rafet Industrial Group). DE 2821972 (1978); US-A 799099 (1977); US-A 801908 (1977).

44. Manufacture of catalysts for ammonia synthesis. (Soc. Ital. Ric. Ind.). US 4073749 (1978).

45. Catalysts for ammonia synthesis consisting of donor-acceptor complexes of alkali metals and transition metal pthalocyanines. (UOP). US 4128621 (1978).

1979

46. Ammonia synthesis process with product recovery by water absorption, with recycling of unreacted gas after drying by solid adsorbent or with liquid aqueous ammonia. A. Pinto (Imperial Chemical Industries Ltd). EP 1324 (1979); US 4242317 (1981).

47. Ammonia synthesis process, with design of air blast head. R. D. Reed and R. R. Martin (J. Zink Co.). DE 2841127; US 4166834 (1979); GB 2004765 (1982).

48. Catalysts for ammonia synthesis containing ruthenium together with potassium and barium as promoters. R. M. Elofson and F. F. Cadallah. US 4142993 (1979).

49. Catalysts for ammonia synthesis containing ruthenium together with potassium and barium as promoters on a carbon support. A. I. Foster, P. J. James, J. J. McCarroll, and S. R. Tennison (British Petroleum Ltd). US 4163775 (1979).

50. Catalyst for ammonia synthesis containing cerium as an additional promoter. (Ammonia Casale SA). IT-A 47920A (1979).

51. Barium promotion of ammonia synthesis catalysts. (Research Council of Alberta). US 4142993 (1979).

52. Ammonia synthesis catalysts of high activity, prepared from alkali metal, e.g., potassium, ferrocyanide with the addition of uranium, aluminum, and/or rare-earth metal. V. S. Badik, V. V. Dovgel, and A. N. Sergeeva. SU 357783 (1979).

53. Ammonia synthesis catalysts of high activity, prepared from alkali metal ferrocyanide with the addition of ytterbium and optionally aluminum. Y. U. A. Lyubchenko and L. M. Dmitrenko. SU 370821 (1979).

54. Ammonia synthesis catalysts of high activity, prepared from alkali metal ferrocyanide with the addition of erbium and aluminum. Y. U. A. Lyubchenko, L. M. Dmitrenko, and B. I. Lure. SU 370823 (1979).

55. Ammonia synthesis catalysts of high activity, prepared from alkali metal ferrocyanide with the addition of aluminum and lutetium and/or thulium. Y. U. A. Lyubchenko and L. M. Dmitrenko. SU 417153 (1979).

56. Ammonia synthesis catalysts consisting of the oxides of iron and potassium, barium aluminate, and cobalt ferrite. V. S. Komarov, M. D. Efros, and L. M. Dmitrenko. SU 697178 (1979).

57. Catalyst containing cobalt for ammonia synthesis. (Imperial Chemical Industries Ltd). EP-A 7830276 (1979).

58. Ammonia synthesis catalysts, resistant to water vapor, consisting of ruthenium and potassium or cerium oxide supported on an alumina carrier. (Nikki Kagaku Kk). JP 54119386 (1979).

59. Multiaxial flow reactor for ammonia synthesis. G. Gramatica (Tecnimont SPA). US 4205044 (1979).

1980

60. Ammonia synthesis process: use of heat of reaction to generate superheated steam. A. Pinto (Imperial Chemicals Industries Ltd). US 4213954 (1980).

61. Ammonia manufacture from lower hydrocarbons, carbon monoxide, steam, and nitrogen in the presence of a ruthenium catalyst. (Shokubai Kasei Kogyo). JP 55047219 A (1980).

62. Iron-based ammonia synthesis catalysts of enhanced activity; alkali promoter, e.g., sodium, added to the finished catalyst by vapor-phase transport. T.A. Gens (Indianapolis Center for Advanced Research). US 4235749 (1980).

63. Metal hydride–nitride catalyst for ammonia synthesis prepared from rare-earth and ferrous metal compounds on a ceramic carrier. L. V. Krivonosov, S. P. Shilkin, and V. V. Burnasheva (AS USSR New Chem PR). SU 740274 (1980).

64. Catalyst for ammonia synthesis comprising barium titanate and metallic technetium on an alumina carrier for increased activity. V. I. Spitsyn, A. M. Alekseev, and I.E. Mikhailenk. SU 671063 (1980).

65. Ammonia synthesis catalysts of increased activity; heat treatment of porous spheres of promoted catalysts. P. D. Rabina, A. A. Daividyuk, and L. D. Kuznetsov. SU 709164 (1980).

66. Catalysts for ammonia synthesis made from iron–titanium alloys. M. N. Ozyagcilar (The Rafet Industrial Group). US-A 112837 (1980).

1981

67. Design of a catalytic converter for an ammonia synthesis process. J. R. LeBlanc and R. B. Peterson (M. W. Kellogg Co.). US 4298589 (1981).

68. Reactor for ammonia synthesis processes with both axial and radial flow. U. Zardi and E. Commandini (Ammonia Casale SA). DE 3146778 (1981); US 4372920 (1983).

69. Granular carrier for an ammonia synthesis catalyst prepared from aluminum oxychloride and boric acid coagulated in kerosine in the presence of a ferric salt gel. S. V. Morozova, L. A. Tarasov, and V. N. Anokhin. SU 793640 (1981).

70. Ammonia synthesis catalyst prepared from potassium and ferric oxides, cobalt ferrite, and barium zirconate. V. S. Komarov, M. D. Efros, and L. M. Dmitrenko. SU 810257 (1981).

71. Ammonia synthesis catalyst prepared by firing an iron and cobalt hydroxide mixture containing a magnesium compound, fusing, and treating with potassium hydroxide solution. V. S. Komarov, M. D. Evros, and P. D. Rabina. SU 818646 (1981).

72. Ammonia synthesis process with nitrogen/hydrogen feed in which the compressed gas mixture is passed over the hot catalyst using cyclic changes in catalyst temperature to increase the yield. G. K. Boreskov, N. M. Zhavoronko, and Y. U. S. Matros (AS Sibe Catalyst). SU 865796 (1981).

73. Preparation of a stable catalyst for ammonia synthesis by precipitation from aqueous solutions of iron, osmium, and ruthenium cyanides with an aliphatic alcohol or acetone. Y. U. A. Lyubchenk, A. N. Sergeeva, and L. M. Dmitrenko. SU 484718 (1981).

1982

74. Ammonia synthesis catalyst comprising alkali metal, alkaline earth metal, iron, or cobalt hexacyanocobaltate or hexacyanoruthenate. M. M. Johnson, D. C. Tabler, and G. P. Nowack (Phillips Petroleum Co.). US 4309311 (1982).

75. Ammonia synthesis catalyst consisting of ruthenium on a pretreated carbon support with a barium promoter. M. R. Logan, J. J. McCarroll, and S. R. Tennison (British Petroleum Ltd). EP 58531 (1982).

76. Catalyst for ammonia synthesis containing a transition metal, especially ruthenium on a graphite-containing carbon with rubidium or potassium promoter. A. M. Lear, J. J. McCarroll, D. A. Pippard, and S. R. Tennison (British Petroleum Ltd). GB 2087746 (1982).

77. Production of a ruthenium dioxide catalyst for ammonia synthesis by treating ruthenium chloride with aqueous alkali, washing the hydroxide with aqueous magnesium nitrate, and firing the resulting product. V. S. Komarov, M. D. Efros, and G. S. Lemeshono. SU 943204 (1982).

78. Granular ammonia synthesis catalysts produced by melting and oxidizing iron and promoters, then granulating and reducing while cooling. V. P. Lytkin, S. N. Menshov, J. S. Frolov, Z. A. Polikarpov, V. S. Sobolevsky, M. G. Selijutina, V. N. Anokhin, and N. D. Barbosov. GB 2092016 (1982); US 4379078 (1983).

79. Metal oxide composition reducible to an ammonia synthesis catalyst, prepared by casting an oxide melt on a surface and then fracturing the layer to form particles.

S. A. Topham (Imperial Chemical Industries Ltd). EP 60622 (1982); US 4797383 (1989).

1983

80. Preparation of ammonia synthesis catalysts by the one-step impregnation of a stable potassium ruthenate solution onto a graphite support. L. Bretherick and S. R. Tennison (British Petroleum Ltd). GB 2034194 (1983).

81. Ammonia synthesis with conversion of purge gas using catalyst based on special graphite support. J. J. McCarroll and S. R. Tennison (British Petroleum plc). GB 2109361 (1983).

82. Method for producing methanol and ammonia. A. Pinto (Imperial Chemical Industries Ltd). US 4367206 (1983).

83. Ammonia production process. A. Pinto (Imperial Chemical Industries Ltd). US 4383982 (1983).

1984

84. Multistage ammonia synthesis process which uses feed and high-pressure steam generation to cool the products of intermediate stages. B. J. Grotz (C. F. Braun Co.). AU 8321381 (1984); GB 2144724 (1985); US 4501123 (1985).

85. Production of ammonia from purified ammonia synthesis gas: more efficient drying and absorption of carbon oxides. A. Pinto (Imperial Chemical Industries Ltd). US 4469665 (1984).

86. Ammonia synthesis process: selective hydrogen adsorption process by pressure swing adsorption with both co-current and countercurrent depressurization steps. A. Fuderer (Union Carbide Corp.). US 4475929 (1984).

87. Ammonia synthesis gas made by primary and secondary reforming of hydrocarbons with partial bypassing of primary reformer. C. L. Winter (Humphreys & Glasgow Ltd). GB 2126208 (1984); US 4613492 (1986).

88. Ammonia synthesis catalyst consisting of ruthenium on a pretreated carbon support with barium and/or potassium promoters. J. J. McCarroll, S. R. Tennison, and N. P. Wilkinson (British Petroleum Ltd). GB 2136704 (1984); EP 120655 (1984); US 4600571 (1986).

89. Precipitated iron catalysts for ammonia synthesis. W. J. J. van der Wal and J. W. Geus. US 4459370 (1984).

1985

90. Reduction of an ammonia synthesis catalyst by heating in pure hydrogen with temperature stages so as to give a finely-crystalline product. B. G. Ovcharenko, S. S. Lachinov, and L. D. Kuznetsov. SU 1070746 (1985).

91. Method of manufacture of an ammonia synthesis catalyst containing iron, alumina, potassium, etc., promoters, with two stages of fusion. E. Dworak, A. Golebiowski, and K. Stolecki (Instytut Nawozow Sztucznych). PL 131490 (1985).

92. Ammonia synthesis process: heat exchanging. A. Pinto (Imperial Chemical Industries Ltd). EP 160412 (1985); US 4689208 (1987).

93. Ammonia synthesis with mechanical power generation from reaction heat by expanding high-pressure liquid ammonia after heat exchange in reactor. L. Silberring. WO 8503501 (1985); EP 170663 (1986).

94. Low-pressure ammonia synthesis process using thermal swing or pressure swing adsorption units for ammonia recovery from production gas. M. Hidaki (Toyo Engineering Corp.). DE 3430979 (1985); GB 2145702 (1985).

1986

95. Iron catalyst for ammonia synthesis. Produced from precursor iron oxide pellets. J. R. Jennings (Imperial Chemical Industries Ltd). EP 174078 (1986); US 4668658 (1987).

96. Iron catalyst for ammonia synthesis containing alumina, cobalt, and an alkali promoter; and a method of producing the catalyst. J. R. Jennings (Imperial Chemical Industries Ltd). EP 174079 (1986); US 4668657 (1987).

97. Catalysts for ammonia synthesis consisting of iron, aluminum, and alkaline earth oxides, and an alkali promoter; and a process for producing the catalyst. J. R. Jennings (Imperial Chemical Industries Ltd). EP 174080 (1986); US 4654320 (1987).

98. New promoted ammonia synthesis catalyst precursor composition contains metal oxides, e.g., iron, cobalt, aluminum, and specified alkali metal, prepared by precipitation and subsequent calcination. J. R. Jennings (Imperial Chemical Industries plc). EP 200315 (1986); US 4689317 (1987).

99. Ammonia synthesis catalyst precursor compositions of high surface area and containing alkali metal acid salts as promoters which allow catalyst activation at lower temperatures. S. P. S. Andrew and J. R. Jennings (Imperial Chemical Industries plc). EP 201215 (1986); US 4698325 (1987).

100. Ammonia synthesis process in which temperature regulation is used to increase the conversion of synthesis gas. B. Grotz (Santa Fe Braun Inc./C.F. Braun Co). WO 8606058 (1986); US 4624842 (1986); GB 2185009 (1987).

101. Ammonia synthesis process. The converter includes a primary reaction vessel with more than two radial-flow catalytic beds, a secondary reaction vessel with more than one catalytic bed, and a separate high-temperature heat exchanger between reaction vessels. R. G. Byington and R. M. Osman (Exxon Research & Engineering Co.). CA 1200673 (1986).

102. Method for increasing the output of existing ammonia synthesis plants. F. C. Brown, C. L. Winter, and T. W. Nurse (Humphreys & Glasgow Ltd). GB 2160516 (1986).

103. Maximum conversion in an ammonia synthesis process by temperature control of a three-bed reactor. A. M. Sokolov. SU 1211217 (1986).

104. Ammonia synthesis process. Hydrogen recovery from purge gas and its addition to the recycle gas. G. B. Mandelik, J. R. Cassata, J. P. Shires, and C. P. van Dijk (M. W. Kellog Co.). US 4568530 (1986).

105. Ammonia synthesis process in which the converter contains a conventional iron catalyst in the inlet zone and a ruthenium/carbon catalyst in the exit zone. C. P. van Dijk, A. Solbakken, and B. G. Mandelik (M. W. Kellog Co.). US 4568531 (1986).

106. Ammonia synthesis process in which the converter contains a conventional iron catalyst in the inlet zone and a ruthenium/carbon catalyst in the exit zone. G. S. Benner, J. R. Le Blanc, J. M. Lee, H. P. Leftin, P. J. Shires, and C. P. van Dijk (M. W. Kellog Co.). US 4568532 (1986).

107. Preparation of an iron-based catalyst for ammonia synthesis by the rapid cooling of a magnetite/metal oxide promoter mixture. N. Pernicone, F. Ferrero, and A. Gennaro (Fertimont SPA). EP 174716 (1986); US 4789657 (1988).

108. Ammonia synthesis catalyst preparation by the electrical reduction of a catalyst precursor mixture, followed by impregnation with a solution containing promoters. K. Yu, K. Li, J. Li, T. Yang, X. Chen, T. Zhang, Y. Chen, and L. Zhao (Yu Kanzhuang). CN 85 00601 (1986).

109. Spherical ammonia synthesis catalyst made by fusion of iron metal/magnetite with alumina, potassium, and calcium promoters. W. Wang, D. Feng, Y. Guo, and L. Li (Zhengzhou University). CN 85 01605 (1986).

110. Ball-shaped high-strength ammonia synthesis catalyst is obtained by smelting magnetite and other raw materials, followed by fluid dispersion, water cooling, and heat treatment. D. Feng (Zhengzhou University). CN 85 01606 (1986).

111. Multistage ammonia synthesis process. S. Lou. CN 8502389 (1986).

1987

112. Metallic catalyst films, suitable for ammonia synthesis catalysts, are formed by thermal spraying, e.g., by spraying metal threads on support material having sufficient cooling capacity to form crystalline, amorphous, or composite films. (Nippon Kagaku Hakko). JP 62033548 (1987).

113. Ammonia synthesis process in which cooling tube bundles in the catalyst bed cause a continuous decrease in reaction temperature, so giving favorable operation. U. Lang and W. Schramm (Linde AG). DE 3522308 (1987).

114. Ammonia synthesis gas: purification of a hydrogen-containing gas stream. A. Pinto (Imperial Chemical Industries Ltd). US 4671893 (1987).

115. Ammonia synthesis process: use of oxygen-enriched air during secondary reforming of hydrocarbons. A. Pinto (Imperial Chemical Industries Ltd). US 4681745 (1987).

116. Ammonia synthesis process. J. B. Johnson and A. Pinto (Imperial Chemical Industries Ltd). US 4695442 (1987).

117. Laminated ammonia synthesis catalyst of increased activity prepared by the reduction of a ferric chloride/graphite compound, with vacuum deposition of potassium promoter. K. Kalucki and W. Morawski (Politechnika Szczecinska). PL 141354 (1987).

118. Preparation of an iron alloy catalyst for ammonia synthesis. K. Kalucki, W. Arabczyk, R. Kalenczuk, W. Morawski, U. Narkiewicz, B. Skowronski, A. Golebiowski, E. Dworak, and Z. Spiewok (Politechnika Szczecinska). PL 142594 (1987).

119. Ammonia synthesis process by photocatalysis from nitrogen and water vapor over titanic catalyst under UV irradiation. Ya. S. Mazurkevich and R. P. Vlodarchik (Chernovtsky State University). SU 1353731 (1987).

1988

120. Ammonia synthesis process. Boiler steam formed from feed-water by heating with ammonia reaction gas circulated in U-tubes from second pressure chamber. H. O. Stahl (Haldor Topsoe A/S). DE 3815572 (1988).

121. Highly active iron oxide catalyst for ammonia synthesis, obtained by adding the promoter of potassium carbonate, ammonium molybdate, and tungstic acid in two stages. S. S. Lachinov, V. I. Tsarev, and A. Z. Lisitsa (Moscow Mendeleev Chemical Institute). SU 1368028 (1988).

122. Higher hydrogen recovery in the production of ammonia synthesis gas. A. Pinto (Imperial Chemical Industries Ltd). US 4725380 (1988).

123. Steam reforming in an ammonia synthesis process: simultaneous heat exchanging from gases leaving first and second zones to endothermic reaction mixture. A. Pinto (Imperial Chemical Industries Ltd). US 4750986 (1988).

124. Ammonia synthesis process: two pressure swing adsorption stages for gas separation. J. B. Johnson and A. Pinto (Imperial Chemical Industries Ltd). US 4772420 (1988).

125. Low-pressure ammonia synthesis process and reactor; fillable space between heat exchanger tubes in catalyst bed. A. Pinto (Imperial Chemical Industries Ltd). US 4778662 (1988).

126. Ammonia synthesis process in which the direction of gas flow over the catalyst beds is periodically changed to minimize the temperature gradient. Yu. Sh. Matros and A. P. Gerasev (Institute of Catalysis, Novosibirsk). WO 88 02737 (1988).

127. Design for ammonia synthesis process with gas recycling and converter cooling by cold gas. H. J. Herbort (Uhde Gmbh). DE 3640823 (1988).

128. Design of catalytic reactors for ammonia synthesis process with concentrically-arranged heat exchangers surrounded by catalyst beds. F. Nast, H. J. Herbort, and H. Graeves (Uhde Gmbh). DE 3643726 (1988).

129. Design for a converter for an ammonia synthesis process. D. V. Quang, P. Han, D. Gelas, and C. Legrand (Institut Francais du Petrole). FR 2609649 (1988).

130. Converter for an ammonia synthesis process comprising two-part vertical cylindrical pressure shell with three annular catalyst beds and two axial heat exchangers. S. A. Noe (M. W. Kellogg Co.). EP 2533350 (1988).

131. Design of catalytic reactor for ammonia synthesis process of improved efficiency. U. Zandi and G. Pagani (Ammonia Casale SA). EP 287765 (1988).

132. Design of an axial-radial flow catalytic reactor for ammonia synthesis process with major flow radial and minor flow axial through each bed. U. Zandi and G. Pagani (Ammonia Casale SA). EP 293546 (1988).

133. Ammonia synthesis catalyst containing iron with calcium, alumina, and potassium promoters, together with ceria. W. Lin, C. Huang, and S. Gan. CN 86 107630 (1988).

134. Preparation of finely-divided iron/carbon catalysts for ammonia synthesis by the controlled reduction of graphite/ferric chloride intercalation compounds. K. Kalucki, W. Morawski, and W. Arabczyk (Politechnika Szczecinska). PL 141907 (1988).

135. Ammonia synthesis catalyst, formed by fusion with successive additions of promoters including molybdenum, tungsten, calcium, potassium, and aluminum compounds. S. S. Lachinov, V. I. Tsarev, A. Z. Lisitsa, V. V. Adrianov, G. I. Pantazlev, T. I. Kushnarenko, and O. I. Bleskin (Moscow Chemical-Technological Institute). SU 1368028 (1988).

1989

136. Ammonia synthesis process with co-production of high-purity carbon dioxide (for, e.g., urea manufacture) by the use of pressure-swing adsorption. S. Sircar (Air Products & Chemicals Inc.). US 4813980 (1989).

137. Interstage cooling scheme for multibed catalytic reactor for ammonia synthesis process. H. J. Herbort (Uhde Gmbh). DE 3725564 (1989).

138. Design of a multibed catalytic reactor for ammonia synthesis process in which each bed is partitioned into two or more zones, alternately a vertical adiabatic

zone and a concentric cooled zone. A. Papillon, P. Lesur, C. Faury, C. Badoual, and G. Lafleur (Societe Chimique de la Grande Pariosse). EP 314550 (1989).

139. Improved flow in a modified axial-flow convertor for ammonia synthesis process to give increased reaction yield. U. Zandi and G. Pagani (Ammonia Casale SA). EP 297474 (1989).

140. Design of a reactor for ammonia synthesis process in which a vertical cylindrical vessel is partitioned by two tube plates into end sections and central sections. K. Murayama and M. Kuwa (Mitsubishi). DE 3832257 (1989).

141. Ammonia synthesis catalyst preparation based on iron promoted with potassium, with activation in a hydrogen/nitrogen mixture, without intermediate calcination. (Consejo Superior In.). ES 2006627 (1989).

1990

142. Production of spherical magnetic material, suitable as ammonia synthesis catalysts, by placing iron and/or iron oxide into a plasma atmosphere for melting and quenching. (Nippon Steel Corp.). JP 2026834 (1990).

LIST OF ASSIGNEES AND PATENTS IN LIST ABOVE

APPENDIX 7

Toxicology of Ammonia and Safety in Use

Compilation of standard advice and procedures from ammonia plants and commercial sales.

PART 1. ANHYDROUS LIQUID AMMONIA

1. CHEMICAL & TRADE NAMES

LIQUID AMMONIA, LIQUEFIED AMMONIA

CAS No 7664-41-7

Appearance

Colorless liquid giving off pungent vapors.

2. SUMMARY

Corrosive Irritant

Liquid ammonia causes severe burns to the skin and permanent damage to the eyes. If ingested it causes severe damage to the tissues of the mouth and the gastrointestinal tract. Vapors above 1500 ppm may damage or destroy tissue.

Eyes may water above 150 ppm.

Explosion of ammonia vapor is possible, but it can only be ignited with difficulty. Ammonia attacks copper, tin, zinc, cadmium, and their alloys.

3. PRECAUTIONS

Storage

Adequate ventilation and egress is required. Liquid ammonia should not be confined without adequate vapor space. Cylinders should be handled with care. Avoid temperatures above 45 °C.

Handling

Avoid skin and eye contact. Do not inhale vapor or ingest liquid.

Personal Protection

For routine operation use chemical gloves and goggles. For other operations where contact with the liquid is a possibility use self-contained breathing apparatus and fully protective ammonia resistant suit, hood, and boots.

Spillages

For small liquid spills, dilute with water and run to drain. For large pools, vacate the area, contain the liquid with barriers, and cover the pool with foam. Use water curtains downwind to reduce vapor emissions.

4. IMMEDIATE TREATMENT

Skin

Contact of vapor or liquid on the skin should be washed with copious quantities of water for 15 minutes. Remove contaminated clothing. Contact *Medical Department* immediately.

Eyes

Vapor or liquid in the eyes requires immediate irrigation with eye wash solution or water, forcing the eyes open if necessary, for a duration of 30 minutes. Contact *Medical Department* immediately.

Inhalation

Remove patient to fresh air. Keep warm and at rest. Administer oxygen if available. Apply artificial respiration if breathing has ceased. Contact *Medical Department* immediately.

Ingestion

Washed out mouth with copious quantities of water. Contact *Medical Department* immediately.

5. TOXICITY

Atmospheric Limits O.E.S. 25 ppm/18 mg/m^3 (8 h TWA) 35 ppm/27 mg/m^3 (10 min TWA).

Acute (Short Term)

Skin

Corrosive. Small splashes cause a local freezing effect. Liquid flooding causes burns affecting the entire exposed area. Ammonia vapor can dissolve in perspiration causing irritation and redness of the skin, depending on the vapor concentration and exposure.

Eyes

Corrosive. Liquid splashes cause permanent painful damage to the eyes. The full effect may not be apparent for 8 to 10 days. Vapor irritates the eyes with lachrymator at 150 ppm and burning effects at higher concentrations.

Inhalation

Irritant. Concentrations of 150–400 ppm cause irritation and discomfort of mucous membranes. Above 1500 ppm, exposure causes coughing and may damage or destroy tissue.

Ingestion

Corrosive. Severe damage to tissue of mouth and gastrointestinal tract.

6. FIRE & EXPLOSION

Flammable vapors are formed on mixing with air, but are only ignited with difficulty. If enclosed it could result in an explosion. Store away from acid, halogens, and other corrosive materials. Ammonia will attack copper, zinc, tin, cadmium, and their alloys. It reacts with halogens, hypochlorite, and mercury to produce unstable compounds likely to explode.

PART 2. AMMONIA SOLUTIONS IN WATER

7. CHEMICAL & TRADE NAMES

AMMONIUM HYDROXIDE, 32–35% AMMONIA IN WATER, AMMONIACAL LIQUOR

CAS No. 7664-41-7

Appearance

Clear, colorless solution with characteristic pungent odor.

8. SUMMARY

Corrosive Irritant

High concentrations of vapor or splashes of liquid may cause severe damage to the eyes. Swallowing the liquid may cause severe internal damage. Inhalation may cause damage to the mucous membranes. Ammonia solution irritates the skin and, on prolonged contact, causes severe burns.

It reacts with halogens, hypochlorites, and mercury to form unstable explosive compounds.

9. PRECAUTIONS

Storage

Store in a cool well-ventilated area. Separate from other chemicals, particularly oxidizing gases, halogens, and acid. Ensure adequate egress is provided. Avoid contact with copper, zinc, brass, or bronze.

Handling

Avoid breathing vapor. Avoid skin, eye contact, or ingestion. Prevent contact with clothing.

Personal Protection

PVC gloves and goggles should be worn.

Spillages

PVC aprons, suits, and rubber boots should be worn when dealing with spillage. Stay upwind of spillage. For major spillages, use breathing apparatus and flush to drain with copious quantities of water.

10. IMMEDIATE TREATMENT

Skin

Remove contaminated clothing. Wash with copious quantities of water for at least 15 minutes. Wash clothing before reuse. Contact *Medical Department.*

Eyes

Speed is essential. Irrigate thoroughly with eye wash solution or water for at least 15 minutes. Contact *Medical Department* and continue with irrigation.

Inhalation

Remove patient to fresh air. Keep warm and at rest. Administer oxygen if available. Apply artificial respiration if breathing has ceased. Contact *Medical Department.*

Ingestion

If conscious give copious quantities of water to drink. Do not induce vomiting. Contact *Medical Department.*

11. TOXICITY

Atmospheric Limits O.E.S. 25 ppm/18 mg/m^3 (8 he TWA) 36 ppm/27 mg/m^3 (10 min TWA).

Acute (Short Term).

Skin

Irritant. Irritates the skin, and prolonged contact may cause severe burns.

Eyes

Corrosive. High concentrations of vapor or splashes of aqueous ammonia may cause temporary blindness and severe eye damage. Early treatment is imperative.

Irritant. Vapor irritates the eyes.

Inhalation

Irritant. Low concentrations of vapor will cause irritation of nose and throat leading to coughing and breathing difficulties. High concentrations can affect the entire respiratory tract leading to severe injury of mucous membranes.

Ingestion

Corrosive. Swallowing of aqueous ammonia results in corrosive action on the mouth, throat, and stomach and may prove fatal.

Chronic. (Long Term).

N/A

12. FIRE & EXPLOSION

Forms flammable vapors which are difficult to ignite, e.g., by burning or welding operations.

Reacts with halogens, hypochlorides, and mercury to form unstable explosive compounds.

INDEX